JAERI-Review
98-016

TIARA Annual Report 1997

October 1998

Advanced Radiation Technology Center

日本原子力研究所
Japan Atomic Energy Research Institute

本レポートは，日本原子力研究所が不定期に公刊している研究報告書です。
入手の問合わせは，日本原子力研究所研究情報部研究情報課（〒319-1195　茨城県那珂郡東海村）あて，お申し越しください。なお，このほかに財団法人原子力弘済会資料センター（〒319-1195　茨城県那珂郡東海村日本原子力研究所内）で複写による実費頒布をおこなっております。

This report is issued irregularly.
Inquiries about availability of the reports should be addressed to Research Information Division, Department of Intellectual Resources, Japan Atomic Energy Research Institute, Tokai-mura, Naka-gun, Ibaraki-ken, 319-1195, Japan.

編集兼発行　　日本原子力研究所

JAERI-Review 98-016

TIARA Annual Report 1997

Advanced Radiation Technology Center

Takasaki Radiation Chemistry Research Establishment
Japan Atomic Energy Research Institute
Watanuki-cho, Takasaki-shi, Gunma-ken

(Received September 17, 1998)

This annual report describes research activities which have been performed with the JAERI TIARA (Takasaki Ion Accelerators for Advanced Radiation Application) facilities from April 1, 1997 to March 31, 1998. Summary reports of 90 papers and breaf discriptions on the status of TIARA in the period are contained. A list of publications, the type of research collaborations and organization of TIARA are also given as appendices.

Keywords: JAERI TIARA, Ion Accelerators, Solid State Physics, Radiation Effects in Materials, Materials for Space, Semiconductors, Organic Materials, Inorganic Materials, Nuclear Fusion Reactor, Functional Materials, Radiation Chemistry, Radiation Biology, Nuclear Medicine, Biotechnology, Radioisotope Production, Nuclear Chemistry, Radiation Shielding, Materials Analysis, Accelerator Technology, Safety Control

---

(Eds.) Ryuichi TANAKA, Masahiro SAIDO, Isamu NASHIYAMA, Hiroshi NARAMOTO, Takeshi SUWA, Yousuke MORITA, Akio TORAISHI, Hiroshi WATANABE, Masanori TANI, Satoshi TAJIMA and Sohei OKADA

JAERI-Review 98-016

原研イオン照射研究施設（ＴＩＡＲＡ）平成９年度年次報告

日本原子力研究所高崎研究所
放射線高度利用センター

（1998年９月17日受理）

本年次報告は、原研イオン照射研究施設で、1997年４月１日から1998年３月31日までの間に行われた研究活動の概要をまとめたものである。１）宇宙用半導体、２）バイオテクノロジー、３）放射線化学および有機材料、４）無機材料、５）材料解析、６）核化学およびラジオアイソトープ製造、７）加速器施設の放射線遮蔽、８）加速器技術の８部門にわたる90編の研究報告に加えて、施設の運転・利用状況、公表された文献、企業・大学等との研究協力関係、研究開発・施設運営組織を収録する。

高崎研究所：〒370－1292　群馬県高崎市綿貫町1233

PREFACE

This report covers research and development activities which have been conducted with TIARA (Takasaki Ion Accelerators for Advanced Radiation Application) during the period from April 1997 until March 1998, and also gives an outline of the operation of TIARA in the same period.

All the accelerators in TIARA, the AVF cyclotron, the 3MV tandem accelerator, the 3MV single-ended accelerator and the 400kV ion implanter, have been operated steadily since the construction were completed in 1993, and have supplied the beam-time to the research programs as had been recognized in advance by the TIARA General Program Committee. In the same time, available species and energy ranges of ions have been widened to meet requests from users, and the quality of ion beams have been improved gradually.

In the field of radiation effects on semiconductor devices for space, experimental data and systematic analyses of radiation resistance on commercial semiconductor devices have been accumulated for space application of the devices which contribute to the reduction the cost of electronic components used in space crafts. It was found that phosphorus is useful for n-type impurity of silicon carbide semiconductor which is expected as a new radiation-tolerant semiconductor , and the implantation technique of phosphorus ions has been developed.

In biotechnology, the studies on application of positron emitting radionuclides to living plants have spread among several varieties of plants. Plant transport, in the chemical forms of labeled compounds such as $^{11}CO_2$, $^{13}NO_3$ and ^{11}C-methionine, have so far been measured by using positron-emitting tracer imaging systems. It was found that in the Fe-deficient plants, the methionine was accumulated in leaf of the severely chlorotic main shoot, whereas it was located in the newest leaf of main shoot in the control plants. In the studies of ion beam-induced mutation, improvement of creeping bentgrass, strawberry, hydrangea, wheat, chrysanthemum and tobacco plant has been performed for the practical use.

In the radiation effect study of inorganic materials, a new type of research came out associated with the hydrogen-selective displacement by electrons. In the materials processing study the importance of interaction between defect and implants has been shown through in-situ dual beam experiment, and in the surface-sensitive structure analysis a new detecting system of secondary electrons has been designed for the crystallography of light elements such as carbon and oxygen.

The synergistic effects of helium formation and displacement damage have been investigated in the field of radiation damage study of fusion materials, using double and/or triple ion beam irradiation and also energy degradation technique for the various fusion relevant materials from austenitic steel to SiCf/SiC composites.

In radiation chemistry, the ion track structure in solid polymer materials has been examined by irradiation of multi-charged high-energy heavy ions. The diameter of the ion track was experimentally evaluated on the basis of formation of cross-linking, scission processes in polysilane and of cross-linking in poly-dimethylsiloxane.

In the fields of radioisotope production and nuclear chemistry, development of the production of positron emitters has been continued for plant study in collaboration with biologists. A series of experiments on the decay of La isotopes using an isotope separator on-line (ISOL) were carried out for determination of the atomic masses of $^{124\text{-}130}$La. The ISOL was also applied to production of a device to be used in the therapy of arteriosclerosis in coronary arteries.

In the field of ion beam engineering, cocktail beam acceleration technique has been developed for quick change of ion species, extracted from the cyclotron, with mass to charge ratios approximately of 4. High-precision beam positioning & single ion hit techniques with the heavy ion microbe system have been developed, which directly meet the users' requirement. Challenging and basic experiments for studies on interaction of microbeams with materials and coulomb explosion of cluster ions have been commenced. Development of micro-PIXE camera has stepped into the observation in an atmospheric environment. The success of ion production with SF_6 plasma is worthy of note.

In nuclear physics, the results of new measurement were reported for double-differential cross sections of charged particle and neutron emission reactions and for fission cross sections of ^{237}Np and ^{238}U using a quasi-monoenergetic neutron source.

The management of TIARA has been smoothly performed on the basis of activity of the TIARA General Program Committee. The committee approved a new beam-time allotment method, which is based on evaluation of each experimental proposal, and the priority system was firstly applied to TIARA management in F.Y.1997.

The reception of users, general management of the facilities, safety management of the radiation controlled areas, supports on utilization of facilities, and other duties have also been practiced smoothly; a computer code system to calculate induced radioactivity, IRAC, have been developed and practically used for the evaluation of radiation safety in irradiation experiments.

The Seventh TIARA Research Review Meeting was held on June 16 and 17 1997 in Takasaki, of which subjects were reported in this issue. 10 oral and 8 poster papers, and one invited lecture were presented in addition to a topical session. 240 people joined in the meeting. In contrast with the earlier meetings, numerous results of TIARA utilization were presented, suggesting the TIARA is now becoming a fruitful facility.

We owe the progress mentioned above to advice of the Consultative Committee for the JAERI-Universities Joint Research Project, the TIARA General Program Committee, and its subcommittee.

田中隆一

Ryuichi Tanaka, Director
Advanced Radiation Technology Center
Takasaki Radiation Chemistry Research Establishment

Contents

This is a blank page.

1. Semiconductors for Space

This is a blank page.

1. 1 Development of a collimated swift heavy-ion microbeam (II)

I. Nashiyama, T. Hirao, T. Hamano, T. Ohshima, and H. Mori
Department of Materials Development, JAERI

1. Introduction

Mechanisms of Single-event effects(SEE) has been studied by the measurement of current pulses generated by the impingement of energetic heavy ions into a pn-junction area in semiconductor devices.[1-3] Since single-event current pulses are extremely fast, their pulse widths are an orders of ten to hundred picosecond, their wave forms are measured using the sampling method, where a series of current pulses having a completely identical wave form is required. To obtain reproducible single event current pulses, ions must strike exactly the same position in the pn-junction area. For this purpose, we applied, for the first time, ion microbeams with the beam size about one micrometer with energies less than 20 MeV.

However, in space environment, galactic cosmic rays of heavy ions with the energy above 100 MeV causes SEE in devices installed on satellites. Therefore, heavy-ion microbeams with the similar energies are needed to perform more accurate and more realistic SEE measurements.

Unfortunately, the present electromagnetic focusing technique cannot be applied to the ion beam with these extremely high-energy heavy-ions obtained from the cyclotron accelerator, because of their insufficient energy purity and beam emittance. Therefore, the only method we can apply to obtain an extremely high-energy heavy-ion microbeam is a micro-aperture method at present.

Though it is simple and convenient, the minimum beam size we can obtain using micro-aperture method is a few tens of micrometer at the best, because a micro-aperture with a very thick metal plate (a 50 μm thick tantalum plate) is necessary to stop all the such extremely high energy ions within the plate, and probability that incident ions are scattered at the inside wall of the aperture increases markedly with decreasing the aperture size.

The purpose of the present work is to develop a new technique to reduce the edge-scattering and to realize an extremely high-energy heavy-ion microbeam using the cyclotron accelerator at TIARA. In this paper, we present some preliminary experimental results on the edge-scattering effect.

2. Beam Collimation and Alignment

By combing a highly collimated ion beam with a micro-aperture, we have been developing a technique to reduce the edge scattering effects at the wall of the micro-aperture. Simple geometrical calculation suggests that beam divergence of the collimated beam should be less than 0.01 degree in order to keep the amount of edge-scattered ions less 2 % of the total ions after passing through a micro-aperture with 1 μm diameter and 50 μm thickness. It is also required that the direction of the micro-aperture is precisely aligned to the collimated beam with accuracy better than 0.01 degree.

In the present experiment, we applied a pair of double slits (1 mm x 1 mm) placed on the beam line with a distance of 1124 cm between each other [4] and a newly developed SEU chamber where the micro-aperture is installed on a remotely controlled double axes goniometer. In order to measure the angular divergence of the ion beam, we used the axial channeling effect around the <111> axis in a thin silicon surface barrier detector (SSD).[5] Using 330 MeV Ar-ion, we obtained that the half angle of the beam divergence is less than 0.01 degree, which is almost equal to that calculated geometrically from the sizes of the double slits and their distance.

3. Spectra of Collimated Ion Beam

The collimated 330 MeV Ar-ion beam is projected normally on micro-apertures with a diameter from 5 μm to 100 μm. Energy spectra of the ions passing through the micro-aperture were measured by a partially depleted silicon surface barrier detector placed behind the micro-aperture.

The result are shown in Fig. 1. A peak at 370 channel corresponds to the ions passed through the micro aperture without the edge-scattering. In the lower energy region below the peak, significant amount of the yield due to ions scattered at the edge of the micro-aperture were observed. The amount of edge-scattered ions increases with decreasing the aperture size, showing that 5% (100 μm), 6% (50 μm), 13% (10 μm), and 89% (5 μm). The abrupt increase in the edge scattering for an 5 μm micro-aperture is due to the poor angular alignment of the micro-aperture to the collimated beam. These results indicates that more precise angular and positional alignment are required.

References

1) Nashiyama, et al. "Single-Event Current Transients induced by High-Energy Ion Microbeams", IEEE Trans. on Nucl. Sci., NS-40, 6, 1935 (1993).

2) Hirao, et al. "Effect of micro-beam induced damage on single-event current measurements", Nucl. Instrum. Methods in Phys. Res. B104, 508 (1995).

3) Hirao, et al. "Effect of ion position on single-event transient current", Nucl. Instrum. Methods in Phys. Res. B130, 486 (1997).

4) Nashiyama, et al. "Collimation of Heavy Ion Beam Produced by Cyclotron for Single-Event Measurements", JAERI-Review 95-019, 8 (1995).

5) Nashiyama, et al. "Development of a collimated swift heavy-ion microbeam", JAERI-Review 97-015, 3 (1997).

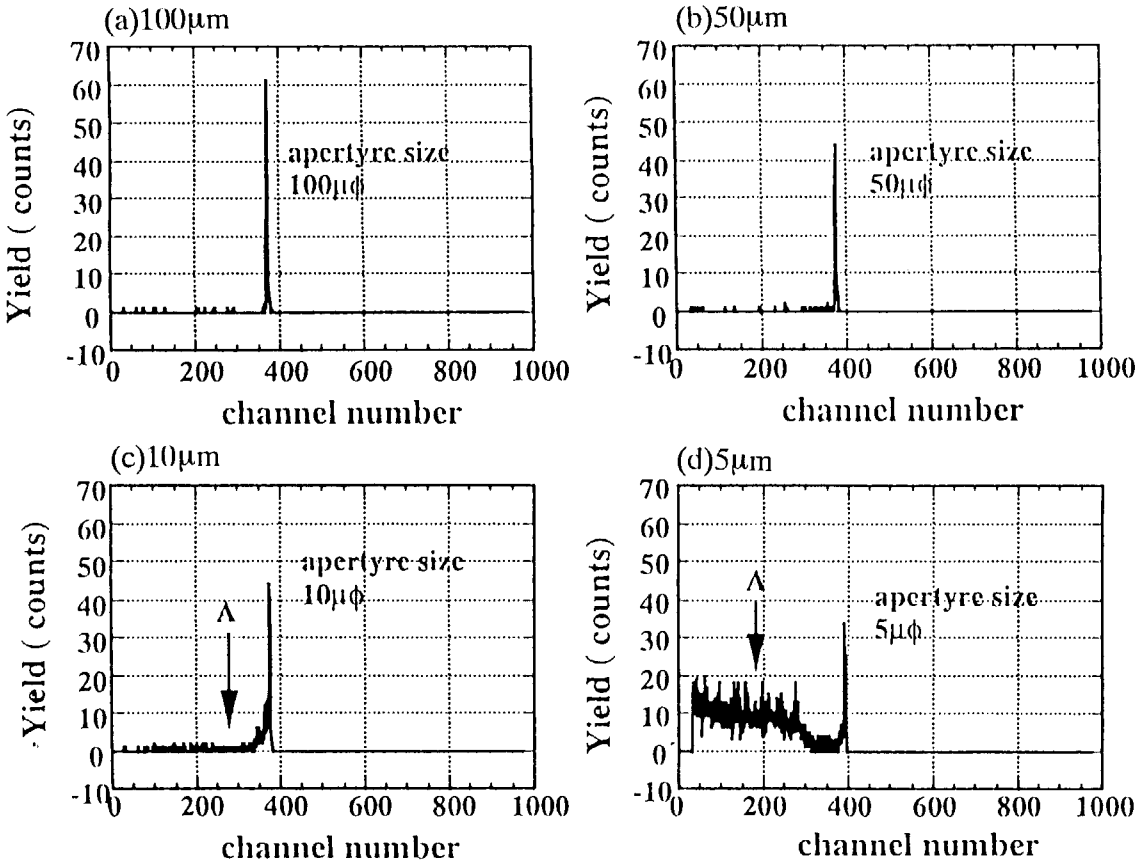

Fig. 1 Energy Spectra of the collimated 330 MeV Ar-ion beam after passing through micro-apertures with (a) 100 μm, (b) 50 μm, (c) 10 μm, and (d) 5 μm in diameter.

1．2 Evaluation of Single-Event Upsets for high-integrated commercial DRAMs

N. Nemoto, H. Shindou, K. Matsuzaki, S. Kuboyama, S. Matsuda,
T. Ohshima*, T. Hirao*, H. Itoh*, I. Nashiyama*

National Space Development Agency of Japan (NASDA)
* Department of Materials Development, JAERI

Abstract

The SEU tolerance has been investigated for the commercial 16Mbit and 64Mbit DRAMs by using high energy heavy ions. Based on the test results, the threshold LET and the saturated cross-section are derived for each DRAM. As a result, the 64Mbit DRAMs are found to have higher radiation tolerance than the 16Mbit DRAMs. The relation of the SEU results with the process technology data is also examined. In highly integrated commercial memories like 64Mbit DRAMs, the SEU tolerance is not always related with the memory cell parameters, e.g., the cell capacitance and size.

1. Introduction

Semiconductor devices used in spacecrafts are exposed to high energy particles such as solar protons and galactic cosmic rays. From this reason, such semiconductor devices have been designed and fabricated according to severe specifications. This fact boosts the device cost and also prolongs the development time of qualified devices. In recent years, lowering of the mission cost is regarded as one of the most important matters, and thus much effort has been made to reduce the cost of electronic components used in spacecrafts without diminishing their performance. On this policy, there has been a growing interest in space application of commercial devices such as highly integrated memory ICs because of low prices and high performance of such devices.

To ensure success in this application, it is indispensable to examine radiation effects, e.g., single-event and total-dose effects, on commercial devices precisely. In National Space Development Agency of Japan (NASDA), the selection methods of commercial devices for space application are being considered. Figure 1 shows a screening process of commercial devices as an example. In the first screening, the reliability and radiation tolerance of commercial devices are examined preliminarily from the information of the design and the structure of the devices. In this examination, irradiation experiments are performed using californium-252. Based on these results, candidates for space usage are selected, and then they are examined in detail. In the second screening, radiation tests are performed by using high energy heavy ions to evaluate the single-event tolerance. The reliability of the devices is also examined by a thermal stress test, a thermal shock test and so on. Taking account of all the test results, the final decision on the actual space application of commercial devices can be made.

In the present study, we have evaluated single-event upset (SEU) tolerance for recent high-integrated memory devices, i.e., 16Mbit DRAMs (the second generation device) and 64Mbit DRAMs (the second and third generation devices) by irradiation of high energy heavy ions such as 175MeV-Ar^{8+} and 450MeV-Xe^{23+}. As a result, the threshold LETs and the saturated cross-sections are derived for each DRAM. We also describe the relation of the SEU tolerance with the process technology of the DRAMs.

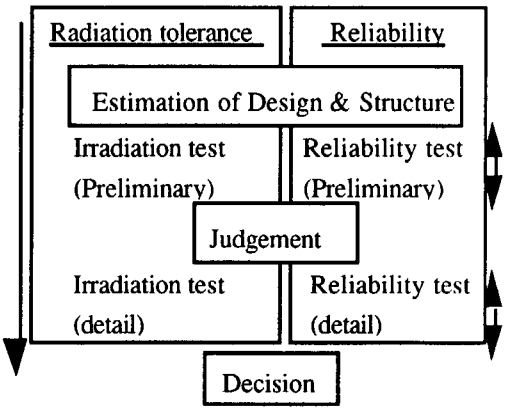

Figure 1. Commercial device screening process for space application

2. Experiments

2.1 Samples

The samples used for our SEU tests were commercial 16Mbit and 64Mbit DRAMs. Figure 2 shows the memory cell cross-section of the 16Mbit DRAM. The device technologies of this device are shown in Table 1[1]. In this device, the memory cell capacitors with the capacitance of 27fF were formed over the bitlines. The capacitance is so high that no SEU occurs by impingement of alpha-rays.

The cross-section of the 2nd generation 64Mbit DRAMs is shown in Figure 3[2]. The memory cells of this device were also produced by the capacitor over bitline technology. The process technologies of the 64Mbit DRAMs are also shown in Table 1.

Table 1. 16Mbit and 64Mbit DRAM process technologies[1-3)]

		16Mbit DRAM	64Mbit DRAM	
		2nd generation	2nd generation	3rd generation
Structure		N well CMOS 2 aluminum layer	3 stacked well CMOS 2 aluminum layer	3 stacked well CMOS 1 aluminum layer/ 1 tungsten layer
Technology rule		0.45 μ m	0.32 μ m	0.28 μ m
Channel length	PMOS	0.9 μ m	0.7 μ m	0.51 μ m
	NMOS	0.7 μ m	0.5 μ m	0.43 μ m
Gate oxide layer		140Å	110Å	100Å
Memory cell	Size	2.48x1.24=3.075μm^2	0.778x1.58=1.25μm^2	0.65x1.3=0.84μm^2
	Structure	Stack (Capacitor Over Bit-line)	Stack (Capacitor Over Bit-line)	Stack(Capacitor Over Bit-line+ Hemi-Spherical Grain Si)
	Capacitance	27fF	25fF	25fF
Supply voltage		5.0±0.5V	3.3±0.3V	3.3±0.3V

The cross-section of the 3rd generation 64Mbit DRAMs is shown in Figure 4[3)], and their process technologies are represented in Table 1. While the capacitor over bitline technology was used in this memory device, an advanced technology was applied in the cell structure: This device has Hemi-spherical grained memory cells, which is shown in Figure 5[3)].

From the data of process technologies for the DRAMs, their radiation tolerance can be estimated. For example, the capacitance of memory cells is related with the critical charge necessary to induce SEU. In addition, the thickness of the gate oxides is an important parameter for total dose effects. The 3rd generation 64Mbit DRAMs are suggested to have higher radiation tolerance than the 2nd generation DRAMs because the memory cell size of the former device is smaller than the latter one.

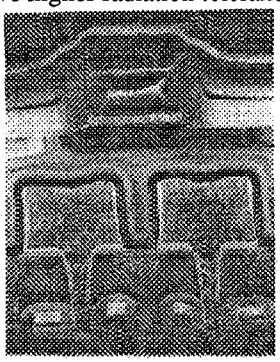

Figure 2. Memory cell cross-section of 16Mbit DRAMs[1)]

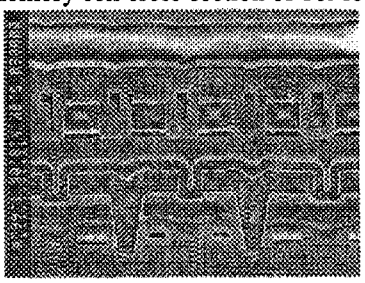

Figure 3. Memory cell cross-section of 2nd generation 64Mbit DRAMs[2)]

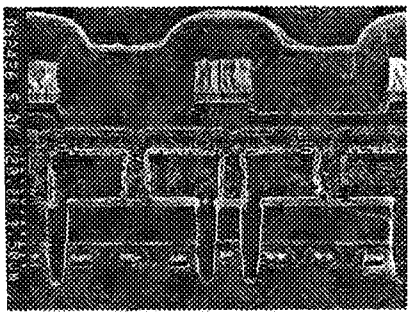

Figure 4. Memory cell cross-section of 3rd generation 64Mbit DRAMs[3)]

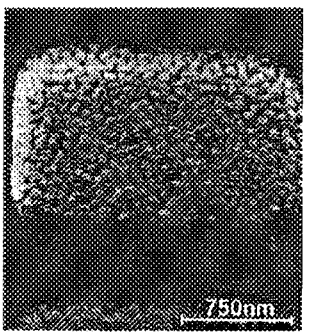

Figure 5. Hemi-spherical grained memory cells of the 3rd generation 64Mbit DRAMs[3)]

2.2 Irradiation tests

The 16Mbit and 64Mbit DRAMs were irradiated with high energy heavy ions such as 120MeV-Ne^{6+}, 322MeV-Kr^{17+}, 520MeV-Kr^{20+} and 450MeV-Xe^{23+} by using an AVF (Azimuthally Varying Field) cyclotron in JAERI Takasaki. The irradiation of such heavy ions was made directly and in a defocused mode. To obtain the SEU cross-section, both the number of memory bits at which upset occurred and the total ion fluence were counted. From the SEU

measurements under several irradiation conditions, we have obtained the SEU cross-sections as a function of LET in silicon for each sample.

3. Results and discussion

The LET dependence of the SEU cross-section for each DRAM is shown in Figure 6. These results are fitted using a weibull distribution function. The fitting results are also shown in Figure 6.

For every DRAM, the threshold LET and the saturated cross-section are derived from the SEU cross-section vs. LET curve. The threshold LETs and the saturated cross-sections obtained are shown in Table 2. From the comparison of the test results, the threshold LET and saturated cross-section for the 2nd generation 64Mbit DRAMs are found to be lower than those for the 16Mbit DRAMs This result can be explained by a difference of the capacitance and size of the memory cell, i.e., the 64Mbit DRAMs have a low memory cell capacitance and a small cell size compared with the 16Mbit DRAMs. The results are consistent with the estimation based on the device process technologies.

From the comparison of the test results for the 2nd and 3rd generation 64Mbit DRAMs which were made by the same company, the threshold LET and the saturated cross-section for the new generation samples are found to be higher. It is estimated from the process technology data

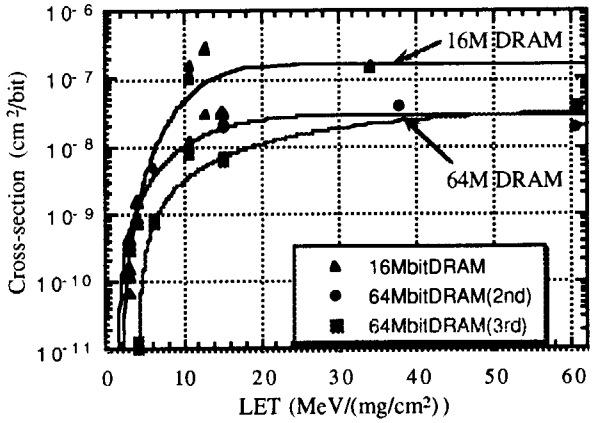

Figure 6. LET vs. cross-section for the 16Mbit and 64Mbit DRAMs

Table 2. Threshold LET and Saturated Cross-section

	Threshold LET (MeV/(mg/cm^2))	Saturated cross-section (cm^2/bit)
16Mbit DRAMs	4.1	1.6×10^{-7}
64Mbit DRAMs (2nd generation)	2.4	3.0×10^{-8}
64Mbit DRAMs (3rd generation)	5.4	3.9×10^{-8}

shown in Table 1 that no significant change in the threshold LET is observed between the two DRAMs due to the same capacitance of their memory cells. In addition, the saturated cross-section of the 3rd generation DRAMs is estimated to be smaller than that of the 2nd generation DRAMs. However, the test results are inconsistent with the results estimated from the process technologies.

This discrepancy of the threshold LET may be related with the difference in the cell structure: Though only an aluminum layer was used in the 2nd generation memories, aluminum and tungsten layers were used in the 3rd generation DRAMs. Concerning the saturated cross-section, the inconsistency may be caused by multiple bit upsets. The cell size of the 3rd generation DRAMs is smaller than 1μm^2. It is known that the diameter of a plasma column generated by the heavy ion impingement is about 1μm. The cell size of the 3rd generation memories is smaller than the plasma column diameter. Thus it is likely that multiple bit upsets occurs by irradiation of heavy ions in a high LET region, which probably raises the saturated cross-section.

4. Summary

We have evaluated the SEU tolerance for the commercial 16Mbit and 64Mbit DRAMs by irradiation of high energy heavy ions. The threshold LET and the saturated cross-section are derived for each DRAM from the SEU cross-section vs. LET obtained. We have also examined the relation of the test results with the process technology data. As the result, we found followings:

1. The 64Mbit DRAMs have high radiation tolerance compared with the 16Mbit DRAMs.
2. The actual SEU tolerance is not always related with the memory cell parameters such as the cell capacitance and size in highly integrated commercial memories. The influence of material used in the cell structure and the effects of multiple bit upsets on SEU should be taken in account.

Acknowledgments

The authors would like to thank the staff of Ryouei Technica Corporation and NEC for their help in the ion irradiation tests and useful discussion.

References

1. S. Koshimaru et al., 2nd Generation 16Mbit DRAM, NEC Technology Journal (1993) 90-92.
2. A. Kagami et al., Development of 64Mbit DRAM (2nd Generation), NEC Technology Journal (1995) 11-15.
3. S. Tsukada et al, Development of 64Mbit DRAM (3rd Generation), NEC Technology Journal (1997) 23-27.

1．3 Degradation Mechanism of Silicon Solar Cells by Large Fluence Irradiation

Tadashi HISAMATSU, Takashi ABURAYA, Sumio MATSUDA,
Takeshi OHSHIMA* and Isamu NASHIYAMA*
National Space Development Agency of Japan (NASDA)
Department of Materials Development, JAERI*

1. Introduction

As previously reported, the accident of The Engineering Test Satellite-Ⅵ (ETS-Ⅵ) provided us an opportunity to find out "The Anomalous Degradation of Space Silicon Solar Cells in Large Fluence Region" (Fig. 1) which could not be predicted from previous data[1,2]. As this phenomenon is of great interest in understanding the degradation mechanism of Si solar cells and it may provide us with new aspects for developing future space solar cells, NASDA has established "The Committee for the Study of Radiation Damage Mechanism of Solar Cells" which comprises specialists in related research-institutes and makers and has performed the analysis in various aspects in cooperated with JAERI Takasaki.

2. Analysis of Degraded Solar Cells

Samples were 50 μmthick Si BSFR (Back Surface Field and Reflector) type solar cells which possessed the about 0.15 μm thick n-type diffused layer on the front surface and the about 0.7 μmthick back-surface-field layer on the rear surface of the B-doped p-type single-crystalline Si substrate (about 10 Ω cm). The Si wafers which have almost the same specification as the substrate of the cells were also used on this study. Irradiations with 1MeV-electrons and 10MeV-protons were carried out by using Cockcraft-Walton type accelerator and AVF cyclotron, respectively, at JAERI Takasaki. From the results of dark I-V and C-V measurements for the degraded cells, the decrease of majority-carrier density in the p-substrate and diffusion-voltage of the pn junction were obtained quantitatively[2]. The decrease of diffusion-length for minority-carrier in medium fluence region (e.g. 1×10^{12}-2×10^{13} p/cm^2 for 10MeV protons and 1×10^{15}-3×10^{16}e/cm^2 for 1MeV electrons) were obtained by EBIC (Electron Beam Induced Current) technique. By using these data, we almost verified the degradation model which was proposed by us for explaining the anomalous degradation[3].

3. Study of Radiation-Induced Defects

The decrease of majority-carrier density with increase of fluence was also confirmed by Hall effect measurements of irradiated Si wafers. Figure 2 shows the fluence dependence of $(1/q\,|\,R_H\,|\,)$ which corresponds to the carrier density. In addition, the type-conversion of substrate from p to n was found due to the large fluence irradiation exceeding 2×10^{14} p/cm^2 for 10MeV protons and 1×10^{17} e/cm^2 for 1MeV electrons. In Fig. 2, the data of n-type were plotted considering the contribution of electrons and holes in conduction[4]. From the results of Positron life time measurement, it was suggested that the radiation-induced defects were oxygen-related complexes. For the electron irradiated samples, it was clarified from DLTS (Deep Level Transient Spectroscopy) measurements that the three levels shown in Table Ⅰ were responsible to the degradation of cell-performance because of the correspondence of thermal-recovery characteristics[5,6]. Figure 3 shows the PL (Photo-luminescence) spectra of B-doped Si samples at 4.2K[7]. For both electron irradiated- and proton irradiated-samples, the increase of back-ground like broad emission with increase of fluence were observed in 0.7-1.0eV regions, besides the variation of specific peak. The intensities of the emission were altered by using wafers doped another impurities such as Al and Ga (in spite of its resistivity was the same as that of B-doped wafer). Thus, we think it may be possible to realize the more radiation-tolerant cells by using Al-doped or Ga-doped wafers instead of conventional B-doped wafers.

4. Conclusion

We investigated the characteristics of irradiated Si solar cells and the radiation-induced defects to clarify the degradation mechanism of space Si solar cells in large fluence regions. We intend to study the radiation-induced defects and would like to identify the origin of them.

[1] O. Kawasaki et al.: JAERI TIARA Annual Report 1994 (Vol.4), April 1994-March 1995, p11-15.
[2] T. Hisamatsu et al.: Solar Energy Materials and Solar Cells, 50 (1998),p.331-338.
[3] T. Ohshima et al.: 33rd Annual International Nuclear and Space Radiation Effects Conference, Indian Wells, California, July 15-19, 1996, G-2.
[4] T. Hisamatsu et al.: Extended Abstracts (The 58th Autumn Meeting, 1997); The Japan Society of Applied Physics, Akita University, Oct. 2-5, 1997,

2a-A-4, p.706 (in Japanese).
[5] S.J. Taylor et al.: Conference Record of 26th IEEE Photovoltaic Specialists Conference, 1997, p.835-838.
[6] T. Yamaguchi et al.: Extended Abstracts (The 45th Spring Meeting,1998); The Japan Society of Applied Physics and Related Societies, University of Tokyo Institute Technology, March 28-31, 1998, 29p-P-7, p.842 (in Japanese).
[7] M. Warashina et al.: Extended Abstracts (The 58th Autumn Meeting, 1997); The Japan Society of Applied Physics, Akita University, Oct. 2-5, 1997, 2a-A-5, p.706 (in Japanese).

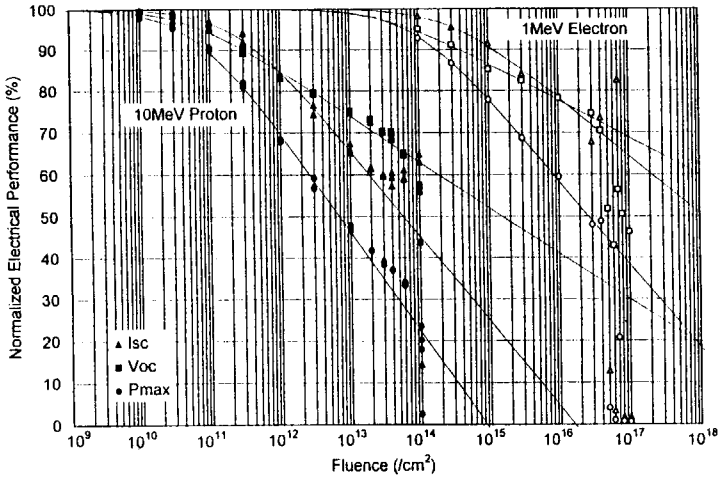

Fig. 1. Normalized electrical performance versus fluence for Si BSFR Solar cells[2]. (black symbols:10MeV proton, white symbols:1MeV electron)

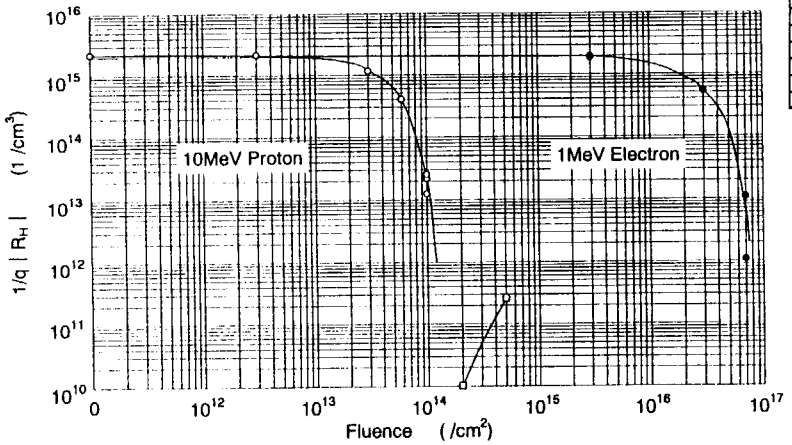

Fig. 2. Carrier Density of 10MeV proton irradiated and 1MeV electron irradiated Si wafer derived from Hall measurements at room temperature(2 carriers). (circular symbols:p-type, square symbols:n-type)

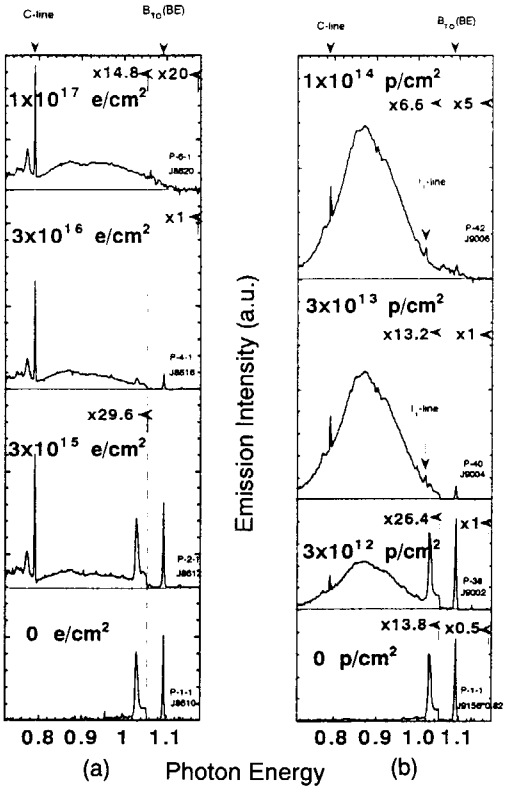

Fig. 3. PL Spectra of B doped CZ-Si (p-type, 10 Ω cm) wafers at 4.2K . (a) 1MeV electron irradiated (b) 10MeV proton irradiated .

Table Ⅰ. Prime defects in 1MeV electron irradiated cells.

Energy level (eV)	Peak temperature (K)	Introduction rate (cm^{-1})	Capture cross section (cm^2)
E_v+0.18	130	3×10^{-3}	8.9×10^{-17}
E_v+0.36	230	7×10^{-3}	7.2×10^{-16}
E_c -0.18	130	1×10^{-2}	1.75×10^{-16}

1．4 ESR Characterization of Ion Implanted Diamond Crystals

J. Isoya, S. Wakoh, M. Matsumoto, Y. Morita* and T. Ohshima*

University of Library and Information Science, *Department of Materials Development, JAERI/Takasaki

1. Introduction

Diamond has much superior physical properties than silicon as potential candidates for applications to electronic devices of high-speed/ high-power performances and those used in a harsh environment. While *p*-type semiconducting crystals are easily obtainable by incorporating boron, the formation of *n*-type semiconducting diamond has not been established. In a high-pressure synthetic diamond crystal grown using phosphorus catalyst, it has been confirmed that phosphorus atom, which has much larger atomic radius than carbon, does substitute for carbon[1]. In this case, unfortunately, the phosphorus is incorporated with accompanying nitrogen atom at the second nearest neighbor site. It has been reported that *n*-type conductivity has been achieved in phosphorus doped homoepitaxial diamond thin film grown by microwave plasma CVD method[2]. These recent developments demonstrate that phosphorus is the most promising *n*-type dopant in diamond.

We have been searching a condition for *n*-type doping by using high energy (9-21 MeV) phosphorus ion implantation. Since the slow-down processes of the implant create lattice damages, and since diamond is a metastable state of carbon at ambient pressures, the doping by ion implantation of diamond is much more complicated than that of silicon. In diamond, not only damage-induced graphitization gives rise to electric conductivity but also clusters of vacancies formed by post-implantation annealing act as donors[3]. To obtain *n*-type doping in which the implants act as donors, it is important to control implantation-induced defects and to drive the implants into the required lattice site. We use electron spin resonance (ESR) technique which is powerful in microscopic identification of defects and impurities. In our previous studies, we clarified that, in an implantation of high-energy phosphorus ions at room temperature, the dangling bond of amorphous phase is produced with a rate of 2.5×10^2 spins/ion, even at a low dose[4]. To suppress the formation of amorphous phase, it is required to use elevated implantation temperature. In our present study, target temperatures of 700°C and 1000°C were employed to facilitate recovery of crystallinity during implantation.

2. Experimental

Synthetic diamond crystals of type IIa were irradiated with phosphorus ions from a 3 MV tandem accelerator. To increase the number of phosphorus ions implanted without too much increasing the density of the lattice damages, crystals were irradiated with

phosphorus ions of nine different energies between 9 MeV and 21MeV. The step of the energy was chosen from the depth profile of implanted phosphorus which was measured by secondary ion mass spectroscopy (SIMS) analysis[4]. High temperature post-implantation annealing was carried out at 1800°C for 14 hrs under high pressure of 6 GPa. The ESR spectra were recorded on a Bruker ESP300 X-band spectrometer by using an Oxford Instrument ESR-900 to control the sample temperature.

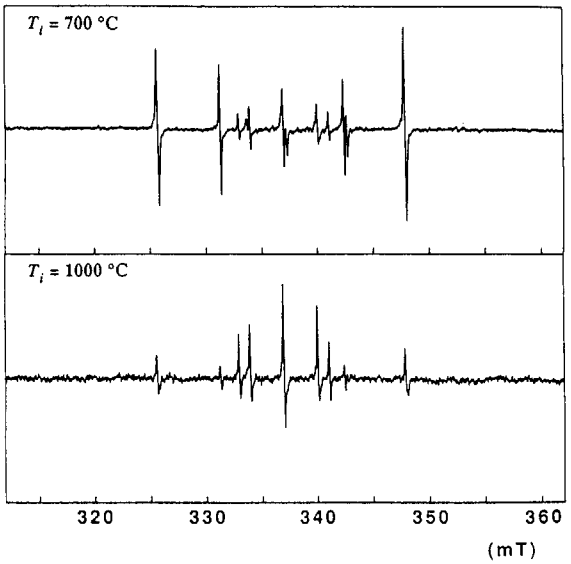

Fig.1 ESR spectrum (B//[111], 120 K) of type-IIa synthetic diamond crystals implanted with phosphorus ions of nine different energies with a dose of $2x10^{12}$ ions/cm^2 at each energy

3. Results and Discussion

The ESR signal of the dangling bond of amorphous phase was not observed after the implantations both at 700°C and at 1000°C (Fig.1). In the case of the implantations at room temperature, the ESR signal of the dangling bond of amorphous phase was observed even after a low total dose of $4x10^{11}$ ions/cm^2. In the case of the target temperature (T_i) of 1000°C, the ESR signal of the dangling bond of amorphous phase was not observed after implantation of phosphorus ions of nine different energies from 9 MeV to 21 MeVwith the dose of $5x10^{13}$ ions/cm^2 at each energy (total dose of $4.5x10^{14}$ ions/cm^2).

In the case of the implantation at room temperature, several ESR signals arising from defects were easily observed even after high temperature (1800°C) post-implantation annealing. The dominant defects which were observed after the annealing depend on the implantation dose. Our samples of synthetic type-IIa crystals contain 0.05 ppm of nitrogen as impurity. In the crystal implanted to a total dose of $4.5x10^{14}$ ions/cm^2 at 1000°C, the intensity of the implantation-induced ESR signals which were observed after the high-temperature (1800°C) annealing was smaller than that of the ^{13}C (I=1/2, natural abundance 1.1%) hyperfine lines of substitutional nitrogen. Since the ESR signals arising from residual defects are extremely weak, the combination of both high-temperature (1000°C) implantation and high temperature (1800°C) annealing has proven to be effective to recover crystallinity.

After the implantations at 700°C and at 1000°C, two dominant ESR centers which are denoted here as center-A and center-B, respectively, were observed . From the pattern of the rotational plots shown in Fig. 2, it is determined that both centers have orthorhombic (C_{2v}) symmetry and spin S=1.

The ESR parameters which were determined from the least-squares fitting of the line positions are summarized in Table I. It is likely that the two centers are arising from vacancy clusters. The size of the clusters are determined from the zero-field splittings **D** to be 6.4 Å and 8.0 Å, respectively, by using point-dipole approximation. With the increase of the target temperature from 700°C to 1000°C, the spin concentration of implantation-induced defects decreases and the fraction of the defect clusters of a larger size increases.

Our purpose is to obtain *n*-type doping in which phosphorus atom substituting for carbon acts as a donor by utilizing ion implantation. Since some defects such as clusters of vacancies act as donors[3], electric measurements alone are not sufficient to confirm *n*-type doping. It is important to determine the lattice locations of the implants. So far, ESR signals that are assignable to be associated with isolated phosphorus occupying a substitutional site have not been found in our phosphorus-implanted diamond crystals. It is likely that most of phosphorus ions implanted might be trapped into defect-clusters.

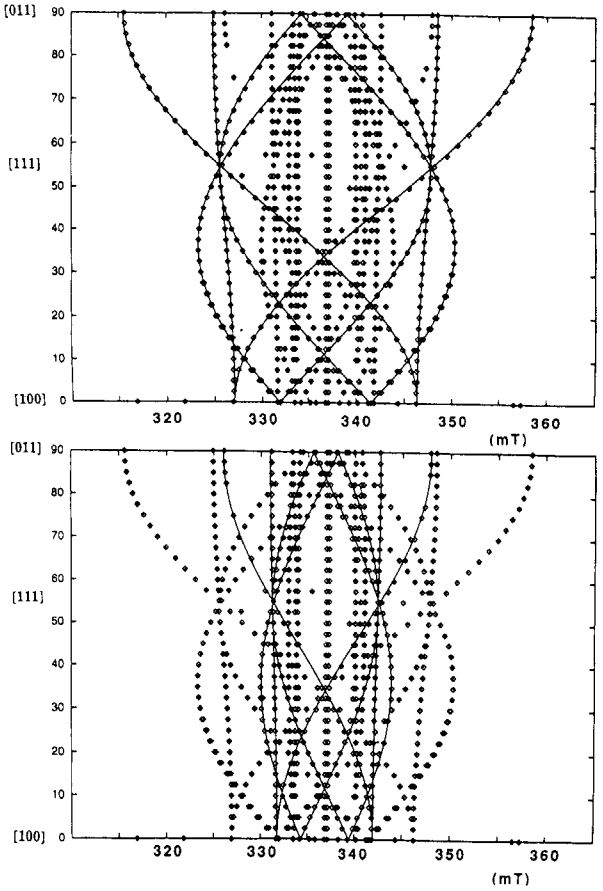

Fig. 2 Angular dependence of the line positions (120 K) of center-A (top) and center-B (bottom). The solid curves are theoretical fit using the ESR parameters obtained.

TABLE I. ESR parameters (120 K)

center-A[*1]	**g**	2.00353	[100]
		2.00301	[011]
		2.00387	[0$\bar{1}$1]
	D /geβ	-6.426	[100]
	(mT)	14.337	[011]
		-7.911	[0$\bar{1}$1]
center-B[*2]	**g**	2.00346	[100]
		2.00286	[011]
		2.00384	[0$\bar{1}$1]
	D /geβ	-3.412	[100]
	(mT)	7.328	[011]
		-3.916	[0$\bar{1}$1]

*1 245 line positions RMSD=0.07 mT

*2 250 line positions RMSD=0.08 mT

References

1. J. Isoya, H. Kanda, M. Akaishi, Y. Morita and T. Ohshima, Diamond Relat. Mater. 6, 356 (1997)

2. S. Koizumi, M. Kamo, Y. Sato, H. Ozaki and T. Inuzuka, Appl. Phys. Lett. 71, 1065 (1997)

3. J. F. Prins, Phys. Rev. B 39, 3764 (1989)

4. J. Isoya, H. Kanda, I. Sakaguchi, Y. Morita and T. Ohshima, Radiat. Phys. Chem. 50, 321 (1997)

1．5 Measurement of Single-Event Transient Current Induced in SOI Devices

Toshio Hirao[1)], Tuyoshi Hamano[1)], Takurou Sakai[1)], Yutaka Naitou[1)], Isamu Nashiyama[1)],Norio Nemoto[2)], Sumio Matsuda[2)],Kazunori Ohnishi[3)]

Japan Atomic Energy Institute[1)], National Space Development Agency of Japan[2)], Nihon university[3)]

I. Introduction

Single-Event-Upset(SEU)is trigged when an amount of electric charges induced by energetic ion incidence exceeds a value known as a critical charge.

This causes a serious problem in electronic components operating in spacecrafts. In order to solve this problem and develop SEU free devices, it is important to clarify the mechanisms of these SEU[1,2,3)].

Silicon-on-insulator (SOI) electronic devices are now being applied to harsh radiation environments of space due to the radiation hardness of the SOI structure.

In order to understand the transportation of charge induced by ion irradiation in SOI, we applied heavy-ion microbeams and a transient-measurement system[4)].

II. Experimental

The test samples used in the present experiments were SOI p^+n junction diodes with a junction area of 50 μmϕ in diameter and the depth of 0.5 μm as shown Figure.1. The sample diode was mounted on a chip carrier with a 50 Ω double-ended microstripline[5)]. The structural parameters of these test devices are listed in Table I.

In order to attain an incident-ion position-

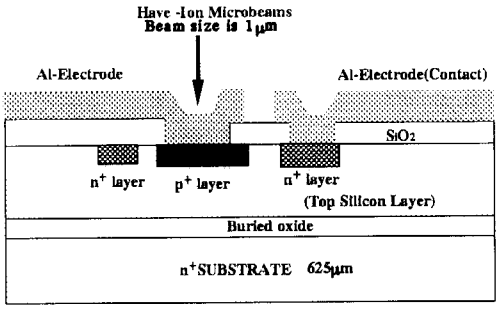

Figure 1. Schematics structure of a SOI p^+n junction diode for SEU experiment

Table 1. list of sample

Sample	Top Silicon	Buried oxide	Substrate
SOI (2.0μm)	CZN(100) 2.0 μm	0.12 μm	CZN(100) 625 μm
SOI(3.0μm)	CZN(100) 2.5 μm	0.19 μm	CZN(100) 625μm
SOI(5.0μm)	CZN(100) 5.7 μm	0.48 μm	CZN(100) 625μm

ing accuracy better than 1μm for current transient measurements, ion microbeams about 1 μm in diameter were provided using a high-energy ion microbe system connected to 3 MV tandem accelerator at JAERI Takasaki.

Heavy ions used were 15 MeV Carbon- and Oxygen-ions. Beam intensity of the microbeams was chosen as low as 200-500 ions/sec in order to reduce the effect of radiation damage[6)].

In measuring ultra-fast current transients, a high speed and wide bandwidth measurement circuit was applied, which consists of a high

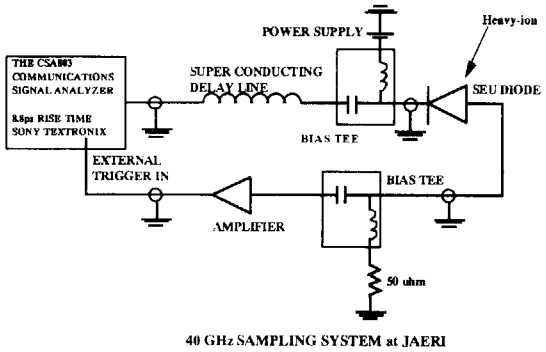

Figure 2. Schmatics of single-event Transient current measurement system

speed digital sampling oscilloscope (Tektronix model CSA803) with 50 GHz bandwidth, a wide bandwidth (40 GHz) bias tee, coaxial cables, connectors, and a super conducting delay line.

The experimental setup is schematically shown in Figure.2.

III. Result and Discussion

a) Single-Event Transient Current

Figures 3 and 4 show the wave forms of the transient currents induced by 15 MeV carbon- and oxygen-ions in the SOI diode with a top silicon layer (5.7 μm) under difference bias

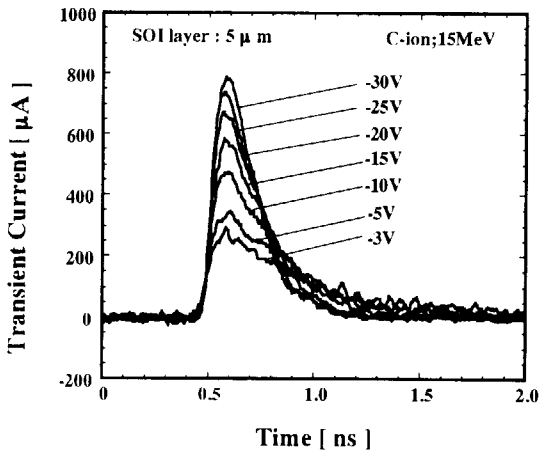

Figure 3. Effect of bias on SEU transient current induced with 15 MeV carbon ions

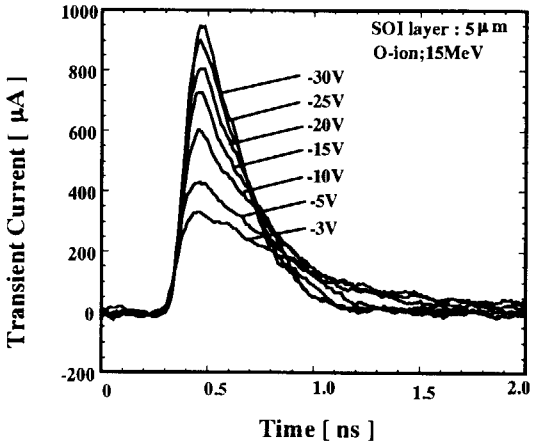

Figure 4. Effect of bias on SEU transient current induced with 15 MeV oxygen ions

conditions. As showns in figures 3 and 4, the peak-height increases with increasing bias voltage and fall time of the current pluse becomes shorter with increasing bias. Figure 5 shows the relation between bias and fall time(Tf),charge collection time(Tc), and FWHM, for the transient current induced by carbon-ion in the SOI diode with top silicon layer 5.7 μm.

As shown in figur 5, Tf and Tc decrease with increasing bias voltage in a similar manner to the reciprocal of the electric field in the depletion layer.

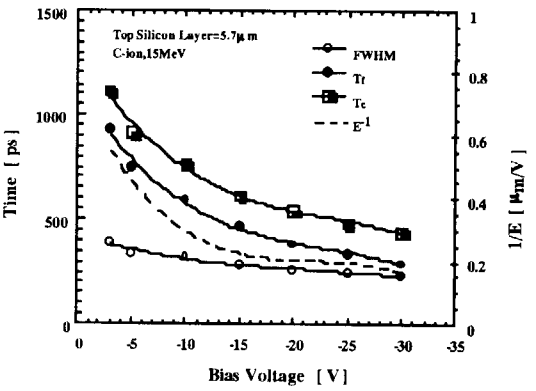

Figure 5. FWHM,Tf, Tc, and reciprocal of the electric field as a function of bias voltage

But, FWHM does not change much with increasing bias voltage.

b) Collected charge

Figure 6 show the relationship between the bias and collected charge obtained from the transient current wave form in figure 3. The straight line(a) and line(b) in the figure shows an amount of charge genereted in the top silicon layer(5.7 μm) and the depletion layer, respectively. The amount of the collected charge show 2 to 3 times larger than an amount of charge in the depletion layer. However, collected charges is less than the charge in the top silicon layer. In addition, an amount of collected charge saturates at the revese bias voltage above 10V. So, the charge collection length is short than the top silicon layer.

Accordingly, the amount of collected charge

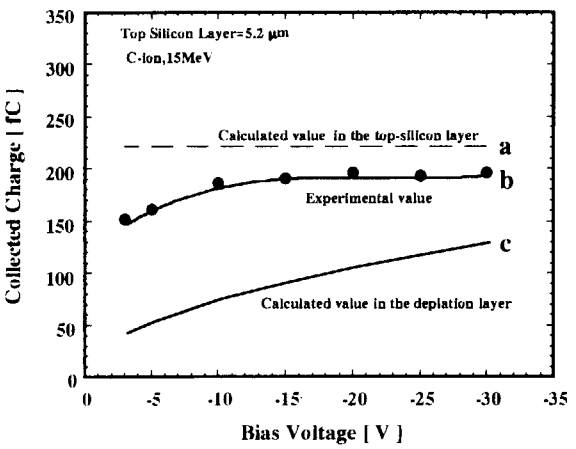

Figure 6. Relationship between collected charge and bias voltage for carbon-ion in SOI diode

is controlled a build-in oxide.

Conclusion

By applying heavy-ion microbeams and wide bandwidth digitizing sampling technique, we measured the effect of the builed-in oxide on the wave form of single-event transient current and the collected charge. We found that SOI structure is effective to increase the radiation haredness of electronic device used in the space environment.

Reference

1)I. Nashiyama, T. Hirao, T. Kamiya, H. Yutoh, T. Nishijima, H. Sekiguti, " Single-Event Current Transients Induced by High-Energy Ion Microbeams," IEEE Tranns, Nucl. Sci., Vol. NS-40, no.6, p-1935,1993

2)T.Hirao, I.Nashiyama, T.Kamiya, T. Nishijima, " Effect of ion posiotion on single-event transient current, " Nuclear In struments and Methods in Physics Research B130 (1997) 486-490

3)T.Hirao, I.Nashiyama, T.Kamiya, T. Suda, "Study of Transient Current Induced by Heavy-ion Microbeams Si and GaAs, "The 7 th International Symposium on Advanced Nuclear Energy Research, p.54, March.1996,Takasaki.

4)T. Kamiya, N. Utsunomiya, E. Minehara and R. Tanaka, "Microbeam sysytem for study of single event upset of semiconductor de vices," Nuclear Instruments and Methods in Physics Research B64 (1992) 326-366

5)H.R.Kaupp, IEEE Trans. Elec. Com.,184(1967)4

6)T.Hirao, I.Nashiyama, T.Kamiya, T. Nishijima, " Effect of micro-beam induced damage on single-event current measurements,"Nuclear Instruments and Methods in Physics Research B104 (1995) 508-514.

1．6 Introduction of Phosphorus into 6H-SiC by Implantation

T. Ohshima, K. Abe*, H. Itoh, M. Yoshikawa and I. Nashiyama

Department of Materials Development, JAERI/Takasaki

1. Introduction

Silicon carbide, SiC, is regarded as a candidate for high-temperature, high-power and high-frequency electronic devices due to its excellent thermal and electrical properties[1]. In addition, since SiC has a strong radiation resistance[2], it is expected to be applied to electronic devices operated in ionizing radiation fields.

For the application of SiC to electronic devices, it is very important to develop impurity-doping techniques. Donor and acceptor impurities N, P and Al have very low diffusion coefficients in SiC. Thus, the thermal diffusion technique is thought not to be applicable to doping of impurities. Ion implantation is considered to be one of the most useful techniques for selective doping of impurities into SiC. For the improvement of the electrical properties of implanted layer, it is necessary to reduce defects remaining after implantation because these defects act as carrier traps and scattering centers. However, optimum implantation and annealing conditions for the electrical activation of donor and acceptor impurities in SiC have not been fully clarified yet.

We have performed P implantation into 6H-SiC at room temperature, RT, and 1200 °C, and subsequent thermal annealing in a temperature range between 1200 and 1500 °C. The electrical properties of P^+-implanted layer have been examined by Hall effect measurements. In this article, we discuss the relation of the electrical activation of P atoms with implantation and annealing temperatures. We also estimated the ionization energies of P donors in 6H-SiC.

*JAERI Research Student from Okayama Univ.

2. Experiments

In this study, *p*-type 6H-SiC epitaxial films (thickness: ~4μm) grown on *p*-type 6H-SiC substrates were used. The net acceptor concentration of the epitaxial films is $3x10^{15}$ /cm^3. Before implantation, a screen oxide with a thickness of 30 nm was formed on the sample surface by pyrogenic oxidation. Four-fold (80, 100, 150 and 200 keV) implantation was conducted at RT and 1200 °C to form a box profile (depth: 250 nm) of P atoms with mean concentrations of $1x10^{18}$ or $5x10^{19}$ /cm^3. The screen oxide was removed using hydrofluoric acid after implantation. Isochronal annealing of the implanted samples was performed up to 1500 °C for 20 min. in pure Ar atmosphere.

Hall effect measurements of implanted samples were performed in a temperature range between 75 and 600 K using the van der Pauw arrangement. Ohmic electrodes were formed on these samples by the evaporation of Al. The electron concentration, n, in P^+-implanted layers was determined from the Hall coefficient, R_H, according to

$$n = \frac{r_H}{eR_H}, \qquad (1)$$

where r_H and e are the Hall scattering factor and electron charge, respectively. The values of r_H values for 6H-SiC have not yet been determined. In this study, r_H is taken as unity.

3. Results and discussion

Figure 1 shows the relation between n at RT and annealing temperature for 6H-SiC implanted with P^+. The Hall mobility at RT

is also shown in Fig. 1. Circles and squares represent the results for RT- and 1200°C-implanted samples, respectively.

For the samples implanted at RT and 1200 °C with $1x10^{18}$ /cm^3 (Fig. 1 (a)), n remarkably increases with annealing temperature up to ≈ 1400 °C. The value of n in the 1200°C-implanted samples is higher than that in the RT-implanted samples. At annealing temperatures above ≈ 1400 °C, no significant increase of n is observed in both the 1200°C- and the RT-implanted samples. As for the Hall mobility, in the 1200°C-implanted samples, no significant change is observed in annealing temperature range between 1200 and 1500 °C. For the RT-implanted samples, Hall mobility remarkably increases with annealing temperature up to 1300 °C, and exhibits almost the same value as that in the 1200°C-implanted samples above 1300 °C. From electron spin resonance[3], it was shown that the defect density in hot-implanted SiC is less than that in RT-implanted one. From positron annihilation spectroscopy, PAS[4], it was found that vacancy-type defects in 6H-SiC implanted with P^+ up to $1x10^{13}$ /cm^2 at RT are removed by 1400°C-annealing. Taking account of findings that some residual defects can act as carrier traps or scattering centers[5], the results shown in Fig. 1 (a) are interpreted by that density of residual defects in the 1200°C-implanted samples is less than that in the RT-implanted samples at annealing temperatures below 1400°C, and that almost all defects in the both 1200°C- and RT-implanted samples are annealed out by 1400°C-annealing.

In the case of the P concentration with $5x10^{19}$ /cm^3 (Fig. 1 (b)), n in the 1200 °C-implanted samples increases with increasing annealing temperature up to 1500 °C. On the other hand, for the RT-implanted samples, n increases by annealing up to 1400°C, and no significant increase of n is observed above 1400°C. From the comparison of the result of 1200°C-implantation with that of RT-implantation, n in the 1200 °C-implanted samples is larger than that in the RT-implanted samples. It was reported that vacancy clusters are formed by annealing in 6H-SiC implanted with P^+ at $1x10^{15}$ /cm^2 at RT and that they still remain after 1400°C-annealing[6]. Thus, the obtained result can be explained by that the density of residual defects in the 1200°C-implanted samples is lower than that in the RT-implanted samples in this annealing temperature range (below 1500 °C).

To estimate the ionization energies of P donors in 6H-SiC, the temperature dependence of n was fitted by using a charge neutrality equation. Here, two donor species of P were considered because of two different lattice locations, *i.e.*, hexagonal and cubic sites, of P in 6H-SiC. From this analysis, we can obtain the donor concentrations at hexagonal, $N(P_h)$, and at

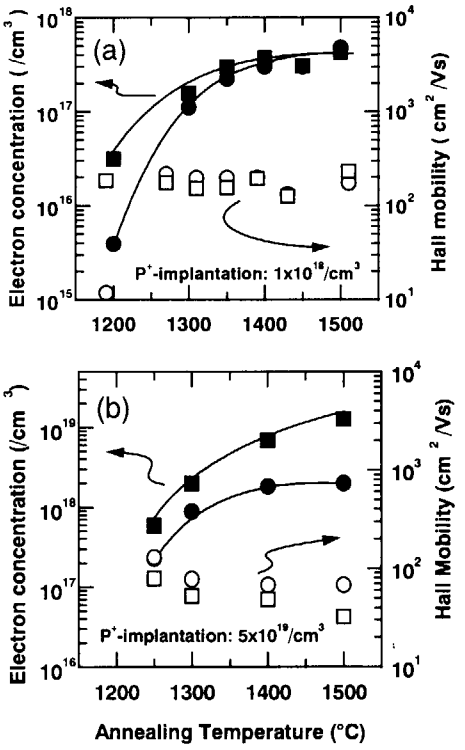

Fig. 1 Annealing temperature dependence of the electron concentration (closed symbols) and the Hall mobility (open symbols) at RT in the 6H-SiC implanted at RT (circles) and 1200°C (squares). The implanted P concentration are **(a)** $1x10^{18}$ /cm^3 and **(b)** $5x10^{19}$ /cm^3.

cubic sites, $N(P_k)$, and their ionization energies ΔE_h and ΔE_k. In this fitting, the ratio of $N(P_h)$ to $N(P_k)$ is assumed to be 1:2 because the ratio of the number of hexagonal lattice sites to that of cubic lattice sites in 6H-SiC is 1:2. For the electron effective mass in the conduction band, $m_{//}=0.68m_0$, $m_{\perp 1}=1.25m_0$ and $m_{\perp 2}=0.13s_0$ [7] were used in this analysis.

Figure 2 shows the temperature dependence of the electron concentration in the RT-implanted and subsequently 1500 °C-annealed sample. The solid line in the figure represents the fitting result using the charge neutrality equation. As a result of the fitting, the concentration of electrically active P atoms, $N(P_h) + N(P_k)$, is estimated to be $1x10^{18}$ /cm^3. This means that the activation ratio of P atoms is approximately 100 %. Here, we should point out that this activation ratio includes some uncertainty because r_H is assumed to be unity. Further information on the temperature dependence of r_H is needed to determine the exact activation ratio of implanted P atoms. The ionization energies of P donor, ΔE_h and ΔE_k, are estimated to be 75±5 and 105±5 meV, respectively. These values are in good agreement with those reported previously (ΔE_h = 80±5 meV and ΔE_k = 110±5 meV)[8]. For nitrogen donors in 6H-SiC, Suttrop et al.[9] reported that they have two ionization energies ΔE_h(N) = 85.5 meV and ΔE_k(N) = 125 meV. The ionization energies obtained for P donors are close to those for N donors. This shows that P as well as N is quite useful donor impurities for the fabrication of *n*-type conducting layers in SiC.

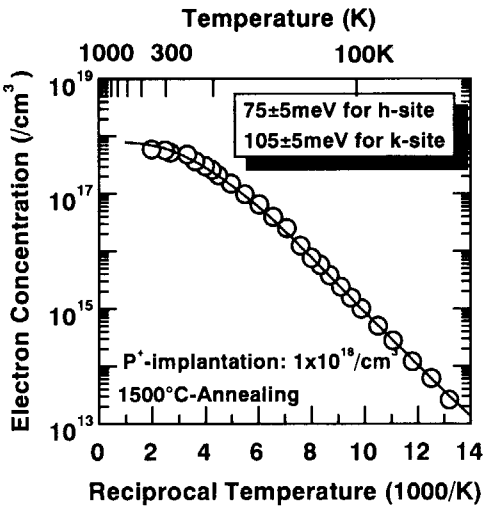

Fig. 2 Temperature dependence of the electron concentration in the 6H-SiC implanted with $1x10^{18}$ P$^+$/cm^3 at RT and subsequently annealed at 1500 °C. The solid line represents the result of the fitting using a charge neutrality equation.

4. Summary

In the case of implantation concentration of $1x10^{18}$ P$^+$/cm^3, *n* in the 1200°C-implanted samples is higher than that in the RT-implanted samples in the annealing temperature range between 1200°C and 1400°C. Above 1400°C, no significant difference of *n* is observed. In $5x10^{19}$ P$^+$/cm^3 implantation, *n* in the 1200°C-implanted samples is higher than that in the RT-implanted samples in the annealing temperature range from 1200 to 1500 °C. These results suggest that hot-implantation is useful, especially high-concentration doping of impurities.

Ionization energies of P donor, ΔE_h and ΔE_k, in 6H-SiC are estimated to be 75±5 and 105±5 meV, respectively, which are similar to those for N donors. It indicates that P atoms are quite useful for device fabrication.

References

1) *For example,* W. E. Nelson *et al.*: J. Appl. Phys. **37** 333 (1966).
2) H. Itoh *et al.*: IEEE Trans. Nucl. Sci. **NS-37** 1732 (1990).
3) K. Abe *et al.*: *Proceeding of ICSCIII-N'97*, Stockholm, September, 721 (1998).
4) T. Ohshima *et al.*: submitted to Appl. Phys. A.
5) G. C. Rybicki: J. Appl. Phys. **78** 2996 (1995).
6) A. Uedono *et al.*: Jpn. J. Appl. Phys. **37** 2422 (1998).
7) P. Kackell *et al.*: Phys. Rev. **B50** 10761 (1994).
8) T. Troffer *et al.*: J. Appl. Phys. **80** 3739 (1996).
9) W. Suttrop *et al.*: J. Appl. Phys. **72** 3708 (1992).

2. Biotechnology

(continue to the next page)

2．1 Detection of structural alterations of the DNA by AFLP technique in ion beam-induced mutants

Naoya Shikazono, Tai Wang, Atsushi Tanaka, Ayako Sakamoto, Hiroshi Watanabe, and Shigemitsu Tano
Plant Resources Laboratory, Department of Radiation Research for Environment and Resources (JAERI)

1. Introduction

In higher plants, cloning a gene defined solely by a mutant phenotype is not yet an easy task. Chromosome walking, which is used to isolate a gene linked to a DNA marker, is still laborious and can be impeded by repetitive sequence. Gene tagging systems that use transposable elements or T-DNA to generate random mutations over an entire genome are being developed but are not yet available for all plant species.

We have been investigating the structural alteration of the DNA in carbon ion-induced *Arabidopsis* mutants and have found that large genetic changes, such as deletions, inversions, or translocations were often induced in these mutants[1]. If these structural alterations of the DNA could be easily detected and linked to the mutated locus, it would provide an useful addition to the chromosome walking and gene tagging approaches for cloning genes corresponding to a mutated phenotype.

We used AFLP(Amplified Fragment Length Polymorphism) technique[2] to detect structural alterations over a genome. In AFLP, the genomic DNA was at first digested by two kinds of restriction enzyme followed by ligation of adaptor sequences at cleavage sites. These fragments were amplified by PCR and then were fractionated by their molecular weights. Structural alterations were detected by identifying polymorphisms between the genome of wild type and of ion beam-induced mutants.

Arabidopsis ast mutant were isolated after exposure of dry seeds to 220 MeV carbon ions[3]. This mutant is a novel mutant and shows a phenotype that pigments on testa accumulate as spots rather than homogeneously spread around. *AST* locus have been mapped at chromosome I. From the mapping experiment, it was found that the nearby markers had slightly different positions in this mutant, suggesting that an inversion might have took place at this region. If this inversion occurred at the *AST* locus, it could be detected easily by AFLP. The *AST* gene product is speculated to regulate the synthesis of the pigments at testa, but its function remains largely unknown.

We planned to clone this gene using AFLP and uncover the function of the gene product. To reach this goal, detection of the structural alterations in the ast mutant and further the linkage of those alterations to the mutated phenotype at the F2 generation were carried out in the present study.

2. Material and Methods

2.1 Plant materials

Arabidopsis wild type ecoytpe Columbia and *ast* mutant, which was induced by exposing 220MeV carbon ions to Columbia seeds at TIARA, were used in this study. Twelve F2 plants derived from a cross between *ast* mutant and wild type Columbia were grown to study the linkage of the structural alterations to the mutated phenotype. Six of the F2 plants had wild type phenotype and the other six had *ast* phenotype.

2.2 Extraction of genomic DNA and AFLP

Genomic DNA was extracted from 3 or 4 weeks-old plants using ISOPLANT kit (Nippon Gene, Co. Ltd.). AFLP was carried out following the manufacture's protocol (AFLP Plant Mapping Protocol of PE Applied Biosystems). In brief, genomic DNA was doubly digested with *Eco*RI and *Mse*I. The digested DNA fragments were ligated with AFLP adaptors, and then were amplified with pre-selective primers. This pre-selective PCR product was used as a template for selective PCR. Selective PCR product was analyzed with ABI PRISMTM 310 Genetic Analyzer. Genomes of *ast* mutant and wild-type(Columbia ecotype) have been analyzed with 61 primers (Table 1).

3. Results and discussion

It was revealed that amplified fragments were detected with high reproducibility by AFLP technique. Therefore, the specific fragments were surveyed whether or not those were detected in ast mutant when compared to those in wild type. From the present study, 8 fragments were identified; 5 of which were present only in wild-type, the rest only present in *ast* mutant (Table 2).

To identify the possibility that these structural alterations had occurred within the *AST* gene, F2 population was analyzed with each of eight AFLP-primer pairs, by which specific DNA fragments were amplified from wild-type or ast mutant.It was suggested that at least two (A44 and C60) of the 8 specific DNA fragments might be linked to the *AST* gene (Table 3). These two fragments are going to be cloned and will be subjected to further analysis for the isolation of the *AST* gene. The rest had interesting segregating character in F2 population and may be useful to investigate the molecular changes by ion beam-irradiation.

AFLP is not labor intensive, and the results reported here indicate that using AFLP to ion beam-induced mutants could be an useful addition to the other gene cloning techniques in plants.

References

1) Shikazono, N. et al., JAERI-Review 97-015, 24-26 (1997).

2) Vos, P. et al., Nucleic Acids Res., 23, 4407-4414 (1995).

3) Tanaka, A. et al., Genes Genet. Sys., 72, 141-148 (1997).

Table1. Primer sets for AFLP

3' end sequence of *Eco*RI primer	3' end sequence of *Mse*I primer: -CAA	-CAC	-CAG	-CAT	-CTA	-CTC	-CTG	-CTT
-AA	1	8	15	23	31	39	47	55
-AC	2	9	16	24	32*	40	48	56
-AG	3	10	17	25	33*	41	49	57
-AT		11	18	26	34	42	50	58
-TA	4		19	27	35	43	51	59*
-TC	5	12	20	28*	36*	44*	52	
-TG	6	13	21	29	37	45	53	60*
-TT	7	14*	22	30	38	46	54	61

* Primer sets that detected specific fragment.

Table 2. Specific fragments detected by AFLP

Fragment	Molecular weight (bp)	Fragment detected in
C14	486	Col (Wild Type)
A28	55	*ast* (Mutant)
C32	339	Col
C33	149	Col
C36	110	Col
A44	54	*ast*
A59	199	*ast*
C60	113	Col

Table 3. Segregation of specific fragments

Fragment	Col	*ast*	F 2 plants*											
			1	2	3	4	5	6	7	8	9	10	11	12
C14	+**	-**	+	+	+	+	+	+	+	+	+	+	-	+
A28	-	+	-	-	-	-	-	-	-	-	-	-	-	-
C32	+	-	+	-	-	-	-	-	+	+	+	+	+	+
C33	+	-	-	-	-	-	-	-	-	-	-	-	-	-
C36	+	-	-	-	-	-	-	-	-	-	-	-	-	-
A44***	-	+	+	+	-	+	+	+	+	+	+	+	+	+
A59	-	+	-	-	-	-	-	-	-	-	-	-	-	-
C60***	+	-	+	+	+	+	+	+	-	-	-	-	-	-

* No.1～6 F2 plants show wild type phenotype and No7～12 F2 plants show *ast* phenotrype.

** +:fragments detected, -:fragments undetected.

*** Fragments that show linkage to the *ast* phenotype.

2. 2 Influence of LET on Repair of DNA Double-Strand Breaks in *Deinococcus radiodurans*

Y. Kobayashi, M. Kikuchi and H. Watanabe
Department of Radiation Research for Environment and Resources, JAERI.

1. Introduction

Induction of double-strand breaks (DSBs) in DNA has been considered to be a predominant determinant of radiotoxicity. Increases in linear energy transfer (LET) were assumed to cause increases in the extents of damage associated with DSBs, and a maximum of the relative biological effectiveness (RBE) for inactivation of mammalian cells has been observed around 100 keV/μm[1]. However, recent data of DSBs yields in cells obtained with protons and heavier ions demonstrate that the yields of DSBs do not vary significantly with increasing LET over a range where RBE varies widely[2,3]. To explain these LET effects, it is assumed that radiations of different quality produce different complexity of lesions which are currently not distinguished in the ordinary assays used to measure DSBs. High-LET-specific-damage such as clustered lesions, that is, more complex DSBs occurring in the LET range of enhanced biological efficiency, are considered as the dominant damage of DNA for cell lethality[4,5]. Accordingly, the maximum of the RBE around 100 keV/μm is likely due to lower repairability of DSBs induced in this LET range, rather than higher yields of DSBs.

Deinococcus radiodurans[6] can repair all DNA lesions including DSBs induced with doses up to 5 kGy[7]. This extraordinary radiation resistant bacterium is also resistant to heavy ion irradiation and the survival curve had a large shoulder[8]. Those facts suggest that this bacterium can also repair DSBs induced by heavy ions.

Therefore we have studied the inactivation of *D. radiodurans* caused by heavy ions; and we have already demonstrated that all survival curves were characterized by a large shoulder of the curves and no final slopes at the exponential part of survival curves for heavy ion irradiation were steeper than that for 2.0 MeV electron irradiation[9,10]. The plots of RBE versus LET showed no obvious peaks suggesting that this bacterium can repair not only DSBs but also clustered damage in DNA which may be induced by heavy ions. Then we analyzed the induction of DSBs in genomic DNA of *D. radiodurans* and the repair process during post-irradiation incubation. Using a pulsed-field gel electrophoresis (PFGE) technique, we detected the reappearance of ladder pattern of genomic DNA digested with a restriction enzyme *Not* I before PFGE analysis to study the LET dependence of the DNA rejoining process.

2. Experimental

Deinococcus radiodurans R_1 strain was cultivated in TGY liquid medium (0.5% Bacto-Tryptone, 0.3% Bacto-Yeast extract, Difco; 0.1% glucose, pH 7.0) with shaking at 30°C for 24 hrs. The cells were harvested in the stationary phase, and then washed and resuspended with 0.1 M sodium phosphate buffer (PB), pH 7.0.

About $3x10^8$ cells were settled on a membrane filter (pore size 22 μm, diameter 47 mm, Millipore Corp.) and the filters were placed on PB agar plates (10 mM sodium phosphate buffer, pH 7.0, containing 2% agar).

The cells on the membrane filters were irradiated in the atmosphere using the method of track segment experiment with 25 MeV/u $^4He^{2+}$ ions (LET = 9 keV/μm), 18 MeV/u $^{12}C^{5+}$ ions (LET = 120 keV/μm) and 17 MeV/u $^{20}Ne^{8+}$ ions (LET = 300 keV/μm) from the AVF cyclotron at TIARA. The particle fluence was determined by microscopic counting of etched particle tracks on track detector CR-39. To convert particle fluence to dose in Gy, the following relationship was used:

$$\text{Dose [Gy]} = 1.6 \times 10^{-9} \times \text{LET [keV/μm]} \times \text{Fluence [particles/cm}^2\text{]}$$

LET values were calculated with ELOSS code developed in JAERI. The cells were also irradiated with 2.0 MeV electron beams (LET = 0.3 keV/μm) from a Cockcroft-Walton accelerator.

After irradiation, the membrane filters were transferred onto TGY agar plates and incubated at 30°C to induce DNA repair enzymes. Then the filters were transferred onto TGY agar plates containing 100 μg/ml of chloramphenicol (CP) to inhibit protein synthesis, and incubated at 30°C to continue DNA repair process without allowing the cells to restart their growth. To determine the total required time to complete the repair process, the incubation time on the CP-containing TGY agar plate was changed after a constant CP-free window sufficient to induce repair enzymes.

The irradiated cells were embedded in agarose plugs and incubated in lysis buffer as previously described[9,10]. The genomic DNA in a plug piece was digested with 30 units of *Not* I restriction endonuclease at 37°C for more than 10 hrs. Then PFGE was performed as previously described[9,10] with a transverse alternative field electrophoresis system, GeneLine™ (Beckman). The agarose gels were stained with 0.5 μg/ml of ethidium bromide (EtBr) for 1 hr and destained twice in distilled water. The ladder pattern of DNA fragments were photographed on the ultraviolet transilluminator.

3. Results and Discussion

The genomic DNA of *D. radiodurans* cells was cleaved into large fragments (*ca.* 50 ~ 500 kbp) with the restriction enzyme *Not* I after post-irradiation incubation, and the fragments were separated and detected using PFGE. Post-irradiation incubation time was prolonged from 2 to 6 hrs, and the total required incubation time to complete the DSBs rejoining process was estimated according to the reappearance of DNA banding pattern.

Figure 1 shows RBE values for cell inactivation and the repair time necessary for the rejoining of DSBs after irradiation with 2 kGy of 2 MeV electrons, 25 MeV/u $^4He^{2+}$ ions, 18 MeV/u $^{12}C^{5+}$ ions and 17 MeV/u $^{20}Ne^{8+}$ ions. The longest repair time was needed after 18 MeV/u $^{12}C^{5+}$ ions irradiation with LET values of 120 keV/μm at the equal dose in Gy, although the RBE for cell inactivation after 18 MeV/u $^{12}C^{5+}$ ions irradiation was lower than those for 2 MeV electrons and 25 MeV/u $^4He^{2+}$ ions irradiation. This result indicates that it takes longer time to repair DNA lesions induced by high LET heavy ions (around 100 keV/μm) compared with low LET electrons and He ions even for *D. radiodurans*, although the DNA lesions are finally to be repaired completely

with lower RBE values.

The minimum incubation time without CP (CP-free window) to complete the induction of DNA-repair related proteins during post-irradiation incubation after exposure to 25 MeV/u $^{4}He^{2+}$, 18 MeV/u $^{12}C^{5+}$ and 17 MeV/u $^{20}Ne^{8+}$ ions are plotted in Figure 2 as a function of dose and LET. The required induction time increased with dose and showed LET dependence. The induction time was longest after irradiation of 18 MeV/u $^{12}C^{5+}$ ions with LET value around 100 keV/μm. This delay in the induction process may cause the delay in rejoining of DSBs shown in Figure 1.

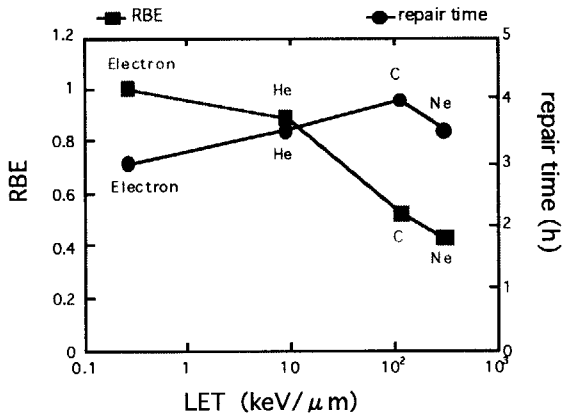

Figure 1. RBE values for cell inactivation after irradiation with electrons and heavier ions (left) and total repair time including the CP-free window necessary for the rejoining of DSBs induced in *D. radiodurans* genomic DNA after irradiation with 2 kGy of 2 MeV electrons, 25 MeV/u $^{4}He^{2+}$, 18 MeV/u $^{12}C^{5+}$ and 17 MeV/u $^{20}Ne^{8+}$ ions (right). The RBE values were determined from the final slope of the surviving curves after irradiation. The total required incubation time to complete the rejoining of DSBs was estimated from time course of the reappearance of the ladder pattern of *Not* I fragments during post-irradiation incubation using PFGE.

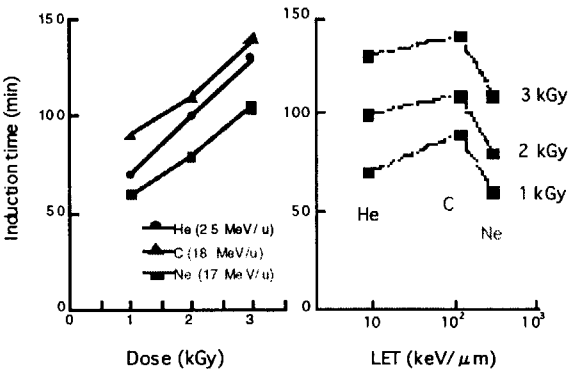

Figure 2. The needed CP-free window for the induction of DNA-repair related proteins after irradiation with 25 MeV/u $^{4}He^{2+}$, 18 MeV/u $^{12}C^{5+}$ and 17 MeV/u $^{20}Ne^{8+}$ ions with doses of 1, 2 and 3 kGy. The required induction time increased with dose (left), and also showed LET dependence (right).

References

1) E. A. Blakely, *Radiat. Environ. Biophys.*, 31, 181-196 (1992)
2) G. Taucher-Scholz, *et al.*, *Radiat. Environ. Biophys.*, 34, 101-106 (1995)
3) J. Heilman, *et al.*, *Int. J. Radiat. Biol.*, 68, 153-162 (1995)
4) K. M. Prise, *et al.*, *Int. J. Radiat. Biol.*, 66, 537-542 (1995)
5) D. T. Goodhead, *et al.*, *Int. J. Radiat. Biol.*, 65, 7- 17 (1994)
6) B. W. Brooks, *et al.*, *Int. J. Syst. Bacteriol.*, 31,353-360 (1981)
7) S. Kitayama and A. Matsuyama, *Biochem. Biophis. Res. Commun.* 33, 418-422 (1968)
8) Y. Kobayashi, *et al.*, *TIARA Annual Report 1994*, 44-46 (1995)
9) Y. Kobayashi, *et al.*, *JAERI-Conf 97-003: 7th International Symposium on Advanced Nuclear Energy Research*, 68-72 (1997)
10) Y. Kobayashi, *et al.*, *TIARA Annual Report 1996*, 27-29 (1997)

2. 3 Microbeam System for Local Irradiation of Biological Systems

Y. Kobayashi, M. Taguchi and H. Watanabe
Department of Radiation Research for Environment and Resources, JAERI.

1. Introduction

The use of a heavy ion microbeam provides a unique way to control the number of particles traversing individual cells and localization of dose within the cell. And the localized dose delivery of a heavy ion microbeam can be applied to inactivation of microscopic region of target organisms: cell surgery technique. Recently laser microbeam irradiation has been used for cell surgery technique, however ion microbeam has not been applied. High-energy ion beams have been applied to radiation therapy development and radiation biology in world-wide scale, however there have been no ion accelerator facility adapted for developmental biology or botanical research. For evaluation of radiation risk on mammalian cells, proton and helium ions with energies of a few and several MeV from Van de Graaff accelerators have mostly been used, however heavy ion beams from those accelerators can not be applied to the study because of the poor penetration. Therefore we have designed and installed a high-energy microbeam apparatus at TIARA to develop a novel cell manipulation technique, and to study radiobiological processes in ways that can not be achieved using conventional random exposures. To investigate the effect of local irradiation of heavy ions on various biological system, for example fertilized eggs of insect and meristematic tissue of plant, the apparatus has been connected to a vertical beam line of AVF cyclotron giving 12.5 MeV/u ^{4}He, 18.3 MeV/u ^{12}C, 17.5 MeV/u ^{20}Ne and 11.0 MeV/u ^{40}Ar ions. This particle spectrum covers a wide range of LET, between 14-2000 keV/μm, giving different biological effectiveness. The relatively deep penetration of heavy ions from the cyclotron allows to analyze the fundamental effect of high-LET radiation to the living organisms in a wider LET range. The heavy ion beams have been collimated to about 10 μm in diameter up to this time using a set of apertures. The final goal is to hit a microscopic target area of cells individually with a single ion using collimated heavy ion beams.

2. Experimental

(1)Beam collimation

Microprobes with various size of the microapertures can be replaced by others according to the desired spot size of local irradiation on the biological samples. The techniques for discharge machining are limited to a maximum hole depth about 5-10 times the hole diameter, depending on the diameter. Using tantalum disk as a microaperture foil, the minimum hole diameter is 10 μm up to this time, being limited by the techniques for fabrication of a fine electrode for electrical discharge. Accordingly 50 μm thick microaperture with non-tapered 10 μm holes, 100 μm thick microaperture with non-tapered 20 μm holes, or 500 μm thick microaperture with non-tapered 50 μm holes were fabricated and used for collimation of the heavy ions. To collimate 13.0

MeV/u ^{20}Ne and 11.0 MeV/u ^{40}Ar ions which can penetrate about 70 μm thick and 42 μm thick tantalum, respectively, two tantalum disks of 50 μm thick with 10 μm holes were doubled (piled) precisely at the position of their holes. To collimate 18.3 MeV/u ^{12}C or 17.5 MeV/u ^{20}Ne ions which can penetrate about 190 μm thick and 110 μm thick tantalum, respectively, orthogonally aligned two sets of slits have been used. The arrangement for the orthogonally aligned 200 μm thick slits is shown in Figure 1. For local irradiation of biological samples with beam spot size of larger than 20 μm in diameter, a series of tantalum disks with electrical discharge perforated holes are used. To make finer hole below 10 μm in diameter, both the orthogonally aligned two sets of slits and the combination of a flat plate and a grooved plate are to be tested near future.

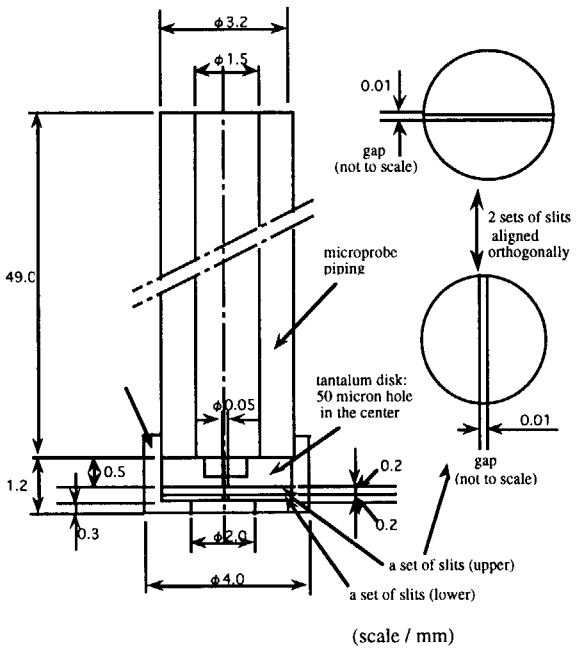

Figure 1. The arrangement for the orthogonally aligned two sets of 200 μm thick tantalum slits with a gap size of 10 μm. The 'pore size' should be 10 μm x 10 μm.

(2) Semi-automatic target positioning system

To find the cells or biological samples to be irradiated, inverted optical microscope and video image processing system were used. We have installed a 'semi-automatic' target finding and positioning system and applied to irradiation of fertilized eggs (1.20 mm long, 0.95 mm wide, 0.63 mm thick) of silkworm *Bombyx mori*. This system can detect the contour of each target egg and draw a circumscribed rectangle overlaying the image of the egg, then finds out a ventrodorsal axis (Ventral midline to Dorsal midline, VD) and an egg-length axis (Anterior pole to Posterior pole, EL). According to the preset X (VD) and Y (EL) co-ordinates, the desired irradiation point on each egg was aimed one after another to the beam position (end of the microprobe) viewed through object lens by remote controlling the sample micropositioning X-Y stage. Then the object lens was replaced with the small PMT (Hamamatsu, type R5600U-06) mounted on the microscope turret to count the number of ions traversed the sample.

3. Results and Discussion

The performance of the collimator was assessed both in terms of the quality of the energy spectrum and its targeting accuracy. The energy spectrum was measured as a pulse height spectrum from the photomultiplier tube assembly in response to the stop of many single heavy ions in 3 mm thick plate of NE110 plastic scintillator. There is no suitable standard to obtain the absolute energy at the energy range of used heavy ions, therefore the pulse height of the signals obtained from the monoenergetic ions detected after passage through a vacuum window was used as a energy value of straight

and properly aligned 'good' beams. A typical energy (pulse height) spectrum from the well aligned microbeam is shown in Figure 2(A). The spectrum is of 440 MeV ^{40}Ar ions that have been collimated by a 10 μm diameter aperture on doubled (piled) 50 μm thick tantalum disk (totally 100 μm thick) perforated by the electrical discharge method. The collimated ions were captured in 3 mm thick plate of NE110 plastic scintillator and the pulse height spectrum from the photomultiplier tube assembly (Hamamatsu, type H3177-50) was accumulated for 100 seconds. Figure 2(B) shows another typical pulse height spectrum of 350 MeV ^{20}Ne ion microbeam collimated by two sets of orthogonally aligned slits with a gap of about 10 μm, therefore the 'pore size' of the aligned slits was about 10 μm x 10 μm. Using the same orthogonally aligned slits, 18.3 MeV/u ^{12}C ions were collimated properly and gave a pulse height spectrum shown in Figure 2(C). It can be estimated from those energy spectrum, more than 95% of the collimated ions were within the monoenergetic peak.

Minimum beam spot size and the projectile range in water of available ion beams at present are listed on Table 1. The beams have been collimated to about 10 μm in diameter; more than 95% of the collimated ions were within the monoenergetic peak and delivered to the aimed locus with 85-90% of targeting accuracy.

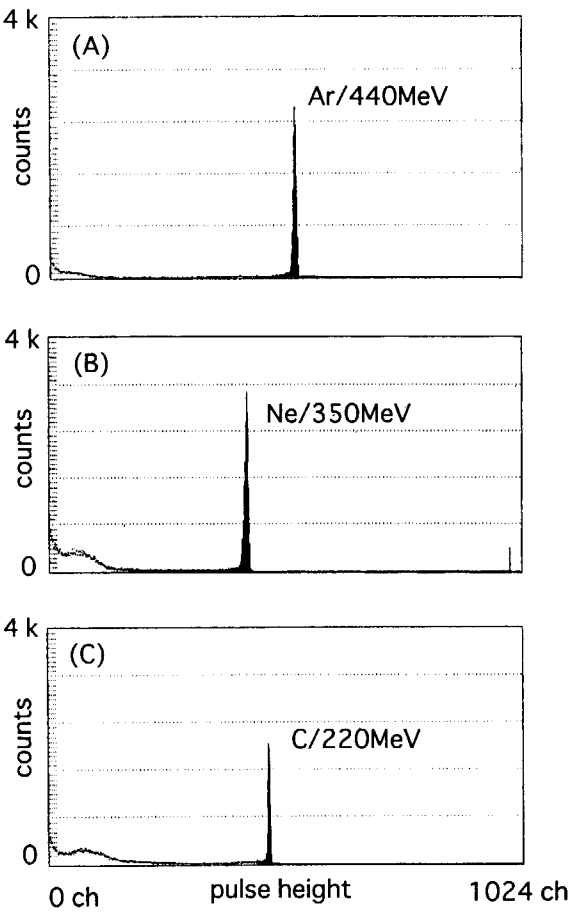

Figure 2. Pulse-height spectrum from the photomultiplier tube assembly in response to the stop of many single heavy ions in 3 mm thick plate of NE110 plastic scintillator.

Table 1 Available microbeams at present for local irradiation of biological systems

Ions	Specific energy (MeV/u)	Minimum beam size (μm in diameter)	Projectile range in water (mm)
$^{4}He^{2+}$	12.5	40	1.8
$^{12}C^{5+}$	18.3	10	1.2
$^{20}Ne^{8+}$	17.5	10	0.7
$^{40}Ar^{13+}$	11.0	10	0.24

2.4 Irradiation effect of phenylalanine aqueous solution on heavy ion

M.Taguchi[a], M.Moriyama[b], Y.Kobayashi[a], H.Watanabe[a], and H.Hiratsuka[b]
[a]Department of Radiation Research for Environment and Resources, JAERI,
[b]Department of Chemistry, Gunma University

1.Introduction

It is well known that relative biological effectiveness shows maximum around 100 keV/μm of Liner Energy Transfer (LET). However, the damage of biological substances was not yet observed which makes LET effects clear. The purpose of this study is to understand LET effects from the viewpoint of the chemical field by analyzing the decomposition reaction showing LET dependence for DNA, protein and amino acid aqueous solutions. In the present report, the decomposition of phenylalanine aqueous solution irradiated with 350 MeV Ne^{8+} ions was studied.

2.Experimental

Phenylalanine(Tokyo Kasei Organic Chemicals, GR) and methanol(Kanto Chemical Co. Cica-reagent) were used without further purification. Water was supplied from a Milli Q (millipore). The concentration of phenylalanine in water was 130 and 13 mM. The irradiations were performed with Ne^{8+} (350 MeV) ions from the AVF cyclotron in TIARA facility. The irradiations were performed using the Irradiation Apparatus for Seed(IAS)[1] connected to the AVF cyclotron. The sample solution has 2 mm depth. Penetration depth of the Ne ions used was about 0.6 mm in water. The ions stopped near the surface of the sample solution, therefore, the sample solution was stirred during the irradiation to keep the homogeneity. Penetration range and LET of the ions were calculated with the IRAC code[2]. Fluence of the ions was determined by counting particle tracks on the track detector, CR-39, irradiated before the sample solution.

Absorption spectra were recorded on the spectrophotometer (Beckman, Du-65) before and after the irradiation. High Performance Liquid Chromatography (HPLC) analysis was performed with a reversed phase column (Waters Symmetry C18) at 254 and 350 nm monitor wavelength. Water with methanol (10%) was used as an eluent and its flow rate was 0.6 ml/minute. The sample solution was also irradiated with 1 MeV electron beam as a low LET radiation.

3.Results and Discussion

Phenylalanine solution has the strong absorption bands in the ultraviolet region as shown by dashed line in Figure 1. After the irradiation with Ne ions the absorbance due to products was observed in the longer wavelength region, 280-450 nm, compared with the original absorption bands, and increased with an increase of dose.

Many peaks on chromatograms of the sample solution were observed for both monitor wavelength at 254 and 350 nm by HPLC measurement after the irradiations of electron and Ne ion beams. Differences in the chromatograms between electron and Ne ion irradiations were observed in the case of 350 nm monitor. Figure 2 shows the

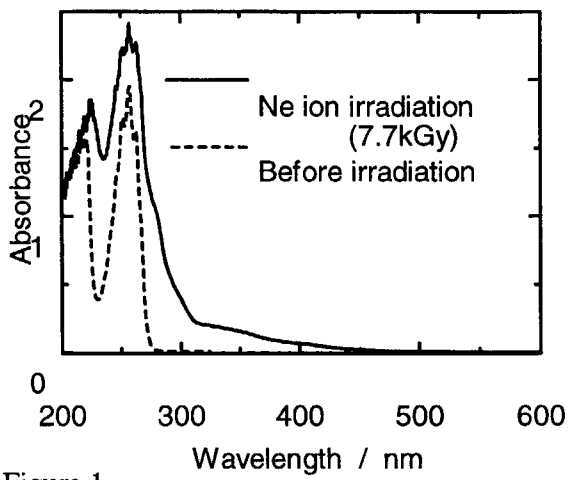

Figure 1
Absorption spectra of phenylalanine aqueous solution before (dashed line) and after(solid line) the irradiation with Ne ion.

chromatograms before and after the irradiation with electron and Ne ions monitored at 350 nm. Many peaks were observed for both electron and Ne ion irradiation until 10 minutes, however, the peak at 16.7 minutes was observed for only Ne ion irradiation. Height of this peak increased up to 6 kGy, and then reached at a plateau.

The peak observed at 9 minutes retention time was assigned to phenylalanine itself, because this peak was also observed before the irradiation and phenylalanine has a weak absorption band (n-π* transition) at this wavelength. The production of tyrosine and DOPA, which are the adducts of one and two OH substituent on benzene ring of phenylalanine, was reported after γ-ray irradiation of phenylalanine aqueous solution[3]. The peaks at 3.5 and 4.2 minutes were assigned to tyrosine and DOPA, respectively, by comparing the retention time of tyrosine and DOPA aqueous solutions. The product due to the peak observed at 16.7 minutes was collected and concentrated. Figure 3 shows the absorption spectrum of the product. No specific bands (for example, vibrational bands around 280 nm for benzene ring) were confirmed, because the absorbance was very small.

Chemical reaction in water is generally induced by OH radical by ionization radiations. Therefore, the common products of electron and Ne ions would be produced by OH radical. The product observed at 16.7 minutes is considered to be produced by the interaction between transient species in the ion track, since transient species are densely produced by high density energy deposition in the ion track.

Further analyses of the characteristic product for Ne ions using FT-IR and GC-MS are in progress.

References

1. M.Kikuchi,A.Tanaka, Y.Kobayashi, R.Nozawa and H.Watanabe, TIARA Annual Report 1,159(1992).
2. S.Tanaka, M.Fukuda, K.Nishimura, W.Yokota, T.Kamiya, H.Watanabe, T.Shiraishi, K.Hata and N.Yamano, TIARA Annual Report, 1, 76 (1992).
3. O.H.Weeler and R.Montalvo, Radiat. Res., 40, 1(1989).

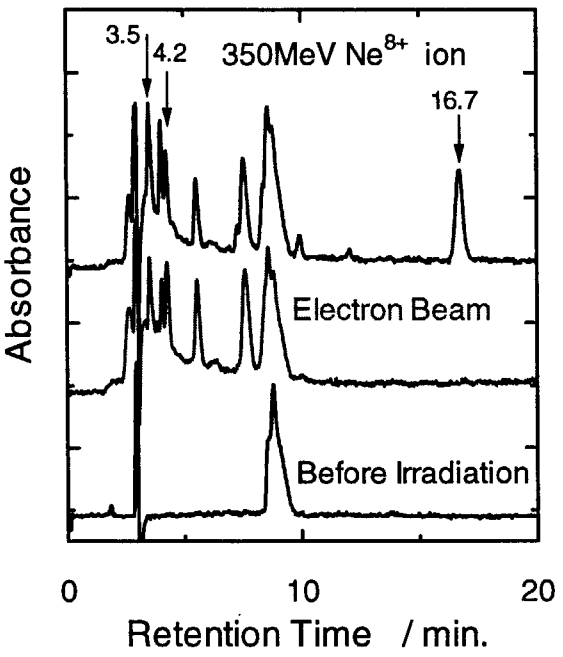

Figure 2
Chromatograms of phenylalanine aqueous solution before and after the irradiations with 1 MeV electron and 350 MeV Ne^{8+} ion monitored at 350 nm.

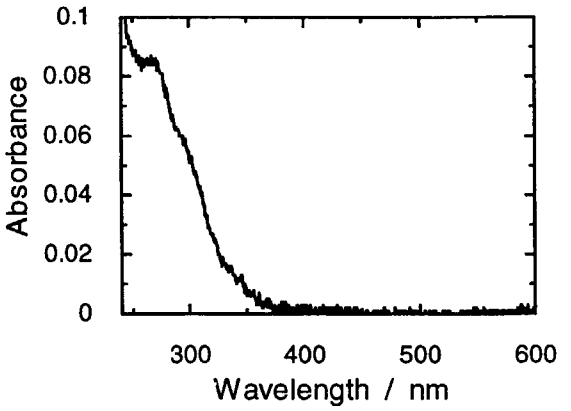

Figure 3
Absorption spectrum of the solution due to the peak observed at 16.7 minutes in the chromatogram of HPLC.

2. 5 Mutation Breeding of *Aspergillus awamori* for Improvement of Raw Starch Digestion

H. Ito, M. Takigami and A. Amsal
Department of Radiation Research for
Environment and Resources, JAERI/Takasaki

1. Introduction

Aspergillus awamori has been utilized as a useful microorganism for fermentation in the South-western islands of Japan and possesses the ability to digest raw starch. In the South Asian countries, carbohydrate-based agricultural commodities such as starchy tubers and crops are found in abundance. Conversion of these commodities to value-added products through enzymatic saccharification is important in the industrial fermentation process. For the saccharification of starches, cooking at 100-140 ℃has been used to liquefy the starch and sterilize the broth. From the view points of energy utilization and process simplicity, industrial direct conversion of raw starches to monosaccharides by amylolytic enzymes is superior to the conventional process which uses pregelatinized starch by cooking. *A. awamori* has an ability to digest uncooked starches at low pH without pasteurization. For the improvement of raw starch digestibility, mutation breeding of microorganisms is one of the important methods in the fermentation process. However, the saccharification ability can not be increased easily by the conventional mutation induction methods by ultraviolet-rays or gamma-rays (Ito and Azizun, 1996).

This paper describes the increase of raw starch digesting activities of crude amylolytic enzymes produced by the mutant strains of *Aspergillus awamori* induced by ion-beams using tropical agricultural commodities.

2. Experimental

(1) Starches

Cassava, sago and sukun starches were obtained from the Center for the Application of Isotopes and Radiation, National Atomic Energy Agency, Indonesia.

(2) Induction of mutation

Aspergillus awamori IFO 4033 was incubated on Potato-dextrose agar (Difco, Detroit, Michigan, USA) plates at 30 ℃ for 1 week and spores (conidia) were suspended in the solution containing 2% peptone, 2% glycerol, 2% poly(vinylalcohol) and 1% sodium glutamate. Then the spores were filtered on a Millipore membrane filter with the pore size of 0.22 μm as a concentration of ca. 1 x 10^6 spores per filter. The spores on the membrane filter were freeze-dried and subjected to 220 MeV C^{5+} or 20 MeV He^{2+} ion-beams from 0.1 to 1.5 kGy in AVF cyclotron in JAERI/Takasaki. Gamma-rays were also irradiated to spores which were freeze dried, vacuum dried, or suspended in 0.067 M phosphate buffer solution. The irradiated samples were inoculated on Potato-dextrose agar plates, and 10 black colonies with bigger sizes were picked up as the test strains from each culture with different sample preparation conditions after cultivation at 30℃for 1 week.

(3) Enzyme assay

The spores of the parent strain and the test strains were inoculated to the 60 ml of Czapek-starch broth (10 g soluble starch, 2 g $NaNO_3$, 0.5 g KCl, 1 g KH_2PO_4, 3 g peptone and 10 mg $FeSO_4$ per liter, pH 5.5) in a 500 ml conical flask with a cotton plug and incubated for 6 days at 30 ℃ by surface culture. A crude enzyme solution was obtained by filtering the culture through No.1 filter paper (ADVANTEC MFS, INC., Japan). The α-amylase activities in the filtrate were assayed using the "Neoamylase Test" (Daiichikagaku). The 0.05 M acetate buffer solutions (pH 3.7 and 4.5) were used during the α-amylase or other kind of enzyme assays. Glucoamylase activities in the filtrate were assayed using the Somogi-Nelson method on glucose after removing ammonia in the filtrate. Saccharification activity of raw starch (raw starch digesting amylase activity) was assayed by the reaction mixture containing 0.3 g of raw starch, 42 ml of 0.05 M acetate buffer (pH 3.7), 6 ml of the crude enzyme solution at 37 ℃ for 10 min. Two ml of 0.5 M NaOH was added to each solution and reducing sugar was determined as glucose.

(4) Digestion of raw starch

Digestibility of raw starch was assayed by the reaction mixture containing 0.3 g of raw starch, 42 ml of 0.05 M acetate buffer (pH 3.7) and 6 ml of the crude enzyme solution in a 100 ml flask. After 24 h incubation at 37℃ with gentle stirring, the reaction mixture was centrifuged at 5000 rpm for 15 min. Two ml of 0.5 M NaOH was added to each solution and then reducing sugar in the supernatant was determined as glucose.

3. Results and Discussion

When the freeze-dried spores were irradiated, the survival curve was exponential for C^{5+} ion-beams, while sigmoidal for gamma-rays as shown in Fig. 1. On the study of mutation induction by gamma-irradiation, only one strain, F9, of 10 isolates from freeze-dried and 2 kGy-irradiated spores (10^{-4} survival fraction) expressed high activity of α-amylase as shown in Table 1 and Fig. 2 . However, the mutant strains with high activity of α-amylase were not isolated from the vacuum dried spores or suspended spores in phosphate buffer even if their survival fractions was 10^{-4}. Many isolates from C^{5+} ion-irradiation expressed high activity of α-amylase of two to threefold (Fig. 2). In this study, a higher mutation ratio of high enzyme activity was obtained with

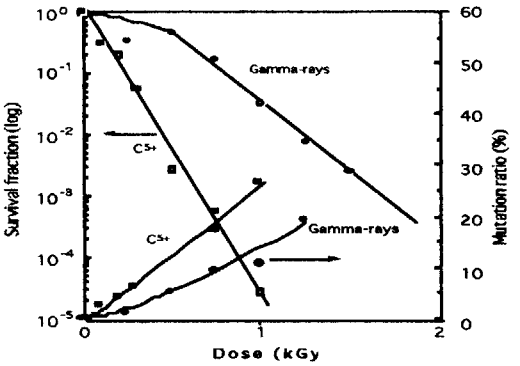

Fig. 1 Survival curves and mutation ratio of freeze-dried Aspergillus awamori IFO4033 irradiated by C^{5+} ion-beam or gamma-rays.

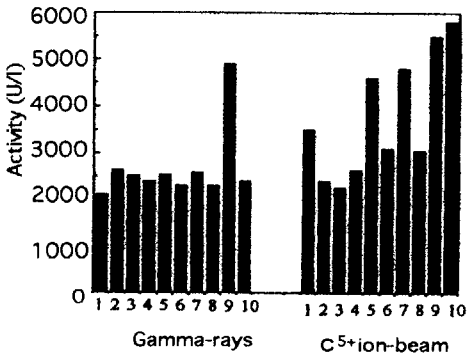

Fig. 2 α-amylase activity of mutant strains of *Aspergillus awamori* obtained by gamma-rays and C^{5+} ion beam irradiation

an increasing absorbed dose in C^{5+} irradiation. The frequency to induce mutant strains with the high α-amylase activity was 5 to 10 times higher in C^{5+} irradiated spores than in gamma-irradiated ones at the survival fractions of 10^{-4}. Saccharification activity and glucoamylase activities were also increased as shown in Table 1. Concerned with the saccharification activities of three kinds of starches, most mutant strains had relatively high activity for sago starch with increased glucoamylase activity.

As shown in Table 2, digestivity of the raw starch was also increased remarkably by the mutant strains obtained by C^{5+} ion-beam irradiation. The result indicates that ion-beam irradiation can induce many types of mutation in one strain as to have increased activities of many kinds of the amylolytic enzymes including α-amylase and glucoamylase. In this study, similar digestivity was observed on cassava and sukun starch. However, digestivity of sago starch was lower than those of other starches even by the mutant strains.

From this study, it is clear that ion-beam irradiation is useful for the breeding of microorganisms, because the irradiation can induce many kinds of mutations simultaneously.

References

1) Ito, H. and Azizum N. (1996) Induction of *Aspergillus oryzae* mutant strains producing increased levels of α-amylase by gamma-irradiation. Radiat. Phys. Chem., 48(6), 811-813.

Table 1 Saccharification activities of uncooked starches by parent and mutant strains

Strain	Amylase activity (U/liter)		Saccharification actiity (U/liter)		
	α-Amylase	Glucoamylase	Cassava	Sago	Sukun
Parent strain	2400	4400	1376	470	1330
C2-1	3050	5200	1550	640	1600
C7-3	5500	5600	1640	710	1700
C7-4	5800	5600	1750	1010	1800
F9	5000	4900	1520	510	1510

Amylase and saccharification activities (means, n=3) were assayed at pH 3.7.
C2-1, C7-3, C7-4 : obtained by C^{5+} irradiation, F9: obtained by gamma-irradiation.

Table 2. Raw starch digestion by parent and mutant strains.

Strain	Amout of glucose in 10 ml reaction mixture (mg)		
	Cassava	Sago	Sukun
Parent strain	8.6	2.3	5.7
C2-1	16.8	5.2	8.2
C7-3	18.1	6.1	11.6
C7-4	19.1	7.0	12.1
F9	11.1	3.8	7.1

Raw starch 57 mg/ 9ml of acetate buffer solution (pH 3.7) + 1 ml of crude enzyme solution. Mixture was incubated at 37 ℃ for 24 h (means, n=2).

2．6 PVY-resistant Mutation induced by Ion Beam Exposure, in combination with Anther Culture of *Nicotiana tabacum* L.

M.Inoue, K.Hamada, Y.Hase, A.Tanaka* and H.Watanabe*

Department of Agriculture, Kyoto Prefectural University,
*Department of Radiation Research for Environment and Resources, JAERI

1. Introduction

In plant breeding, it is necessary to enlarge the range of genetic variation and to select a gene(s) controlling character to be improved. Therefore, it is important to develop the selection method for obtaining a desirable gene(s) efficiently. From this point of view, haploid generation, *e.g.* pollen, is very valuable as a material for detecting gene expression.

Ion beams have higher LET (Linear Energy Transfer), in comparison with that of X-rays or Gamma-rays, and can be controlled the range in the target material. Accordingly, a lot of energy can be depositted on the focused point of material exposed to ion beams. Taking advantages of these characteristics of ion beams, we have already established the procedure for overcoming cross-incompatibility between distantly related species of *Nicotiana* [1~3]. In *N. gossei* Domin × *N. tabacum* L., the interspecific hybrid seeds can be obtained by conventional cross, and can germinate. However, seedlings can not survive , because of hybrid inviability. On the other hand, the cross with pollen exposed to He ion beams produced the viable hybrid plants at the rate of 1×10^{-2}, which was much higher than that of gamma-rays.

Furthermore, we found phenomenon specific for ion beam exposure, "leaky pollen", in which internal substance leaked through an opening in the outer wall of pollen grain. After leakage, the outer wall remained open or closed. Leaky pollen is thought to result from a physical lesion(s) induced in outer wall (probably, exine) of pollen grain by ion beam[4]. If exogenous DNA can be transferred into pollen through cleavage induced by ion beam, pollen can be used as a gene vector, in combination with crossing. Now, researches on transfer of exogenous DNA to pollen, its expression in pollen and production of progeny seed with gene-transferred pollen are in progress[5].

In the present paper, we describe PVY(potato virus Y) - resistant mutation

in haploid plants derived from the anthers exposed to He and C ions.

2. Materials and Methods

Plants of *N. tabacum* cv. Bright Yellow 4 (BY-4) were used as experimental materials. BY-4 is known to be susceptible to PVY.

The anthers with pollen at the mid-to late-uninuclear stage were collected and cultured on the modified Nakata's medium under light condition at 26 ℃. And, they were exposed to 220 MeV C ions (penetration depth, 10 mm) of 0～200 Gy and 50 MeV He ions (15 mm) of 0～400 Gy from AVF Cyclotron, respectively. Four days after exposure, they were transferred to the fresh medium and cultured. Anther culture response, percentage of the anthers producing a plantlet(s), was determined 50 days after initiation of culture. Considering RD_{50} on anther culture response, the anthers were exposed to C ions of 0, 5 and 10 Gy, and He ions of 0, 5, 7 and 10 Gy , respectively, and cultured by means of same procedures as mentioned above. The plantlets obtained, were transferred to pot and allowed to grow in a greenhouse at 25 ℃. During the course of plantlet growth, number of chromosomes was determined in root tip cells.

When the haploid plants differentiated 5 to 6 leaves with 4～5 cm in length, two leaves of each plant were dusted with carborundum (600 mesh) and inoculated with a suspension of PVY (race T) extracted from infected leaves of *N. tabacum* cv BY-4. According to symptom appearance and survival, the PVY-resistant mutants were identified 21 days after inoculation.

3. Results and Discussion

Anther culture response was reduced in proportion to exposure dose: 78.3 % in the non-exposed; 43.0 and 18.5 % in C ions of 5 and 10 Gy ; 65.0 and 17.5 % in He ions of 7 and 25 Gy, respectively. RD_{50} on anther culture response was 5 Gy for C ions and 10 Gy for He ions. RD_{50} for each ion beam was much lower than that of 40 Gy reported in gamma-ray-irradiated anther of *N.tabacum* [6].

Frequencies of the chromosome aberrations were observed in root tip cells of the plantlets (Table 1). In the exposure regime, aberration frequency significantly increased, compared to that in the control regime. However, there was no difference in the aberration spectrum between the exposure regimes.

The haploid plants were inoculated with PVY (Table 2). In plants derived from the non-exposed anther, veins turned brown 10 days after inoculation and, subsequently, necrotic symptom expanded over whole area of the leaves and stem. Finally, all plants died up to 21 days after inoculation. On the other hand, the survival plants were obtained in the exposure regime. Among 487 plants

derived from the anthers exposed to C and He ions, 15 plants had no disease-symptom at 40 days after inoculation. Thereafter, they continued to grow in a greenhouse, although slight symptom was observed in some of them at various times after 50 days. Thus, those 15 plants were evaluated to be resistant to PVY. Mutant frequencies in C ions of 10 Gy, He ions of 5 and 10 Gy were 2.9, 3.9 and 3.4 %, respectively. Particularly, one mutant obtained in 5 Gy of He ions, had no disease-symptom during observation, and grew vigously.

References

1) M.Inoue, H.Watanabe, A.Tanaka and A.Nakamura, JAERI Annu. Rep.**3** (1993) 44.
2) T.Yamashita, M.Inoue, H.Watanabe, A.Tanaka and S.Tano, JAERI Annu. Rep.**4** (1994) 37.
3) T.Yamashita, M.Inoue, H.Watanabe, A.Tanaka and S.Ttano, JAERI Annu. Rep.**5** (1995) 44.
4) M.Inoue, H.Watanabe, A.Tanaka and A.Nakamura, JAERI Annu. Rep.**2** (1992) 50.
5) A.Tanaka, H.Watanabe, S.Shimizu, M.Inoue, M.Kikuchi, Y.Kobayashi and S.Tano, Nuc. Inatr. and Meth. in Phys. Res. **B 129** (1997) 42.
6) H.Hasegawa, S.Takashima and A.Nakamura, Plant Tissue Culture Letters **12** (1995) 281.

Table 1 Frequency of cells with chromosome aberrations in the root tip cells of haploid plants

Ion・Dose	Mitotic index	Number of cells	Chromosome aberration			Frequency
(Gy)	(%)	observed	Bridge	Fragment	Lagging	(%)
non-exposed	6.5	258	4	3	1	3.1
C・5	5.8	549	11	42	25	14.2
C・10	6.7	217	7	13	6	12.0
He・5	6.5	390	10	32	22	16.4
He・7	6.0	162	3	14	6	14.2
He・10	6.3	522	13	28	21	11.9

Table 2 Frequency of mutants resistant to PVY-T in haploid plants

Ion・Dose	Number of plants	PVY-T		Frequency
(Gy)	tested	Susceptible	Resistant	(%)
non-exposed	91	91	0	0
C・5	42	42	0	0
C・10	104	101	3	2.9
He・5	255	245	10	3.9
He・7	13	13	0	0
He・10	58	56	2	3.4

2. 7 Effects of Heavy Ions on Embryogenesis in the Silkworm, *Bombyx mori* : Comparison of Radiation Effects Among Three Different Ions

K. Kiguchi*, S. Yamasaki*, Z. L. Tu*, Y. Kinjoh*, Y. Kobayashi** and H. Watanabe**

* Faculty of Textile Science and Technology, Shinshu University,

** Department of Radiation Research for Environment and Resources, JAERI.

1. Introduction

Since Henneberry and Sulivan (1963) first suggested that silkworm eggs were useful experimental materials for the study of the biological effects of cosmic and other radiations [1], the radiosensitivity of silkworm eggs have been investigated by X- and γ- radiations [2,3]. However, little information has yet accumulated on the effects of low-fluence high-energy heavy particles (HZE particles), which would be one of the problems encountered in space flight.

In JAERI TIARA, a novel micro-beam apparatus has been installed under the vertical beam line of an AVF cyclotron. This apparatus is expected to contribute not only to the development of cell surgery technique but also to the study of the biological effect of HZE particles in a space environment. In this study, we first investigated the sensitivity of the silkworm eggs to the heavy ion ($^{12}C^{5+}$) beams throughtout their embryonic development. Next, the radiation effects of three different ions on the embryonic development were examined as a basis of the studies mentioned above.

2. Materials and Methods

The larvae of the *pnd* (pigmented non-diapausing) mutant of the silkworm, *Bombyx mori*, were routinely reared on a commercial artificial diet (Yakult). Since *pnd* mutant embryos do not enter diapause, this mutant is considered particularly suitable for such studies. Egg collection was made on a polyester film every 20 minutes. The eggs were kept at 25°C and subjected to ion beams at various developmetal stages. Eggs were generally exposed to three different ions from an AVF cyclotron or locally irradiated by the beams collimated with a 250 μmø aperture. The ions used were $^{4}He^{2+}$(12.5MeV/u; range in water=1.8mm), $^{12}C^{5+}$(18.3MeV/u; range= 1.2mm), and $^{20}Ne^{8+}$ (17.5MeV/u; range= 0.7mm). After irradiation, the treated eggs were kept at 25°C, and the morphology of the embryos developed from the irradiated eggs was examined carefully under a dissecting micro-scope.

3. Results and Discussion

1) Changes of sensitivity to carbon ion-radiation during embryonic development

When kept at 25°C, eggs of *pnd* mutant hatch into larvae 10 days after oviposition. The eggs were exposed to $^{12}C^{5+}$ of three different doses every 24 hrs post oviposition (PO), and the radiation effects were examined based

on their hatchability. As shown in Fig.1, hatchability was strongly inhibited when the eggs were irradiated during the first 3 days PO, but little influence was observed thereafter. Thus, early embryos seemed to be highly sensitive to the ion-beam radiation in the period from the oviposition to the shortening stage (30% development), but thereafter they became rather resistant. 50% lethal doses for C ions showed almost the same results (5 to 10 Gy) at the before-fertilization stage (~2hr PO), the cellular blastoderm(12hr PO), and germband stages(36hr PO) (data not shown).

2) Comparison of radiation effects among three different ions

Eggs of the blastoderm stage (12-13hrs PO) were generally exposed to three different ion beams, $^{4}He^{2+}$, $^{12}C^{5+}$, and $^{20}Ne^{8+}$. Percentages of non-hatched eggs (lethality) and abnormal embryos (mostly partial embryos) induced after exposure are shown in Fig.2. As seen in the Figure, 50% lethal doses were delivered at almost the same levels (8 to 10 Gy) among the three ions. However, the radiation effects of Ne ions were significantly different from those of He and C ions. Namely, serious morphological defects including deletion, fusion, and partial embryonic development were observed in the eggs irradiated with 10-36 Gy of C or He ions, but embryogenesis was completely inhibited when the eggs were exposed to the dose of 40 Gy or more. By contrast, in the case of eggs irradiated with Ne ion beams, partial embryonic development was still induced by the dose of 95 Gy at high frequencies (80%<). Moreover, most defects were observed on both side of the embryos when irradiated with C and He ions. On the other hand, in many cases after Ne ion irradiation, defects apeared only on either side (right or left) of the embryos. Similar results were also obtainded by localized spot irradiation with a 250 μmø beam. The factor most possibly responsible for inducing this difference is the range (penetration depth) of each ion beam. Accelarated He and C ions are considered to pass through the eggs because of their long ranges. However, Ne ion beams may not be able to pass through, and thus form a bragg peak inside the egg. This was confirmed by use of a CR39 track detector. As illustrated in Fig.3, eggs in the cellular blastderm stage are composed of cells of different phases [4]. Such heterogeneity in the embryonic cells might be another possible factor involved in the induction of partial embryos due to the differences in sensitivity to the ion-beam exposure. The results obtained will afford the basis for further research not only on the biological effects of low-fluence HZE particles, but also on the development of radio-micro cell surgery tecniques.

4. References

1) T. J. Henneberry and W. N. Sullivan, Nature, 200,1121 - 1122 (1963)

2) A. Murakami, Int.J. Radiat.Biol., 15, 315-322 (1969)

3) A. Murakami and M. Miki, J. Radiat.Res., 13, 183-192 (1972)

4) L. Nagy, L. Riddiford and K. Kiguchi, Develop. Biol., 165, 137-151 (1994)

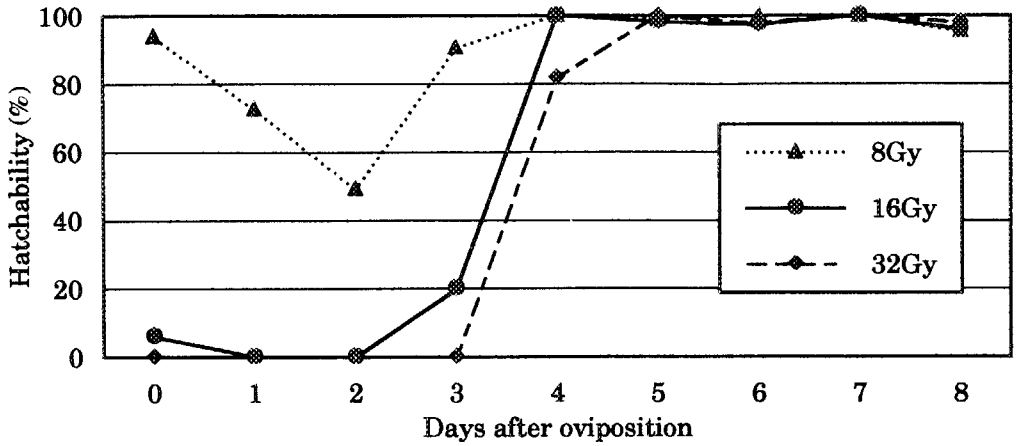

Fig.1 Changes of sensitivity to carbon ion radiation during embryonic development in the silkworm, *Bombyx mori*.

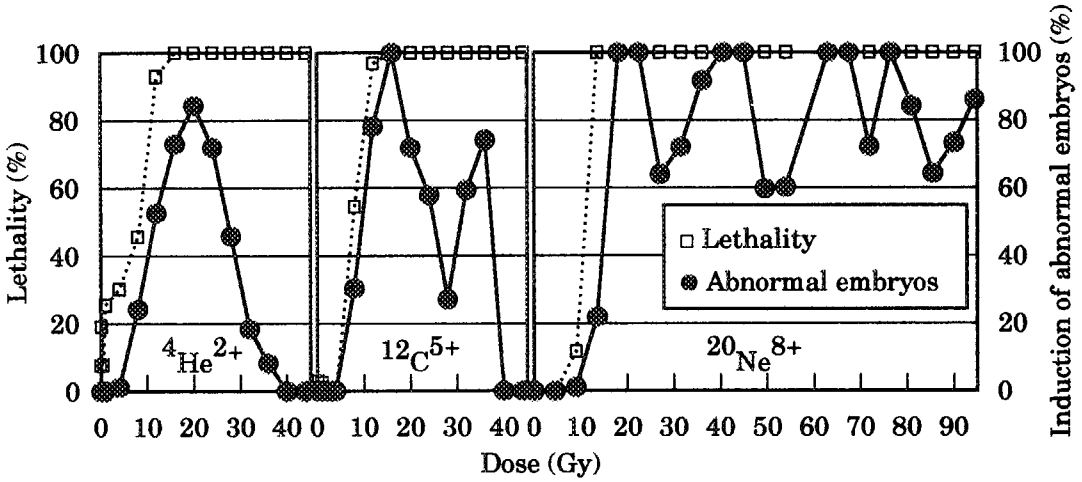

Fig.2 Comparison of radiation effects among three different ions.
Eggs at cellular blastoderm stage were generally irradiated with each ion beams.

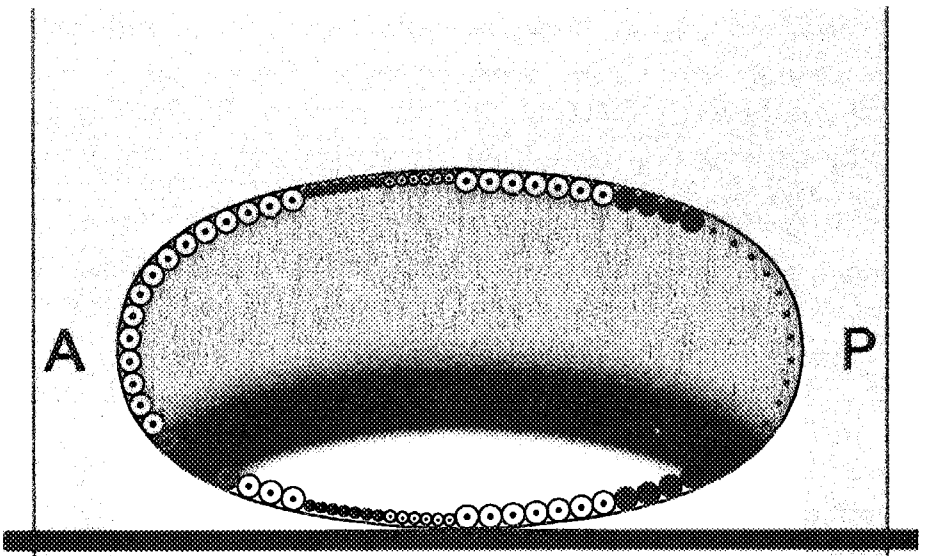

Fig.3 A schematic illustration of Ne ion irradiation to the cellular blastoderm stage embryo.

2. 8 Mutation Induction through Ion Beam Irradiations in Rice and Chrysanthemum

S. Nagatomi[1], A. Tanaka [2], A. kato[1], H. Yamaguchi[1],
H. Watanabe [2] and S. Tano [2]
Institute of Radiation Breeding, NIAR[1]
Takasaki Establishment, JAERI [2]

I. Introduction

A new mutagen is required to develop a plant mutation. Most mutagens used for registered crop mutant varieties in the world are gamma rays and X rays. Ion beams are expected to be widely utilized as new mutagens, because they have very high LET and RBE at controlled penetration depths.

The present study was conducted to develop an effective mutation breeding method using ion beams and to investigate the radiosensitivity and induced mutants in two reproductive model crops, rice and chrysanthemums.

II. Experimental methods

The plant materials were irradiated with various doses of accelerated ion particles, $^{4}He^{2+}$(100 MeV, 20nA), $^{12}C^{5+}$ (220 MeV, 0.02 nA), and $^{20}Ne^{8+}$(350 Mev, 0.02 nA) using an AVF Cycrotron in JAERI. Seeds of the rice cultivars "Nippon-bare" and "Hitome-bore" were investigated for germination ability after irradiation, and the culm length, shoot number per stool, and seed fertility of the plants transferred to a paddy field were recorded. The selfed seeds collected from each panicle of the plants were sown. The plants were grown in a paddy field as panicle-row lines to the M_2 generation and were studied for visible mutant traits. The genetic transmissibility of the selected mutants was investigated in the M_3 generation. Gamma-ray-irradiated generations were also established for a comparison.

Explants of the floral petals and leaves of the chrysanthemum cultivar "Taihei," cultured on the callus induction media, were irradiated with ion beams and their survival ratio, callus induction, and regeneration were investigated. The regenerated plants were established and the mutants were selected during the flowering. The mutant lines propagated through cuttings were grown in the field and their mutated traits were investigated during flowering.

III. Results and discussion

The median lethal dose (LD_{50}) of the rice cultivar "Nippon-bare" seed was 200 Gy with $^{4}He^{2+}$ ions and 40-50 Gy with $^{12}C^{5+}$. In the case of $^{20}Ne^{8+}$ ions, the seeds irradiated at 400 Gy survived, probably due to the thin beam penetration. The LD_{50} of the seeds of the rice cultivar "Hitome-bore" was estimated to be 80 Gy with $^{4}He^{2+}$, 40 Gy with $^{12}C^{5+}$, and 20-30 Gy with $^{20}Ne^{8+}$. Various visible mutant traits were found in the M_2 generation derived from the $^{12}C^{5+}$ ion beams and a gamma rays (Table 1). In general, mutation was induced more frequently at 40-60 Gy with $^{12}C^{5+}$ and at 250-300 Gy with a gamma rays. The average mutation rate by $^{12}C^{5+}$ and $^{4}He^{2+}$ irradiations were comparable to the rate by gamma rays. The mutated traits of 69 lines out of 172 variants selected from the M_2 generation of the cultivar "Nippon-bare" were also recognized in

the M_3 generation and proved to be a genetic mutation (Table 2).

The LD_{50} of the chrysanthemum explants was 20 Gy for the floral petals and 10 Gy for the leaves with $^{4}He^{2+}$, and 15 Gy for both the floral petals and the leaves with $^{12}C^{5+}$. However, the penetration depth of the $^{20}Ne^{8+}$ ion appeared to be so weak that the explants irradiated at a high dose, 400 Gy, retained their viability. The mutation rates of the flower color of the regenerated plants were 21.1, 12.5, 26.8, 7.1, 6.2, and 6.4% from the floral petals and leaves with $^{4}He^{2+}$, $^{12}C^{5+}$ and $^{20}Ne^{8+}$ (Fig. 1). A higher mutation rate and broader flower color spectrum were induced more from the floral petals than the leaves with $^{4}He^{2+}$ and $^{12}C^{5+}$, while no difference in the explants was observed with $^{20}Ne^{8+}$. Complex flower color mutants, distinctive of ion beam induction, were obtained by the three kinds of ion beams; the most were derived from floral petal irradiations.

The optimal irradiation methods were evident in our results and the induced mutants were recognized in rice seeds and cultured chrysanthemum explants using $^{4}He^{2+}$ and $^{12}C^{5+}$ ions. Since distinctive mutants in the chrysanthemums were recognized, we can conclude that ion beams can be utilized as novel mutagens. However, further investigation is required into $^{20}Ne^{8+}$ irradiation.

References

1) S. Nagatomi et al., Breed. Sci., 48(Suppl.1), 220 (1998).
2) S. Nagatomi et al., TIARA Ann. Rep., 6: 127-128 (1997).
3) S. Nagatomi, Seminar for Regional Cooperation in Asia, Bangkok. p. 24-32 (1996).
4) S. Nagatomi, Proc. Rad. Process Symp., 7:97-100(1997).
5) S. Nagatomi et al., Tech. News, Inst. Rad. Breed.,60: 1-2.

Table 1. No. of mutants observed on M2 generation of rice cultivar "Nippon-bare" irradiated with ion beam and gamma ray.

Mutagen	Dose (Gy)	No. of lines	Chloro-phyll	Dwarf	Semi-dwarf	Late heading	Early lethal	Less tiller	Upper tiller	Mal-formed spike	Total	Muta-tion (%)
$^{12}C^{5+}$	20	150	7	4	8	2	0	8	0	0	29	19.3
	40	300	26	11	23	6	6	24	2	0	98	32.7
	60	300	23	7	30	5	4	25	0	3	97	32.3
γ ray	200	150	7	6	15	3	0	10	0	0	41	27.3
	250	150	11	4	10	2	2	13	0	0	42	28.0
	300	150	7	2	15	1	1	12	2	0	40	26.7
	350	150	2	1	10	0	2	9	1	0	25	16.7
Control	0	149	0	0	3	0	0	8	0	0	11	7.4

Table 2. No. of mutants observed on M2 and M3 generations of rice cultivar "Nippon-bare" irradiated with ion beam

Ion beam	Dose (Gy)	No. of lines planed	No. of mutants on M2	No. of mutants on M3	Mutation rate (%)
$^{4}He^{2+}$	100	433	57	15	2.8
	125	179	27	13	7.3
	150	300	58	23	6.7
	200	118	24	16	11.0
	250	29	6	2	6.9

Fig. 1. Mutation rate of flower color on regenerated plants from cultured petal and leaf with ion beams

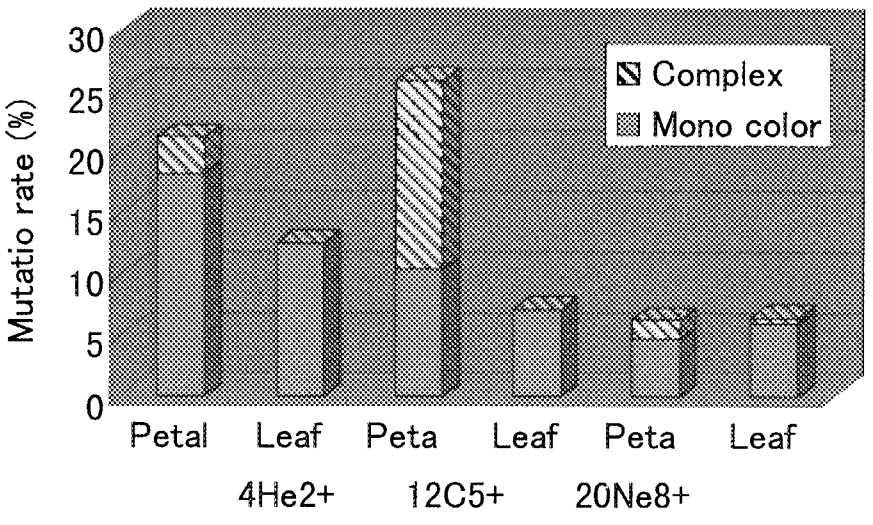

Fig. 2. Flowering of mutant lines with complex-colored flower in the experimental field in November 1997.

2．9 Application of Positron Emitting Tracers for the Study of Living-plant Functions

- Effect of Environmental Condition on theUptake of $^{11}CO_2$ and Translocation of Photosynthetic Products-

S. Matsuhashi, T. Ito, T. Kume, N. S. Ishioka*, S. Watanabe*, A. Osa**, T. Sekine**, H. Uchida***, and A. Tsuji***

Dept. Raidat. Res. Environ. Resources, JAERI/Takasaki, *Dept. Isotope, JAERI/Tokai, **Dept. Mater. Sci., JAERI/Tokai, ***Hamamatsu Photonics Co. Ltd.

【Introduction】 In the study of the response of plant against change of the environmental condition, it is important to know the changes of translocation of the essential materials in plant. We measured the change of translocation of ^{11}C-compound as photosynthetic products of wheat, especialy at ear part which is the sink of photosynthetic products by PETIS (positron emitting tracer imaging system) under the regulated conditions.

【Experiment】 Wheat (cv. Norin 61, harvested in Gumma prefecture) was cultured in commercial nutrient solution (HYPONeX, the ratio of N:P:K=8:12:6) at room temperature. Wheat plants with 5～6 leaves were used for the measurement of ^{11}C translocation from leaf to leaf (4 weeks after germination) and plant with young ear were used for the measurement of ^{11}C translocation from leaf to ear (6 weeks after germination) by PETIS. $^{11}CO_2$ gas was produced from nitrogen gas according to the reaction of $^{14}N(p,\alpha)^{11}C$ by bombardment of $^{1}H^{+}$ beam which was generated from TIARA AVF cyclotron. $^{11}CO_2$ gas was collected by a liquid nitrogen trap and supplied to the leaf of wheat through the cell which enclosed a part of leaf connected to the circulating pipes. Translocation of the photosynthetic materials were measured by PETIS as a movment of ^{11}C.

【Results and Discussion】

(1) Effect of light condition to the translocation of ^{11}C from leaf to leaf of

wheat was analyzed. The photosynthetic products translocated from the leaf supplied $^{11}CO_2$ gas, to the youngest leaf which was covered with alminum foil to keep in dark condition. However, the products did not translocate to the matured leaf coverd with alminum foil.

(2) Effect of light condition at the ear as a sink on the translocation of ^{11}C from leaf to ear was analyzed. Figure 1 shows the imaging pictures of accumulation of ^{11}C into the ear under normal light condition. The photosynthetic products reached to the ear 45min after the supply of $^{11}CO_2$ gas to the leaf, and the amount of ^{11}C was continuously increased during 2hr measurement (Fig. 2, Table 1). On the other hand, the plant which only the ear was covered with aluminum foil, ^{11}C compounds took 75min (30min delayed) to reach the ear from the leaf. The amount of accumulated ^{11}C was only 40% after 2hr those of the wheat in the normal condition. Furethermore, the plant in dark condition during the measurement (light condition was only 10min during the $^{11}CO_2$ gas supply), ^{11}C compounds took 101min (delayed 56min) to reach the ear and the accumulated amount of ^{11}C was only 3% those of in normal condition, respectively. The maximum accumulation speed was calculated from the measurement of the amount of translocated ^{11}C into the ear. The relative speed of translocation in wheat, when the ear was covered or turned light off after 10min $^{11}CO_2$ gas supply were 39% and only 7%, respectively.

From these results, light condition of the ear as a sink organ is quite important to the translocation and accumulation of the photosynthetic products.

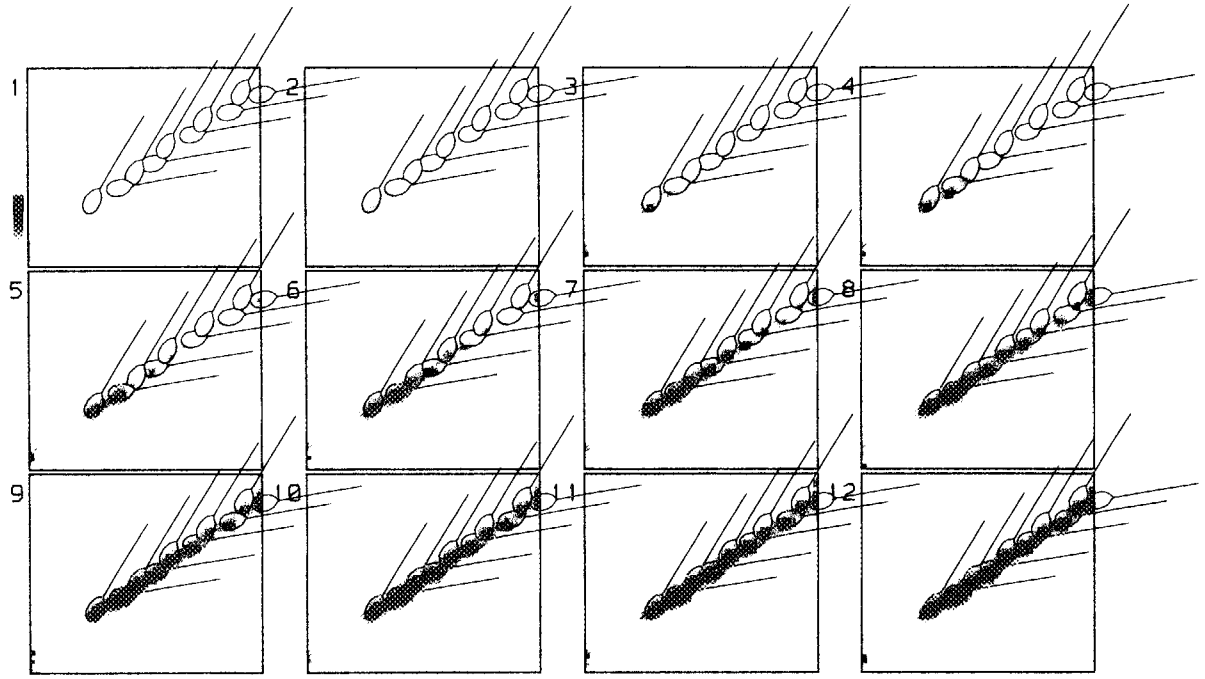

Fig. 1 Translocation of photosynthetic products to the ear (imaging pictures of ^{11}C by PETIS). Wheat under normal condition was supplied $^{11}CO_2$ for 10min. Accumulation of the radio activity, in every 5min from 60min to 120min.

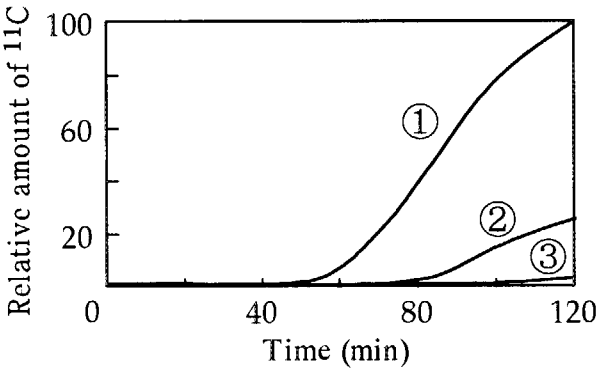

Fig. 2 Accumulation of ^{11}C into ears
① : normal light condition
② : dark only the ear
③ : dark condition after $^{11}CO_2$ supply

Table 1 Maximum accumulation speed of photosynthetic products into ears

	light condition		distance cm	arrival time min	maximum speed (%/10min)
	$^{11}CO_2$ supply	measurement			
ear	blight	blight	46.3	53	100
plant	blight	blight			
ear	blight	dark	40.2	101	7.1
plant	blight	dark			
ear	dark	dark	44.2	79	39.3
plant	blight	blight			

2．10 $^{13}NO_3^-$ uptake- and assimilation-sites on common bean single root visualized by a positron emitting tracer imaging system : A study relating to the locality of *Rhizobium* infection site.

H. Matsunami*1, Y. Arima*1, K. Watanabe*1, N. S. Ishioka*2, S. Watanabe*2, A. Osa*3, T. Sekine*3, H. Uchida*4, A. Tsuji*4, S. Matsuhashi*5, T. Itoh*5 and T. Kume*5

*1:Fac. of Agric., Tokyo Univ. Agric. and Tech., *2:Dept. Radiisotopes, JAERI, *3:Dept. Chem. Fuel Res., JAERI, *4:Hamamatsu Photonics,K.K., *5:Dept. Radiat. Res. Environ. Resources, JAERI

1.Introduction

Common bean is one of the most important legume crop as well as soybean in the world. Efficient utilization of root-nodule functions is much meaningful for establishing sustainable agricultural system. However, it is generally difficult to get high level yield of common bean depending on nodule nitrogen fixation, because nodule activity is insufficient and/or unreliable in the plants grown in fields. [1,2].

With the artificial medium containing little amount of combined nitrogen, common bean plants revealed considerable capacity in nodulation and nitrogen fixation, while growth of the plant was inferior[3,4]. When application level of nitrogen was increased, capacity of nodulation and nodule activity was more sensitively repressed in common bean than in soybean[5]. Results of a experiment, in which plant roots were fed with ^{15}N-nitrate, suggested that such a higher sensitivity of common bean to combined-nitrogen corresponded to higher activity in uptake, reduction and assimilation of ^{15}N-nitrate comparing to that of soybean.

In this study, nitrate uptake- and assimilation-sites were specified on common bean root using ^{13}N and a positron emitting tracer imaging system (PETIS). And then positional relationship of the nitrate uptake- and assimilation-site with the region of just elongating root hair, where *rhizobium* capably initiate infection, was discussed.

2.Materials and Methods

Common bean (*Phaseolus vulgaris* L. cv. Himetebou) were grown for ca. 10 days after sowing in 300 mL pots filled with vermiculite. The pots were supplied with a nutrient solution containing 5 or 60ppm NO_3^--N. The plants were transplanted to the 200 mL plastic bottle

prior to PETIS experiment. One of the lateral roots generating on upper part of the tap root was taken out from the bottle and introduced into a poly-propylene tube filled with ca.7mL of a nutrient solution containing 14nM, 1.4 μ M or 140 μ M of NO_3^- (^{14}N-medium).

^{14}N-medium in the tube was replaced by a corresponding radioactive nutrient solution containing 14nM, 1.4 μ M or 140 μ M of $^{13}NO_3^-$ (ca. 11-16MBq/tube). After feeding the radioactive medium for 2 min, ^{13}N-medium was discarded followed by washing several times with corresponding ^{14}N-medium for 2 min. The tube was filled with renewed ^{14}N-medium, and then imaging process by PETIS was started by 1min time-frame and continued for 30min.

3.Results and Discussion

As shown in Fig. 1, ^{13}N atoms incorporated into the root were acquired by PETIS, and successfully gave their distribution images under different applied concentration of nitrate in the medium. So, PETIS is applicable for plant root studies fed with ^{13}N-medium having wide range of specific activity.

Dense distribution of ^{13}N was located at two positions of 0.5 - 1 and 3 - 5 cm from the root apex. This distribution pattern did not change through detection period, and common in the all plants grown with different concentration of the nitrate in medium (Fig. 1 and Fig. 2). These facts suggest that common bean single root has two sites of active nitrate uptake and assimilation. Because the sites of dense ^{13}N distribution are near or at the region of elongating root hairs, it is likely that *rhizobium* infection is directly affected by nitrate assimilation in common bean roots.

4.Conclusion

PETIS is a powerful tool to obtain direct evidences for location of the site where ^{13}N-nitrate is actively uptaken and assimilated. The sites of nitrate uptake and assimilation are located closely to the site of *Rhizobium* infection in common bean single root.

5.Reference

1)LaRue, T. A. and Patterson, T. G.,1981, *Adv. Agron.*, 34, 15-38.

2)Nishimune, A., Konno, T., Saito, G. and Fujita, I., 1983, *Res.Bull Hokkaido Natl. Agric. Exp. Stn.*, 137, 81-106.

3)Arima, Y., 1993, Jpn.J.Soil Sci. Plant Nutr., 64, 118-125.

4)Piha, M. I. and Munns, D. N., 1987, Plant Soil., 98, 169-182.

5)Arima, Y. and Shirai, M., 1996, Jpn. J.Soil Sci. Plant Nutr., 67, 605-612.

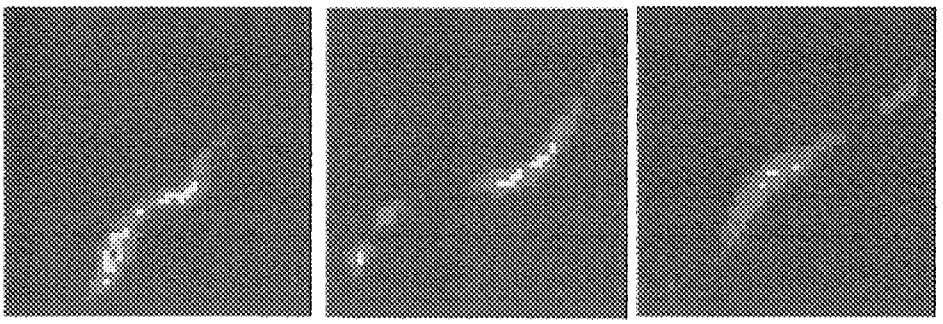

with 14nM NO_3 with 1.4 μ M NO_3 with 140 μ M NO_3

Fig.1 Distribution images accumulated for 30 min by PETIS of ^{13}N atoms incorporated into the root under different applied concentration of the nitrate in medium. The plants were grown in a pot filled with vermiculite for ca 10 days after sowing supplied with a nutrient solution containing 5ppm NO_3^--N.

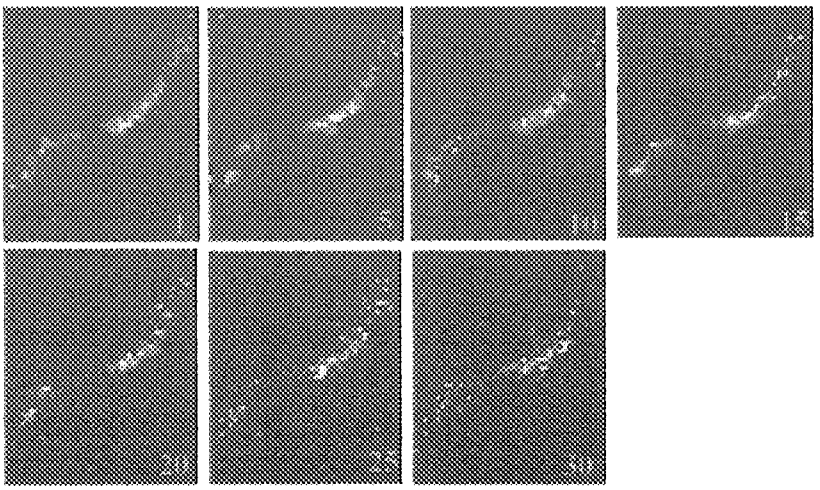

Fig.2 The 1 min time frame distribution images by PETIS of ^{13}N atoms incorporated into the root. Images were shown at 5 min intervals. The plant was grown under the same condition as Fig.1.

2．11 Development of Novel Resistant Lines to Tobacco Yellow Spotted Streak Disease by Ion Beam Irradiation

Tomonori SUZUKI, Hiroshi TANAKA, Toshiake MATSUZAKI,
Atsushi TANAKA* and Hiroshi WATANABE**
JAPAN TOBACCO INC., Leaf Tobacco Research Laboratory,
*Advanced Sci. Res. Center at Takasaki, JAERI,
**Department of Radiation Research for Environment and Resources, JAERI

Introduction

Ion beams have a higher LET than X and gamma rays. The irradiation of ion beams has a high potential of inducing the mutant plants with novel characters which might be impossible to obtain by commonly used mutagens.

Fig. 1 The plant inoculated with PVY-T. Burley 21 (commercial cultivar susceptible to the disease).

Tobacco yellow spotted streak disease (Fig. 1) caused by potato virus Y (PVY) is one of the serious diseases in tobacco cultivation and only limited sources of resistance for the disease are available now. The final goal of this study is to develop the novel resistant lines by ion beam irradiation to tobacco seeds.

Materials and Methods

To make it easier to select the mutant plants with susceptibility gene, six tobacco lines, mainly F1 plants, were used in this study: F1 plants from crosses of Coker 319 ×VAM; Coker 319×Perevi; Burley 21 × VAM and Burley 21×Perevi; inbred plants of Coker 319; and Burley 21. Coker 319 and Burley 21 are commercial cultivars susceptible to the disease. VAM and Perevi are resistant source lines to the disease. The ion beam used was $^{12}C^{5+}$ with the doses of 10 - 80 Gy. Ion beams were irradiated to tobacco seeds of each of these lines.

The survival plants grown from about 13,700 irradiated seeds were inoculated with PVY-T. The plants not attacked by the disease were selected. Visible morphological mutations (leaf size and shape, number of leaves, stalk height and flowers) were investigated. Seeds were gathered from the selected plants. These seeds were sown, their seedling were cultured, and the resistance of the next generation was examined. The

examination of resistance of the next generation was done for 25 plants per line for improvement of reliability.

Results and Discussion

About 13,700 irradiated seeds were sown and a total of 5,579 surviving plants were obtained from these seeds. These survival plants were inoculated with PVY-T and 174 of them were not attacked by the disease. The mutations caused by the ion beam irradiation were observed more in flowers than in the elements related to vegetative growth, such as leaf size and shape, number of leaves and stalk height (Table 1). The seeds were collected from the 126 plants not attacked by the disease.

As a result of the PVY-T inoculation examination of the F2 generation of those 126 plants which produced seeds, one resistant line with no symptoms of the disease (Fig. 2) and three lines showing the delayed occurrence of the disease (Table 2) were obtained. These lines had less pollen and more leaves than the commercial cultivars in the greenhouse. There is the need of investigating these plants in a field.

In the future, the four resistant lines obtained in the experiment will be cultivated in a field to investigate their cultivation characters. In addition, several individuals having less variations yet adequate resistance will be obtained by the irradiation of ion beams of the dose more suited to the induction of mutation ($^{12}C^{5+}$: 10 - 40 Gy, $^{4}He^{2+}$: 100 - 200 Gy)[1] or a lower dose, and additional promising lines will be selected from these individuals.

Reference

1) T.Suzuki et al., TIARA Ann. Rep., 97-015: 54-56 (1997)

Table 1 Number of mutants of the plants not attacked by the disease by the dose of $^{12}C^{5+}$ irradiation

Dose (Gy)	Leaf shape		No. of leaves		Stalk height		Flower			Seed		Total	No. of the lines whose F2 generation shows resistance
	N	A*1	N	A	N	A	N	A	N b*2	G	N*3		
10	19	0	19	0	12	7	14	5	0	19	0	19	0
20	26	2	27	1	19	9	12	16	0	26	2	28	1
30	23	5	27	1	12	16	16	9	3	24	4	28	1
40	37	14	42	9	23	28	19	29	3	36	15	51	1
50	9	6	12	3	7	8	3	11	1	7	8	15	1
60	7	12	18	1	10	9	2	17	0	11	8	19	0
70	5	6	9	2	4	7	0	10	1	3	8	11	0
80	2	1	2	1	0	3	0	3	0	0	3	3	0
Total	128	46	156	18	87	87	66	100	8	126	48	174	4

The morphology was investigated for the 174 plants (No. of plants not attacked by the disease / No. of surviving plants / No. of sowed seeds = 174/5579/13700) which had the PVY-T inoculation examination in the present age (F_1) and were not attacked by the disease.
*1: N:normal, A:abnormal
*2: N:normal, A:abnormal, N b:no blooming
*3: G:gathered, N:not gathered

Table 2 Lines whose F2 generation showed resistance

Line	Dose	Tobacco yellow spotted streak disease
Burley 21×Perevi F2	$^{12}C^{5+}$: 40 Gy	Resistant
Coker 319×Perevi F2	$^{12}C^{5+}$: 20 Gy	Occurrence of the disease delayed
Coker 319×Perevi F2	$^{12}C^{5+}$: 30 Gy	Occurrence of the disease delayed
Coker 319×Perevi F2	$^{12}C^{5+}$: 50 Gy	Occurrence of the disease delayed

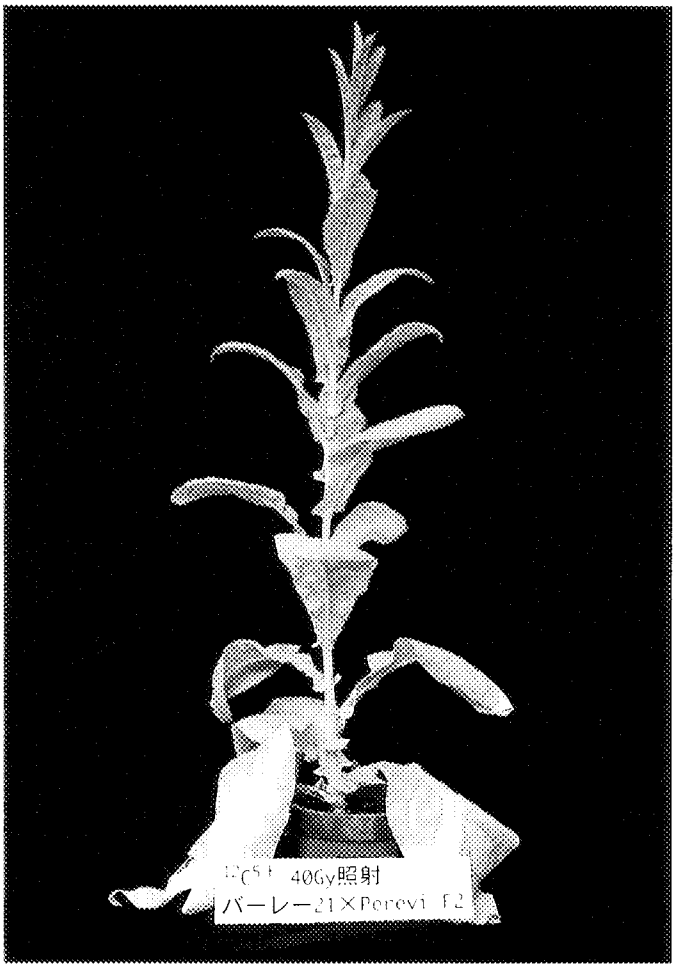

Fig.2 The plant inoculated with PVY-T.
The resistant individual which was created by the experiment.
The F2 generation of Burley 21×Perevi F1 with $^{12}C^{5+}$ 40 Gy irradiation.

2. 12 Analysis of nitrate absorption and transport in soybean plants with $^{13}NO_3^-$

T. Sato, N. Ohtake, T. Ohyama, N. Ishioka*, S. Watanabe*, A. Osa*, T. Sekine*, S. Matsuhashi**, T. Ito**, T. Kume**, H. Uchida*** and A. Tsuji***

Facul. Agric., Niigata Univ. *Dept. Radioisotopes, JAERI, **Dept. Radiat. Res. Environ. Resources, JAERI, ***Hamamatsu Photonics Co.

1. Introduction

Nitrogen is an essential element of plants, and the availability and utilization is stringently related to the growth, yield and quality of crops. The studies of N absorption, transport and metabolism are very important topics in the field of plant nutrition. Radioactive ^{13}N (half life 10 min) and stable isotope ^{15}N are available for the tracer studies of plant N nutrition. Recently, the positron emitting tracer imaging system (PETIS) has been devised for observing two dimensional image of positron emittion in plant part supplied with the positron emitting atoms such as ^{13}N, ^{11}C and ^{18}F produced by cyclotron.

In this report, ^{13}N labeled nitrate was supplied to the culture medium, and the distribution of ^{13}N in the petiole and leaves was observed by PETIS or bioimaging analyzer (BAS).

2. Experimentals

Soybean plants were cultivated with hydroponics and young seedlings were used for the experiments. $^{13}NO_3^-$ was produced from $^{18}O(p, \alpha)^{13}N$ reaction by TIARA AVF cyclotron. $^{13}NO_3^-$ solution was added to the culture solution, and the transport and distribution of the absorbed ^{13}N was observed in the first trifoliate leaf by PETIS (Fig. 1). Real time observation was conducted for 40 min after $^{13}NO_3^-$ addition within the detection area of 48 mm × 50

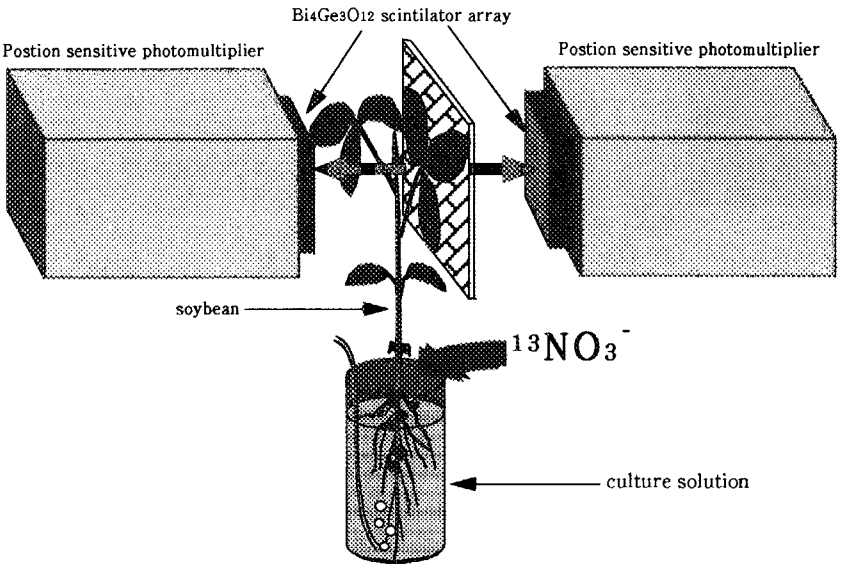

Fig.1 PETIS (Positron-emitting tracer imaging system)

mm square.

In the first experiment, the nodulated soybean plants (cultivar Williams) inoculated with *Bradyrhizobium japonicum* (strain USDA 110) were supplied with $^{13}NO_3^-$ in the rooting medium and the distribution of the positron emitting atoms (^{13}N) was observed by PETIS. The plants were pretreated with or without 1 mM NO_3^- for 1 day before ^{13}N supply. The $^{13}NO_3^-$ were added to the culture solution containing 0.1 mM NO_3^- or 1 mM NO_3^- as carrier.

In the second experiment, nodulating (T202) and non-nodulating (T201) isolines of soybean were cultivated and the transport and distribution of ^{13}N in the leaves were compared between two isolines.

In the third experiment, one leaflet of the first trifoliate was covered with aluminum foil or plastic vinyl sheet, and the effect on ^{13}N transport was observed by PETIS. After 40 min observation by PETIS, the plant was subjected to bioimaging analysis by BAS.

3. Results and Discussion

In experiment 1, the imaging picture by PETIS was monitored every minute, but the summation of 5 min images are shown in Fig. 2. The ^{13}N image appeared in the petiol at first between 6 and 10 min interval. The count was gradually increasing in the petiole until the end of the treatment. After 11 min ^{13}N was also detected in the leaf blade. After 26 min, back ground spots became remarkable especially in the peripheral part possibly due to the artifact of calibrations for decreased radioactivity. Therefore, the observation by PETIS for this type of experiment was done in 40 min.

The total count of detected area was plotted for each plant with various treatment (Fig. 3A). The total count were markedly varied among plants and the consistent tendency was not observed in nitrate pretreatment and nitrate carrier concentrations (0.1 mM or 1 mM). In order to compare the relative patterns of absorption such as time lag and linearity, the relative count was calculated as Fig. 3B. In this figure, most of the plants transported ^{13}N to the leaves linearly after about 5 ~ 10 min time lag. The variation in total

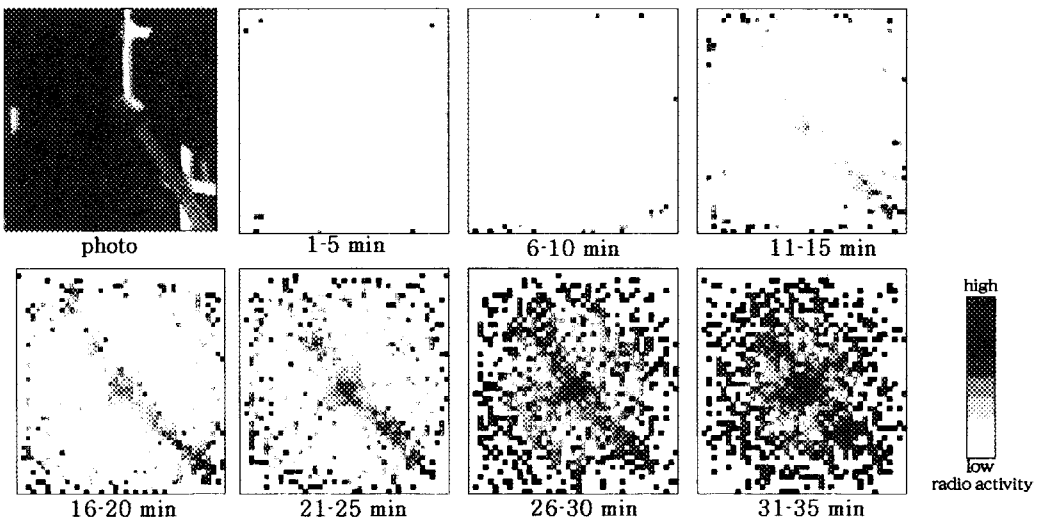

Fig. 2 The imaging picture by PETIS.

count may be due to the difference in NO_3^- absorption activity, NO_3^- transport to the first trifoliate, or the other physiological differences.

In experiment 2, the total count increased linearly after about 5 min time lag (Fig. 4). The pattern of ^{13}N count was almost identical between nodulated (T202) and non-nodulated (T202) plants. Based on this result, it was suggested that nodulation might not affect the NO_3^- absorption in roots and transport to the leaves.

In the experiment 3, ^{13}N transportation to the leaflet covered with aluminum foil or plastic vinyl was severely inhibited compared with the leaflets without covering, as shown in BAS image (Fig. 5). The aluminum foil interrupt light but vinyl sheet does not. So the lack of ^{13}N transport to the covered leaflet may be due to the lack of transpiration. Hence, the initial transport of nitrate derived N to the leaflet may depend on the transpiration stream through stomata.

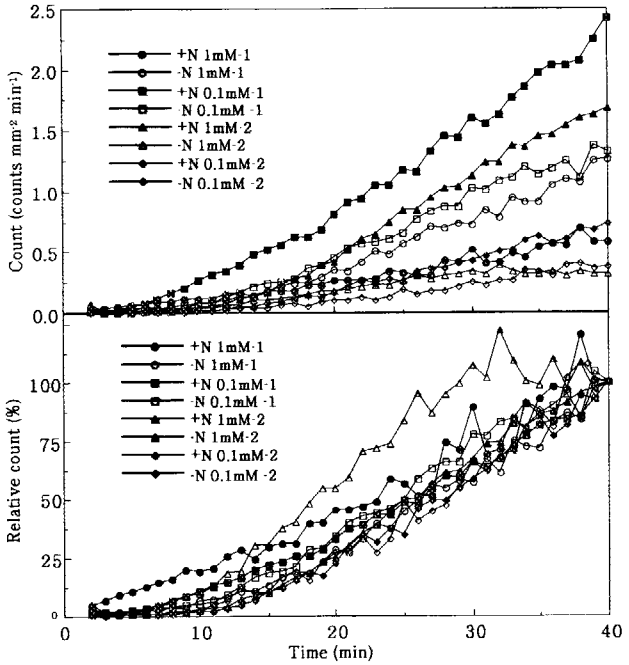

Fig. 3 The total count(A) and the ralative count of detected area ploted for each plant with various treatment.

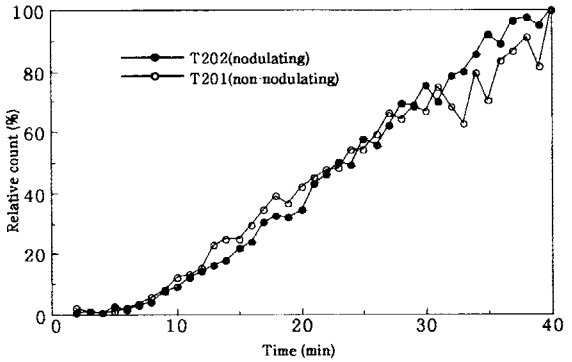

Fig. 4 The relative count of detected area ploted for nodulating (T202) and non-nodulating(T201) soybean.

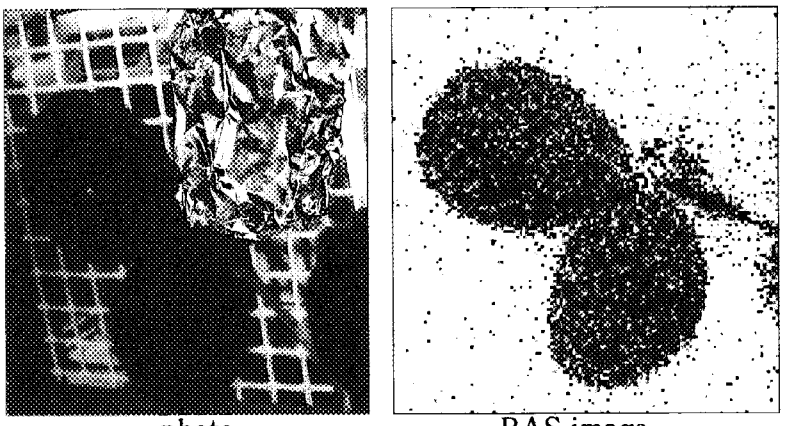

photo BAS image

Fig. 5 The photo of detected area and the BAS image.

2. 13 Mutation Induction on Protoplasts of Chrysanthemum with Irradiation of $^4He^{2+}$ Ion Beams

T. Nakahara[1], K. Hirashima[1], M. Koga[1], A. Tanaka[2],
N. Shikazono[2] and H. Watanabe[2]
Fukuoka Agricultural Research Center[1]
Department of Radiation Research for Environment and Resources, JAERI[2]

1. Introduction

Chrysanthemum is one of the most economically important horticultural plant and many cultivars have been developed. Most of chrysanthemum cultivars have been improved by intra-specific crosses or bud mutation. Recently tissue culture techniques of chrysanthemum such as floral petal culture and leaf protoplast culture were established. Somaclonal variations occured in the regererated plants through tissue cultures were used to develop new cultivars. But, the chromosome number of the regenerated plants varied from parent and these characteristics are not for practical use. Then new cultivars developed by the combined method of gamma ray irradiation with floral petal culture[1,2]. Furthermore, Nagatomi[3,4] showed that ion beams were effective to induce mutation of chrysanthemum.

In this study, we conducted irradiation of the leaf protoplasts of chrysanthemum with $^4He^{2+}$ ion beams to regenerate mutant plants.

2. Experimental methods

Chrysanthemum cultivar, 'Shuho-no-chikara' (White flower) was used for the experiments. The protoplasts were isolated from aseptic plant established from the meristem tip culture. One gram of leaf was digested for 16 h at 25°C in 10 ml of enzyme solution which consisted of 0.1% Pectolyase Y-23, 0.5% Cellulase Onozuka RS, 0.1% Driselase and 0.5 M mannitol. After digestion, cell suspension was sieved (0.05mm pore size) and the filtrate was centrifuged at 100xg for 5 min. The protoplasts were resuspended in 10 ml of 0.57 M sucrose solution and centrifuged at 100xg for 10 min. The floated protoplasts were washed twice with 0.5 M mannitol solution. Freshly isolated protoplasts were diluted to $5x10^4$cells/ml with NN67 medium (Nitsch and Nitsch) supplemented with 0.4 M sucrose, 1 mg/l NAA (Naphtalene acetic acid) , 0.5 mg/l BA (Benzylaminopurine) . One-tenth ml of the protoplast suspension was spread on 2 ml of the same medium solidified with 0.8% agarose in petri dish (35x10 mm) , which were covered with Kapton film. The protoplasts were

irradiated with 50 MeV $^{4}He^{2+}$ ion beams from the AVF cyclotron in JAERI. After irradiation, the protoplasts were transferred to the new petri dish which contained 1 ml of the same NN67 medium. At 7 and 14 days after irradiation, 1 ml of the same medium containing 0.2 M sucrose, and 2 ml of the same medium containing 0.1 M sucrose were added, respectively. At 21 days after irradiation, calli were transferred to the MS medium (Murashige-Skoog) containing 30 g/l sucrose, 0.5 mg/l NAA and 2 mg/l BA, and solidified with 2 g/l gellan gum. After 4 weeks, the protoplast-derived calli were transferred for shoots induction onto MS medium supplemented with 30 g/l sucrose, 2 mg/l BA, 0.2 mg/l GA_3 (Gibberellic acid) and solidified with 2 g/l gellan gum at 4 weeks intervals. The cultures were maintained at 25°C under 16 h photoperiod (3,000 lux) .

3. Results and Discussion

The dose response curve of callus induction derived from the protoplast irradiated with $^{4}He^{2+}$ ion beams was shown in Fig.1. According to the increase of dose from 2 Gy to 10 Gy, the callus induction decreased gradually. At higher than 10 Gy, the callus induction decreased acutely and only few calli were induced at 20 Gy. No callus was induced at higher than 30 Gy. The LD_{50} was estimated to be existed between 10 Gy and 20 Gy. The evaluation of more detailed response curve of callus induction and traits of the regenerated plants are in progress.

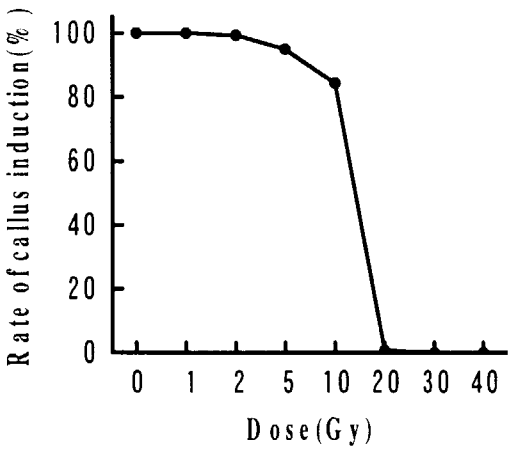

Fig. 1. The dose response curve of protoplast irradiated with $^{4}He^{2+}$ ion beams. The number of callus were estimated at 8 weeks after irradiation. Average values of three replications were expressed as percent of non-irradiated control.

References

1) S.Nagatomi et al., Breed. Sci. 44 (Suppl.1) :292 (1994) .
2) S.Nagatomi et al., Breed. Sci. 46 (Suppl.1) :62 (1996) .
3) S.Nagatomi, A.Tanaka, A.Kato, H.Watanabe and S.Tano, TIARA Annual Report 5:50-52 (1996)
4) S.Nagatomi, A.Tanaka, H.Watanabe and S.Tano, TIARA Annual Report 6:48-50 (1997)

2．14 Breeding new shiitake(*Lentinus edodes*) variety at high temperature using ion beam irradiation.

H. Akaishi, N.Nakahara, S. Tanimoto, I. Narumi*, M. Kikuchi* and H. Watanabe*

Research and Development Division, Mori and Company, LTD,
*Department of Radiation Research for Environment and Resources, JAERI

1.Introduction

Shiitake(*Lentinus edodes*) is cultivated at all seasons. But it is difficult to obtain the high quality mushroom in summer. Ion beams, which belong to high LET radiation, are considered to be an efficient mutagenic agents applicable to mutation breeding of shiitake. The present studies were initiated aiming to obtain high quality mutant mushroom at high temperature by ion beam irradiation. In this paper, we report the survival rate after ion beam irradiation of shiitake protoplasts.

2.Material and Method

(1) Protoplast isolation

Liquid-cultured mycelia of shiitake were incubated in an enzyme solution at 30℃ for 4hr shaking at 200 rpm. The enzyme solution at pH 5.5 consisted of Cellulase(1.0%) and mannitol(0.6M).The protoplasts were washed 3 times with mannitol solution by centrifugation at 2000 rpm.

The density of the protoplast suspension was adjusted to about 1 x 10^6 per ml for the following experiment.

(2)Irradiation

The protoplasts suspension was put into a petri dish of 50mmØ, and irradiated by ion beams from the AVF cyclotron in JAERI. The ion beams used were 220 MeV $^{12}C^{5+}$ with the dose of 5-100 Gy and 50 MeV $^{4}He^{2+}$ with the dose of 5-250 Gy.

(3)Protoplast Culture

The protoplasts were incubated at 25℃ for 6 days.

3.Results

The Table shows the survival rates of the protoplasts irradiated with C and He ions. The survival rates were expressed as a percent of the non-irradiated control(100%).

The survival rates after $^{12}C^{5+}$ irradiation were about 90%, 35% and almost none with the doses of 5-10 Gy, 50 Gy and 100 Gy respectively. The survival rates after $^{4}He^{2+}$ irradiation were 92%, 34% and 3% with the doses of 25 Gy, 125 Gy and 250 Gy respectively.

It is concluded from these results that the best doses for obtaining mutants at high temperature with minimum change in other characteristics will be 5-10 Gy of $^{12}C^{5+}$ or 25 Gy of $^{4}He^{2+}$.

Further experiments in detail on biological effects of ion beams are in progress.

Table Survival rates of protoplast irradiation with C ions and He ions.

Dose (Gy)	Survival rates(%)*	
	C ions	He ions
0	100	100
5	87	110
10	92	98
15	71	n.d.
20	62	n.d.
25	58	92
50	35	71
75	10	78
100	0	56
125	n.d.	34
150	n.d.	26
200	n.d.	11
250	n.d.	3

* : The survival rates were expressed as a percent of the non-irradiated control.

n.d. : no data

2．15 Mutation induced by ion beams (C^{5+} and He^{2+}) irradiation in wheat

T.Takahashi,A.Tanaka* and H.Watanabe*
Gunma Agricultural Experiment Station, *JAERI, Takasaki, Biotech, Lab.

1 Introduction

Ion beams, which belong to high LET (linear energy transfer) radiations, are considered to be efficient mutagenic agents applicable to mutation breeding of wheat plant. The present studies were initiated aiming to obtain mutants with practically useful traits. However , little has been studied the effect of ion beam irradiation on induction of mutaion in wheat. Therefore, we have examined emergence rate of seedling after irradiation by C^{5+} or He^{2+} ions beam .

2 Materials and Methods

Seeds of a wheat cultivar ,`Gunma W 2' of Tritcum aestivum were used in this study. Seeds were irradiated with ion beams (220 MeV C^{5+} and 100 MeV He^{2+}) at various doses (5 to 20 Gy and 25 to 300 Gy) .The irradiated seeds were sown and grown in a field.

3 Results and discussion

C^{5+} ion beam

Seeds which received higher than 10 Gy showed a delay in emergence of 5 to 7 days. Fig. 1 and Table.1 shows that emergence rate of seedling from the irradiated seeds at various doses. At 10 Gy irradiation, 100% of seeds could emerge the seedling and have grown to normal, however, culum length became shorter. We are performing morphological studies to investigate the characteristics for cultivation of the mutants.

He^{2+} ion beam

Seeds which received higher than 200 Gy showed a delay in emergence of 3 to 5 days. Fig. 2 and Table. 1 shows that emergence rate of seedling from the irradiated seeds at various doses. less than 150 Gy irradiation, about 100% of the seeds could emerge the seedling and have grown to normal, however, culum length became shorter. We are performing morphological studies to investigate the characteristics of the mutants.

Table 1. Result of growth

Ion beams	C^{5+}					He^{2+}						
Dose(Gy)	0	5	10	15	20	25	50	100	150	200	250	300
Heading date	20 Apr	22 Apr	23 Apr	23 Apr	ns	21 Apr	21 Apr	21 Apr	22 Apr	22 Apr	23 Apr	ns
Culm length(cm)	78	71	63	63	52	72	75	70	72	64	67	56
C V %	3.0	3.1	4.2	2.7	4.2	2.6	3.7	2.9	2.3	3.6	2.4	2.8
Panicle length(cm)	9.3	9.4	8.7	9.5	7.6	9.7	9.8	8.7	9.6	8.1	10.0	9.1
C V %	4.5	8.8	9.2	6.3	10.2	8.2	5.6	8.9	8.7	9.0	5.7	8.8

ns : after 10.May
CV: Conefficient of variation

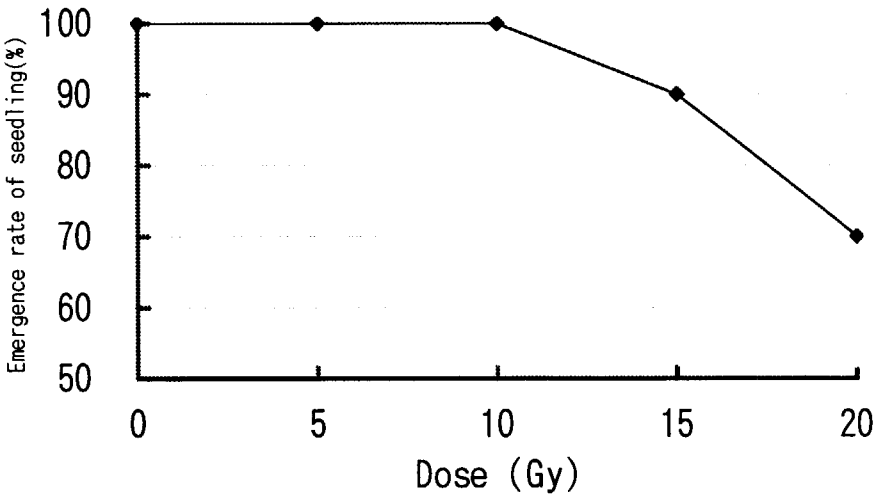

Fig.1 Effect of C^{5+} ion beams on dose response of emergence rate of seedling .

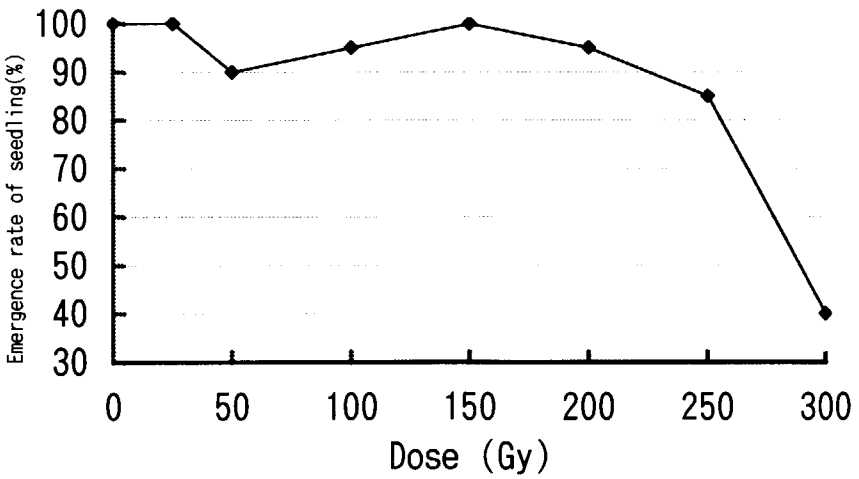

Fig.2 Effect of He^{2+} ion beams on dose response of emergence rate of seedlings .

2．16 Induction of Mutation in Strawberry and Hydrangea by Ion Beam Irradiation. Effects of Ion Beam Irradiation on Shoot Regeneration of Strawberry Callus and Germination of Hydrangea Seed.

Nobuhiro KUDO[1], Masahide IIZUKA[1], Yasuo KIMURA[1], Atushi TANAKA[2], Naoya SHIKAZONO[2] and Hiroshi WATANABE[3]

[1]Gumma Horticultural Experiment Station,

[2]Advanced Sci. Res. Center at Takasaki,

[3]Department of Radiation Research for Environment and Resources, JAERI.

Introduction

Ion beams, which have a higher linear energy transfer (LET) than X and gamma rays, are one of the efficient mutagenic agents, which is applicable to mutation breeding of many horticultural plants. However, there have been few studies on the effects of ion beam irradiation on the induction of mutation in fruits, vegetables and ornamental plants.

At present paper, we examined the effects of ion beam irradiation on shoot regeneration of strawberry callus and germination of hydrangea seed.

Materials and Methods

Strawberry

GSC-1 line of strawberry (Fragaria ×anannasa) was used in this study. Leaf segments were cultured on the modified Murashige and Skoog's (MS) medium supplemented with 0.1 mg/l 2.4-D and 1mg/l BA for callus induction. Callus proliferated on the cut end of the segment 30 days after culture. Formed callus was cut into small pieces and transferred to the fresh medium. The callus was irradiated with ion beam (100 MeV $^4He^{2+}$) at various doses (10 to 200 Gy). After irradiations the callus was transferred to the fresh medium, Threshold of injury of the callus growth was determined and the efficiency of shoot regeneration from the irradiated callus was examined. Regenerated shoots were excised and transferred to the hormone-free rooting medium. Plantlets were acclimatized and grown in a greenhouse and morphological changes of the plantlets were observed.

Hydrangea

Seeds of two cultivars, 'Hanuna' and 'Blue diamond' of Hydrangea macrophylla were used in this study. Seeds were irradiated with $^4He^{2+}$ ions (100 MeV) at various doses (10 to 50 Gy). Surface of irradiated seeds were sterilized with 70% ethanol and 1% sodium hypochlorite solution and washed three times in sterile water. They were inoculated on a modified MS medium without plant growth regulators and cultured at 25 °C and 16 hr-photoperiod. Germination rate was examined 30 days after culture. Survived seedlings were acclimatized and transferred in soil. Morphological changes of the seedlings were investigated.

Results and Discussion

Strawberry

Regeneration frequency of calli decreased as dosage increased (Fig. 1). Irradiation at 100 Gy suppressed shoot regeneration almost completely and calli irradiated at higher than 150 Gy lost regeneration capacity. Regeneration frequency of control calli which received no irradiation expressed 90 to 80%. Calli which received higher than 25 Gy had tissue damage, showing a delay in shoot regeneration. Plantlets from higher dosage (>75Gy) showed morphological abnormality. We are currently screening mutants resistant to the serious fungal pathogen (Glomerella cingulata).

Hydrangea

Seeds which received higher than 20 Gy showed a delay in germination of 3 to 5days. The rate of germination decreased with increasing dosages. Seeds irradiated at dosage of 50 Gy lost germination capacity. No difference between cultivars was obsved at germination rate of the irradiated seeds. Germination rate of the seeds that received no irradiation display about 85%. Germination of the control seeds occurred about 5 days after sowing. Suzuki et al. (1997) found that less than 300 Gy irradiation of $^{4}He^{2+}$ ion beam did not inhibit germination of tobacco seeds. Hydrangea seeds are probably more radiosensitive than tobacco seeds. Dwarf type and branch type mutants were obtained from irradiated seeds with 20 and 30 Gy. Other types of morphological changes were not observed. A result obtained from this experiment showed threshold of inury of the seed was 30 Gy. It has been estimated that 30 Gy was the maximum dosage of $^{4}He^{2+}$ ions that could be tolerated by hydrangea seeds. We would decrease irradiation dosage to less than 30 Gy that are less injurious to the seeds. We are investigating horticultural values of the mutants.

References

1.T. Suzuki et al. TIARA Ann. Rep., 15:54-59. (1997)

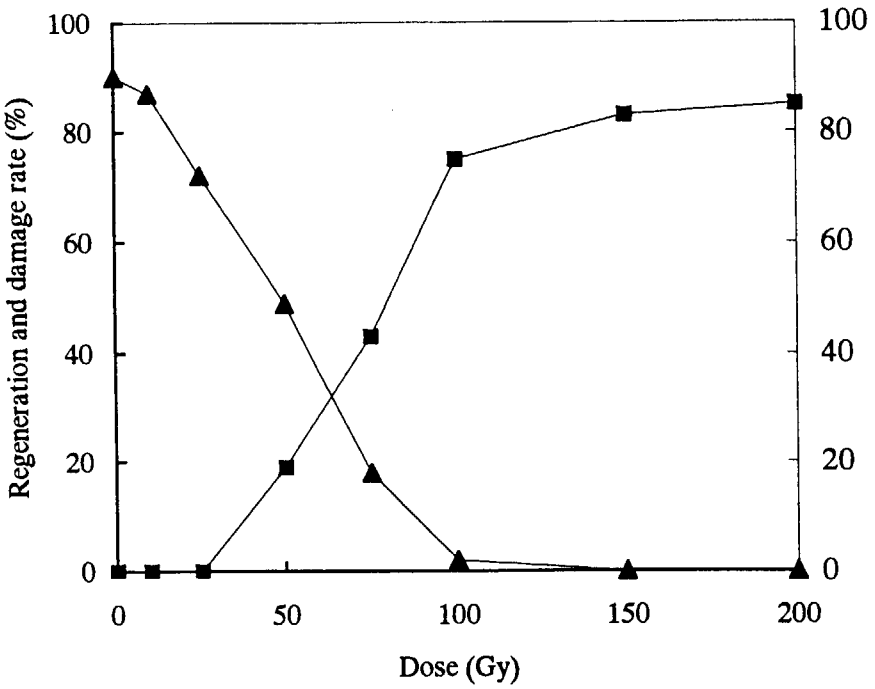

Fig. 1 Dose response of shoot regeneration of strawberry callus.
Regeneration rate (▲). Damage rate (■).

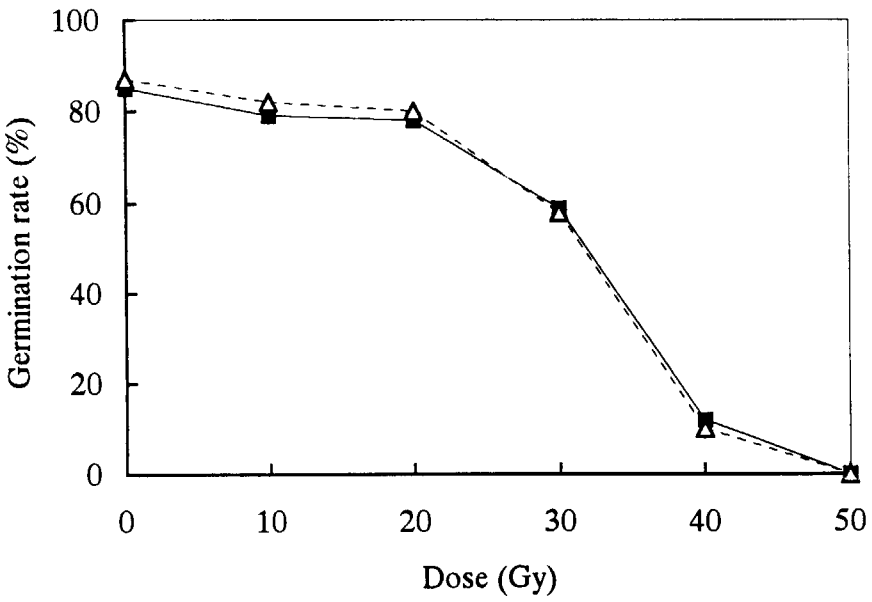

Fig. 2 Dose response of germination of hydrangea seed.
'Haruna'(△), ''Blue diamond(■).

2．17 Effects of Ion Beams on The Seed Germination and In Vitro Regeneration of Creeping Bentgrass

Yasuyuki Ito, Atushi Tanaka*, Naoya Shikazono*, Hirosi Watanabe*, Mari Ohara and Azusa Fujiie
Chiba Prefectural Agricultural Experiment Station and
*Advanced Science Research Center at Takasaki, JAERI.

1. Introduction

Creeping bentgrass (*Agrostis palustris Huds*), the most commonly used turfgrass on golf course putting greens, is highly susceptible to pests, diseases and unwanted weeds. They are usually controlled by agricultural chemicals, occasionally causing the problems of degrading the water quality in the surrounding area, etc.

Threfore, the production of bentgrass varieties with disease and pest-resistance, will be of significant value to the turfgrass manegers and also to the neighbors.

To date many investigations on the effects of several mutagens have been reported for inducing useful mutation in plants. For example, evergreen mutant lines were selected in Manila grass (*Zoysia matrella*) by chronic irradiation with gamma rays. Since ion beam has a higher LET than X-rays and gamma rays, it was expected to enlarge the mutation frequency and spectrum, and to minimize unexpected variation in mutation breeding of the agricultural crops.

A regenerable embryogenic tissue cultures of creeping bentgrass have been developed, and we have already obtained protplast-to-plant system applicapable to gene transfer.

In this paper, we report the effects of heavy ion irradiation on germination of the seeds and in vitro regeneration from suspension cultures of creeping bentgrass.

2. Materials and methods

1) *Plant materials*

The mature dry seeds and embryogenic suspension cultures were used as irradiation target materials. More than 2,000 seeds of bentgrass cultivar 'Penncross' were sandwiched between kapton films (50 × 50mm, 7.5 μ m thickness) to make a monolayer of seeds for homogeneous irradiation. Suspended calli of brown patch disease (caused by *Rhizoctonia solani*)-resistant cultivar 'Chiba green B-1' which were plated on gelrite solidfied MS medium in plastic plates (ϕ 50mm) and covered with sterilized kapton films were also used.

2) *Irradiation*

The Irradiation Apparatus for Seed, connected to a vertical beam line of the AVF-cycrotoron in JAERI, was used for the 220MeV carbon and 50MeV helium ion irradiation. All irradiations to the seeds and calli were performed under atmospheric pressure, within about three minutes for all doses.

3) *Seed germination and in vitro*

regenaration

After irradiation, seed germination and in vitro regenaration rates were determined. Each of a hundred seeds from three independent experiments with three replicates at each dose, was sown in soil and germinated in greenhouse under natural day light at 15-20 ℃ for 14 days.

Irradiated calli were transferred onto the fresh regenaration medium (1/2MS + 1.0mg/lBAP + 0.8%gelrite) in plastic petri dishes and incubated under fluorescent light (16h/day photoperiod) at 25 ℃ for 4 weeks.

3. Results and discussion

1) *Seed germination*

The effects on the germination of creeping bentgrass seeds by irradiation of carbon and helium ions were compared. Tables 1 and 2 show the degrease of seed germination rates as dose levels increase. Some differences were observed between each seed lot in germination rates, but the tendency of suppression compared to unirradiated control was similar in all experiments.

Carbon ions of up to about 50 Gy had almost no effect on germination rate. But with above 100 Gy, suppression of germination by irradiation was apparently observed. So the median lethal dose with carbon ion was estimated to be about 75-100 Gy. While, in helium ion, it was estimated 200-500 Gy. These results were similar to those results in tabacco seeds. The survival seedlings grew normally, except delayed growth in initial stage at higher dose irradiation, but recovered later.

The irradiated seeds will be used for pathogen inoculate examination in the test tubes for screening the useful mutation.

2) *Regenaration from suspension cultures*

In the case of calli, they appeared to be more sensitive compared to the seeds. Even 5 Gy of carbon ions affected regenaration rate of 'Chiba green B-1' calli.(Table 3) According to incresing of dose, the regeneration rates did not decresed. 62.7% relative regeneration rate was obtained at the maximum of 100 Gy dose. At this time, optimum dose level was not obtained in the case of carbon ion.

In contrast, as the dose increased, regeneration rate decresed in the case of helium ion. An apparant effect was recognized at 20 Gy, and very few regenerants were obtained at 50 Gy.(Table 4) The median lethal dose was estimated to be about 10-20 Gy.

By combining in vitro culture and heavy ion beam irradiation, it mihgt be expected to enlarge the mutation frequency.

References

1) Y.Asano, Y.Ito, M.Fukami, M.Morifuji, and A.Fujiie, *International Turfgrass Society Reserch Journal*, vol. 8, 261-267 (1997)

2) S.Nagatomi, K.Mitui, K.Miyahara, *Institute of Radiation Breeding Technical News*, No.44,(1993)

3) T.Suzuki, H.Tanaka, T.Matsuzaki, A.Tanaka and H.Watanabe, *TIARA Ann. Rep. 1996*, 54-56(1997)

4) A.Tanaka, N.Shikazono, Y.Yokota, H.Watanabe and S.Tano, *Int. J. Radiat. Biol.*, 72, 121-127(1997)

Table 1 Effect of carbon ion beam on germination of bentgrass seeds

Dose (Gy)	Germination rate (%)		
	Exp. 1	Exp. 2	Exp. 3
0	95.3 (100)	43.8 (100)	88.3 (100)
5	90.8 (95.3)	37.4 (85.4)	—
25	94.1 (98.7)	40.0 (91.3)	83.3 (94.3)
50	90.0 (94.4)	40.0 (91.3)	80.2 (90.8)
75	—	—	58.1 (65.8)
100	39.3 (41.2)	17.1 (39.0)	16.6 (18.8)
150	—	—	0 (0)
200	0.1 (0.1)	0 (0)	—

( ) : Relative germination rate to control

Table 2 Effect of helium ion beam on germination of bentgrass seeds

Dose (Gy)	Germination rate (%)		
	Exp. 1	Exp. 2	Exp. 3
0	92.1 (100)	38.1 (100)	84.9 (100)
10	91.7 (99.6)	31.4 (82.4)	90.8 (106.9)
30	93.2 (101.2)	37.4 (99.2)	—
100	90.6 (98.4)	36.2 (95.0)	81.8 (96.3)
200	92.2 (100.1)	35.0 (91.9)	74.0 (87.2)
500	55.1 (59.8)	4.4 (11.5)	0.8 (0.9)
1000	—	—	0.3 (0.4)

( ) : Relative germination rate to control

Table 3 Effect of carbon ion beam on regeneration of bentgrasscallus

Dose (Gy)	Regeneration rate (%)
0	61.8 (100) ± 6.1
5	31.4 (50.9) ± 3.0
10	29.4 (47.6) ± 6.9
25	54.9 (88.8) ± 5.2
50	44.8 (72.5) ± 8.3
100	38.8 (62.7) ± 2.5

( ) : Relative regeneration rate to control

Table 4 Effect of helium ion beam on regeneration of bentgrass callus

Dose (Gy)	Regeneration rate (%)
0	65.6 (100) ±29.0
10	53.5 (81.6) ± 4.9
20	15.1 (23.0) ± 4.4
50	2.2 (3.3) ± 2.0
100	2.4 (3.7) ± 1.4
200	2.3 (3.4) ± 0.5

( ) : Relative regeneration rate to control

2.18 Induction of Somatic Mutation by Ion Beam Irradiation in Lethal Chlorophyl Mutant

M. Maekawa, A. Tanaka* and N. Shikazono*

Res. Inst. for Biores., Okayama University. *JAERI/Takasaki

1. Introduction

So far, any transpozons (movable elements) have not been discovered in rice. If endogenous transpozon were discovered in rice, it could be used easily as a powerful tool for gene-tagging in open environments. As *Mu* in maize[1], transpozons may be found in mutagenized rice. As ion beams are a type of high linear energy transfer (LET) radiation and can deposit high energy on a target compared to low LET radiations, the novel mutants or larger deletions are expected to be induced by ion beam irradiation[2]. So, it is expected that transpozon may be induced by ion beam irradiation. Visualization of transpozon activity is made by variegation in chlorophyll mutant or anthocyanin accumulation. Maekawa[3] found a variegated chlorophyl mutant in F2 of the cross between distantly related rice varieties. Although a near isogenic line (NIL) for this mutant gene with T-65 genetic background was bred, this line did not show any variegations through generations. So, if variegation could be induced by mutation in this NIL, it is highly expected that this mutant line carries transpozon. Thus, this study aims to induce somatic mutation at M1 in this chlorophyl mutant line by ion beams.

2. Experimentals

As a chlorophyll mutant (referred yl) is highly lethal, large amount of mutant seeds enough for inducing mutation at M1 can not be obtained. So, a single heterozygote (Cr14-1) for mutant gene was ratooned and large amount of F2 seeds were yielded for irradiation. Ion beams used were Helium and Carbon. Irradiated seeds were sterilized with 1% sodium chlorite and sown in planters containing commercial substrate. After three weeks, presence/absence of variegations were examined because yl mutants start withering from this time.

3. Results

Cr14-1 segregates yl plants with a frequency of 39.2% in control (Tab.1). This frequency is excessively high in comparison with 25% expected from a recessive gene. Helium ion beam irradiation with 50 MeV in Cr14-1 reduces germinatin rate markedly in

comparison with 100 MeV. This result might be caused by higher energy deposit with 50 MeV than with 100 MeV. On the other hand, a large reduction of germination rate in Cr14-1 by Carbon ion beams was not observed. All 3216 of yl plants derived from irradiated Cr14-1 by both Helium and Carbon ion beams did not show any variegations. Any variegations were not observed at M1 of irradiated T-65 used as a control with the ion beams. Since reduction of germination rate by Carbon ion beam irradiation was not observed, it was considered that real effect for variegation-induction at M1 by Carbon ion beam was not monitored in this study. So, Carbon ion beam irradiation experiments with higher absorbed doses will be needed.

References

1)D. S. Robertson, Mutat. Res. 51 (1978) 21.

2)A. Tanaka, Y. Yokota, N. Shikazono, H. Watanabe and S. Tano, Jaeri-Review 95-019 (1995) 29.

3)M. Maekawa, Modification of Gene Expression and Non-Mendelian Inheritance. eds. K. Oono and F. Takaiwa.(Natl. Inst. Agr. Res.)(1995) 379.

Tab. 1. Germination rates and frequencies of yl plants and variegated yl plants by Helium or Carbon ion beam irradiation in Cr14-1 and T-65

Radiation	Energy (MeV)	Absorbed dose(Gy)	Strain	No. of seeds sown	No. of plants germinated	Germ. rate(%)	No. of yl plants	Freq. of yl plants(%)	No. of var. yl plants
$^{4}He^{2+}$	50	15	Cr14-1	2921	541	18.5	105	19.4	0
			T-65	2532	1877	74.1			
		25	Cr14-1	2965	387	13.1	100	25.8	0
			T-65	1295	1214	93.7			
		50	Cr14-1	533	127	23.8	34	26.8	0
			T-65	495	237	47.9			
		100	Cr14-1	717	53	7.4	19	35.8	0
			T-65	666	204	30.6			
$^{4}He^{2+}$	100	15	Cr14-1	2331	2033	87.2	683	33.6	0
		25	Cr14-1	2346	2025	86.3	675	33.3	0
		50	Cr14-1	1201	347	28.9	344	99.1	0
$^{12}C^{5+}$	220	5	Cr14-1	1022	961	94.0	330	34.3	0
			T-65	972	931	95.8			
		10	Cr14-1	1005	939	93.4	299	31.8	0
			T-65	958	878	91.6			
		15	Cr14-1	969	913	94.2	320	35.0	0
			T-65	959	938	97.8			
		25	Cr14-1	1026	847	82.6	307	36.2	0
			T-65	959	894	93.2			
Control			Cr14-1	637	569	89.3	223	39.2	0
			T-65	136	133	97.8			

Note. Cr14-1 segregates yl with T-65's genetic background.

2．19 Effects of Helium Ions irradiation in Sexual Reproductive Stages on Seed Production and Germination of *Brassica napus* L.

H.Minami, N.Sakurai, A.Tanaka* and H.Watanabe**

Tokyo Metropolitan Industrial Technology Institute; *Advanced Science Research Center, JAERI; **Department of Radiation Research for Environment and Resouces,JAERI

1.Introduction

Plant mutation ratio induced by ionizing rays is varied in life stages of plant. It is well known that reproductive organs ranging from differentiation to development and immature embryos during embryogenesis are more radiosensitive than the other organs[1].

The purpose of this study is to investigate the effects of ion beam in sexual reproductive stages on embryogenesis and mutation of *Brassica napus* through the flower culture method[2]. In this paper, we report the effects of helium ions in the horizontal division stage of zygote and early embryo stage on seed production, seed germination and ovary elongation.

2.Materials and Method

2.1 Plant

Brassica napus cv.Lisandra were grown at 15/10℃ under natural daylight. Flowers of the terminal racemes were used. Whole flowers included pedicels, which were unpollinated in the morning of anthesis during middle flowering period, were collected to be transferred on 2ml plastic tubes in Murashige and Skoog'macro and micro elements medium[3] supplemented with 3 % sucrose, pH 5.8 using a procedure modified from that of Lardon *et al.*[2]. The flowers were pollinated with pollen of other plants and cultured at 25℃ under 24 h light. The flowers produce mature seeds as a half to one third in average as that of intact flowers. The embryogenesis of sexual reproductive stages proceeds synchronously.

2.2 Reproductive stages after pollination

The reproductive stages after pollination were preliminarily determined under fluorescence microscope. The horizontal division stage of zygote and early embryo stage were 57 h and 81 h after pollination, respectively.

2.3 Helium ions irradiation

Whole flowers, cultured on 2 ml plastic tubes, were irradiated 57 h and 81 h after pollination at 15, 30 and 50 Gy using helium ions(100MeV) at room temperature.

2.4 Measurements

The number of mature seeds in a pod, seed germination rate and ovary length were measured 50 days after pollination. All experiments were carried out using 20

flowers.

3.Results

The mature seed production of flowers irradiated in early embryo stage, were strongly repressed at more than 15 Gy(Table 1). The flowers irradiated in horizontal division stage, did not reduce the number of mature seeds per pod with 15 and 30 Gy. The flowers, however, reduced the number to 70 % of unirradiated flowers with 50 Gy.

Helium ions irradiation on flowers inhibited the seed germinatin with increasing dose(Table 2). In paricular, the germination rates were repressed to 80 % and 70 %, for irradiation in horizontal division stage of zygote and early embryo stage, respectively, with 50 Gy.

The ovary elongation of irradiated flowers was not repressed and ranged from 3.6 to 3.9 cm(Figure 1). Minami *et al.*[4] reported that gamma irradiation in early embryo stage did not repress the ovary elongation up to 87 Gy in *Brassica napus*.

4.References

1)H.Gaul:Radiation Bot.4(1964)155-232

2)A.Lardon, A.M.Triboi-Blondel and C.Dumas :Sexual Plant Reprod. 6(1993)52- 56.

3)T.Murashige and F.Skoog Plant Physiol. 15(1962)217-227.

4)H.Minami, N.Sakurai T.Muroyama and D.Hogetsu : Bulletin of The Tokyo Metropolitan Isotope Res. Ctr. 13(1996)41-49(In Japanese).

Table 1 Effects of helium ions in repoductive stages on number of mature seeds per pod

Dose(Gy)	Stages	
	Horizontal division of zygote	Early embryo
	Number of mature seeds/pod	
0	11.1±3.83	
15	11.6±3.12	9.7±3.92
30	13.1±4.16	9.2±4.45
50	7.6±3.65	8.5±3.85

Values are means±S.D of 20 flowers.

Table 2 Effects of helium ions in reproductive stages on seed germination

Dose(Gy)	Stages	
	Horizontal division of zygote	Early embryo
	Seed germination(%)	
0	98.6±4.67	
15	88.5±21.98	94.8±8.76
30	86.9±10.87	83.8±15.41
50	79.8±18.50	66.3±22.28

Values are means±S.D of 20 flowers.

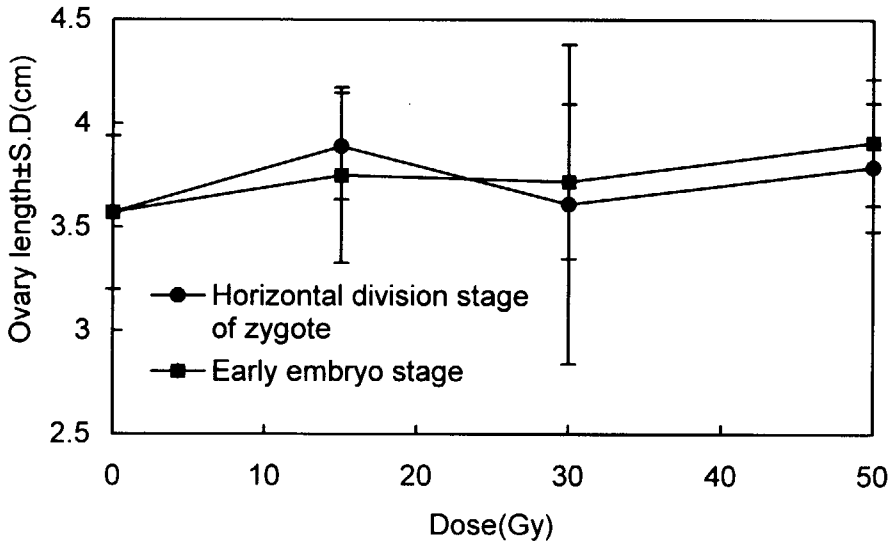

Figure 1. Effects of helium ions on the ovary elongation

2.20 Visualizing ^{11}C-Methionine Movement in Plant by Positron Emitting Tracer Imaging System (PETIS)

S. Mori[1], H. Nakanishi[1], N. Bughio[1], N. S. Ishioka[2], S. Watanabe[2], A. Osa[2], T. Sekine[2], H. Uchida[3], A. Tsuji[3], S. Matsuhashi[4] and T. Kume[4]

[1]Graduate School of Agricultural and Life Sciences, The University of Tokyo; [2]Tokai Res. Estab., JAERI; [3]Hamamatsu Photonics Co.; [4]Takasaki Radiation Chem. Res. Estab., JAERI

1. Introduction

Despite of low resolution (2.5mm), positron emitting tracer imaging system (PETIS) offers several advantages over other methods of imaging used for dynamic movement of radiolabelled molecules in the plant. It has a high time resolution (about 5 seconds) and can be used for imaging of intact plants. In this report we will discuss the movement of ^{11}C-methionine in intact barley plants by using PETIS and BAS imaging techniques. The reason behind the use of methionine is that it has a short synthesis time ($\sim$35 min) therefore it is the most suitable among all amino acids for the production of a labeled molecule of as short half life as 20.39 min. Secondly, when the plants suffer from the problem of Fe deficiency in the growth medium, root cells immediately perceive that signal and release the low molecular weight substances (mugineic acids) in the rhizosphere. The mugineic acids chelate insoluble Fe and convert it into a soluble form which is readily absorbed by the plants[1]. The mugineic acids are synthesized from methionine via a metabolic pathway in the barley roots. The object of this study is to investigate whether leaf supplied methionine can absorbe and actively translocate to the mugineinc acid producing roots or not.

2. Materials and Methods

Barley plants were cultured hydroponically for 3-4 weeks which had 3-6 leaves and 1-3 tillers. Iron deficiency treatment was started when the plants were 2 weeks old. Methionine was synthesized by an organic synthesis reaction using $^{11}CO_2$ ($^{11}CO_2 \rightarrow {}^{11}CH_3I \rightarrow$ [^{11}C-methyl]methionine). The ^{11}C-labeled methionine was supplied to the Fe-deficient and Fe-sufficient (control) plants either from roots or from cut leaves for 1-1.5 h and real time ^{11}C-methionine movement was chased by PETIS method. After ^{11}C-methionine absorption, the plants were exposed to a BAS imaging plate and the image was analyzed by an image analyzer (BAS1500, Fuji Film).

3. Results and Discussion

3-1. As revealed by PETIS, when

^{11}C-methionine was supplied through roots, the plants were rapidly labeled in their basal part just at the junction of roots and shoot (designated as "discrimination center"). In the case of the Fe-deficient plants, discrimination center was labeled within 1 minute of the commencement of the experiment and reached a saturation plateau after 90 minutes. In the case of control plants, the lag phase lasted 8 minutes and a log phase curve was obtained after 90 minutes from the start of the absorption (Fig. 1).

BAS image of the Fe-deficient plants showed methionine accumulation pattern in the order of leaf of the severely chlorotic main shoot > the newest leaf of the severely chlorotic tillers > the old leaves of tillers = the newest leaf of the main shoot > the oldest leaf of the main shoot. Whereas the control plants showed the order of the newest leaf of main shoot > the newest leaf of tillers. Almost no translocation was observed to older leaves.

3-2. Methionine supplied through cut leaf of the main shoot of the Fe-deficient and control plants reached the discrimination center within 2 and 5 minutes from the start of the experiment respectively and then maintained almost a straight line. As expected, the distance from cut leaf part to the discrimination center was long, therefore it took a longer time to reach the discrimination center. BAS image revealed the accumulation pattern in the order of new leaf of the severely chlorotic main shoot > the newest leaf of the severely chlorotic tiller. In the control plants, the accumulation was observed in the new leaf of the main shoot only.

3-3. It was hypothesized that being a precursor of the mugineic acids, methionine would move to the tips of the lateral roots and root hairs where it would take part in the mugineic acid synthesis, but that hypothesis

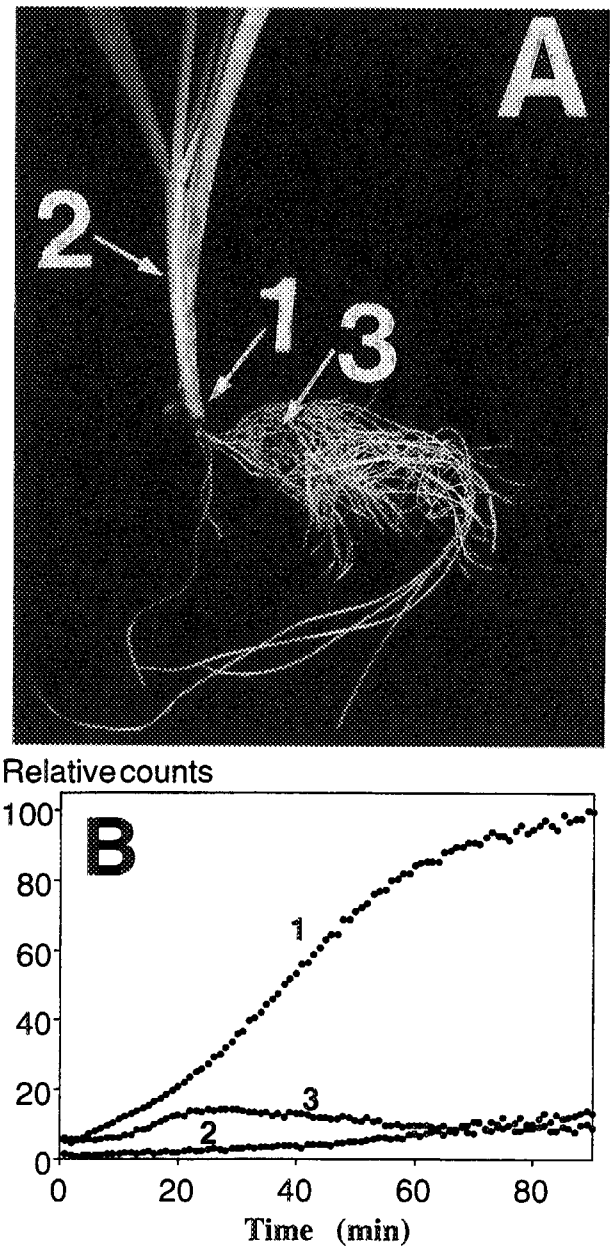

Fig. 1 Methionine absorption through roots of Fe-deficient barley plant: A. plant; B. PETIS data curves.

could not be proved. However, the movement from the leaf to the root tip was higher in control plants. Therefore, it was suggested that during Fe deficiency, methionine synthesis might be originating from ATP, produced by metabolism of photoassimilate like sucrose, after entering into Yang cycle and then used in the synthesis of the mugineic acids.

3-4. From above mentioned facts, it became clear that the root or leaf supplied methionine accumulates in plant body in the sink strength order of discrimination center > chlorotic leaves > new leaf of the Fe-deficient plant whereas in the control plants it was in the order of discrimination center > the newest leaf.

3-5. While handling plant tissues, PETIS affords a high efficiency of imaging in thick tissues like the discrimination center or leaf veins because positrons after hitting a thick target convert into gamma rays which are then traced and produce an image. But the thin tissues like intervenal spaces, it has a low efficiency. Contrary to that in BAS method of imaging, positron is not converted into gamma rays, so it gives a good image of the thin tissues but has low efficiency for the thick tissues like the discrimination center and leaf veins. Therefore, while interpreting the imaging results above points should be kept in mind.

Reference

1) S. Mori (1998) Iron transport in graminaceous plants. *In* Metal Ions in Biological Systems: iron transport and storage in microorganisms, plants, and animals. Edited by A. Sigel and H. Sigel, pp. 216-238. Marcel Dekker, Inc., New York.

2.21 Detection and characterization of nitrogen circulation through the sieve tubes and xylem vessels of rice plants.

H.Hayashi*, Y.Okada*, H.Mano*, T. Kume**, S.Matsuhashi**, N. S-Ishioka**, H.Uchida*** and M.Chino*

*Dept. of Applied Biol.Chem., The Univ. of Tokyo
**Dept.Radiation Research for Environ.and Resources,JAERI
***Central Research Laboratory, Hamamatsu Photonics Co.

1. Introduction

Nitrogen absorbed by roots is transported to the leaves through xylem vessels and then retranslocated to the new leaves, root and storage organs through sieve tubes. It is very important to know how this nitrogen movement occurs in the plant and what mechanisms are involved in controlling this movement in order to increase the efficiency of fertilyzer.

^{15}N has also been used to detect the nitrogen circulation in plants[1-3]. However, this method cannot be used to detect the short-term movement of nitrogen in plants and cannot therefore be used to visualize the dynamics of nitrogen movement.

Radioactive nitrogen(^{13}N) which has a half life time of 9.9 minutes is a positron emitting isotope and can be detected by a positron-emitting tracer imaging system[4]. This detection technique is useful for displaying the nitrogen distribution in plants.

In this paper, we will describe a method to detect the nitrogen circulation in plant using a combination of sap collection and nitrogen isotope techniques.

2.Experiments

Rice plants(*Oryza sativa* L. var. Kantou) were grown in a complete nutrient solution [5], with nitrate (0.71 m*M*) as the only source of nitrogen.The plants of the 7th- or 8th- leaf stage and of the one week after anthesis were used for the experiments.

An aqueous solution containing $^{13}NO_3^-$ (a positron emitter with a half life of 9.9 minutes) was produced from the reaction of $^{16}O(P, \alpha)^{13}N$ by bombarding water with 1μA of 20 MeV H^+ particles from the TIARA AVF cyclotron. The water containing $^{13}NO_3^-$ was purified through a cation exchange column. A 126 MBq solution of $^{13}NO_3^-$ was added to the 20 mL of the nutrient solution already in a small box (5cm x 0.5cm x 10cm) from which the rice plant was absorbing the nutrients. For the study of nitrogen transport, the plant was placed in the $^{13}NO_3^-$ solution at the midposition between two separate two-dimensional block detectors(5 x 6 cm square) which were composed of a $Bi_4Ge_3O_{12}$ scintillator array coupled to a position sensitive photomultiplier tube(Hamamatsu Photonics Co., Japan). Two

annihilation γ-rays from samples are detected in coincidence. The original position of the annihilation is localized at the intersection of the object plane, where the plant is set, in a line connecting the two detection points on the detectors.

3. Results

The current paper is the first to report the use of a positron-emitting tracer imaging system for the detection of the nitrogen distribution in plants. The results show that it provides a convenient system for displaying such data even though the spatial detection limit is only 2mm and measurement lasting more than 30 minutes may be difficult.

Our results show that in rice plants supplied with nitrate as the sole nitrogen source, the absorbed nitrogen is translocated through the xylem to the leaf within 8 minutes and starts to retranslocate through sieve tubes within 10 minutes.

References

1)T.Mae and K.Ohira, Plant Cell Physiol.**22**(1981)1067.
2)J.S.Pate,M.B.Peoples and C.A.Atkins, Plant Physiol. **74**(1984)499.
3)T.Yoneyama and C. Sano, Soil Sci. Plant Nutr. **24**(1978)191.
4)T.Kume,S.Matsuhashi,M. Shimazu,H.Ito,T.Fujimura, K.Adachi,H.Uchida,N.Shigeta, H.Matsuoka,A.Osa and T.Sekine, Appl. Radiat. Isot. (In press).
5)H.Hayashi and M.Chino,Plant Cell Physiol. **26**(1985)325.
6)H.Hayashi,Y.Okada,H.Mano, T.Kume,S.Matsuhashi,N.S-Ishioka,H.Uchida and M. Chino,Plant and Soil, 196 (1997)233.

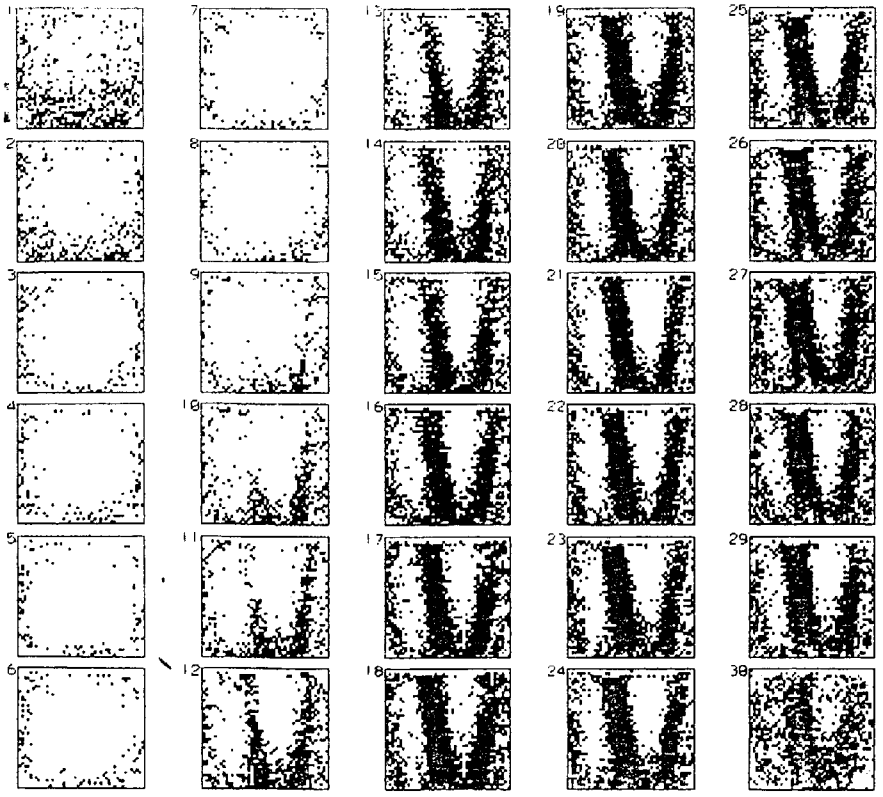

Fig.1 Illustration of ^{13}N in rice plantusing a positron-emitting tracer imaging system. Images were aquired at 1 minute frame intervals for 30 minutes.

2.22 Water and Trace Element Behavior in Plant

T.M.Nakanishi, J.Furukawa, N.S.Ishioka*, S.Watanabe*, A.Osa**, T.Sekine**, T.Ito***, S.Matsuhashi***, T.Kume***, H.Uchida*****, A.Tsuji*****

Graduate School of Agric. & Life Sci., The Univ. of Tokyo;
*Dept. of Radioisotopes, JAERI/Tokai;
**Dept. of Materials Science, JAERI/ Tokai;
Dept. of Radiat. Res. Environ. Resorces, JAERI/Takasaki;*Hamamatsu Hotonics, Co.

1. Introduction

Cowpea has been grown in semi-arid area in Asia and Africa as an important crop, for it maintains high photoshythesis rate under dry climate. The size of the internode between the first leaf and first trifoliate leaf in cowpea is large compared with those of the other internodes. Though this tissue has been considered as a water storing tissue, the function of the internode has not been known well. In this research, we tried to know how the water in the internode has been supplied or moved up to the other tissues by PETIS (Positron Emitting Tracer Imaging System). Through water kinetics in the internode, we investigated the activity of the plant after drying treatment.

2.Experimentals

Cowpea and common bean were cultured for ten days and when the first trifoliate was developed, the plants were transported to Takasaki Establishment, JAERI to carry out PETIS. To get ^{18}F labeled water, He ion was accelerated by AVF cyclotron and 6ml of distilled water was irradiated for 40 min. After irradiation, the activity of the water was found to be about 100MBq/6ml. The energy and current of the He ion irradiated were 50MeV and 1.0 μ A, respectively. The water was purified by passing through a cation exchange resin and was supplied for 2 min.to the plant which root was excited. Then the labeled water was exchanged by distilled water and labeled water distribution was measured up to 60 min.

Positrons emitted from the water was detected by a $Bi_4Ge_3O_{12}$ scintillation counter (BGO) block. The detector block was consisted of an array of small BGO detectors, each 2mmx2mm with 20mm in depth. Twenty three small detectors were lined up until 27 lows, with every 2.2mm of an interval. The area that the detector could measure was 5cmx6cm. The internod between the first leaf and the first trifoliate, as well as the first trifoliate was fixed on an acrylic board or board with many holes with a tape. The measurement was carried out at room temperature with sufficient light. Drying treatment was performed for 30 min. at room temperature. After drying, about 2cm of the lowest stem was cut off under water and the labeled water was supplied again for 2 min. in the same way.

3.Results

The distribution of the labeled water in the target was measured every 1min. until 60 min. The water accumulation of the target stem and the first trifoliate was relatively rapid. After 5 to 10 min., the radioactivity of the water both in the stem and the leaf showed constant. The amount of the water in leaf was about 1/3 of that in the stem. However the radioactivity of the water absorbed in the tissue could not be calibrated to the water amount in our experiment.

After 30 min of drying treatment, only common bean was drooped. Then the labeled water was supplied again to both plant samples in the same way. In the case of cowpea, the water absorption manner did not show any difference by drying. However in the case of the common bean, the water supply to the stem and the leaf was drastically decreased, about one third and less than a half, respectively, as those before the treatment.

The result indicated that cowpea maintained high water absorption activity through drying treatment. We are going to compare the water absorbing activity of the stem with those of the other tissues in cowpea.

References

1)T.M.Nakanishi et al., Proc. Fifth World Conference on Neutron Radiography.

2) T.M.Nakanishi et al., J.Plant Phys. **151**(1997)442

3) T.M.Nakanishi et al., Nuclear Instruments and Methods, in press

2.23 Development of pollen-mediated gene transfer technique using penetration controlled irradiation with ion beams

Y.Hase, A.Tanaka, I.Narumi, H.Watanabe and M.Inoue*
Department of Radiation Research for Environment and Resources, JAERI
*Department of Agriculture, Kyoto Prefectural University

Introduction

There are several gene transfer techniques in plants such as *Agrobacterium*-mediated technique and direct gene transfer using electroporation. However application of the *Agrobacterium*-mediated technique is restricted by the host range. Further protoplasts preparation for electroporation and the cultivation require a great deal of labor. If pollen can be used as a DNA vector, it could make up a large part of those disadvantage.

In the previous studies[1,2], we have reported that ion beam irradiation with shallow depth (4 μm in pollen) can induce leaky pollen effectively and also that transient GUS expression was observed at the highest frequency (55.1 %) when those irradiated pollen were incubated in a DNA (pBI221) solution. Those results suggest that foreign DNA can be efficiently transferred into pollen using the penetration controlled irradiation with ion beams. To establish the pollen vector technique, foreign gene expression in the progeny must be observed.

Pollen is covered with two layers of envelopes, outer pollen exine and inner cell membrane. One of the major obstacles in DNA transfer into pollen is those envelopes because DNA are hard to pass those envelopes. Although measuring the leaky pollen is an endpoint to examine pollen envelope damage, it is presumably caused by damage only on pollen exine. To optimize the DNA transfer condition, cell membrane damage should also be observed.

In this study, seeds were produced following pollination with DNA transferred pollen, and screening of the transformant was attempted. Tripanblue dyeing test was also carried out to examine pollen cell membrane damage.

Materials and Methods

Irradiation

Irradiation Apparatus for Cell (IAC) for penetration controlled irradiation has been connected to a beam line of 3 MV tandem accelerator as previously described by Tanaka et.al.[3]. Dry pollen of *Nicotiana tabacum* L. (cv.BY-4, 20 μm in thickness) was monolayered on a plastic plate and irradiated with 18 MeV C^{5+} beams. The penetration depth into a target and the beam currents were controlled as described by Tanaka et.al.[3].

Gene transfer

The irradiated pollen was collected and suspended in a DNA solution (200 μg/ml pCH containing the CaMV 35S promoter, the sequence of hygromycin B phosphotransferase gene and NOS terminator, 10 % sucrose and 100 μg/ml boric acid) at the concentration of 2000-5000 pollen/μl. Two μl of the solution containing pollen was pollinated to each emasculated flower. The ripe capsules were harvested 3-4 weeks after pollination and the seed weight per capsule was recorded. The seeds were sown on the screening medium containing 5 μg/ml hygromycin B and 0.3 % agar.

Dye exclusion test

The irradiated pollen was suspended in a solution containing 1 mg/ml tripanblue, 10 % sucrose and 100 μg/ml boric acid for one hour and the rate of dyed pollen was counted.

Results and Discussion

Table 1 shows the effects of penetration controlled irradiation with C^{5+} beams on the pollen fertility. Fertile seeds were produced in all irradiation conditions. The flowers pollinated with

Table 1 Effects of penetration controled irradiation with ion beams on the pollen fertility

Fluence (p/ cm^2)	Penetration depth in pollen(μm)	Fertile capsules / pollinated(No.)	Mean seed weight per capsule(mg)
Control	—	25/ 25	82±30
4×10^{9}	2	10/ 10	87±40
4×10^{9}	4	30/ 30	70±37
4×10^{10}	2	11/ 11	65±30
4×10^{10}	4	10/ 10	55±37

unirradiated pollen produced the seeds of 82 mg on average. Seed weight per capsule was reduced as the fluence and/or the penetration depth increased. From these results it was suggested that the pollen fertility was more affected by the fluence than the penetration depth. Furthermore it was recognized that irradiation with a fluence at 4×10^9 p/cm^2 and a range of 2 μm did not suppress the pollen fertility.

In the previous report[3], transient GUS expression rate was the highest following 6 MeV He^{2+} irradiation with a fluence at 4×10^9 p/cm^2 and a range of 4 μm. In this study, pollen was irradiated at the same condition except that we used 18 MeV C^{5+}. The irradiated pollen was suspended in the DNA solution and then pollinated. The obtained seeds (approx.10000 seeds) were sown on the screening medium. Most of those seeds germinated but all of them died except for 18 seedlings. Those 18 seedlings were seemed to be viable on the screening medium (Fig.1). Cotyledons of viable plants were green

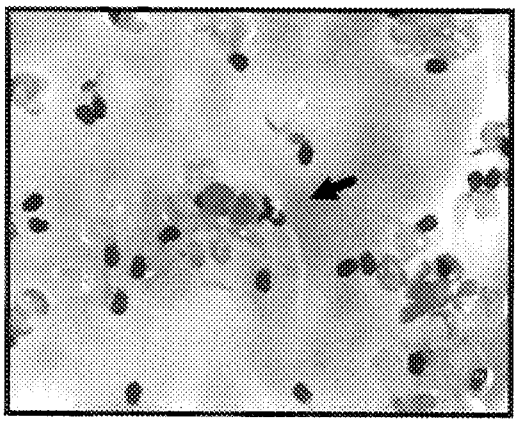

Fig.1 Viable plants observed on the screening medium.

and root length were over two times longer than the other died seedlings. To make clear whether foreign gene is incorporated into nuclear DNA, reproducibility of this experiment must be confirmed.

Cell membrane damage was examined by tripanblue exclusion test (Fig.2 and Table2). Tripanblue penetrates into the cells that have damage on cell membrane. Although

Table 2 Tripanblue uptake rate (%) following penetration controlled irradiation

Fluence (p/ cm^2)	Penetration depth in pollen(μm)	Uptake (%)
Control	—	24.6±5.7
4×10^{9}	1	34.4±4.9
4×10^{9}	4	41.4±3.6
4×10^{10}	1	32.1±7.4
4×10^{10}	4	90.6±2.3

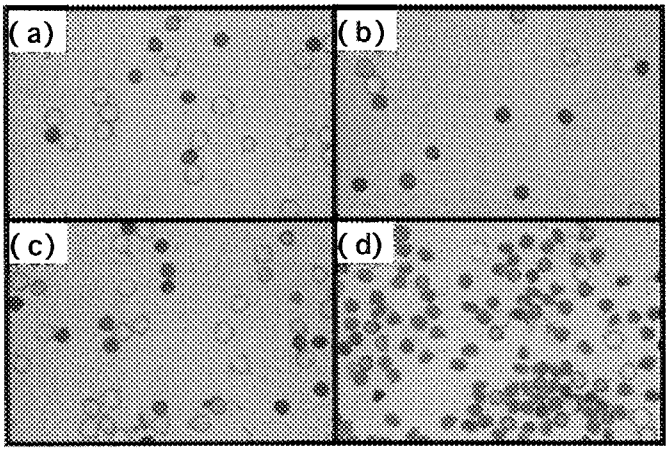

Fig.2 Pollen stained in tripanblue solution following penetration controlled irradiation.
(a);control,(b);Fluence 4×10^{9}p/cm^{2}·range 4μm,(c);4×10^{11}p/cm^{2}·1μm,(d);4×10^{11}p/cm^{2}·4μm

tripanblue uptake occurred in 24.6 % of unirradiated pollen, the irradiated pollen with a fluence at 4×10^{9} p/cm^{2} and a range of 4 μm was dyed at the rate of 41.4 %. In case the penetration depth was 1 μm, tripanblue uptake rate was not significantly different between the fluence of 4×10^{9} p/cm^{2} and 4×10^{11} p/cm^{2}. Since tobacco pollen exine is 1.0 μm in thickness[3], ion beams may not give any effective damage on cell membrane at this depth. The irradiation with a fluence at 4×10^{11}p/cm^{2} and a range of 4 μm caused dyeing in over 90 % pollen and those pollen was seemed to be sterile. Irradiation conditions should be further examined to find an optimum irradiation condition for DNA transfer into the pollen.

References

(1) A.Tanaka, T.Yamashita, T.Shimizu, M.Kikuchi, Y.Kobayashi and H.Watanabe(1994). *JAERI Rev.* 95-019:27-28.
(2) A.Tanaka, H.Watanabe, Y.Hase, M.Inouc, M.Kikuchi, Y.Kobayashi and S.Tano (1997). *JAERI Rev.* 97-015:21-23.
(3) A.Tanaka, H.Watanabe, T.Shimizu, M.Inouc, M.Kikuchi, Y.Kobayashi and S.Tano (1997). *Nucl. Instr. and Meth. in Phys. Res. B* 129:42-48.

This is a blank page.

3. Radiation Chemistry/Organic Materials

This is a blank page.

3. 1 Distribution of Fluorescence of Gaseous Nitrogen around Energetic Ar ion

M.Taguchi[a], K.Furukawa[b], M.Moriyama[c], H.Namba[a], and S.Ohno[d]

[a]Department of Radiation Research for Environment and Resouces, JAERI,

[b]Department of Chemistry and Fuel Research, JAERI,

[c]Department of Chemistry, Gunma University,

[d]Research Institute of Science and Technology, Tokai University

1.Introduction

We have been studying on spatial distribution of energy deposited by high energy heavy ions traveling through matters, which gives the nature of ion irradiation effects, such as in chemical reactions and in cell's death. We have estimated the distribution of an absorbed dose in water. Water is among the most important substances from the point of view of microdosimetry relating to health physics, because it is the main component of living bodies. The experimental results showed a steep decrease in dose with radial distance from the incident ion beam[1].

Two types of emissive transitions were observed for nitrogen irradiated with 330 MeV Ar^{11+} ion[2]. The (0,0) transition of the first negative system of nitrogen molecular ion observed at the wavelength of 391.4 nm has an excitation cross section proportional to the total ionization cross section[3]. On the other hand, the (0,0) transition of the second positive system of nitrogen molecules observed at 337.1 nm is known to be induced exclusively by low energy electrons[4]. Thus the analysis of the distribution of these transitions may be important to understand the energy distribution in the track in detail.

In the present report, the excited states produced in gaseous nitrogen irradiated with 175 MeV Ar^{8+} ions are identified and their radial distributions were studied.

2.Experimental

Ion irradiation and fluorescence measurement were performed at the beam port of HX-1 of the AVF cyclotron in TIARA facility, which is called the Experimental Apparatus for Basic study of Radiation Chemistry with Heavy Ions (EA-BRACHI)[5-8]. The ion used in this study was 175 MeV Ar^{8+}. Figure 1 shows the simple diagram of the gas pressure control system and the single photon counting system. The target chamber is evacuated through throttling valve (MKS 253A-2-4CF-2) by a turbo-molecular pump (Osaka Vacuum TG1000M) and a rotary pump. The pressure of nitrogen gas was controlled to 0.4, 2.7, and 27 Pa at ambient temperature, using pressure sensors (MKS Baratron 122A and 127A), a throttling valve (MKS253A-2-4CF-2), pressure controller (MKS 113A) and mass flow controller (MKS 147B). Ar ions were induced through a tantalum collimators with 2 mm hole, which was sealed Kapton film (5μm thick) to keep the gas pressure in the target chamber, set on the upper reaches of the ion beam to a target chamber. The fluence of the Ar ion has been measured by counting protons from plastic scintillators induced by one Ar ion irradiation before and after measurements, and was 2×10^6 ions/sec. LET of Ar ion with the incident energy of 175 MeV in water were calculated to be less than 2010 eV/nm by the IRAC code[9].

Optical system was constructed with optical lens and three slits to collect photons of the excited nitrogen molecules from the restricted three-dimensional area. The space resolution of the area was ±0.6 mm. The photons were measured by a single photon

counting system with a photomultiplier tube (HAMAMATSU H3177) using the interference filter of 338 nm. The distance of the restricted area from the center of ion beam was changed with moving target chamber itself. In this study the optical system was placed at the radial distance of from –50 mm to 50 mm.

3.Results and Discussion

The (0,0) transition of the second positive system of nitrogen molecules observed at 337.1 nm($C^3\Pi_u$-$B^3\Pi_g$) is known to be induced exclusively by low energy electrons, about 20 eV[8]. Thus it is suitable for estimation of the contribution to the energy deposition from the low energy electrons.

The number of photons of nitrogen gas was accumulated for 10 second.

The distance from the ion beam reduced to the unit density, r (mm), is expressed with the distance from the ion beam in gas, r_{gas} (mm)

$$r=r_{gas} \times \rho_{gas} / \rho_{water} \quad (1)$$

where ρ_{gas} is the density of the gas and r_{water} is the unit density ($1g/cm^3$). The relative emission density at distance r, D(r), is expressed as follows;

$$D(r)=N_p / F_i / \rho_{gas} \times (\rho_{water} / \rho_{gas})^2 \quad (2)$$

where N_p is number of photons measured by the photomultiplyer, F_i is ion fluence.

Figure 2 shows the relative emission density in water of low energy secondary electron around 175 MeV Ar ion obtained with equations. Track radius was treated as maximum range of secondary electron in matter by theoretical assumption. However, the experimental results indicate that energy is deposited very wider than that (800 nm) obtained by theoretical prediction[10] Furthermore, similar result was obtained for total ionization measurement.

The emission density decreased proportionally to square of the distance. This slope is similar to that of total ionization.

Reference

1. M.Taguchi H.Namba, Y.Aoki, K.Furukawa and S.Ohno, Submitted for TIHANY symposium 1998.
2. M.Taguchi, H.Namba, Y.Aoki, K.Furukawa and S.Ohno, JAERI-Review, 97-015, 72(1996).
3. W.L.Borst and E.C.Zipf, Phys. Rev., A1,834-840(1970)
4. M.Imai and W.L.Borst, J. Chem. Phys., 61,1115-1117(1974).
5. H.Namba, Y.Aoki, M.Taguchi and K.Furukawa, TIARA Annual Report 1,163(1992).
6. M.Taguchi, H.Namba, Y.Aoki, R.Watanabe, Y.Matsumoto and H.Watanabe, JAERI Tech., 96-046.
7. H.Namba, Radioisotopes, 44,69(1995)
8. M.Taguchi, Y.Aoki, H.Namba, R.Watanabe, Y.Matsumoto and H.Hiratsuka, Nucl. Instr. Method B132,135(1997).
9. S.Tanaka, M.Fukuda, K.Nishimura, W.Yokota, Kamiya, H.Watanabe, T.Shiraishi, K.Hata and N.Yamano, TIARA Annual Report, 1,76(1992).
10. J.L.Magee and A.Chattegee, J. Phys. Chem., 84,3529(1980).

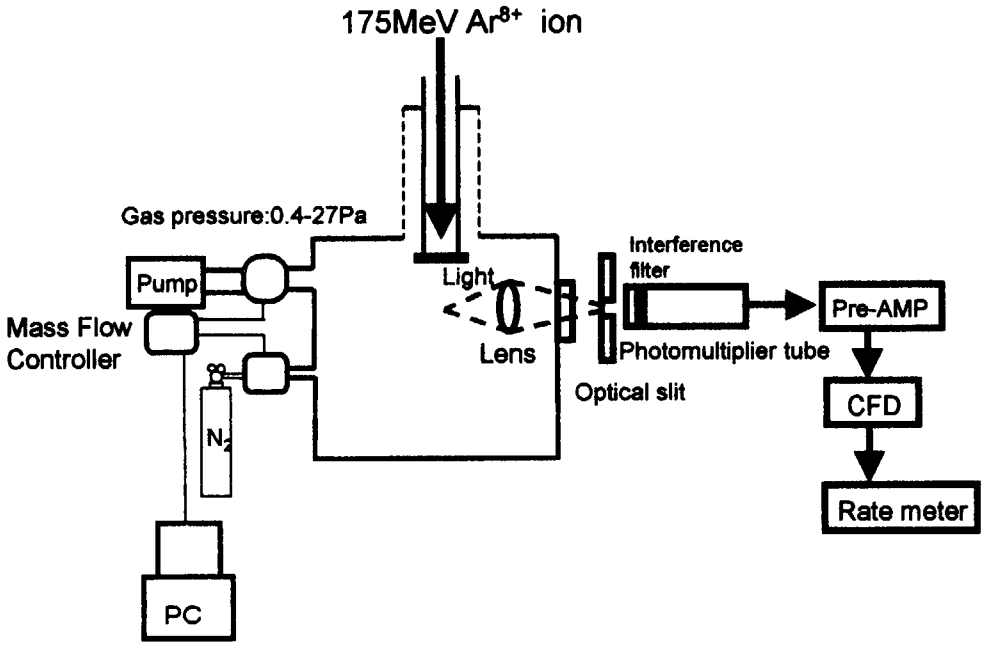

Fig. 1 Schematic presentation of the experimental apparatus for the irradiation with Ar ions and the detection of the fluorescence from gaseous nitrogen.

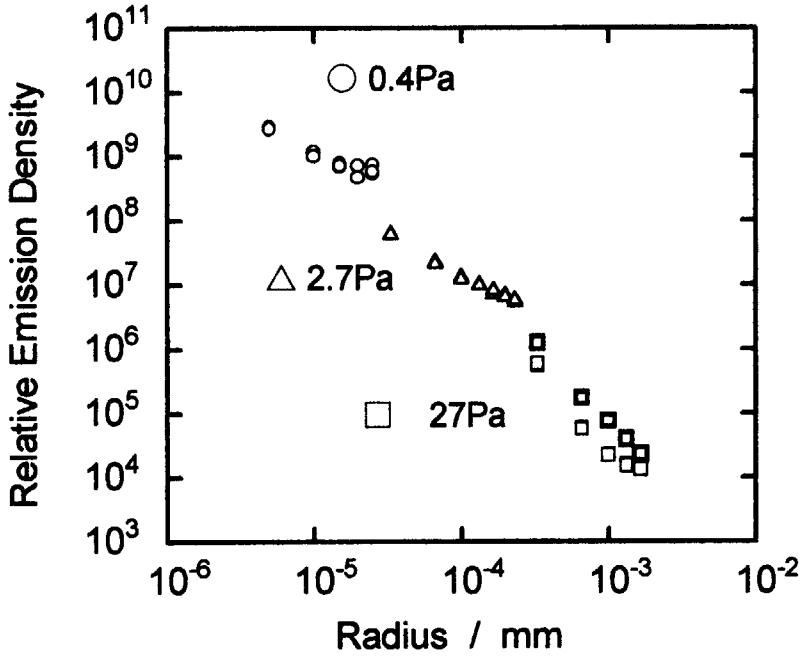

Fig. 2 Distribution of fluorescence intensity around 175 MeV Ar ion's trajectory in gaseous nitrogen.

3. 2 Cross-linking of Polydimethylsiloxanes in Heavy Ion Tracks

H. Koizumi, M. Taguchi* and T. Ichikawa

Division of Molecular Chemistry, Graduate School of Engineering, Hokkaido University; *Department of Radiation Research for Environment and Resources, JAERI/Takasaki

1. Introduction

Heavy ions deposit energy along the ion tracks with high density. The high local dose may cause chemical effects different from those by γ-rays and fast electrons. Dose distribution in the ion tracks is inhomogeneous: dose at the center of the ion tracks is highest, and it decreases with increasing the distance from the center. Relationship between the dose distribution and chemical effects of ion beam irradiation will be important to develop new applications of ion beams for material modification and fabrication of micro-structure[1-4].

In the present study, we have examined cross-linking of polydimethylsiloxanes (PDMS) by ion irradiation. As gelation dose of PDMS is 10^4-10^6 Gy[5,6], dose in heavy ion tracks may exceed the gelation dose[1-4]. Gel particles are hence generated in the ion tracks. Measurements of the size and the yield of the particles will give information on the chemical reactions in heavy ion tracks.

2. Experimental

Polydimethylsiloxanes supplied by Shin-Etsu Chemical Co., Ltd. were degassed under vacuum. They were put in metal cells with a window of Harvar foil of 6 μm thickness. Ion beams from the AVF cyclotron at JAERI Takasaki were irradiated through the window. The irradiated samples were dissolved in hexane. The gel particles were separated by filtration with membrane filters (Millipore LSWP02500, pore size 5.0μm). The gel particles were dispersed in hexane with ultrasonic wave. A few drops of the solvent were put on mica film, and the solvent were evaporated. The residue was observed with atomic force microscope (AFM, Digital Instruments, Nanoscope III-H) and scanning electron microscope (SEM, JEOL JSM-5310LV). AFM was operated in tapping mode.

3. Results and Discussion

The tapping-AFM images of the insoluble residue obtained from ion-irradiated PDMS are shown in figures 1 and 2. Small particles of 50-500nm in diameter and of several nm in thickness are observed. No particle was observed for unirradiated PDMS. Figure 1 is the AFM image for the irradiation of 350 MeV $^{20}Ne^{8+}$ with the fluence of 10^{10} ions cm^{-2},

and figure 2 is the AFM image for the irradiation of 520 MeV $^{84}Kr^{20+}$ with the fluence of 10^{10} ions cm^{-2}. Molecular weight of PDMS is 6,700 for both the samples.

G-value for cross-linking of PDMS is 3.0[5,6]. Gelation dose for PDMS of 6,700 in molecular weight is calculated to be 2.4 x 10^2 kGy. Average dose in the volume between the surface and the range of the ions is 7.3 kGy for the Ne irradiation, and 74 kGy for the Kr irradiation. Gel particles are generated with the dose less than the gel dose.

The radial dose distributions are proposed by several authors[7,8]. The size of the gel particles, however, is much smaller than the size expected from the dose distribution. The doses in the tracks of 350 MeV Ne and 520 MeV Kr ions within several nm in diameter are larger than the gel dose. The formation of gel rods of several nm in diameter and of several hundreds of μm in length is expected from the radial dose distribution. The discrepancy between the observed and the estimated size of the gel particles might be ascribed to randomness in ionization events in the ion tracks. The radial dose distribution continuously changes. However, it is an average distribution of many ion tracks. The actual dose distribution in an ion track will be more inhomogeneous. Domain with higher dose than the gelation dose will be scattered in an ion track.

References

1) H. Koizumi, M. Taguchi, H. Namba, T. Ichikawa, H. Yoshida, Nucl. Instr. and Meth. B, **132** (1997) 633.
2) H. Koizumi, T. Ichikawa, H. Yoshida, H. Namba, M. Taguchi, and T. Kojima, Nucl. Instr. and Meth. B, **117** (1996) 431.
3) H. Koizumi, T. Ichikawa, H. Yoshida, H. Shibata, S. Tagawa, and Y. Yoshida, Nucl. Instr. and Meth. B, **117** (1996) 269.
4) H. Koizumi, T. Ichikawa and H. Yoshida, Appl. Radiat. Isot. **47** (1996) 1205.
5) R. Folland and A. Chalesb y, Radiat. Phys. Chem. **10** (1977) 61.
6) C. G. Delides and I. W. Shephered, Radiat. Phys. Chem. **10** (1977) 379.
7) A. Chatterjee, H. J. Schaefer, Radiat.Environ. Biophys. **13** (1976) 215.
8) R. Katz, S. C. Sharma, and M. Homayoonfar, Nucl. Instr. and Meth. **100** (1972) 13.

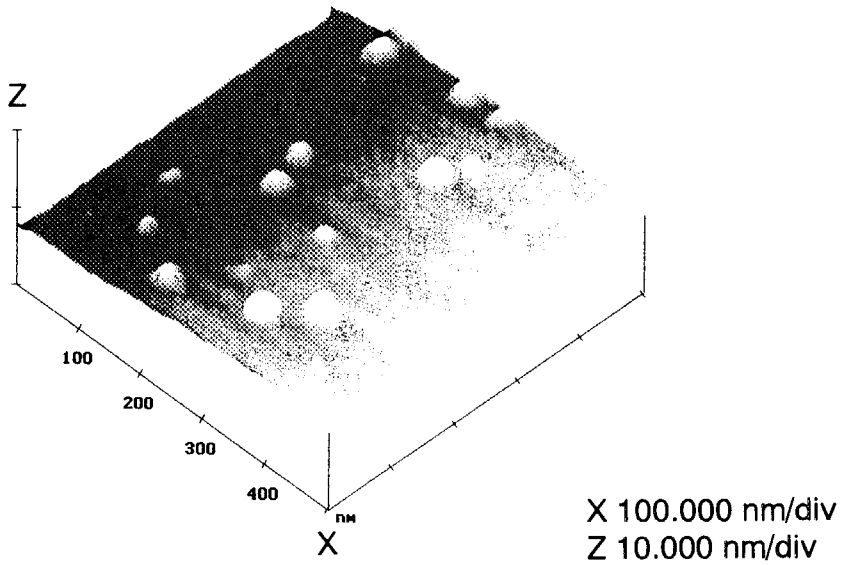

Figure 1. Tapping AFM image for insoluble residue obtained from polydimethylsiloxane (PDMS) irradiated with 350 MeV $^{20}Ne^{8+}$; the fluence of the ions is 10^{10} ions cm^{-2}; the molecular weight of PDMS is 6,700.

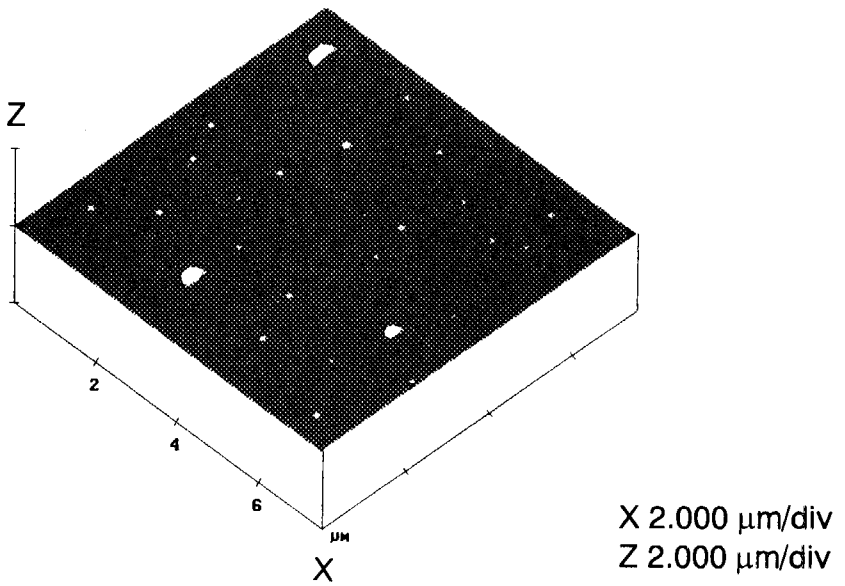

Figure 2. Tapping AFM image for insoluble residue obtained from polydimethylsiloxane (PDMS) irradiated with 520 MeV $^{84}Kr^{20+}$; the fluence of the ions is 10^{10} ions cm^{-2}; the molecular weight of PDMS is 6,700.

3. 3 LET Effect of Heavy Ion Irradiation on Photostimulated Luminescence

Ken Abe, Masahiro Takebe, Tsuyoshi Hamano, Yasuaki Murakami, Takuji Suzuya, Kiwamu Saito, Kentaro Toh, and +Takuji Kojima and +Takuro Sakai

Graduate School of Engineering, Tohoku University, +Advanced Radiation Technology Center, JAERI

1. Introduction

The imaging plate (IP, here BAS UR, Ⅲ, TR) is one of the cumulative image sensors formed of $BaFBr:Eu^{2+}$ storage phosphors. It is widely used in various radiation fields, specially in weak X-ray imaging because of both its super high sensitivity and wide dynamic range of detection for the range from extremely weak dose to higher one.

The radiation sensitivity of the IP including windowless type TR is inclusive but depends on radiation types, such as VUV, X(γ), SR, $e^{\pm}$ ($\beta^{\pm}$), n (through neutron converters), α and heavy ions, and also on their incident particle energies.

It is therefore desired to equip the IP with features of discrimination among radiation types and/or energy ROI (region of interest) and dose ROI. We have investigated in detail the response of the IP to many types of radiations to develop a radiation imaging technique equipped with radiation type discrimination. We have already found and elucidated a simple method to extract the radiation types and the incident energies of X(γ) rays, electrons, protons and alpha particles from the IP images[1].

We intended to extend the experiments to get a new response characteristic to heavy ions of higher LET (linear energy transfer), i.e. 220MeV $^{12}C^{5+}$, 160MeV $^{16}O^{6+}$, 350MeV $^{20}Ne^{8+}$, 330MeV $^{40}Ar^{13+}$, 520MeV $^{84}Kr^{20+}$ and 450MeV $^{120}Xe^{23+}$ ion beams. Various thickness aluminum absorber foils were used to degrade the top energies for getting lower energies and getting the particle energy responses with them.

2. Results and a discussion

Heavy ion irradiation onto the IP was done in a vacuum chamber at LD-1 port of TIARA AVF cyclotron using the uniformly scanned beam of 100 x100 mm^2 in area. The PSL (photo-stimulated luminescence) excitation spectra of the IP were measured over the range of 450nm - 750nm in wavelength on a timetable up to 48 hours after the irradiaion.

Discussion is here on the basis of the spectra 24 hours after the irradiation when the fading becomes negligibly small.

The PSL excitation spectra (stimulation spectra) obtained by 520MeV $^{84}Kr^{20+}$ ions are shown in Fig.1, as an example. Twin peaks at 500nm and 600nm in wavelength are characteristic of the IP. Comparing many PSL excitation spectra obtained by various ion beams with various energies mentioned above, we found some small component peaks, e.g. shown in the figure, are common to other spectra and making the main form of the twin peaks and then their changes changing the main form with time. There seems a strong correlation between some of the components and the causes of the fading of latent image of the IP.

It has been established for the blue IP, e.g. BAS-UR, that the PSL ratio of the twin peaks corresponds to the penetration depth of an incident particle, e.g. proton or alpha particle, into the IP through the dependence of the attenuation

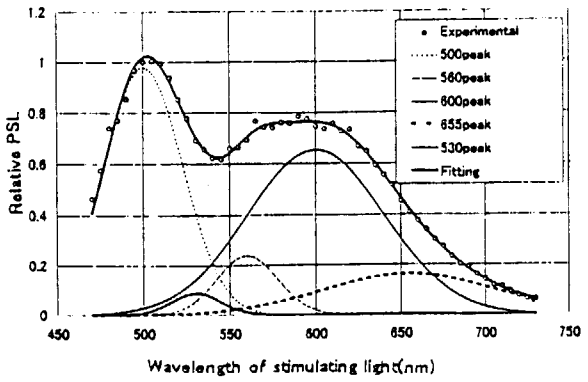

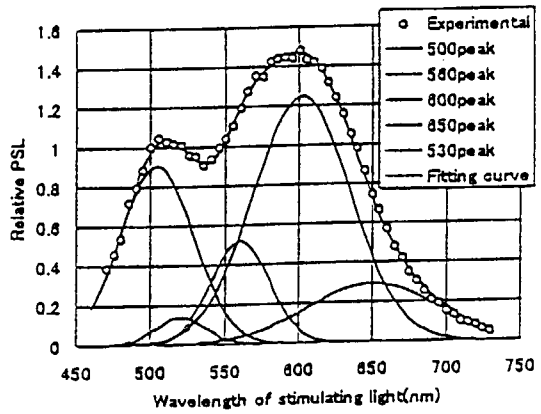

Fig.1. PSL excitation spectra of 520MeV $^{84}Kr^{20+}$ irradiation on IP. The upper: BAS-UR, the lower: BAS-Ⅲ.

length of the stimulating light on the wavelength as long as the particle stops within the IP's phosphor, which we call "depth effect" or "dye effect". But it was found that there is something yet to clear the relation of the penetration depth versus the PSL ratio of the twin peaks in the case of heavy ion irradiation. The depth effect was evaluated with both TRIM code and measured attenuation length of the stimulating light[1] in the IP. Fig.2 shows the average LET of the heavy particles versus the deviation of the PSL ratio from the one of the depth effect, where the average LET was also evaluated with the TRIM code over the whole track of the particles. Heavier ions show a larger deviation from the depth effect. We call this deviation "LET effect". A radiation damage of the IP may play some role in the LET effect in the case of heavy ion irradiation. The damage is, however, expected little in this case according to the fact that the present irradiation fluence is about $10^{10}/cm^2$ or less and the PSL signal is reported to decrease to 80% of initial PSL signal at $8x10^{13}$ He^+/cm^2 for 2 MeV[2]. The radiation damage of the IP is not yet well known.

Fig.3 shows that the unfolded components of the PSL spectrum as shown in Fig.1 depend separately on the intensity of the stimulating light, where the intensity varies by 30% and 70% using ND filters. Fig.4 shows the different representation of the Fig.3, whose relative PSL is the one renormalised by the light intensity (devided by the number of

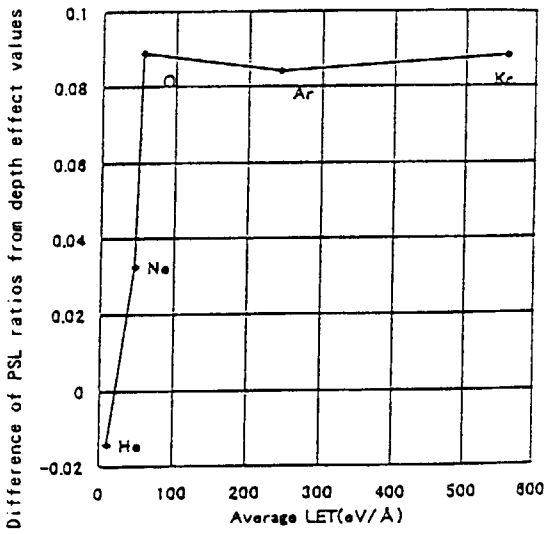

Fig.2. Average LET vs deviation of PSL ratio off the depth effects. He 10MeV, Ne 350MeV, O 160MeV, Ar 330MeV, Kr 520MeV.

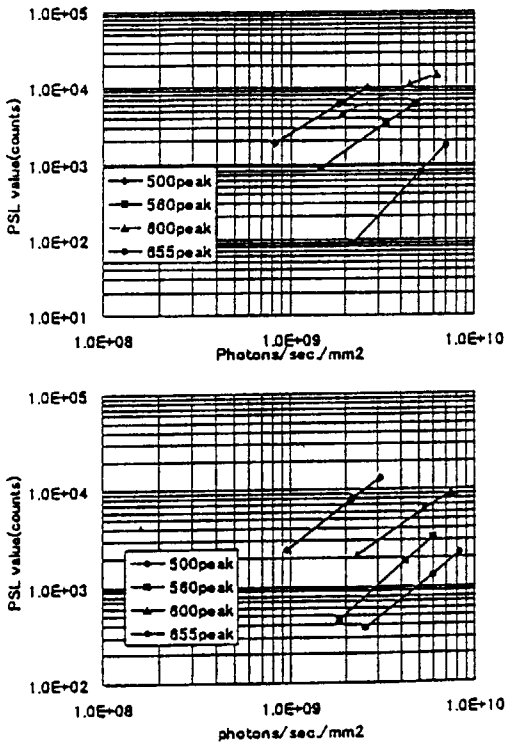

Fig.3. Stimulating light vs unfolded components of the PSL excitation spectrum of ^{60}Co-γ irradiation. The upper: BAS-Ⅲ, the lower: BAS-UR.

photons). Fig.3 and 4 suggest that the use of different intensity of stimulating lights can also enhance the particle discrimination among heavy ions, and in another side be expected to elucidate the details of PSL and fading mechanism of the IP.

The reason is not yet clear why the photo-bleaching and/or stimulation with different intensity of lights enhance the difference of the particle responses.

In conclusion, it is clear that the particle discrimination between the light ions and heavier ones is simple and easy. Moreover, the discrimination among heavy ions can be expected through a combination of the LET effect and the enhancement of the difference of the PSL ratio with photo-bleaching[3].

References

(1) M.Takebe et al., Nucl.Instr.Meth. **A345** (1994)606, **A359** (1995)626, **A363** (1995)614. Jpn.J.Appl.Phys. **34** (1995)4197. Radiation detectors and their uses, KEK Proceedings 98-,(1998).
(2) H.Kobayashi et al., Nucl.Instr.Meth. **B135** (1998)229.
(3) K.Toh et al., Extended Abstracts (Jpn. Soc. Applied Phys.) 1 (1997, Fall)110.

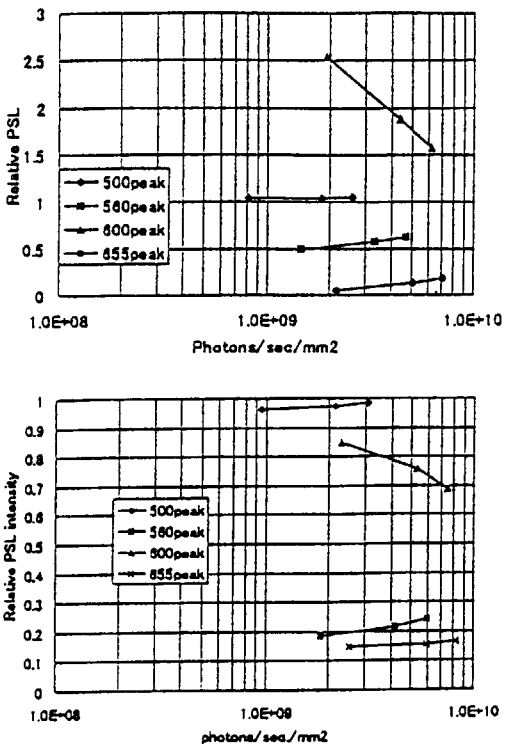

Fig.4. Stimulating light vs renormalised components of the PSL excitation spectrum of ^{60}Co-γ irradiation. The upper: BAS-Ⅲ, the lower: BAS-UR.

3. 4 Study of LET Effects on Polystyrene Excited States by Means of Ion Pulse Radiolysis

Y.Yoshida, S. Seki, Y. Mizutani, S Tagawa,
Y. Aoki*, M. Taguchi*, H. Nanba*
ISIR, Osaka University, *JAERI/Takasaki

1. Introduction

It is important to realize the mechanism of the irradiation effect of high energy ion beams which shows the different effects from the low LET radiation such as γ rays and electron beams. To investigate the irradiation effects, the behavior of the excited states of polymers and liquid alkanes was studied by using the ion beam pulse radiolysis [1-3]. The lifetimes of the lowest excited state of n-dodecane were reduced with increasing of the values of LET. On the other hand, the excimer of solid polystyrene showed a constant lifetime against the various LET values. To make a clear of the difference between n-dodecane and solid polyethylene, the time-dependent behavior of the excimers was studied in cyclohexane solutions.

2. Experimental

The time-resolved emission spectroscopy was done at HX1 irradiation port by using 520 MeV Kr^{+20} ion pulse beams from the AVF cyclotron. The repetition of the continuous pulse train was reduced to be 1/6 by using the s-chopper. The time-dependent emission was measured by a photon counting system. A start signal was gotten from the photomultiplier, and a signal from the s-chopper was used as a stop signal.

A specially-designed cell (made of stainless steel) for liquid samples was used. The sapphire window for the UV-emission was used.

The molecular weight of the polystyrene was 10000. All samples were degassed and irradiated at the room temperature.

3. Results and Discussion

Figure 1 shows the time-dependent behavior of the emission from polystyrene excimer obtained in the 520 MeV Kr^{+20} ion pulse radiolysis of 3, 10, and 100 mM polystyrene solutions in cyclohexane monitored at 330 nm. The emission intensities at various concentrations were normalized at the ion pulse end. In the 100 mM solution, the lifetime of the excimer was 20 ns which was agreement on the lifetime of solid polystyrene. In 10 and 3 mM, the fast and slow decay components were

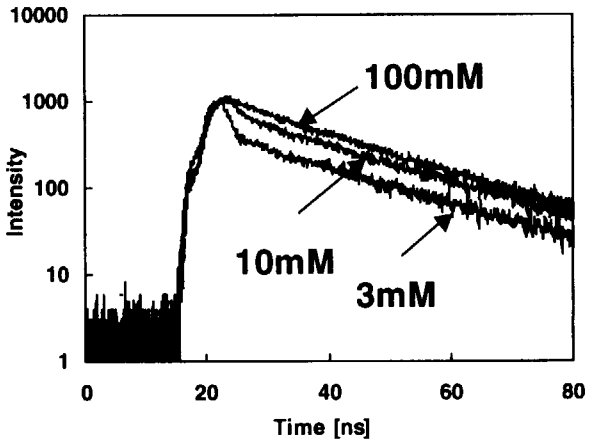

Fig. 1 Time-dependent behavior of polystyrene excimer obtained in 520 MeV Kr^{+20} pulse radiolysis of polystyrene solution in cyclohexane monitored at 330 nm.

observed. The lifetime of the slow components corresponded with 20 ns. The ratio of emission intensity of the fast component to that of the slow component increased with decreasing of the concentration of polystyrene.

From the former result of the ion beam pulse radiolysis of liquid n-dodecane and solid polystyrene, the LET effect on the excited states was closely related with the lifetimes, the mobilites and the concentration of the excited states. The lifetimes of the lowest excited state of n-dodecane decrease with increasing of the LET. The excited states should react with other excited states (or unknown short-lived intermediates) due to the high concentration in the truck. While the lifetime of polystyrene excimer is longer than that of n-dodecane, the excimer show a constant lifetime against the various LET values. It means that polystyrene excimers do not react with other polystyrene excimers (or unknown short-lived intermediates) due to the low mobility.

From the view points of the above discussion, the present experimental result will be discussed. It would be predicted that the LET effect on polystyrene excimer would be observed in the solution, because the excimer could move in the solution. If the excimer reacts with other excimer (or unknown short-lived intermediates), the LET effect should appear in the high concentrated solution. However, the behavior of the excimer was the same as the solid polystyrene at the high concentrated solution (100 mM). In the low concentration (10 mM and 3 mM), the LET effect was observed.

To understand the present result, the following reaction mechanism is proposed. The polystyrene excimer do not react with other polystyrene excimer both in the solution and solid phases. The movement of the polystyrene molecule is necessary for the reaction, the lifetime of the excimer must be shorter than the movement. Therefore, the lifetime of the slower component is 20 ns which is the same as the solid polystyrene. The fast decay is due to the reaction with other short-lived intermediates. One of the intermediates should be the cyclohexane excited state, because the lifetime of the fast decay is almost the same as the lifetime of the cyclohexane excited states observed at 220 nm.

The LET effect on the excited states was observed in this experiments. However, quantitative analysis has not been done, because the emission spectroscopy was not good at the quantitative measurement. We have a plan of the absorption spectroscopy to elucidate the problem.

References

1) H. Shibata et al. Nuclear. Instrum. Meth.,A327, 53, 1993
2) Y. Yoshida et al., Nuclear. Instrum. Meth, A327, 41, 1993
3) H. Shibata et al., Nucl. Instrum. Meth., B105, 42, 1995

3．5 Ion Beam Induced Crosslinking Reactions in Poly(di-n-hexylsilane)

S. Seki*, Y. Kunimi[a], K. Maeda S. Tagawa, Y. Yoshida,
H. Kudoh, M. Sugimoto, Y. Morita, T. Seguchi, H. Shibata
ISIR Osaka University, JAERI Takasaki, and RCNST University of Tokyo

Introduction

Recent studies on polysilanes have suggested many interesting features of polysilanes, such as semiconductive properties(Trefonas et al., 1985), nonlinear optical properties (Kajar et al., 1986), and photoconductivity(Fujino, 1987). These features of polysilanes have been determined to be due to their conjugated silicon skeleton, which has σ electrons delocalized along the skeleton. The UV-light photolysis phenomena of polysilane derivatives has been widely studied because of the possibility for use in the field of microlithography.

The UV light induced scission reactions, however, become a problem to use the polysilanes as electro-optical materials making the best use of the electronic properties of the polymers. The crosslinking reactions should play a significant role in the practical use of the polymer materials. Our previous study reported on reactive intermediates of polysilane derivatives irradiated by ion, electron and γ-rays(Seki et al., 1995). Predominant reactive intermediates in polysilane derivatives were assigned to silyl radicals showing great stability in comparison with carbon centered alkyl radicals(Seki et al., 1996). The ion beam irradiation effects on polysilanes also reported in the previous study (Seki et al., 1996). Reactions in the polymers were changed with the energy deposition rate of incident particle : LET of radiation sources.

Models of the energy distribution was proposed experimentally and theoretically as "Track Core" and "Penumbra" models by Magee et al.(1987), Varma et al.(1975), and Wingate et al.(1976). In spite of the theoretical modeling effort, the size of ion tracks has not shown good agreement with the values of intratrack reaction radius that was experimentally obtained by the analysis of irradiation products(Koizumi et al., 1996). Licciardello et al.(1988) and Calcagno et al.(1994) also reported the effects of ion beam bombardment to polystyrene leading to the aggregation of molecules and crosslinking reactions.

We discuss the efficiency of crosslinking and main chain scission reactions induced by ion beams, EB, and γ-rays with a variety of LET ranging from 0.2 to 1620 eV/nm. The molecular weight of the polymer is traced as a function of absorbed dose giving G-values (number of reactions per absorbed 100 eV) of the reactions. Both reactions in polysilanes are able to regard as reactions occurred in an individual ion track ; intratrack reactions. The simulation model of intratrack reactions reveals the chemical core to have different sizes with changing LET.

*e-mail : seki@sanken.osaka-u.ac.jp

Experimental

PDHS was prepared by the procedure in Seki et al.(1996). The molecular weight of PDHS was measured by gel permeation chromatography (GPC System, Shimadzu Class VP-10) with tetrahydrofuran as an eluent. The chromatograph equipped with four columns : Shodex KF-805L from Showa Denko Co. LTD. PDHS has initially bimodal molecular weight distribution. The high or low molecular weight peak was cut off by separatory precipitation leading to the low molecular weight PDHS (PDHS-L) and high molecular weight PDHS (PDHS-H) with monomodal distribution. The molecular weights of the polymers were Mn = 0.98 ~ 1.3 x 10^4 and Mw = 3.9 ~ 5.6 x 10^4 for PDHS-L, and Mn = 5.6 x 10^5 and Mw = 1.4 x 10^6 for PDHS-H, respectively. The PDHS samples were dissolved in toluene and spin-coated on Si wafers (0.5 μm thick). The polysilane films were 1-3 μm thick for all ion beam irradiation. These films were irradiated in a vacuum chamber (< 5 x 10^{-6} hPa) by 2 MeV $^1H^+$, $^4He^+$, and $^{14}N^+$ ion beams from a Van de Graaff accelerator at the RCNST, University of Tokyo. The ion beams from a cyclotron accelerator was also of use at JAERI, Takasaki. The irradiation was performed under vacuum (< 5 x 10^{-6} hPa) at room temperature using 20 ~45 MeV $^1H^+$, 20 MeV $^4He^{2+}$, 220 MeV $^{12}C^{5+}$, 225 MeV $^{16}O^{7+}$, 160 MeV $^{16}O^{7+}$, and 175 MeV $^{40}Ar^{8+}$ ion beams. After irradiation, molecular weight distribution of irradiated PDHS films was measured by the GPC system. The loss of kinetic energy of ions in traversing polymer films was estimated by the TRIM 92 code.

Results and discussion

The MeV order ion beam irradiation already re-

vealed to cause crosslinking reactions in polysilane derivatives making negative tone in the thin solid films. The behavior of PDHS drastically changed with the irradiation temperature and the value of LET of incident ions, i.e., the predominant reaction changed from crosslinking into main chain scission with increasing temperatures upon irradiation to high LET ion beams. The main chain scission reactions also became predominant in PDHS irradiated with the low LET ion beams even below phase transition temperature, ca. 312 K. Figure 1 displays the diagram of ion beam induced reactions in PDHS. The efficiency of crosslinking reactions is expected to depend on the values of LET, thus the change in the molecular weight is traced as a function of absorbed dose.

According to the statistical theory of crosslinking and scission of polymers induced by radiation(Charlesby-Pinner relationship : Charlesby, 1954a, 1954b, Charlesby and Pinner, 1959), G-values of main chain scission and crosslinking are estimated for ion beams. Figure 2 and 3 plots 1/Mn vs. D. The Charlesby-Pinner relationship apparently gives good interpretation to the change in 1/Mn for low LET radiation such as γ-rays, EB, and high energy proton beams. However, the linear relationship is no longer effective to fit 1/Mn vs. D of high LET ion beams at high dose (> 1 MGy) as displayed in figure 2. The solid PDHS films become partially insoluble against THF in the range of D, which is responsible to the non-linearity at high dose region. The slope of the plotting mainly reflects the probability of chain scission, and it suddenly drops down at the LET increased from 2.7 to 17 eV/nm. The irradiated part of PDHS films actually turns from positive to negative tone, thus the threshold of LET seems to locate around 10 eV/nm. Mw of PDHS is also plotted to D. The linear relationship in equation (2) also gives better fittings. Generally, Mw is more sensitive than Mn to the change in the molecular

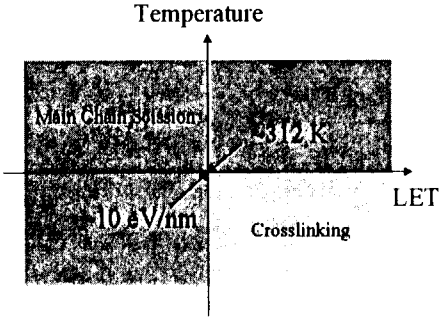

Figure 1. Schematic diagram of predominant reactions in PDHS.

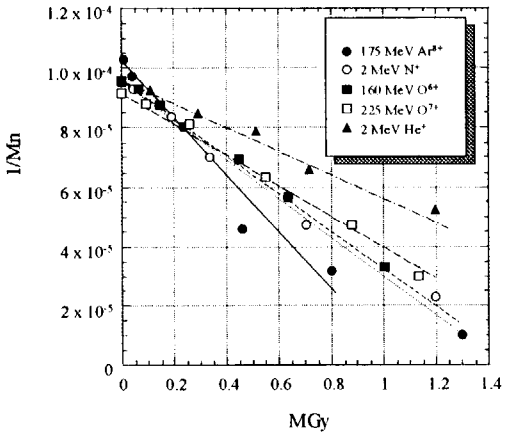

Figure 2. Charlesby-Pinner plotting of Mn to absorbed dose for 2MeV $^{4}He^{+}$, 225 MeV $^{16}O^{7+}$, 160 MeV $^{16}O^{7+}$, 2MeV $^{14}N^{+}$, and 175 MeV $^{40}Ar^{8+}$.

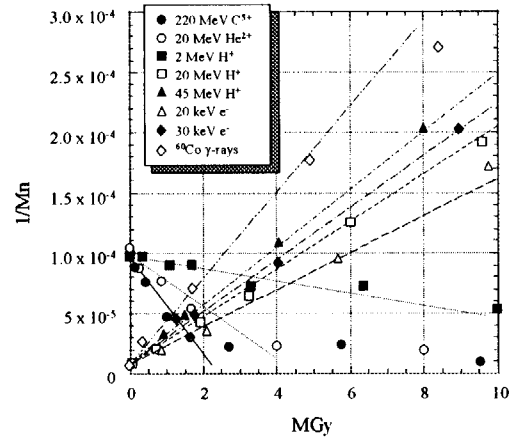

Figure 3. Charlesby-Pinner plotting of Mn to absorbed dose for ^{60}Co γ-rays, 20~30 keV e^{-}, 2 ~45 MeV $^{1}H^{+}$, 20 MeV $^{4}He^{2+}$, 220 MeV $^{12}C^{5+}$.

weight distribution, and it reflects the rapid decrease of 1/Mw. The negative slope of the fitting indicates that crosslinking reactions become predominant for the irradiation, and the slope turns from positive into negative at the same threshold of ca. 10 eV/nm.

Figure 4 shows semi-logarithmic plotting of the calculated G(x) against LET. G(x) increases with the increasing LET. The G(x) is estimated in both PDHS-L and PDHS-H for 2MeV $^{1}H^{+}$ and $^{4}He^{+}$ ion beams. However little difference is observed as shown in figure 4, indicating G(x) not to depend on the initial molecular weight of PDHS. G(x) is also plotted as a function of particle velocity in figure 5. Apparently, figure 4 gives a better fitting than that in figure 5. Our previous study reported anomalous change in the molecular weight distribution of PDHS irradiated by high LET ion beams. It was attributed to microscopically heterogeneous reactions caused along incident ion projectile,

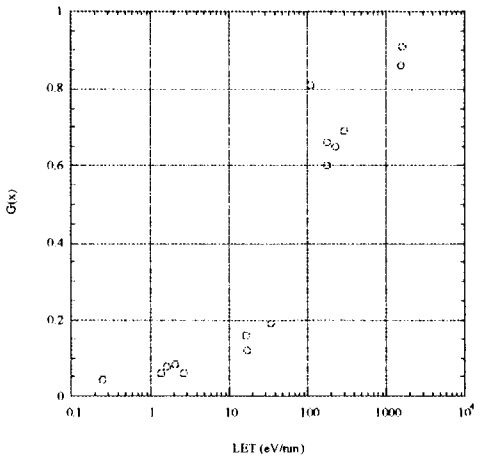

Figure 4 Semi-logarithmic plotting of the G(x) vs. LET.

giving ion track radii for a variety of ion beams. The LET dependence of ion track radii is similar to that of G(x). The volume of a single ion track should be responsible to the increasing G(x). The radius of a ion track by 2 MeV $^{4}He^{+}$ was reported to be 5.9 ± 1.5 nm, where G(x) is 0.66 in the present study. Thus, the track radii of 2 MeV $^{4}He^{+}$, 175 MeV $^{40}Ar^{8+}$, and 220 MeV $^{12}C^{5+}$ are predicted to be ca. 7.1, 6.9, and 6.2 nm, respectively. Several previous experimental studies also have been suggested a variety of radii for tracks induced by ion beams(Pulgsi and Licciardello, 1994, Licciardello and Puglisi, 1994. Values of radii were determined by Koizumi et al. (1996) in the same LET range of incident ions, which were varying from 2 nm to 5 nm. The present values of radii indicate similar values of radii to the experimentally obtained values, and locate in the middle of "Core" and "Penumbra" sizes speculated by theoretical aspects(Magee and Chatterjee, 1987). The sizes of "Core" and "Penumbra" have been considered as a function of rather particle velocity than LET. However the present results suggest that the energy deposition rate of incident particle gives better interpretation to the chemical track structure in the present polymeric materials.

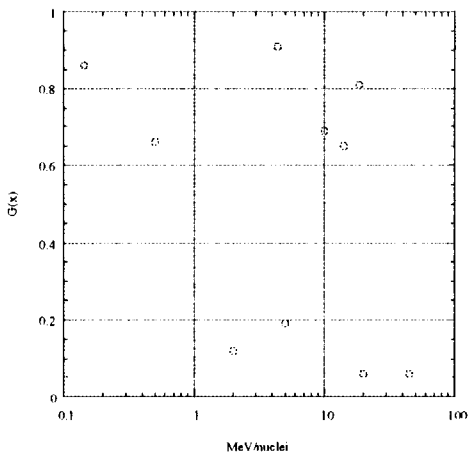

Figure 5 Semi-logarithmic plotting of the G(x) vs. particle velocity : MeV/nuclei.

Conclusion

Crosslinking and main chain scission reactions were investigated for ion beam irradiation to PDHS films. The changes in Mn and Mw of PDHS showed good agreement with the Charlesby-Pinner relationship at the range of low absorbed dose. The G-value of crosslinking increased from 0.014 to 0.91 with increasing values of LET. The expanding chemical track along a ion projectile may be responsible to the increasing crosslinking G-values. The reaction model in a single track was applied to the phenomena, suggesting the track radii of 2 MeV $^{4}He^{+}$, 175 MeV $^{40}Ar^{8+}$, and 220 MeV $^{12}C^{5+}$ to be ca. 7.1, 6.9, and 6.2 nm.

Acknowledgements

The authors thanks to Mr. K. Nishida at ISIR Osaka University and Mr. M. Narui and Mr. T. Omata at the University of Tokyo for their experimental supports.

References

Calcagno, L., Percolla, R., Foti, G. (1994) Nucl. Instr. Meth. Phys. Res. **B91**, 426.
Charlesby, A. (1954a) Proc. R. Soc. London Ser. A, **222**, 60
Charlesby, A. (1954b) Proc. R. Soc. London Ser. A, **224**, 120.
Charlesby, A., Pinner, S. H. (1959) Proc. R. Soc. London Ser. A, **249**, 367.
Fujino, M. (1987) Chem. Phys. Lett. **136**, 451.
Kajar, F., Messir, J., Rosillio, C. (1986) J. Appl. Phys. **60,** 3040.
Koizumi, H., Ichikawa, T., Yoshida, H., Namba, H., Taguchi, M., Kojima, T. (1996a) Nucl. Instr. Meth. Phys. Res. B **117**, 431
Licciardello, A., Puglisi, O., Calcagno, L., Foti, G. (1988) Nucl. Instr. Meth. Phys. Res. **B32**, 131.
Magee, J. L., Chattarjee, A. (1987) Kinetics of Nonhomogenious Processes G. R. Freeman Ed. Chapter 4, pp.171
Seki, S., Ando, M., Yamaki, T., Nakashiba, Y., Asai, K., Ishigure, K., Tagawa, S. (1995) J. Photopolym. Sci. Technol. **8**, 89.
Seki, S., Tagawa, S., Ishigure, K., Cromack, K. R., Trifunac. A. D. (1996a) Radiat. Phys. Chem. **47**, 217.
Seki, S., Shibata, H., Yoshida, Y., Ishigure, K., Tagawa, S. (1996b) Radiat. Phys. Chem. **48**, 539.
Schnabel, W., Klaumuenzer, Z. (1991) Radiat. Phys. Chem. **37**, 131.
Varma, M. N., Baum, J. W., Kuehner, A. J. (1975) Radiat. Res. **62**, 1.
Wingate, C. L., Baum, J. W. (1976) Radiat. Res. **65**, 1.

3. 6 Change in Mechanical and Optical Properties of Polymer Materials by Ion Irradiation.

H. Kudoh, M. Sugimoto and T. Seguchi
Department of Materials Development, JAERI

1. INTRODUCTION

The radiation resistance of polymers, the changes in mechanical and optical properties of polymers upon irradiation of high LET (linear energy transfer) ion beams, is the important factor for their application in space environment or around a fusion reactor. We found that change in mechanical property induced by light ion beam is the same as that induced by gamma rays or electron beam when the irradiation effect is compared at the same dose level[1]. Ion irradiation effects on optical properties of polymers have been studied in some reports. Kasai et al.[2] studied the depth profile of ultraviolet light absorbance for stacked aromatic polymers irradiated with Ni^{4+} ions, and found an excellent agreement in depth profiles between the absorbance and the calculated stopping power. Hama et al.[3], and Sugimoto et al.[4], studied depth-distribution of trans-vinylene bonds induced by ion beam irradiation in polyethylene by using micro-FTIR. They found a good agreement for many kinds of ions between observed absorbance and calculated stopping power. In this work we report changes in mechanical and optical properties induced by higher LET ion beam.

2. EXPERIMENTAL

Specimens for mechanical property test are polyethylene (medium density, MDPE, 150 μm thick) and poly-methylmethacrylate (PMMA, 3mm thick). Material for optical property change is cellulose tri-acetate (CTA, 125 μm thick). Ion irradiation was carried out with an AVF cyclotron accelerator in TIARA at RT under vacuum by beam scanning. Ions were Ne^{8+} (350 MeV) and Xe^{23+} (450 MeV). The stopping powers and penetration ranges based on TRIM 95 code are shown in Table 1. For MDPE, stopping powers of Ne^{8+} and Xe^{23+} are larger by 1.6×10^3 and 4.4×10^4 times than that of 2 MeV electron (ICRU 37). For PMMA, these ions stop at the inside of the specimen. The spot beam of about 10 mm diameter was scanned at 50 Hz in horizontal direction and 0.5 Hz in vertical direction on 10 cm x 10 cm area of the specimen at the currents of 100 nA for Ne and 20 nA for Xe ions. Dose was evaluated as a product of the fluence and the averaged stopping power in the specimen (TRIM 95 code).

Tensile tests were performed on MDPE at RT at a crosshead speed of 200 mm/min, and changes in elongation at break and tensile strength were examined. Three-

point flexural test was carried out for PMMA at RT at a crosshead speed of 2 mm/min with a span / thickness ratio of 16.7, and change in flexural strength was investigated. Change in optical density at 280 nm was measured for CTA with an UV spectrometer.

Table 1 Stopping power (S: keV/μm, at surface) and range (R: μm) of ions (TRIM 95 code).

Ion	PE		PMMA	
(MeV)	S	R	S	R
Ne(350)	2.9×10^{2}	7.2×10^{2}	3.4×10^{2}	6.1×10^{2}
Xe (450)	9.1×10^{3}	5.9×10^{1}	1.1×10^{4}	5.2×10^{1}

3. RESULTS

Figure 1 shows the changes in elongation at break and tensile strength as a function of dose averaged in the specimen, together with the previous data[1]. The decay in elongation at break until at around 0.3 MGy is almost the same for any irradiation sources from electron beam (2 MeV) to Ne^{8+} (350 MeV), though the stopping power of Ne^{8+} (350 MeV) is as high as 1.6×10^{3} times than that of 2 MeV electron beam. Tensile strength decreases with dose but keeps a constant around 25 MPa over 0.3 MGy. The behaviors of elongation and tensile strength indicate that the crosslinking proceeds by ion irradiation.

The Ne and the Xe beams do not thoroughly penetrate the PMMA specimens of 3 mm thickness. To analyze the spatially inhomogeneous degradation, we irradiated 500 keV electron beams on

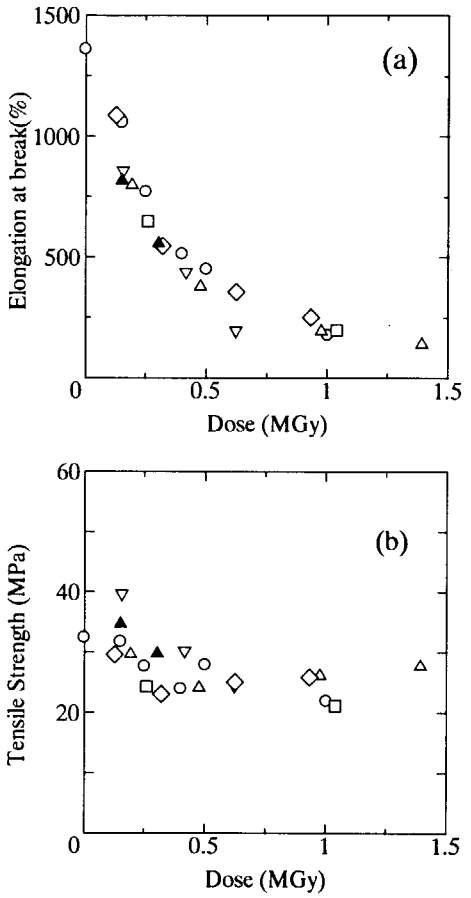

Fig.1 Change in elongation at break (a) and tesile strength (b) of MDPE by irradiation (○ : e^{-} 2MeV, △ : H^{+} 10MeV, ◇ : He^{2+} 50MeV, □ : He^{2+} 20MeV, ▽ : C^{5+} 220MeV, ▲ : Ne^{8+} 350MeV).

the PMMA specimens for modeling of ion beams. In the LET region of low energy electron, the LET-dependence of decrease in flexural strength is negligible[1]. We compared the decrease of flexural strength between 500 keV electron beam and gamma rays. The strength was plotted as a function of the averaged dose from the surface to the penetration range. When the tensile stresss was added to the irradiated side, a

good agreement was obtained. Then we analyzed flexural strength in the same procedure for ion irradiation. Ne^{8+} (350 MeV) and Xe^{23+} (450 MeV) showed a similar degradation behavior to the cases of gamma rays and electron beam. The stopping power of Ne and Xe is $1.6x10^3$ and $5x10^4$ times higher than that of gamma rays, respectively. It was confirmed that the degradation behavior of flexural strength does not depend on the LET.

Stacked CTA films were irradiated to Ne^{8+} 350 MeV. Change in optical density at 280 nm was measured for each CTA to get a depth profile. Figure 2 shows the change in optical density (OD) at 280 nm together with dose evaluated as a product of fluence and stopping power (TRIM code). This implies that the depth-profile of experimental OD change almost equals to the stopping power from TRIM code. Coloration increases in proportion to dose based on TRIM code. The sensitivity of coloration is 0.76 times of that to electron beam through the first layer to the fourth layer. For Xe^{23+} 450 MeV ions, we obtained similar distributions between the coloration and the stopping power.

4. CONCLUSION

Change in mechanical properties of MDPE showed little LET dependence. Decease in flexural strength of PMMA showed also little LET effect if the strength is measured with the irradiated side under tensile stress and studied as a function of averaged dose from the surface to the range. Depth profile of change in optical density for CTA is the same as that of calculation code. The sensitivity of coloration decreased for high LET.

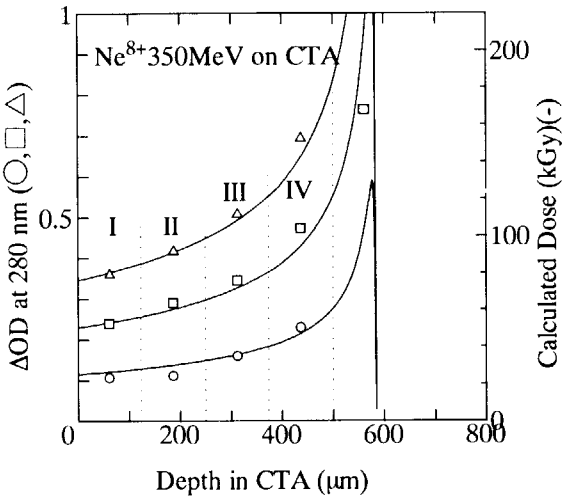

Figure 2. Comparison of depth-profile between OD change of CTA at 280 nm (○,□,△) and dose in CTA by TRIM code (solid line) for Ne^{8+}350MeV.

References

1) H. Kudoh, T. Sasuga and T. Seguchi, JAERI-Review 94-005, 79 (1994)

2) N. Kasai, H. Kudoh and T. Seguchi, JAERI-Review 97-015, 80 (1997)

3) Y. Hama, T. Takano, K. Inoue, M. Kitoh, H. Kudoh, M. Sugimoto, and T. Seguchi, JAERI-Review 97-015, 59 (1997)

4) M. Sugimoto, H. Kudoh, T. Sasuga, T. Seguchi, Y. Hama, K. Hamanaka, H. Matsumoto, JAERI-conf 97-003, 269 (1997).

3. 7 Permeation of p-nitrophenol through membrane containing thermally responsive graft-polymers on the surface

MASAHARU ASANO, MASARU YOSHIDA, TAKESHI SUWA

Department of Material Development, Takasaki Radiation Chemistry Research Establishment, Japan Atomic Energy Research Institute, 1233 Watanuki-Machi, Takasaki, Gunma 370-1292

AKIHIRO HIROKI, RYOICHI KATAKAI

Department of Chemistry, Faculty of Engineering, Gunma University, Kiryu, Gunma 376-8515

1. INTRODUCTION

Our goal is to create a pore-size-controllable functional film which responds selectively to environmental signals, here temperature, by a combination of ion beam technology and functional materials technology. For this purpose, a thermo-responsive N-isopropylacrylamide (NIPAAm) polymer was grafted onto a newly synthesized etched-track copolymer film consisting of diethyleneglycol-bis-allylcarbonate (DG) and NIPAAm by post-polymerization after previous γ-irradiation. Many researchers have reported that NIPAAm polymer is easily grafted onto films such as poly(ethylene/vinyl alcohol), nylon, poly(vinylidene fluoride), and poly(vinyl alcohol). However, we confirmed that a polymer of NIPAAm is difficult to graft onto bulk DG films by means of radiation-induced polymerization. To solve this problem, we synthesized a copolymer film by introducing NIPAAm into DG. The thermo-response of the corresponding NIPAAm-grafted etched-track films is reported using p-nitrophenol (PNP) as a permeant.

2. EXPERIMENTAL

A 50 μm thick copolymer film was prepared by the cast polymerization technique. The cast polymerization was performed at 70°C for 24 hours in nitrogen atmosphere. The films obtained were fixed on a glass plate (50 mm x 50 mm x 1 mm) after being cut into 4 cm x 4 cm squares. The ion species used were ^{84}Kr ion with an energy of 6.19 MeV/n and a fluence of 10^7 ions/cm^2. The etching of the latent tracks obtained was performed in aqueous 5M NaOH solution at 70°C for 45 minutes, resulting in the formation of cylindrical pores passing through the film with a diameter of 2.5 μm. A linear polymer of NIPAAm was grafted onto the etched tracks of the copolymer films by post-polymerization after pre-irradiation. The etched-track copolymer films were first irradiated at 25°C in dry air at a dose rate of 10 kGy/h, using γ -rays from a ^{60}Co source (irradiation time between 1 and 5 hours), then immersed

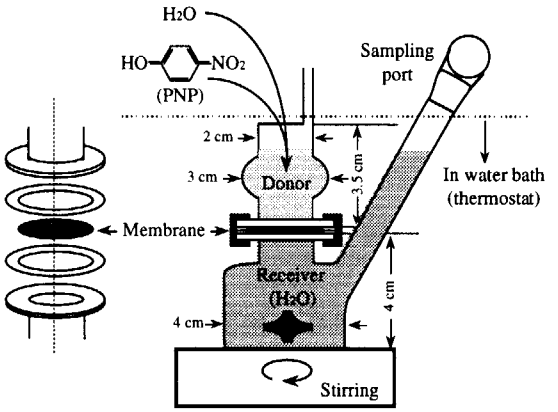

Fig. 1 Modified Franz cell used for PNP permeation.

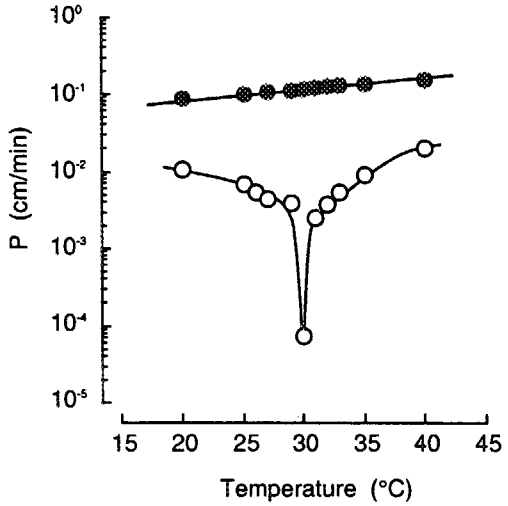

Fig. 2 Temperature dependence of the permeability constant (P) of PNP from (O) NIPAAm-grafted and (●) NIPAAm-ungrafted copolymer films after track etching.

immediately in a glass ampoule filled with aqueous 10% (w/w) NIPAAm solution and treated at 60°C in a sealed ampoule in vacuo to perform the graft-polymerization, namely, a pre-irradiation and post-grafting technique. The permeability constant (P) of PNP from NIPAAm-grafted etched-track copolymer films was measured using a modified Franz cell apparatus, as shown in Fig. 1. The apparent permeability constant (P, cm/min) was calculated from the following equation [1, 2]:

$$P = \frac{kV}{AC}$$

where k is the slope of the release-time curve, V is the volume of the outer water phase (receiver chamber), A is the surface area of a film, and C is the concentration of PNP trapped in the donor chamber. Samples were collected from a side arm at various intervals. The concentration of permeated PNP was assayed at 317.5 nm with a Hitachi U-3210 UV spectrophotometer.

3. RESULTS AND DISCUSSION

Using a NIPAAm-grafted etched-track film with a surface graft yield of 0.18 mg/cm^2, the temperature dependence of the permeation of PNP was investigated. The results are shown in Fig. 2. In NIPAAm-ungrafted film, the permeability constant (P) monotonically increased with the increase in temperature in the range of 20°C to 40°C used in this study. In contrast, for NIPAAm-grafted films the P values exhibited a greatly different permeation characteristic around 30°C. In particular, at

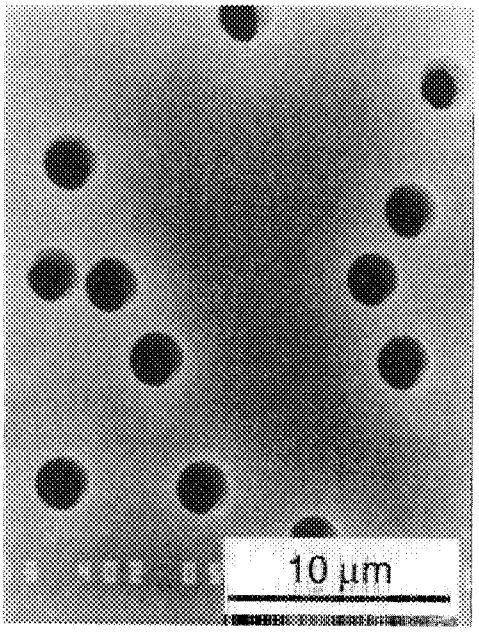

Fig. 3 A SEM view of etched-track copolymer film without grafting. The etched-track copolymer films with a pore diameter of 2.5 μm were obtained by treatment in aqueous 5M NaOH solution for 45 minutes at 70°C after a 6.19 MeV/n ^{84}Kr ion irradiation.

temperatures of 29°C, 30°C, and 31°C the P values were found to be 3.84 x 10^{-3}, 7.12 x 10^{-5}, and 2.46 x 10^{-3} cm/min, respectively, indicating that the permeation of PNP is markedly depressed only at 30°C. Such sudden permeability depression can be explained by the existence of a theta-point (Θ) temperature. Tanaka reported that this Θ temperature is 30.59°C, at which the hydrophilic interaction between the NIPAAm polymer chain and water apparently disappears, as the permeation of water-soluble PNP is retarded by the appearance of a strong

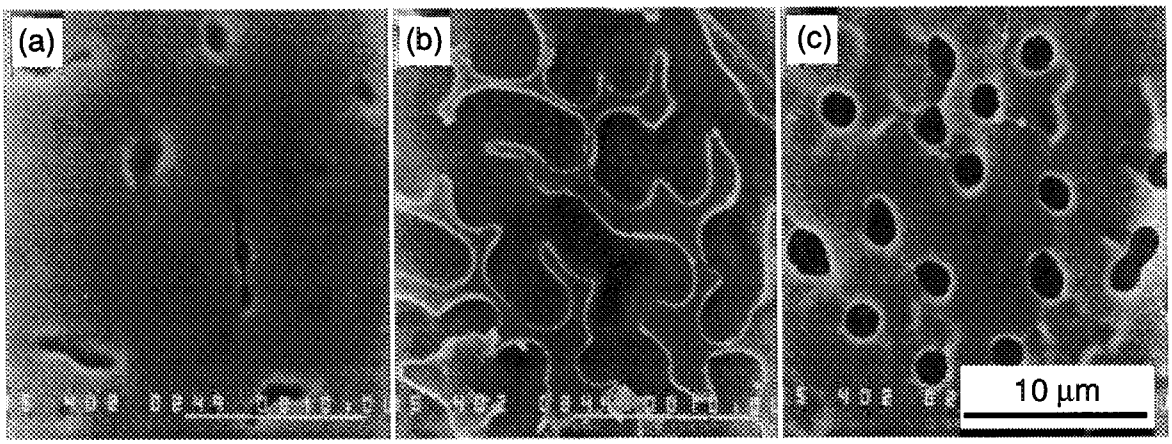

Fig. 4 SEM views of NIPAAm-grafted etched-track copolymer films treated in water kept at temperatures of (a) 20°C, (b) 30°C, and (c) 40°C for 24 hours after pre-swelling to saturation in water at 0 °C (ice-water). The etched-track copolymer films were obtained by etching in aqueous 5M NaOH solution for 45 minutes at 70°C after a 6.19 MeV/n ^{84}Kr ion irradiation. The grafting of NIPAAm was done by post-polymerization at 60°C for 30 minutes *in vacuo* after pre-irradiation of 30 kGy in dry air. The graft surface yield is 0.18 mg/cm^2.

of this polymer swells below the LCST, but shrinks above the LCST. Such a hydrophobic effect was also suggested by the results of laser light scattering studies [5, 6].

Fig. 3 shows a SEM view of pores at the surface of etched-track copolymer films without grafting, in which the cylindrical pores obtained with uniform diameter of 2.5 μm pass through the film. It was confirmed here that the pore geometry remains unchanged between 0°C to 50°C. On the other hand, Fig. 4 shows SEM views of the grafted pores of NIPAAm-grafted etched-track copolymer films as a function of temperature. The polymer chains of NIPAAm grafted on the wall of etched-track copolymer films are greatly expanded by inclusion of water at 20°C, as the pores are almost completely covered with the grafted layer (Fig. 4a). In this case, the permeation of PNP is dominated by the diffusion in the surface graft. At 30°C, the grafted NIPAAm layer showed a discontinuous shrinking on the film surface (Fig. 4b), in which the permeation of PNP is markedly depressed in close relation to the existence of a Θ temperature. Contrary to these results, pores in the film fully opened when the sample was treated at 40°C because of the aggregation of NIPAAm polymer chains. The resulting permeation level of PNP jumped near to that at 20°C again, but the permeation mechanism is markedly different from that at 40°C.

1) C. C. Hsu, J. Y. Park, N. F. H. Ho and W. I. Higuchi, *J. Pharm. Sci.* **72** (1983) 674.
2) Y. Okahata, H. J. Lim, G. Nakamura and S. Hachiya, *J. Am. Chem. Soc.* **105** (1983) 4855.
3) T. Tanaka, *Phys. Rev. Lett.* **40** (1978) 820.
4) C. Wu and S. Zhou, *Macromolecules* **28** (1995) 8381.
5) S. Fujishige, K. Kubota and I. Ando, *J. Phys. Chem.* **93** (1989) 3311.
6) K. Kubota, S. Fujishige and I. Ando, *J. Phys. Chem.* **94** (1990) 5154.

3．8 Dosimetry Systems for Characteristics Study of Thin Film Dosimeters (Ⅲ)

T. KOJIMA, *H.SUNAGA, H.TAKIZAWA, H.TACHIBANA
Advanced Radiation Technology Center, TRCRE, JAERI

1. Introduction

Estimation of absorbed dose and its distribution in interested materials is necessary for evaluation/interpretation of radiation effects of charged particle beams on organic materials used in nuclear research facilities, semi-conductors used in space environment, and biological substances in mutation research. Such radiation effect studies have been carried out using ion beams with a few tens of MeV/amu which are provided from the AVF cyclotron of TIARA. Dose measurement techniques for these studies in dose range of 0.01-200kGy should have an accuracy of about 5%, which includes the overall uncertainty in the film dosimeter system (about ±3%). Thin film dosimeters of about 10 to 200 μm in thickness such as cellulose triacetate (CTA) dosimeter and alanine film dosimeter, have been well-characterized for ^{60}Co γ rays and MeV electron beams. These dosimeters, when calibrated, are promising to be applied also to ion beam. Reliability check of the real-time beam monitoring technique using a Faraday cup is also indispensable in advance of dose response characteristics studies.

Uncertainty study in the fluence measurement has been carried out by simultaneous use of a Faraday cup (Fig.1) and a total absorption calorimeter (Fig.2)[1,2]. The fluence measurement above about 10 nC/cm^2, which is required for radiation effect studies on organic materials, is achievable within ±2% for most of studied ion beams using the present Faraday cup measurement. The result suggests, however, need of improvement in the lower fluence range which is required for the radiation effect studies in biology.

In the present work, fluence measurement lower than 10 nC/cm^2 was preliminarily studied considering contribution of undercurrent in Faraday cup measurement and optimization of the procedure of calorimetry for temperature rise to about 0.1℃.

2.Experimental

The total absorption calorimeters were designed and fabricated for evaluation of

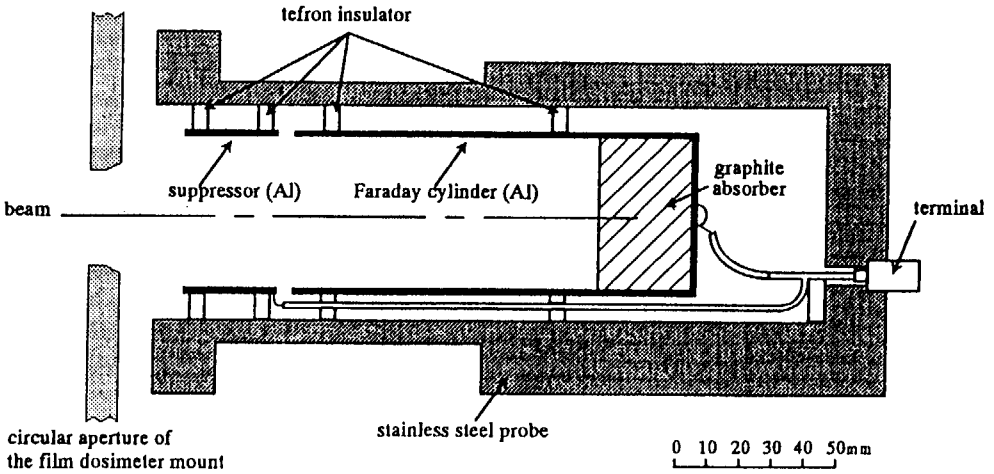

Fig.1 Elevation schematic drawing of the Faraday cup for 5-20MeV/amu ion beams. It consists of the Faraday cylinder (Al) with the graphite absorber at the bottom and the suppression electrode tube (Al) upstream to the beams.

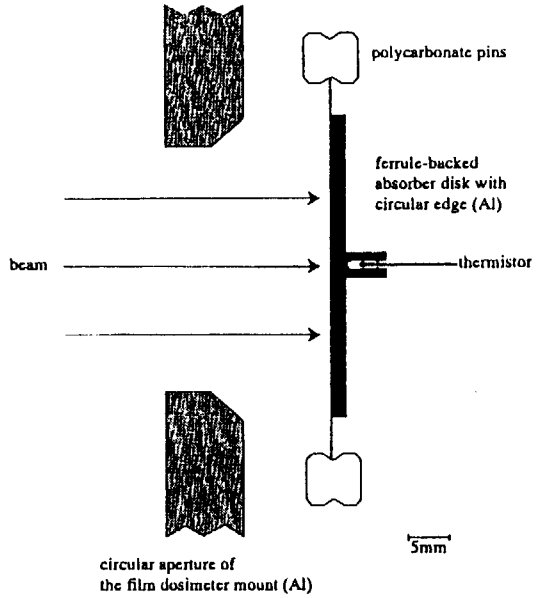

Fig.2 Sectional scheme of the total absorption calorimeter with 3 mm thick aluminum absorber disk, as an example, where temperature sensing thermistor is mounted on the opposite side from the incident ion beam. Different disk absorbers of 0.5 and 1 mm in thickness were also fabricated of the same structure according to penetration range of incident ions.

uncertainties in Faraday cup measurement. These calorimeters have different absorbers of 0.5-3 mm in thickness according to the required penetration ranges to stop ion beams completely. The simultaneous irradiation technique of a Faraday cup, a calorimeter and film dosimeters was also developed to use them in the wide-uniform fluence irradiation field of 100x100 mm^2 with scanning ion beams of 5-20 MeV/amu provided from the AVF cyclotron[1,2]. The Faraday cup (suppression voltage:-100V) and the calorimeters [the specific heat capacity of aluminum (Al): Ca(T)=0.8612+0.00126T (J℃/kg), T=10-40℃] are exposed to ion beams passing through 5-mm thick Al plate with the circular aperture of ϕ30 mm in diameter (7.07 cm^2 in area). The film dosimeters mounted on this aperture plate are also irradiated in vacuum (about $2x10^{-4}$Pa) with current/charge measurement using the Faraday cup. This method allows us to minimize uncertainty due to instability of beam current.

Two different irradiation experiments were performed using 20 MeV $^4He^{2+}$ and 160 MeV $^{16}O^{6+}$ up to the integrated charge of 2-8 nC/cm^2 for each ion as a preliminary study on lower fluence measurement. The integrated charge of about 16-60 nC/7.07 cm^2 is resulted into temperature rise of about 0.1 Celsius in the calorimeter absorber within about 45 sec. The contribution of undercurrent in the Faraday cup measurement without ion beam exposing was estimated to be about 0.03 nA and taken into account for correction of charge integration. These measured fluence values were compared with calculated values Φ using the following formula: $\Phi = \Psi / E$, where Ψ is the energy fluence derived from calorimeter measurement and E is the nominal energy given from cyclotron operation parameters.

3.Results and discussion

Table 1 summarizes the results of the ratio of measured fluence and estimated value based on the nominal energy, and the variation coefficients among at least three repeating fluence measurements. The ratios obtained in this work(☆) for lower fluence measurement are in the range 0.991-1.073 (average:1.024) and within the variation coefficients of ±2% (1σ), which are similar to the previous result for higher fluence measurement[1,2], although there are a few experimental results. This suggests that the uncertainty in measurements of both higher and lower fluence range mostly meets to ±5% precision which is required in dosimetry for radiation effect studies on polymers as well as those on biological substances, including specified uncertainty of film dosimeter systems (± 3%). The overestimation of about 2% in fluence values suggests need of uncertainty check in nominal energy values of the cyclotron.

On the basis of this real-time current/charge monitoring, dose response characteristics of several film dosimeters were studied preliminarily for ion beams of 3.5-45 MeV/amu with mass collision stopping power ranging about 12-84,000 MeV/(g/cm^2). Dose responses in terms of dosimeter responses, e.g. optical density change per unit dose, were estimated only using linear dose range of 10-200 kGy for CTA, 200-400 Gy for Gaf chromic and 2-10 kGy for alanine and Radiochromic

Table 1 Uncertainties in fluence measurement ☆this work

ion beams	energy*1 (MeV)	measured charge*2 (nC)	fluence ratio*3	v.c.*4 (%)	
$^{1}H^{+}$	20(20)	780-1,900	1.056	±0.8	
$^{4}He^{2+}$	20(5)	390-540	1.073	±3.0	
		26-27	1.015	±2.1	☆
	50(12.5)	360-550	0.993	±1.3	
$^{12}C^{5+}$	220(18.3)	160-300	0.991	±1.4	
$^{16}O^{6+}$	160(10)	150-200	1.040	±4.0	
		16-60	1.044	±0.7	☆
$^{20}Ne^{8+}$	350(17.5)	110-140	0.997	±4.7	
$^{40}Ar^{11+}$	330(8.3)	200	1.043	±0.3	
$^{84}Kr^{20+}$	520(6.2)	40	1.001	±1.8	

*1 nominal energy of incident ions (MeV/amu).
*2 integrated charge measured in the circular area of 7.07cm^2.
*3 the fluence ratio of the measured ones to those estimated on the basis of the nominal energy.
*4 variation coefficients at a 68% confidence level which were estimated from at least three repeating measurements.

(FWT-60) films, and normalized them to those for low LET radiation e.g. ^{60}Co γ rays and 45 MeV protons. These values are plotted as the function of mass collision stopping power $(S/\rho)_{col}$ of interested materials for incident ion beams. Absorbed dose in dosimeter materials was derived from the product of fluence measured by the Faraday cup and $(S/\rho)_{col}$ calculated using ELOSS code[3] on the basis of Ziegler's data tables[4]. In the present work, average value of $(S/\rho)_{col}$ was calculated from integral of total stopping power over the entire dosimeter thickness. Average $(S/\rho)_{col}$ values were 10 % at the maximum higher than $(S/\rho)_{col}$ values calculated based on the initial particle energy.

Relative dose response for all the dosimeter decreases with increase of mass stopping power at above 100 MeV/(g/cm^2), for instance, about 0.6 and 0.3 at about 1,000 and 10,000 MeV/(g/cm^2), respectively. For further discussion to interpret the LET dependence of the dose responses, their saturation characteristics at very high doses attributed to localized high energy deposition along the ion pass and/or fading characteristics of dose responses.

References

1)T.Kojima et al.: JAERI-Review 96-017 (1996) 79 :JAERI-Review 97-015(1997)75
2)T.Kojima et al.: *Radiat.Phys.Chem.*, **53** (1998) 115
3)K.Hata and H.Baba: JAERI-M 88-184(1988)
4)J.F.Ziegler, J.P.Biersack and U. Littmark : "The stopping power and range of ions in solids", Vol.1(Permagon Press, Oxford, 1985).

3．9 Heavy Ion Irradiation Effects on Optical Properties of Polymer Materials - 2.

Noboru KASAI, Hisaaki KUDOH, and Tadao SEGUCHI
Department of Materials Development, JAERI

1. Introduction

Poly-ether-ether-ketone (PEEK) and poly-ethylene-naphthalete (PEN) films containing aromatics have excellent thermal, optical, and mechanical properties, and are expected for use as temperature controlling material or an optical reflector in a space satellite. Under the space environment, the materials are exposed to high energy radiation such as electrons, protons and heavy ions, and the characteristics of the materials degrade. Radiation resistance of the polymers, especially against ion irradiation, is of critical importance in the environment. PEEK and PEN films were irradiated by heavy ions, and the changes in optical properties such as light transmittance were investigated. In our previous report[1, 2], decreases in transparency were much large by Ni^{4+}, Si^{4+}, Fe^{4+}(15 MeV) irradiations carried out at Tandem accelerator in comparison with those by electron beam (2 MeV), Ar^{8+} (175 MeV), Xe^{23+} (450 MeV). The big difference was thought to be induced by the beam heating related to the high dose rate. In this report, effects of ion species and the dose rate were studied.

2. Experimental

Materials are PEEK film of 6 μm thickness, and PEN film of 1 μm thickness. Ion beam irradiation was carried out under vacuum. The ion energy, the stopping power and the penetration range are shown in Table 1. Ni^{4+}, Fe^{4+}, Si^{4+} and O^{4+} ions were irradiated with Tandem accelerator under vacuum by sample scanning. Each polymer film was put on a cylindrical holder (Al, 75 mm ϕ), and the holder was rotated at 200 or 400 rpm, and moved repeatedly along the rotational axis at 200 cm/min. For comparison, beam scanning was also tried. A spot beam of 1 cm diameter was scanned at 999 Hz in horizontal direction and 606 Hz in vertical direction over an area of 2.5 cm x 2.5 cm. Ar^{8+} and Xe^{23+} ions were irradiated with Cyclotron accelerator by beam scanning. The absorbed dose by ion irradiation was evaluated by the product of fluence and stopping power from TRIM code. For the reference, electron beam (EB, 2 MeV) irradiation was carried out under vacuum. The dose was measured by using CTA film dosimeter. Absorption spectra of irradiated PEEK

and PEN films were obtained by an UV spectrometer at room temperature in the wavelength region of 200 -900 nm after storage over ten days under air at room temperature.

Table 1. Ion Energy (E), range (R) and stopping power (S, averaged in 6 μm thickness) for PEEK.

Ion	E (MeV)	R(μm)	S (keV/μm)
Ni^{4+}	15	6.4	$2.31x10^3$
Fe^{4+}	15	6.6	$2.31x10^3$
Si^{4+}	15	8.0	$2.28x10^3$
O^{4+}	15	11.5	$1.38x10^3$
Ar^{8+}	175	58.6	$2.59x10^3$
Xe^{23+}	450	51.0	$1.14x10^4$
e^-	2	8 mm	0.234

3. Results and Discussion

(1) Depth profiles

Figure 1 shows depth profiles of absorbance (optical density, OD) and stopping power for TRIM code for PEN film, where O^{4+} (15 MeV) was exposed to a stack of 1 μm thick films, and the OD was measured at 400 nm. Increase in OD is almost proportional to the fluence. The depth profile of OD shows a difference from that of stopping power. That is, OD shows a steeper and deeper peak than TRIM. Ni^{4+} ion irradiation to PEN in our previous study[2] showed the same depth profile between OD and TRIM. For these multi-charged ions, the stopping power calculated from TRIM code should be checked.

(2) Effect of dose rate

The effect of dose rate was investigated by changing the irradiation procedure. Figure 2 shows the OD of PEEK film at 400 nm as a function of dose for Ni^{4+} (15 MeV) ions. As shown in the figure, the sample scanning at the rates of 200 and 400 rpm gave the same changes. Moreover, no difference in OD was observed between the beam scanning and sample scanning. In the dose rate ranges in this case, the coloration of PEEK was not affected by the dose rate.

(3) Effect of ion species

Figure 3 shows increases in OD as a function of dose for PEEK (6 μm) upon irradiation of various ions. Irradiation of O^{4+} (15 MeV) gave appreciably less increase compared with Ni^{4+}, Fe^{4+}, and Si^{4+} ions of 15 MeV. The increase by O^{4+} was the same as in the cases of Xe^{23+} (450 MeV) and Ar^{8+} (175 MeV). This difference would come from that whether ions penetrate throughout the specimen or not. Namely, for Ni^{4+}, Fe^{4+} and Si^{4+}, the ranges of ions are almost the same with specimen's thickness (6 μm). Whereas, for O^{4+}, Xe^{23+} and Ar^{8+}, the range is much large and all of ions can completely penetrate the specimen. In a case of the former ions, that is, their penetration ranges are almost the same with the specimen thickness, a part of

ions stop inside the specimen and the charges are accumulated. The charge might accelerate the coloration in the polymers.

References

1) N. Kasai, T. Arakawa, and T. Seguchi, TIARA Annual Report, **vol. 5**, 82 (1996)

2) N. Kasai, H. Kudoh, and T. Seguchi, TIARA Annual Report, **vol. 6**, 80 (1997).

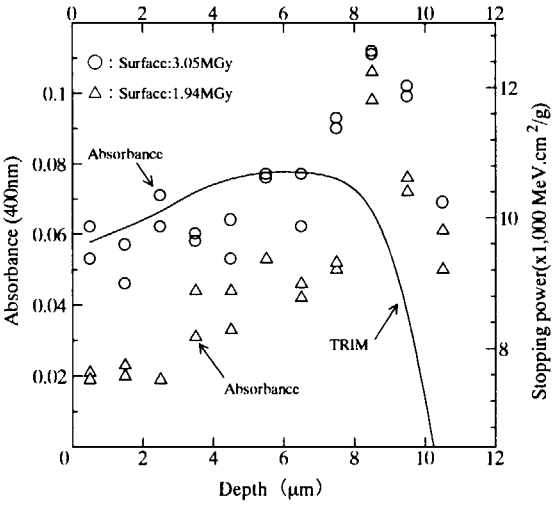

Figure 1. Depth profiles of absorbance at 400 nm and stopping power of PEN (a stack of 1 μm thick films) by O^{4+} (15 MeV) irradiation. (○:Absorbance of PEN at 400 nm irradiated to 3.05 MGy, △:Absorbance of PEN at 400 nm irradaited to 1.94 MGy, solid line : stopping power by TRIM.)

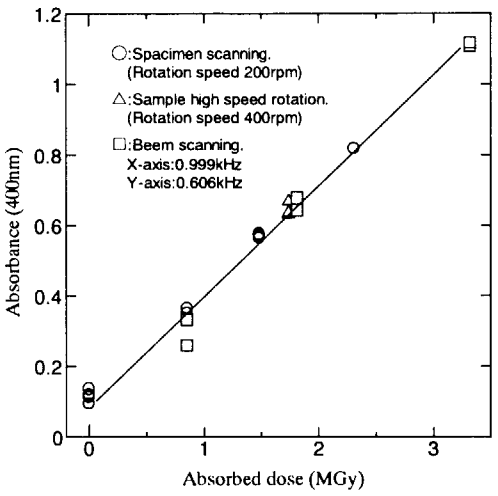

Figure 2. Effect of irradiation procedure on absorbance of PEEK film(6 μm) at 400 nm absorbance by Ni^{4+} (15 MeV) irradiation. (○:sample scanning at 200 rpm, △:sample scanning at 400 rpm, □:beam scanning)

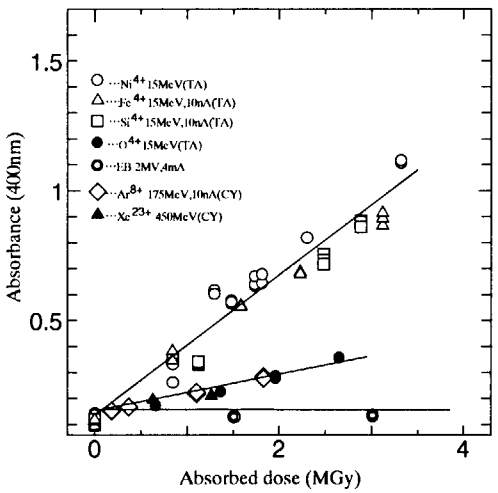

Figure 3. Change in absorbance at 400 nm of PEEK (6 μm thick) film for various ions and dose rates. (○ : Ni^{4+} 15 MeV, △ : Fe^{4+} 15 MeV, □ : Si^{4+} 15 MeV, ● : O^{4+} 15 MeV, ◇ : Ar^{8+} 175 MeV, ▲ : Xe^{23+} 450 MeV,◎ : EB 2 MV)

3. 10 Preliminary experiment of ion implantation into organic electroluminescence device

Tomoyuki Shirasaki, Hitoshi Yamamoto, *M. Tamada, *H. Koshikawa, *T. Suwa
CASIO Computer Co.,ltd, *Dep. of Mater. Develop., JAERI/Takasaki

1. Introduction

Organic electroluminescence device (OELD) can be driven by a low voltage of DC, and is expected as one of the promising flat displays such as Plasma display panel and Field emission display in next generation. Especially, only OELD is composed of all solid state material, and has a light weight, thin panel, never shattering and an easy process for large sizes. Therefore it has a great predominant potential against the above competitive technology.

OELD has multi-layer structures in which organic thin layers between cathode and anode electrode. The cathode electrode is one of the most important parts of electron injection to improve properties of OELD. We expect to improve the electron injection efficiency. There are several techniques such as co-deposition of a low work-function metal and the addition to insulation thin film, about 20 Åthick, between cathode and organic layer.

In this report, potassium ions were implanted into the cathode as a preliminary experiment.

2. Experimental

Figure 1 shows the OELD structure. Generally it is composed of two or three layers which play roles of carrier injection, transport, and light emission, respectively. In this experiment, we chose a single light emitting layer structure of tris(8-quinolinol) aluminum, called Alq_3, to simplify the analysis. This OELD has a good rectification even though it's a single structure. Aluminum of work function 4.3 eV was deposited as the cathode. It is higher than 3.8eV of magnesium often used as OELD cathode. Potassium as implanted ions has a low work function; 2.24eV, electron affinity; 0.5eV, electronegativity; 0.8eV. Therefore if potassium ion could be implanted, it would be supposed to make the result much clearer.

Potassium ions were implanted into the devices by TIARA 400kV ion implantation equipment. Table 1 shows the injection current and injection time. After implantation, the

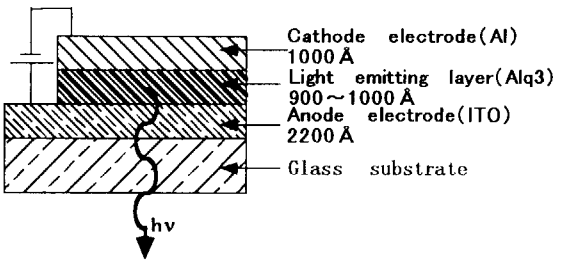

Figure 1 The structure of EL device

Table1 Implantation Parameter

Injection current (nA)	Injection Time (hr)	
50	1	→ Fig.4
50	2	
100	0.5	
100	1	

Ion specie K^+, Accelerate Voltage80 keV

OELD were evaluated by voltage/current density and brightness (VIL) characteristics, and voltage and frequency/capacitance and conductance ones.

3. Results and discussion

Figure 2 shows a simulated potassium doping profile. Potassium is concentrated near the boundary between the cathode and the light emitting layer, and distributed in cathode and light emitting layer, respectively. The implantation effects are supposed to be as follows:

1. Potassium in Aluminum cathode can improve electron injection because of its lower work function. It has already been done by co-deposition of Aluminum and Lithium; 2.5 eV. However we might mention the low concentration of Potassium in Aluminum by means of the implantation if it is compared to 0.5 to 2 weight % potassium in Aluminum in the case of co-deposition.
2. Potassium in the light emitting layer can make trap sites and increase the possibility of the tunnel current.

Figure 3 shows the VIL characteristic of unimplanted device. It reveals a good rectification characteristic, and a light emitting at 8 V and higher.

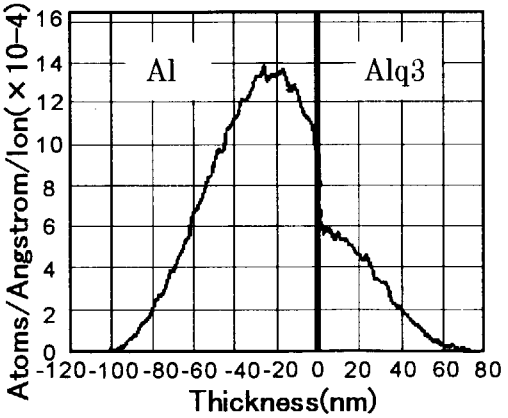

Fig. 2 The potassium doping profile simulated by Trim code

Figure 4 shows the VIL characteristics of implanted devices of which the implantation conditions are 50 nA for 1hr. The light emitting of all the implanted devices were not observed by implantation of potassium. Instead, their voltage/current density characteristics have V curves like Metal-Insulator-Metal types. They show a conspicuous tendency with the doze quantity. This phenomenon was shown at 100nA, also.

These results indicate that the implanted ion made the light emitting layer decomposed and turn it into insulator. Incidentally, we cannot clarify whether this damage was caused by heating or irradiation in the ion implantation.

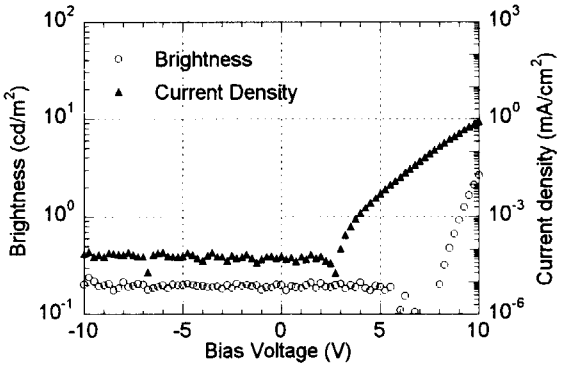

Fig. 3 The VIL characteristic of unimplanted device

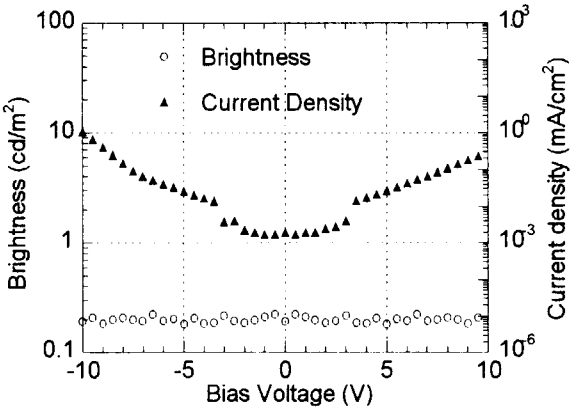

Fig. 4 The VIL characteristic of implanted Device, 80keV,50nA,1hr

4. Inorganic Materials

(continue to the next page)

4. 1 Damage depth profile in austenitic stainless steels using energy degrader

Y. Miwa, T. Tsukada, K. Tsuchiya*, S. Hamada and H. Tsuji

Dept. of Nuclear Energy System, JAERI.
* Dept. of JMTR Project, JAERI.

1. Introduction

Repair of in-core components by welding is one of the key issues of plant maintenance not only for light water reactors but for the fusion reactor. Weldability of irradiated materials is affected by a concentration of helium generated by some transmutation reactions[1]. During welding, the He precipitates as bubbles at grain boundary in the heat affected zone (HAZ), and may lead to the weld cracking.

To study the effect of He on mechanical properties and corrosion resistance, an irradiation apparatus was installed in Light Ion Room No.2 of cyclotron facility at TIARA. Using this equipment, He ions can be implanted uniformly into bulk specimens by a function of energy degraders. This report describes design of the energy degraders which will be used for material irradiation.

2. Energy degrader

Energy degrader is a device to change the energy of incident ions and distributes the ions homogeneously in a direction of specimen depth. This energy degrader is consisted of metal foils, which thickness could be changed from 0 to about 1 mm, every 1 μm step. Using the energy degrader and a X-Y beam scanner, it is possible to control implanted depth and area, and consequently incident ions are homogeneouly implanted into specimens.

Three types of energy degraders were equipped in our irradiation facility. Using these energy degraders, 4 types of distribution of He concentration and displacement damage could be obtained. The He concentration and amount of displacement damage were calculated using the TRIM85 computer code[2], which was improved to include the effect of energy degrader. The materials applied for calculation were Fe-18Cr-12Ni and type 316LN stainless steels. Displacement threshold energy was set up at 40 eV. The calculation results of He concentration and displacement damage described below were normalized by the incident ion number, which corresponds to an irradiation condition of 1 particle μA /cm^2 for 1 h.

(a) No degrader

Figure 1 shows the distributions of He and displacement damage in Fe-18Cr-12Ni irradiated by 50 MeV He^{2+} for a case without degrader. Displacement damage increased gently from irradiation surface to 200 μm in depth, and then peaked at 380 μm deep. The displacement damage (dpa) in the range from surface to 250 μm was approximated by a following equation;

$$dpa=7.36\times10^{-11}z^3-7.68\times10^{-9}z^2+4.14\times10^{-6}z+2.39\times10^{-3},$$

where z is depth in unit of μm. He was implanted in a region ranged from 380

to 384 μm in depth.

(b) Degrader A

The degrader A is consisted of aluminum foils, which thickness vary from 0 to 600 μm, every 1 μm step. Figure 2 shows the distributions of He and displacement damage in Fe-18Cr-12Ni irradiated by 50 MeV He^{2+} using a degrader A. He ions were implanted uniformly from 145 to over 250 μm in depth. The average concentration of He is about 10.8 at.ppm. In the region from surface to 135 μm in depth, only displacement damage was given.

(c) Degrader B

The degrader B is consisted of aluminum foils, which thickness vary from 350 to 950 μm, every 1 μm step. Figure 3 shows the distribution of He and displacement damage in Fe-18Cr-12Ni irradiated by 50 MeV He^{2+} using a degrader B. The degrader B can distribute He homogeneously in the range from surface to 240 μm in depth. The average concentration of He is about 10.6 at.ppm. Displacement damage had a maximum near surface, and decreased along implanted depth.

(d) Degrader C

The degrader C is consisted of aluminum foils, which thickness vary from 5 to 934 μm, every 1 μm step. Figure 4 shows the distribution of He and displacement damage in type 316 LN irradiated by 50 MeV He^{2+} using a degrader C. The degrader C can distribute He homogeneously in the range from surface to 380 μm in depth. The average concentration of He is about 6.7 at.ppm. Displacement damage had a maximum near surface, and decreased along implanted depth.

3. Status of irradiation experiment

Figure 5 shows an irradiation matrix of type 304 stainless steel. In some of these irradiated specimens, transmission electron microscopy were carried out[3]. The results were reported elsewhere. Farther testing of mechanical property, corrosion property and microstructural characterization will be carried out.

Reference

1) S. A. Fabristiev et al., ASTP STP 1270 (1996) p.980
2) J. F. Ziegler et al.,"The Stopping and Range of Ion in Solids" Vol.1, PREGAMON PRESS (1985)
3) Y. Miwa et al., TIARA annual report 1996 (Vol. 6)

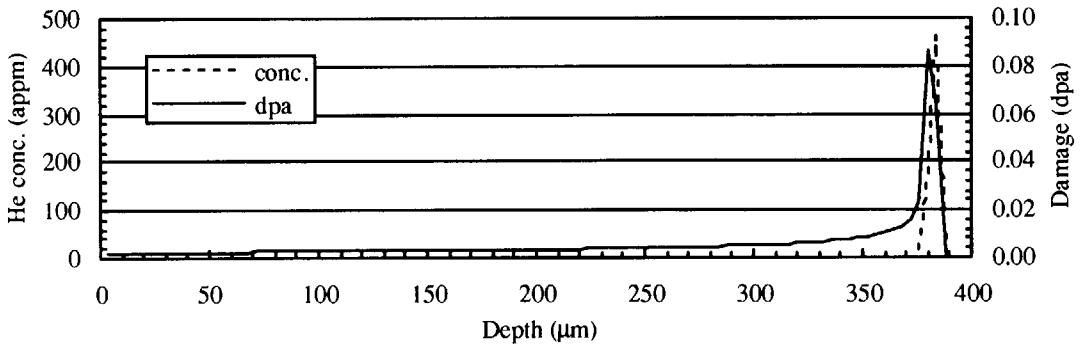

Figure 1 Distribution of implanted He and displacement damage in Fe-18Cr-12Ni irradiated by 50 MeV He^{2+} without a degrader.

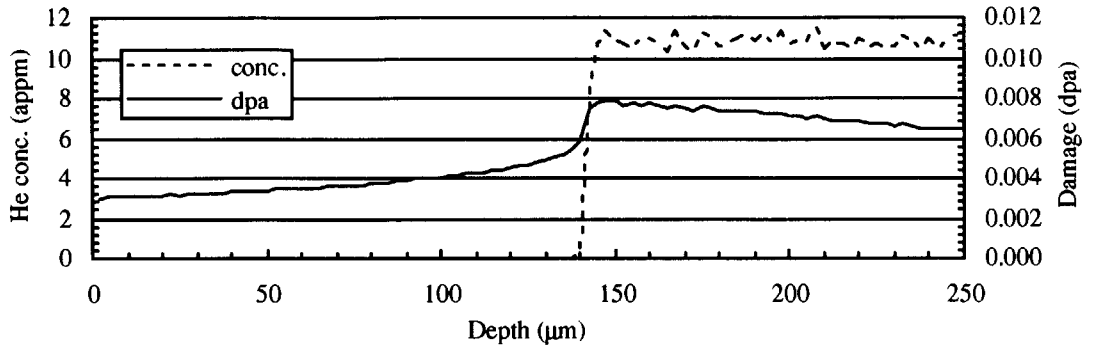

Figure 2 Distribution of implanted He and displacement damage in Fe-18Cr-12Ni irradiated by 50 MeV He^{2+} with a degrader A.

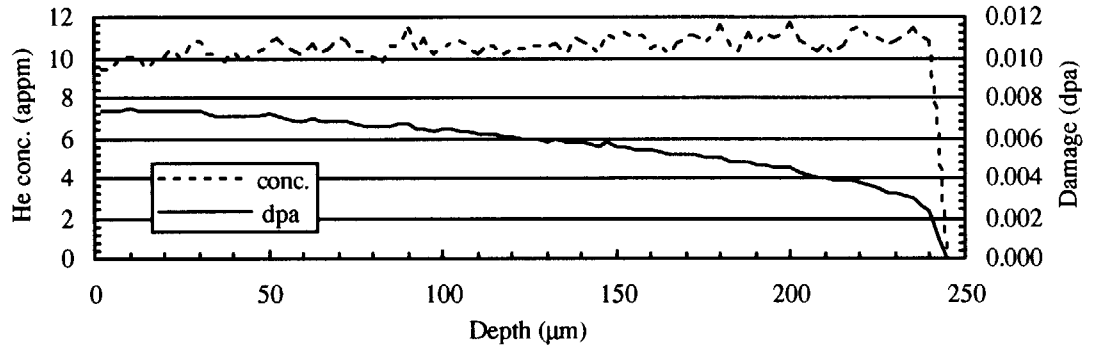

Figure 3 Distribution of implanted He and displacement damage in Fe-18Cr-12Ni irradiated by 50 MeV He^{2+} with a degrader B.

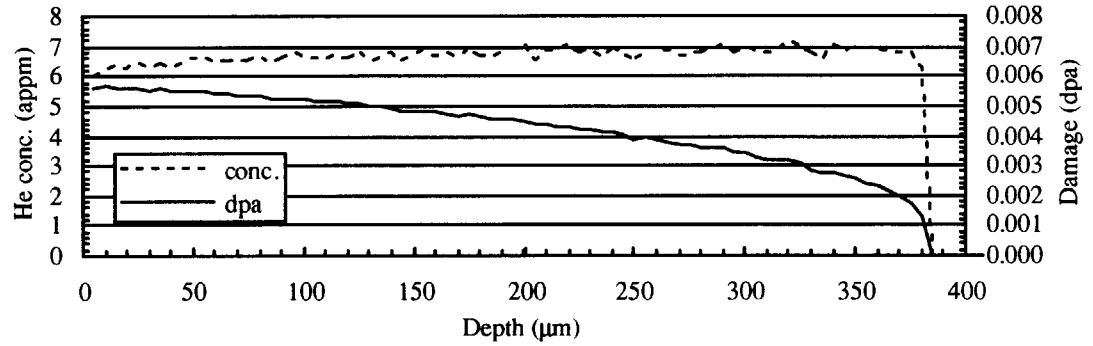

Figure 4 Distribution of implanted He and displacement damage in 316LN irradiated by 50 MeV He^{2+} with a degrader C.

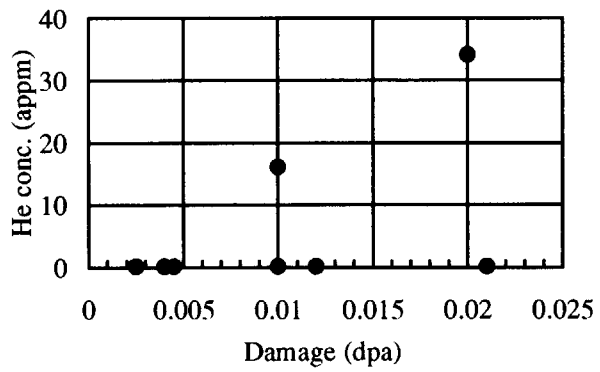

Figure 5 Status of irradiation matrix of Type 304 statinless steels.

4. 2 Effect of He and minor elements on vacancy diffusion in austenitic stainless steels

Y. Miwa, T. Tsukada, A. Naitou and H. Tsuji

Department of Nuclear Energy System, JAERI

1. Introduction

Depletion or enrichment of alloying and impurity elements at grain boundary due to the radiation induced segregation (RIS) are considered as a primary cause of the irradiation assisted stress corrosion cracking (IASCC) of austenitic stainless steels[1]. RIS is caused by a flow of vacancy to sink, i.e., grain boundaries, and a simultaneous flow of atoms such as Fe and Cr which migrate away from sinks[1]. In this study, effect of He and minor alloying or impurity elements on diffusion mechanism of vacancy was studied by the ion-irradiation and post-irradiation annealing experiments.

2. Experimental

The materials used in this study were high-purity, solution-annealed Fe-18Cr-12Ni base alloy and its alloys doped with C, Si, P, S and Ti separately or together. Prior to irradiation, 3-mm-diameter discs were mechanically polished and finished by electrochemical polishing. Those discs were irradiated under vacuum solely with 1 MeV He^+ or synergistically with 12 MeV Ni^{3+} and 1 MeV He^+ below 253K using triple beam irradiation facility at TIARA. Figure 1 shows the distributions of implanted He ions and displacement damage of Fe-18Cr-12Ni using a TRIM85 computer code[2]. After irradiation, specimens were electroplated by Ni and machined to 3-mm-diameter discs in order to observe the microstructure along the irradiation range. Some of disks were annealed at 973K for 200 h in vacuum. Microstructural observation was carried out using a transmission electron microscope (JEOL-2000FX).

3. Results and discussion

Figure 2 shows a distribution of the mean diameter of cavities and swelling values in Fe-18Cr-12Ni-0.69Si. The cavities were observed in a range from near-surface to about 20 μm in depth. A mean diameter of cavities near He-implanted zone was 16 nm, and it decreased as the depth from surface. The mean diameter of cavities near He-implanted zone was larger than that reported by Carsughi et al[3].

The region where cavities were observed is much wider than He-implanted region as seen in Fig. 1. In this region, He diffused during the heat treatment after irradiation. Sekiguchi et al., reported that a diffusivity of He in AISI 316 stainless steel. By a vacancy mechanism, the one-dimensional diffusion equation is described as follows;

$<x^2>=2tx0.05\exp(-2.06/k_BT)$

where t is time in unit of s, k_B is the Boltzmann constant in unit of eV and T is annealing temperature in unit of K. Diffusion distance is calculated as 12.4 μm after the heat treatment at 973 K for 200 h. This distance seems to be smaller than that width of cavity-distributed zone in Fig. 2. It may be considered that the diffusion of vacancy is affected by He, Si and/or irradiation defects.

In order to reveal a detail about the effect of He and minor element, it is necessary to examine materials treated under the different heat treatment condition; temperature, aging time etc.

Reference

1) S. M. Bruemmer et al., Mat. Res. Soc. Symp. Proc. Vol.373 (1995) p.119
2) J. F. Ziegler et al., "The Stopping and Range of Ion in Solids" Vol.1, PREGAMON PRESS (1985)
3) F. Carsughi et al., J. Nucl. Mater. 212-215 (1994) p.336
4) H. Sekiguchi et al., J. Nucl. Mater. 133&134 (1985) p.468

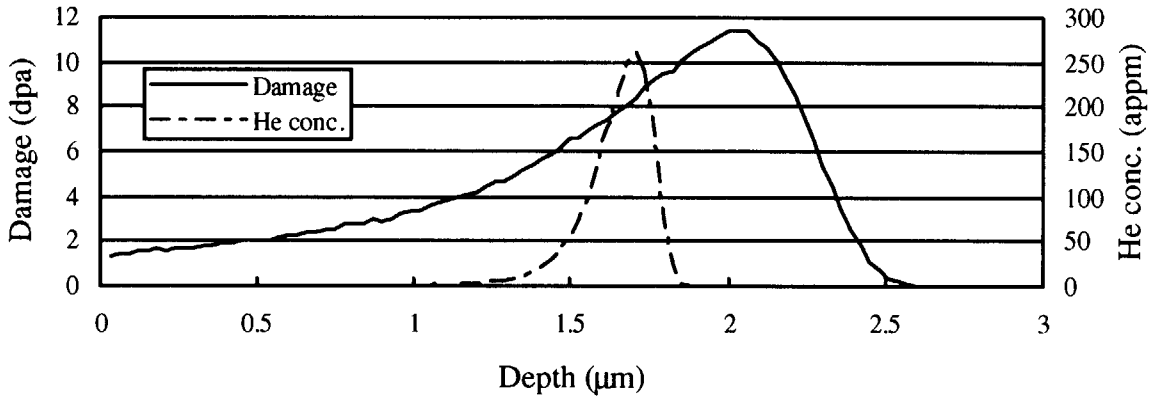

Figure 1 Distributions of implanted He and displacement damage.

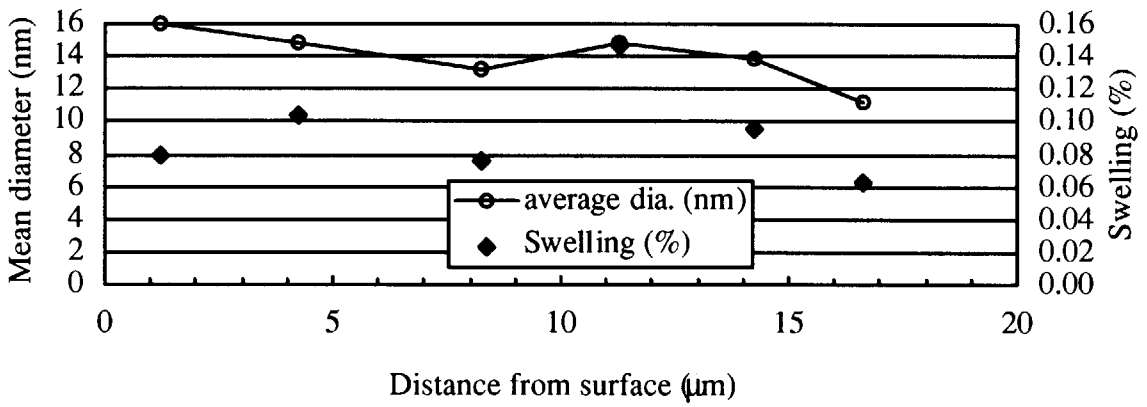

Figure 2 Mean diameter of cavities and swelling

4．3 Effect of Displacement Damage on Corrosion of the Reprocessing Materials

S. Hamada and Y. Miwa
Dept. of Nuclear Energy System, JAERI

1. Introduction

The nuclear fuel reprocessing facility has been constructed at Rokkasho-mura in Aomori Prefecture and new materials for major equipments such as an acid recovery evaporator and a dissolver have been developed in JAERI. These materials are exposed in very severe corrosive nuclear environments and the lifetime of them become important keys to maintain the equipments. The lifetime of the materials is mainly controlled by the corrosion resistance and the property strongly depends on nitric acid and radiation.

So far, the effects of nitric acid on the corrosion resistance have been studied[1]. However, there are no studies of the effects of radiation, especially displacement damage by α, β and γ rays, on the corrosion resistance.

In this study, it is objective to investigate the effect of displacement damage on the corrosion resistance of the materials for major equipments of nuclear fuel reprocessing facility.

2. Experimental

The materials used in this study are three alloys of 304 stainless steel (SUS304ULC) and Ni base alloy (RW), pure zirconium. The chemical compositions of these materials are shown in tables 1 and 2. The samples for corrosion test and TEM (transmission electron microscope) observation of these materials were prepared. The specimen sizes for these test are 10 x 10 x 0.36' mm and 30ϕ x 0.2'mm, respectively.

Irradiation was carried out in the irradiation apparatus for common use installed in Light Ion Room No. 2 of the cyclotron facility[2]. The specimens were installed on the substrate made of copper and the substrate was cooled by circulated cold water during irradiation.

The displacement damage levels were evaluated to be about 10^{-2} dpa (displacement per atom) at maximum in major equipments have been employed for forty years[3]. So, 50 MeV He ions were used and irradiated to be about 10-2 dpa into the specimens.

The experiments of the corrosion tests and TEM observation are in progress.

3. References

1) For example, K. Kiuchi, J. Atomic Energy Society of Japan, 31(1989)229.
2) Y. Nakamura et al., TIARA annual report (1995)232.
3) Annual Report of Demonstration test for nuclear fuel reprocessing facility, second period (1997).

Table 1 Chemical composition of the materials used (wt%)

	C	Si	Mn	P	S	Ni
304ULC	<0.015	0.14	<0.10	<0.01	<0.002	12.6
RW	<0.005	2.7	<0.10	<0.10	<0.002	bal.

	Cr	Mo	W	Nb	Ti	Fe
304ULC	19.3	<0.01	<0.01	<0.01	0.25	bal.
RW	30.1	<0.045	9.9	<0.01	<0.05	<0.02

Table 2 Chemical composition of pure zirconium (wt%)

	C	Zr+Hf	Hf	H	N	O	Fe+Cr
Pure Zr	0.001	99.7	0.07	8E-04	0.003	0.135	0.06

4．4 Coincidence Doppler Broadening Measurements on Si Containing Internal Positron Source of ^{22}Na

M. Hasegawa, Y. Nagai, Z. Tang, T. Shimamura, A. Kawasuso* and S. Okada*

Institute for Materials Research, Tohoku University;
*Department of Materials Development, JAERI/Takasaki

1. Introduction

Vacancies, their agglomerates and complexes with impurities are introduced in Si during the crystal growth and the subsequent processing for the Si devices. Then it is very important to identify them and to understand their atomic and electronic structures. Several experimental techniques, such as electron spin resonance (ESR), infrared (IR) absorption and deep-level transition spectroscopy (DLTS), have been used for these studies.

Positron annihilation method has been widely known to be very sensitive to vacancy-type defects and to be complementary to the other method; for example, positron annihilation can be used for detection of paramagnetic as well as diamagnetic vacancy-type defects, while ESR is only applicable to paramagnetic defects.

Recently a new positron annihilation technique, two Ge-detector coincidence Doppler broadening method, has been developed to make chemical analysis of vacancy-impurity complexes; the two-detector coincidence is employed to reduce the background and then to measure higher momentum components from core electrons of specific chemical species[1,2]. In this study we employed this method to study vacancies and their impurity complexes in Si. Furthermore to reduce ambiguity from the positron source component (Myler or Kapton film component) we use an internal (in-situ) positron source of ^{22}Na produced by nuclear reactions of high energy protons [$^{28}Si(p, ^{7}Be)^{22}Na$].

2. Experimentals

In this study we prepared floating zone grown(FZ) and Czchralski-grown Si single crystal wafer samples (20x20x0.5mm): undoped (1000 Ωcm) and B-doped (200-500 Ωcm) FZ Si, and P-, As- and Sb-doped (0.05-0.2 Ωcm) Cz-Si. The content of oxygen in Cz-Si is a few tens of appm while less than 1 appm in Fz-Si. These samples were stacked and attached to an aluminum holder, cooled by running water, for irradiation. To introduce the internal positron source of ^{22}Na, the stacked samples were irradiated with 70 MeV-protons from TIARA cyclotron to a fluence of $1x10^{17}$ cm^{-2}. The maximum sample temperature was about 350 ℃.

Two annihilation gamma photons were detected with two pure Ge detectors arranged at 180° to each other. Their output signals were fed into multi-parameter multichannel pulse height analyzer to register the two photon energy (E_1 and E_2) respectively from every coincidence event. The energy E_1 and E_2 are correlated to the longitudinal momentum p_L along the direction of emission of one of the photons from the annihilating pair as follows,

$$E_1 = mc^2 - cp_L/2, \quad (1a)$$

$$E_2 = mc^2 + cp_L/2, \quad (1b)$$

where m, c and p_L are the electron (positron) rest mass, the speed of light in vacuum. In the present study, the measurements on p_L along the (100) crystal orientation were performed.

3. Results and Discussion

Figure 1 shows a two-dimensional $(E_1\text{-}E_2)$ coincidence Doppler broadening spectrum of the proton-irradiated undoped Si. We can see an intense central peak around the center of $E_1=E_2=$ 511keV, which comes from positron annihilations with the valence electrons[1]. The peak has an ellipsoidal shape extending along the E_2 =511keV - E_1 line. This shape reflects the momentum distribution of the valence and core electrons; especially the long tails of the high momentum are due to the core electrons which are almost unchanged by chemical bonding. It should be noted that this tail region is nearly free from accidental background counting. A cut along the sum energy window,

$$511\text{-}2.4\ (\text{keV}) < (E_1 + E_2) < 511 + 2.4(\text{keV})$$

can be analyzed to extract the longitudinal momentum distribution of the annihilating pairs.

In Fig. 2 the $(E_1 - E_2)$ projection is plotted together with an single-detector energy (E_1) spectrum (Detector 1) obtained by integration of the coincidence spectrum with respect to energy E_2. As seen from Eq. (1), this projection represents the longitudinal momentum distribution. It is clearly seen that the back ground counting at the high momentum region is much reduced. Then this allow us to obtain the momentum distribution associated with the core electrons.

To clarify the differences among the various kinds of the samples, in Fig. 3 we plot the ratios of the projection curves to that of the undoped FZ-Si (reference) sample after normalizing to the same height at $(E_1 - E_2) = 0$. The ratio curves for all the CZ-Si samples are much enhanced around 514keV, while that for the B-doped FZ-Si sample is very close to unity over all the energy region. A theoretical calculation with a simple superimposed-atom model shows that in the ratio curve to bulk Si (perfect crystal) vacancy-oxygen complexes, such as V_2O (divacancy-oxygen), is enhanced around p_L=10mrad, which correspond to about 513.5keV, by the annihilation with oxygen core electrons. Then it is strongly suggested that in the proton-irradiated samples vacancy-oxygen complexes trap positrons and lead to annihilation with the core electrons of oxygen atoms of the complexes. Our previous study demonstrate that vacancy-oxygen complexes, such as divacancy-oxegen (V_2O) and trivacancy-dioxygen (V_3O_2), are stable up to about 450℃[4]. Then these vacancy-impurity complexes can survive during the irradiation at about 350℃ and remain in the samples after the irradiation. Small but definite difference can be seen among the curves for the CZ-Si samples, which reflects different chemical species of the dopants. Now detailed experimental and theoretical studies are in progress.

References

(1) P. Asoka-Kumar, M. Alatalo, V.J. Ghosh, A.C. Kruseman, B. Nielsen and K.G. Lynn: Phys. Rev. Lett. 77 (1996) 2097.

(2) S. Szpala, P. Asoka-Kumar, B. Nielsen,

J.P. Peng, S. Hayakawa and K.G. Lynn: Phys. Rev. **B54** (1996) 4722.

(3) J. Kuriplach, T. Van Hoecke, B. Van Waeynberge, C. Dauwe, D. Segers, N. Balcaen, A.L. Morales, M.-A. Trauwaert, J. Vanhellemont and M. Sob: Mater. Sci. Forum **255-257** (1997) 605.

(4) A. Kawasuso, M. Hasegawa, M. Suezawa, S. Yamaguchi and K. Sumino: Appl. Surf. Sci. **85** (1995) 280.

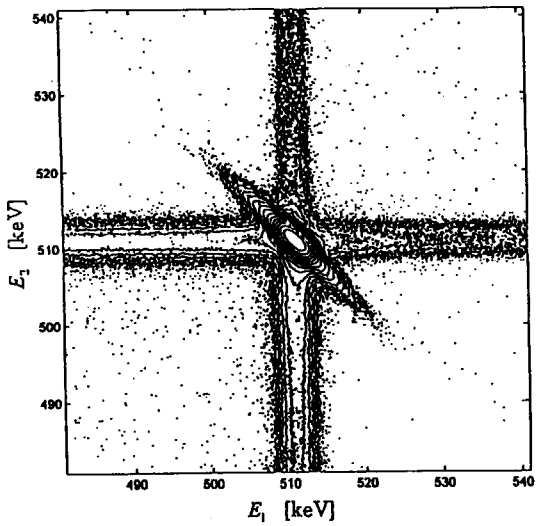

Figure 1. The coincidence Doppler broadening spectrum of proton irradiated FZ-Si (undoped) samples obtained by internal positron source (^{22}Na) method.

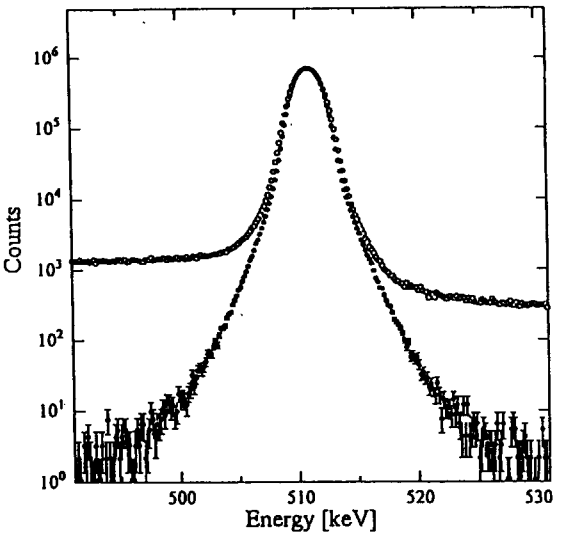

Figure 2. The (E_1 - E_2) projection spectrum (open circles) and single-detector energy (E_1) spectrum (full circles).

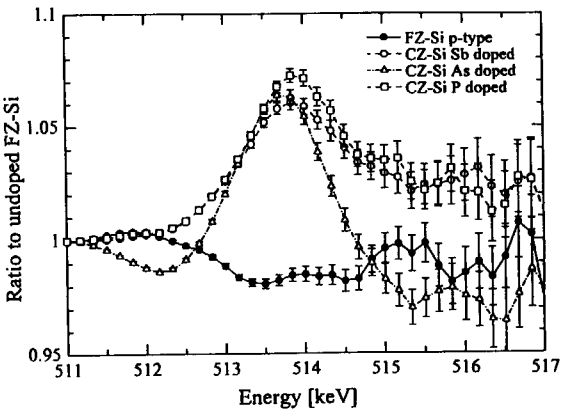

Figure 3. The ratio curves for the CZ-Si and B-doped FZ-Si samples.

4. 5 Point-defect clustering and atomic disordering in $MgO-Al_2O_3$ crystals under irradiation with ions and/or electrons

K. Yasuda, T. Soeda, S. Matsumura, C. Kinoshita, M. Ohmura,
H. Abe* and H. Naramoto*

Department of Applied Quantum Physics and Nuclear Engineering, Kyushu University,
Hakozaki, Fukuoka 812-8581, Japan
* Department of Materials Development, Japan Atomic Energy Research Institute-Takasaki,
Takasaki, Gunma 370-1292, Japan

1. Introduction

Search and development of radiation resistant ceramics have being strongly motivated in the course of the development of fusion devices, such as International Thermonuclear Experimental Reactor (ITER). α-Al_2O_3 and $MgO{\cdot}nAl_2O_3$ ($n \geqq 1$) are expected to be applied as insulators and transmission windows of ITER. Especially, $MgAl_2O_4$ has received strong interests because of its excellent radiation resistance: this compound shows negligiblly weak void swelling under neutron irradiation in fission reactors up to 200 dpa (displacement per atoms) [1]. Furthermore, nucleation of dislocation loops in $MgAl_2O_4$ is suppressed if high ionizing radiation coexists with dispacement damage [2,3]. These evidences of radiation resistance of this material brought us to study fundamentals of defects in this material, to extend the development of radiation resistant ceramics for fusion devices.

In this report, we will describe our recent progress on radiation damage study of $MgO-Al_2O_3$ crystals, including research topics (1) formation process of defect clusters under concurrent irradiation with displacement and ionization, and (2) quantitative evaluation of cation distribution in $MgO{\cdot}nAl_2O_3$ crystals. These works were done in part at TIARA by using a transmission electron microscope facility interfaced with ion accelaratos.

2. Microstructure evolution under concurrent irradiation with ions and electrons

Single crystals of $MgO{\cdot}\,nAl_2O_3$ (n=1 and 2.4), pure α-Al_2O_3 and α-Al_2O_3 doped with V or Ni were irradiated concurrently with 300 keV ions and 200 keV electrons to provide a wide irradiation spectrum. Table 1 summarizes the microstructure of those ceramics irradiated at 870 and 1070 K. Dislocation loops of interstitial type were observed in all samples under 300 keV ion irradiation, except for 300 keV He^+ ions at 870 K. The formation of dislocation loops is suppressed in $MgAl_2O_4$ under concurrent irradiation with 200 keV electrons. However, no significant effect of concurrent irradiation is observed in pure α-Al_2O_3: a high density of tiny dislocation loops was observed even under the concurrent irradiation with 200 keV electrons. In $MgO{\cdot}2.4Al_2O_3$ and Ni- or V-doped α-Al_2O_3 samples, the formation of dislocation loops is slightly suppressed under concurrent irradiation with 200 keV electrons.

Dislocation loops are observed in α-Al_2O_3 under irradiation solely with 300 keV O^+ ions after a fluence of $2x10^{17}$ ions/m^2, and increased their density with increasing fluence. The saturation density of dislocation loops is about $3x10^{22}$ /m^2. On the other hand, in $MgAl_2O_4$ and $MgO{\cdot}\,2.4Al_2O_3$ crystals, loops show up their contrasts after irradiation of $1x10^{19}$ ions/m^2, and their density is saturated at $1x10^{21}$/m^2. These results indicate that disloaction loops in $MgO{\cdot}nAl_2O_3$ is much more difficult to nucleate than in α-Al_2O_3.

Fig.1 shows a sequence of the weak-beam dark-field images of α-Al_2O_3 under irradiation at 300 K with 200 keV electrons. The sample was originally irradiated with 6 keV Ar^+ ions to induce tiny dislocation loops. These loops are seen to be eliminated with 200 keV electron irradiation. Such extinction of loops are observed under electron irradiation in all crystals used in this study. The disappearing rate of loops is found to be higher under electron irradiation with lower energies. Comparing the dis-appearing rate among the crystals, the stability of loops is high in the order of $MgO{\cdot}2.4Al_2O_3$, α-Al_2O_3 and $MgAl_2O_4$.

These results have led to an idea that the loop formation under the concurrent irradiation is contolled by a competitive process between the nucleation rate of loops with ion irradiation and the extinction rate of loops with electron irradiation. This idea supports that $MgAl_2O_4$, which has the lowest production rate and the lowest stability of loops, is most remarkable for the suppression of dislocation loops.

3. Cation distribution under irradiation with electrons and ions

The excellent radiation resistance of $MgAl_2O_4$ is believed to be associated with results of site exchanges of cations under irradiation, which contribute to the high recombination rate of point defects in this crystal. In order to understand the correlation between disordering process and radiation resistance, we have evaluated quantitatively the lattice site of cations in $MgO{\bullet}nAl_2O_3$[4]. We followed a new analysing method [5] based on quantitative electron microscopy, including two techniques, those are, large angle convergent beam electron diffraction (LACBED) and electron channeling enhanced microanalysis (ECEM). Detaild discusson of the analysing method can be seen in reference [5].

Fig.2 shows a typical example of LACBED pattern where incident electrons were illuminated into $MgAl_2O_4$ under 220 systematic excitation. A transmission electron microscope equipped with an energy filter, JEM-2010 FEF, was used taking fig.2 to reduce diffuse background caused by inelastic collision, and zero-loss electrons with a energy width of 15 eV forms the LECBED pattern in fig.2. It is clearly seen in fig.1 that the energy-filtering considerably removes inelestic scattered electrons, leading to an precise evaluation of the structure factor.

Two EDX spectra were obtained by ECEM (data are not shown) under (a) a dynamical excitation of 400 reflection with positive s_{400}, and under (b) a quasi-kinematical condition where no reflections were strongly excited. Here, the X-ray intesity of O($K\alpha$) was controlled to be same at both conditions of (a) and (b). It was seen from the two spectra that the emission of Mg($K\alpha$) is enhanced by the dynamical excitation of 400, while the intensity of Al($K\alpha$) is almost identical between the two conditions. This result qualitatively indicates that considerable amount of Mg^{2+} ions exsist on the tetrahedral sites, while most of Al^{3+} ions are located on the octahedral sites.

Table 2 summarizes the results of our analyses, or the occupation probability P_i (i stands for Mg, Al and vacancy) in the tetrahedral sites. It is found in the samples prior to irradiation that 70% of Mg^{2+} and 20% of Al^{3+} are located on the tetrahedral sites in both crystals of $MgAl_2O_4$ and $MgO{\bullet}2.4Al_2O_3$. The values of P_i are almost independent of the stoichiometry of spinel compounds. The most of structural vacancies are found to be at the tetrahedral sites prior to irradiation.

Irradiation with 300 keV O^+ ions induce remarkable decrease of P_{Al}, although P_{Mg} is almost constant. However, it is clear from table 1 that electron irradiation does not induce significant change for P_{Mg} nor P_{Al}. The irradiation dose for 1 MeV electrons and 300 keV ions were almost same, or 1.5 dpa. These results suggest that Al^{3+} dominant in the disordering process, and that displacement cascade is more effective in the disordering than isolated Frenkel defects.

It is also worthy to note the change in P_V caused by irradiation. The remarkable decrease of P_V under electron irradiation implies that the vacancies are moved from the tetrahedral to the octahedral sites during irradiation. Also, this result suggests that recombination of interstitials and vacancies occur mainly at the tetrahedral sites. Furthermore, the excess value of P_V in $MgO{\bullet}2.4Al_2O_3$ ($P_V = 270\%$) indicates that empty

Table 1 Summary of the microstructure in $MgO\text{-}Al_2O_3$ crystals irradiated with 300 keV ions, and that concurrently with 200 keV electrons.

sample	ion	irra. temp. (K)	charateristics of microstructure	
			ions	ions and electrons: retardation of dislocation loops ?
$MgO{\bullet}1Al_2O_3$	300 keV He^+	870	bubbles	bubbles
	300 keV O^+	870	dislocation loop	○
	300 keV Mg^+	870	dislocation loop	○
$MgO{\bullet}2.4Al_2O_3$	300 keV O^+	870	dislocation loop	△
$\alpha\text{-}Al_2O_3$	300 keV He^+	870	dislocation loop	×
	300 keV O^+	870	dislocation loop	×
	300 keV Ar^+	870	dislocation loop	×
$\alpha\text{-}Al_2O_3$ (Ni-doped)	300 keV O^+	1070	dislocation loop	△
$\alpha\text{-}Al_2O_3$ (V-doped)	300 keV O^+	1070	dislocation loop	△

○: dislocation loop formation was suppressed with concurrent irradiation with 200 keV electrons
△: dislocation loop formation was slightly suppressed with concurrent irradiation with 200 keV electrons
×: no significant changes were observed compared with the microstructure irradiated only with 300 keV ions.

interstitial sites of stoichiometric spinel compounds may play a role for the disordering process, though it is not taken into consideration of the analyses [5].

4. Summary

In MgO-Al_2O_3 system, $MgAl_2O_4$ has been found to be most resistant to nucleate dislocation loops under concurrent irradiation with ions and electrons, indicating that $MgAl_2O_4$ is most sensitive to irradiation spectrum effects. This feature is considered to come from the lowest production rate and the lowest stability of dislocation loops in $MgAl_2O_4$. The lowest production rate of loops in $MgAl_2O_4$ is known as the large nuclei of loops compared with α-Al_2O_3 [3]. However, the physical mechanism responsible for the stability of loops under electron irradiation is uncertain at the present time. Although, it is obvious from the present study that the unstability of loops is from non-displacement effects, such as ionization and/or athermal motion of point defects driven by subthreshold displacement.

It is also found in this syudy that the motion of Al^{3+} ions is donimant in the disordering process of $MgO{\cdot}nAl_2O_3$. Furthermore, displacement cascades are more effective for the disordering process of cations in $MgO{\cdot}nAl_2O_3$. Further studies are necesarry to understand the disordering process of $MgO{\cdot}Al_2O_3$ under irradiation, leading to a complihensive understanding of radiation resistance of $MgAl_2O_4$.

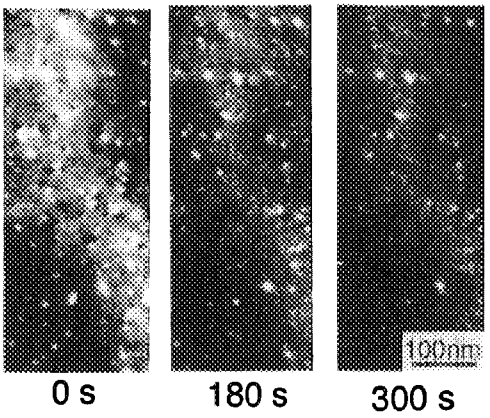

Fig. 1: Week-beam dark-field images of pure Al_2O_3 irradiated originally with 6 keV Ar^+ ions followed by 200 keV electron irradiation at 300 K. Dislocation loops were disappeared with increasing irradiation time of 200 keV electrons.

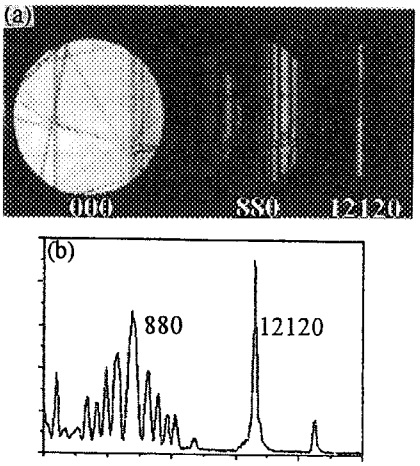

Fig.2: LACBED pattern (a) and its profile (b) of 220 systematic reflections of $MgO \cdot nAl_2O_3$ (n=1.0).

Table 2: Occupation probabilities P_i (i=Mg, Al or V) on the tetrahedral site under irradiation with electrons (a) and O^+ ions (b) in $MgO{\cdot}\,nAl_2O_3$.

(a) 1 MeV electron

n=1.0	before	after
P_{Mg}	69±15 %	69±17 %
P_{Al}	19± 2 %	12± 6 %
P_V	-	-

n=3.0	before	after
P_{Mg}	69±31 %	80±24 %
P_{Al}	17± 4 %	23± 8 %
P_V	155±54 %	6±44 %

(b) 300 keV O^+ ion

n=1.0	before	after
P_{Mg}	69±15 %	71±12 %
P_{Al}	19± 2 %	2± 2 %
P_V	-	-

n=2.4	before	after
P_{Mg}	73±21 %	68± 6 %
P_{Al}	20± 2 %	9± 2 %
P_V	97±28 %	270±10 %

References

[1] C. Kinoshita *et al.*, J. Nucl. Mater., 233-237 (1996) 100.
[2] S.J. Zinkle, J. Nucl. Mater., 219 (1995) 113.
[3] K. Yasuda, C. Kinoshita *et al.*, Philos. Mag. A, (1998) in press.
[4] S. Matsumura, J, Hayata and C. Kinoshita, Ann. Rep. of HVEM Lab. Kyushu University, 20 (1996) 9.
[5] T. Soeda, S. Matsumura and c. Kinoshita, submitted to proceedings of 14th Int. Con. for Electron Microscopy, Mexico (1998).

4. 6 Transport Properties of Pyrolytic Carbon Irradiated with 2-MeV Electrons at Low Temperature

A. Iwase*, N. Ishikawa*, T. Iwata*, Y. Chimi* and T. Nihira**

*Department of Materials Science, JAERI-Tokai
**Faculty of Engineering, Ibaraki University

1. Introduction

Our previous report has shown that the magneto-resistance of poorly graphitized pyrolytic carbon (PC) at low temperature becomes more and more negative by electron irradiation[1]. We also have shown that the zero-magnetic-field resistivity decreases and the Hall coefficient increases by 2-MeV electron irradiation[2], which indicates that the effect of electron irradiation on the transport properties of PC cannot be analyzed in terms of one carrier model. Therefore, we use a simple two band model (STB) to explain the change in magneto-resistance of PC by electron irradiation.

2. Data Analysis

According to STB, the Hall coefficient, R_H, and the electrical resistivity, ρ, under the magnetic field, H, are given by,

$$R_H = \frac{1}{ne}\frac{(a-1)(1+\mu^2H^2)}{(a+1)^2+(a-1)^2\mu^2H^2} \quad (1)$$

$$\rho(H)=\frac{1+\mu^2H^2}{ne\mu(a+1)\left[1+\mu^2H^2\left(\frac{a-1}{a+1}\right)^2\right]} \quad (2)$$

where, n is the electron concentration, $a=p/n$, p the hole concentration, and μ the mobility of electron and hole. We assume here that the mobility of electron and hole is 0.5 m^2/VS.

By using the experimental results on the magnetic field dependence of R_H and $\rho(H)$, carrier concentrations, n and p, can be obtained as a function of magnetic field and electron fluence. Figure 1 shows the total concentration, $n+p$, as a function of magnetic field taking the electron fluence as a parameter. The dependence of $n+p$ on H is little changed by irradiation. Figure 2 shows the carrier concentrations, $n+p$, n and p for unirradiated specimen are plotted against the square of H. The figure shows that the carrier concentration is proportional to H^2. In Fig. 3, the carrier concentrations, n, p, and $n+p$ are plotted as a function of electron fluence. Although the total concentration, $n+p$, is little changed by irradiation, as is also seen in Fig. 1, the hole concentration, p, increases, while the electron concentration, n, decreases with increasing the electron fluence.

3. Discussion

Yazawa explained the negative magneto-resistance in PC as due to the increase in carrier concentration under the magnetic field, which was induced by the formation of the two dimensional (2D) Landau level[3] Afterward, Bright refined Yazawa's model by adding the effect of disorder-induced broadening of Landau Level and that of band overlapping[4]. Bright model shows that the carrier concentration under the magnetic field, H, is proportional to H^2. This relation is the same as obtained in the present study. Therefore, the magnetic field dependence of the carrier concentration can be explained by the broadened 2D Landau level which is induced by disorder and the magnetic field.

Change in carrier concentration by irradiation can be explained as follows; it is well known that the irradiation-produced vacancies induce the acceptor level below the Fermi level. This acceptor level lowers the Fermi Level, resulting in the increase in hole concentration and the decrease in electron concentration.

The present study shows that the enhancement of the negative magneto resistance by electron irradiation can be explained within a framework of Yazawa-Bright model.

References

[1] A. Iwase et al., TIARA ANNUAL REPORT 1995, p.91(1996).
[2] A. Iwase et al., TIARA ANNUAL REPORT 1996, p.91(1997).
[3] K. Yazawa, J. Phys. Soc. Jpn. 26(1969) 1407.
[4] A. A. Bright, Phys. Rev. B20(1979) 5142.

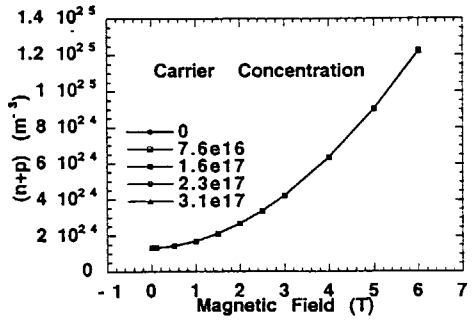

Fig. 1 Total carrier concentration as a function of magnetic field taking the electron fluence as a parameter.

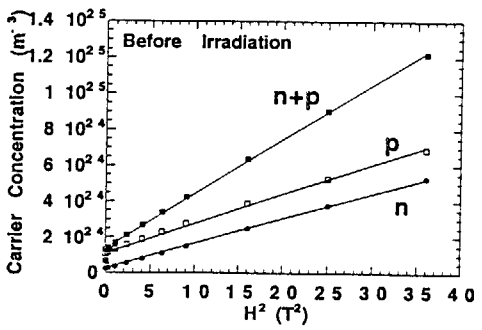

Fig. 2 Total carrier concentration, electron concentration, and hole concentration as a function of H^2.

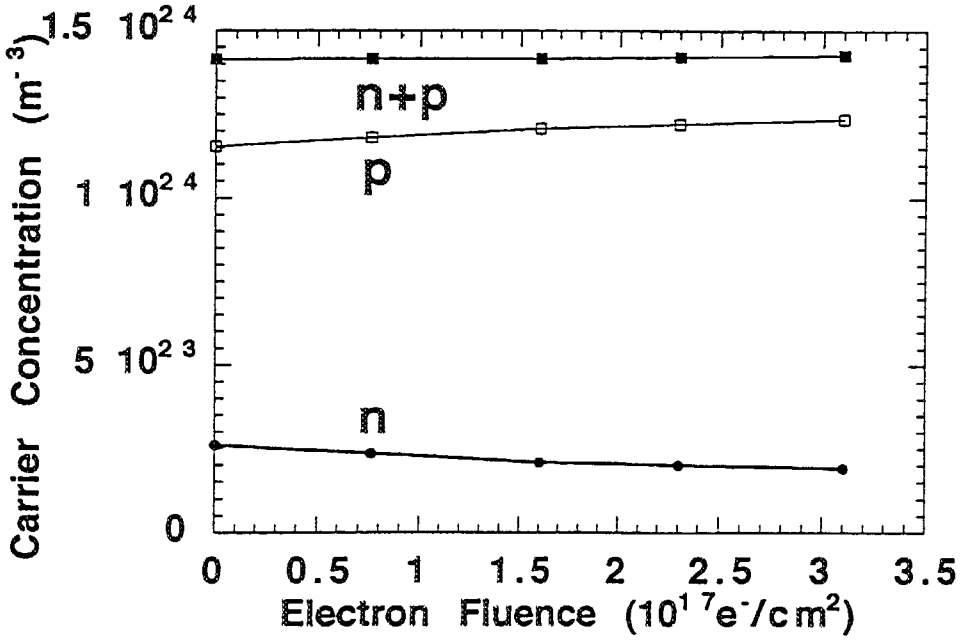

Fig. 3 Total carrier concentration, electron concentration, and hole concentration as a function of electron fluence. .

4. 7 Investigation of the resonant vibration modes of self interstitial atoms in FCC metals by low temperature specific heat measurement

M.Watanabe, N.Ishikawa and Y.Chimi
Department of Materials Science, JAERI

1.Introduction

Some theories[1] predict the resonant vibration modes due to self interstitial atoms in metals, which have a large amplitude and a low frequency. The occurrence of kind of modes for a single defect is quite unusual. To verify the existence of these modes, we measured the specific heat of electron-irradiated Cu and Al at low temperatures.

2.Experimental

The specimens used in this work were Cu and Al single crystals with shape of $12\times12\times0.5$ mm^3 and $15.6^{\Phi}\times0.5$ mm^3. The irradiations with 2-MeV electrons to the dose of 7.73×10^{17}/cm^2, 1.2×10^{18}/cm^2 and 6.67×10^{17}/cm^2 at 19K,at 20K and at 22K, respectively, were performed by using the a low temperature irradiation facility interfaced to TIARA 3MV single-ended accelerator. The aperture of 6×6 mm^2 was used to define the electron beam. Before and after irradiation, we measured the specific heat of the specimen under the adiabatic condition between 2K-40K.

3.Results and discussion

Figure 1 shows the change in specific heat for Cu<100> after irradiation to the dose of 7.73×10^{17}/cm^2 at 19K and subsequent 60K annealing[2]. The peak of two specific heat changes was found. This temperature range is lower than the first stage of the recovery, and it can not be detected by electric resistance measurements, etc..

Figures 2 and 3 show the change in specific heat for Al<100> after irradiation to the dose of 1.31×10^{18}/cm^2 and 6.67×10^{17}/cm^2 at 20k and at 22K. The change in specific heat which depends on the radiation value is shown. It is proven that with the generation of the interstitial by the irradiation, it holds the atomic lattice vibration, and that a specific heat decreases with it.

Figure 4 shows the change of specific heat after 300 K annealing for Al<100> irradiated to the dose of 6.67×10^{17}/cm^2 at 22K. In 300K anneal temperature, the lattice defect of Al is supposed to be recovered. However, it does not recover in the measurement of a specific heat, as is shown in figure 4.

Figure 5 shows the change in specific heat after 300 K annealing for Al<100> irradiated to the dose of 6.67×10^{17}/cm^2 at 22K and after measured specific heat from 5K at 60K(Fig.4)(time required 15 hours for the measurement to 60K). The peak in which a specific heat decreased at about 16K was found, as it was shown in figure 5.

Reference

1) A.Scholz and Chr.Lehmann, Phys.Rev.B6(1972)813.
2) M.Watanabe,A.Iwase,N.Ishikawa and Y.Chimi, TIARA Annual Report 1996, p92 (1997).

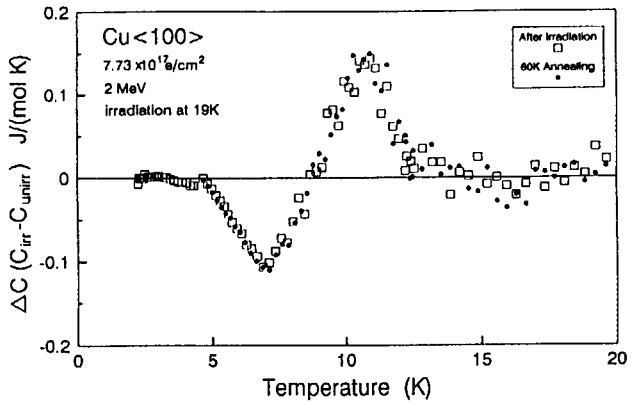

Fig.1. Change in specific heat for Cu<100> after irradiation to the dose of 7.73×10^{17}/cm ^{2} at 19K and 60K annealing.

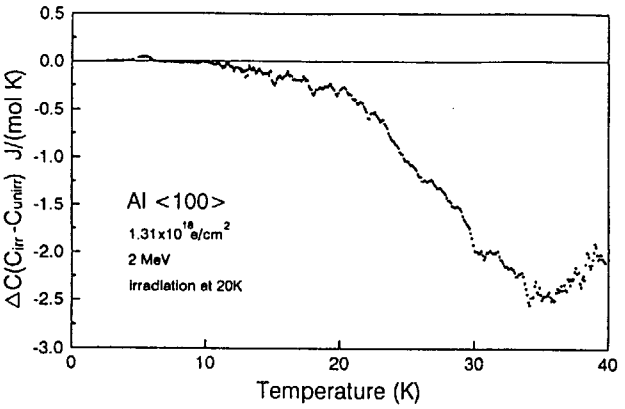

Fig.2. Change in specific heat for Al<100> after irradiation to the dose of 1.31×10^{18}/cm ^{2} at 20K.

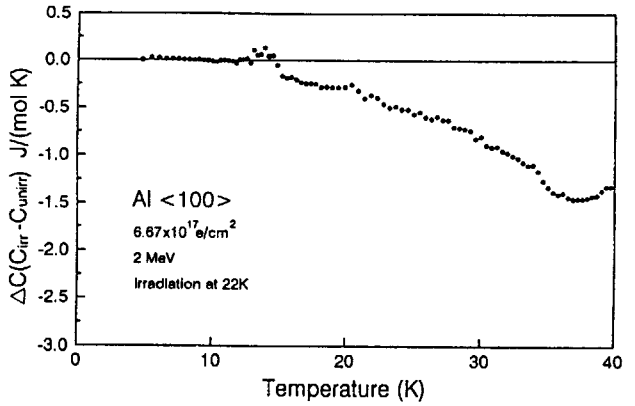

Fig.3. Change in specific heat for Al<100> after irradiation to the dose of 6.67×10^{17}/cm ^{2} at 22K.

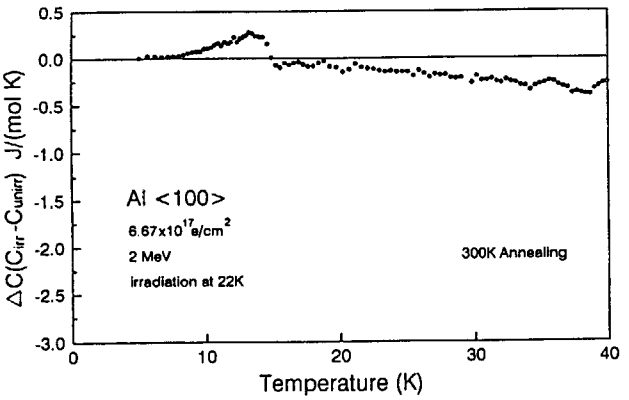

Fig.4. Change in specific heat after 300 K annealing for Al<100> irradiation to the dose of 6.67×10^{17}/cm ^{2} at 22K.

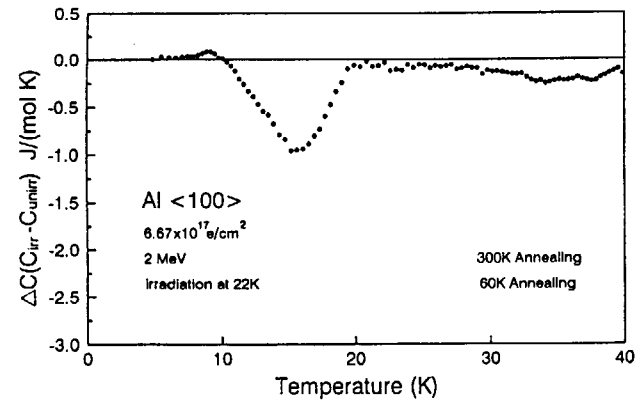

Fig.5. After 300 K annealing for Al<100> irradiation to the dose of 6.67 $\times 10^{17}$/cm ^{2} at 22K, change in specific heat after measured specific heat from 4K to 60K(Fig.4).

4．8 Electron Irradiation Effects on Superconducting Properties in $Bi_2Sr_2CaCu_2O_y$ Single Crystal

N.Ishikawa[1], T.Sueyoshi[1,2], Y.Chimi[1], A.Iwase[1], N.Kuroda[1,3], H.Ikeda[4], and R.Yoshizaki[4]

[1]Department of Materials Science, JAERI, [2]Kumamoto University, [3]Japan Science and Technology Corporation, [4]University of Tsukuba

1.Introduction

A single crystal $Bi_2Sr_2CaCu_2O_y$ (Bi-2212) superconductor has been irradiated with electrons, and in-situ measurement of resistivity in a magnetic field has been performed. The purpose of this work is to study the effect of irradiation-induced point defects on pinning properties of Bi-2212.

2.Experimental

A Bi-2212 single crystal was grown by traveling solvent floating zone method[1]. The sample was irradiated at low-temperature(100K) with 2MeV electrons from a single-ended accelerator in TIARA. The in-situ measurement of temperature dependence of resistivity under magnetic field was performed before and after the irradiations.

3.Results and Discussion

In order to study the effect of defects introduced by electron irradiation on the pinning of vortices, we focused on the low-resistivity data in a magnetic field. By plotting the resistivity data on a logarithmic scale versus inverse temperature as in Fig.1, we find this Arrhenius plot shows a straight line, indicating that the resistivity is thermally activated[2]. By assuming the activation energy U, the low-resistivity data can be expressed as

$$\rho = \rho_0 \exp\left(-\frac{U}{T}\right),$$

where ρ is the resistivity, ρ_0 the field-independent constant, U the activation energy in a temperature scale, k_B the Boltzmann constant, and T the temperature. Fig.2 shows the fluence dependence of activation energy. This shows the activation energy increases as increasing the fluence up to $9\times10^{17}cm^2$.

References

1)R.Yoshizaki and H.Ikeda, J. Phys. Soc. Jpn., 65 (1996) 1533.

2)T.T.M.Palstra, B.Batlogg, R.B.van Dover, L.F.Schneemeyer and J.V.Waszczak, Phys. Rev. B41 (1990) 6612.

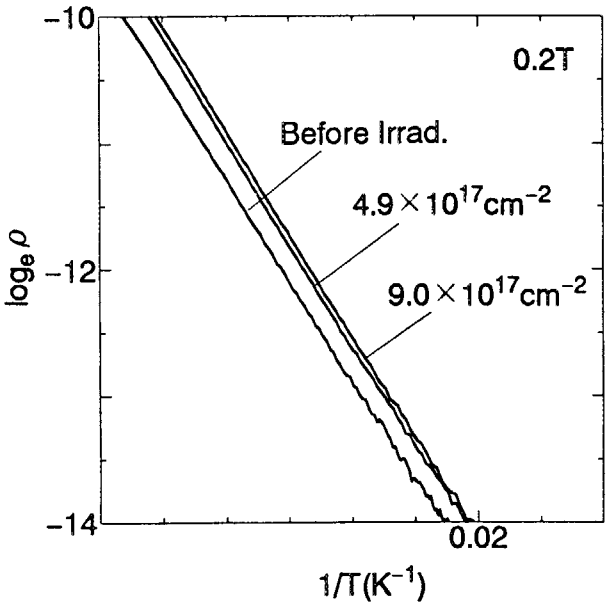

Fig.1 Arrhenius plot of the resistivity in the field 0.2T for the sample before and after the electron irradiation.

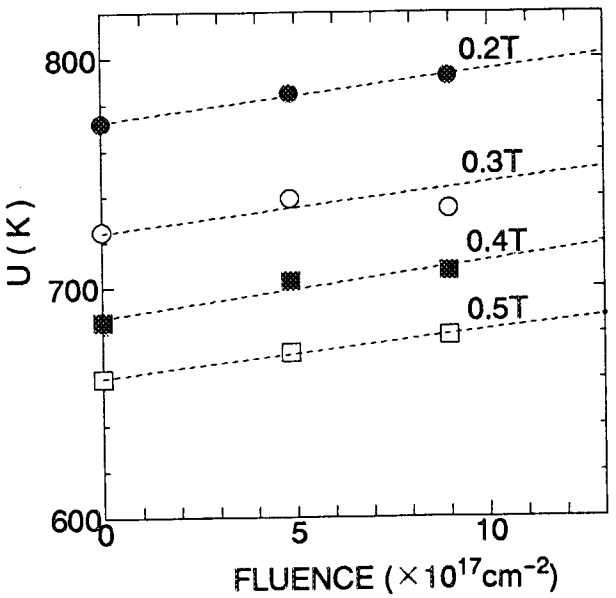

Fig.2 Activation energy plotted against electron fluence for different fields(0.2T-0.5T).

4. 9 Cavity formation behaviors observed in Al_2O_3 irradiated with multiple beams of H, He and O ions

Y. Katano[a], T Aruga[a], S. Yamamoto[b], T. Nakazawa[a], D. Yamaki[a] and K. Noda[a]

[a]*Department of Materials Science, JAERI-Toaki*

[b]*Department of Materials Development, JAERI-Takasaki*

1. Introduction

We have so far studied synergetic effects of atomic displacement damage and implanted H, He atoms in Al_2O_3, which has been proposed for electrical insulators and diagnostic materials in fusion reactors, using samples irradiated with multiple beams of hydrogen (H), helium (He) and oxygen (O) ions from TIARA. It has been found that hydrogen atoms enhance the growth of dislocation loops decorated with tiny cavities under a displacement damage as low as 0.2 dpa, while the concurrent existence of He atoms under a high damage of 3.6 dpa retards the dislocation growth[1,2].

In the present study, we have investigated the damage structures in Al_2O_3 samples simultaneously irradiated with beams of H, He and O ions by cross-sectional transmission electron microscopy (XTEM). The results are discussed in terms of mobilities of point defects influenced by the presence of H and He atoms using the depth profiles of implanted H atoms measured for the irradiated samples.

2. Experimental procedure

The materials used in this study were single crystal alumina (α-Al_2O_3). The procedures of sample preparation and irradiations have been described elsewhere [3]. The samples were irradiated with either triple ion beams (0.25MeV H^+, 0.6MeV He^+ and 2.4MeV O^{2+}) or dual ion beams (0.25MeV H^+ and 2.4MeV O^{2+}) at 923 K (0.4Tm). The ion energies were so chosen that the projected ranges of the irradiated ions in Al_2O_3 coincides with depths of 1.38~1.41 μm. Table 1 summarizes the irradiation conditions examined and respective damage parameters obtained with TRIM89 code [4], using a common displacement energy of 40 eV. After irradiation, XTEM observations were performed using a JEM-2000FX electron microscope operating at 200kV.

Depth profiles of implanted H atoms in the both as-irradiated samples were measured utilizing a resonant nuclear reaction analysis (NRA) of ^{15}N, $^{15}N(H, \alpha\gamma)^{12}C$ [5], which occurs at ^{15}N ion energy of 6.385 MeV,

Table 1 Irradiation conditions and corresponding damage parameters obtained by TRIM calculations.

Ion beams	Energy/Ion (MeV)	Flux (10^{16} ions/m^{2}s)	Fluence (10^{20} ions/m^2)	Calculated value (TRIM)			
				Damage peak depth (μm)	Peak damage (dpa)	Average projected range (μm)	Peak ion concentration (at.%)
Triple #94-05	0.25 H^+	3.6	2.3	1.35	0.04	1.38	1.7
	0.6 He^+	2.4	1.5	1.34	0.3	1.39	0.9
	2.4 O^{2+}	3.3	2.1	1.34	3.3	1.41	1.3
Dual #95-11	0.25 H^+	4.0	5.0	1.35	0.09	1.38	3.7
	2.4 O^{2+}	6.0	7.6	1.34	10.5	1.41	2.8
Single #97-01	0.25 H^+	6.0	6.6	1.35	0.10	1.38	4.8

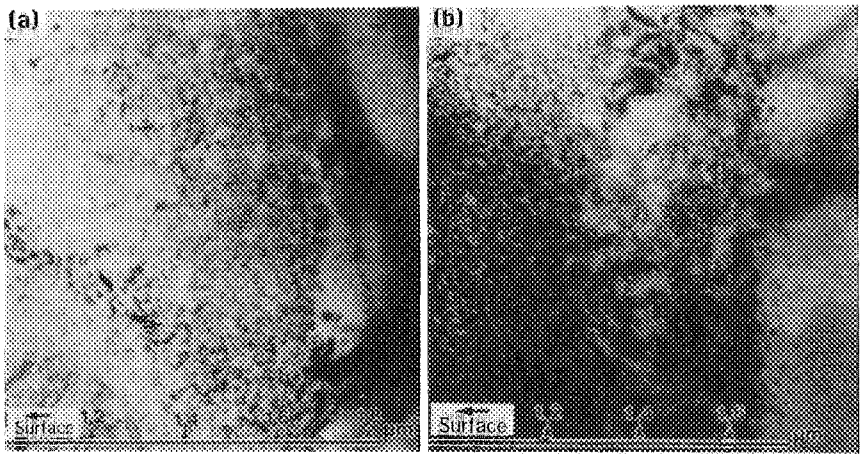

Fig.1. Cross-sectional damage structures in single crystal α-Al_2O_3 irradiated with triple(H^+, He^+ and O^{2+}) beams at 923K (a) and with dual (H^+, and O^{2+}) beams at 923K (b).

using an apparatus described in ref. [6]. Counts of γ-rays emitted from the resonant nuclear reaction and detected through a channel window around ~4.43 MeV as a function of ^{15}N ion energies varied from 9 to 11.2 MeV, were converted to a depth scaled function using stopping powers for ^{15}N provided in TRIM89. The γ-ray yields were accumulated for the total incident ^{15}N ions of 5 μC for every energy.

3. Results and discussion

3.1 Cavity formation behaviors

The cross-sectional microstructure of Al_2O_3 irradiated with triple (H^+, He^+ and O^{2+}) beams to a total peak damage of 3.6 dpa at 923 K and the one irradiated with dual (H^+ and O^{2+}) ions to a total peak damage of 10.6 dpa at 923 K are shown in fig.1(a),(b). The damaged region extends from the position very close to the ion-incident surface to a depth of 1.8 μm (fig.1(a),(b)).

As has been already described [7], cavities in the triple beam irradiated sample are observed to form in the restricted region of depths from 1.2 to 1.7 μm, where the displacement damage is greater than 1.5 dpa and most of H, He and O ions are predicted to be stopped (fig.2(b)). The depth profile of cavity densities peaked with a maximum value of 1.7 x $10^{23}/m^3$ at depths of about 1.3~1.4 μm. In the dual beam irradiated sample, the irregularly shaped cavities are seen to grow two times larger than those observed in the triple beam irradiated sample. Moreover, tiny cavities smaller than 5 nm are formed in the region of smaller depths down to 0.5 μm and the damage level there is as low as 1.0 dpa (fig.2(b)). These facts suggest that He atoms trap the radiation-produced point defects, thus lowering the mobility of the point defects and suppressing the formation of visible cavities.

3.2 Depth profile of H atoms in the irradiated samples

The depth profiles of H atom densities in both the triple and dual beam irradiated samples are shown in fig.2(a), along with that for the sample irradiated with single beam of 0.25 MeV H^+ at 923 K (table 1), for comparing the diffusivity of H atoms under various irradiation conditions. Note that the depth scale was merely converted from incident ^{15}N-ion energies using its stopping powers provided by TRIM89 code. It is seen that the depth profile of H atoms implanted with single beam is peaked at a depth of 1.55 μm, while the peaks occur at 1.25 μm and 1.45 μm for the triple and dual beam irradiations, respectively. Besides, the second peak is clearly observed at 1.45 μm for the triple beam irradiation.

The ratios of peak heights of the triple and

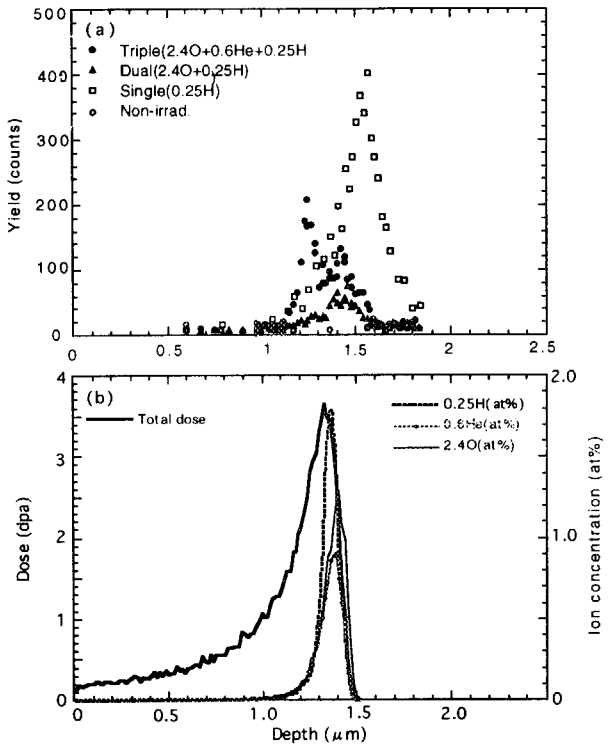

Fig.2. Depth profiles of H atom densities in the Al_2O_3 irradiated with triple and dual beams along with single beam of H ions at 923 K measured by a NRA (a) and depth profiles of damage parameters for the triple beam irradiation obtained by TRIM89 (b).

dual beam case to that of the single beam case are, respectively, 1/2 and 1/4. Note that the ratio of 1/2 is large compared with the ratio of implanted H atom density predicted to that of single beam case (table 1), i.e., about 1/3, for the triple beam case. On the other hand, the ratio of 1/4 is much smaller than the corresponding ratio 3/4, for the dual beam case; suggesting a reduced mobility of H atoms under coexistence of He atoms.

The reduction of the point defect mobility under the influence of coexisting He atoms is supported also by this fact that a larger fraction of H atoms implanted with the triple beam irradiation to 3.6 dpa remain, without being diffused away, at the stopped positions, compared with that measured for single H-ion beam irradiation to a low dose of 0.1 dpa (fig.2(a), table 1). Furthermore, we have already observed that cavities sized to be 8 nm in an average were formed along grown-in dislocation loops in Al_2O_3 sample irradiated at 923 K with 0.33 MeV H-ions to a comparable dose [2]: grown-in loops sized as large as 80 nm being formed under the low displacement damage level of 0.2 dpa.

In the case of dual beam irradiation, as is observed in the depth profile of H atoms (fig.2(a)), most of implanted H atoms are considered to be diffused away from the distributed ranges along the gradient of the displacement damage toward the surface, and play a role of aiding cavity formation down to a depth of 0.5 μm where damage level is as low as 1.0 dpa. On the other hand, H atoms stopped in association with He atoms seem to be bound to defect clusters and may efficiently trap the radiation produced point defects, with the clusters being hardly to grow into visible cavities even at 1.5 dpa.

In summary, in the both irradiations at 923 K, the depth profile of cavity density distribution for the triple beam irradiation appeared in a more restricted region of depths around the damage peak, compared with that in the dual beam irradiation, exhibiting that a coexistence of He atoms suppresses the growth to visible cavities, whereas H atoms in the absence of He atoms enhance cavity growth.

Reference

[1] Y. Katano, T. Nakazawa, D. Yamaki, T. Aruga, K. Hojou, K. Noda, Nucl.Instr & Meth. B116 (1996) 230.

[2] Y. Katano, T. Nakazawa, D. Yamaki, T. Aruga, and K. Noda, J. Nucl.Mater. 233-237 (1996) 1325.

[3] Y, Katano, H. Ohno and H. Katsuta, J. Nucl. Mater. 155-157(1988)366.

[4] J.F. Ziegler, J.P. Biersak and U.L. Littmark, The stopping and Range of Ions in Solids (Pergamon, New York, 1985).

[5] W. A. Lanford, Nucl. Instr.and Meth.B 66 (1992) 65.

[6] S. Yamamoto, P. Goppelt-Langer, H. Naramoto, Y.Aoki, H. Takeshita, J. of Alloy an Compounds 231(1995) 310.

[7] Y.Katano, T. Aruga, S. Yamamoto, T. Nakazawa, D. Yamaki, and K. Noda, Nucl. Instr. and Meth. B 140 (1998) 152.

4.10 Cavity Formation and Swelling in Ion-Irradiated F82H Steel

A. Naito, S. Jitsukawa and Y. Miwa
Department of Materials Science, JAERI.

1. Introduction

The swelling in ferritic steels has been almost out of consideration because it is lower compared with austenitic steels. However it is also possible to be important consideration under actual irradiation environment of fusion reactors. The objective of this study is to investigate the swelling behavior in a ferritic steel by the ion-irradiation experiments with high accuracy.

2. Experimental

The material used is a reduced activation ferritic/martensitic steel F82H. The main chemical composition is Fe-8Cr-2W-0.2V-0.04Ta in wt%. Samples with 3mm in diameter and 0.2mm in thickness were simultaneously irradiated with 11.3MeV Fe^{3+} and 1MeV He^{+} at 723 and 823K in the triple beam irradiation facility of TIARA. The theoretical depth profiles of displacement damage produced by iron ions and concentration of injected helium were calculated with TRIM-85 code.

After the irradiation, specimens for TEM observation of a cross sectional view perpendicular to the incident surface were prepared from the irradiated samples. Nickel was electroplated on the both sides of an irradiated sample to a thickness greater than 3mm. The electroplated sample was sliced into 0.2mm thick sheet using a low speed diamond saw, and cut into 3mm disk. Then it was electropolished to perforation. The cross sectional microstructures were observed with a JEOL-2000FX operated at 200kV.

3. Results

Cavities were observed in the depth of 1.6μm corresponding to the injected depth of helium both in the irradiated specimens at 723 and 823K. Those TEM micrographs are shown in Fig. 1. Displacement damage is 11.8dpa and He/dpa is 202appm/dpa at 723K irradiation, and they are 10.4dpa and 220appm/dpa at 823K irradiation, respectively. The cavities are uniformly distributed in the matrix at 723K, while the biased distribution along dislocation lines is observed at 823K. Fig. 2 shows the size distribution of cavities at each temperature. The mean diameters are 1.5nm at 723K, and 2.7nm at 823K. The number densities are 8.0 x $10^{22}m^{-3}$ and 1.8 x $10^{22}m^{-3}$, respectively. The swellings are 0.03% at 723K, and 0.04% at 823K, and they are comparable at both temperatures. These values are shown in Table 1. No cavity was observed except in the injected depth of helium both in the irradiated specimens.

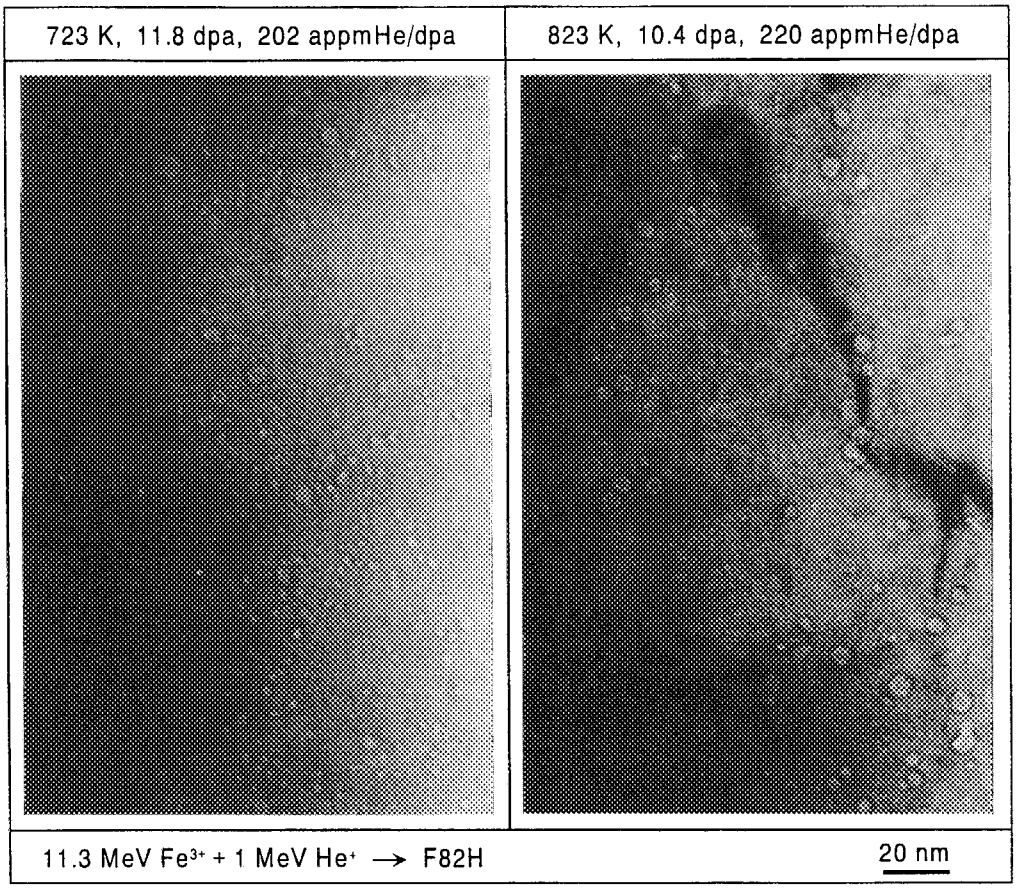

Fig. 1 Cavities formed in F82H irradiated at 723K and 823K.

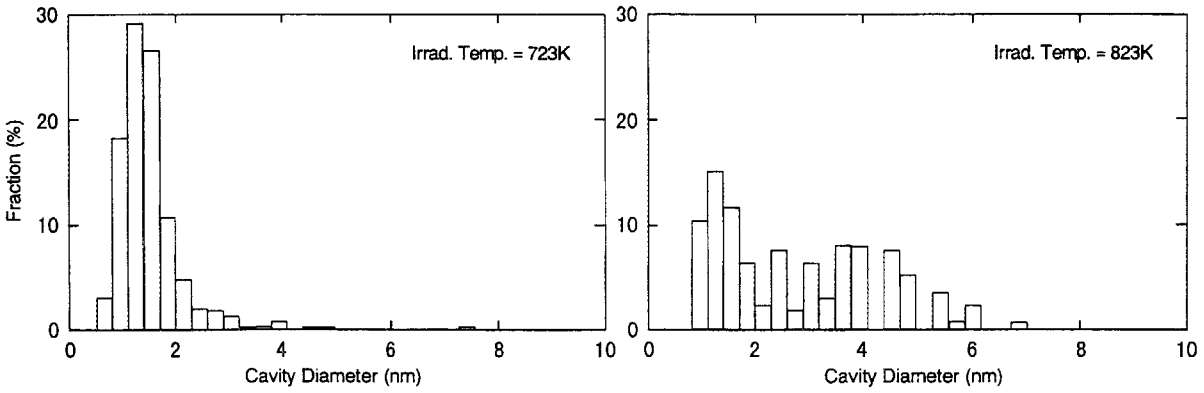

Fig. 2 Size distribution of cavities.

Table 1 Quantitative data of cavity structures.

Irrad. Temp.	723K	823K
Mean Cavity Diameter (nm)	1.5	2.7
Cavity Number Density (m^{-3})	8.0×10^{22}	1.8×10^{22}
Swelling (%)	0.03	0.04

4. 11 Damage evolution in high energy ion-irradiated metals and the interaction between gas atoms (H and He) and damage defects

Y. Shimomura, I. Mukouda, T. Iiyama, Y. Katano*, T. Nakazawa*, D. Yamaki* and K. Noda*

Applied Physics and Chemistry, Faculty of Engineering, Hiroshima University,
*Department of Materials Science, JAERI/Tokai

1. Introduction

On operating environment of fusion reactor, materials which compose the first wall receive a high flux of 14MeV neutron-irradiation and a large concentration of damage cascades is formed as such amount as a few dpa. At the same time, hydrogen and helium atoms are generated by nuclear transmutation of (n, p) and (n, α) reaction. These gas atoms play an important role on the evolution of damage structure. It is generally believed that helium atoms nucleate voids by suppressing a collapse of vacancy clusters. In the present work, the quantitative experiments are carried out to study the role of gas atoms on the evolution of damage structure in irradiated materials. It is the only possible to dope controlled concentration of gas-atoms in irradiated metals by ion irradiation of high energy. We examined the void formation in Ni-ion irradiated Fe-15Cr-20Ni and pure Cu by a dual-beam irradiation (5MeV Ni-ion and 260 keV H ion, and 5MeV Ni-ion and 600 keV He ion) and a triple-beam irradiation (5 MeV Ni-ion, 260 keV H-ion and 600 keV He-ion).

Experimental results are compared with those of computer simulation of molecular dynamics to disclose the atomistic mechanism of void formation in irradiated metals.

2. Experimentals

Projectiles of ions stop in the depth of 1 - 2 microns from surface level and damage formed inside this depth of metals. For the quantitative investigation, damage structure

a) FIB RT thinning

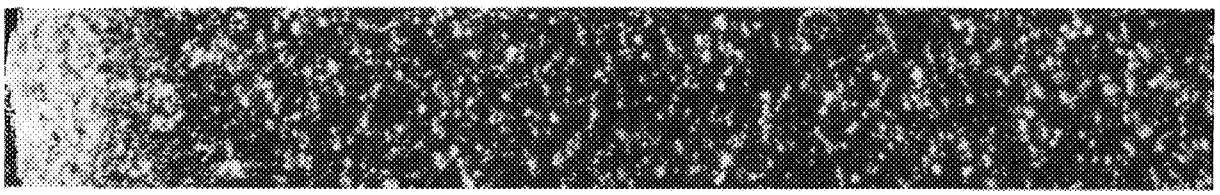

b) FIB 100K thinning

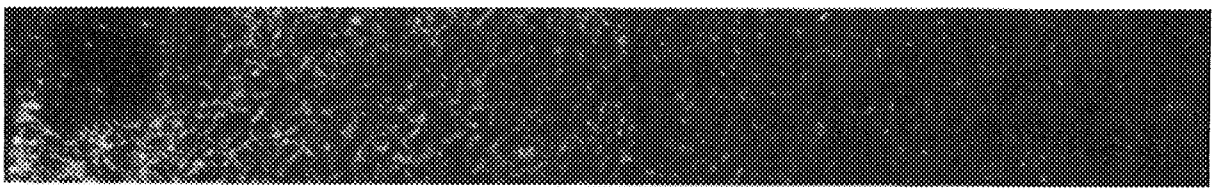

c) FIB 100K thinning and RT annealing

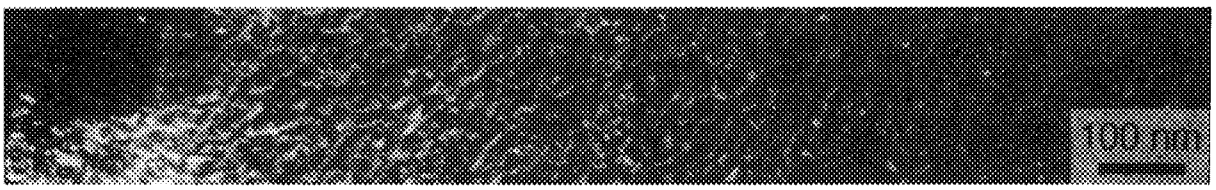

Fig.1 Weak beam dark field images of TEM (a) FIB thinning at RT, (b) FIB thinning at 100K, (c) after RT annealing of area (b).

have to be observed as a function of the depth. We utilized the focussed ion beam device (FIB). FIB generates 30 keV Ga ions and illuminates specimen surface with glancing angle. Atoms on surface are removed by sputtering. To reserve the surface position of ion-irradiated metals, we deposited the W on surface to prevent the sputtered out of surface atoms due to low sputtering yield of W. In our previous work, it was found that interstitial atoms form their clusters throughout FIB-thinned specimens. It is very difficult to distinguish damage defects which are formed by high energy-ion-beam irradiation and FIB damages. To solve this problem, we developed the cryotransfer-FIB thinning technique, in which specimen is cooled down at 100K on FIB thinning holder [1] (Thin holder is the TEM holder of side-entry type.) and transfer to a transmission electron microscope without warm-up specimens. This technique makes it possible to observe voids, even very small ones, in high energy ion irradiated metals. In ion-irradiated metals at high temperature, voids, interstitial clusters and dislocation are formed. Even with the FIB technique mentioned above, it is difficult to observe dislocation structure which is developed by clustering of interstitial atoms in irradiated specimen. To overcome this difficulty, we invented the TEM specimen preparation method which is a combination of FIB thinning and an electro-polishing. It is found that damage structure of ion-irradiated metals such as copper can be observed without FIB damages.

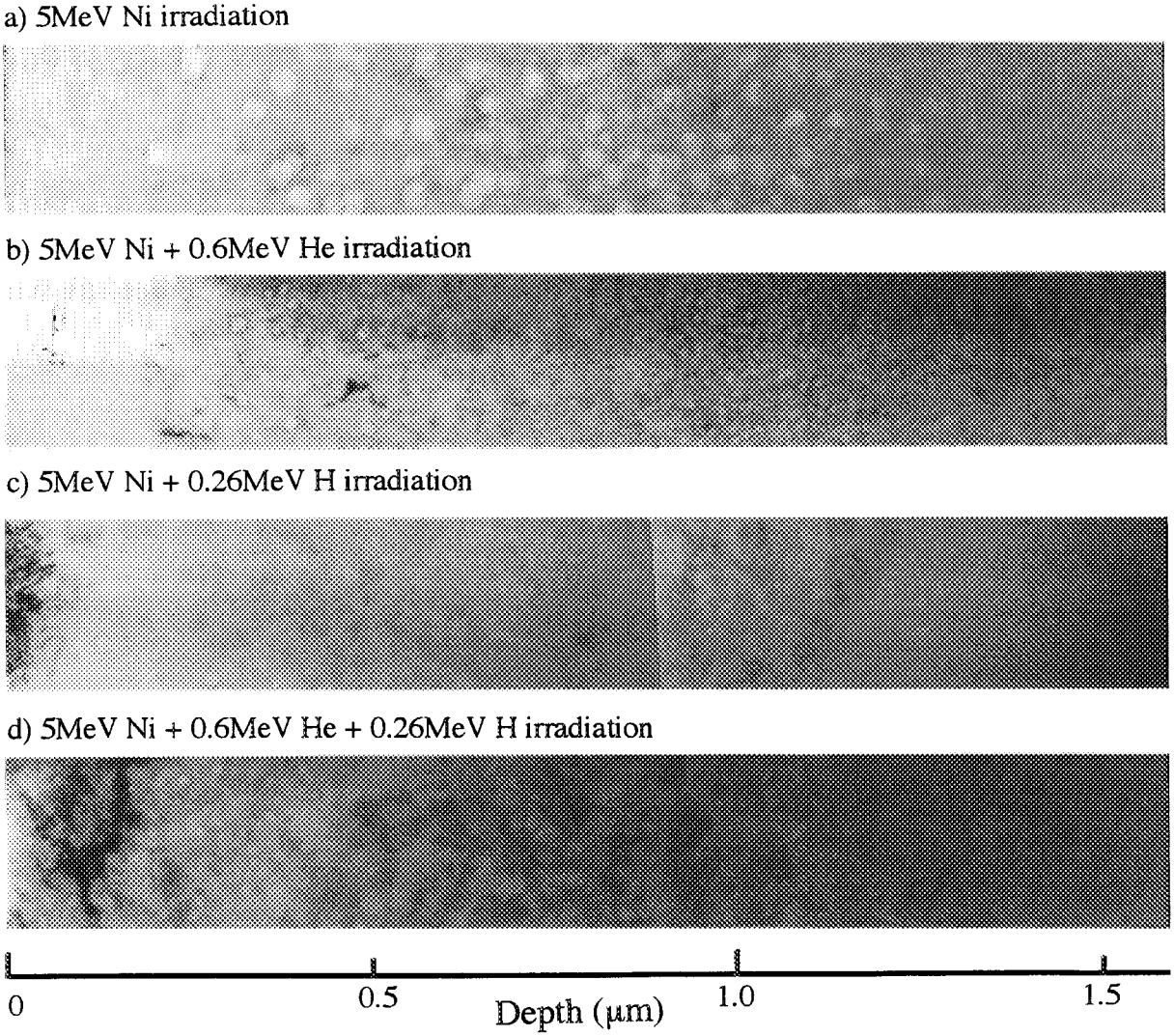

Fig.2 Void contrast bright field images of Fe-15Cr-20Ni irradiated at 500°C.

a) 5MeV Ni irradiation

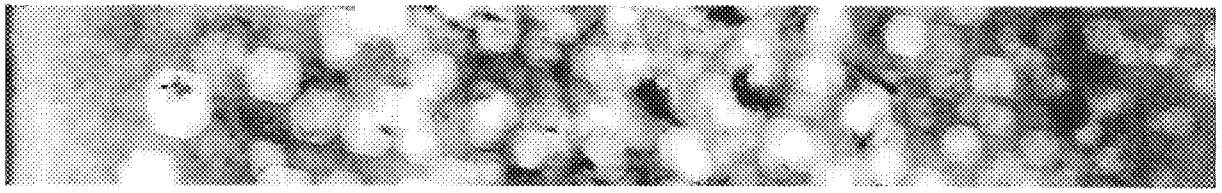

b) 5MeV Ni + 0.6MeV He irradiation

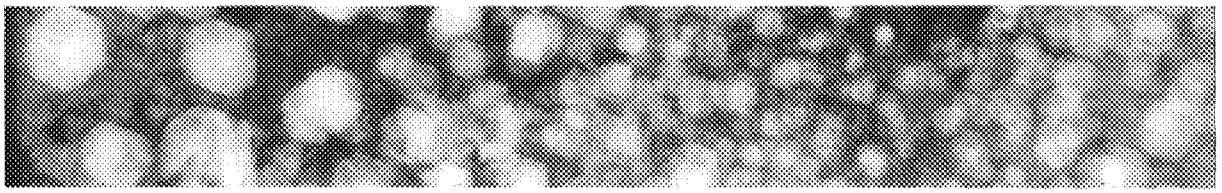

Fig.3 Void contrast bright field images of Fe-15Cr-20Ni irradiated at 600°C.

3. Results

Figure 1 shows defects which are created during FIB thinning. Observation was carried out with the weak beam dark field technique. Fig. 1(a) shows defects which were observed in FIB thinned Fe-Cr-Ni at room temperature. All white dotted defect due to FIB damages. Fig. 1(b) and (c) show FIB damages observed in warmed specimen after 100K thinning and cryotransfered specimen. It can be seen that FIB damage formation can be suppressed by using a cryotransfer FIB technique. It should be noted that FIB damages are interstitial clusters which are formed uniformly inside specimen. Figure 2(a) to (d) show the voids which are observed in single-, dual- and triple-beam irradiated Fe-Cr-Ni at 500°C. The number of vacancies which were accumulated into voids was calculated as a function of specimen depth. The value of vacancy concentration seems to show agreement with deposited damage energy which was calculated by TRIM code. At the range of Ni-ion of single beam, the number density of voids increases with the depth which mean that the number density of voids depends on the damage production rate. In dual-beam (Ni-ion and He-ion) irradiated Fe-Cr-Ni, the number density of voids increases remarkably at the stopped range of helium atoms. In dual-beam (Ni-ion and H-ion) irradiated Fe-Cr-Ni, only voids of very small size were observed. It is believed that a large number of sub-TEM size of voids are formed in the irradiated specimen with Ni-ions and H-ions. In specimen irradiated by a triple-beam, voids are observed while their size is smaller than that in dual-beam (Ni-ion and He-ion) irradiated specimens. These results suggest that vacancy clusters which trap hydrogen atoms are suppressed the movement as reserving a cluster. Vacancy clusters which trap helium atoms can migrate in specimens. At 600°C, the growth of voids in irradiated Fe-Cr-Ni is significantly enhanced as shown in Fig. 3.

A computer simulation on dynamical behavior of small vacancy clusters in copper and nickel shows that a hydrogen atom which is trapped into void moves on the void surface. A helium atom which is trapped into a void tends to stay in the central part of voids. In order small vacancy cluster to move at high temperature, vacancy cluster has to relax to a string-like shape. In this string-like vacancy clusters, a helium atom still can be trapped while a hydrogen atom can not be trapped.

References

1) Y. Shimomura, I. Mukouda, T. Iiyama, K. Noda, Y. Katano, T. Nakazawa and D. Yamaki: JAERI TIARA Ann. Rep. 1996 (1997) 121-123.

4.12 Effect of Transmutation Gas Atom on Microstructure Development by Displacement Damage of SiCf/SiC Composites for Fusion Systems

S. Nogami[1], A. Hasegawa[2], M. Saito[1],*, K. Abe[2], S. Hamada[3], Y. Miwa[3]

[1] Graduate School of Engineering, Tohoku University, [2] Department of Quantum Science and Energy Engineering, Tohoku University, [3] Dept. of Mater. Science and Engineering, JAERI/Tokai *Present address; JEOL Japan,

1.Introduction

Silicon carbide (SiC) is considered as one of the candidates of low activation structural materials for fusion systems because the induced radioactivity of SiC by 14MeV-neutron is inherently lower. So the development of SiC-fiber reinforced SiC composites (SiCf/SiC) has been advanced in order to alleviate the brittleness of monolithic SiC. The ratio of helium (He) gas concentration (unit:at.ppm) produced by nuclear reaction (typically (n,α)-reaction) to the displacement damage (unit:dpa) by 14MeV neutron will be about 130at.ppmHe/dpa (maximum) in SiC, which is larger than for the other candidate materials such as ferritic steels and vanadium alloys. He gas atoms combine with lattice defects easily and become stable because they are not soluble in almost all materials and consequently these defect clusters influence microstructure of materials. So it is important to investigate the effects of He on microstructure development and mechanical properties of SiCf/SiC under fusion conditions. Since threshold energy of (n,α) reaction of SiC is larger than several MeV, introducing high concentration of He into SiC using a fission reactor is almost impossible. Using He it is easy to introduce high concentration of He into SiC. The purpose of this work is to investigate the effects of displacement damage under high concentration He on the microstructure of SiCf/SiC with ion irradiation by accelerators.

2.Experimentals

The materials examined in this work were 2D-SiCf/SiC composites (produced by DuPont in USA), which consist of layers of 2D-textiles of Hi-Nicalon™ fibers with carbon coating (thickness: 1.2 or 0.2μm) and β-SiC matrix fabricated by CVI-process. These samples were cut perpendicularly to the layers of textile into 500μm thickness and then polished and thinned to 300μm thickness by mechanical lapping machine and cut into TEM disk-specimens.

These specimens were implanted 3.0MeV Helium ions (He^+) with DYNAMITRON

accelerator of Tohoku university at room temperature using an Al-foil energy-degrader in order to obtain the uniform He distribution in the specimens toward the depth of about 1~5μm. And then these specimens were irradiated 6.5 or 8.0MeV carbon ions (C^{2+}) with a tandem accelerator of TIARA at temperature of 600 and 800℃. The concentration of pre-implanted He was 0, 100, 1000 and 10000at.ppm and the maximum displacement damage by the carbon irradiation is about 10dpa.

After irradiation these specimens were sandwiched between monolithic β-SiC plates which were bonded by the resin to prepare TEM specimens. These specimens were cut perpendicularly to the irradiated surface into 300μm thickness. The "sandwiched specimens" were mechanically thinned to less than 50μm thickness and ion-milled with Argon ions at 4kV to less than 100nm thickness.

Cross sectional transmission electron microscopy was performed on these specimens using a HITACHI HF-2000 microscope using 200kV.

3. Results and Discussion

Microstructure of Hi-Nicalon™ fiber in composite specimens pre-irradiated He to 10000at.ppm and followed by 10dpa carbon ion irradiation at 600℃ is shown in Fig.1. This micrograph is the dark field image using {111} reflection of β-SiC and each white spot corresponds to the SiC micro grain. But at the peak damage region of carbon ions these white spots are a little as is shown in Fig.1. The microstructure change may be attributed to amorphization by displacement damage. In the case of β-SiC matrix, microstructure change such as amorphization were not observed. The threshold irradiation dose for amorphization of monolithic SiC after ion irradiation had been reported[1], but that of Hi-Nicalon™ had not been well known using ion irradiation. It is likely that the cause of amorphization of Hi-Nicalon™ fiber in this work are relatively small size of SiC grain in Hi-Nicalon™ fiber (~5nm) compared to matrix (~μm) and relatively high contents of carbon and oxygen compared to stoichiometry component. On the other hand, amorphization was not observed in both Hi-Nicalon™ fiber and matrix in specimen irradiated at 800℃. It may be attributed to recovery of amorphised at higher temperature.

Helium bubbles were not observed in both Hi-Nicalon™ fiber and matrix of specimens pre-implanted He and irradiated carbon ions at 600 and 800℃. Helium bubbles in matrix of specimens which was irradiated He ions up to 10000at.ppm and annealed at 1400℃ in 1 hour are shown in Fig.2. In Hi-Nicalon™ fiber of the same specimen helium bubbles were not observed. Helium might present in matrix as small clusters combined with vacancy after carbon irradiation and bubbles were formed during annealing at 1400℃. The results of this work show that pre-implanted He did not form bubbles in the matrix, fiber and then interface even after 10dpa irradiation at 600 and 800℃. Amorphization at 600℃ shows diffusion is not large enough to

recover displacement damage at 600℃. Further experiment will be needed to clarify the difference between fiber and matrix.

In 1998, we are planning to study the effect of He gas atoms on microstructural development of SiCf/SiC composites due to displacement damage with dual-irradiation of He ions and carbon ions above 900℃ which corresponds to operating temperature of SiCf/SiC composites in fusion reactor.

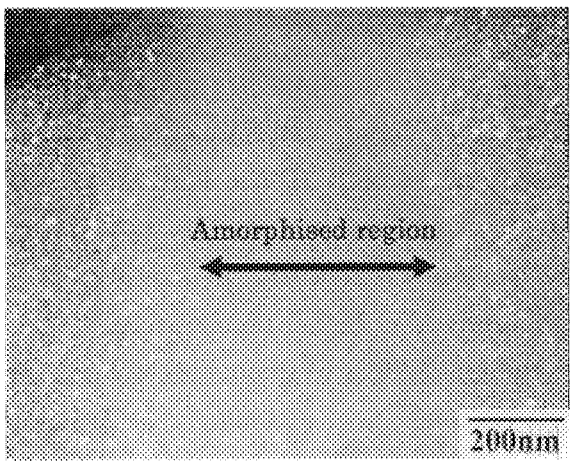

Fig.1 Dark field image of He ion pre-implanted and carbon ion irradiated Hi-Nicalon™ fiber of SiCf/SiC composite. Pre-implanted He concentration was 10000at.ppm and carbon ions irradiated up to 10dpa at 600℃.

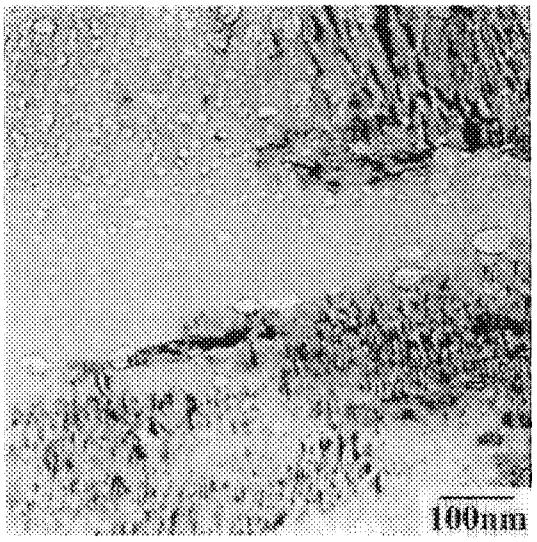

Fig.2 TEM micrograph of He bubbles in β-SiC matrix of He pre-implanted SiCf/SiC composites after annealing at 1400℃ for 1h. (Pre-implanted He concentration: 10000at.ppm)

References

(1) L.L. Snead and S.J. Zinkle, Fusion Mater. DOE/ER-0313/21 Semiannual Progress Report for Period Ending December 31, 1996 P99.

4. 13 Effect of Synergistic Irradiation on Microstructural Structure in Duplex Stainless Steel

S. Hamada, Y. Miwa and T. Taguchi*
Dept. of Nuclear Energy System, *Dept. of Materials Science, JAERI

1. Introduction

Structural materials for water-cooled components in a fusion reactor are required to possess excellent resistance to stress corrosion cracking (SCC) in pressurized water at elevated temperature. In general, ferritic stainless steels are known to have better resistance than austenitic stainless steels. Ductility loss, however, of ferritic stainless steel is greater than that of austenitic stainless steel under irradiation. Ferrite/austenite duplex stainless steel consisting of both, ferrite and austenitic phase, have mixed characteristics of these steels. There are a few previous papers on studies of radiation effects of ferrite /austenitic duplex stainless steels [1,2]. They have focused on void swelling at high damage levels. It is important to get information concerning phase stability, which will affect other characteristics of the materials, as well as swelling behavior under irradiation.

In this study, phase stability of the ferritic and the austenitic phase of duplex stainless steel under synergistic irradiation by multi beam was investigated.

2. Experimental

The material used in this study is a stainless steel of 0.019C-0.49Si-1.01Mn-0.02P-0.003S-9.0Ni-21.3Cr-2.5Mo-0.013N-Fe balance, all in weight percent. The material is composed of both, ferritic and austenitic phases and contains α–ferrite phase of 47%. It was solution-annealed for 30 min at 1323K. The irradiation conditions were shown in table 1. Some samples were simultaneously irradiated with multi beam. The theoretical depth profiles of displacement damage produced by nickel ions and the concentrations of both helium and hydrogen injected in 316 stainless steel were calculated using the E-DEP-1 code[3] with threshold energy of 40 eV.

After the irradiation, thin foils were prepared for TEM (transmission electron microscope) examination by using the cross-section technique[4]. The cross sectional microstructures were observed with a TEM operated at 200 kV.

3. Results and discussion

Fig. 1 shows a scanning electron micrograph of a cross section normal to the incident

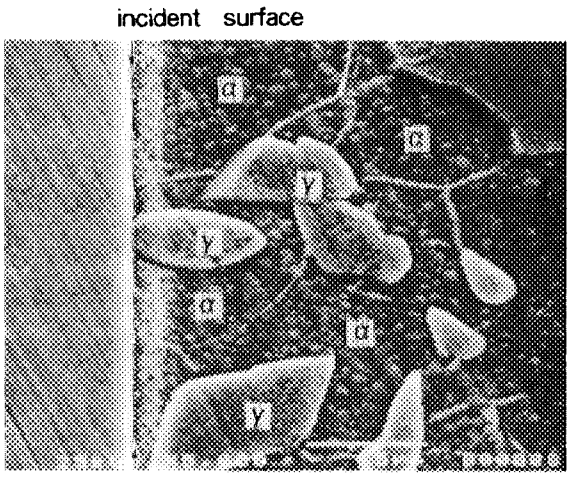

Fig. 1 SEM micrograph of cross section normal to the incident surface etched by a $CuCl_2$ saturated solution.

Table 1 Irradiation condition

Mode	Irra. temp. (°C)	Displacement damage(dpa)	H level (at.ppm)	He level (at.ppm)
Ni	500	10	0	0
Ni+H	400	8	970	0
Ni+He	400	10	0	700
Ni+H+He	400,500	10	200	300

surface in the nickel-ion irradiated sample etched by a saturated $CuCl_2$ solution. Some precipitates appeared to be in a parallel band to the incident surface at a depth of 3.5 to 1.5 μm from the incident surface. The band was observed only in ferritic phases, not in austenitic ones.

The microstructural evolution formed in the ferritic phase is shown in fig.2. Precipitates with round shape (10-30nm in diameter) were produced in a depth of 0.3 μm from the incident surface, where the dose is evaluated to be about 3 dpa. They grew as the depth increased, that is, damage level increased, and formed warped and elongated shapes in a depth of 1 μm, which corresponds to damage level of 10 dpa. These results mean the precipitates in this alloy grow fast with increasing dose. The precipitates distributed like a band in fig. 1 are ensured to correspond to the elongated ones in fig. 2. These precipitates have a moire fringe contrast on them. The diffraction pattern and EDS analysis results identified the precipitates in a ferritic phase to be χ-phase and the chemical composition is 4.3Si-13Mo-27.1Cr-36Fe-18.7Ni (in wt%).

The appearance of the χ-phase in the ferritic phase is characteristic for the nickel-ion irradiated α/γ duplex stainless steel. This phase in the α/γ duplex stainless steels has not been reported by other irradiation studies [1,2]. The χ-phase has not appeared in other ferritic steels such as HT-9[5] and 9Cr[6] steels except only for work[7] during heavy ion irradiation. The χ-phase under nickel-ion irradiation may significantly depend on the chemical composition of the ferritic phase. In comparison of the chemical composition of the material used in this study with that of the other ferritic steels, the former reveals Ni, Si and Mo content to be higher and carbon content to be lower relative to the latter. Further, the chemical composition of the χ-phase in this study shows enrichment of Ni and Si relative to that of the χ-phase thermally formed[8]. These results indicate that Ni and Si have so influence on the formation of the χ-phase. Ni and Si are undersized atoms in iron-base alloys, which then tend to be enriched at point defect sinks[9]. Point defect clusters produced at the initial period of irradiation may play a role as sinks for Ni and Si atoms. Subsequently these atoms will form a radiation-induced segregation (RIS) zone at point defect clusters. Here, the behavior of RIS during additional irradiation may depend on carbon content of the ferritic phase. If enough carbon is contained of it, this RIS may proceed to form carbides such as M_6C. Actually, car-

bides such as M_6C enriched with Ni and Si easily form under irradiation in 316 austenitic stainless steel, which contains higher carbon levels (0.04-0.06 wt%) than the materials in this study[10,11]. Although the carbon level of the ferritic phase has not been determined yet, the carbon of ferritic/austenitic duplex stainless steels generally tends to enrich more in the austenitic than in the ferritic phase. This means the carbon content of the ferritic phase is probably lower than 0.019 wt%, which is that of the alloy used in this study, and is much lower relative to the carbon levels of other ferritic steels as described above. Eventually, Ni and Si atoms may segregate at the point defect cluster and the nucleus of χ-phase is formed at the initial period of irradiation. Lower carbon content will lead it to form an intermetallic compound of χ-phase. This grows fast with increasing dose.

4. Summary

The ferritic/austenitic duplex stainless steel was nickel-ion irradiated at 500 °C to 10 dpa at peak. The results are characterized by appearance of plenty of χ-phase precipitates are radiation-induced precipitated and are enriched in Ni, Si and Mo.

The experiments of dual and triple beam irradiated specimens are in progress.

5. References

1) D. Blasl, H. Tsunakawa, K. Miyahara, and N. Igata, J. Nucl. Mater. 133&134(1985)517.
2) W.G. Johnston, J.H. Rosolowski, A.M. Turkalo and T. Lauritzen, J. Nucl. Mater. 54(1974)24.
3) I. Manning and G.P. Mueller, Comput. Phys. Commun. 7(1974)85.
4) S. Hamada, M.P. Tanaka and K. Shiraishi, J. Nucl. Mater. 114(1983)338.
5) G. Ayrault, DAFS Quart. Prog. Rep. Octo.-December 1981, DOE/ER-0046/8, Vol.1.
6) K. Farrell and E.H. Lee, Pro. 12th Int. Symp. on Effects of Radiation on Materials, Williamsburg, 1984, ASTM-STP 870, pp. 383-393
7) J.J.Kai, G.L. Kucinski and R.A. Dodd, DAFS Quart. Prog. Rep. January-March 1985, DOE/ER-0046/21.
8) B. Weiss and R. Sticker, Metall. Trans. 3(1972)851.
9) T.R. Anthony: radiation-Induced Voids in Metals, CONF-71060, pp. 630-646.
10) S. Hamada, P.J. Maziasz, M.P. Tanaka, M. Suzuki and A. Hishinuma, J. Nucl. Mater. 155-157(1988)838.
11) E.H. Lee, P.J. Maziasz and A.F. Rowcliffe, Proc. Symp. on Phase Stability During Irradiation, Pittsburgh, 1980, pp. 191-218.

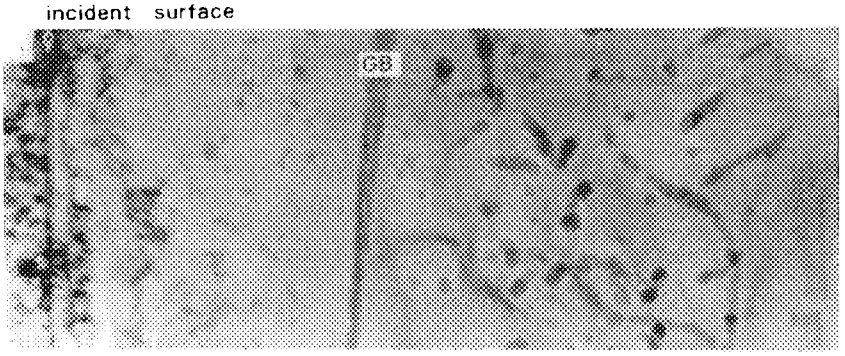

Fig. 2 Depth profile of precipitates observed in the ferritic phase

4.14 The Effect of Helium and Hydrogen on Microstructural Evolution in Vanadium as Studied by Triple Beam Irradiation

N. Sekimura[1], S. Yonamine[1], Y. Arai[1], T. Iwai[2], T. Okita[1], T. Morioka[1], S. Hamada[3] and Y. Miwa[3]
Department of Quantum Engineering and Systems Science, Univ. of Tokyo [1]
Research Center for Nuclear Science and Technology, Univ. of Tokyo[2]
Materials Research Division, JAERI/Tokai[3]

1. Introduction

Vanadium alloys are one of the candidate materials for blanket structures in fusion reactors, because of their good mechanical properties at high temperature and low activation under 14 MeV neutron irradiation[1, 2].

Microstructural evolution in vanadium alloys is considered to be strongly influenced by nuclear transmutants under 14MeV neutron irradiation. Here, the effect of helium and hydrogen on swelling behavior in pure vanadium was investigated to construct fundamentals of predictive modeling of microstructural evolution and mechanical property changes in irradiated vanadium alloys.

2. Experimental

Vanadium alloys are prepared by arc-melting and rolled to sheets of 0.2 mm in thickness. These are cut into 3mm disks and annealed at 1273 K for 1 hour in high vacuum, followed by rapid cooling. These specimen are irradiated with 12 MeV Ni^{3+} ions to 30 dpa at 1700 nm from the surface with simultaneous implantation of helium and hydrogen by 1 MeV He^+ and 350 keV H^+ ions in the TIARA facility. He(appm)/dpa and H(appm)/dpa ratios are fixed at 10. Fig.1 shows the distribution of damage by Ni ions and implanted He and H particles. In this paper, we report the microstructural results in 99.8 % pure vanadium specimens irradiated at 873 K, comparing dual beam irradiation with 12MeV Ni^{3+} and 1MeV He^+, or 12MeV Ni^{3+} and 350KeV H^+, and single beam irradiation only with 12MeV Ni^{3+} to 30 dpa at the identical temperature.

3. Results and discussion

Cavities are formed in irradiated vanadium regardless of helium and hydrogen implantation modes. Fig. 2 and 3 show average diameter and density of cavities in irradiated pure vanadium, respectively.

In the triple beam irradiated specimens with He(appm)/dpa and H(appm)/dpa ratios of 10, cavities are found to grow larger than other cases. As nucleated cavities grow very rapidly, total density of cavities are considered to be smaller than other cases. In the neutron-irradiated vanadium with co-production of helium in the DHCE experiments[3], cavity density becomes

larger than He free cases. However, it has not been recognized that co-injection of both He and H increases swelling. This will have great impact in modeling of swelling

Fig. 5 shows total cavity volume faraction in pure vanadium with and without simultaneous injection of He and/or H at 873 K.

References

1) D.L. Smith, J. Nucl. Mater. 122&123 (1984) 51.
2) D.R. Dieercks and B.A. Loomis, J. Nucl. Mater. 141-143 (1986) 1117.
3) M. Satou, K. Abe and H. Kayano, J. Nucl. Mater. 212-215 (1994) 794.

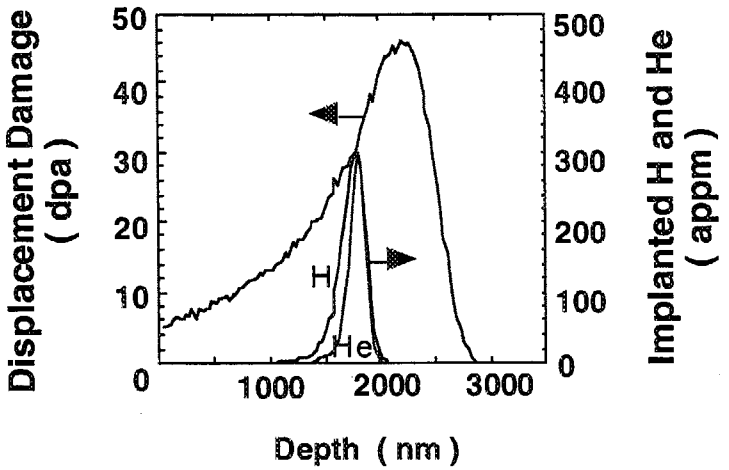

Fig. 1. Depth distributions of displacement damage and implanted He and H calculated by the TRIM92 code.

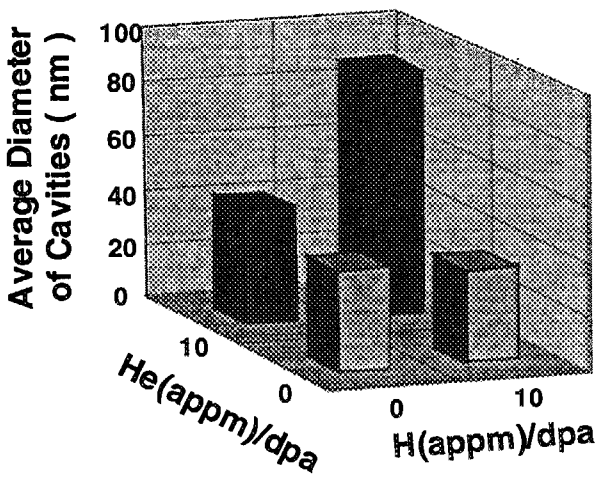

Fig. 2 Average cavity diameter in pure vanadium irradiated with 12 MeV Ni^{3+} ions to 30 dpa at 873 K with and without simultaneous irradiation of He and H.

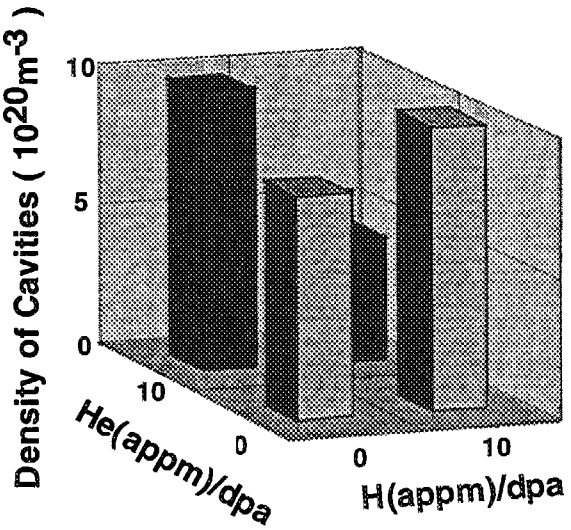

Fig. 3 Cavity density in pure vanadium irradiated with 12 MeV Ni^{3+} ions to 30 dpa at 873 K with and without simultaneous irradiation of He and H.

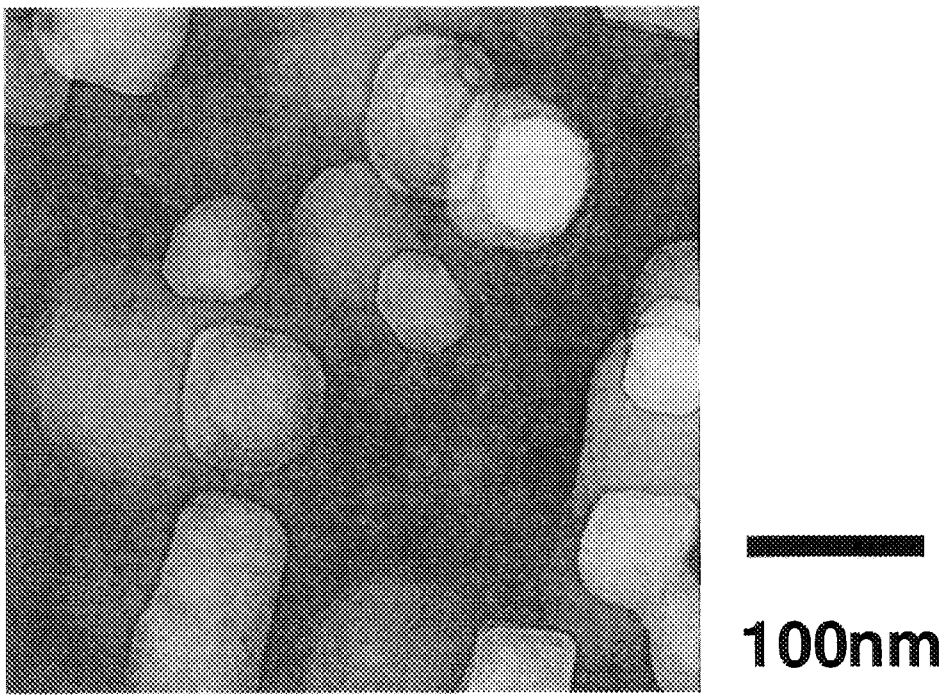

Fig. 4. Microstructure observed in pure vanadium irradiated with 12MeV Ni^{3+}, 1MeV $He^{+}$and 350KeV H^{+}ions (triple beam irradiation) at 873K to 30dpa.

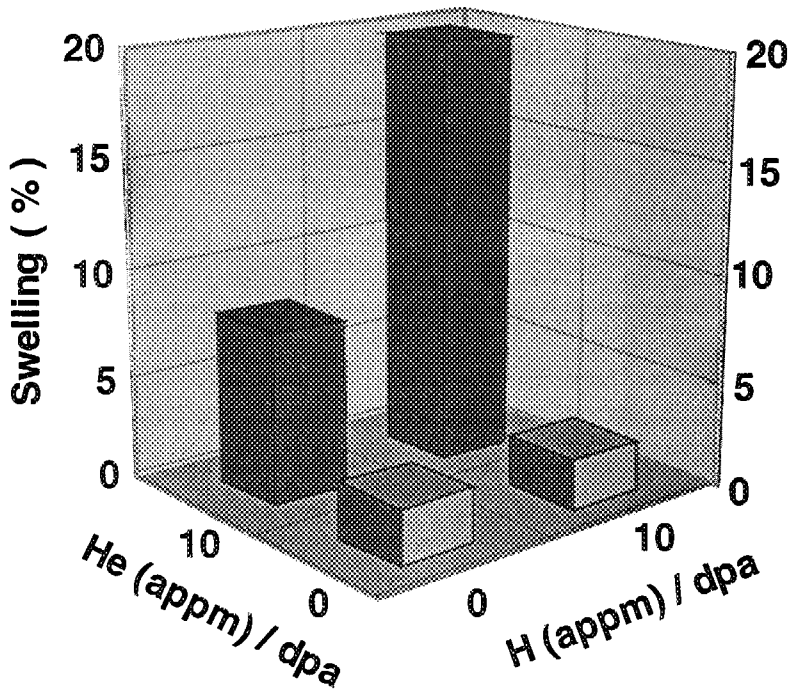

Fig. 5 Cavity volume fraction in pure vanadium irradiated with 12 MeV Ni^{3+} ions to 30 dpa at 873 K with and withou simultaneous irradiation of He and H. Triple beam irradiation strongly enhances swelling in vanadium.

4. 15 Hardening of Fe-0.6%Cu Alloy by Electron Irradiation

T. Tobita*, M. Suzuki*, Y. Idei*, A. Iwase**, and K. Aizawa**
Dept. of Reactor Safety Research* & Materials Science **, JAERI / Tokai

1. Introduction

Fluence and dpa (displacement per atom) associated with fast neutron irradiation are generally used as a scaling parameter for irradiation embrittlement of RPV steels. But other factors , such as γ -ray and thermal neutrons, are also known to contribute to irradiation embrittlement. The accelerated embrittlement revealed by the HFIR (High Flux Isotope Reactor) surveillance test was attributed to the γ -ray irradiation embrittlement[1]. The effect of the γ -ray irradiation on RPV steels has, however, not been fully understood.

Fast neutron irradiation forms cascade damages, while γ -ray produces simple Frenkel-pairs(interstitial atom & vacancy) through the generation of high-energy electrons by Compton effect (Fig.1). Therefore, we simulated γ -ray irradiation by electron irradiation, and measured the change of mechanical properties by hardness tests. The effect of electron irradiation was compared with that of fast neutron.

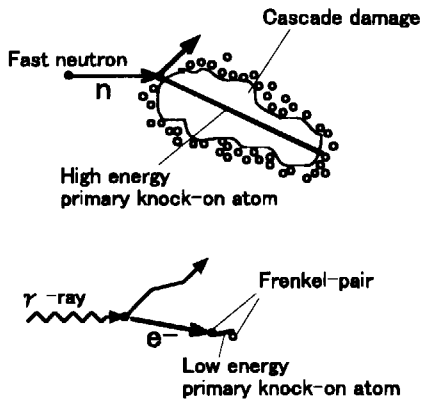

Fig.1. Difference in irradiation damage processes between fast neutron and γ -ray irradiation.

2. Experimental

2.1 Specimen

Chemical compositions of the specimen used(Fe-0.6%Cu) are shown in Table 1. This material contains Cu richer than actual RPV steels, which is one of the series designed for irradiation embrittlement study.

Table 1. Chemical compositions of the material. [wt%]

ID: Z-3	Fe	Cu	C	Si	O	N
Spec.	Bal.	0.52~0.66	≦0.003	≦0.003	≦0.003	≦0.002
Heat Treatment*	Bal.	0.61	0.002	0.002	0.015	0.0006

*850°C-2H & Rapid cooling

2.2 Electron Irradiation

Fig.2 shows specimen set up for electron Irradiation. Electron energy used for irradiation was 2MeV. Target temperature was 250°C, and irradiation times were 5, 10, and 15 hours.

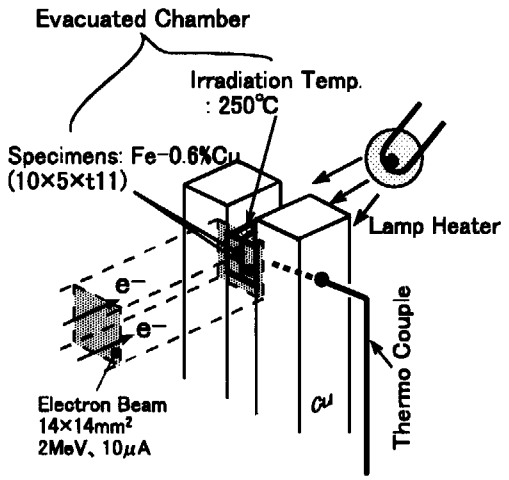

Fig.2. Specimen set up for electron irradiation.

2.3 Calculation of dpa Distributionin the Target Specimen

Distribution of energy spectrum, flux, and dpa were calculated using Monte Carlo

simulation code EGS4 (Electron Gamma Shower ver.4 [2]). Threshold energy of Fe atom used in this calculation was 40 eV.

2.4 Hardness Test

Hardness(Hv) distribution through the specimen thickness was measured using a micro Vickers hardness tester at 500gf, and was compared with dpa distribution calculated by the code.

3. Results and Discussion

3.1 Hardness Distribution

Fig.3 shows the hardness distribution on 5, 10 and 15 hour irradiated specimens. The hardness increases with increasing electron fluence.

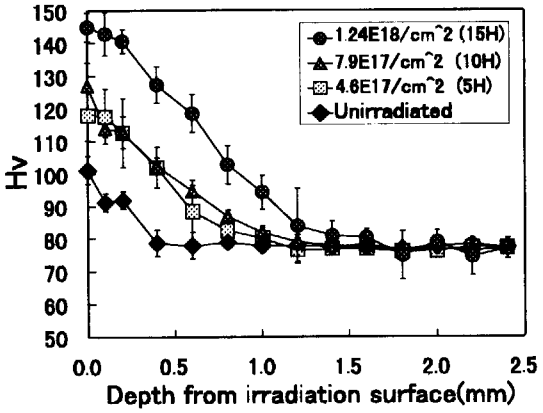

Fig.3. Hardness distribution

3.2 Distribution of dpa and Hardening

Fig.4 shows the distribution of calculated dpa and ⊿Hv(= $Hv_{(irr.)}$ - $Hv_{(unirr.)}$) as a function of depth. In this figure, also shows experimental result corresponding to the maximum fluence. Both dpa and ⊿ Hv decrease with the depth.

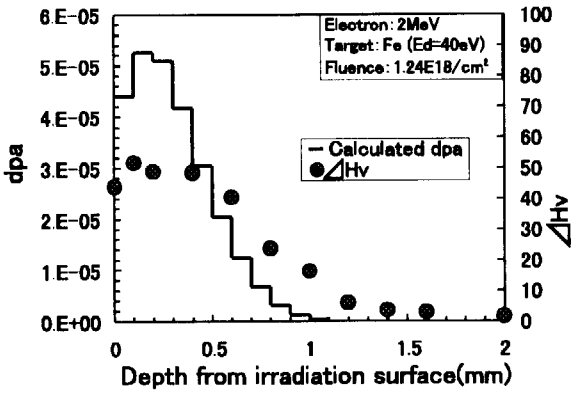

Fig.4. Distribution of dpa and ⊿Hv

3.3 Correlation between dpa and Hardening

Fig.5 shows dpa and ⊿ Hv for all specimens. Assuming 0.5 power rule dependence of ⊿Hv on dpa, an approximate correlation(shown as gray zone) is observed.

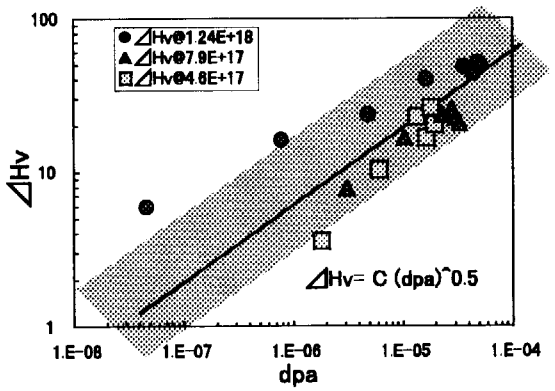

Fig.5. Correlation between dpa and ⊿Hv

3.4 Comparison with the Fast Neutron Irradiation

Fig.6 compares the irradiation hardening by electrons and fast neutrons. Materials for both irradiations are almost the same. Fast neutron irradiation was performed at the Yayoi reactor[3] and JMTR. Hardening caused by electron appears at lower dpa of approximately one-tenth than by neutron.

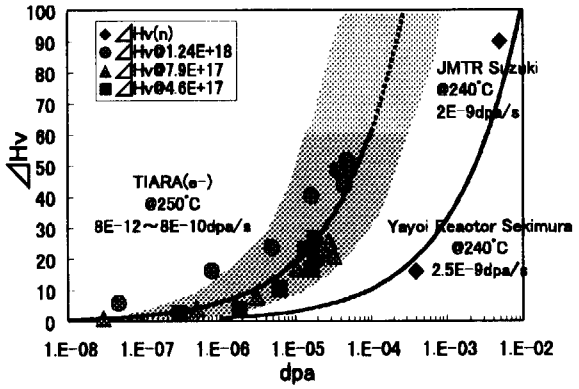

Fig.6. Comparison of hardening between electron irradiation and fast neutron irradiation.

4. Smmary

To study the irradiation effect of γ -ray, electron irradiation and hardness tests were performed.

1) Irradiation hardening caused by electron on Fe-0.6wt%Cu alloy was confirmed.
2) Hardening caused by high-energy electron appears at lower dpa than by fast neutron.

References

[1] I.Remec, J.A.Wang, F.B.K. Kam and K.Farrell, J. Nucl.Mater. 217(1994)258.

[2] W.R.Nelson, H.Hirayama, D.W.O.Rogers, "The EGS4 Code System,"SLAC-265, (1985)

[3] N.Sekimura, et al., to be published in ASTM STP.

4. 16 Positron Annihilation Study for Ion-Induced Structural Change of Semiconductors

— Damages and their influence on luminescence in rare-earth-implanted silicon related materials —

H. Arai, K. Hirata*, T. Sekiguchi**, A. Kawasuso, Y. Kobayashi*, S. Okada
Dept. of Mater. Develop., JAERI/Takasaki, NIMC*, IMR, Tohoku Univ.**

1. Introduction

Rare-earth (RE) elements in host materials show characteristic optical and magnetic properties due to their incomplete 4f electronic shell which is electrostatically shielded by outermost 5s and 5p shells from the hosts. For instance, trivalent erbium (Er^{3+}) shows sharp luminescence peaks at around 1.54 μm. This wavelength corresponds to the minimum loss of optical transmission in the silica-based optical fibers. Accordingly, Er is a promising element for applications in optoelectronics[1]. The development of RE-implanted optical materials has been extensively carried out so far.

Ion implantation is an established method in the semiconductor device processing. However, a number of lattice defects are unintentionally introduced by incident ions. The ion-implanted layer is also amorphousized depending on the ion doses and its mass. These "damages" act as non-radiative recombination centers, and degrade RE-implanted materials by decreasing their radiative efficiency. To activate RE-implanted layer optically, it is indispensable to eliminate these damages by appropriate thermal annealing. It is therefore important to research damage recovery stages and their influence on the optical properties.

Positron annihilation spectroscopy is a powerful tool to detect open-volume-type defects. Using energy variable slow positron beam, depth profile of defects near subsurface region and buried interface can be investigated[2]. In this paper, we show the damage profiles of Er-implanted Si and SiO_2/Si monitored by slow positron beam. We also show how these damages affect the luminescence properties related to Er ions through annealing experiments.

2. Experiments

Samples used in this study were floating-zone grown (FZ-) Si, Czochralski grown (CZ-) Si and SiO_2 films (500 Å thick) grown on Si substrates by thermal oxidation. These samples were implanted with 30 keV Er^+ ions up to a dose of 1.5×10^{15} Er^+/cm^2 at room temperature using the ion implanter of TIARA. The mean implantation depth of Er ions is about 210 Å. After implantation, they were annealed at 300, 600, 900 and 1200 °C for 30 minutes in a dry argon atmosphere. Then cathodoluminescence (CL) measurements were done in the temperature range from 22 K to room temperature. Doppler broadening measurements of positron annihilation gamma rays using slow positron beam were performed at room temperature.

3. Results and discussions

Figure 1 shows the most intense CL spectra measured at 22 K for each sample after an annealing at 900 °C. The observed peaks are originating from intra-4f transitions of Er^{3+}. It is found that the 1.54 μm peak intensity of the SiO_2/Si:Er sample is about two times higher than that of the CZ-Si:Er sample. The luminescence of the FZ-Si:Er sample is the weakest. Since SiO_2 is composed of Si and oxygen (O) atoms and CZ-Si contains supersaturated O atoms (about 1.0×10^{18} cm^{-3}) as compared to FZ-Si, it is inferred that O atoms play an important role for the luminescence of Er ions.

The peak intensities of the FZ and CZ-Si:Er samples were found to decrease at elevated temperatures. At room temperature, their intensities lowered by two orders of magnitude as compared to those at 22 K. On the contrary, the peak intensity

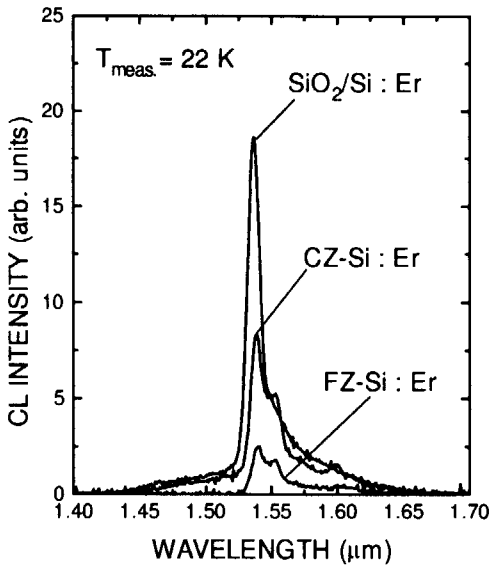

FIG. 1. CL spectra for the Er-implanted samples at 22 K (30 keV, 1.5×10^{15} Er/cm^2, annealed at 900 °C).

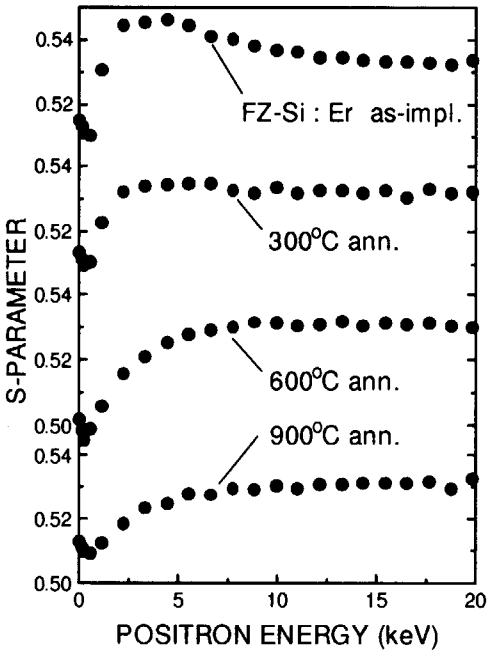

FIG. 2. Annealing behavior of S-parameter vs. positron energy curves for the FZ-Si:Er sample at room temperature.

of the SiO_2/Si:Er sample was found to decrease only 50% by changing temperature from 22 K to room temperature. This indicates that SiO_2/Si:Er holds a potential as an infrared light-emitting material.

No luminescence peak at 1.54 μm was observed from each sample after Er-implantation. After an annealing at 300 °C, the luminescence appeared and the peak intensities showed a tendency to increase at 600 and 900 °C annealing. It is suggested that damages introduced by Er-implantation act as non-radiative recombination centers and optical transitions occur accompanying by their recovery.

Figure 2 shows Doppler-broadened line-shape parameters (called S-parameters) as a function of incident positron energy for the FZ-Si:Er sample. At the as-implanted state, the S-parameters for positron energy range of 2 – 10 keV are greater than the S-values for bulk Si (> 15 keV). This indicates that open-volume-type defects are introduced by Er-implantation. These high S-values recover to that for bulk Si after an annealing at 300 °C. This suggests the recovery of point defects such as divacancies. Considering the fact that the CL peak at 1.54 μm appears after the 300 °C annealing, it is presumed that the luminescence appears with the disappearance of the point defects. The S-values at 3 – 7 keV slightly lower than the S-values for bulk Si after annealing at 600 and 900 °C. It was found that broad spectra under the CL peak at 1.54 μm decreased at 600 and 900 °C annealing. Since it is known that an amorphousized layer in Si substrate recrystallizes at about 500 – 600 °C [3], it is inferred that amorphousized layer of Er-implanted regions recovered at over 600 °C and hence the luminescence peak increased. The S-values at Er-implanted regions (0 – 1 keV) are considerably small. This implies that positrons annihilate with high-momentum core electrons of Er^{3+} and/or in a native oxide layer at the surface.

Reference

1) A. Polman, J. Appl. Phys. **82**, 1 (1997).
2) P. Asoka-Kumar, K. G. Lynn and D. O. Welch, J. Appl. Phys. **76**, 4935 (1994).
3) B. L. Crowder and F. F. Morehead, Jr., Appl. Phys. Lett., **14**, 313 (1969).

4. 17 Structural Analysis of Crystalline Materials Using Very Weak Ion Beams

Hiroshi Kudo, Kiyomitu Takada, Shunya Yamamoto*,
Kazumasa Narumi*, and Hiroshi Naramoto*
Institute of Applied Physics, University of Tsukuba
*Department of Materials Development, JAERI

1. Introduction

Ion-induced electron emission from a crystal target is strongly influenced by the periodic atomic structure along the incident paths of the ions.[1] Actually, the electron yield in the continuum spectrum reflects the high-energy shadowing effect which is the initial stage of ion channeling. The experiment using ion-induced electrons is applicable not only to metal and semiconductor targets, but also to insulator films unless the film thickness exceeds the mean penetration distance (projected range) of the ions.

The ion-induced electrons have been so far energy-analyzed mostly using electrostatic analyzers with a solid angle of acceptance less than ~10^{-2} sr. If the emitted electrons are energy-analyzed and detected over a solid angle on the order of one steradian, the high-energy shadowing effect is expected to be observed with weak ion beams or extremely low beam doses that have been impractical for backward measurements. For example, an ion beam of picoampere currents might be practically used for analysis of thin insulator films that suffer serious radiation damage due to electronic excitations in a typical ion backscattering analysis using nanoampere beams. Also, nondestructive microbeam analyses in a backward direction will be surely established. Furthermore, it is of technical interest to investigate the possibility of observing shadowing and related phenomena using a beam of secondary particles such as positrons gererated by accelerators.

Figure 1 is a schematic diagram illustrating the electron analyzer of the cylindrical mirror type developed and investigated in the present work.[2] The electrically grounded grid of the cylindrical shape (30-mm diameter) fixed inside the analyzer consists of an array of 0.2-mm-diameter Cu wires stretched ~4-mm-apart parallel to the cylinder axis. A microchannel plate (MCP) electron multiplier with a 4-mm-diameter center hole is used for detection of the energy-analyzed electrons. The incident ion beam passes through the 3-mm-diameter aluminum tube (Al thickness of 0.08mm) along the cylinder axis and incident on the target crystal. This tube and the 7-mm-diameter disk fixed at the end of the tube (the left end in Fig. 1) geometrically prevent the backscattered ions from entering the MCP.

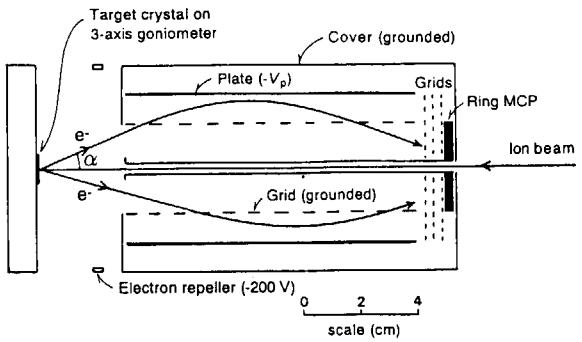

Fig. 1. Schematic diagram of the CMA.

The three parallel grids in front of the MCP are used to set the lowest measurable electron energy. Negative voltage $-V_g$ is applied to the center grid while the others are electrically

grounded. When the distance L from the entrance of the analyzer to the target crystal is 30 mm, the ion-induced electrons emitted from the crystal surface in an angular range of 7-27 degrees with respect to the cylinder axis enter the analyzer. They are then deflected towards the cylinder axis by the electrostatic field between the cylindrical grid and the coaxial cylindrical plate to which negative voltage $-V_p$ is applied. The ring-shape electron repeller (-200V) is used for accurate measurement of the ion beam current. The emission angle α with respect to the cylinder axis and the kinetic energy E of the electrons that are properly deflected and come onto the MCP can be numerically calculated by assuming the logarithmic electrostatic field in the analyzer. For a given value of α, the electron orbit in the analyzer depends on the dimensionless parameter E/eV_p, where e is the electronic charge. Examples of the electron orbits are shown in Fig. 1 for the two pairs of the parameters $(\alpha, E/eV_p)$=(24°, 5.0) and (15°, 7.0). For the setup at a distance between the target and the entrance of the spectrometer, L=30 mm, a wide angular range of approximately $8° \leq \alpha \leq 25°$ with respect to the cylinder axis, which corresponds to a solid angle of 0.53 sr, is accepted for $4.5 \leq E/eV_p \leq 6.0$. A slight change of L by 1 mm, for example, caused by the crystal tilt sensitively affects the measured electron yield only at $E/eV_p \approx 8$.

Operation and performance of the electron analyzer can be demonstrated by the measurements of the shadowing patterns obtained by tilting the target crystal, as mentioned ealier. The maximum depth contributing to the shadowing pattern is typically in the range of 10-100 nm for the present experimental conditions. Figure 2 shows the shadowing pattern around Si<100> axis for an angular range of 3°×3° (tilt angles of θ and ϕ), measured using the electrons induced by 1.5 MeV He^+. In this case, we applied V_p=0.16 kV and V_g=0.82 kV, which lead to the measured range of E/eV_p

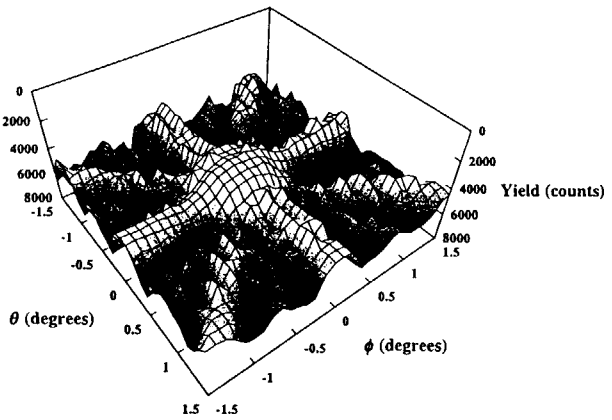

Fig. 2. Shadowing pattern around Si<100> for an angular range of 3°×3° (θ- and ϕ-tilt).

from 0.82/0.16=5.1 to 8.3 i.e., E=0.82-1.33 keV. For the beam spot size of ~0.8-mm diameter on target, the He^+ beam current was 0.45-0.50 nA which allows a count rate of ~6000 counts/s (including a negligible contribution from background signals) for random incidence conditions. The shadowing pattern consists of the electron counts for 31 × 31 pixels of tilt angle, each of which was measured for 1.0-1.3 sec corresponding to a fixed beam dose of 6.2×10^{11} He^+/cm^2 (0.5 nC on the 0.8-mm-diam spot size).

The clear shadowing pattern shown in Fig. 2 confirms the availability of the electron analyzer of the cylindrical mirror type for analysis of crystalline materials under low beam current, i.e., low beam dose conditions. In the present case, the beam dose required for practical measurement of the electron yield in the channeling case, which provides structural information near the surface (up to a depth of 10-100nm), is as low as ~10^{11} ions/cm^2. This value is extremely smaller than those at least required in typical ion backscattering spectroscopy (for example, ~10^{14} He/cm^2 for Si target) by a factor of ~10^{-3}.

References

1) H. Kudo, A. Tanabe, T. Ishihara, S. Seki, Y. Aoki, S. Yamamoto, P. Goppelt-Langer, H. Takeshita, and H. Naramoto, Nucl. Instr. and Meth, B115 (1996) 125, and references therein.
2) H. Kudo, S. Yamamoto, K. Narumi, Y. Aoki, H. Naramoto, Nucl. Instr. and Meth. B 132 (1997) 41.

4. 18 Diffuse X-ray Scattering from defect clusters in materials irradiated with electrons

Hideki Yuya, Hiroshi Maeta[1], Hideo Ohtsuka[1],
Hiroyuki Sugai[1], Haruhiko Motohashi[1], Akihiro Iwase[1],
Kohji Yamakawa[2] and Tsuneo Matsui

Department of Quantum Engineering,
Graduate School of Engineering, Nagoya University
[1]Tokai Research Establishment, JAERI/Tokai
[2]Faculty of Engineering, Ehime University

1. Introduction

Radiation defects induce diffuse X-ray scattering (DXS) around the Bragg peaks. The intensity distribution of this diffuse scattering contains detailed information on the radiation defects. The DXS technique has, therefore, become a unique field of an application for the determination of the defect structures [1].

We calculated the q-dependencies of diffuse scattering amplitude for both a single vacancy loop and a single interstitial loop with different loop radius for investigating the average size of interstitial loops in pure Ni irradiated with electrons in this study.

2. Experimental

High purity single-crystal sample of pure Ni was spark-cut from large single crystals grown by the Czochoralski method. The samples were irradiated with 2 MeV electrons up to a total dose of $3\times10^{18}e^{-}/cm^{2}$ near liquid-nitrogen temperature.

The DXS experiments were performed at room temperature at Photon Factory of National Laboratory for High Energy Physics in Tsukuba. The diffuse scattering intensities were obtained by taking a difference between the intensity from an irradiated and that from a non-irradiated region of the same sample.

3. Theory

The intensity of diffuse X-ray scattering from dislocation loops is given by the following equation

$$I_{diffuse} = N_D (r_e f_a)^2 |A(K)|^2, \qquad (1)$$

where N_D is the concentration of dislocation loops, r_e the classical electron radius, f_a the atomic scattering factor, K the scattering vector and $A(K)$ the scattering amplitude associated with a dislocation loop. In this expression, $A(K)$ is written as follows [2] ;

$$|A(K)| = \left| \sum_m e^{iKr_m} (e^{iKs_m} - 1) \pm \sum_n e^{iK(r_n + s_n)} \right| . \qquad (2)$$

The first term in Eq.(2) describes the sum of diffuse scattering amplitudes from the m-th lattice atom displaced from its ideal position r_m by s_m due to the presence of the dislocation loops. The second term

represents the sum of the scattering amplitudes from the n-th additional or missing atom, which defines a lattice defect. The scattering vector K is given by the sum of the reciprocal lattice vector h and the vector q relative to h, ($K = h + q$).

4. Numerical calculations

For the calculation of the terms in Eq.(2) the displacement field of lattice atoms around a loop has to be evaluated numerically. The calculation of the displacement field was carried out using a formula reported by Ohr [3]. The result of the theoretical diffuse scattering amplitude calculated by Eq.(2) from an interstitial loop with radius R=10Å in Al is shown in Fig.1. The result of the calculation is in good agreement with that of other researchers [2].

5. Results and Discussion

The size distribution of the dislocation loops in pure Ni irradiated with electrons could be obtained by assuming the coexistence of the several dislocation loops with different radii and fitting the calculated q-dependence for Ni to the experimental data. The size of loops was 5-60Å in pure Ni. The result of the fitting, that is given by the dashed lines is shown in Figs.2 in comparison with the experimental data points.

The result of fitting showed that the major defects in electron irradiated pure Ni was interstitial loops. The average size of interstitial loop was about 12Å and the concentration of interstitials was estimated to be about 9 ppm. The fact that the major defects was interstitial loops was thought to be originated from the difference of the mobility between interstitials and vacancies.

References

1) P.Ehrhart, J. Nucl. Mater. **216** (1994) 170.

2) P.Ehrhart, H.Trinkaus and B. C. Larson, Phys. Rev. B **25** (1982) 834.

3) S.M.Ohr, Phys. Status. Solidi B **64** (1974) 317.

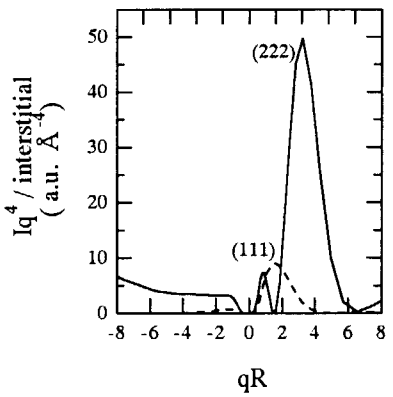

Fig.1. Scattering amplitude for an interstitial loop (R=10Å) in Al.

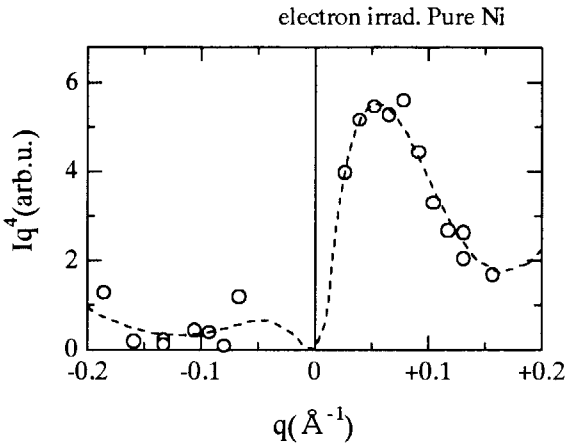

Fig.2. Diffuse scattering intensity obtained experimentally from Ni with the dashed line fitted to the data.

4. 19 Chemical Effect on X-ray Spectra Induced by Multiple Inner-shell Ionization (I)

T. Inoue, A. Uesugi, T. Igarashi, N. Terazawa, K. Kawatsura, Y. Aoki*, S. Yamamoto*, K. Narumi* and H. Naramoto*

Faculty of Engineering and Design, Kyoto Institute of Technology,
*Department of Materials Development, JAERI/Takasaki

1. Introduction

X-ray emission spectroscopy by excitation of X rays and electrons has shown wide applications from analytical and physical chemistry, materials science, and atomic, molecular and solid state physics[1]. It is well known that X-ray transitions including valence electrons of atoms, molecules and condensed matters cause large chemical binding effects. Moreover, X-ray emission spectra induced by heavy ion impacts have shown a large effect to produce multiple inner-shell ionization due to strong coulomb interactions between heavy projectile ions and target atoms or molecules. For heavy ion impacts on transition metals, it is found that the L X-ray spectra show broadening to the lower energy side and more complicated structures at the high-energy side of the $L\alpha_{1,2}$ and $L\beta_1$ lines.[2,3]

In this paper we report excitation and deexcitation processes of inner-shell electrons in a Cu metal target and chemical bonding effects from chemical shift and shape variation of high resolution Cu L X-ray spectra induced by 0.075 to 0.75 MeV/u C, F, and Si ion impacts.[4] The experiment using metal oxides targets is now in progress.

2. Experimentals

The experiments were performed at the TIARA accelerator facility of JAERI, Takasaki using a 3 MV tandem accelerator. A heavy ion beam has been irradiated on a Cu solid target. Emitted Cu L X rays have been measured by using an X-ray crystal spectrometer at the MD1 beam line. The analyzing crystal was a flat RbAP single crystal. The X-ray detector used was a gas flow-type proportional counter with an entrance window of a 1.0 μn thickness polyester film.

3. Results

Figure 1 shows high resolution Cu L X-ray spectra produced by 0.75 MeV/u C and F, and 0.64 MeV/u Si ion impacts with 1.0 MeV/u H ion impact as a reference. It is found that the relative intensity, $L\beta_1/L\alpha_{1,2}$ for F ion impact is larger than that for C ion impact, and that for Si ion impact is the highest one. It is also found that the peak energies of $L\iota$ and $L\eta$ transitions, and that for the $L\beta_{3,4}$ transition shift to the higher energies with an increase of

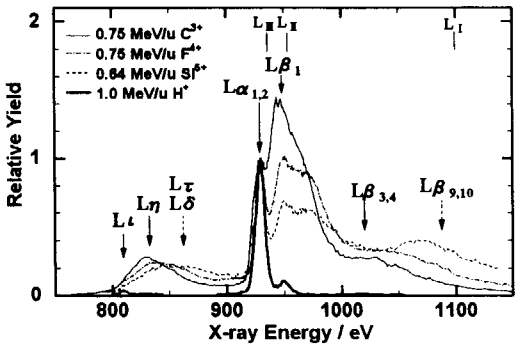

Fig.1 Cu LX-ray spectra produced by high energy ion impact

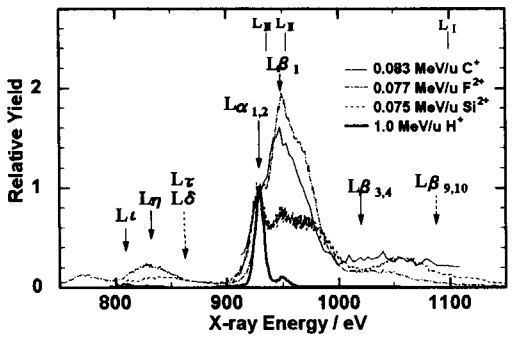

Fig.2 Cu LX-ray spectra produced by low energy ion impact

projectile Z.

Figure 2 shows high resolution Cu L X-ray spectra produced by 0.083 MeV/u C, 0.077 MeV/u F, and 0.075 MeV/u Si ion impacts with 1.0 MeV/u H ion impact as a reference. The relative intensity, $L\beta_1/L\alpha_{1,2}$ for 0.077 MeV/u F ion impact is larger than those for C and Si ion impacts, and that for Si ion impact is the lowest one. It is not found that an energy shift of $L\iota$ and $L\eta$ X-ray region, and the $L\beta_{3,4}$ line. For 0.077 MeV/u F ion impact, a broad band is found at 770 eV but not for 0.75 MeV/u F ions .

4. Discussion

The broad band structures on Cu L X-ray spectra induced by C, F, and Si ion impact are attributed to satellite and hypersatellite lines due to multiple inner-shell electron excitation/ionization induced by heavy ion impacts. This is shown from the calculated results using HFS method.[4,5] It is also shown that for high energy ion impacts, the L-shell excitation/ionization processes are caused by the direct Coulomb interactions from the calculations using the ECPSSR theory.

References

1) A. Meisel *et al*, X-Ray Spectra and Chemical Binding (Springer-Verlag, Berlin, 1989)

2) H. Kageyama *et al.*, I. J. PIXE, 5 (1995) 203.

3) H. Kageyama *et al.*, Nucl. Instr. and Meth. Phys. Res., B107 (1996) 47.

4) K. Kawatsura *et al.*, I. J. PIXE, 7(1997) in press.

5) F. Herman and S. Skillman, "Atomic Structure Calculations" (Prentice Hall, Englewood Cliffs, NJ, 1963).

4. 20 Surface Modification of Corrosion Resistant Materials by Ion Implantation

J.Saito, K.Hayashi, S.Kano, N.Kasai*, H.Kudo* and Y.Morita*

Frontier Technology Section, PNC / OEC,
* Dep. of Mater. Develp., JAERI / Takasaki

1. Introduction

The structural materials for a fast breeder reactor are used in severe environment such as high temperature, neutron irradiation and liquid sodium. It is demanded for high thermal efficiency and high security for safety of nuclear energy plants to develop the new structural materials possessing excellent material properties.

A surface modification technique using an ion implantation is one of beneficial method to create new materials. Ion implantation can dramatically transform several material properties, increasing the hardness and wear resistance or improving the corrosion or oxidation resistance of the surface[1].

In order to improve the material properties, especially corrosion resistance in liquid Na, the material development has been carried out using the ion implantation[2)3)]. The purpose in this study is to form MgO layer as a protective layer on the top of the material surface utilizing the ion implantation. It was reported in previous investigation that MgO which was one of advanced ceramics showed higher corrosion resistance against liquid Na[4)5)].

2. Experimental

Three kinds of substrates, SUS316FR, Mod. 9Cr-1Mo steel and Nb-1mass%Zr, were prepared as substrates. The specimen size was 20mm×6mm rectangle and 2mm thickness. One side of each specimen was polished to make a mirror surface. They were implanted with Mg ions up to a dose of either 3×10^{17}Mg/cm^2 or 6×10^{17}Mg/cm^2 at the energy of 150keV under high vacuum of 10^{-5} Pa at room temperature. Subsequent to the implantation, the heat treatment was carried out at various temperature (473K, 673K or 873K) for 7.2ks in air to forward the forming MgO layer. Furthermore in order to form MgO layer without the heat treatment, oxygen ions at the energy of 120keV were implanted after Mg implantation. The depth profiles of some of specimens was measured using the secondary ion mass analysis (SIMS) and the X-ray photoemission spectroscopy (XPS) to clarify the formation of MgO layer.

3. Result and Discussion

The SIMS depth profiles of Mg, O, Fe and Cr in the implanted SUS316FR are shown in Fig.1 for (a) 6×10^{17}Mg/cm^2, (b) 3×10^{17}Mg/cm^2 and (c) 6×10^{17}Mg/cm^2 with heat treatment at 673K for 7.2ks. They show that the implanted element was successfully doped in the surface layer.

In figure(a), there was a large peak of Mg concentration and its top was located at the near-surface region. It was higher than either Fe or Cr concentration which were ones of constitutional elements of substrate. And it decreased gradually toward inside of specimen. It was interesting that similar trace of profile was observed in oxygen concentration. For the result of XPS narrow scanning spectra, Mg 1s spectrum was shifted between the ionic and metallic states at the

near-surface region. On the contrary, the chemical shift of O 1s spectrum which was due to MgO was observed to 70nm in depth from the surface. These results indicated that some of implanted Mg atoms reacted with oxygen atoms in the near-surface region, and then they might be formed MgO compound. However, implanted Mg atoms which were in the deeper region exsisted as solute metallic elements.

In figure(b), there was a narrow peak of Mg concentration in 3×10^{17}Mg/cm^2 implanted SUS316FR at the near-surface region. By comparing figure (a), there was a remarkable decrease of Mg concentration. Also, the oxygen concentration was high at even the near-surface layer. The difference of depth of Mg concentration between 3×10^{17}Mg/cm^2 and 6×10^{17}Mg/cm^2 implanted SUS316FRs was caused by a dose of implantation. For the result of XPS, the chemical shift of O 1s spectrum which was due to MgO was also observed certainly to 30nm in depth. Thus it was evident that MgO was formed, however the implanted Mg atoms were transferred from the ionic state to the metallic state in the deeper region, as was similar to the 6×10^{17}Mg/cm^2 impalnted one.

Figure(c) shows the SIMS depth profiles of Mg, O, Fe and Cr in the implanted SUS316FR for 3×10^{17}Mg/cm^2 with heat treatment. It was clear from this figure that Mg concentration at the near-surface region decreased exactly and the peak of that was shifted to about 100nm in depth from the surface. On the contrary, Fe, Cr and O concentration showed the sharp peak, hence their concentration became higher than Mg

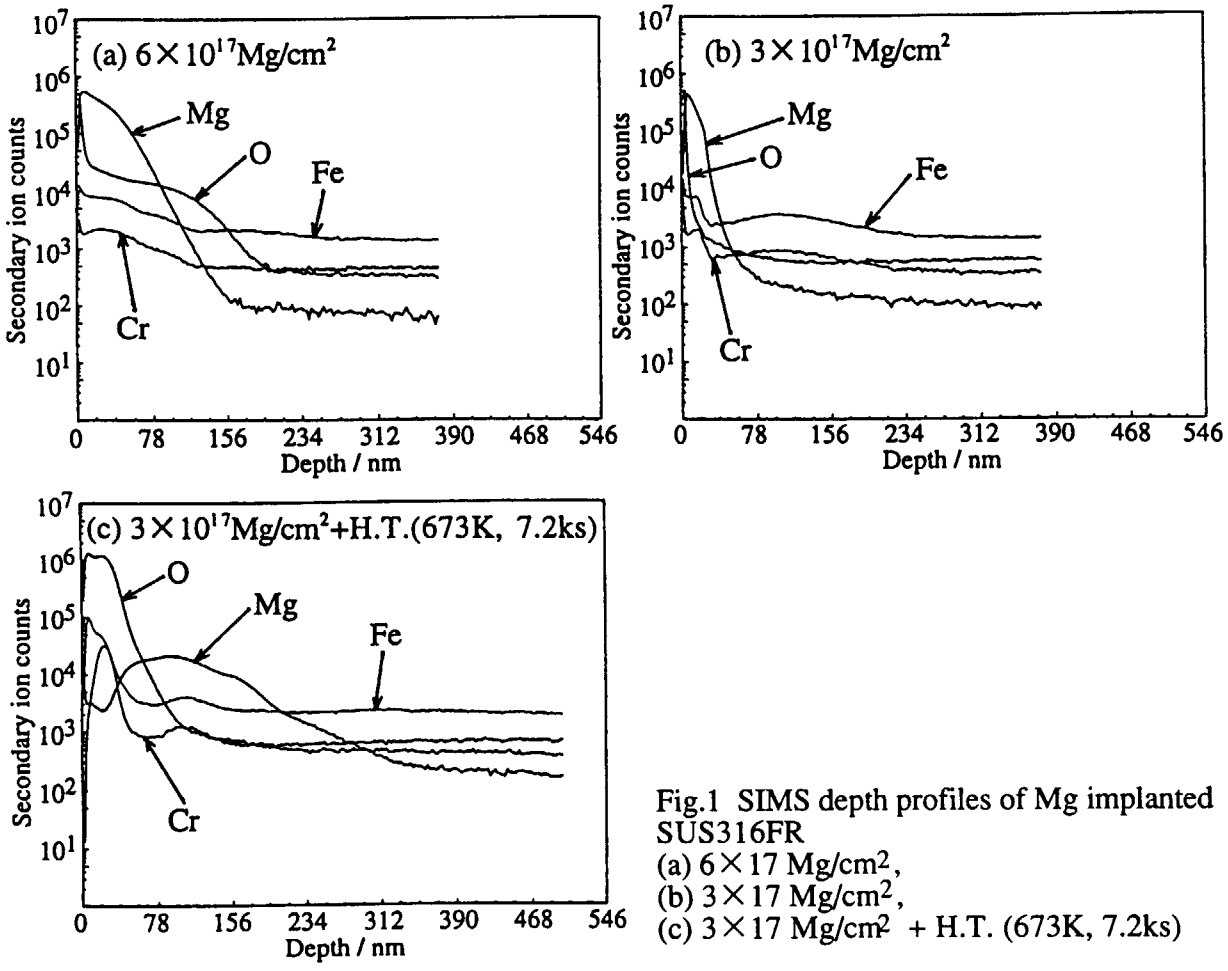

Fig.1 SIMS depth profiles of Mg implanted SUS316FR
(a) 6×17 Mg/cm^2,
(b) 3×17 Mg/cm^2,
(c) 3×17 Mg/cm^2 + H.T. (673K, 7.2ks)

concentration at the near-suface region. O 1s spectra which were due to Fe_2O_3 and Cr_2O_3 were observed by XPS. Therefore, the formed MgO by implantation was decomposed by heat treatment and oxygen atoms were reacted with Fe and Cr, and then Fe_2O_3 and Cr_2O_3 were formed at the near-surface region. According to the Fe-Mg binary phase diagram[6], although Mg has no solubility against fcc-Fe, it was diffused deeply toward inside of specimen from the surface. The redistribution of implanted Mg did not occur at the near-suface region.

The specimens which were carried out the heat treatment at other temperatures and were implanted Mg and O ions are analyzed now. Also, the corrosion test will be performed in liquid Na at 923K for 3.6Ms. The corrosion resistance of Mg implanted materials will be evaluated on the basis of those results.

References

1) S.T.Picraux and P.S.Peercy, MRS Bulletin, Feb. (1987), 22.
2) J.Saito et al.: JAERI TIARA Ann. Rep., 5(1996) 135.
3) K.Hayashi et al.: JAERI TIARA Ann. Rep., 6(1997) 139.
4) L.A.Lay, Corrosion Resistance of Technical Ceramics, (1985)
5) Y.Tachi, Ceramics, 30 (1995) 989.
6) Binary Phase Diagrams, 2nd Edition : ed. by Massaski (ASM international) 1990.

4. 21 Selectively Knocked-on Hydrogen Atoms in Pd-H Alloys and Their Diffusivity

K. Yamakawa, Y. Chimi*, A. Iwase*, H. Maeta* and N. Ishikawa*

Ehime University, *JAERI/Tokai

1. Introduction

Various properties such as electrical resistivity and specific heat of Pd-H(D) alloys show an anomaly at around 50K. It is disclosed that this anomaly is caused by ordering of hydrogen isotopes by neutron scattering[1]. The electrical resistivity of the alloy increases with the hydrogen ordering and decreases with hydrogen disordering[2,3].

In the present work, the diffusivity of hydrogen in Pd has been studied by the measurement of an electrical resistance change by the ordering during the annealing around 50K.

2. Experimental

Before charging hydrogen, pure Pd specimens were annealed in vacuum for 5h at 1070K. Charging of hydrogen was done by electrolysis in 0.1N H_2SO_4 in H_2O. Both hydrogen charged specimen and no charged(pure Pd) specimen were mounted at the same time on a specimen holder in the electron-irradiation equipment of JAERI/Takasaki. To obtain the same ordering state of hydrogen, the specimen was cooled down with constant cooling rate, 0.1K/min to 20K from 80K. Then 0.5MeV electrons were irradiated. The fluence was determined to obtain the same resistance decrease due to the disordering of hydrogen for the Pd-H alloy. The irradiation temperature was always below 30K. After the irradiation, the specimens were heated with constant heating rate. These procedures were repeated for few times with different heating rates for the same specimen.

3. Results

A part of ordered hydrogen atoms in interstitial sites (O sites) of FCC lattice are selectively knocked out from the occupied positions by 0.5MeV electron irradiation due to the large mass difference of a hydrogen atom and palladium atom. The resistivity of Pd-H alloy decreased by 3×10^{-10} Ω m with fluence of 2.6×10^{12}e/m^2 of the electron irradiation but the resistivity of pure Pd did not changed. The irradiated specimens were annealed with

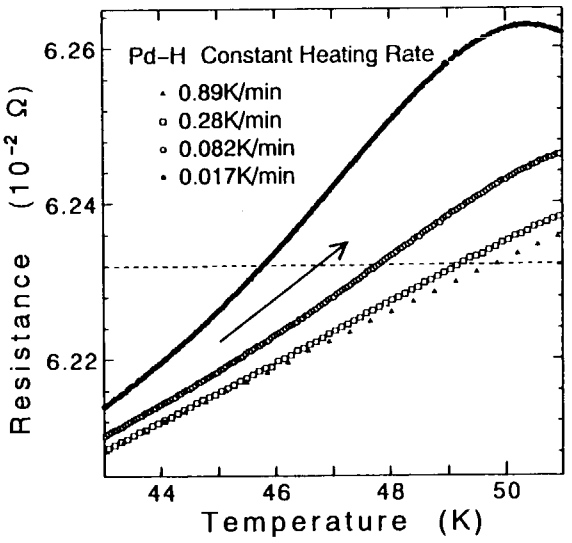

Fig.1 Apparent annealing curves for Pd-H alloy for various heating rates. The resistance was measured at the temperature.

constant heating rates. The annealing curves are shown in Fig.1. The resistance are measured at the temperatures. Therefore the resistance contain the part of resistance increase due to temperature increase and due to hydrogen ordering. The curves shift to lower temperature with decrease of heating rate α. From the shifts the migration energy of hydrogen should be derived generally but in this case the situation differs from usual one. On the cooling rate of 0.1K/min to order hydrogen atoms, the ordering is not perfect. Disordered hydrogen atoms already exist before the electron irradiation. The hydrogen atoms disordered by the irradiation order during the annealing and simultaneously the hydrogen atoms disordered before the irradiation also order. Furthermore, even if the specimen is annealed from the same ordering state,

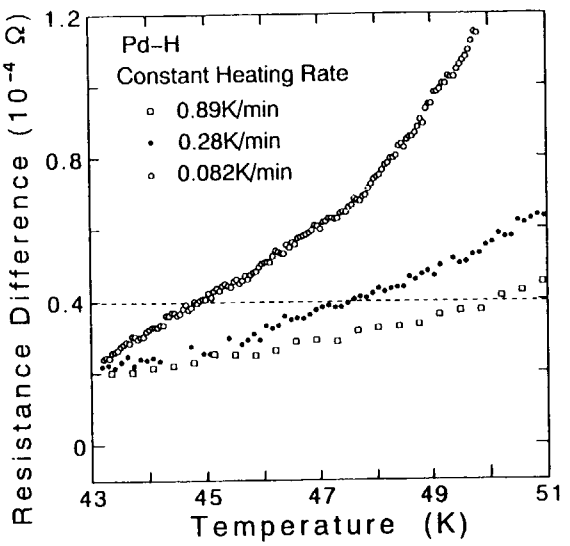

Fig.2 Annealing curves of hydrogen atoms disordered by the irradiation.

the amount of ordered atoms depends on the heating rate. Therefore, it is needed that the amount of ordering of hydrogen atoms disordered by the irradiation is estimated. The amount is obtained from the difference between the resistance of irradiated specimen and the resistance of unirradiated specimen for the same heating rate and the same specimen. The resulting curves are shown in Fig.2. The temperature T to obtain the same amount of ordering(in this case 0.4×10^{-4} Ω) is obtained for each heating rate α. The values are plotted in Fig.3 together with the results of fast cooled specimens. (Disordered hydrogen atoms also obtained by fast cooling from high temperatures.)

The slope of the line is the migration energy of hydrogen atom. The value of the energy is similar for the irradiated and fast cooled case.

References

1.O. Blaschko, P. Fratzl and R. Klemencic, Phys. Rev. B24(1981)277.

2.K. Yamakawa, H. Maeta and Y. Shimomura, Scripta Met. Mater. 25(1991)1129.

3. K. Yamakawa, H. Maeta, Def. Diff. Forum, 95-98(1993)311.

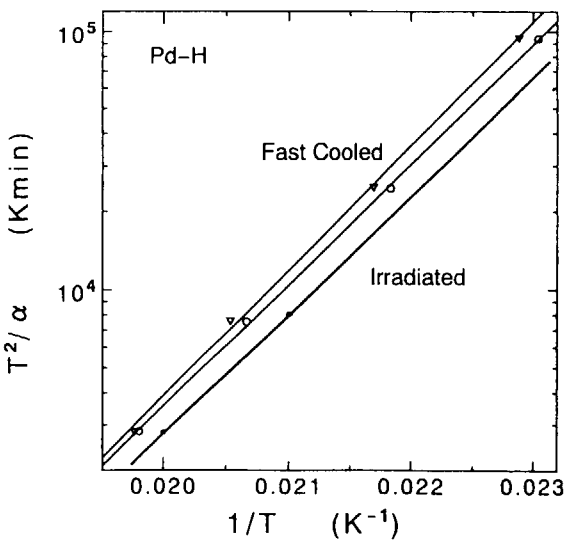

Fig.3 Arrhenius plot for constant heating rate. α: heating rate.

4. 22 Ion Implantation and Annealing of Crystalline Oxides

K. Takahiro, S. Nagata, A. Kunimatsu, S. Yamaguchi,
S. Yamamoto*, Y. Aoki* and H. Naramoto*

Institute for Materials Research, Tohoku University
*Dept. of Mater. Develop., JAERI/Takasaki

1. Introduction

It is necessary to develop new technologies to realize new micro-optics components such as diffractive components or integrated optics circuits. Ion implantation presents many advantages in contrast to other techniques because the implanted dose and the depth of implantation can be well controlled. In a dielectric, ion implantation induce changes in optical absorption and refractive index. The dielectric containing nano sized metal particles such as gold, silver and copper exhibit not only the optical absorption, but also the third-order optical nonlinearity. The optical absorption depends on particle size, surrounding medium as well as particle shape and spatial distribution.

In the present work, we will examine the response of several crystalline oxides to ion implantation and subsequent thermal annealing. We have studied ion-induced defects and optical absorption change in MgO, $SrTiO_3$ and $LiNbO_3$ crystals from Ag^+ and Au^+ implantations, and the effects associated with thermal annealing. The characteristics of the Ag^+ and Au^+ implanted crystals were studied using ion scattering/channeling techniques and optical absorption.

2. Experimentals

Single crystals of MgO, $LiNbO_3$ and $LiNbO_3$ were implanted with Ag (350 keV) and Au (550 keV) to doses from 1×10^{15} to $4 \times 10^{17}/cm^2$ at room temperature. MgO and $SrTiO_3$ have cubic NaCl type and perovskite type structure, respectively, and {100} face was used. $LiNbO_3$ has a hexagonal structure and y- and z-oriented faces were used. Following implantation, these crystals were annealed in vacuum at temperatures in the range of 300 - 873 K for time periods ranging from 1 h to several days.

Crystals were examined in the as-implanted state and after thermal annealing using 2- 3.6 MeV He^+ Rutherford backscattering (RBS) and channeling techniques. The absorption spectrum was measured in the visible range.

3. Results and discussion

A. Implantation and annealing of MgO

After Au^+ implantation, the surface of MgO was changed to light brown and its color grew richer with increasing dose. A broad absorption peak is observed around 560 nm.

Fig. 1 shows [100]-aligned RBS spectra for the as-implanted state and the after thermal annealing (873 K/1h) state. In addition, the random spectrum of an unimplanted sample is also given. Aligned yield for the implanted Au atoms decrease a little compared with the scattering yield in the random spectrum, suggesting that a small amount of the implanted Au is substitutional in the lattice. After annealing, the aligned yield from the implanted region, which increases due to direct scattering and dechanneling of the probing beam at the irradiation induced damage, is almost un-

changed. This indicate that the irradiation induced defects in MgO are not recover by annealing at 873 K.

B. Implantation and annealing of $SrTiO_3$

After Au^+ implantation, the surface of $SrTiO_3$ was changed to reddish brown. A broad absorption peak is observed around 590 nm.

Fig. 2 shows [100]-aligned RBS spectra for the as-implanted state and the after annealing state. The random spectrum of virgin sample is also shown in this figure. Aligned yield in the implanted region reaches the random value in the Sr sublattice and the step in the aligned yield from the Ti sublattice is equivalent to the increase in the random spectrum at the energy corresponding to the Ti leading edge. This result shows that the implantation of Au at dose of $3 \times 10^{16}/cm^2$ turns the near-surface region amorphous. The depth of the amorphous region is about 280 nm. After annealing, the aligned yield from the implanted region is greatly reduced demonstrating that the amorphous layer was crystallized by annealing and that the recrystallized region is epitaxial with the underlying substrate. On the other hand, the implanted Au profile was unchanged by the annealing at 873 K for 1 hour.

C. Implantation and annealing of $LiNbO_3$

After Au^+ implantation, the surface of $LiNbO_3$ was changed to dark brown. A broad absorption peak is observed around 560 nm.

Fig. 3 shows the y-axis aligned RBS spectra for the as-implanted state and the after annealing state. Aligned yield in the implanted region reaches the random value in Nb sublattice, indicating that the near-surface region turned to amorphous. After annealing, the near-surface region of the aligned spectrum appears to be still amorphous, but the annealing treatment has caused the amorphous /crystal interface to advance toward the surface. These results suggest the type of layer-by-layer crystallization that is expected when the regrowth occurs by solid-phase epitaxy. The depth profile of the implanted Au atoms, however was unchanged by the annealing.

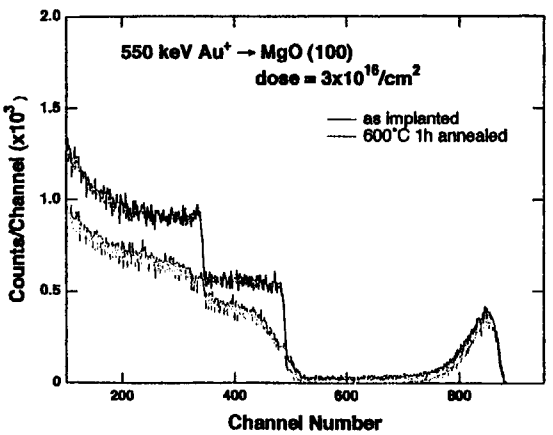

Fig. 1 RBS spectra of the as-implanted and the after annealing (873 K/ 1 h) MgO samples.

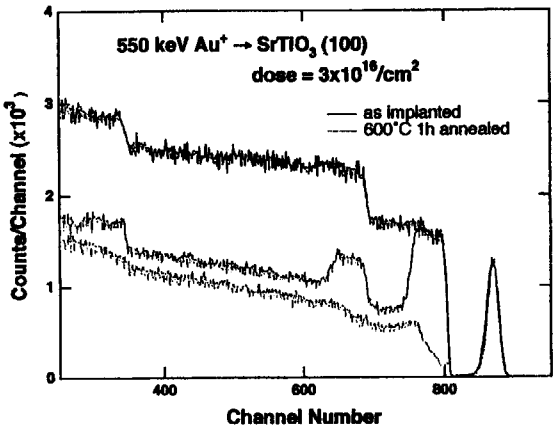

Fig. 2 RBS spectra of the as-implanted and the after annealing (873 K/1h) $SrTiO_3$ samples.

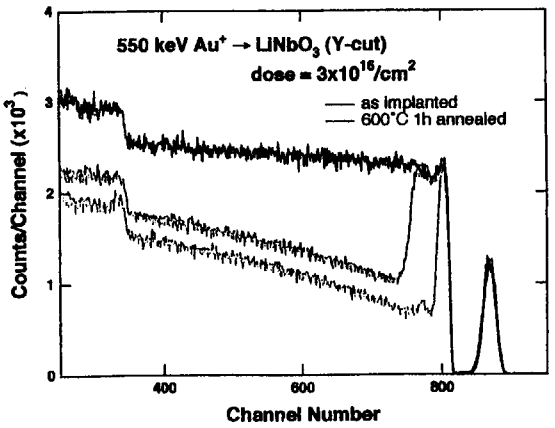

Fig. 3 RBS spectra of the as-implanted and the after annealing (873 K/1h) $LiNbO_3$ samples.

4. 23 Formation and stability of metallic silicides during ion-beam mixing

S.Ohnuki, T.Suda, M.Takeda, F.Arimoto,
H.Abe* and H.Naramoto*
Faculty of Engineering, Hokkaido University
*Department of Materials Development, JAERI

1. Introduction

Metallic silicides using as electrode materials of LSI devices are compounds consisting of silicon and metals. The LSI process is due to thermal and chemical process, however, a low temperature process has been required. The objective of this study is applying ion-beam mixing for the silicide formation at low temperature. This method is a mixing process using kinetics energy of incidence particles, which consists of two effects, radiation-enhanced diffusion and recoil-mixing. In the former case, the diffusion is enhanced by the large amount of irradiation defects. In the latter case, the direct atomic motion due to incident ion and knock-on atom produce a recoil-mixing, which shows no temperature dependence. Those two processes occur at the same time, and are complex phenomena in usual condition. In this study, the effects of metal species, ion fluence, and temperature on the silicide formation are examined and the interdiffusion coefficient is estimated.

2. Experimentals

Si wafer with (100) was used for the experiment following Mo or Ti vapor deposition with thickness of 60 or 70nm, respectively. Si^+ ion irradiation of 1MeV was carried out at TIARA facility, JAERI Takasaki. The ion flux was 0.9~1.6 μ A/cm^2, and the temperature was at several level between room temperature and 200℃. The maximum fluence was 6×10^{16}/cm^2. After irradiation, TEM specimens were prepared by a cross-cut method. The cross sectional observation was performed by 200kV TEM. The depth distribution of elements was analyzed by EDS attached with TEM.

3. Results

Composition of mixing layer:

In the case of Mo/Si irradiated at high temperature to high dose (200℃ and 3×10^{16}/cm^2), the mixing layer was crystalline phase ($MoSi_2$). After the irradiation at low temperature (RT to 6×10^{16}/cm^2), the layer was composed of amorphous and crystalline ($MoSi_2$). At lower doses, the mixing layer was only amorphous. The width of the layer increased with temperature and dose in general. In the case of Ti/Si, the mixing layer was only amorphous at all of the irradiation condition. The width of mixing layer was increased with increasing temperature and dose, however, the surface sputtering can be confirmed at some condition (150℃ and 200℃). The Si substrates of both Mo/Si and Ti/Si turned to amorphous at low temperature, and stayed in crystalline with dislocation loops and lines at high temperatures.

Compositional changing due to mixing:

Fig.1 shows compositional profiles for each irradiation conditions. A high level of Si can be expressed in the Mo layer, however, this included large error come from the analysis for thin areas. The concentration profiles between deposited and substrate layers were steep before the irradiation, and the profile changed to smooth with increasing temperature and dose. The phenomena indicated the progressing of mixing due to the irradiation.

Estimation of interdiffusion coefficient:

The temperature dependence of interdiffusion coefficient estimated by finite difference method is shown in Fig.2. The both Mo/Si and Ti/Si shows slightly temperature dependence at higher temperature side, which means that the diffusion was enhanced in comparison with thermal diffusion. However, the interdiffusion coefficient recognizing crystalline $MoSi_2$ at 200℃ stayed and deviated from extrapolated line. This phenomena imply that the diffusion coefficient of amorphous layer (Da) is larger than that of crystal layer formation (Dc).

4. Discussion

Structural change by ion-beam mixing:

In the experimental results, the formation process of mixing layer should include two stages; from crystal to amorphous and its re-crystallization (Fig.3). The first stage can be caused by the atomic mixing by recoil-mixture and the radiation-enhanced diffusion where both produce amorphization. In this case, amorphous

region has the composition close to crystalline compound [1]. In the second stage, it is suggested that a critical level of the irradiation dose and temperature should be exist for giving driving force of re-crystallization, because the nucleation and growth of re-crystallization can start from composition of $MoSi_2$ in amorphous region. For determination of nucleation site, a high-resolution electron microscopy will be carried out in near future.

Stability of crystal phase :

There is phenomenological reasons for the formation of amorphous; features in phase diagram, melting point and crystal structure. In generally, the system existing liquid-phase until more low temperature in phase diagram was known to do easily amorphization [2]. The slope of liquidus line of Mo/Si system is steep comparing with Ti/Si system, which means that Mo/Si system has a tendency of forming amorphous easily. In the case of radiation-induced amorphization was progressed and the composition was closed to intermetallic compound, amorphization depends on a tendency of forming amorphous of intermetallic compound. In the case of difference in melting point, $MoSi_2$ and $TiSi_2$ are 1900℃ and 1330℃, respectively. Consequently, it can be estimated that amorphous of $TiSi_2$ is more stable than $MoSi_2$ at experimental temperature, which is corresponding with experimental results. The crystal structures of $MoSi_2$ and $TiSi_2$ are I4/mmm and Fddd, respectively. $TiSi_2$ has more complex structure than $MoSi_2$. From these results it can be suggested that the melting point and crystal structure are predominate for the stability of mixing layer formed by ion-mixing.

5. Summary

Si ion irradiation of 1MeV for Mo/Si and Ti/Si was performed. The changings of microstructures and local concentration were observed, and the interdiffusion coefficient was evaluated. In Mo/Si, the crystalline mixed later was formed at either high fluence or high temperature. In Ti/Si, the amorphous mixed layer was formed at all irradiation condition. The interdiffusion coefficient for both system was in the order of 10^{-16} ~ $10^{-15}cm^2/sec$ and indicated a slightly temperature dependence.

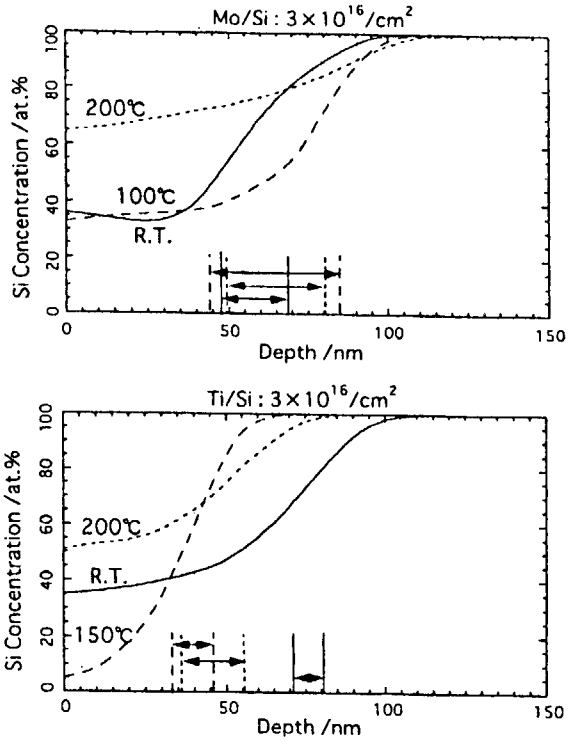

Fig.1 Si concentration profile by EDS.

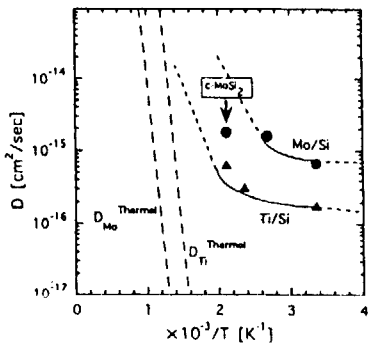

Fig.2 Temperature dependence of interdiffusion coefficient.

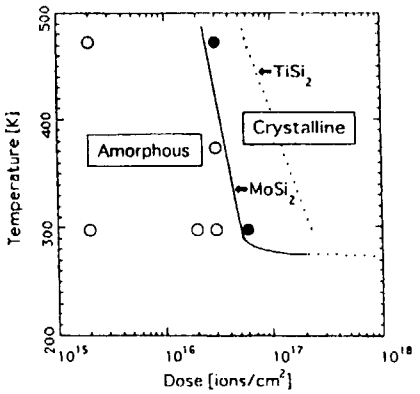

Fig.3 Phase/Dose/Temperature diagram.

Reference

[1]J.W.Mayer et al., Nuclear Instruments and Methods 182/183 (1981) 1-3

[2]K.Kimura, A master's thesis at Hokkaido University (1988)

5. Materials Analysis

This is a blank page.

5. 1 Characterization of epitaxial Cu/Nb multilayer with RBS/channeling

S. Yamamoto, K. Narumi, A. Miyashita, Y. Aoki, H. Naramoto

Dept. of Materials Development, JAERI

1. Introduction

The growth of high-quality single-crystalline Nb films has attracted much interest from the view points of basic science and applications, and systematic studies have been made on the orientation relationship and also the interface structure between Nb and other substance. In the present study, the efforts are described to prepare the epitaxially grown multilayer structure. It is demonstrated that the hetero-epitaxial multilayers composed of Nb and Cu on α-Al_2O_3 substrates with different orientations are realized with the good crystal quality by controlling the substrate temperatures under UHV condition.

2. Experiment

Cu/Nb multilayers were deposited on $(11\bar{2}0)$, $(1\bar{1}02)$, (0001) α-Al_2O_3 substrates using an MBE chamber equipped with four electron-beam guns. Each of α-Al_2O_3 substrates (10×10 mm) was annealed at 1450 °C for 12 hours in air to eliminate the strain induced during polishing. Nb(99.95%) and Cu(99.9999%) pellets were used for evaporation sources. The thickness of each layer was monitored with quartz oscillators, which were calibrated with Rutherford backscattering spectroscopy (RBS). The Nb and Cu layers were deposited at the rate of about 0.2 nm/s onto the α-Al_2O_3 substrate kept at 750 °C for Nb and less than 200 °C for Cu. The typical thicknesses of Nb and Cu layers were in the range of 50 nm to 260 nm, respectively.

The multilayer samples were analyzed with RBS/channeling using 3 MV single stage accelerator in JAERI/Takasaki. The analyzing beams of $^4He^+$ ions with the broad energy range (1.5 - 2.7 MeV) were incident by considering the enough energy mass separation between Cu and Nb layer in RBS spectra. Backscattered particles were detected by standard surface barrier detectors (SSD) at 110° to 165° to the incident beam. The exact orientation relationship among Cu, Nb layers and α-Al_2O_3 substrate was obtained through the mapping of planar channeling points at each layer of Nb, Cu and α-Al_2O_3. XRD was also employed to determine the orientation relationship between Cu and Nb layer.

3. Results and discussion

Fig. 1 illustrates the RBS/channeling results of 2.7 MeV ^4He ions in Cu/Nb on α-$Al_2O_3(11\bar{2}0)$ substrate with the thicknesses of 64.7 nm and 51.8 nm for Cu and Nb layers, respectively. The substrate temperature was kept at 750 °C for the Nb layer growth on α-Al_2O_3 and was then changed into 200°C for the further Cu layer growth. By using rather higher energy ions (2.7 MeV $^4He^+$), the mass-resolution in the spectra has become good enough to judge the interface sharpness. χ_{min} in Nb and Cu layers are 0.13 and 0.23, respectively. Several samples with different thicknesses of Cu layers on Nb were prepared under the same condition. The RBS/channeling

analysis of these samples revealed a tendency that the crystal quality is improved with the increase of Cu layer thickness. In the 260 nm thick Cu layer on Nb(110)/α-Al_2O_3(11$\bar{2}$0), χ_{min} of the Cu layer specified at the depth (~20 nm) just behind the surface peak is 0.075 which is almost the same level as in a bulk Cu single crystal.

The crystal growth feature of Cu layers on other Nb single-crystalline layers are different from the above. The Cu single-crystalline layer on Nb(001)/α-Al_2O_3(1$\bar{1}$02) was grown only around RT. At the temperature higher than 200 °C there appeared the columnar structure different from Cu(111) growth on Nb(110)/α-Al_2O_3(11$\bar{2}$0). As the last case, the Cu deposition was made on Nb(111)/ α-Al_2O_3(0001) and the non-columnar structure was realized only around RT but any channeling phenomena were not observed. XRD analysis shows the textured Cu(111) growth on Nb(111) layer.

The third layer deposition of Nb was tried on Cu/Nb/α-Al_2O_3(11$\bar{2}$0) substrate with the same thickness of 50 nm. In this series of deposition, the substrate temperature was kept at 750 °C for the first Nb layer on α-Al_2O_3 substrate, 200 °C for the second Cu layer and 500 °C for the top (third) Nb layer during the deposition. The results of RBS/channeling measurements are shown in Fig. 2. The crystallographic axes close to the surface normal in Cu and Nb layers are parallel to the α-Al_2O_3<11$\bar{2}$0> crystallographic axis. The Nb(110) single-crystalline growth was confirmed for the top Nb layer through the angular mapping of planar channeling around the major axis. χ_{min} of the top Nb layer is 0.13, which suggest the decrease of crystal quality with the increase of the stacking number. The rather higher yield under the aligned condition at the other Nb layer adjacent to the substrate is from the dechanneling effect when passing through the upper Nb and Cu layers. It is concluded that Cu(111)/Nb(110) with Cu[1$\bar{1}$0]//Nb[001] is crystallographically reasonable stacking in this system. The insertion of Cu thick layer will result in the better crystal quality of top Nb layer because the crystal quality of Cu layer can be improved with the thickness increase.

Fig. 3 summarizes the crystal quality changes as a function of the substrate temperatures by referring to χ_{min} values at the three kinds of the top layers in Nb(110) layer on α-Al_2O_3(11$\bar{2}$0), Cu(111) layer on Nb(110)/α-Al_2O_3 and Nb(110)layer on Cu(111)/Nb(110)/α-Al_2O_3 samples. The thickness of each layer was kept to be the same (50 nm) not to induce the overlapped component in RBS spectra. It is demonstrated that the optimum temperature for the growth of single-crystalline Nb(110) on α-Al_2O_3 substrates is higher than 700 °C and around 200 °C for Cu(111) growth on Nb(110). χ_{min} in the Nb(110) layer on Cu(111)/Nb(110) decreases sharply around 400 °C and then saturates at the temperature higher than 500 °C. It has become clear that the minimum temperature for the growth of Nb single-crystalline layer on Cu (111) is around 500 °C, which is lower than that for the direct growth of single-crystalline Nb on α-Al_2O_3 substrates under the same depositing condition. It is amazing that the Cu layer once grown in a single-crystalline form on Nb(110) at 200 °C can keep its crystal quality up to 700°C without forming the columnar structure.

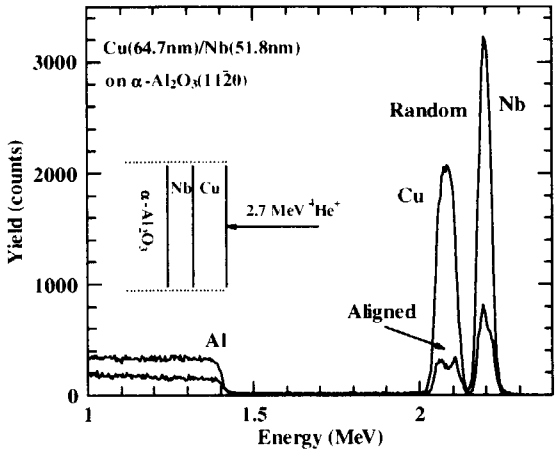

Fig. 1: RBS/channeling spectra of 2.7 MeV $^4He^+$ ions from Cu(64.7 nm)/Nb(51.8 nm) hetero-epitaxial film on α-$Al_2O_3(11\bar{2}0)$. Aligned spectrum was taken around the major axis close to $<11\bar{2}0>$ in α-Al_2O_3.

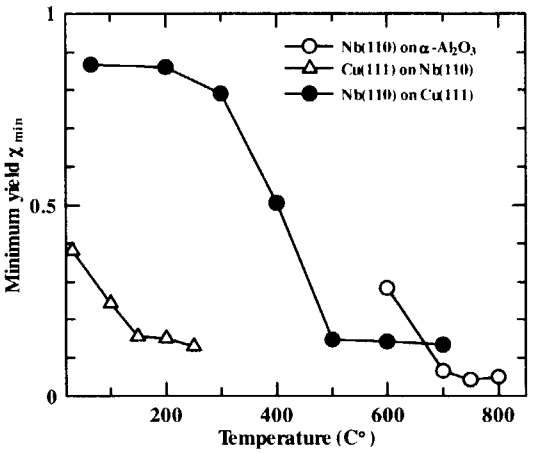

Fig. 3: χ_{min}, relative fraction of the axial channeling minimum yields for Cu and Nb layers on α-$Al_2O_3(11\bar{2}0)$ substrate is plotted as a function of substrate temperature.

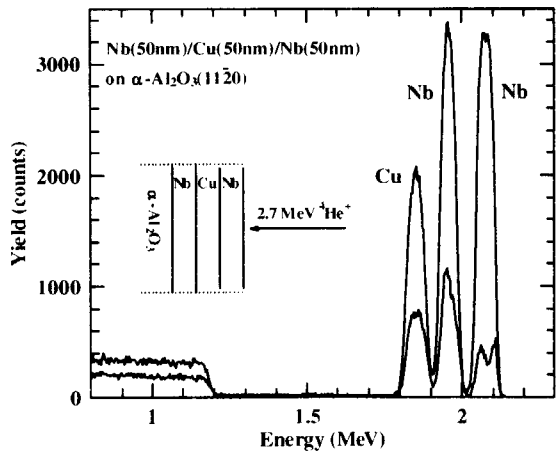

Fig.2: RBS/channeling spectra of 2.7 MeV $^4He^+$ ions from Nb(50nm)/Cu(50 nm)/Nb(50nm) hetero-epitaxial multilayer on α-$Al_2O_3(11\bar{2}0)$.

5. 2 Hydrogen adsorption sites on a Pt{111}-(1×1)-H and a Ni{111}-(2×2)-H: a LERS study

K. Umezawa, S. Nakanishi, S. Yamamoto*, K. Narumi*, Y. Aoki* and H. Naramoto*

Dept. of Materials Sciences, Osaka Prefecture Univ.; *Dept. of Mater. Develop., JAERI/Takasaki

1. Introduction

The determination of the surface structure of the adsorbate-metal system is a topic of continuing interest in surface science. Low energy recoil scattering (LERS) techniques offer the possibility of directly observing and locating surface hydrogen by analyzing the angular anisotropy of recoiled hydrogen. The concept of shadowing and blocking based on simple classical mechanics is very effective for surface structure analysis[1-3] There are two different recoil processes of hydrogen atoms: surface recoil (SR) and direct recoil (DR).

When a hydrogen molecule approaches Pt and Ni surfaces, it readily dissociates and is adsorbed. In what follows, we report the information on the position of hydrogen on Pt(111) at 150 K and Ni(111) at 220 K coupled with trajectory simulations. Calculations were performed using the Thomas-Fermi-Moliére (TFM) potential with Frisov's screening length a_F, and using procedures described in other papers [4, 5] . Also, the experimental value of the incident critical angle is defined as the angle where the intensity curve attains 70 % of the maximum.

2. Experimentals

The experiments presented here were performed in an ultrahigh vacuum system with LEED, AES and LERS facilities. The base pressure during the experiments was maintained below 3×10^{-8} Pa. The crystal was cleaned in situ by repeated cycles of 500 eV-Ar^+ bombardment followed by annealing at 700 °C to remove the surface damage. After this treatment no carbon, oxygen, or sulfur surface impurities were detectable by AES and LEIS. Sharp LEED patterns were thus obtained. Hydrogen adsorption onto the sample was made by introducing H_2 gas into the chamber for Pt(111) at 150K and Ni(111) at 220 K, respectively. The LERS flight time spectra were taken by chopping the primary 1 keV-Ne^+ beam with a pulse width of about 100 ns and the forward scattered particles, after a free flight through a drift tube of 30 cm, and were recorded by a micro channel plate (MCP). The detection system was located at 45° with respect to the incident beam. The recoiled hydrogen were detected as a function of the polar angle α, and the azimuthal angle ϕ between the Ne^+ ion beam incident direction and the crystal axes. In

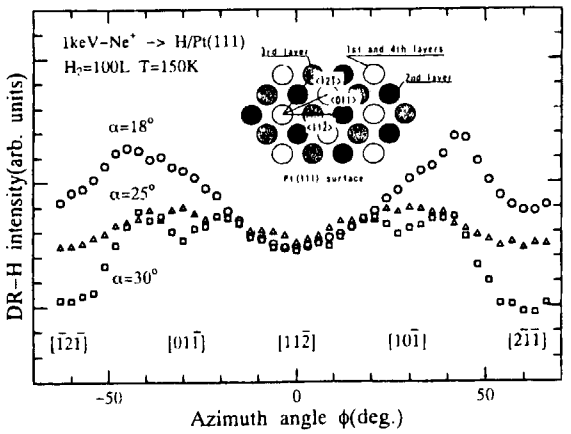

Fig. 1 DR hydrogen intensity profiles as a function of the azimuthal (ϕ) angles along α=16°, 24° and 32° of the incident beam. A sample is H/Pt(111).

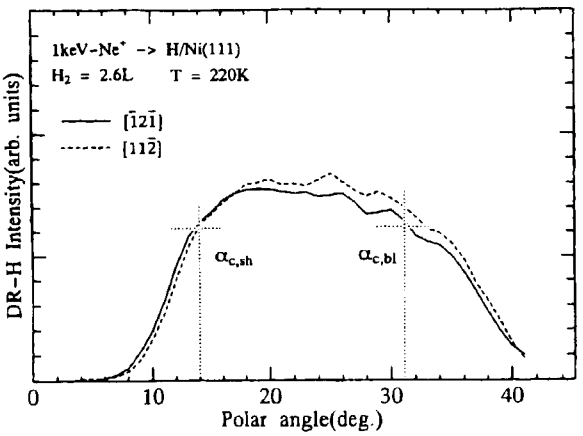

Fig. 2 DR hydrogen intensity profiles as a function of the polar (α) angles obtained from H/Ni(111) sample. The angle regions below and above 22.5° are associated with the shadowing and blocking effects, respectively.

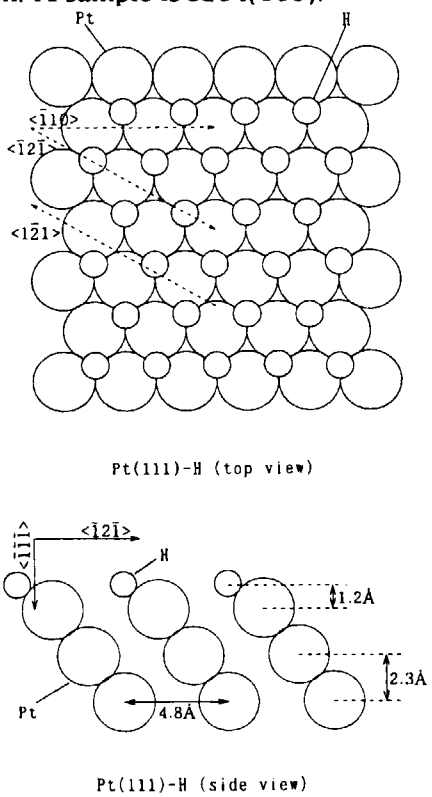

Fig. 3 Structural models of Pt{111}-(1×1)-H at 150K.

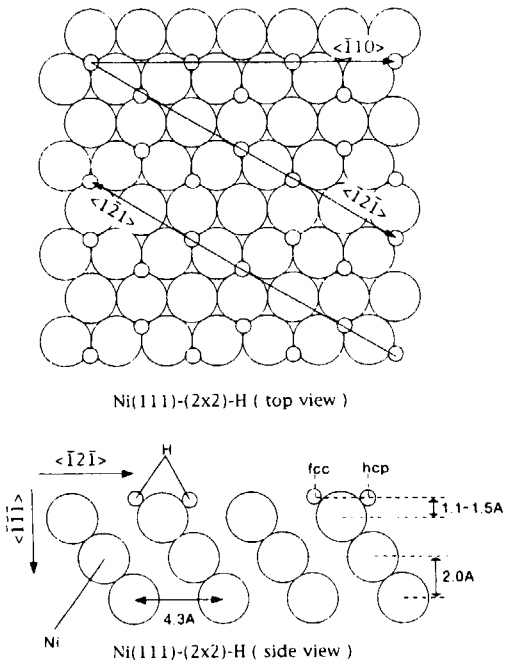

Fig. 4 Structural models of Ni{111}-(2×2)-H at 220K.

addition, RBS measurements were performed to check the reconstruction of substrate surfaces using 2 Mev-He^+ ions.

3. Results and discussion

Figure 1 shows the variation of the intensity of DR hydrogen as a function of ϕ along the polars α=18°, 25° and 30° of the Ne^+ ion incident direction obtained from Pt{111}-(1×1)-H. The intensity drops observed at ϕ=0°([1$\bar{1}$2]), ϕ=60°([$\bar{2}\bar{1}$1]) and ϕ = -60°([$\bar{1}$2$\bar{1}$]) show the shadowing effects for α=18°, 25°and blocking effects for 30°, respectively. Also, the intensity peaks around ϕ = ±40° are due to the focusing effect. The magnitude of the intensity at ϕ = 0° drops off more deeply than that at ϕ =60°. These profiles clearly show an observed periodicity of 120° for the azimuthal angle (a 3-fold symmetry). Figure 2 shows the variation of the H intensity as a function of the polar angle a obtained from the Ni{111}-(2×2)-H sample along the [$\bar{1}$2$\bar{1}$] and [1$\bar{1}$2] azimuths. The DR-H intensity is the same along both azimuths. It suggests that two atomic hydrogen occupy the hcp- and fcc- sites (3-fold sites, the honeycomb (2×2)-2H model). To investigate the H position on sample surfaces, we conducted two-dimensional trajectory simulations. They were carried out by solving Newton's equations of motion for 1 keV-Ne^+ projectiles impinging on a finite two-dimensional slice of the surface along the two azimuths. The targets were modeled by a four layered composite of H/Pt(111) and H/Ni(111). Selected trajectories representing typical DR-H events for incident beams scattering from the model depending on the H positions were reached into a detector at 45°. The impact parameters for these trajectories lie on the long axis of the surface cell, consequently, the trajectories are planner [2, 3]

The experimental data and the calculations of the critical angles for shadowing and blocking result in the final structural model shown in Figs. 3 and 4. In these models, the H atoms occupy fcc-sites on the Pt(111) terraces at a height of approximately 1.2 Å above the first layer of Pt atoms, and (2) the H atoms occupy the fcc- and hcp-site on the Ni(111) terraces at a height of approximately 1.1~1.5 Å above the first layer Ni atoms.

4 Conclusion

We have shown that LERS can be used to detect hydrogen on a Pt(111) at 150 K and a Ni(111) surface at 220 K, respectively. It was found: (1) the H atoms occupy the fcc-site on Pt(111) terraces at a height of approximately 1.2 Å above the first layer of Pt atoms, and (2) the H atoms occupy the fcc- and hcp-site on the Ni(111) terraces at a height of approximately 1.1~1.5 Å above the first layer Ni atoms.

References

1) S. V. Teplov, V. V. Zastavnjuk, V. Byok, J. W. Rabalais, Surf. Sci. 310 (1994) 374.
2) K. Umezawa, T. Ito, M. Asada, S. Nakanishi, P. Ding, W. A. Lanford, B. Hjörvarsson, Surf. Sci. 387 (1997) 320.
3) K. Umezawa, T. Ito, S. Nakanishi, Nucl. Instr. and Meth. B 136/138 (1998) 1121.
4) O. B. Firsov, Sov. Phys. -JETP 6 (1958) 534.
5) M. Aono, Nucl. Instr. and Meth. B 2 (1984) 127.

5. 3 Precipitates of Vanadium Oxide Formed by Ion Implantation and Heat Treatment

K. Narumi,[1] S. Yamamoto,[2] A. Miyashita,[2] Y. Aoki[2] and H. Naramoto[1]
[1]Advanced Research Center, JAERI, [2]Department of Materials Development, JAERI

1. Introduction

Due to the relatively many possible valence states, vanadium has a lot of oxide phases. It has been reported that some of vanadium oxides show semiconductor-to-metal transitions at some transition temperatures.[1] The changes are related to a first-order crystallographic transition, which affects the electrical, magnetic and optical properties of the materials. For example, vanadium dioxide (VO_2) exhibits a reversible phase transition from a semiconductor (monoclinic) to a metal (tetragonal) on heating above a transition temperature of about 70℃. Because of such interesting properties and the possibility of applications of optical switches and so on, many groups have reported preparing methods and related results of characterization for bulk and thin films.[2-5]

Ion implantation is a noble method to make a new or expected physical and chemical properties on the surface. Any element can be introduced into a solid in a controlled and reproducible way by the method, which is nonequilibrium in nature; a feature that often leads to the formation of compositions and structures that cannot be obtained by conventional processing methods. This technique has been applied not only to semiconductor technology but also to altering the near-surface optical, electrical, or mechanical properties of ceramic materials or crystalline oxides.[6]

Oak Ridge group has investigated to form a vanadium-oxide phase in a sapphire substrate by coimplantation of vanadium and oxygen ions and subsequent thermal annealing.[7-9] They succeeded in getting coherent precipitates of V_2O_3[7] and VO_2[8] in c-axis-oriented α-Al_2O_3, where the implants are not stoichiometric for the former but stoichiometric for the latter.

As described above, there are many oxide phases of vanadium, so relative oxygen dose seems to be critical in precipitation of the oxides. In the present study, taking oxygen dose and crystallographic orientation of a substrate as parameters, sapphire is coimplanted with vanadium and oxygen ions. We observe behavior of the substrate and the implant to thermal annealing with the use of Rutherford backscattering spectroscopy. Effect of oxygen on the precipitation of vanadium oxides in sapphire is reported.

2. Experimental

Single crystals of sapphire (0001) (c-axis oriented) and (11$\bar{2}$0) (a-axis oriented) which had been optically polished were used as substrates. Prior to ion implantation, the substrates were annealed in air at 1500℃ for 12 hours to remove damage due to the polishing process. Vanadium and oxygen ions were implanted into the substrates at room temperature with the use of the ion implanter of JAERI/Takasaki. The energy of the ions were 250 and 90 keV, respectively, and the fluences of the ions are shown in Table I. Typical current density was around 0.5 A/cm^2. The thermal annealing of the implanted substrates was carried out in a reducing atmosphere (3% H_2 in Ar) at 900℃ for an hour. After the thermal annealing, the substrates were analyzed using RBS/channeling techniques to observe the depth profile of V and the behavior of the substrate to the annealing. In the RBS measurement, 2-MeV $^4He^+$ ions were used and the angle of scattering was 165°. X-ray-diffraction (XRD) techniques were employed in order to identify the precipitates after the annealing.

3. Results and Discussion

Figure 1 shows RBS/channeling spectra for c-axis-oriented α-Al_2O_3 coimplanted with V and O ions at room temperature. In the following, we call the specimens 1 and 3 where the oxygen fluence is more than that of vanadium oxygen-rich one and the other oxygen-poor one. For simplicity, only the spectra for the annealed specimens are shown. The as-implanted spectra for each specimen are almost

Table I
Summary of Conditions for Ion Implantation

Sample No.	Orientation	Temperature	Fluences	
			V (/cm^2)	O (/cm^2)
1	(0001)	RT	8.9×10^{16}	1.2×10^{17}
2	(0001)	RT	8.4×10^{16}	4.8×10^{16}
3	(11$\bar{2}$0)	RT	9.1×10^{16}	1.2×10^{17}
4	(11$\bar{2}$0)	RT	8.7×10^{16}	4.8×10^{16}

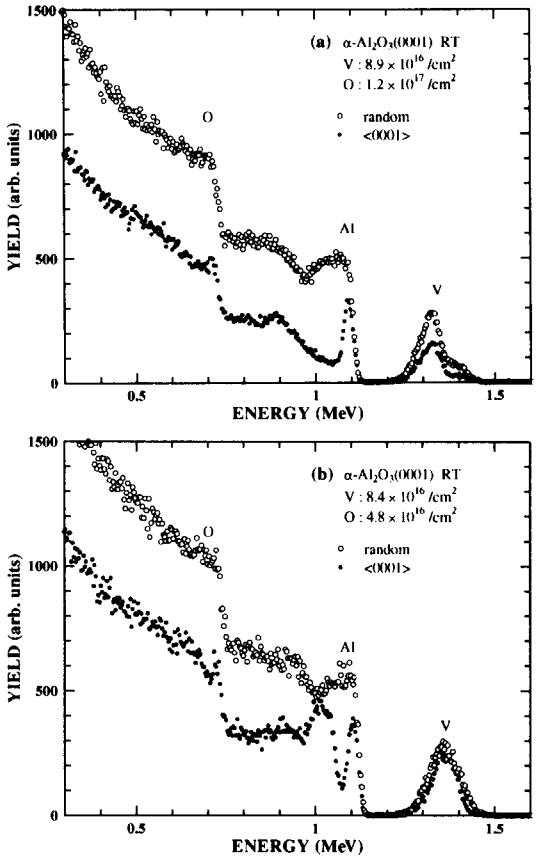

Fig. 1. RBS/channeling spectra for c-axis-oriented sapphire coimplanted with V and O ions after annealing at 900℃ for an hour; (a) oxygen-rich and (b) oxygen-poor samples.

the same: The channeling spectra show an almost amorphous layer only around the projected range of implanted V. The surface region keeps crystallinity to some extent, and a damage peak is observed. After the thermal annealing in the reducing atmosphere at 900°C for an hour, significant changes are not recognized in the spectra for oxygen-poor specimen, as shown in Fig. 1(b): The crystallinity of the Al sublattice was recovered a little. On the other hand, the behavior of the oxygen-rich specimen to the annealing is different as shown in Fig. 1(a). Although a damage peak is still observed, the Al sublattice in the region where the implanted V atoms exist recovers its crystallinity significantly. The distribution of the implanted V atoms also changes and almost a half of the V atoms is substitutional in the Al sublattice. This substitution and the recovery of the crystallinity in the Al sublattice suggest that a phase containing some V that is oriented with respect to the substrate lattice has formed. For a-axis-oriented α-Al_2O_3 coimplanted with V and O ions, the similar as-implanted spectra were observed. After the thermal annealing, however, we did not observe significant recovery of the crystallinity and the spectra hardly depend on the oxygen fluence.

Figure 2 shows the X-ray-diffraction results for 2θ-θ scans of the coimplanted c-axis-oriented sapphires after the annealing. As shown in the figure, (020), (002), (040) and (004) reflection of VO_2 are observed for both oxygen-rich and -poor specimens besides (0006) and (00012) reflection of the sapphire substrate. It is noted that it is difficult to distinguish (020) and (040) reflection of VO_2 from (002) and (004) reflection, respectively. For the oxygen-rich specimen, $(11\bar{2}0)$ and $(22\bar{4}0)$ reflection of V_2O_3 are also recognized. The results indicate that the VO_2 and V_2O_3 precipitates were formed coherently with respect to the c-axis-oriented sapphire substrates. Taking account of the results of the RBS measurements, however, it is considered that the VO_2 precipitates are less coherent than V_2O_3. On the other hand, no reflection of vanadium oxide was observed for the 2θ-θ scans of the a-axis-oriented sapphires. So coherent vanadium-oxide precipitates were not formed, which is consistent with the results of the RBS measurement.

In the present study, the ratio of the oxygen to the vanadium is 1:1.3 and 1:0.56 for the oxygen-rich and -poor specimens, respectively. The precipitates of V_2O_3 were formed in the oxygen-rich c-axis-oriented sapphire where the coimplantation was almost stoichiometric. However, the precipitation of VO_2, which is not so coherent with the sapphire substrate, is not dependent on the oxygen fluence. These results are not interpreted clearly at present. On the other hand, no vanadium-oxide precipitates were formed in the a-axis-oriented sapphire, *i.e.*, no effect of the oxygen fluence was observed. Thus the crystallographic orientation is also considered to be crucial to the precipitation of the vanadium oxides. In fact, under implantation of

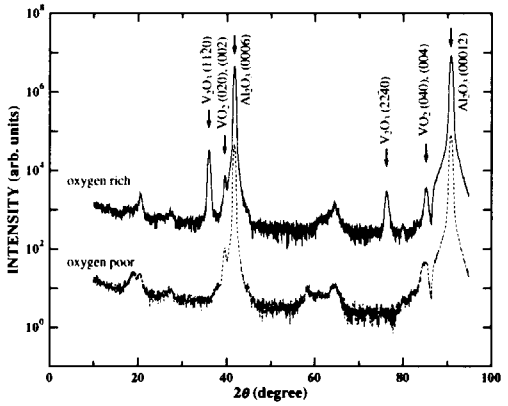

Fig. 2. X-ray-diffraction 2θ-θ scan of c-axis-oriented sapphire; solid and broken lines show the results for oxygen-rich and -poor specimens, respectively.

sapphire.[10] In order to advance the investigation into the process of the precipitation, it is required to study the behavior of the oxygen, both implanted and of the substrate, to the heat treatment associated with the crystallographic orientation.

4. Summary

The single-crystal sapphire coimplanted with V and O ions and annealed subsequently was analyzed using RBS/channeling and XRD techniques. The behavior of the substrate and implanted vanadium to the thermal annealing are closely related to the precipitation of the vanadium oxides. It is found that the vanadium-oxide precipitates in sapphire depend on the oxygen fluence relative to vanadium one and the crystallographic orientation of the substrate.

References

1) D. Adler, Rev. Mod. Phys. **40** (1968)714.
2) F. C. Case, J. Vac. Sci. Tchnol. A **9** (1991) 461.
3) D. P. partlow, S. R. Gurkovich, K. C. Radford and L. J. Denes, J. Appl. Phys. **70** (1991) 443.
4) M. -H. Lee, M. -G. Kim and H. -K. Song, Thin Solid Films **290** (1996) 30.
5) D. Manno, A. Serra, M. Di. Giulio, G. Micocci, A. Taurino, A. Tepore and D. Berti, J. Appl. Phys. **81** (1997) 2709.
6) H. Naramoto, C. W. White, J. M. Williams, C. J. McHargue, O. W. Holland, M. M. Abraham and B. R. Appleton, J. Appl. Phys. **54** (1983) 683.
7) L. A. Gea, L. A. Boatner, J. Rankin and J. D. Budai, Mat. Res. Soc. Symp. Proc. **354** (1995) 269.
8) L. A. Gea and L. A. Boatner, Appl. Phys. Lett. **68** (1996) 3081.
9) L. A. Gea, L. A. Boatner, H. M. Evans and R. Zuhr, Nucl. Instrum. Methods B **127/128** (1997)553.
10) H. Abe, H. Naramoto and S. Yamamoto, Mat. Res. Soc. Symp. Proc. in press.

5. 4 Temperature-dependent Defect Growth in Sapphire ($11\bar{2}0$) Implanted with 250keV $^{51}V^{+}$ Ions

H. Naramoto♦, S. Yamamoto*, K. Narumi♦, Y. Aoki† and D. Ishikawa#
♦Takasaki-Branch, Advanced Science Research Center, JAERI,
*Dept. of Mater. Develop., JAERI/Takasaki, †Research Institute for Sumitomo Heavy Industry, #JAERI Research Student(1997FY)

1. Introduction

The defect production in sapphire has been studied since 1980's and main concerns were on how to accommodate the implants into the crystal lattice to utilize the surrounding crystal filed[1, 2]. Recently it has become more important to understand the detailed process of defect accumulation for the controlled materials processing[3]. Influential factors in the defect-introduction are the defect-implants interactions, the anisotropic diffusion and temperature-dependence. For example, the implant-stabilization by defects at the fixed depth can realize the uniform buried layer with a new function without the precipitation of different phase[4].

For these purposes, several institutes have installed "dual beams system" and they have studied the defect introduction at the initial stage of ion implantation[5], the temperature-dependent amorphization and the ion-beam-induced crystalization[6].

In the present study, the ion implantation and the analysis are made *in-situ* on sapphire ($11\bar{2}0$) at typically different temperatures using a dual beam analysis system[3].

2. Experimentals

Sapphire platelets with (0001) and ($11\bar{2}0$) crystallographic planes were employed to know the possible anisotropic behaviors.

In the dual beam experiment, implanting beam was incident 40 degrees off the surface normal and scanned laterally. The analyzing $^{4}He^{+}$ ion beam is incident almost parallel to the surface normal.

3. Results

Fig. 1 shows 2.0 MeV $^{4}He^{+}$ RBS/channeling spectra from sapphire ($11\bar{2}0$) implanted with 250 keV $^{51}V^{+}$ ions at room temperature(RT). The features in this figure are almost the same as those in sapphire (0001) which should have different nature in impurity diffusion. The depth at the maximum defect concentration shifts from one at the expected maximum defects production in TRIM simulation to the projected range possibly because of the formation of defect-implant aggregates. During the implantation, one can see the appreciable change of surface peak suggesting the reordering around the subsurface regions at RT. The substitutional fraction of implanted V atoms is less than that in the (0001) case, which implies that the V-atoms can be accommodated mainly along the <0001> Al-string.

Fig. 2 shows the implantation result at 250K. It has the mixed nature between the

results at RT and low temperature. The defect growth feature is rather close to that at RT, but one can see the first evidence of the defect-recovery at the doses of $7.5x10^{15}/cm^2$ and $1.5x10^{16}/cm^2$, and more careful considerations should be taken for the precipitation process in the implanted samples at low temperatures. After the heavy implantation there appears a huge surface peak reflecting rather thick distorted region. This is also different from the results at RT.

Fig. 3 is the RBS/channeling spectra at 40K and no reordering is observed around the surface region. After $4.7x10^{14}/cm^2$, the implanted region has become amorphous at the depth corresponding to the maximum defect production. Further implantation extends the amorphous region towards the inside.

References

1) H. Naramoto, C. W. White, J. M. Williams, C. J. McHargue, O. W. Holland, M. M. Abraham and B. R. Appleton, J. Appl. Phys. **54**(1984)683.
2) C. W. White, G. C. Farlow, H. Naramoto, C. J. McHargue and B. R. Appleton, Mater. Res. Soc. Proc. **24**(1984)163.
3) H. Naramoto, S. Yamamoto, Y. Aoki and K. Narumi, Mater. Science and Eng. A(1998). In print.
4) Z. J. Zhang, H. Naramoto, A. Miyashita, B. Stritzker and J. K. N. Lindner, Phys. Rev. B(1998). Accepted for publication.
5) H. Naramoto, Y. Aoki, S. Yamamoto and H. Abe, Nucl. Instr. Meth. **B127/128** (1997)599.
6) M. Nastasi, J. W. Mayer, Mat. Sci. Eng. **B12**(1994)1.

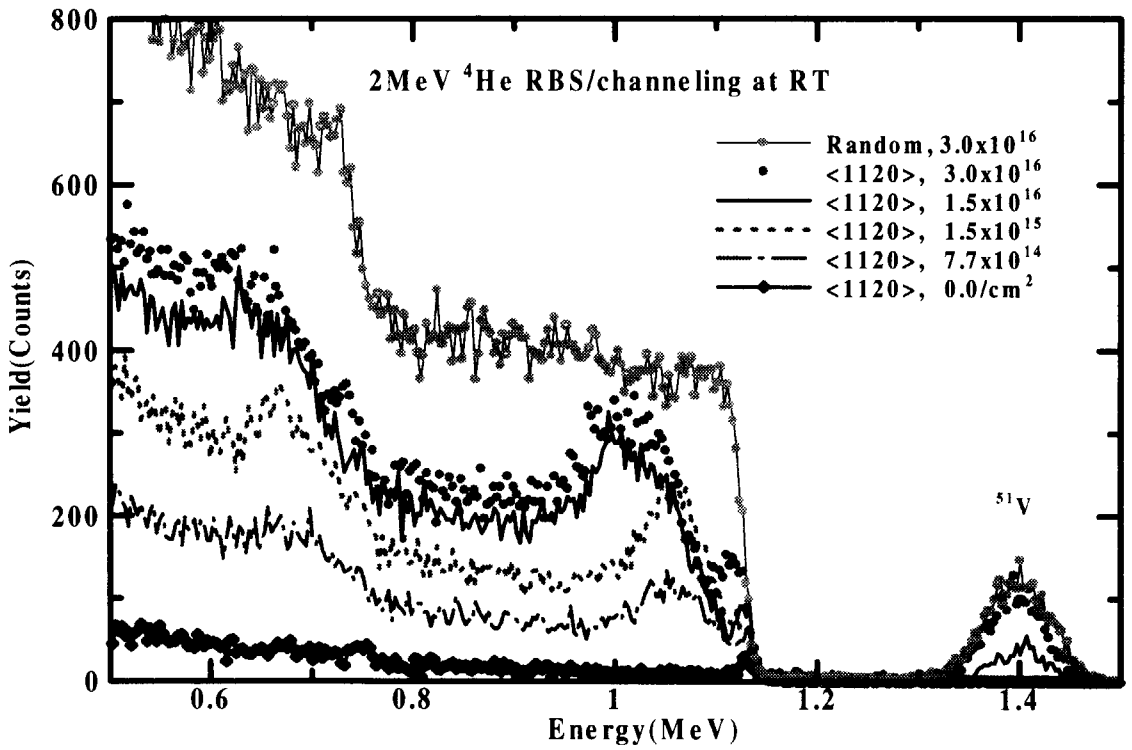

Figure 1: RBS/channeling analysis at RT on sapphire $(11\bar{2}0)$ implanted with 250keV $^{51}V^+$ ions. Yield of backscattered counts are in the order of implanted doses. Except the two-stage-spectra with the maximum yield, the remainings are $<11\bar{2}0>$ aligned spectra.

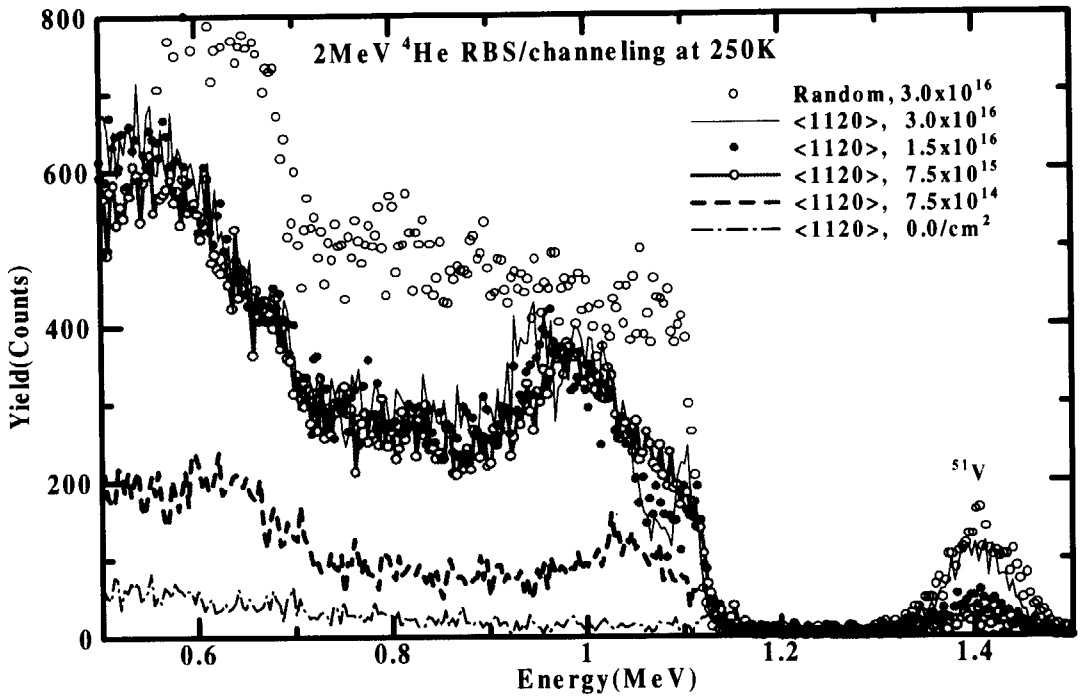

Figure 2: RBS/channeling analysis at 250K on sapphire ($11\bar{2}0$) implanted with 250keV $^{51}V^{+}$ ions. The order of yield increase corresponds to the implanted doses.

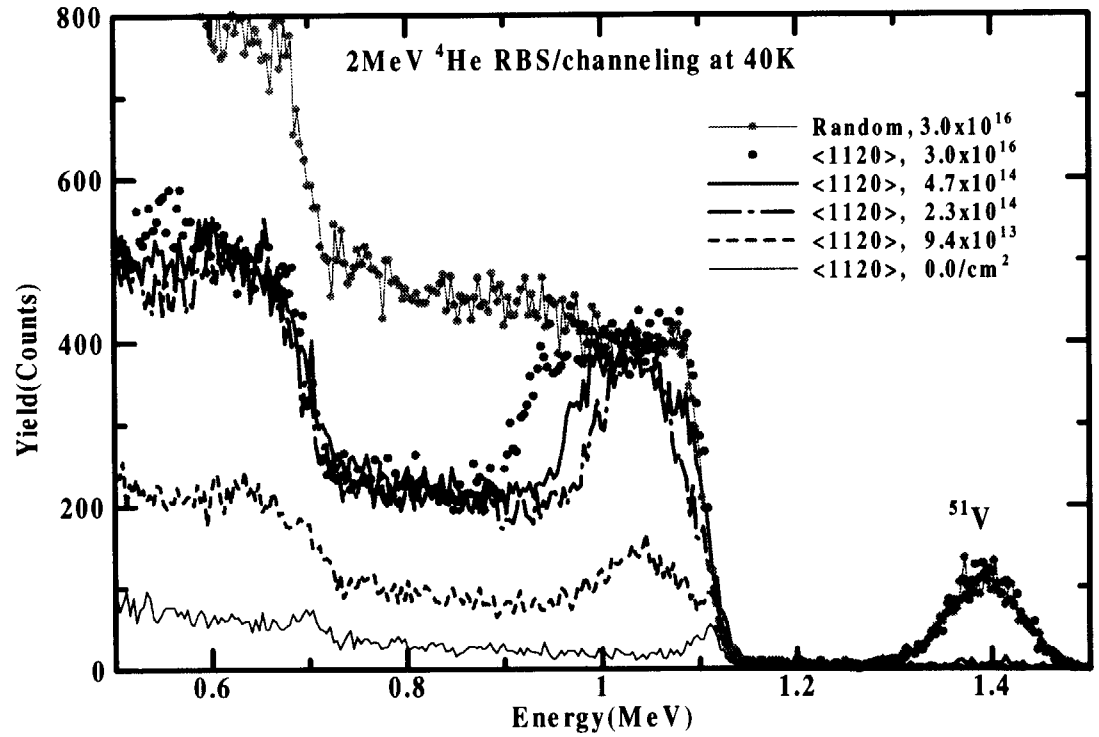

Figure 3: RBS/channeling analysis at 40K on sapphire ($11\bar{2}0$) implanted with 250keV $^{51}V^{+}$ ions. The dose employed here are relatively low to know the effective defect production.

5. 5 Transmission Channeling Study of High Energy Heavy Ions through a Ag/Au Deposited Si(111) Thin Film

K. Morita, D. Ishikawa, J. Yuhara, D. Nakamura, K. Soda, S. Yamamoto[A], K. Narumi[A], H. Naramoto[A], K. Saito[B]
School of Engineering, Nagoya Univ.,
Dept. of Mater. Develop., JAERI Takasaki[A], National Industrial Research Institute of Nagoya[B]

1. Introduction

Ag/Au/Si(111) surface has a variety of structure such as $\sqrt{21}\times\sqrt{21}$, $\sqrt{3}\times\sqrt{3}$, and $2\sqrt{3}\times2\sqrt{3}$ depending on the Au and Ag coverages[1]. However, these real space structures have not been clarified yet. In this study, we have applied the transmission channeling of high energy heavy ion beam to determine the adsorbed sites and to clarify the atomic structure of the Ag/Au/Si(111) surface.

Transmission ion channeling is the powerful tool to determine the site of a adsorbate on a crystalline surface[2]. It utilizes the fact that the flux distribution of the ions reaches an equilibrium after they travel through a substrate thickness ~100nm, which can be calculated quite precisely. The site determination can be performed by fitting the calculated angular dependence of the scattering yield from the adsorbate to the experimental one. The benefit of this technique using high energy ion is a sensitivity to the subsurface layer structure, which can hardly be achieved with conventional low energy ion scattering techniques such as CAICISS, which is sensitive to only the surface structure due to a high neutralization probability of ions scattered from the subsurface layers.

It is reported from the experimental results on the RHEED-TRAX[3] and the ion impact desorption[4] that the adsorbate structure on the Ag/Au/Si(111) surface are composed of a top Ag layer and an underlying Au second layer. To determine the layer structure of the Ag/Au/Si(111) surface, the information on the lattice sites of them on the Si(111) surface is necessary. In this paper, we report the preliminary result on site determination of Au and Ag adsorbates on the Ag/Au/Si(111) surface by means of the transmission channeling of high energy heavy ion beam.

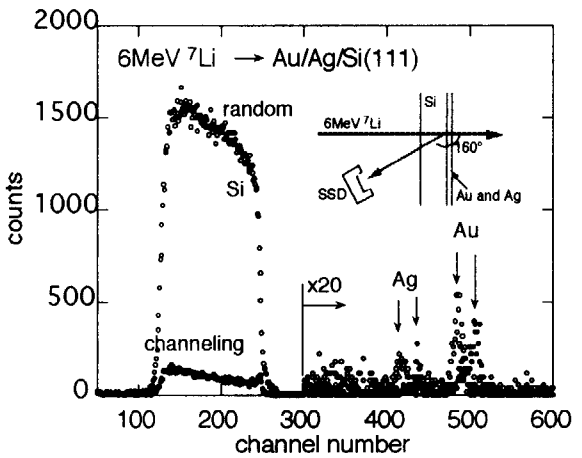

Fig.1 Energy spectra of ions scattered from the Ag/Au/Si(111) surface at channeling and random incidence. Present experimental geometry is also inserted in the figure.

2. Experiment

Thin crystalline Si(111) samples were prepared by ion implantation and selective wet etching[5]. The thickness of the sample used in the present study was 1.3μm. Au and Ag were deposited to the Si(111) thin crystal at room temperature in a UHV chamber. The

coverages of Au and Ag were 0.7 and 1.1ML, respectively. The sample was then transferred to MD1 chamber which is connected to the Tandem accelerator of TIARA facilities of JAERI. 6MeV ^{7}Li ion is used for the probe beam, and backscattered ions were detected by a solid state detector placed at 160° to an incident direction. The purpose of use of the high energy heavy ion beam for the probe and the backscattering geometry are to obtain a wide separation between energies of ions scattered by Au and by Ag enough to analyze them separately. The experimental geometry is shown in Fig. 1.

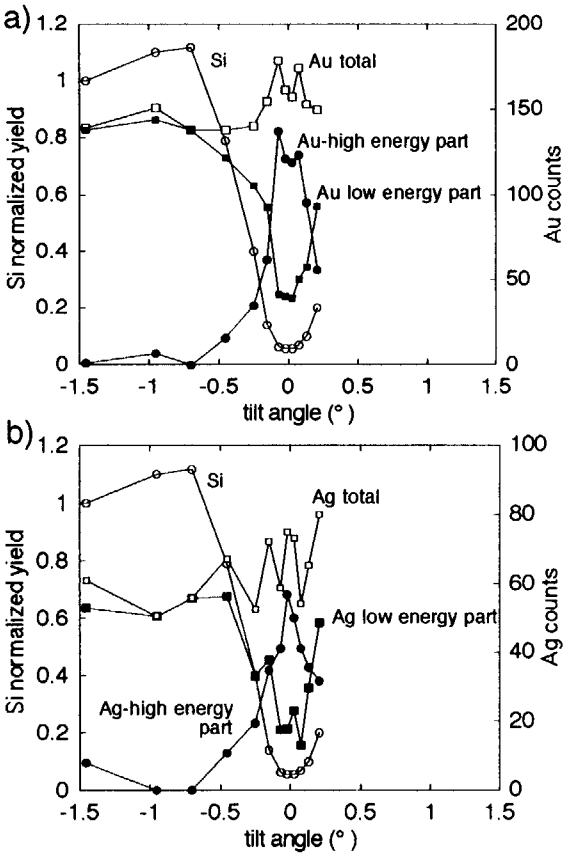

Fig. 2 Plots of the a) Au and b) Ag yields as a function of incident angle relative to the <111> axis. High and low energy parts are plotted separately.

3. Results

Backscattering spectra of 6MeV ^{7}Li ions scattered from the Au/Ag/Si(111) surface at the <111> channeling and random incidence are shown in Fig. 1. It can be seen that Au and Ag peaks are sifted towards high energy side at channeling incidence, which indicates that the energy loss of Li ions passing through under channeling condition is lower than that under random condition. Fig. 2 a) and b) show the angular scans of Au and Ag yields, respectively, as a function of the tilt angle relative to the <111> axis. Low and high energy parts of the corresponding peaks are plotted separately. In the angular scans of the Au yield, it can be seen that the high energy part shows off-axis peaks at the angle of 0.07°, which indicates that Au is located at a site between the channel center and the Si lattice position. On the other hand, the angular scan of the high energy part of Ag shows a single peak at the <111> direction, which indicates that Ag are located close to the channel center. It can also be noticed that a shoulder appears in the angular scan of the low energy part. This fact suggests that some Ag atoms are located at a site between channel center and the Si lattice position.

4. Discussion

In order to locate the adsorbed sites of Au and Ag at the Ag/Au/Si(111) surface, the angular dependences of the scattering yields have been calculated and compared with the experimental results. At first, the calculation of the ion flux distribution in a channel was done as a function of the tilt angle. The flux distribution was calculated using the continuum model[6] which used the string potential, and the Moliere approximation to the Thomas-Fermi potential. Thermal vibration of the Si atoms was taken into account for the potential calculation[7]. Then the thermal vibration of the adsorbate was also taken into account for calculation of the site dependence of the scattering yield

profile. The result is shown in Fig.3 for a variety of positions in a channel. The positions are indicated as a distance of the adsorbed site from the Si lattice position. The off-axis peak appeared in the experimental angular scan of Au yield is consistent with the peak position appeared in the calculated angular scan for the site 0.72Å apart from the Si lattice.

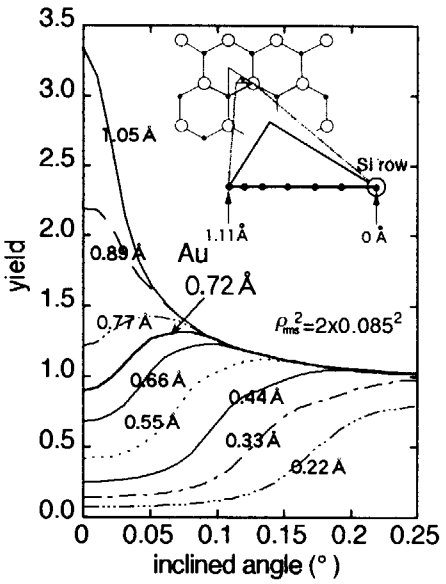

Fig.3 Calculated angular scans of scattering yields as a function of tilt angle relative to the <111> axis at a variety of positions in the channel. Numbers are the distance of the assumed adsorbed site from the Si lattice.

Using the data described above, we determine the surface atomic structure of the Ag/Au/Si(111) surface. The surface structure of the surface used in the present study is assumed to be the Si(111)-2√3x2√3-(Au,Ag), judging from the Au and Ag coverages. We assume that the Au site at the Si(111)-2√3x2√3-(Au,Ag) surface is similar to that of Au at the Si(111)-√3x√3-Au surface and Au atoms form trimer structure at both surfaces. Considering the distance of 0.72Å between Au and Si lattice sites, it suggests that the Au trimer is rotated by 16°. For Ag sites, the experimental results indicate the existence of two sites; one is the channel center site and another is off-center site, however, the latter site can not be determined in detail in the present analysis. A model proposed in Fig.4 is the preliminary one derived from the present experimental data on the transmission channeling. A complete site location would require more data (i.e. angular scan in the other major axes should be measured to get adsorbate displacement along the surface normal).

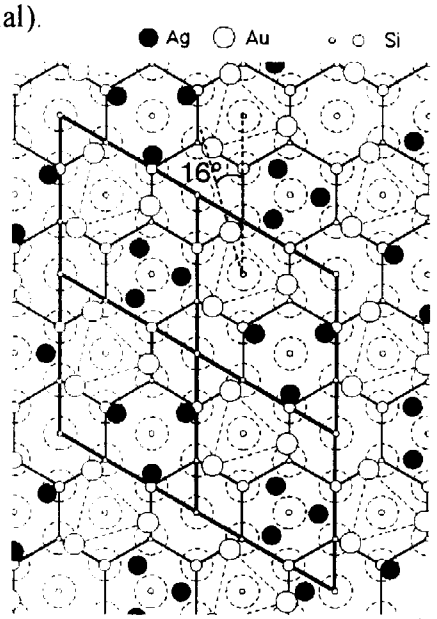

Fig.4 Proposed model for the Si(111)-2√3x2√3-(Au.Ag) surface.

Reference

1) J. Yuhara, M. Inoue and K. Morita, Surf. Sci. **283** (1993) 327.
2) I. Stensgaard and F. Jacobsen, Phys. Rev. Lett. **54** (1985) 711.
3) T. Yamanaka, A. Endo and S. Ino, Surf. Sci. **294** (1993) 53.
4) D. Ishikawa, J. Yuhara, K. Soda and K. Morita, Surf. Sci. **374** (1997) 306.
5) K. Saito, S. Nakao, H. Niwa, M. Ikeyama, Y. Miyagawa and S. Miyagawa, Jpn. J. Apl. Phys., **31** (1992) 4020.
6) B. Bech Nielsen, Phys. Rev. **B37** (1988) 6353.
7) B. R. Appleton, C. Erginsoy and W. M. Gibson, Phys. Rev. **161** (1967) 330.

5. 6 Investigation of Quantitative Analysis Method of Hydrogen Using Fast Neutrons

K.Saitoh, S.Nakao, H.Matsuda, H.Niwa, Y.Saitoh, Y.Nakajima*, S.Tajima* and H.Naramoto*

Nat. Ind. Res. Inst. Nagoya, *JAERI/Takasaki

1. Introduction

The analysis of hydrogen isotopes has been extensively carried out by elastic recoil detection analysis (ERDA) or by nuclear reaction analysis (NRA). Although these techniques provide high depth resolution, the accessible depth is limited within a few μm, which is, in most cases, insufficient for the characterization of surface structure.

Recently, elastic recoil detection analysis induced by fast neutron (NERD) has been developed[1]. There are several advantages of this method. Firstly, the accessible depth is far greater than that attained by the above method; at least more than a few tens of μm, depending on the neutron energy. Secondly, there is a great suppression of irradiation damage than that for the conventional ion beam methods. However, the NERD method has technical difficulties, because charged particles must be detected in a fast neutron field.

We started the research of NERD using relatively lower energy neutrons than 5MeV. In this report, we describe a brief principle and some results of preliminary tests of NERD measurement using a 3MV single-ended accelerator of TIARA facility.

2. Brief Principle

When mono-energetic neutrons are irradiated normal to a planar sample which contains light atoms, such as hydrogen, some of the atoms are recoiled by neutron elastic collisions, and emitted from the opposite sample surface. If a recoil atom is emitted normal to the surface, the relation between the initial depth z of the atom and the emission energy E(z) at the surface are as follow:

$$E(z) = E_r - \int_0^z [dE/dx]_{E(x')} dx' \qquad (1)$$

where E_r is the recoil energy, $[dE/dx]_E$ the stopping power depending on the energy E, and E(x') the energy of recoil atom as a function of path length x'. The energy spectrum f(E) of recoil atoms emitted normally from the opposite surface is presented as

$$f(E) = \frac{\Phi_n\, t_m\, N_p(z)\, S_m\, \sigma_r(\theta_r)\, \Omega_D}{[dE/dx]_{E(z)}} \qquad (2)$$

where Φ_n is the neutron flux rate, t_m the measurement time, $N_p(z)$ the concentration of atoms as a function of depth z, S_m the effective sample area. $\sigma_r(\theta_r)$ the differential cross section of the recoil atoms, Ω_D the detector solid angle and E(x) the energy of the emitted atom. Note that eqs. (1) and (2) are an approximation when the source neutrons are incident normally to the sample with perfect mono-energetic, and the solid angle of detector Ω_D is small enough.

3. Experimental

Figure 1 shows the neutron source and the counter telescope. Fast neutrons were produced by nuclear reactions of $D(d,n)^3He$ (Q=3.27MeV) with 2MeV deuterons, and $^7Li(p,n)^7Be$ (Q=-1.65MeV) with 2.3 MeV protons. The Target were TiD_2 films of about 3μm thickness and LiF

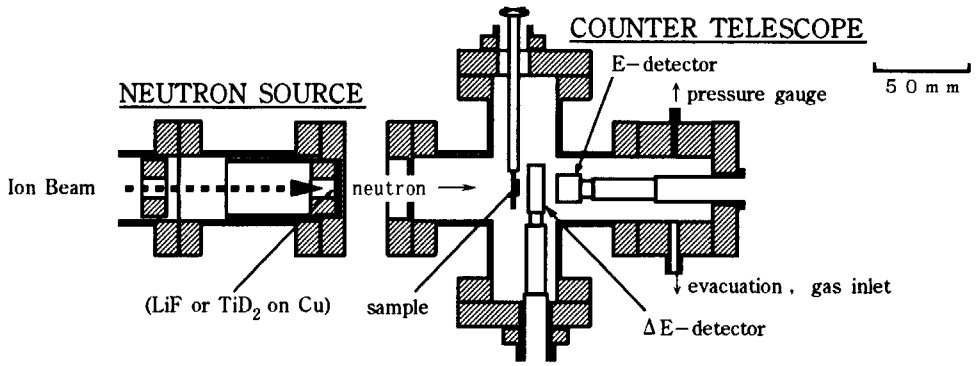

Fig.1 A cross-sectional view ofthe neutron source and the counter telescope.

films of about 4μm thickness respectively, which were deposited on copper substrates of 1mm thickness..

The energy of neutron is about 5.2 MeV for $D(d,n)^3He$ reaction and about 0.55 MeV for the $^7Li(p,n)^7Be$ reaction at the forward direction. The neutrons were irradiated to the sample from the back surface in the counter telescope.

Recoil atoms were detected by a ΔE-E counting system. In this study, two types of ΔE-detectors are used. One is a Si totally-depleted surface-barrier detector of 15μm thickness, and the other is a compact proportional counter whose shape is the same as the Si ΔE-detector (wire diameter 0.02mm and the effective length is about 6mm). In the case of the proportional counter, the telescope was filled with Ar gas with 5% CO_2 to a pressure of 100Torr. For the E-detector, conventional Si surface barrier detector (active thickness 100μm or 300μm) was used. Outputs signals from these detectors are analyzed by a two-dimensional pulse height analyzing system.

4. Results and discussion

Figure 2(a) shows a ΔE-E pulse height distribution of recoil hydrogen atoms from a thick polyethylene sample induced by 5.2 MeV neutrons. In this case the 15μm Si ΔE-detector and the 300μm thickness E-detector were used. A bow-shaped dark area is recognized on the ΔE-E space, which corresponds to the recoil hydrogen. The relation between ΔE and E signals is reasonable, taking into account the energy loss and the straggling of hydrogen in the ΔE- detector.

A projection of the dark area on the E-axis is shown in Fig.2(b). This is the energy spectrum of the recoil hydrogen atoms after penetrating ΔE-detector. Taking into account the neutron energy width and the finite geometrical effects, the measured spectrum is consistent with equation (2).

Figure 3(a) shows a ΔE-E pulse height distribution of recoil hydrogen and deuteron atoms from a TiD_2 film induced by 0.55MeV neutrons. The thickness of the TiD_2 film is about 3μm and it contains hydrogen and oxygen impurities which may be caused by sputtering gas impurities.

Different from the above case, the ΔE-E pulse height distribution shows a complex shape. It consists of three distribution groups. The highest ΔE-signal group corresponds to the recoil deuteron atoms, and the second highest ΔE-signal group is the recoil hydrogen atoms contained in the films as an impurity. The lowest ΔE-signal group corresponds to chance coincidence with noise elements from ΔE-detector and E-detector. Therefore the third group should be ignored in the analysis.

Fig.3 (b) shows the energy spectra of recoil hydrogen and deuterium atoms, which were obtained by the projection of

each group on the energy axis. Since the low energy discriminator is set relatively high, the low energy region of each spectra were lost but the result shows a reasonable spectra of recoil hydrogen and deuterium atoms from the TiD_2 film. It should be noted that, in the case of the 0.55MeV neutrons, the energy loss of the recoil atoms in the proportional gas is significantly affects the measured energy spectra.

5. Summary

The preliminary test of the NERD measurement was performed using 0.55MeV and 5.2 MeV neutrons which were generated with proton and deuteron beams from the 3MV single-ended TIARA accelerator. Recoil hydrogen and deuterium atoms induced by the fast neutrons were successfully detected by the ΔE-E counter telescope. This indicates that the such relatively low energy neutrons can be used for the analysis of light atoms, such as hydrogen and helium isotopes, included in solid surface layer.

Acknowledgements

The authors are grateful to Dr. M.Baba and his group in University of Tohoku for their useful suggestions.

References

1) B. G. Skorodonov, I. O. Yatsevich and Y. O. A. Zhukovsk, Nucl. Instr. Meth. B85 (1994) 301.

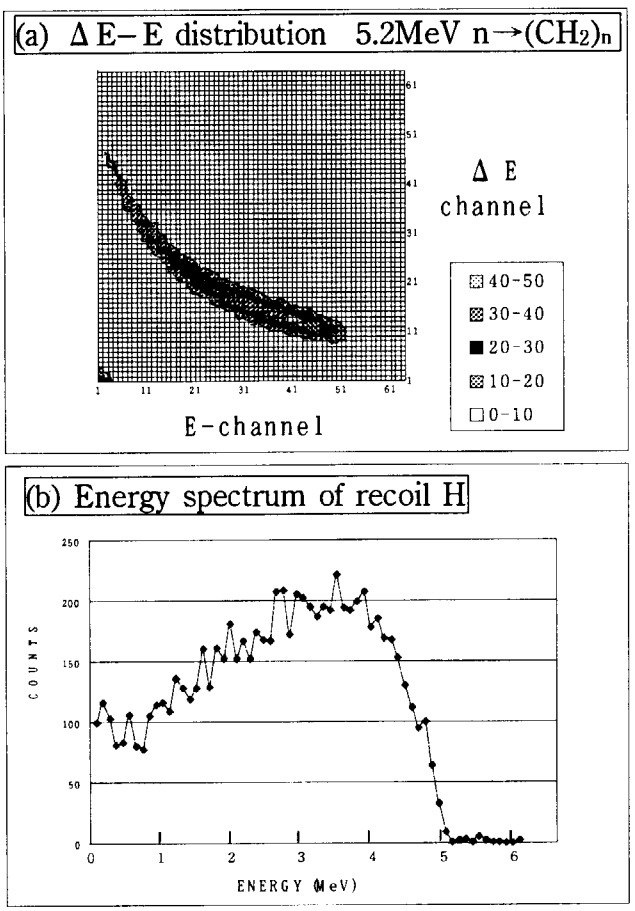

Fig.2 (a) A ΔE-E distribution of recoil hydrogen atoms from a thick polyethylene by 5.2 MeV neutrons. (b) The energy spectrum of recoil hydrogen atoms measured by the E-detector.

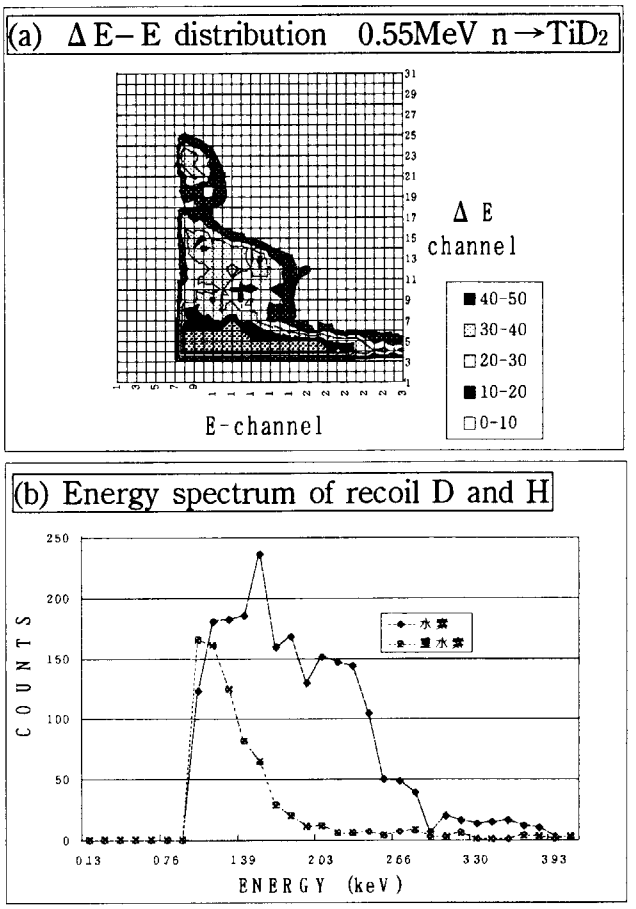

Fig.3 (a) A ΔE-E distribution of recoil hydrogen and deuteron atoms from a TiD2 film by 0.55 MeV neutrons. (b) The energy spectra of recoil hydrogen and deuterium atoms measured by the E-detector.

6. Nuclear Chemistry and Radioisotope Production

This is a blank page.

6. 1 Production of Positron Emitter-Labeled Compounds for Plant Study Using an AVF Cyclotron

N. S. Ishioka, H. Matsuoka, S. Watanabe, A. Osa*, M. Koizumi*and T. Sekine*
Department of Radioisotopes, JAERI, and *Department of Materials Science, JAERI

1. Introduction

In the TIARA facility, since the positron emitting tracer imaging system (PETIS) was developed[1] together with production methods of positron emitters such as ^{13}N, ^{18}F and ^{11}C,[2] the physiological function of plants *in vivo* has been studied with these positron emitters. This technology, including the PETIS and radioisotope production, is a version of the technique of positron emission tomography (PET), which uses positron emitters, in nuclear medicine, although the PETIS is not tomography but a dynamical two-dimensional imaging system. Production methods of positron emitters for plant study are expected to be developed. A variety of radioisotopes, including positron emitters, can be produced using the TIARA radioisotope-production system characterized by irradiation of targets in solid, gas and liquid with energetic proton, deuteron and α beams from the AVF cyclotron.

We have continued the development of the water target system for the production of ^{13}N and ^{18}F and have started the production of medium-mass positron emitters of metallic element such as ^{48}V. The water target system was designed to keep the purity of a target and to automatically transport a target from the hot cell to the irradiation position as described elsewhere.[3] Further, we have modified the system to recover and purify an irradiated water target in the hot cell for routine production of [^{13}N]nitrate ion ($^{13}NO_3^-$) and [^{18}F]fluoride ion ($^{18}F^-$) instead of a manual operation in a fume hood. In this paper, the modification of the water target system and the production method of ^{48}V are described.

2. Production of $^{13}NO_3^-$ and $^{18}F^-$: the system for recovery and purification of an irradiated water target

The new system provides the ability to remotely transfer the irradiated water target from the target vial to a vessel without exposing the operating personnel to radiation. As shown in figure 1, the system consists of a peristaltic pump and disposable columns. As the irradiated water target contains an impurity of ^{48}V from proton and α-particle activation of the Ti window, and, in the production of $^{13}NO_3^-$, an impurity of $^{18}F^-$ from proton activation of ^{18}O (0.2% natural isotopic abundance and 0.02% in depleted water), the impurities were separated rapidly together with $^{13}NH_4^+$ ion from the target by cation exchange and basic alumna chromatography. Using the system we can recover and purify rapidly the irradiated water target in the hot cell. A $^{13}NO_3^-$ solution is routinely available for a plant study in 22 min from the end of bombardment.

Using the water target system eighty-three batches of $^{13}NO_3^-$ were produced during the past year and each of them was analyzed by HPLC before plant experiment for the concentrations of, radioactive and non-radioactive, nitrate ion and nitrite ion. We found that these final solutions contained 0.2 ppm of NO_3^- and 0.1 ppm of NO_2^-. The admixture of NO_2^- to the NO_3^-, however, may obscure the experiments on plants. The reduction or removal of NO_2^- will be studied.

3. Production of vanadium-48

Vanadium-48 with a half-life of 16 day, emitting β^+-rays, can be produced in the $^{45}Sc(\alpha,n)^{48}V$ reaction. In vanadium radioisotopes, the ^{48}V radionuclide offers considerable advantages as a biomedical tracer,

and the ^{48}V can be used to make clear the effect of its ions to the process of plant growth.

A commercially available 500 μm thick scandium foil (purity: 99.9%, ESPI) was used as a target. The irradiations were carried out using a 30-MeV α-particle beam. An incident energy of the α-particles after passing through the window (100 μm-thick Ti) was estimated to be 22.7 MeV. The production yield obtained was about 1.5 MBq of ^{48}V using a beam current of 0.8 μA for 5.4 hours. Figure 3 outlines the preparation of ^{48}V by the (α,n) reaction with high specific radioactivity for plant studies. The impurities identified were ^{44m}Sc and ^{46}Sc produced by (α,αn) and (α,2pn) reactions. These radionuclides were useful for the check of the entire radiochemical separation.

The radiochemical separation developed for the isolation of carrier-free ^{48}V is based on cation exchange chromatography with retention of Sc^{3+} and elution of ^{48}V as anionic pentavanadate ions. The irradiated metallic Sc foil was dissolved in a 2 ml of 6M HCl containing 1% H_2O_2 and then placed on a column (15 mm ϕ × 25 cm) of 50W-X8 (Muromac) in the hydrogen form (100/200 mesh). The ^{48}V was eluted with 1M HCl containing 1% H_2O_2. The radiochemical yield of the ^{48}V in the eluate was in the order of 80% in the first 50 ml. Another 50 ml was poured for more elution of ^{48}V. The ^{48}V-eluate was evaporated to dryness and the residue dissolved in 2 ml of ultra pure water. Radioactive concentrations of the order of 0.8 MBq of ^{48}V/ml were obtained. The chemical yield of ^{48}V from the target was 91%. The chemical form of the ^{48}V obtained was considered to be the anionic pentavarent ^{48}V form, $H_2VO_4^-$. The radiochemical purity of the ^{48}V in the eluate was determined by γ-ray spectrometry using a HPGe detector (crystal diameter 56.7 mm, length 71.3 mm) coupled to SEIKO 7800 MCA and was found to be better than 99.8%. Figure 2 shows γ-ray spectrum of the ^{48}V solution after chemical separation. The final products were free from γ-peaks of ^{44m}Sc and ^{46}Sc. Radioactive scandium was strongly absorbed on the top of the column.

The yield of ^{48}V produced by the (α,n) reaction is lower than the corresponding production via (p,xn) reactions on metallic titanium.[4] However, the radiochemical separation of the ^{48}V from the irradiated Sc is much simpler and more rapid (it took 12 h in our experiment) than the corresponding multi-step and time-consuming separation of ^{48}V from proton bombarded Ti (complete within 4-5 days).[4]

References

[1] T. Kume, S. Matsuhashi, M. Shimazu, H. Ito, T. Fujimura, K. Adachi, H. Uchida, N. Shigeta, H. Matsuoka, A. Osa and T. Sekine, Appl. Radiat. Isot., **48** (1997) 1035.

[2] N. S. Ishioka, H. Matsuoka, S. Watanabe, A. Osa, M. Koizumi T. Kume, S. Matsuhashi, T. Fujimura, A. Tsuji, H. Uchida and T. Sekine, J. Radioanal. Nucl. Chem., (in press).

[3] N. S. Ishioka, H. Matsuoka, S. Watanabe, A. Osa, M. Koizumi and T. Sekine, Synthesis and Applications of Isotopically Labelled Compounds 1997, Wiley, Chichester (1998), p.669.

[4] E. Sabbioni, E. Marafante, L. Goetz, C. Birattari, Radiochem. Radioanal. Letters, **31** (1977) 39.

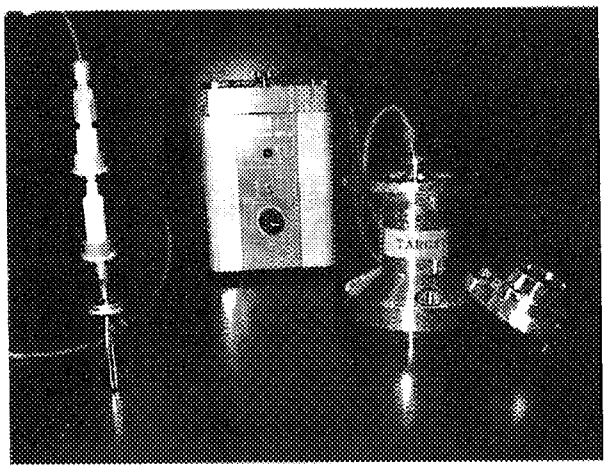

Fig.1 The recovery system of the irradiated water target for producing ^{13}N and ^{18}F in water. The operation is done with manipulators.

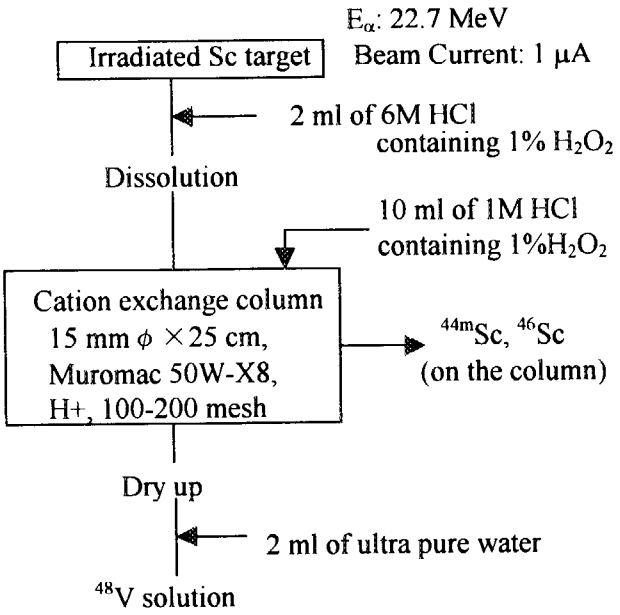

Fig.3 Chemical procedure of the separation of ^{48}V from a Sc target.

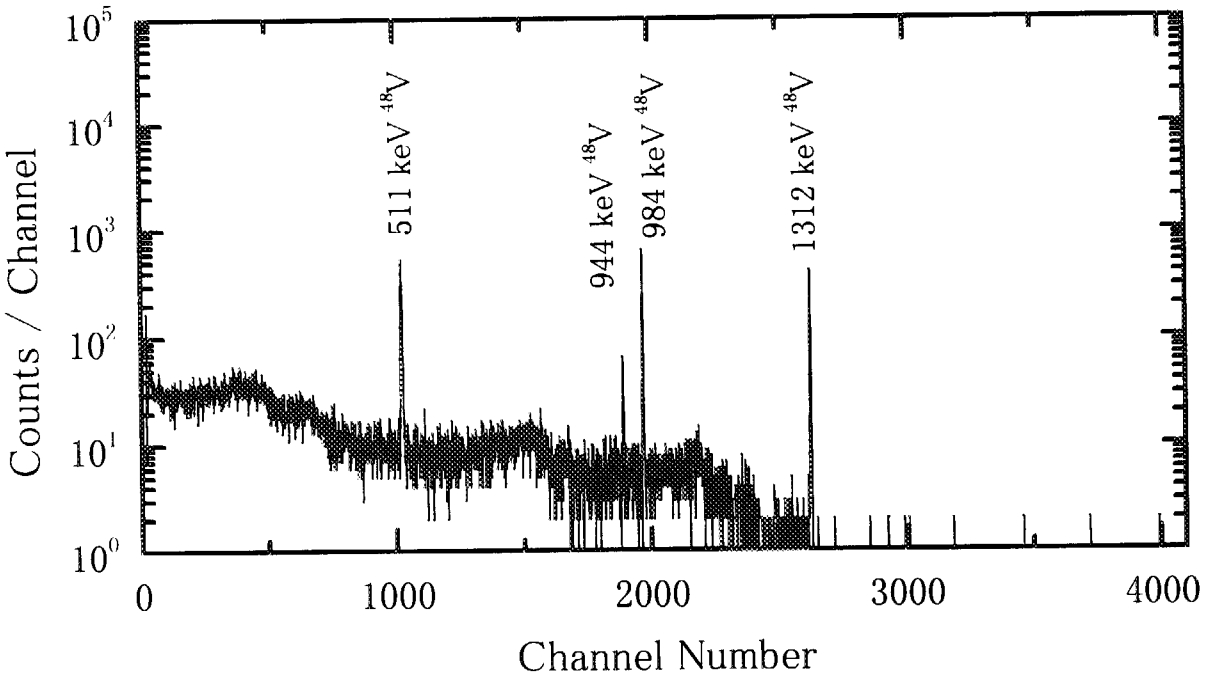

Fig 2 A γ-ray spectrum of the purified ^{48}V solution.

6. 2 Development of a Laser Ion Source for the TIARA-ISOL

M. Koizumi[1], A. Osa, T. Sekine[1], T. Wakui[2], M. Kubota[2], W.G. Jin[2], T. Minowa[2], and H. Katsuragawa[2]
[1] Department of Materials Science, JAERI
[2] Department of Physics, Faculty of Science, Toho University

1. Introduction

We have continued the development of a laser ion source (LIS), which is based on a technique of resonance ionization of atoms [1], for element selection in on-line isotope separation. In this ion source, atoms are excited stepwise to the ionization state through the atomic levels by two or three laser beams. The combination of an LIS with a mass separator, therefore, has the capability of providing mono-isotopic radioactive beams [2-3]. The resulting reduction of isobars of the isotope of interest is useful for low background measurements in decay spectroscopy and laser spectroscopy. As reported previously [4-5], a hot-cavity-type LIS, named FLINT-IS, was constructed for the TIARA-ISOL. This report describes on-line experiments on the effect of a primary beam to photoionization.

2. Experimental

Experiments were carried out for different mountings, as shown in fig. 1, of a catcher that catches recoiling products from the target. When a catcher is mounted at position 1, radioactive products, after diffusing through the catcher, have to pass through the gap between the catcher and the body of the ion source to reach the ionization cavity. The on-line experiment reported in ref. 5. was done with a catcher mounted at position 1. When a catcher is mounted at position 2, on the other hand, radioactive products reach the ionization cavity rather directly.

Ionization by the FLINT-IS was tested with the radioactive isotope, ^{128}Ba ($T_{1/2}$ = 2.43 d) produced with the ^{nat}Mo (^{36}Ar, 4pxn) ^{128}Ba reaction. The incident $^{36}Ar^{8+}$ beam used was 195 MeV in energy, and about 1.5 eμA in beam current. A schematic diagram of the target-ion-source of the FLINT-IS is shown in fig. 1. The target was mounted about 5 mm away from the window. Radioactive fusion-reaction products were stopped in a catcher of 25 mg/cm^2 in thickness. The thickness of the target and the window were 3 mg/cm^2, and 8.3 mg/cm^2, respectively. The mass-separated $^{128}Ba^+$ ions were detected with a particle detector (Murata, Ceratron EMT-6081B) at the

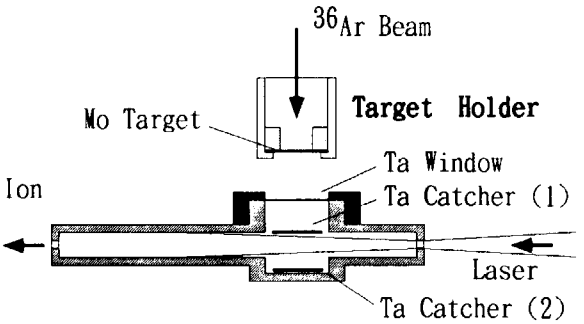

Fig. 1. A schematic diagram of the FLINT-IS. A Ta catcher foil was mounted at position 1 (between the laser beams and the Ta window) or at position 2 (at the bottom of the cavity).

end of the TIARA-ISOL beam line. The particle signals were counted with a multi-channel scaler (MCS); the start signal was given by the laser shot.

We employed a two-color two-step ionization scheme, as described preciously [5], using the laser system shown in Fig. 2. This laser system is characterized by a long pass of lasers, including a 30-m quartz fiber, from ISOL Room to the target room, Light-Ion Room 1. Within the pass of lasers there must be a number of mirrors and lenses. The number of mirrors and lenses were reduced, and mirrors with high reflection were applied.

3. Results and discussion

The laser powers at the entrance window of the FLINT-IS was increased by a factor of about 10 compared with those of the previous report [5]. The energies of the laser beams were about 800 μJ for the 553.5-nm first-step, and about 160 μJ for the 396-nm second-step.

Photoions were detected with the catcher mounted at position 1, but they could not be detected with the catcher mounted at position 2. This result is ascribable to the effect of a plasma produced by the incident beam, which sputters the surface of the catcher and produces ions and electrons, as known for an ion-guide ion source [6]. The plasma may cause recombination of photoions with electrons. The catcher at position 1 can prevent the plasma from affecting atoms in the ionization cavity.

References

[1] V.S. Letokhov, Laser Photoionization Spectroscopy (Academic Press. 1987).

[2] V.I. Mishin, V.N. Fedoseyev, H.-J. Kluge, V.S. Letokhov, H.L. Ravn, F. Scheerer, Y. Shirakabe, S. Sundell, O. Tengblad and the ISOLDE Collaboration, Nucl. Instr. Meth. B73 (1993) 550.

[3] V.N. Fedoseyev, Y. Jading, O.C. Jonsson, R. Kirchner, K.-L. Kratz, M. Krieg, E. Kugler, J. Lettry, T. Mehren, V.I. Mishin, H.L. Ravn, T. Rauscher, H.L. Ravn, F. Scheerer, O. Tengblad, P. Van Duppen, A. Wöhr, and The ISOLDE Collaboration, Z. Phys. A353 (1995) 9.

[4] M. Koizumi, A. Osa, T. Sekine, and M. Kubota, Nucl. Instr. and Meth. B126 (1997) 100.

[5] M. Koizumi, A. Osa, T. Sekine, T. Horiguchi, and M. Asai, JAERI TIARA Ann. Rep. 15 (1997) 183.

[6] K. Morita, T. Inamura, T. Nomura, J. Tanaka, H. Miyatake, M. Fujioka, T. Shinozuka, M. Yoshii, H. Hama, K. Taguchi, K. Sueki, Y. Hatsukawa, K. Furuno, and H. Kudo, Nucl. Instr. and Meth. B26 (1987)406.

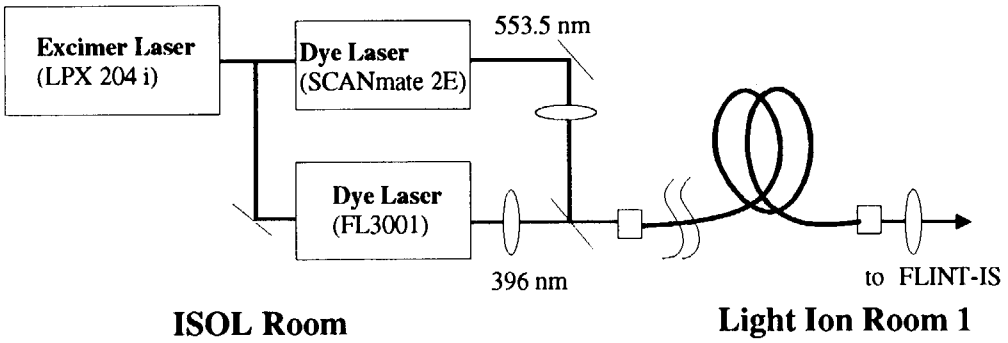

Fig. 2. A schematic diagram of the laser system. The excimer laser was triggered by a pulse generator. The mirror in front of the entrance of the optical fiber has a dielectric-multiple-layer coating for reflection of 532-nm Nd:YAG laser.

6. 3 Production of polarized unstable nuclear beam by grazing ion - surface scattering

T. Ohtsubo, S. Ohya, H. Kimura*, K. Hori*, S. Yachida*, S. Muto**, T. Sekine***, M. Koizumi*** and A. Osa***

Department of Physics, Niigata University, *Graduate School of Science and Technology, Niigata University, **KEK ***Department of Materials Science, JAERI

The polarized unstable nuclear beams are very useful for investigating not only nuclear physics but also material science. The nuclear magnetic resonance (NMR) of the polarized unstable nuclei can be detected by observing the change of the angular distribution of the radiation. The high sensitivity of the NMR with radiation detection allows the study of extremely dilute samples in condensed matter or the determination of nuclear moments.

The technique of the ion beam surface interaction at grazing incidence (IBSIGI) is one of the method for production of the polarized ion beam [1,2]. After the interaction of fast ions with a solid surface at grazing angle, a large atomic polarization yields for the scattered ion. During flight in free space, a fraction of the atomic polarization is transferred to nuclei via the hyperfine interaction. Andrä observed the large nuclear polarization for ^{14}N stable nuclei by IBSIGI method [1]. The purpose of the present investigation was to observe directly the nuclear polarization of unstable nuclei created by IBSIGI method.

A 60 keV ^{124}Cs ($T_{1/2}$ = 30.8 s) beam from the on-line isotope separator (ISOL) at the Japan Atomic Energy Research Institute (JAERI), Takasaki. was used in this study. The Cs activities were produced using Mo(^{36}Ar, xnyp) reactions with a 195 MeV ^{36}Ar beam. They were ionized in a surface-ionization ion source of the mass separator and ^{124}Cs ions were separated from other isotopes. The ^{124}Cs beam was collimated by a narrow slit and bent onto the target of Si single crystal by an electric field of 440 V/cm. The scattered ions passed through a free space and implanted in a KBr single crystal stopper. The static magnetic field B_0 of 0.1 T parallel to the polarization axis was applied at the KBr stopper in order to maintain the nuclear polarization during the implantation. The cancellation-magnetic field were applied between the target and stopper, because the strong leakage field of B_0 decouples the atomic and nuclear spins. Typical magnetic field in the flight path was less than 10 gauss. To detect the β-ray asymmetry , two sets of the plastic scintillator of 40 x 40 x 2 mm were placed at 0° and 180° with respect to the polarization axis. For the NMR, an rf oscillating field was applied perpendicular to B_0. The magnetic moment of ^{124}Cs is known as $\mu(^{124}\mathrm{Cs}) = +0.673(3)\ \mu_N$ [3]. With the value of the magnetic moment and B_0 an expected value of the resonance frequency is calculated to be 515 kHz. Therefore we applied the rf frequency of 500 ± 100 kHz. The nuclear polarization was observed by the β-ray asymmetry change with the rf filed. Figure 1 shows the experimental set up.

Fig. 2 shows the experimental results. Open circles are the experimental data and closed ones are the weighted mean. The observed polarization was 0.15(9) %. This small value is mainly due to the low beam velocity. Freier studied the beam velocity dependence of the atomic and nuclear polarization of ^{14}N [5]. The observed polarization is in agreement with their data on the present condition of the velocity.

For the next step, we will use the ^{21}Na beam. Since the electromagnetic properties of ^{21}Na are well known, it is suitable for

observing the nuclear polarization. The velocity of ^{21}Na from ISOL is about 6 times faster than one of ^{124}Cs. Therefore the large nuclear polarization is expected from the velocity dependence of the polarization in IBSIGI method.

Reference

[1] H.J. Andrä, *Hyperfine Interactions* 5 (1978) 403.
[2] H. Winter and R. Zimmy, *Hyperfine Interactions* 22 (1985) 237.
[3] P. Raghavan, *Atomic Data and Nuclear Data Table* 42 (1989) 190.
[4] S. Momota, Doctor Thesis, Osaka University, 1995.
[5] R. Freier and H. Winter, *Hyperfine Interactions* 73 (1992) 323

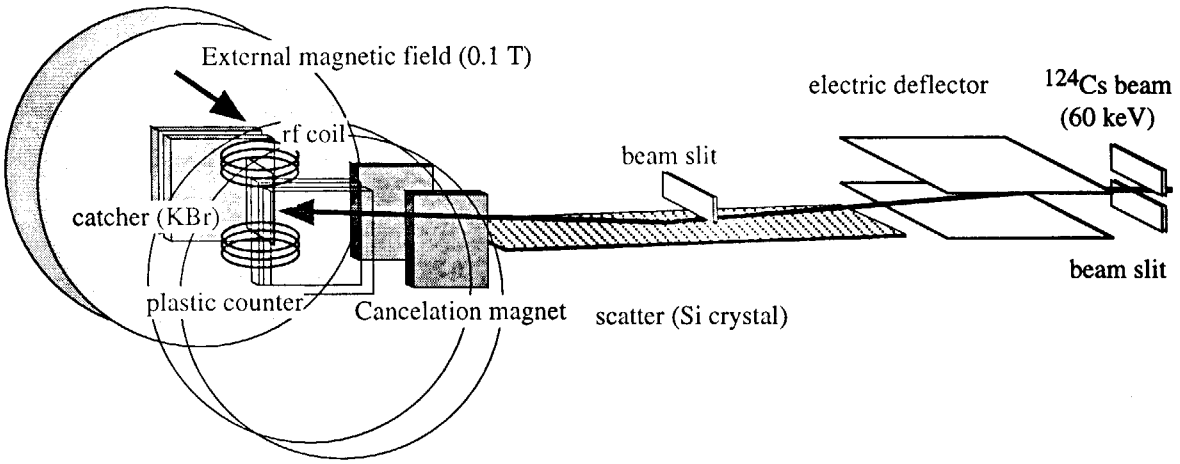

Fig. 1. Experimental setup.

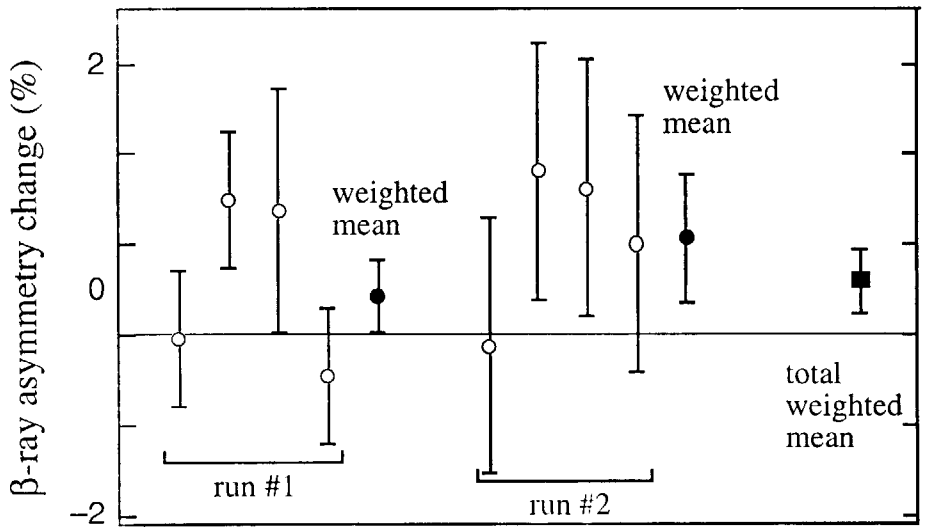

Fig. 2 Summary of experimental result.

The vertical axis shows the β-ray asymmetry change with the nuclear magnetic resonance. Open circles show the experimental data. Closed circles show the weighted mean of each run. A closed square shows the weighted mean of total data.

6. 4 Q_{EC} Measurement of ^{124,125,129,130}La

Y. Kojima, T. Hirose, M. Shibata, H. Yamamoto, K. Kawade,
A. Osa*, S. Watanabe**, M. Koizumi* and T. Sekine*
School of Engineering, Nagoya University, * Department of Materials Science and **Department of Radioisotopes, JAERI

1. Introduction

Atomic masses are one of the most fundamental quantities because they manifest all interactions contributing to nuclear binding. Precise experimental values on atomic masses of unstable nuclei provide an essential input to theoretical efforts to refine and develop nuclear models. The comparison between experimental masses and theoretical predictions tests the reliability of extrapolation of mass formulas into unknown mass regions.

The measurement of Q_{β}-values with a small HPGe detector is convenient to determine atomic masses, especially for short-lived nuclei[1]. In the present work, this method was applied to measurements of β^+-ray maximum energies of ^{124,125,129,130}La at the TIARA isotope separator on-line. In order to check the reliability of atomic mass models, the atomic masses derived from the Q_{EC}-values were compared with theoretical predictions.

2. Experiment

The ^{124,125,129,130}La activities were produced by heavy-ion fusion-evaporation reactions at the TIARA-ISOL connected with the JAERI AVF cyclotron[2]. The 195-MeV $^{36}Ar^{8+}$ beam with an intensity of about 0.12 particle μA was delivered upon a 3 mg/cm^2 thick molybdenum target foil. The targets used for producing of ^{124,125}La and ^{129,130}La nuclides were ^{92}Mo and ^{nat}Mo, respectively. Reaction products were ionized in a thermal ion source and mass-separated as a chemical form of LaO. The mass-separated ions were implanted into an aluminum-coated Mylar tape in a tape-transport system. The sources were periodically transported to a detector station for γ-ray measurements at time intervals adjusted to individual half-life of ^{124,125,129,130}La[3].

Beta-ray singles and β-r coincidence measurements were performed with a planar-type HPGe detector (25mm ϕ x13mm^t) for β-rays and a 28.4% n-type HPGe detector for γ-rays. Beta-ray spectra were measured through a 50 μm^t Mylar window. In the β^+-ray measurements, the main amplifier was operated in a short shaping time constant of 0.5 μs, and the counting rate of the singles spectrum measurement was kept below 3000 cps to reduce a pulse-pileup effect. The coincidence data were recorded in event by event mode. About 6×10^7 coincidence events were accumulated during a measuring period of 36 ~74 h for each nuclide.

Energy calibration of the β^+-ray detector was made up to 8.6 MeV using a standard γ-ray source of ^{56}Co and prompt γ-rays in the thermal neutron capture of ^{35}Cl. The thermal neutrons were generated by a ^{252}Cf neutron source of about 700 kBq.

Overall energy loss was estimated to be 120keV for positrons in an energy of 1-6 MeV. The systematic error of the β^+-ray maximum energy determination was estimated to be 10~20keV in an energy range below 5 MeV. The detailed analysis procedure of a β^+-ray spectrum was described in ref 5.

3. Results and discussion

After each of the β^+-ray spectra obtained was unfolded with experimental response functions for monoenergetic positrons[4-6], the Fermi-Kurie plot was produced. The endpoint energy of the β^+-rays was derived from the fit of a straight line using the maximum likelihood

method for Poisson distribution.

^{124}La ; There are two isomers in ^{124}La. Relatively strong β^+/EC feeding to the levels of 2690.6 (~4%) and 3094.9keV (~10%) were observed in the decay of the high-spin isomers. Endpoint energies of the β^+ rays were determined to be 5200 (160) and 4830 (140) keV, respectively. The resulting Q_{EC}-value of 8930 (110) keV is somewhat larger than the evaluated one of 8800 (300) keV by Audi and Wapstra.

^{125}La ; Fermi-Kurie plots of the unfolded β^+-ray spectra feeding the levels of 1284.2 and 1311.0 keV are shown in Fig.1. Beta-ray maximum energies to these levels were found to be 3650 (90) and 3610 (100) keV, respectively. The resulting Q_{EC}-value of 5950 (70) keV is 310keV higher than the value evaluated from the systematic trends.

^{129}La ; Beta-ray maximum energies to the levels of 110.6 (14%) and 278.6 (25%) keV were determined to be 2600 (70) and 2440 (50) keV, respectively. The resulting value of 3740 (40) keV was adopted for the Q_{EC}-value of ^{129}La. The present value is in good agreement with the previous result.

^{130}La ; Beta-ray maximum energies feeding the levels of 357.2 (19%) and 907.7 keV (22%) were determined to be 4260 (120) and 3740 (90) keV, respectively. The deduced Q_{EC}-value of 5660 (70) keV agrees with the evaluated value of 5600 (210) keV.

The present result are summarized in Table1, together with the evaluated Q_{EC}-values by Audi and Wapstra[7]. The Q_{EC}-values of ^{124,125,130}La nuclides were newly obtained from the present study. For ^{129}La, the present value was in agreement with the previous result. The Q_{EC}-values of ^{124,125}La are 100-300keV more heavier than the evaluated values, while the masses of ^{129,130}La are in good agreement with the evaluated ones. These Q_{EC}-values provide useful input data to the atomic mass evaluation.

The experimental masses were compared with theoretical predictions, as shown in Fig. 2. The best agreement with the experimental masses is observed for the empirical mass formula of Tachibana et al.

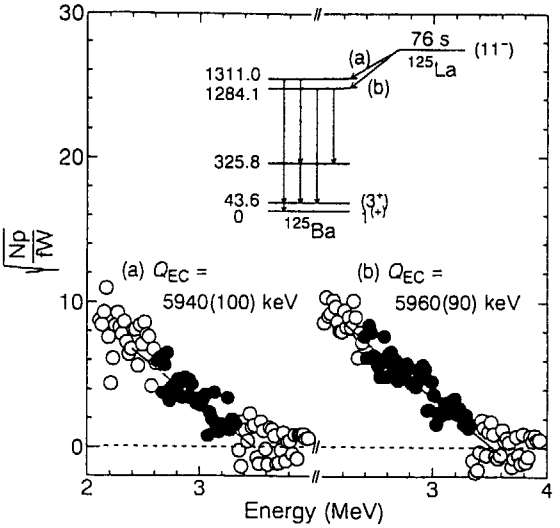

Fig. 1. Fermi-Kurie plots of the unfolded β^+-ray spectra of ^{125}La feeding the 1284.1 and 1311.0 keV levels of ^{125}Ba. Fitting regions are represented by closed circles. A partial decay scheme is shown in the inset.

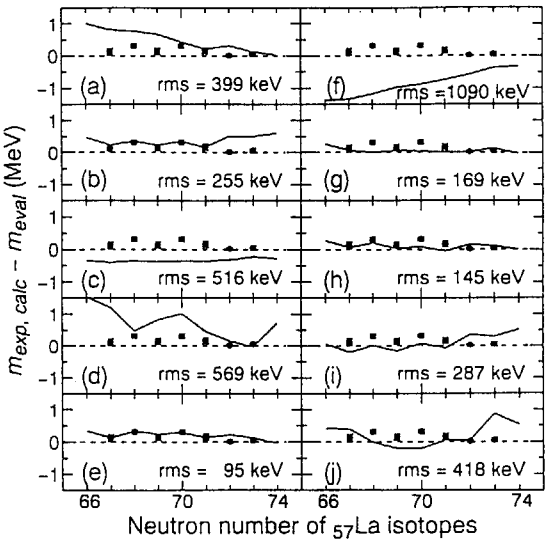

Fig. 2. Deviation of the experimental atomic masses, m_{exp}, and the calculated values by mass formulas, m_{calc}, from the evaluated values, m_{eval}, of La isotopes by Audi and Wapstra. The present values are represented by closed circles. The following mass formulas are considered : (a) Dussel et al., (b) Moller and Nix, (c) Comay et al., (d) Satpathy and Nayak, (e) Tachibana et al., (f) Spanier and Johansson, (g) Janecke and Masson, (h) Masson and Janecke, (i) Moller et al., (j) Aboussir et al., The root-mean square of the mass differences is given for each formula.

Atomic masses of ^{124,125}La are well reproduced by the unified model of Moller and Nix[8]. For ^{129,130}La isotopes, however, calculated masses are about 500 keV larger than the present results. Large discrepancies from the present results are observed for the formula of Spanier and Johansson[9]. All predicted values are smaller than the experimental masses. The differences increase with decreasing neutron number.

4. Conclusions

By unfolding the β^+-ray spectra using experimental response functions, the Q_{EC}-values of ^{124,125,129,130}La were newly obtained. The Q_{EC}-values of ^{124,125}La are 100-300 keV more heavier than the evaluated values. The best agreement was observed for the mass formula of Tachibana et al. All predicted values are smaller than the experimental masses.

References

[1] A.Osa,T.Ikuta,K.Kawade, H.Yamamoto and S.Ichikawa, J. Phys. Soc. Jpn. 65 (1996) 928.

[2] T.Sekine,A.Osa,M.Koizumi,S.Ichikawa, M.Asai,H.Yamamoto and K.Kawade, Z. Phys. A349 (1994) 143.

[3] M.Asai,K.Kawade,H.Yamamoto,A.Osa, M.Koizumi and T.Sekine, Nucl. Instr. and Meth. A398 (1997) 265

[4] A.Osa,T.Ikuta,M.Shibata,M.Miyachi, H.Yamamoto,K.Kawade,Y.Kawase and S.Ichikawa, Nucl. Instr. and Meth. A332 (1993) 169.

[5] Y.Kojima,T.Ikuta,M.Asai,A.Taniguchi, M.Shibata,H.Yamamoto and K.Kawade, Nucl. Instr. and Meth. B126 (1997) 419.

[6] Y.Kojima,M.Asai,A.Osa,M.Koizumi, T.Sekine,M.Shibata,H.Yamamoto, K.Kawade and T.Tachibana, J. Phys. Soc. Jpn., in press

[7] G.Audi and A.H.Wapstra, Nucl. Phys. A595 (1995) 409.

[8] P.Moller and J.R.Nix, Atomic Data and Nucl. Data Tables 39 (1988) 213.

[9] L.Spanier and S.A.E.Johansson, Atomic Data and Nucl. Data Tables 39 (1988) 259.

Table 1: Experimental Q_{EC}-values of $^{124-130}$La deduced from the present study compared with the previous and the evaluated values.

Nuclide	Half-life	Level (keV)	Endpoint energy[c] (MeV)	Q_{EC}-value Present (MeV)	Averaged (MeV)	Evaluated[b] (MeV)
^{124}La	29 s	2690.6	5.20(16)	8.91(16)	8.93(11)	8.80(30)#
		3094.9	4.83(14)	8.95(14)		
^{125}La	1.3 m	1284.1	3.65(9)	5.96(9)	5.95(7)	5.64(39)#
		1311.0	3.61(10)	5.94(10)		
^{129}La	11.6 m	110.6	2.60(7)	3.73(7)	3.74(4)	3.72(5)
		278.6	2.44(5)	3.74(5)		
^{130}La	8.7 m	357.2	4.26(12)	5.64(12)	5.66(7)	5.60(21)#
		907.7	3.74(9)	5.67(9)		

[a] The experimental error of the β^+-ray endpoint energy is obtained by quadratic addition of the statistical and the systematic uncertainty.

[b] Audi and Wapstra. The mark of # represents a value estimated from the systematic trends.

6. 5 Development of a Radioactive Endovascular Stent by Implantation of ^{133}Xe Ions

S. Watanabe[1], A. Osa[2], T. Sekine[2], N. S. Ishioka[1], M. Koizumi[2], T. Kojima[3], A. Hasegawa[4], M. Yoshii[4] and R. Nagai[4]

[1]Department of Radioisotopes, [2]Department of Materials Science and [3]Advanced Radiation Technology Center, JAERI and [4]School of Medicine, Gunma University

1. Introduction

The application of radioisotopes is now extending to the therapy of arteriosclerosis in coronary arteries. Radiation therapy is expected to limit restenosis that seriously matters in percutaneous transluminal coronary angioplasty (PTCA) and is the re-narrowing of the blood vessel after PTCA. Because ionizing radiation, β- or γ-ray, may give an antiproliferative effect to intimal cells of the blood vessel, endovascular irradiation techniques are under development both for balloon angioplasty and for stent angioplasty. The irradiation techniques on the former, developed better than those on the latter, are summarized by Waksman.[1] The latter is the concern of the present work.

In stent angioplasty, stents, which are made of alloy and are expandable, are implanted into a narrowing artery to expand it. About 40% of the operations of PTCA involve stent implantation.[1] However, restenosis occurs in about 20% of patients.[2-5] There are two ways in endovascular irradiation for stent angioplasty: short-period irradiation with a sealed β- or γ-ray source before stent implantation; and activation of stents with β- or γ-ray emitters. The former is almost the same as the technique for balloon.[1]

Stents can be activated by charged-particle irradiation using a cyclotron.[6] Charged particle-induced reactions may produce many radioisotopes, some of which are not wanted. On the other hand, ion-implantation, which uses an electromagnetic isotope separator, allows us to activate stents with a single radioisotope. Electroplating is also proposed for the activation of stents with ^{48}V.[7] Ion-implantation can be applied even to a non-metallic element, if it is ionized.

In the literature, ion-implantation has been applied to activation of stents only with ^{32}P. It was reported that ^{32}P-implanted stents inhibited neointimal hyperplasia, which cause restenosis after stent placement, in rabbit iliac arteries[8] and in porcine coronary arteries.[9]

Because the entire mechanism of the inhibition of neointimal hyperplasia by endovascular irradiation has not been cleared yet, a minimum range of effective endovascular irradiation is not known. Phosphorus-32, decaying with a half-life of 14.3 d, emitting a β-ray with a maximum energy of 1.711 MeV, has a rather long range (maximum range in water: 8.5 mm) corresponding to its high β-ray maximum energy. Therefore, use should be made of another radioisotope with a smaller β-ray maximum energy than that of ^{32}P. A search of the nuclear chart has suggested that ^{133}Xe is a nuclide adequate for this aim because of its nuclear characteristics and the easy ionization of xenon atoms. Xenon-133 decays with a half-life of 5.25 d, emitting a beta-ray with a maximum energy of 0.346 MeV (maximum range in water: 1.0 mm), followed by a gamma-ray of 81 keV or a conversion electron competing in the 81-keV γ transition. If ^{133}Xe-implanted stents can inhibit restenosis, they will reduce the risk to surrounding nontarget tissues further than ^{32}P-implanted stents.

The present work aims at developing a method of implantation of ^{133}Xe ions into stents. Although completely homogeneous implantation on the surface of a stent is not realized within this paper, stents obtained can be used in an animal experiment. Some characteristics of the ^{133}Xe-implanted stents are described together with the

first animal experiments using them.

2. Experimental

Implantation of ^{133}Xe ions into stents was carried out with the isotope separator installed at the TIARA (Takasaki Ion Accelerators for Advanced Radiation Application) facility in Japan Atomic Energy Research Institute. The isotope separator has a 55° analyzing magnet 1.5 m in radius and a Nielsen ion source (Danfysik model 910). Its mass resolution $M/\Delta M$ is 1000, and its mass dispersion on the focal plane 1500 mm/M. Use was made of tubular slot stainless steel stents 14 mm in length and 1.4 mm in outer diameter and a standard gas containing 40 MBq of ^{133}Xe supplied by the Radiochemical Center Amersham. The ^{133}Xe gas was transferred from the ampoule to a 3.8 L stainless steel bomb through a glass vacuum line and was diluted with about 3 cm^3 of enriched ^{129}Xe gas; the ^{129}Xe atoms worked as a mass marker in mass separation. Xenon atoms supplied from the bomb through a stainless steel tube were ionized in the ion source of the isotope separator. Xenon-133 ions were accelerated to an energy of 40 or 60 keV, mass-separated and implanted into six or eight stents mounted on a target-holder table which was set on the focal plane of the isotope separator. Three different target-holder tables were used to distribute $^{133}Xe^+$ ions within a stent as well as among the stents, as described later. It took 20 h to use up a substantial portion of the xenon gas. Immediately after ion-implantation, a γ-ray spectrum of each of the stents was measured with a germanium detector. The ^{133}Xe radioactivity was determined from the 81-keV γ-ray intensity in comparison with that of a calibrated ^{133}Ba source. The radiation dose of a stent was measured for some of the stents with a GAF film. A GAF film with a 0.01 mm-thick sensitive layer for radiation was exposed to a stent in contact with each other for 3 weeks.

Figure 1 shows the arrangement of stents on three different target-holder tables against the ^{133}Xe beam. An approximate FWHM (full width at half maximum) of the ^{133}Xe beam, calculated from the mass resolution and mass dispersion, is also indicated. The first target-holder table (Fig. 1a) is stationary, having six pins 20 mm long and 1 mm in diameter to hold stents. The second one (Fig. 1b) can revolve on the center of the table, having ten pins. Eight stents were mounted on it, as shown in Fig. 1b, and it was rotated once an hour by 90°. The third one (Fig. 1c) can revolve with an additional movement up and down the revolving axis by 10 mm, having eight pins. This target-holder table revolved continuously ten times a minute, and moved up and down sixteen times a minute.

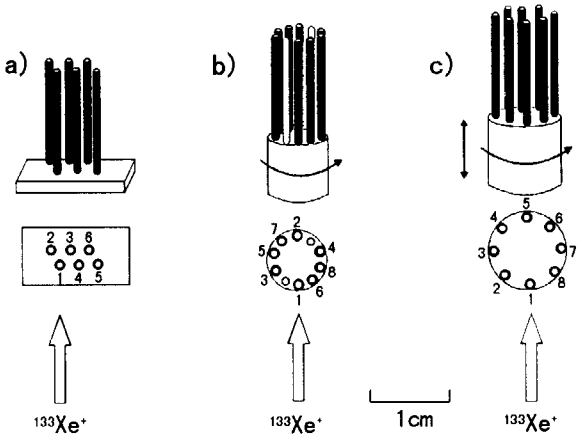

Fig.1 Three target-holder tables to arrange stents against the $^{133}Xe^+$ beam: (a) a stationary target-holder table; (b) a revolving target-holder table; (c) a revolving and moving up and down target-holder table.

3. Results and Discussion

Radioactivity of stents

The radioactivity of the stents produced is listed in Table 1. Runs 1, 2 and 3 correspond to the experiments using the first, second and third target-holder tables mentioned above, respectively. In each run stents are numbered in descending order of radioactivity, and the same numbers are given in Fig. 1. The results of Run 1 indicated that ^{133}Xe ions were implanted effectively only into stents No. 1 and No. 2, and the amount of ^{133}Xe radioactivity in a stent decreases very rapidly with increasing distance from stent No.1. This method could not produce more than two stents

with the same radioactivity level within one experimental run. Homogeneity for radioactivity among the stents was increased very much with the second target-holder table, although an effect of intermittent rotation can be seen in the radioactivities of the stents. With its continuous rotation, the third target-holder table gave almost the same radioactivities to the stents.

Table 1 Radioactivity and radiation dose of the ^{133}Xe-implanted stents produced.

Run	Stent No.	Radioactivity / kBq	Radiation dose / kGy
1	1	3.02±0.07	
	2	1.53±0.04	
	3	0.583±0.015	
	4	0.474±0.012	
	5	0.041±0.02	
	6	0.035±0.02	
2	1	97.9±2.0	
	2	93.4±1.9	
	3	74.5±1.5	
	4	40.7±0.8	
	5	36.9±0.8	
	6	24.9±0.5	
	7	22.9±0.5	maximum: 0.16
	8	12.8±0.3	maximum: 0.21
3	1	81.8±1.7	
	2	77.1±1.6	
	3	74.5±1.5	
	4	73.8±1.5	
	5	71.7±1.5	
	6	65.9±1.3	
	7	15.0±0.4	<0.1
	8	11.8±0.3	<0.1

Radiation dose

Experimental data on the radiation dose within a range of 0.01 mm from a stents is also listed in Table 1. Different values of radiation dose were observed on a GAF film because of incomplete homogeneity of radioactivity distribution on a stent. Therefore, a maximum of observed values is listed in Table 1. Owing to the same reason, the maximum radiation dose of a stent is not proportional to its radioactivity, as seen from the data on the 2-7 and 2-8 stents. However, it should be noted that the value 0.21 kGy is considered enough to give biomedical effects.

Though the radioactivity of the 3-7 and 3-8 stents are in the same order of magnitude with that of the 2-7 and 2-8 stents, the radiation dose of the 3-7 and 3-8 stents was lower than the detection limit of the GAF film which was about 0.1 kGy. This is because the distribution of ^{133}Xe in the 3-7 and 3-8 stents is more homogeneous than that of the 2-7 and 2-8 stents.

Animal experiment with ^{133}Xe-implanted stents

Some of the radioactive stents produced were applied to an animal experiment with New Zealand white rabbits. A stent was implanted in an abdominal aorta injured by balloon overstretch. Four weeks after stent implantation, the animals were sacrificed. The abdominal aortas were harvested, and the regions in which stents were implanted were sliced, stained with hematoxylin-eosin and analyzed by histomorphometry. The same experiments were carried out with non-radioactive stents for comparison. The results indicate that, in a few cases, neointimal thickening was suppressed by the ^{133}Xe-implanted stents. To obtain a concrete conclusion, however, we need further biological studies.

Acknowledgment

The present work is partially supported by the REIMEI Research Resources of Japan Atomic Energy Research Institute.

References

1) R. Waksman, Am. J. Cardiol. **78[suppl 3A]**(1996)23.
2) D. L. Fischman et al., N. Engl. J. Med. **311**(1994)496.
3) M. P. Savage et al., J. Am. Coll. Cardiol. **24**(1994)1207.
4) A. Kastrati et al., Circulation **96**(1997)462.
5) R. Albiero et al., Circulation **96**(1997)2997.
6) C. Hehrlein et al., Circulation **92**(1995)1570.
7) R. J. Nickles et al., J. Nucl. Med. **38[5 suppl](1997)**7P.
8) C. Hehrlein et al., Circulation **93**(1996)641.
9) A. J. Carter et al., Circulation **94** (1996)2364.

This is a blank page.

7. Radiation Shielding for Accelerator Facility

This is a blank page.

7. 1 Measurements of Residual Radionuclides by ^{12}C-induced Reactions on Co

Su. Tanaka, K. Nishimura, M. Hosono, M. Fukuda, S. Meigo[2], S. Chiba[3], T. Fukahori[3], O. Iwamoto[3], T. Nakamura[4]

Advanced Radiation Technology Center, JAERI/Takasaki, Center for Neutron Science, JAERI/Tokai [2], Dept. Reactor Engineering, JAERI/Tokai [3], Cyclotron R.I. Center, Tohoku Univ.[4]

1. Introduction

Recently high-energy accelerators are widely used for a variety of purposes. Radioactivity is induced in the accelerator components and target samples irradiated with energetic ion beams and secondary produced neutrons. In the planning stage of irradiation, estimation of the induced radioactivity is important for radiation protection to reduce the radioactivity and to minimize radiation exposure to personnel as well as the amount of radioactive wastes. An IRACM code system[1] has been developed at JAERI to calculate the radioactivity and a gamma-ray dose rate. However, the radioactivity calculated by the IRACM has a large ambiguity because activation cross sections for heavy ion induced reaction have not been properly evaluated yet. The IRACM code system is required to be improved by comparing the calculated values with the experimental data. Hence we first start measuring residual radionuclides generated by ^{12}C-induced reactions on a target element Co using conventional gamma-spectrometry.

2. Experiment

The residual radionuclides were measured by the activation method using the stacked-foil technique. The irradiated target had 25 mm x 25 mm in area. The target was high purity material containing 99.9% Co. The stacked-file consisted of 0.01 mm thick foils. The thickness of the stacked-foil was selected overall to be longer than the projected range of a 220-MeV ^{12}C ion in Co.

The 220-MeV $^{12}C^{5+}$ ions accelerated by the TIARA AVF cyclotron were delivered to a simultaneous irradiation system[2] consisting of a Faraday cup and the target foils. The beam was uniformly scanned on the target foils and the Farady cup. The number of $^{12}C^{5+}$ ions was estimated from the integrated charge measured with the Farady cup. The irradiation time was 3.75 hours with a beam current of 0.74 enA. After the irradiation, gamma-rays emitted from the irradiated foils were measured by the HP-Ge detector. The gamma-ray spectra obtained after the decay of all the parent nuclei were used for the analysis of the residual radionuclide production. The production rates of radionuclides identified from the gamma-ray spectra were estimated by the same method as the neutron experiment done by E. Kim[3]. Correction was not made for the decay of the parent in the calculation. Cumulative residual radionuclides investigated are shown in Table 1.

Table 1 Cumulative productions by the reactions of ^{12}C with ^{59}Co

Residue	Cumulative productions
^{52}Mn	$^{52}Mn + {}^{52}Fe$
^{55}Co	$^{55}Co + {}^{55}Ni$
^{56}Mn	$^{56}Mn + {}^{56}Cr$
^{56}Co	$^{56}Co + {}^{56}Ni$
^{57}Co	$^{57}Co + {}^{57}Ni$
^{58}Co	$^{58}Co + {}^{58m}Co$
^{61}Cu	$^{61}Cu + {}^{61}Zn$
^{62}Zn	$^{62}Zn + {}^{62}Ga$
^{63}Zn	$^{63}Zn + {}^{63}Ga$
^{66}Ga	$^{66}Ga + {}^{66}Ge + {}^{66}As$
^{66}Ge	$^{66}Ge + {}^{66}As$

3. Results and discussion

The total of measured activities corresponding to thick target yields are shown as a function of cooling time after the irradiation in figures 1 - 3, comparing with the activities calculated by the IRACM. Figures 1 and 2 show typical examples of activities of ^{56}Mn, ^{63}Zn, ^{66}Ge, ^{55}Co, ^{61}Cu, ^{62}Zn and ^{66}Ga

with half-lives shorter than 50 hours. The measured activities of ^{66}Ge, ^{66}Ga and ^{61}Cu were consistent with the calculated values within a factor of 3, but a large discrepancy was observed between the other measured activities and calculated values. Regarding the radionuclides with long-half-lives shown in the figure 3, the measured activities of ^{52}Mn, ^{56}Co and ^{57}Co agreed with the calculated values within a factor of 3, but the measured activities of ^{58}Co were larger than the calculated values over a factor of 10.

On all the three figures there were obvious discrepancies between the measured and calculated activities. In order to confirm the applicability of the IRACM code system, a detailed analysis of the residual nuclides is in progress.

The authors are indebted to M. Shimoyama, K. Matumoto and S. Kaneya for their helps in the irradiation and gamma-ray measurement.

References

1. Su. Tanaka et al., JAERI-Data/Code 97-019 (1997)
2. T. Kojima, Radiat. Phys. Chem. (in press)
3. E. Kim et al., Nucl. Sci. Eng., 129, 209(1998)

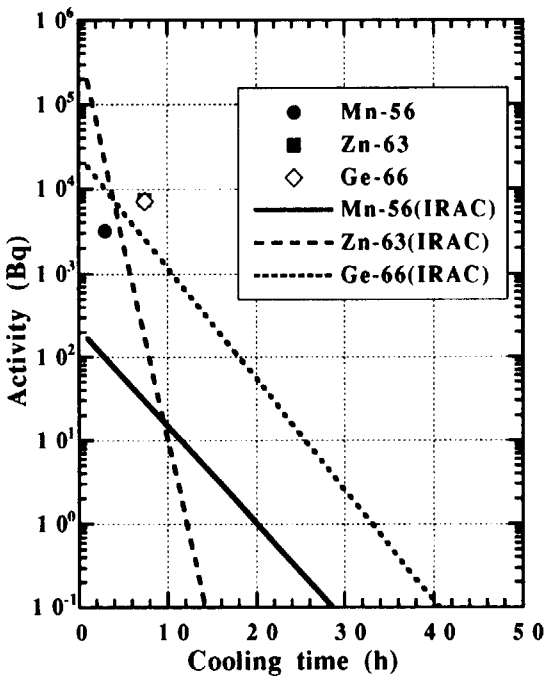

Fig.1 Comparison between the measured and calculated activities of ^{56}Mn, ^{63}Zn and ^{66}Ge in the bombardment of thick ^{59}Co target with 220-MeV ^{12}C ions.

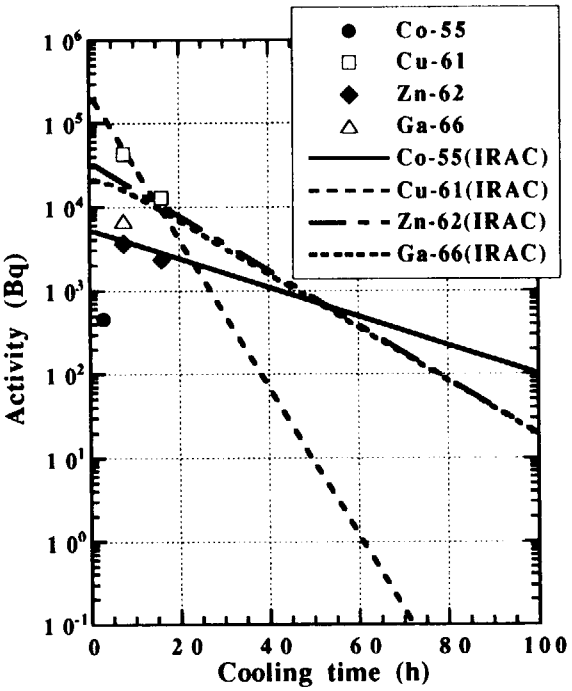

Fig.2 Comparison between the measured and calculated activities of ^{55}Co, ^{61}Cu, ^{62}Zn and ^{66}Ga in the bombardment of thick ^{59}Co target with 220-MeV ^{12}C ions.

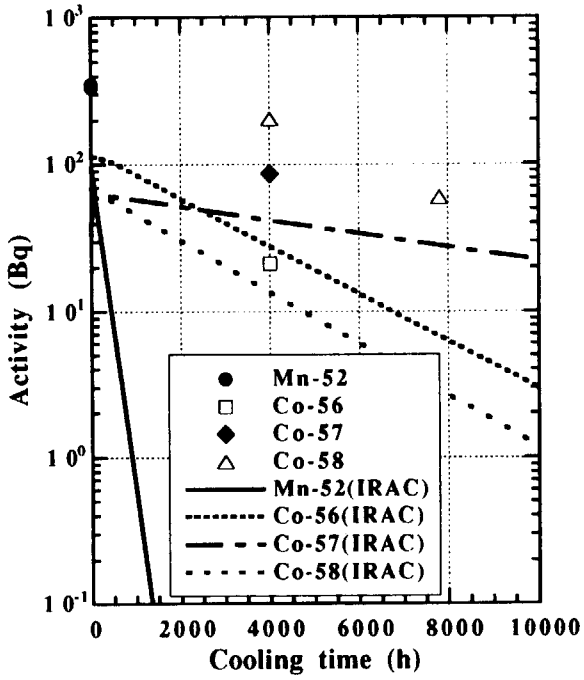

Fig.3 Comparison between the measured and calculated activities of ^{52}Mn, ^{56}Co, ^{57}Co and ^{58}Co in the bombardment of thick ^{59}Co target with 220-MeV ^{12}C ions.

7. 2 Study of secondary charged particle production from nuclear reactions induced by charged particles

M. Harada, A. Yamamoto, Y. Watanabe[2], K. Shin[3], S. Meigo[4], H. Nakashima[4], H. Takada[4], T. Sasa[4], T. Fukahori[5], O. Iwamoto[5], S. Chiba[6], and Su. Tanaka[7]

Dept. of Energy Conversion Engineering, Kyushu Univ.,
[2]Dept. of Advanced Energy Science Engineering, Kyushu Univ.,
[3]Dept. of Nuclear Engineering, Kyoto Univ.,
[4]Center for Neutron Science, JAERI, [5]Nuclear Data Center, JAERI,
[6]Advanced Science Research Center, JAERI,
[7]Advanced Radiation Technology Center, JAERI

1. Introduction

Neutron and proton nuclear data for ^{12}C are required in various applications, such as advanced cancer therapy using high-energy proton or neutron beam. Some of the authors have recently evaluated the neutron nuclear data and kerma factor of ^{12}C for energies up to 80 MeV[1]. As the next step, we have started evaluation of proton nuclear data for ^{12}C in the energy region up to 200 MeV.

Double-differential cross sections (DDXs) are needed for calculations of particle transport in matter. However, there is few systematic experimental data for the p+^{12}C reaction in the energy region from a few tens of MeV to 200 MeV.

In the present work, we have developed a system for measuring DDXs at the AVF cyclotron facility, TIARA, and have carried out two measurements with a carbon target:
(I) α-particle induced reaction at 50 MeV and (II) proton-induced reaction at 68 MeV. In this paper, preliminary results of the measurements are reported.

2. Measurement

The experiments were carried out using the HB-1 beam line at the AVF cyclotron facility. A 60 cmϕ scattering chamber was installed in the beam line as illustrated in Fig. 1. A beam dump made of carbon was placed at a distance of 3 m from the chamber for reduction of γ-ray backgrounds. A self-supporting natural carbon foil (0.5 mg/cm^2 in thickness) was located at the center of the chamber as a target.

In order to measure energy spectra of emitted charged-particles, we have used a counter telescope consisting of three detectors: two thin silicon ΔE-detectors (30 μm and 500 μm in thickness, respectively), and a CsI(Tl) E-detector (18 mmϕ x 30 mm) with photo-diode read-out. Those thickness and size were optimized using a Monte Carlo simulation of energy deposit in the detectors in which the effect of energy straggling was considered. The counter telescope was placed at a distance of 14.5 cm from the target in the scattering chamber and detected light-charged particles over a wide dynamic energy range, e.g. outgoing energies from 1.5 MeV to 90 MeV for proton.

Energy signals from each detector have been converted to digital data by using conventional NIM and CAMAC modules, and those data were stored event by event on an MO disk with SDAQ system[2]. Off-line data processing was made with PAW in CERNLIB[3].

In the experiment (I), DDXs of α-particles and protons were measured at angles of 20, 30, 50, 70, 90, 120 and 150 degrees in the laboratory system. In (II), all light charged particles (protons, deuterons, tritons, ^3He and α-particles) were measured at 25, 30, 35, 45, 60, 75, 90, 120 and 150 degrees in the laboratory system.

3. Results

Figure 2 shows measured differential cross sections of (α,α) scattering from ^{12}C at 50 MeV together with other data[4] and an optical model calculation[5]. The present experimental data are in excellent good agreement with Abele's data.

In Fig. 3, experimental differential cross sections of proton elastic scattering from ^{12}C at 68 MeV are compared with other data[6] and calculations based on the spherical optical model[7] and the soft-rotator model (SRM)[8]. The SRM prediction is in better agreement with the experimental data

Experimental DDXs of emitted protons and α-particles are shown from proton-induced reactions on ^{12}C at 68 MeV in Figs. 4 and 5. No data are seen in an energy interval of 1.5 MeV around 8 MeV in Fig. 4 and in an energy interval of 6 MeV around 33 MeV in Fig. 5, because of higher discrimination level that was set to eliminate the electric noise. Also, continuum proton spectra measured at angles less than 45 degree may include a background component due to edge-penetration of elastic protons in a defining collimator. The background component is now under investigation in detail.

To check the reliability of our measured data, the DDXs are compared with other experimental data[6,10] and LANL evaluation[9] in Fig. 6. Our data show overall agreement with other experimental data, although they are slightly smaller than the data of Bertrand and Peelle[6] at lower outgoing energies. The LANL evaluation underestimates the measured DDXs in the continuous region between 15 and 50 MeV at 30 degree, while it shows reasonable agreement with the expermental data for the other angles.

4. Summary

We have succeeded in measuring the DDXs of light charged particles (p, d, t, ^3He and α) produced from reactions induced by 68 MeV-proton and 50 MeV-α–particle for ^{12}C. The measurement system developed in the present work was found to be reliable and useful, although there was a difficulty on elimination of electric noise.

In the future, we plan further measurements of DDXs for some different incident energies (45 and 90 MeV) and other targets (^{27}Al and ^{90}Zr). These data will be useful for intermediate energy nuclear data evaluation.

Acknowledgments

This work was undertaken as the Universities-JAERI Collaboration Research Project. We wish to thank the staff of AVF cyclotron team for their cyclotron operation during our experiment.

References

1) M. Harada et al., J. of Nucl. & Technol. **34**, 116 (1997).
2) PAW-Physics Analysis Workstation CERN Program Library entry Q121 (1993).
3) K. Sato, Master thesis, Kyushu Univ,. (unpublished) (1993).
4) H Abele et al., Z. Phys. **A326**, 373 (1987)
5) V. Avrigeanu et al., Phys. Rev. C **49**, 2136 (1994).
6) F. E. Bertrand and R. W. Peelle., ORNL report ORNL-4799, (1973).
7) M. Ieiri et al., J. Phys. Soc. Jpn. **55**, suppl., 1106 (1986).
8) S. Chiba et al. Nucl. Phys. **A624**, 305 (1997).
9) M. B. Chadwick et al., Los Alamos LA150 Library (1997).
10) H. Sakai et al., Nucl. Phys. **A344**, 41 (1980)

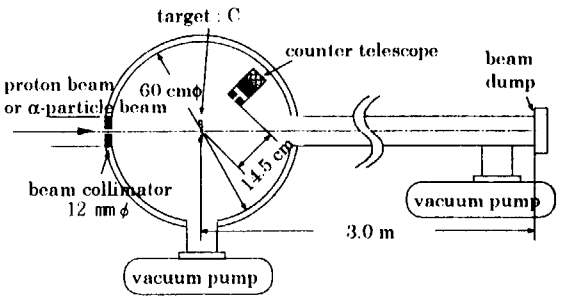

Fig. 1 Schematic view of the scattering chamber installed in the HB-1 beam line.

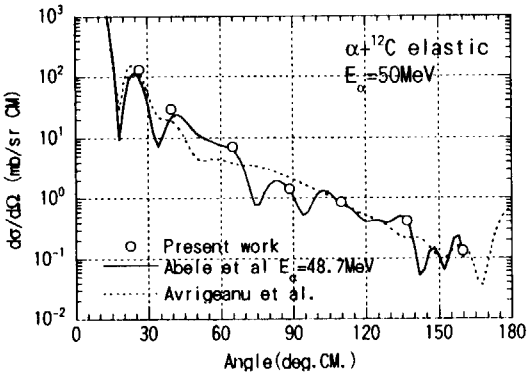

Fig. 2 Differential cross sections of α-particle elastic scattering from ^{12}C at 50 MeV.

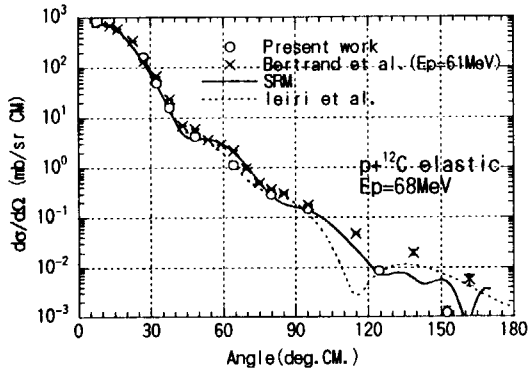

Fig. 3 Differential cross sections of proton elastic scattering from ^{12}C at 68 MeV.

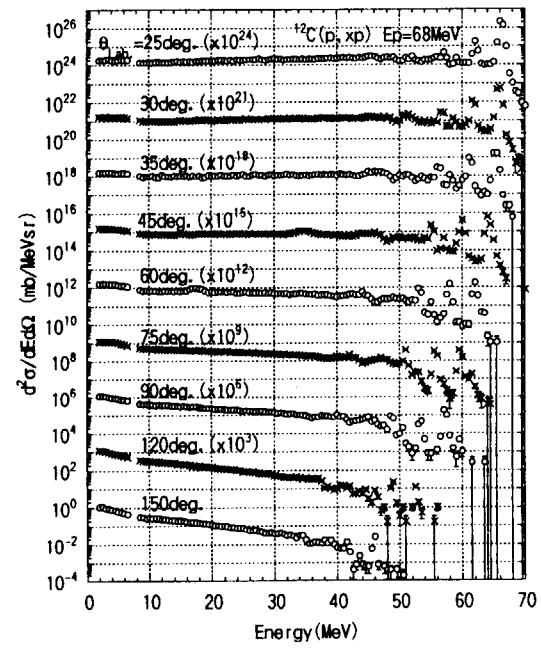

Fig. 4 Measured DDXs of $^{12}C(p,xp)$ at 68 MeV.

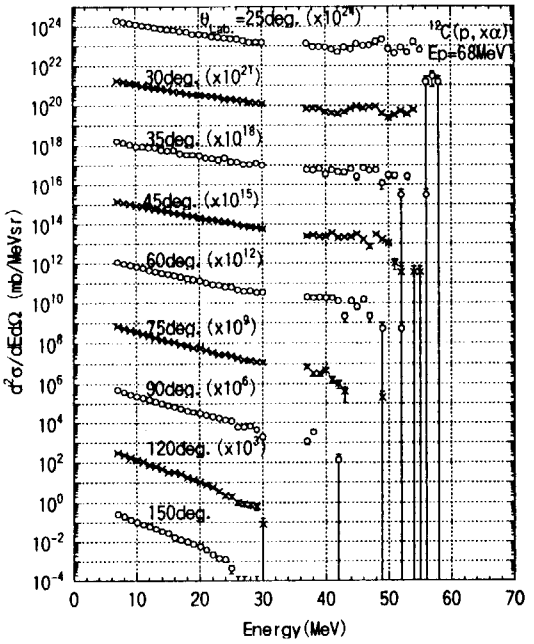

Fig. 5 Measured DDXs of $^{12}C(p,x\alpha)$ at 68 MeV.

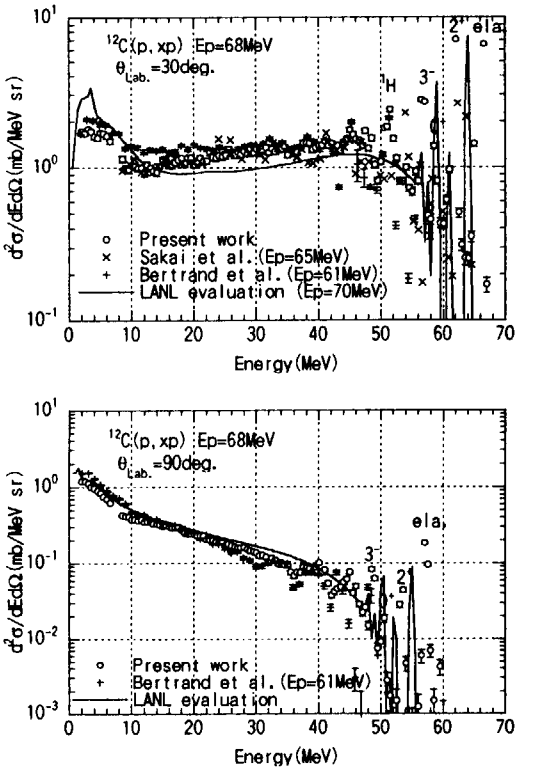

Fig. 6 Comparison of measured DDXs of emitted protons with other experiments and evaluation at 68 MeV.

7. 3 Application of Self-TOF high energy neutron detector for neutron scattering cross section measurements

Sasaki M., Nakao M., Nakamura T., Nakao N.*, Shibata T.*

CYRIC, Tohoku Univ; *KEK

Introduction

A self-TOF which measures the neutron-induced proton time of flight (TOF) has been developed[1,2] for high energy neutron spectrometry. This detector is composed of a VETO counter for elimination of charged particles, START and STOP detectors for measurement of recoiled proton energy by the TOF method. The VETO counter is a 150 mm × 150 mm × 5 mm-thick, the START detector is a 80 mm diam. × 0.5 mm-thick and the STOP detector is a 200 mm × 200 mm × 20 mm-thick NE102A plastic scintillator. The performance of this detector was tested under a quasi-monoenergetic p-Li neutron field at CYRIC[3] (Cyclotron and Radioisotope Center, Tohoku University) and TIARA (Takasaki Ion Accelerator for Advanced Radiation Application). This detector is planned to be applied for measurements of neutron scattering cross section.

Experiment at CYRIC

The proton beams accelerated up to 35 MeV by a cyclotron were transported to the scattering chamber through a beam swinger in the No. 5 target room. A proton beam was focused onto a 2 mm thick natural Li target which has about 2 MeV loss of incident proton energy. The proton beam was inclined at 10° to the horizontal line with a beam swinger in order to shield neutrons produced from a Faraday cup. The neutrons emerging from the Li target at 10° were transported down to the TOF extension room.

The VETO counter was used to discriminate the neutrons and charged particles incident to the radiator, since neutrons do not scintillate the VETO counter. The radiator was put between the VETO counter and the START detector and the recoiled protons from the radiator due to the H(n,p) elastic scattering reaction were measured between the START and the STOP detectors by the TOF method. The proton energy E_p is obtained from the proton flight time and the neutron energy E_n is then determined by $E_n = E_p / cos^2\theta$ where θ is the scattering angle.

In the experiment, three types of radiators, polyethylene, graphite and nothing, were used to subtract the contribution of protons produced from carbon in the polyethylene radiator and from other detectors.

Data analysis

The pulse height distributions of scintillation light outputs from the VETO, START and STOP detectors were stored with integrating-type ADC(LeCroy 2249W) which was gated by coincidence signals of the START and STOP detectors . The proton TOF spectra were stored with TDC together with the neutron TOF spectra using the RF (Radio Frequency) signal from a cyclotron as a start signal for comparison.

As the events to be analyzed for estimation of neutron energy spectra are the proton events

produced from a radiator, the VETO pulse height was fixed to be noise level to avoid the primary charged particles and the START pulse height to be high enough to discriminate the protons induced in the START detector.

The proton energy spectra given for three radiators, polyethylene (f_{POLY}), graphite (f_{GRA}) and nothing (f_{BLANK}), were determined from relativistic kinematics using the recoiled proton TOF spectra after correction of energy loss in the START scintillator. The proton events induced by only H(n,p) elastic scattering from polyethylene radiator($f_{H(n,p)}$) can be obtained by using the above three neutron energy spectra from the following formula which subtracts unnecessary components,

$$f_{H(n,p)} = (f_{POLY} - f_{BLANK}) - (f_{GRA} - f_{BLANK}) \times \eta,$$

where η is the ratio of carbon density of the polyethylene radiator to that of the graphite radiator.

Results and discussions

Fig. 1 shows the experimental data together with the neutron spectrum obtained by the PRT (Proton Recoil Telescope).The peak energy is about 1 MeV lower and the fluence of peak component is about 15 % smaller compared with the PRT spectrum. The difference of peak energy is reduced to the neglection of energy loss correction caused by proton flight of 1 m in air. The underestimation of peak fluence comes from various factors which are necessary to be corrected. We are now considering these corrections while analyzing data at TIARA experiment.

Conclusions

The performance test of the self TOF detector for measurements of neutrons was done at CYRIC. By using three type of radiators, the contribution of carbon reaction in polyethylene radiator and background was able to be subtracted. This detector is now applying for the neutron scattering cross section measurements.

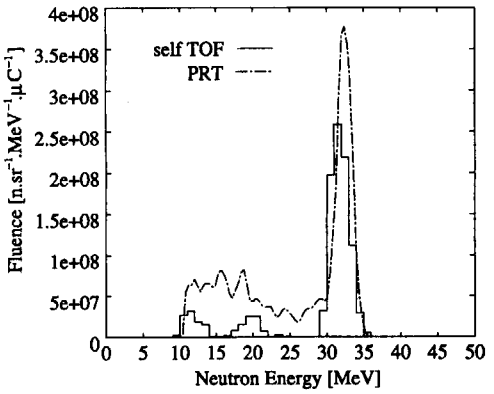

Figure 1. Comparison of neutron energy spectra given by the self-TOF detector(line) and of the PRT (proton recoil telescope).

References

(1) M. Nakao et al., KEK Proc. of 11th Workshop on Radiat. Detec. and Their Uses, p102, (1997)

(2) N. Nakao et al., RIKEN Accel. Prog. Rep. **29** (1996)

(3) M. Takada et al., Nucl. Instrum. Methods, A 372, p253 (1996)

7. 4 Fission Rate Distributions of ^{237}Np and ^{238}U for 65 MeV Quasi-Monoenergetic Neutrons in Al, Fe and Pb

Takashi TABEI, Tomohiko IWASAKI, Yasushi NAUCHI, Naohiro HIRAKAWA
Hiroshi NAKASHIMA[1], Yukio SAKAMOTO[1], Hiroshi TAKADA[1]
Susumu TANAKA[2]
Department of Quantum Science and Energy Engineering, Tohoku University
[1]Center for Neutron Science, JAERI
[2]Advanced Radiation Technology Center, JAERI

I. INTRODUCTION

Various accelerator-driven systems have been proposed for transmuting minor-actinides (MA) and long-lived fission products (LLFP) in high level waste (HLW) [i]. In all such systems, protons are accelerated up to about 1 GeV and many neutrons are generated via the spallation reaction in a heavy element target. The energy of the spallation neutrons extends to several hundreds MeV. For designing an accelerator-driven transmutation system, it is necessary to prepare a code that is able to simulate transport of neutron in the energy region. Some codes have been proposed to design these systems and the NMTC/JAERI[ii] is one of the codes.

The NMTC/JAERI is an improved version of the NMTC[iii] by Japan Atomic Energy Research Institute (JAERI). Owing to the improvement, the NMTC/JAERI can treat high energy fission process and calculate neutron transport for nuclei with a wide range of mass number of A=1 and 6<A<250. However, it is supposed that the codes as NMTC/JAERI based on the intra-nuclear cascade/evaporation model are insufficient to analyze neutron transport at low particle energies below 100 MeV or for light elements [iv].

Considering these backgrounds, we performed a measurement of fission rate distributions of ^{237}Np and ^{238}U in different mass number systems with a 65 MeV mono-energetic neutron source and analyzed the experimental results using the NMTC/JAERI code. In the previous report, we discussed about polyethylene (CH_2) system[v]. Then it was found that NMTC/JAERI overestimates both fission rates of ^{237}Np and ^{238}U in the system. The C/E values were about 2.0 at 72cm of polyethylene thickness. In this paper, we report same experiment and analysis about aluminum, iron and lead systems. We compare C/E value about each systems and discuss accuracy of the code about different mass number systems.

II. EXPERIMENT

The present experiment was carried out using $^{7}Li(p,n)$ neutron source facility at LC course.

The characteristic of the neutron spectrum was described in detail elsewhere[vi]. Figure 1 shows the neutron energy spectrum used in the present work. The peak energy was 65 MeV and the FWHM of the peak was 2.5 MeV.

The experimental system was composed of an iron collimator and some sample blocks as shown in Fig.2. The dimensions of the sample systems are shown in Table 1. The sample blocks were placed keeping a gap of about 3cm in order to insert detectors.

Table 1 Measuring points in each sample systems

Sample	Dimension (cm)	Measuring Point
Polyethylene	118 x 118 x 70	0, 30, 40, 70 cm
Aluminum	15 x 15 x 60	0, 15, 30, 45 cm
Iron	120 x 120 x 70	0, 10,20,30 cm
	15 x 15 x 64	0, 8, 16,32 cm
Lead	15 x 15 x 45	0, 7.5, 15, 22.5 cm

*0cm is just outside the collimator

Two sealed fission chambers of ^{237}Np and ^{238}U were employed. The specification of the detectors is shown in Table 2. The diameter was about 0.6 cm and the active length was about 2.5 cm.

The ^{237}Np and ^{238}U fission chambers were bunched and were placed in the gap between the blocks and on the center of neutron beam at the same time. Fission counts of the two fission chambers were measured at points shown in Table1 for each samples. Then, those were

normalized to source neutron fluence to obtain the fission rates distribution as function of the depth of sample. The maximum errors of the experimental results were about 7% and 4% for ^{237}Np and ^{238}U respectively.

Table 2 Specification of Np237 and U238 FC

Detector	Active Length (cm)	Diameter (cm)	Coated Thickness (μ g/cm^2)
Np237 FC	2.48	0.64	~300
U238 FC	2.48	0.64	~1000

III. ANALYSIS

The present experiment was analyzed using the code system of NMTC/JAERI and MCNP4A [vii]. The analysis was carried out following three steps. In the first step (A), the NMTC/JAERI was used for the neutrons above 15 MeV included in the source neutron beam. For the neutrons slowed-down below 15 MeV from the step (A), the MCNP4A was employed in the second step (B). Finally, the MCNP4 was also employed in the third step (C) only for the neutrons below 15MeV included in the source neutron beam.

By the three steps, neutron energy spectra were calculated at the detector positions of ^{237}Np and ^{238}U. From those neutron energy spectra, the fission reaction rates per source neutron were derived by multiplying fission cross sections of ^{237}Np and ^{238}U. The total fission rates were obtained by summing up the fission rates of the three steps. A typical statistical error of the Monte-Carlo calculations was 2.0 % for the total fission rates of both ^{237}Np and ^{238}U. The maximum error was 3.5%. In this study, the fission cross sections were taken from the JENDL-3 below 20MeV and from the data of Lisowski [viii] above 20MeV. Figure 3 shows the fission cross sections of both nuclides.

IV. RESULT

Figure 4 compares the C/E values for ^{237}Np in all systems. In the figure, the number of nucleons per unit area (10^{24}/cm^2) was adopted as the depth of blocks because we should research about the sample effect on the reaction rate between neutron and a sample nucleon. It is clearly found from the figure that the NMTC/JAERI provides better accuracy for a sample with larger mass number and for the lead system, the calculated values fairly agreed with the experimental ones at every measuring point. This trend is also found in the case of ^{235}U.

V. CONCLUSION

In this study, we measured fission rates of ^{237}Np and ^{238}U in polyethylene, aluminum, iron and lead systems irradiated by 65 MeV quasi monoenergetic neutrons at the LC course of TIARA. By the present experiment, relative fission rate distributions dependent on sample thickness were obtained for ^{237}Np and ^{238}U. These fission rate distributions of actinides are supposed to be valuable as experimental benchmark data.

An analysis for the present experiment was performed by the NMTC/JAERI that is currently used in the design study of accelerator-driven transmutation systems. The calculation results fairly agreed with the experimental ones for both ^{237}Np and ^{238}U in the lead system. The accuracy of the NMTC/JAERI was not good for polyethylene, aluminum and iron. It can be remarked that some efforts are required to improve the accuracy of the NMTC/JAERI for light elements.

REFERENCE

[i] S.Matsuura et al.: NEA/NSC/DOC(94)11, OECD/NEA(1994).

[ii] Y.Nakahara and T.Tsutsui: JAERI-M 82-198 (1982) [in Japanese].

[iii] W.A.Coleman and T.W.Armstrong: The Nucleon-Meson Transport Code NMTC, ORNL-4606 (1970).

[iv] H.Takada: J. Nucl. Sci. Technol., 33, 75 (1996).

[v] T.Iwasaki et al.: JAERI TIARA Annual Report. 1996 p212-214.

[vi] T.Nakamura et al.:Proc.int.Conf.Nucl.Data.Sci. Technol. May, 1997,Trieste p1508-1512.

[vii] J.F.Briesmeister(Ed.): MCNP Version 4A, LA-12625 (1993).

[viii] P.W.Lisowski et al.: Proc. September. Meet. on Neutron Cross Section Standards for Energy Region above 20 MeV, Uppsala, Sweden, 21-23 May, 1991, 177 (1991).

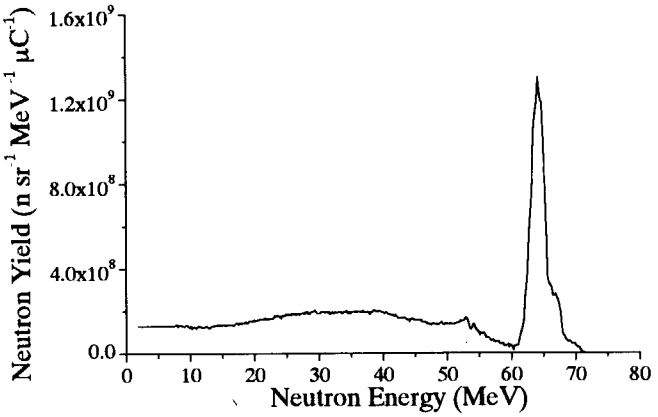

Fig.1 Energy spectrum of source neutrons

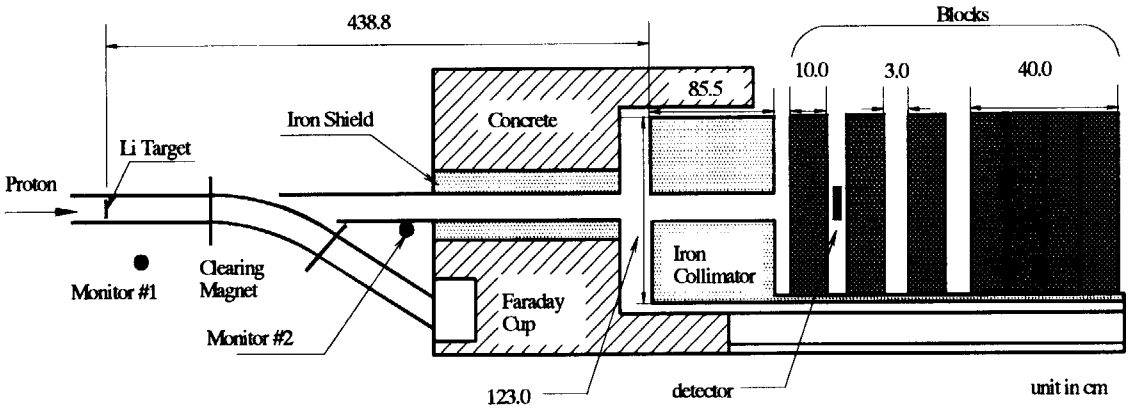

Fig.2 Experimental set up of Iron

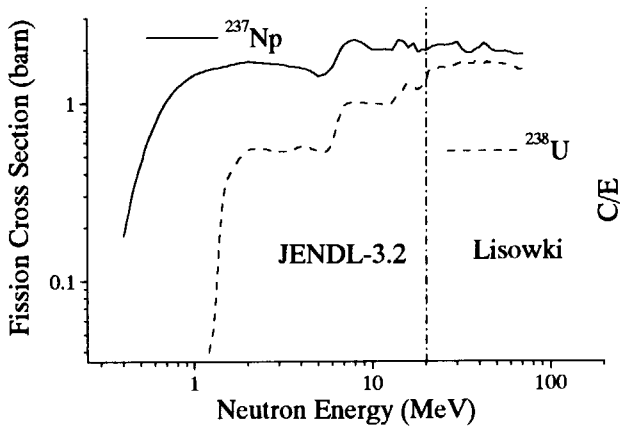

Fig3.Fission cross section of Np237 and U238

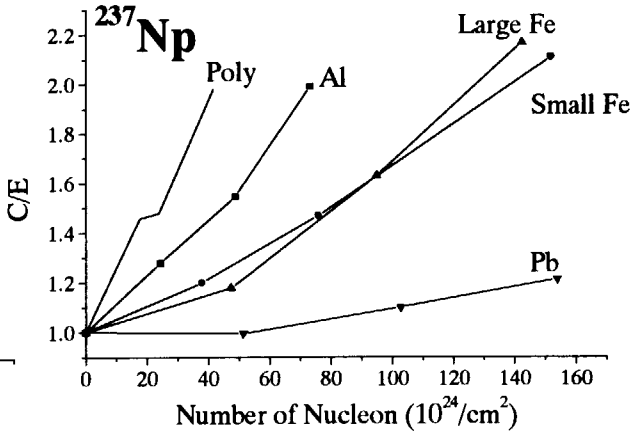

Fig4.Comparison of C/E for Np237 fission rate distributions in four sample systems

7．5 Charged-particle and neutron production in 75 MeV neutron induced reactions

Y. Nauchi, M. Ibaraki, M. Baba, T. Nunomiya, T. Miura, Y. Hirasawa, H. Nakashima[1], S. Meigo[1], Su. Tanaka[2]
Dept. Quantum Science and Energy Engineering, Tohoku University,
Center of Neutron Science, JAERI[1], Advanced Radiation Technology Center, JAERI[2]

1.Nuclear Data Measurements at TIARA

Double differential cross sections (DDXs) of charged particle and neutron emission reactions for ten's MeV neutrons are of great importance for many kinds of accelerator applications. To obtain these data, we had studied the spectra of ^{7}Li(p,n) neutron sources of LC course of TIARA[1)], then started the measurements (n,xp) and (n,xd) DDXs at forward angles down to 12 ° using a conventional counter telescope[2)]. However, high threshold energy, high background and low count rate restricted the measurements.

During the last year, we developed a (n,xz) spectrometer characterized by its wide dynamic range large enough to measure a few MeV α particles as well as 80 MeV protons. Besides, a neutron TOF spectrometer was set at just downstream of the (n,xz) spectrometer as shown in fig. 1, to measure the neutron elastic scattering cross section utilizing the ^{7}Li(p,n) source neutrons transmitting the upstream spectrometer. Owing to these development, measurements of (n,xz) DDXs and neutron elastic scattering can be done concurrently, that would promote the nuclear data studies in the intermediate energy region.

2.Charged Particle Measurement

2.1 New Spectrometer

A vacuum reaction chamber shown in fig. 1 was adopted to lower the detection threshold to obtain α particles, and to reduce background charged particles from the air. A sample of disk shape, 5cm in diameter, located at the center of the chamber is viewed by 3 counter telescopes set at 20° intervals. The chamber has 3 neutron entrance – exit ports, and by rotating the chamber, the DDXs data are obtained at angles from 25° to 155° with 10° angle step.

Each telescope consists of a low pressure gas proportional counter, a SSD(900mm^2, 150μm thick) and a BaF_2 scintillator as shown in fig.2. As the window between the chamber and the gas (0.1atm Ar +5% CO_2) counter, 5.4μm thick mylar films were used to reduce the energy loss of α particles. Low energy α particles (<16MeV) which stop in the SSD are detected and identified by the usual ΔE-E (gas-SSD) method. For identification of high energy protons which loose little energy in the gas counter, ΔE(SSD)-E(BaF_2) spectra was used. By combining the two ΔE-E spectra, particle identification and spectra measurements are achieved over a wide range .

2.2 Measurements of Charged Particle Spectra

The first test of the new spectrometer was performed for C(n,xz) DDX measurements at En=75MeV. The pulse heights data from the three counter of each telescope were accumulated event by event using the conventional CAMAC data acquisition system[3)]. Figure 3 shows the gas-SSD particle identification spectra. In the experiments, the telescope viewed an ^{241}Am α source behind the sample for energy calibration. The distinct peak in fig.3 is due to the ^{241}Am, and the high energy edge in SSD axis means the maximum energy loss. (E_α=16MeV for 150μm thick SSD). Thus we achieved α particle measurements from low threshold around 4MeV by using the low energy loss spectrometer.

Figure 4 shows the ΔE(SSD)-E(BaF_2) spectra. Proton, deuteron and triton are separated clearly. As the results, particle identification and spectra

measurements over a wide dynamic range can be achieved by using the new spectrometer.

3.Elastic scattering measurements

3.1 Experiment

Neutrons of 75 MeV by the ^{7}Li(p,n) reaction were used as incident neutrons for the measurements of elastic scattering cross sections. The scattering samples, carbon (5cmϕ×8cm), iron(4cmϕ×6cm) and lead(3cm ϕ×6cm), were placed at 10m from neutron production target. Elastically scattered neutrons were measured by time of flight method(TOF) using five NE213 liquid scintillation detectors (12.7cmϕ× 12.7cm) concurrently. The TOF spectra were obtained at 25 laboratory scattering angles between 2.6° and 53.0° in. The scattering angle was changed by rotating the detector array around the sample. The flight paths were around 5m at forward angles and 2m at backward angles. The absolute cross sections were determined relative to the incident neutron flux measured by the NE213 detectors which were used for scattering measurements.

Elastic cross sections deduced were further corrected for the effects of the finite sample size, flux attenuation and multiple scattering, and for the contributions of inelastic scattering neutrons. The last corrections was done by calculating the yield ratio of the inelastic scattering neutrons to the total (elastic and inelastic) ones considering experimental energy resolution. In this calculation, we used the evaluated data by Chadwick et al.[4] as the input data for the neutron-sample nuclide interaction. Because of strong forward peaking of the elastic scattering angular distribution, inelastically scattered neutrons do not affect the results for the forward angle, but the correction factors reach 20% around 30 degree to 40% around 50 degree.

3.2 Results

Figure 5 shows present results with the evaluated data by Chadwick et al.[4] and the experimental data(WNR/LAMPF) in ref 5). Our experimental data agree well with the evaluation except for forward angles of carbon, but WNR/LAMPF data incline gradually than our data and the evaluation. The present data will contribute to provide new information to update the nuclear models and codes in intermediate energy region.

Acknowledgement

The present research was performed as a part of the special project research between universities and JAERI.

References

1)Y.Nauchi et al.: JAERI-Review 97-015 "TIARA Annual Report 1996" p. 206
2)Y.Nauchi et al.: Proc. Int. Conf. Nucl. Data for Sci. Technol(May 1997, Trieste) p. 613
3)K.Omata et al.:INS-Rep. –884 (July 1991)
4)M.B.Chadwick et al., Nucle. Sci. Eng. 123, 17(1996).
5)J.H.Osborne,Ph.D.Dissertation,University of California, Davis, 1995.

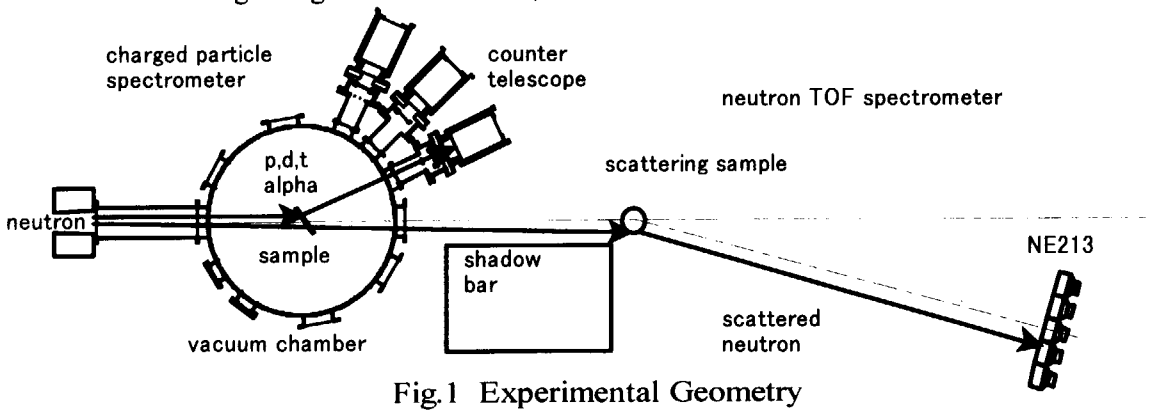

Fig.1 Experimental Geometry

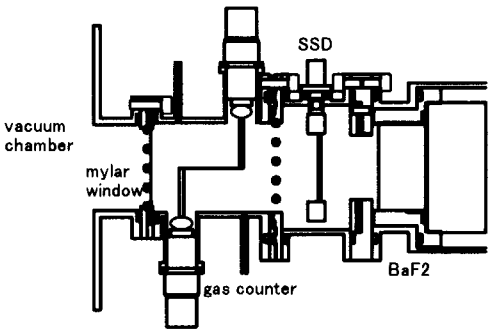

Fig.2 3-element counter telescope

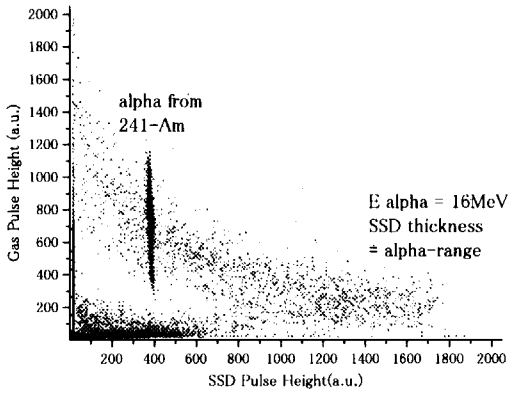

Fig.3 Gas-SSD spectra

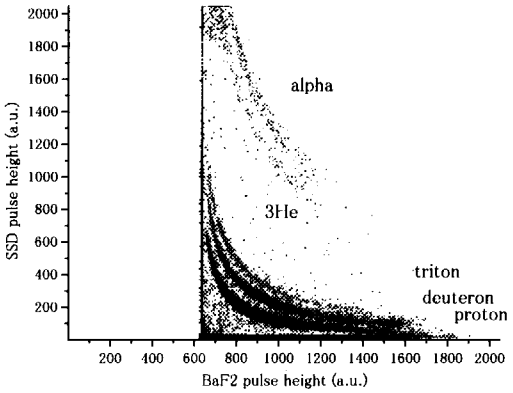

Fig.4 SSD-BaF2 spectra

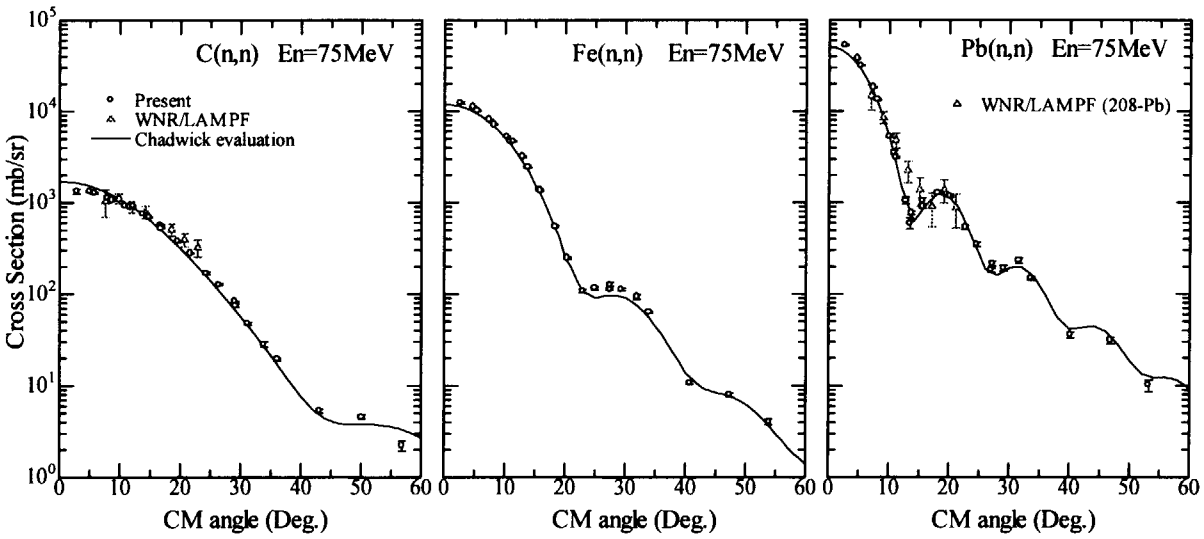

Fig.5 Elastic Scattering Cross Sections

This is a blank page.

8. Accelerator Technology

This is a blank page.

8. 1 Diagnostic Technique for Low Beam Current and for Beam Profile

I. Ishibori, T. Agematsu, S. Okumura, M. Fukuda, H. Tamura,
K. Arakawa, A. Matsumura* and S. Kanou*

Advanced Radiat. Tech. Center, JAERI/Takasaki.
*Beam Operation Co.,LTD.

1. Introduction

The extracted beam currents from a cyclotron are measured by a Faraday cup (FC) which is distributed over the beam transport line of the cyclotron. The FC is of cylindrical-shaped with a suppressor ring biased at -500V. However the FC can not measure the low intensity beam less than 1 nA because large dark currents are induced by a cooling water. For providing accurate measurements of currents as low as nA and pA, FCs of air cooling type were tested.

Cellulose triacetate (CTA) film dosimeter has been successfully applied to measurement of the two-dimensional relative fluence distribution as an integration method for ion beams. Since this method can not be used for real time measurement, we have developed a system to measure the relative fluence distribution of ion beam by using a fluorescent screen and a CCD camera.

2. Accurate measuerment of beam current

For accurate measurements of the net current, a FC of duct type which collects the secondary electron generated at a cup surface is used as a standard one. Figure 1 shows the schematic drawing of the FCs used in this work. Table 1 shows the dimensions of the FCs. W_FC and T_FC are a water cooling Faraday cup and an air cooling one, respectively. As materials of the FC, copper (Cu) and carbon (C) were used because production efficiency of the generated secondary electrons by impact of ions depends on materials. The most unique feature of highly charged ion beam is

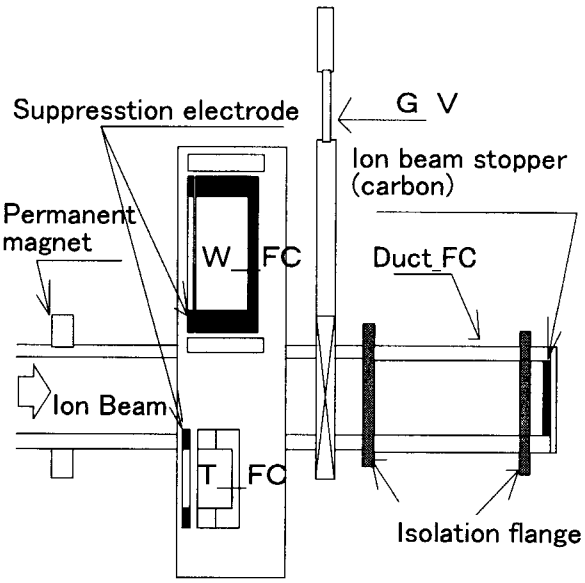

Fig.1: Constitution of Faraday cups

its power to produce secondary electrons when impacted on a surface of a material. Therefore we used the following beam conditions in this work ; 10 MeV H^+, 100 MeV $^{16}O^{4+}$, 150 and 175 MeV $^{40}Ar^{8+}$, and 250 MeV $^{40}Ar^{10+}$. Figure 2 shows the current ratio measured for 10 MeV H^+ and 250 MeV $^{40}Ar^{10+}$ as a function of the suppressor

Table 1: Size of Faraday cup [mm]

	Duct_FC	T_FC	WFC
Depth of cup	1,142	39	64
Inside diameter of cup	146	40	80
Thickness of sup -pressor	—	5	3
Inside diameter of suppressor	—	40	80

voltage. In Fig. 2, I_{DUCT_FC} is beam current measured by the FC of duct type. In the case of 10 MeV H^+, the dependence on the dimensions of the FC is a little and the relative current error, the deviation from I_{DUCT_FC}, is less than 4%. On the other hand, the dependence of the dimensions of the FC is observed in the case of 250 MeV $^{40}Ar^{10+}$ ions. It is clear that the W_FC can not collect enough secondary electrons generated by heavier multiply charged ions although the suppressor ring is biased at -500V. The

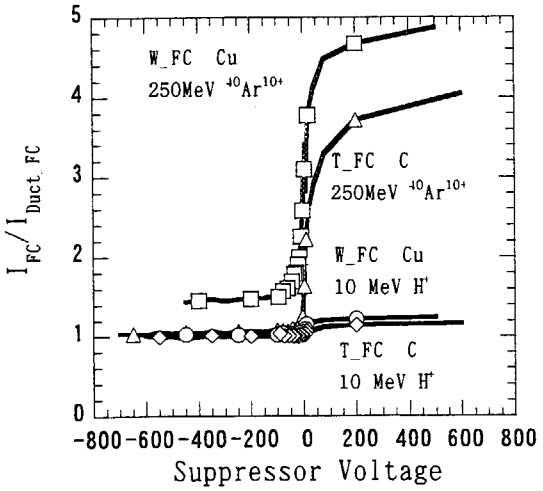

Fig 2: Measurement of beam current for T_FC and W_FC

electric potential on the surface of the FCs was evaluated by a TOSCA code. The suppressor potentials of W_FC and T_FC were -60V and -300 V, respectively. It is clear that the suppressor potential at W_FC is reduced by the metallic cover for protection of the FC. For accurate measurement of beam current, we need to remove the metallic cover of the W_FC.

3. Real time measurement of beam profile

Sample materials of the fluorescent screens were chromium-activated alumina ceramics (AF995R, Desmarquest), magnesia ceramics, alumina ceramics and quartz glass. The fluorescent materials were irradiateed with 10 MeV H^+ and an 175 MeV $^{40}Ar^{8+}$ ions and luminescences of the samples were measured by a CCD camera and image processor. Two camera systems were used

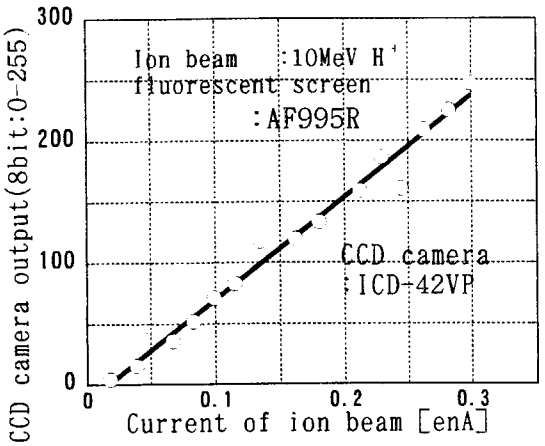

Fig.3: Light intensity vs ion beam current

for measurement of the luminescence. One is a high sensitivity black & white video camera (ICD-42VP, Ikegami Tsusinki Co., Ltd.), and the other is a home video camera (CCD-G100,SONY). The video signals are converted to the beam profile by the image processor (MVS-5040, Hamamatsu Photonics K.K.). For the image processor, we have developed the programs including four principal functions as follows: 1) an indication of beam profile in real-time, 2) a calibration of the γ-characteristics of the CCD camera, 3) an indication of the digitized

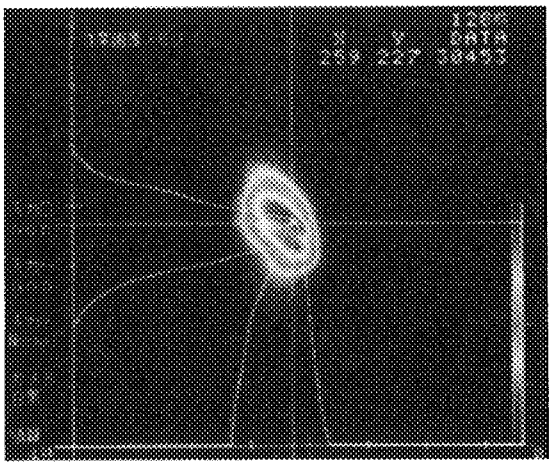

Fig.4: Result of profile monitor test

data from video signal, and 4) an integration of video image with time. Figure 3 shows that the linearity of the peak light intensity against the beam current is ensured over the whole region of the measurement. Figure 4 shows the result of a profile monitor test. The available range of the beam current for the fluorescent materials are shown in Table 2. The method of a luminescence is very easy to measure the beam profile in real-time and the playback function of the video camera is very convenient to confirm of the beam profile repeatedly.

References

1) S. Mattson and M. Anicolet, Nuclear Instruments and Method 160(1979) 301-311.
2) Martin P. Stockli and S. Winecki, Proceedings of the 12th International Workshop on ECR Ion Source. (1995), P.90.
3) T. Agematsu, S. Okumura and K. Arakawa, JAERI-M 94-071 (1994).
4) T. Agematsu, S. Okumura and K. Arakawa, Proc. 6th Japan-China Bilateral Symp. Radiat. Chem. (Tokyo, Nov.6-11, 1994), JAERI-Conf 95-003 p.467.

Table 2: Available range of beam fluence for fluorescent materials by using a CCD camera (unit:eA/cm^2)

Camera	ICD-42VP camera, Ikegami		CCD-G100 camera, SONY	
screen\beam	H^+ 10MeV	$^{40}Ar^{8+}$ 175MeV	H^+ 10MeV	$^{40}Ar^{8+}$ 175MeV
AF995R	0.4p～4n	0.8p～2n	0.4n～4n	0.06n～0.6n
Magnesia (MgO)	16p～40n	8p～20n	4n～40n	0.6n～6n
Alumina (Al_2O_3)	40p～200n	40p～200n	20n～200n	0.6n～3n
Quartz glass	6n～2000n	1.4n～400n	100n～1000n	20n～200n

8. 2 Present Status and Beam Acceleration Tests on Cyclotron

K. Arakawa, Y. Nakamura, W. Yokota, M. Fukuda, T. Nara,
T. Agematsu, S. Okumura , I. Ishibori and H. Tamura.

Advanced Radiation Technology Center, JAERI

1. Introduction

The operation of the JAERI-AVF cyclotron[1] for experiment was started from January 1992 in daily operation mode on a trial base. The weekly continuous operation was started from September 16, 1992. The total operation time attained to 20000 hours in April 1998.

There are two major reasons driving the need for fast energy/ion switching. The first is the requirement of material science research (for example single event upset studies) for beams of a wide range of energies and ion species. The second is the need for economic and efficient operation of the accelerator. To meet the requirement, we have been developing a cocktail beam acceleration technique at the JAERI-AVF cyclotron[2].

2. Present status

2.1 AVF cyclotron

The AVF cyclotron was smoothly operated for experimental utilization in FY 1997. The beam time for experiments was 3202 hours in FY 1997. The AVF cyclotron provides a wide range of ions, energies, and intensities in support of the experimental program. Thirty-eight kinds of ion species were provided for experiments.

It is clear that the power supplies for the magnets, constructed nearly 10 years ago, cannot keep the regulation stability. Stability of the current outputted from the power supply is preserved by monitoring the voltage of the shunt resistor. We have replaced the shunt resistors of the power supplies for the main magnet and the analyzing magnets. After replacement of the shunt resistors, the stability of the power supplies for the main magnet and the analyzing magnets are less than $\pm 1 \times 10^{-5}$ for 8 hours. It is better than the stability before the replacement.

We have had the following machine troubles:

(1) A high voltage of an ECR ion source broke down by increasing a humidity in the room.

(2) A leakage from bellows, which are used for pressing the contact fingers of the movable shorting plate against the wall of the coaxial type resonator with high pressure air, caused a vacuum in the acceleration chamber worse.

(3) A cooling water leakage from the baffle slit of the magnetic channel in the acceleration chamber of the cyclotron.

The accumulation of induced radioactivity in the acceleration chamber is making it more

difficult to conduct maintenance work inside the cyclotron. The strong sources of radiation are the electrostatic deflector (100 mSv/h) and the magnetic channel (160 mSv/h). For the protection against radiation hazards, some of the strongly activated parts, such as the electrode of the electrostatic deflector, main probe, magnetic channel and magnetic channel probe, were replaced in January 1998.

2.2 Ion source

ECR ion beams are presently used for two purposes; (1) injection of highly charged ion beam into the AVF cyclotron, (2) study and development of the ECR for highly charged ion beams of gases. Total operation time for the ECR ion source was 2445 hours. The breakdown of the high voltage occurred frequently by a discharge in the ECR ion source because the humidity is not good condition in the room. Total operation time for a multi-cusp ion source was 924 hours. The multi-cusp ion source was smoothly operated without any trouble.

3. Beam development

3.1 Cocktail beam acceleration

Cocktail beam acceleration is one of the most time-saving methods for changing the ion species and/or the energy. Ion "cocktail", which are composed of ions with the same or very close mass to charge ratio (M/Q), are produced in an ECR ion source, injected into the cyclotron, accelerated at the same time and extracted separately by a fine tuning of the magnetic field or a slight changing of the RF frequency.

Particle identification was carried out by measuring a pulse height from a SSD. The results of the cocktail beam acceleration test are summarized in Table 1. The extracted beam current for 56 MeV $^{15}N^{3+}$ increased from 0.7 to 3.2 eμA. The extracted beam current for 100 MeV $^{16}O^{4+}$ is 4.0 eμA.

The time required for changing the ion species and/or energy is only one minute for the cocktail beam acceleration. The details of the cocktail beam is reported in a separate paper at this annual report.

Table1: Parameters of a cocktail beam acceleration tests.

Ion	M/Q	Frequency (MHz)	Energy (MeV)
$^{15}N^{3+}$	4.9995	13.868	56
$^{20}Ne^{4+}$	4.9976	13.873	75
$^{40}Ar^{8+}$	4.9948	13.881	150
$^{84}Kr^{17+}$	4.9354	14.047	323
$^{4}He^{+}$	4.0021	11.908	25
$^{12}C^{3+}$	3.9995	11.916	75
$^{16}O^{4+}$	3.9982	11.919	100
$^{20}Ne^{5+}$	3.9979	11.920	125
$^{40}Ar^{10+}$	3.9957	11.927	250
$^{84}Kr^{21+}$	3.9952	11.928	525

3.2 Other new beam acceleration

The beam acceleration tests have been conducted for 20 MeV D^{+} and 400 MeV $^{84}Kr^{18+}$. Protons are generated by the multi-cusp ion source, and $^{84}Kr^{18+}$ ions by the ECR ion source. The results of the beam acceleration test are summarized in Table 2.

The 20 MeV D^+ beam current is limited within 5.0 μA for the present to avoid unnecessary induced radioactivity of the machine parts.

3.3 Extraction current and transmission

Particles accelerated and extracted so far are listed in Table 2. The extraction efficiency is defined by the ratio of the beam current measured with the main probe at r=900 mm to that with the Faraday cup (FC) just after the cyclotron. The average extraction efficiencies for harmonic 1, 2 and 3 are 54 %, 65% and 58 %, respectively.

The overall transmission efficiency is defined by the ratio of the beam current with the FC just after the analyzing magnet at the injection line to that with the FC just after the cyclotron. The average transmission efficiencies for harmonic 1, 2 and 3 are 13 %, 17% and 13% , respectively.

4. Reference

1) K. Arakawa, Y. Nakamura, W. Yokota, M. Fukuda, T. Nara, T. Agematsu, S. Okumura, I. Ishibori, T. Karasawa and R. Tanaka, Proc. 13th Int. Conf. on Cyclotrons and their Applications, Vancouver, Canada, (1992) 119.

2) M. Fukuda, K. Arakawa, S, Okumura, T. Nara, Y. Nakamura, T. Agematsu, I. Ishibori, W. Yokota and H. Tamura, Proc. 11th Sympo. on Accele. Sci. and Tech., Harima Science Garden City, (1997) 139.

Table 2. Results of extracted intensity and overall transmission.

Ion	Energy (MeV)	Extracted Intensity (emA)	Extraction Efficiency (%)	Overall Transmission (%)
H^+	10	12	80	27
	20	5	77	23
	30	5	67	22
	45	30	79	14
	50	5	44	14
	55	5	63	14
	60	5	57	22
	65	7	62	12
	70	5	42	12
	80	3	47	13
	90	10	48	7.7
D^+	10	11	29	3.7
	35	40	59	13
	50	20	49	7.2
$^4He^{2+}$	20	5.5	69	12
	30	10	42	10
	50	20	62	22
	100	10	32	10
$^{12}C^{3+}$	220	0.25	77	22
$^{16}O^{3+}$	100	4	34	21
$^{16}O^{6+}$	160	1.9	58	21
$^{16}O^{7+}$	225	1	82	13
$^{16}O^{7+}$	335	0.1	41	6
$^{20}Ne^{6+}$	120	1.6	53	18
$^{20}Ne^{7+}$	260	0.33	70	19
$^{20}Ne^{8+}$	350	1.5	63	23
$^{36}Ar^{8+}$	195	2.5	73	13
$^{36}Ar^{10+}$	195	0.1	43	1.2
$^{40}Ar^{8+}$	175	3	73	15
$^{40}Ar^{11+}$	330	0.7	86	22
$^{40}Ar^{13+}$	460	0.03	63	24
$^{84}Kr^{18+}$	400	0.04	60	2
$^{84}Kr^{20+}$	520	0.06	72	22
$^{129}Xe^{23+}$	450	0.2	72	11

8. 3 Development of a Cocktail Beam Acceleration Technique

M. Fukuda, K. Arakawa, S. Okumura, T. Nara, I. Ishibori,
T. Agematsu, Y. Nakamura, H. Tamura, W. Yokota and T. Karasawa
Advanced Radiation Technology Center, JAERI

1. Introduction

An ion beam has become one of the most effective tool for research in materials science and biotechnology. A wide variety of characteristics depending on the research are required for a cyclotron beam. The beam characteristics are defined by an ion species, energy, a beam current, a size of a beam spot and a beam pulse frequency and width, etc.

There is a growing demand for utilization of different ion beams without loss of time during the same beam time. An immediate change of the ion species and energy enhances efficiency of beam utilization during the finite beam time, and expands the feasibility of the research on radiation effects in a material. Generally half an hour is required for re-excitation of a cyclotron magnet and for replacement of a gas supplied to an ECR ion source. Another half an hour is needed for optimization of parameters in all the systems. If acceleration harmonics are changed, another one hour is required for replacing electrodes of an inflector and a puller. Thus it takes one through two hours in all to change the ion species and energy.

The cocktail acceleration technique[1,2] saves the time required for changing the ion species and energy. Cocktail ions with almost the same mass to charge ratio(M/Q) are injected into the cyclotron simultaneously, and one of the cocktail ion species is fully accelerated by setting an RF frequency for an optimum value. Other ion species gradually slip from an isochronous condition, and finally enter a phase region for deceleration. The change of the ion species was completed within a few minutes, since the only RF frequency was adjusted to the ion species to be accelerated. We developed $M/Q \approx 5$ and 4 cocktail beams[3,4] so far. The $M/Q \approx 5$ cocktail ions have already been provided for users. In case of the $M/Q \approx 4$ cocktail beam acceleration, separation of different cocktail ions was incomplete due to insufficient M/Q resolution of the cyclotron. The smallest difference of the M/Q values between the nearest cocktail ions is $\Delta(M/Q)/(M/Q) = 0.6 \times 10^{-4}$. A specific method for preventing intermixture of the different ions has been developed.

2. Cocktail beam acceleration of $M/Q \approx 4$ ions

Parameters of the $M/Q \approx 4$ cocktail ions are listed in Table 1. The difference of the M/Q values between the nearest cocktail ions is $\Delta(M/Q)/(M/Q) = 0.6$ to 6.6 $\times 10^{-4}$. A pulse height spectrum of the cocktail ions obtained at an RF frequency of 11.919 MHz, which is an optimum value for 100 MeV $^{16}O^{4+}$, is shown in ref. 3) and 4). In this case, $^{12}C^{3+}$, $^{20}Ne^{5+}$ and $^{40}Ar^{10+}$ ions were injected into the cyclotron together with the $^{16}O^{4+}$ ion. The $^{40}Ar^{10+}$ ion was not observed in the pulse height spectrum. The $^{12}C^{3+}$ and $^{20}Ne^{5+}$ ions were, however, contained in the 100 MeV $^{16}O^{4+}$ beam extracted from the cyclotron. The insufficient separation of the cocktail ions resulted from large phase acceptance of the cyclotron that determines M/Q resolution of the cyclotron.

Table 1: Parameters of the cocktail ions with $M/Q = 4$.

Ion	M/Q	Δ(M/Q)/(M/Q)	Energy (MeV)	RF frequency (MHz)
$^{4}He^{+}$	4.00210		25	11.9073
		6.6×10^{-4}		
$^{12}C^{3+}$	3.99947		75	11.9152
		3.2×10^{-4}		
$^{16}O^{4+}$	3.99818		100	11.9190
		0.6×10^{-4}		
$^{20}Ne^{5+}$	3.99794		125	11.9197
		5.6×10^{-4}		
$^{40}Ar^{10+}$	3.99569		250	11.9264
		1.1×10^{-4}		
$^{84}Kr^{21+}$	3.99524		525	11.9278

3. Evaluation of M/Q resolution

In order to assess the capability for separating different cocktail ions, M/Q resolution of the cyclotron was evaluated experimentally and theoretically. An isochronous condition for acceleration is expressed as

$$2\pi\frac{f_{RF}}{h} = \frac{Q}{M}B, \qquad (1)$$

where f_{RF} is the RF frequency, h the acceleration harmonics number, Q a charge of an ion, M an ion mass and B a magnetic field. If the B is constant, we get $\Delta(M/Q)/(M/Q) = -\Delta f_{RF}/f_{RF}$ by differentiating the equation (1). Thus the M/Q values with which ions can be fully accelerated is evaluated from the extent of the RF frequency at which an ion can be extracted from the cyclotron. Dependence of a beam current on the RF frequency for 25 MeV $^{4}He^{+}$ beam is shown in Fig. 1. The extent of the RF frequency is $\Delta f_{RF} = 4.5$ kHz FWHM, and we get $\Delta f_{RF}/f_{RF} = 3.8 \times 10^{-4}$ that is equivalent to the M/Q resolution of 2600, where the M/Q resolution R is defined as

$$R \equiv \left|\frac{M/Q}{\Delta(M/Q)}\right| = \left|\frac{f_{RF}}{\Delta f_{RF}}\right|. \qquad (2)$$

Assuming that the extent of the RF frequency for full acceleration corresponds to $2 \times FWHM$, the M/Q difference to eliminate different ion species from the extracted beam is estimated to be $|\Delta(M/Q)/(M/Q)| > 3.8 \times 10^{-4}$.

A phase slip of the ion with an M/Q difference $\Delta(M/Q)$ is given by

$$\Delta \sin\phi = 2\pi\frac{\Delta(M/Q)}{M/Q}Nh, \qquad (3)$$

where ϕ is a beam phase and N a number of turns. Assuming that the phase acceptance for acceleration is $\pm30°$ RF and an average turn number is 400, the M/Q resolution is estimated to be 3300. The difference between the experimental and theoretical estimation comes from ambiguity of the assumption.

The M/Q difference of $^{12}C^{3+}$ and $^{20}Ne^{5+}$ from $^{16}O^{4+}$ is less than the resolvable M/Q difference of 3.8×10^{-4}. This results in the insufficient separation as shown in Fig. 1. In order to enhance the M/Q resolution, an acceleration voltage should be lowered to increase the turn number. The change of the acceleration voltage was not, however, so efficient, because optimization of several parameters was required for removing the different cocktail ions completely and for keeping beam intensity.

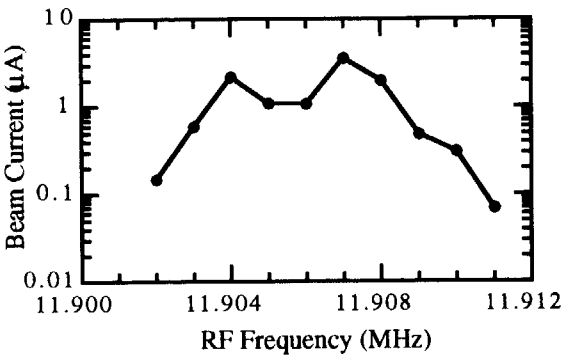

Figure 1: Dependence of a beam current on the RF frequency for 25 MeV $^{4}He^{+}$.

4. Fast change of gases in the ECR ion source

One of the most effective solution for eliminating different ion species is acceleration of a single ion species using the cocktail beam acceleration technique. The single ion species can be changed by replacing a main gas supplied to the ECR ion source by another gas. A gas supplying system of the ECR ion source was modified to save the time for replacing the gas. Volume of gas feeding pipes was minimized to reduce the evacuating time for rinsing unnecessary gases. A nitrogen gas was used as support for all the main gases in common, because the M/Q of the nitrogen ion is largely different from 4 and because the time for changing the support gas is omitted. Change of the ion species in the ECR ion source was completed within seven minutes. Another three minutes was required for changing the RF frequency to the optimum value of the injected ion species. As a result, a pure ion beam can be obtained within ten minutes.

The $^{16}O^{4+}$ is always contained in the $^{12}C^{3+}$ beam, since the $^{12}C^{3+}$ ion is produced from a CO_2 gas. In this case, the $^{16}O^{4+}$ ion can be separated by slightly changing the RF frequency from the optimum value.

Although a $^{84}Kr^{21+}$ ion was produced from a krypton gas, background ions like $^{56}Fe^{14+}$, $^{52}Cr^{13+}$, $^{40}Ar^{10+}$ and $^{36}Ar^{9+}$ were observed in a pulse height spectrum of the $^{84}Kr^{21+}$ beam as shown in ref. 3) and 4). The $^{56}Fe^{14+}$ and $^{52}Cr^{13+}$ ions came from a plasma chamber wall made of stainless steel, because electrons in plasma hit the wall. The $^{40}Ar^{10+}$ and $^{36}Ar^{9+}$ ions were considered to originate from a little air leakage. Separation of the background ions was extremely difficult, because the M/Q difference was less than 3.8×10^{-4}.

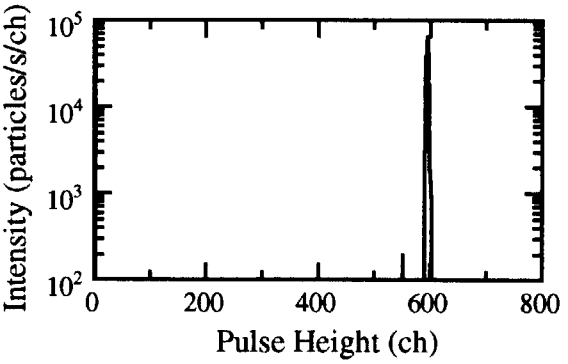

Figure 2: Pulse height spectrum of the $^{78}Kr^{19+}$ beam.

5. Acceleration of isotope ions

The krypton gas contains six kinds of stable isotopes. The M/Q difference of the isotope ions is of the order of 10^{-2}, which is large enough to separate the background ions. A pulse height spectrum of a $^{78}Kr^{19+}$ beam, as an example, is shown in Fig. 2. No background ions were observed in all the pulse height spectra of isotope ion beam. In this case, the ion species was changed within ten minutes.

References

1) M.A. McMahan, et al., Nucl. Instr. and Meth. A253 (1986) 1.
2) M. Fukuda, et al., TIARA Annual Report 1995, 229-231 (1996).
3) M. Fukuda, et al., TIARA Annual Report 1996, 229-231 (1997).
4) M. Fukuda, et al., Proceedings of the 11th Symposium on Accelerator Science and Technology, 139-141 (1997)

8. 4 Estimation of Charge Exchange Cross Section for Heavy Ions Accelerated in the JAERI AVF Cyclotron (III)

Y. Nakamura, I. Ishibori, K. Arakawa and T. Nara

Advanced Radiation Technology Center, JAERI/Takasaki

1 Introduction

The charge exchange reactions which occur with high probabilities in ion-atom collision have been studied[1)-4)] from a standpoint of theoretical and experimental situations since the 1960s. However, reliable experimental data and comprehensive empirical formulae for many kinds of ions almost have been not reported so far.

We experimented to get the charge exchange cross section (CECS) which is estimated from an attenuation of beam intensity by aggressive gas feeding into the vacuum chamber of the JAERI AVF cyclotron. We have already described some preliminary data[5)-8)] such as pressure control, pressure distribution and attenuation of beam.

2 Estimation of Charge Exchange Cross Section

The beam loss along the perpendicular injection line where the pressure is made to rise on account of the contribution from the vacuum chamber needs to be corrected carefully. The relative attenuation of the beam intensities along the injection line at several pressure levels is corrected surely using the exponential functions as shown in Fig. 1.

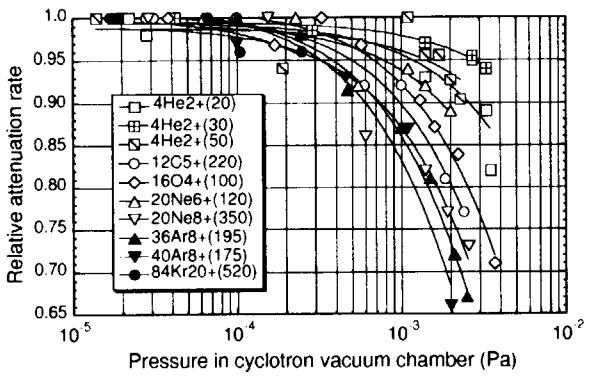

Fig. 1 Relative attenuation rate for various ions along the perpendicular injection line. The numbers in parentheses correspond to nominal energy of accelerated ions in unit of MeV.

Figure 2 summarizes the CECS's dealt with polynomial approximation for typical kinds of experimented ion beams. Although a little big variations appear in a lot of data points, whole tendency shows that the CECS's for various ions decrease with increase of the ion velocity. Furthermore, the CECS's for highly charged ions are relatively larger than those of lowly charged ones.

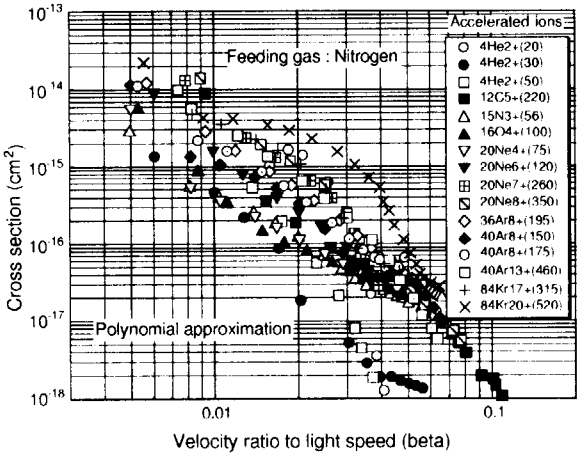

Fig. 2 Typical charge exchange cross sections estimated based on beam attenuation.

3 Derivation of Empirical Formula

We tried to get a reliable empirical formula which is available over the range of ion energy and charge state as wide as possible based on above data. It is found out that the CECS (σ) for each ion can be expressed in the power form of $\sigma = a\,\beta^{-b}$ by means of the experimental result. Where β is the ratio of the ion velocity to light speed.

Both coefficients "a" and "b" are determined as a function of the ratio of ionization, Q_r which equals Q/Z, from two straight lines in Fig. 3a and 3b with the exception of some $^{4}He^{2+}$ ions and 520 MeV $^{84}Kr^{20+}$ one, because the CECS for each accelerated ion can be roughly approximated by power fitting. Where, Q is charge state, Z atomic number of the ion.

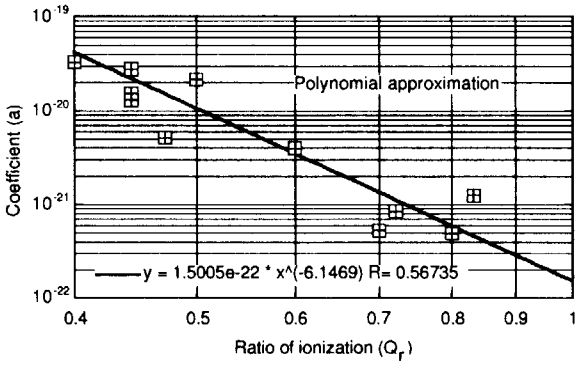

Fig. 3a Plotting of coefficient "a" to the ratio of ionization.

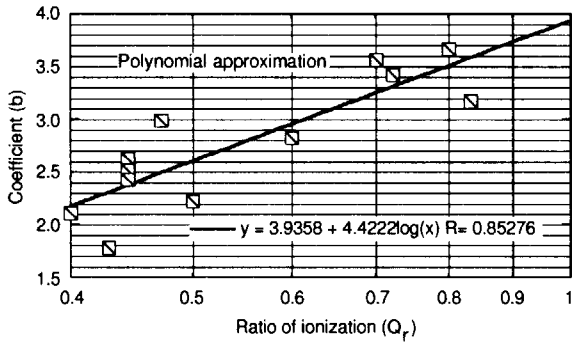

Fig. 3b Plotting of coefficient "b" to the ratio of ionization.

Finally, we derived a following comprehensive empirical formula which is given as a function of β and Q_r, within the range of β which is less than 0.1.

$$\sigma = 1.5 \times 10^{-22} \bullet Q_r^{-6.1} \bullet \beta^{-(3.9+4.4 \bullet \log Q_r)} \quad (1)$$

4 Comparison with Other Formulae

Some theoretical and semi-empirical formulae have been proposed so far as described in following formulae (2), (3) and (4) corresponding to references 9), 10) and 11), respectively.

$$\sigma = 2\pi a_0^2 \left(Z^{1/3} + Z_T^{1/3}\right) \bullet \left(v_0/v\right)^2 \quad (2)$$

$$\sigma = \pi a_0^2 \left\{ Z_T^{2/3} Z^{4/3} Q^{-3} \left(v/v_0\right)^2 + Z_T^{1/3} Q^2 \left(v_0/v\right)^3 \right\} \quad (3)$$

$$\sigma = 9 \times 10^{-19} Q^{-0.4} \beta^{-2} + 3 \times 10^{-28} Q^{2.5} \beta^{-7} \quad (4)$$

Where a_0 is Bohr radius, Z_T is atomic number of the target medium, v and v_0 are velocities of the ion and an electron around 1s orbit in a hydrogen atom, respectively.

A comparison of these formulae and experimental result for $^{40}Ar^{8+}$ ion is shown in Fig. 4. The formula (2) theoretically suggested by Bohr is the most similar in shape to our formula among these formulae in case of this ion.

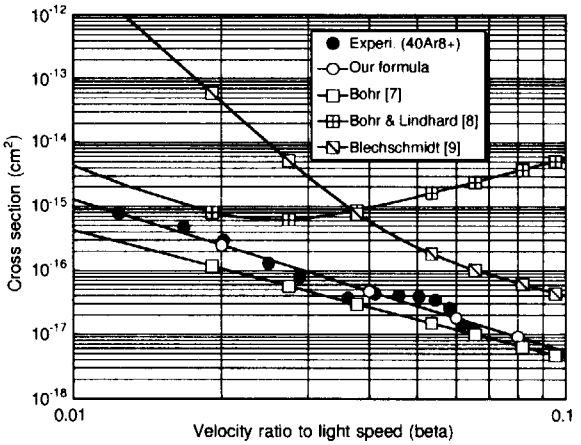

Fig. 4 Comparison of some formulae and an example of experimental result for $^{40}Ar^{8+}$ ion.

5 Beam Attenuation Through the Cyclotron

An example of beam attenuation through the cyclotron in case of pressure increase is shown in Fig. 5. At TS1 just downstream the cyclotron, as the pressure in the cyclotron rises up two orders, the beam intensity extracted from the cyclotron reduces about three orders.

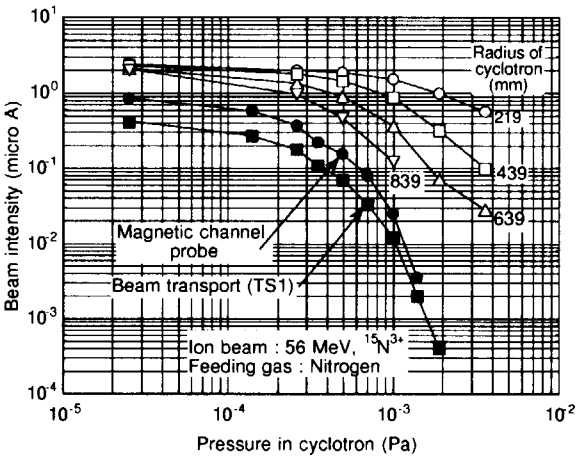

Fig. 5 An example of beam attenuation at several positions in the cyclotron and TS1 in the beam transport line just downstream one.

In regard to the acceleration of relatively low energy ion such as 56 MeV, $^{15}N^{3+}$ ion which is a kind of cocktail beams[12] with M/Q=5, we have to maintain the pressure in the cyclotron below 8×10^{-5} Pa from 2.5×10^{-5} Pa at original equilibrium pressure, if the beam loss through the cyclotron by charge exchange reaction needs to be restricted within 30 % which is equal to general transmission rate along an electrostatic deflector.

References

1) H. D. Betz, Rev. Mod. Phys., vol. 44, No.3, p465 (1972).
2) C. L. Cocke, Phys. Rev. A, vol. 20, No.3, p749 (1979).
3) P. D. Miller, IEEE Trans. on Nucl. Sci. vol. NS-26, No. 1, p1111 (1979).
4) R. A. Gough and M. L. Mallory, IEEE Trans. Nucl. Sci., NS-26, No. 2, p2384 (1979).
5) Y. Nakamura, I. Ishibori, *et al.*, TIARA Annual report, vol. 5, p227 (1995).
6) Y. Nakamura, I. Ishibori, *et al.*, TIARA Annual report, vol. 6, p227 (1996).
7) Y. Nakamura, I. Ishibori, *et al.*, Proc. 14th Int. Conf. on Cyclo. and Their Applic., Cape Town, South Africa, p276 (1995).
8) Y. Nakamura, I. Ishibori, *et al.*, Proc. 11th Sympo. Accel. Sci. Technol., Hyogo, Japan, p368 (1997).
9) N. Bohr, Kgl. Danske Viedenskab. Selskab, Mat.-Fys. Medd. 18, No. 8 (1948).
10) N. Bohr and J. Lindhard, Kgl. Danske Viedenskab. Selskab, Mat.-Fys. Medd. 28, No. 7 (1954).
11) D. Blechschmidt and H.J. Halama, Proc. HIF Work-shop, 136 (1977).
12) M. Fukuda, K. Arakawa, *et al.*, TIARA Annual report, vol. 6, p229 (1996).

8. 5 Preliminary Test for High Precision Measurement of Main Coil Current

Y. Nakamura and T. Agematsu

Advanced radiation Technology Center, JAERI/Takasaki

1. Introduction

The JAERI AVF cyclotron has been already utilized for various research fields since the installation in 1991. The ion beam extracted from the cyclotron needs to be supplied steadily, because it is delivered continuously from Monday morning to Friday evening.

However, we are sometimes observing the phenomenon that the ion beam decreases gradually owing to the magnetic field deviation which is predicted as the effect caused by temperature rising at the cyclotron pole and yoke. Now, we try to investigate the instability of the ion beam for this phenomenon. A lot of checking quantities, such as ion beam phase, relative distribution of magnetic field, main coil current, temperatures at cyclotron yoke and cooling water, are monitored during several days on the beam acceleration test.

In order to maintain the excellent beam stability, main coil current which is one of the most important parameters has to be controlled under very steady state for one week at least. The power supply[1] for the main coil magnet has been designed to equip with superior stability less than 10 ppm.

2. Outline for precise current measurement

We are planning to monitor the main coil current with high precision. Both quantities of the direct voltage across the shunt resistor and output voltage from the direct current - current transformer (DC-CT) through the bus bar in the power supply box are measured simultaneously. The DC-CT calibrated with rated current of 1000 A was purchased from Hollec International Co. in the Netherlands. A measuring head of the DC-CT which is assembled in plastic housing is installed as shown in Photo. 1. This plastic housing made of bakelite is fixed at perpendicular copper bus bar by plastic screws.

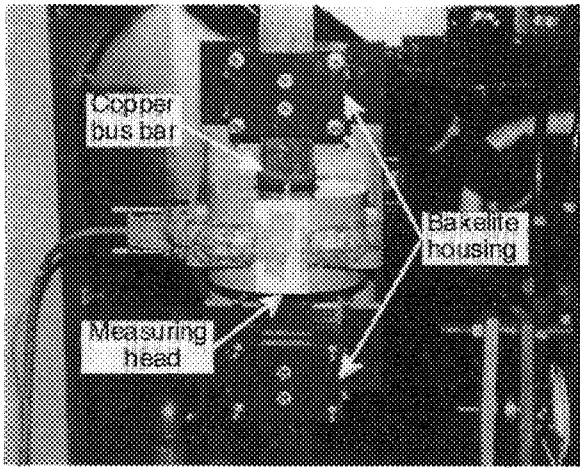

Photo. 1 Installation of the measuring head for DC-CT.

Two calibrators were used in the measurement as the DC standard sources. One is 5440B and the other is new 5720A which is rather expensive. Both calibrators[2] equipped with excellent stability much less than 1 ppm were manufactured by Fluke Co. in USA. An outline for the precise measurement is illustrated in Fig. 1. Some temperatures and voltages should be checked for the purpose of data correction. The measuring environment for the DC-CT in the power supply can be enough allowed because the magnetic field surrounding the measuring head is 8 G (specification value[3] : below 20 G) and the distance far from the modified return bus bar is 30 (more than 20) cm.

3. Basic measurement circuit

Basic measurement circuit is shown in Fig. 2. A null voltmeter with high input impedance detects slight difference voltage between DC standard and shunt resistor/DC-CT output. The output voltage from the shunt resistor or DC-CT, V_M, is given by a simple following equation.

$$V_M = V_S + V_N$$

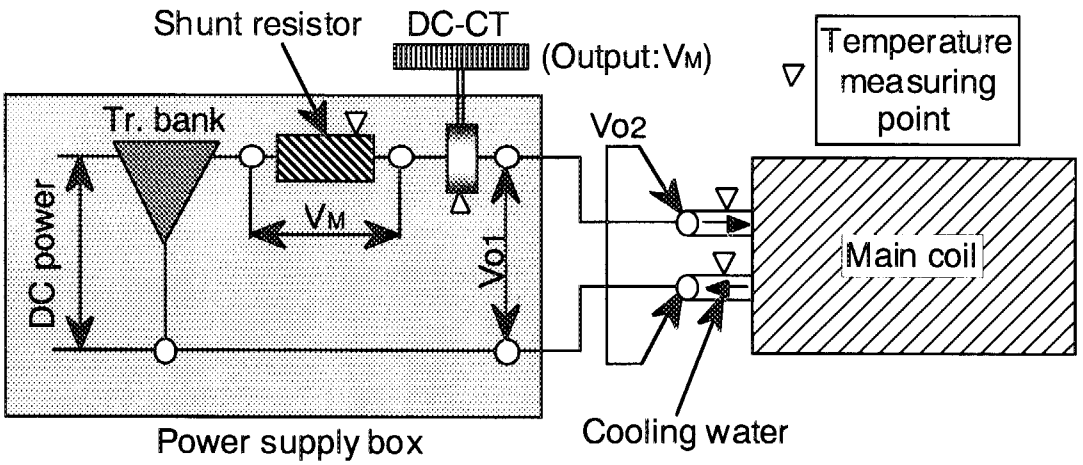

Fig. 1 An outline for precise measurement of main coil current.

Where, V_S is the output voltage from the DC standard, V_N the voltage detected by the null voltmeter, respectively. The output signal of V_N is usually drawn on an analogue recorder.

In general, the method of grounding is a severe technical problem on precise measurement. The grounding cable for chassis is connected to the general grounding line because of person security. And, the guard terminals in the instruments should be also connected to an exclusive grounding line for the cyclotron system by way of the prevention against external noise interference.

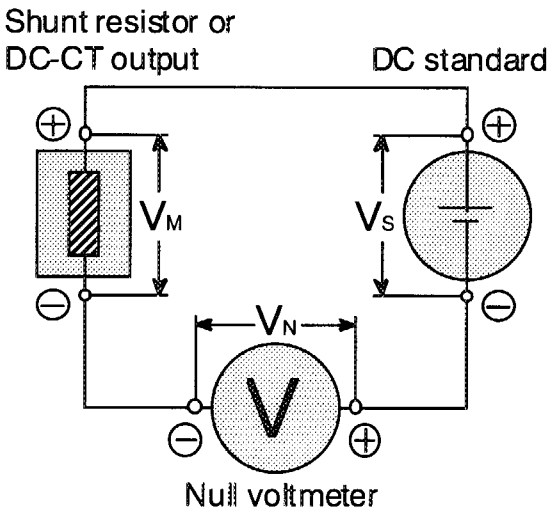

Fig. 2 Basic circuit for precise current measurement.

4. Test result

The output response from the shunt resistor and DC-CT was made sure by each step of 0.01 A minimum increment for the main coil current. The change of both outputs is shown in Fig. 3.

Two stepwise output signals are similar in shape to the unit increment of the main coil current. A magnitude of the third step for the

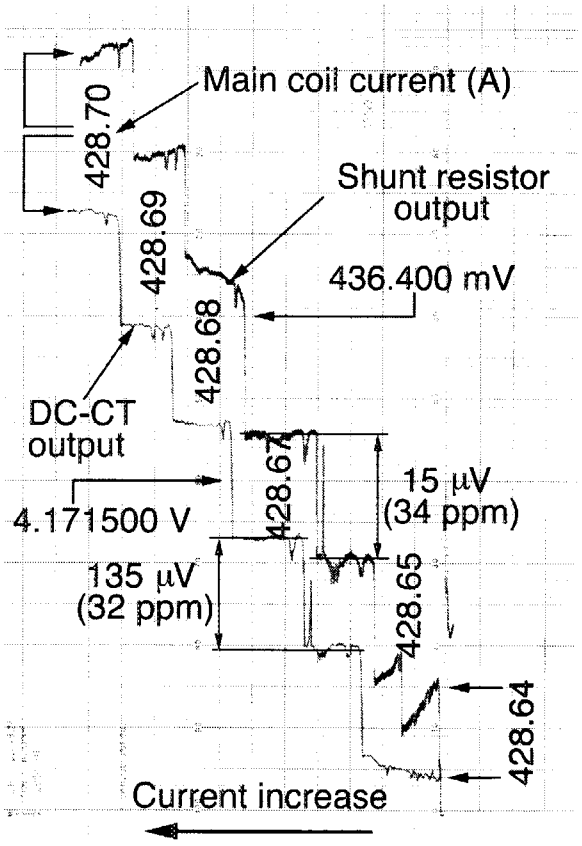

Fig. 3 Output response of the shunt resistor and DC-CT to 0.01A increment of the main coil current.

shunt resistor is 15 μV to the output voltage of 436.4 mV, on the other hand, one for DC-CT is 135 μV to 4.1715 V output. Since these steps are estimated at almost same rates corresponding to about 32-34 ppm between 428.64 and 428.70 A of main coil current, this accordance shows that both responses are enough reliable to carry out precise measurements.

References

1) K. Arakawa, Y. Nakamura, *et al.*, TIARA Annual report, vol. 1, p3 (1992)
2) Catalogue, High performance multifunction calibrator, Fluke Co., (1997)
3) User manual, "System TOPACC 1.0, Zero-flux current transformer", Hollec International, Co. (1996)

8. 6 Development of High Precision Beam Positioning and Single Ion Hit Techniques with the Heavy Ion Microbeam System.

T.Kamiya, T.Sakai, Y.Naitoh and T.Hirao*.
Advanced Radiation Technology Centre, JAERI/Takasaki
*Department of Materials Development, JAERI/Takasaki

1. Introduction

Beam positioning technique and single ion hit one have been established in the TIARA heavy ion microbeam system[1-4]. These provide methods to observe individual phenomena induced by single ion injections to semiconductor devices or to biological cells. However, these phenomena take place so statistically that one can not extract enough information from small amounts of events induced by manually controlled single ion hits. In biological cell irradiation, for example, more than 10^5 cells should be irradiated by single ions on particular local area of them in a few hours. An automated beam positioning and single ion hit system was required to perform such actual experiments. In this report, development of the system is outlined and results of performance tests are described.

2. Apparatus and experimentals

A schematic diagram of the automated beam positioning and single ion hit system is shown in Fig. 1. A single ion hit system consisting of a single ion detector and a fast beam switch is controlled by a personal computer (PC) which sets hit positions in a microbeam scanning area of a sample.

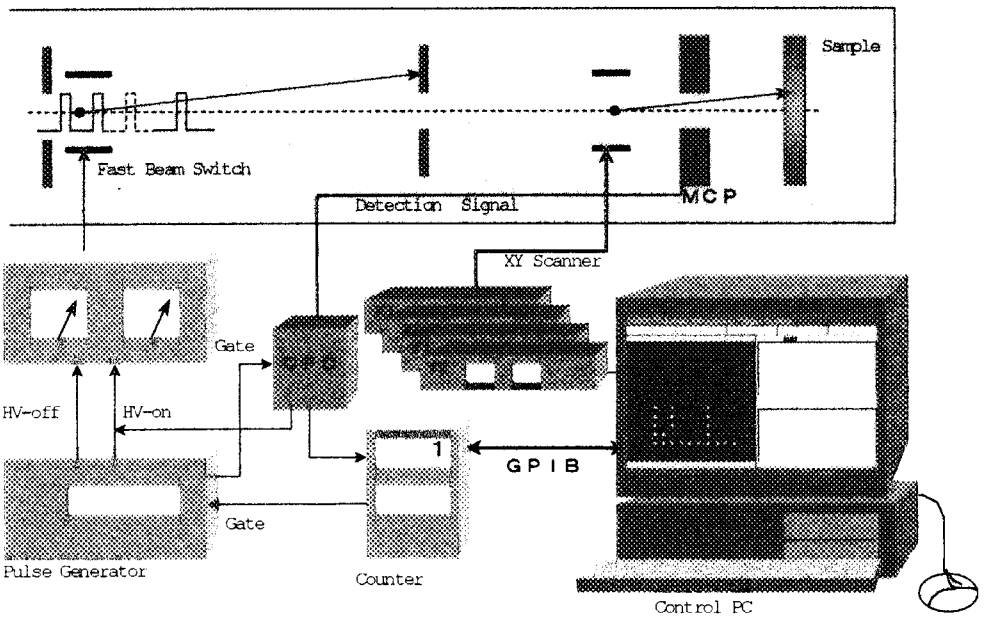

Fig. 1 Schematic diagram of automated beam positioning and single ion hit system

Hit positions defined by the scanner voltages are set according to stored data in the PC. Hit times defined by preset times on a counter are set through a GPIB interface.

An experiment of single ion (15 MeV Ni) irradiation to a plate of CR-39, a nuclear track detector, was performed in order to draw a 'daruma' dot pattern in a 200 x 200 μm^2 area automatically as shown in Fig. 2. Each etch pit was formed at just a single ion hit position by chemical etching with 60 °C 6 N NaOH solution for half an hour.

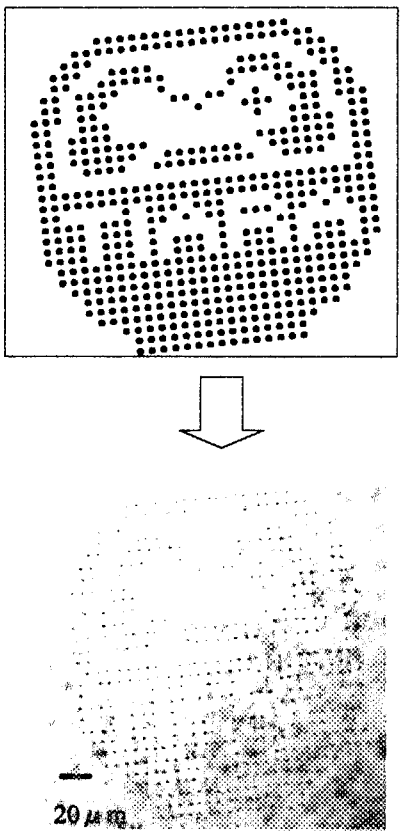

Fig. 2 'Daruma' dot pattern set in the computer program (upper) and etch pits on CR-39 irradiated by 15 MeV Ni single ions, respectively (lower).

In order to test the hit positioning accuracy, another CR-39 was irradiated by the same ions with 16 x 16 matrix patterns in two ways as shown in Fig. 3; (a) one scan of 50 continual hits onto the matrix positions, (b) 50 repeating scans onto the other matrix. It takes 3 minutes to make the former irradiation and 60 minutes the latter. Clusters of etch pits seem to have similar shapes for both the irradiation methods. These also show that the positioning accuracy is kept less than ±1 μm for an hour and that it takes about 0.5 second to move a hit position to the next.

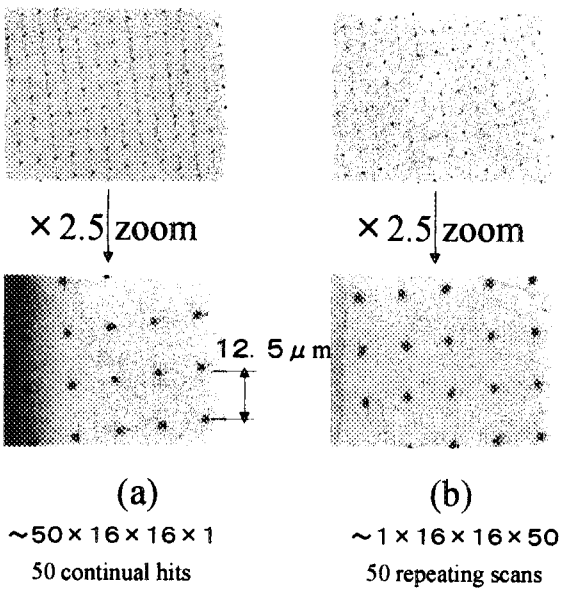

Fig. 3 Matrix patterns of clusters of etch pits on CR-39 irradiated by 50 15 MeV Ni ions. Each cluster was formed by (a) one scan of 50 continual hits and by (b) 50 scans of single hit on the same points.

3. Conclusion

An automated beam positioning and single ion hit technique was developed in the TIARA heavy ion microbeam system, in order to perform single ion irradiation to plenty of positions of samples. Feasibility of the system was demonstrated using CR-39's, nuclear track detectors as target samples for making single ion hit tracks visible. In the future project, this technique will be introduced to a high energy heavy ion microbeam system connected to the TIARA AVF-cyclotron, so that various phenomena can be simulated by irradiation of single ions with the actual energy range. We are also thinking of utilizing this system for observation of individual processes of interactions induced by single ions, such as luminescence or radiation damage effect in various materials.

References

1) T.Kamiya, N.Utsunomiya, E.Minehara, R.Tanaka and I.Ohdomari, Nucl. Instr. And Meth. B64 (1992) pp362-366.
2) T.Kamiya, T.Suda and R.Tanaka, Nucl. Instr. And Meth. B118 (1996) pp362-366.
3) T.Kamiya, T.Sakai, T.Hamano, T.Suda and T.Hirao, Nucl. Instr. And Meth. B130 (1997) pp285-288.
4) T.Sakai, T.Hamano, T.Suda, T.Hirao and T.Kamiya, Nucl. Instr. And Meth. B130 (1997) pp498-502.

8. 7 Component analysis of emitted gas from CR-39 during light ion microbeam irradiation

Takuro SAKAI, Yutaka NAITOH and Tomihiro KAMIYA
Advanced Radiation Technology Center, JAERI

1. Introduction

Interactions between ionizing radiation and organic materials have been studied widely and the research still has been an interesting field. Recently we found out that tracks of light ion microbeam in CR-39 films, a well known track-detector [1], were observable without chemical etching and these tracks became deeper as the dose increase [2]. The tracks in the organic material were considered to be induced by extremely high current density ion beam. The polymer was supposed to be decomposed by the irradiation, namely chemical bonds in irradiated region were broken along the trajectory of the ion beam resulting in the formation of tracks. There are few reports about effects of high brightness microbeam irradiation to a small local point. We have measured partial pressures of gas from CR-39 generated by the microbeam irradiation so as to see basic processes of this phenomenon. This work has also practical aspects. Thin organic films are a promising material for a beam exit window which is a partition between high vacuum beam-line and atmospheric side. Organic films consist of light elements which reduce the beam broadening by multiple-scattering and generate no hard x-rays and furthermore they have relatively high mechanical strength, cheaper cost and so on. This window is one of essential parts for external scanning microbeam system that is under development for PIXE analysis here. This study will also contribute to developing suitable materials for this window.

2. Experimental

Fig. 1 shows the schematic diagram of the experimental setup. Beam-induced gases were analyzed by a quadrupole mass spectrometer (ANELVA M-QA200TS) which was located at 135 mm apart from the target position. The background pressure was in the order of 10^{-8} Torr. A CR-39 sheet was irradiated by 2 MeV proton and helium microbeams. The size for each ion beam was about ø1.5 μm with the current of 150 pA and 130 pA, respectively. Point and scanning irradiations over 250 μm x 250 μm area have been performed with proton

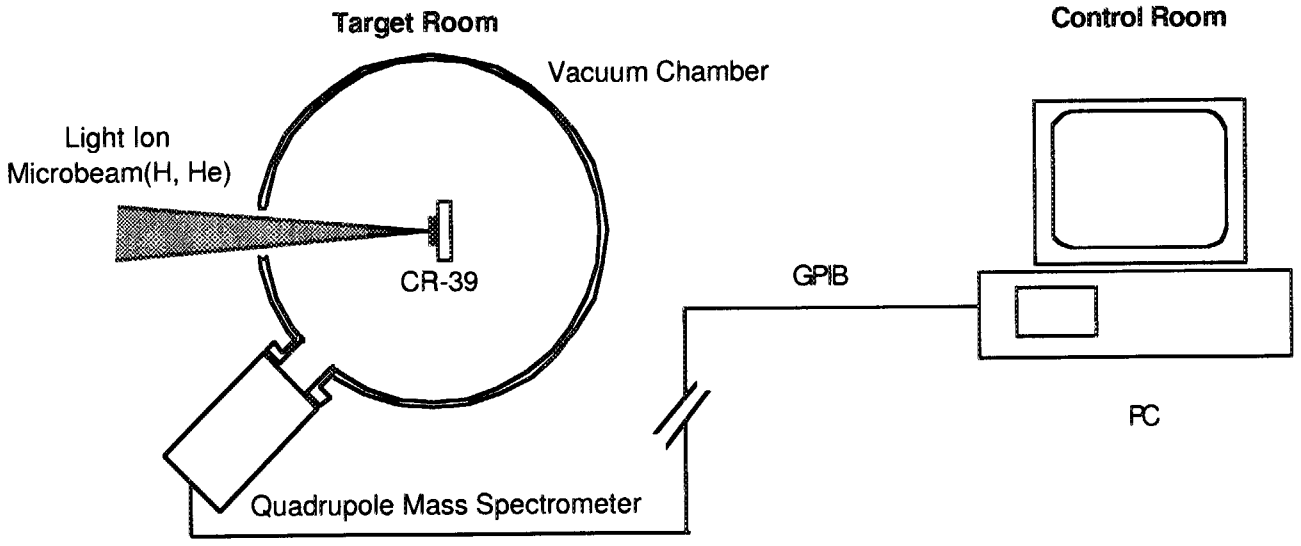

Fig. 1 Schematic diagram of experimental setup

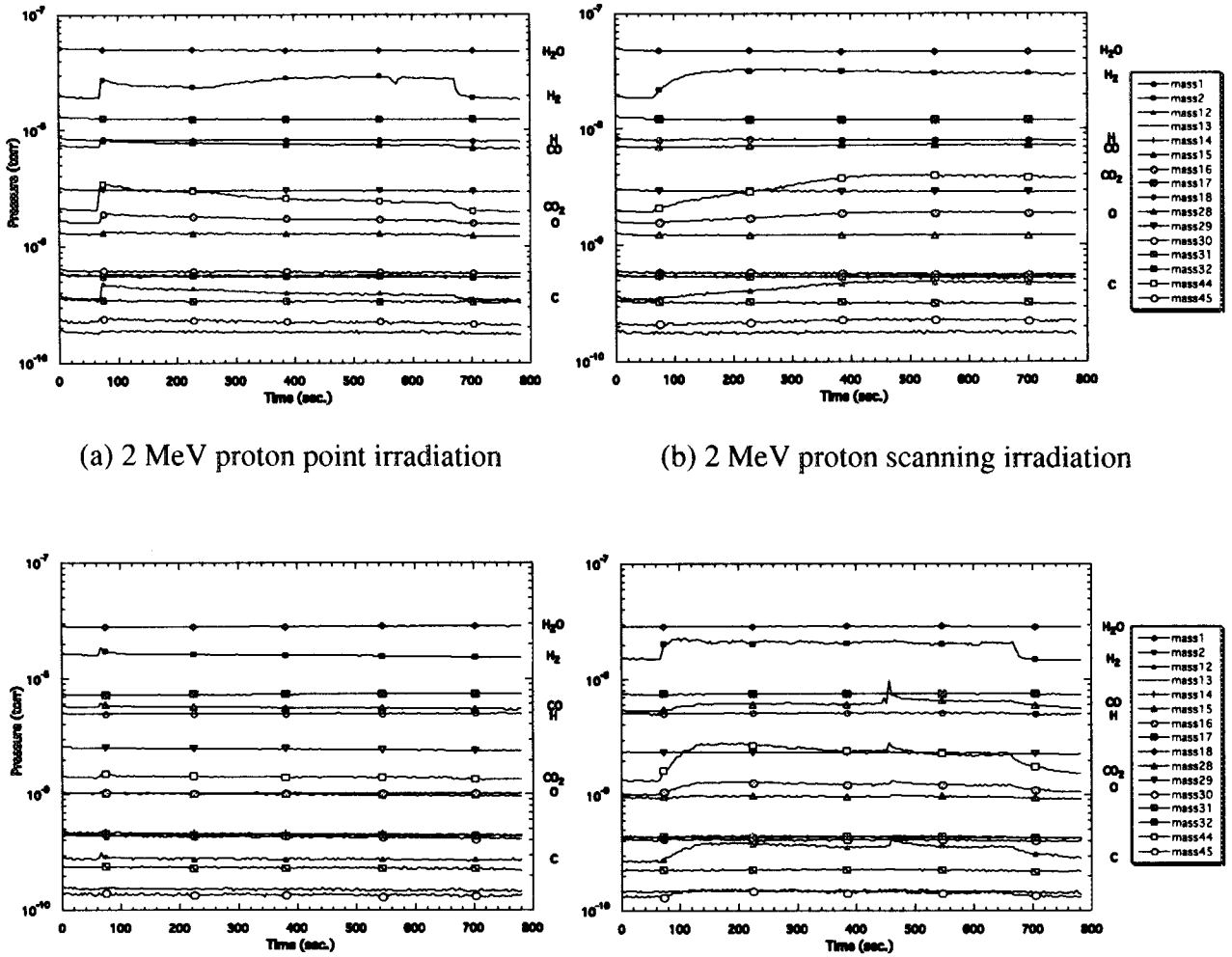

(a) 2 MeV proton point irradiation

(b) 2 MeV proton scanning irradiation

(c) 2 MeV helium point irradiation

(d) 2 MeV helium scanning irradiation

Fig. 2 Trends of partial pressures measured by the mass spectrometer

and helium beams. A trend of partial pressures was measured in each condition by the mass spectrometer. Results are shown in fig. 2. The irradiated CR-39 sheet was taken from the chamber and observed with an optical microscope. The microscopic photographs of 2 MeV helium ion irradiated sheet are shown in fig. 3.

3. Results & discussions

The partial pressures of mass number 2(H_2), 12(C), 16(O, CH_4), 28(CO, C_2H_2) and 44(CO_2, C_3H_8) in measured sixteen components were increased during the beam irradiation. Because fragments of hydrocarbons (i.e. 13=CH, 14=CH_2 and so on) didn't increase by the irradiation, components of mass number 16, 28 and 44 were identified as O, CO and CO_2. O was considered to be fragment of CO or CO_2. Decomposed gases from the CR-39 were hydrogen, carbon monoxide and carbon dioxide.

Although the trend of pressure varies in different conditions, the components which were related to the irradiation were the same. The gas production was larger in scanning irradiation than in point one. These results suggest that the CR-39 was mainly decomposed by ionization rather than thermal effect.

Amount of the gas production was remarkably small in point irradiation of helium

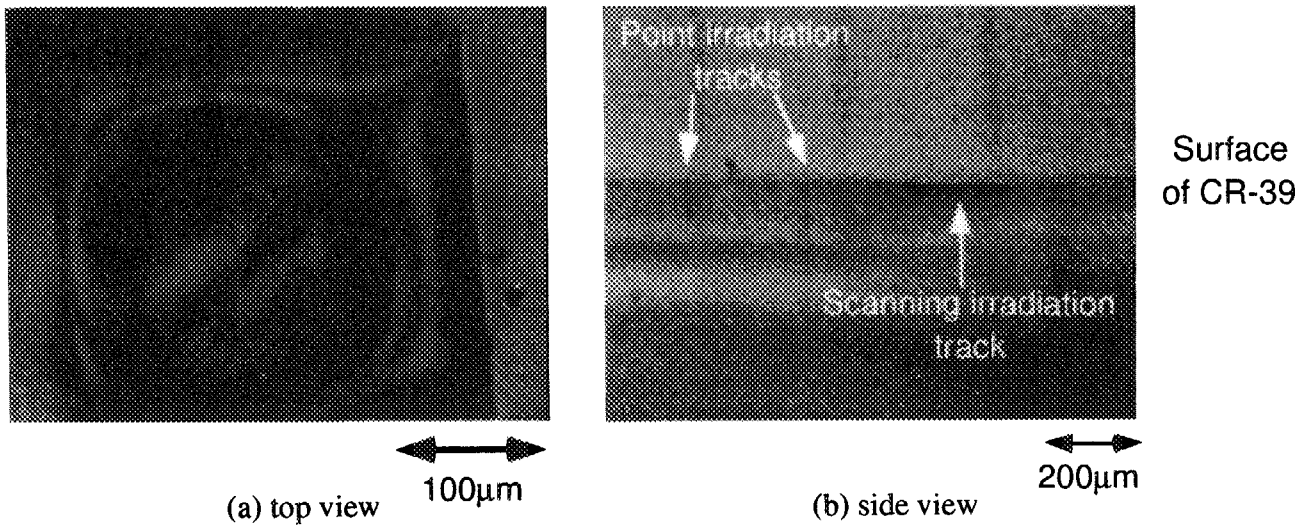

Fig. 3 Microscopic photographs of 2 MeV irradiated CR-39 sheet

ion. However the observed tracks exceeded its range in CR-39. Helium ion has the lager value of LET, namely, dense ionization would be caused in smaller area. Fine holes might be formed rapidly, so diffusion of gases would be limited or some products might recombine.

Our present work revealed some new effects induced by intense ion microbeams, and further study is expected for more detail discussion.

Acknowledgement

We are grateful to Dr. M. Asano for the supply of CR-39 track detector and kind guidance. We would like to thank all the staffs of JAERI electrostatic accelerator group for their assistance.

References

[1] R. L. Fleischer, P. B. Price, and R. M. Walker, Nuclear Tracks in Solids, Principles and Applications, University of California Press

[2] T. Sakai, T. Hamano and T. Kamiya, Proc. of the 34th seminar on science and technology, small accelerators and their application, Tokyo 1997, p261

8．8 Coulomb Explosion Image Experiment in TIARA

Y. Saitoh, T. Sakai, T. Kamiya, Y. Naito, K. Mizuhashi, S. Tajima

Advanced Radiation Technology Center, JAERI/Takasaki

1. Introduction

We are developing MeV energy molecular and cluster ion beams by using the 3 MV tandem accelerator in the TIARA. MeV clusters transfer energy of large density in materials, so that deferent phenomena from those induced by irradiating elemental ions should be expected. These beams are used for investigation of non-linear effect and materials modification. Six sorts of MeV energy cluster and molecular beams, B_{2-4}, C_{2-8}, O_2, Al_{2-4}, Si_{2-4}, Cu_{2-3}, LiF and AlO, are available[1] so far. Different kinds of ions, Li^+ and F^+ for instance, can be implanted simultaneously in a very small aria of target by using LiF and AlO beams. The information of the structures of the clusters is important to analyze fundamental interactions between the beams and targets. Therefore, we are going to investigate the structures by Coulomb Explosion Imaging (CEI). The preparation of a detection system of CEI and the preliminary experiments for carbon clusters (C_n:n=2-6) are reported.

2. Coulomb Explosion Imaging[2]

The CEI has been developed in this decade. Structure of a molecule or a cluster which is actually implanted to a target is directly measured by the CEI. The schematic view of CEI is presented in fig.1. When a swift molecule passes through a thin solid film, it loses all of its binding electrons. The remaining positive ions repel each other by Coulomb repulsion force, which transforms the micro-structure into a macrostructure that can be measured precisely. The measured traces of each fragment nucleus for individual molecules are then transformed into the original molecular structure.

3. Cluster acceleration and experiment

Singly negative charged carbon cluster ions are produced by a conventional Cs sputter ion source (SNICS Ⅱ) and transported to the tandem with the injection energy of 70 keV. Clusters injected to the tandem are accelerated toward the high
voltage terminal positioned in the middle of the accelerator vessel. Most of the carbon clusters are dissolved into the elements by collision with the stripper gas (N_2) in the terminal. However, small amount of clusters are survived and stripped to singly positive charged ions, and accelerated toward the ground level. In the experiment,

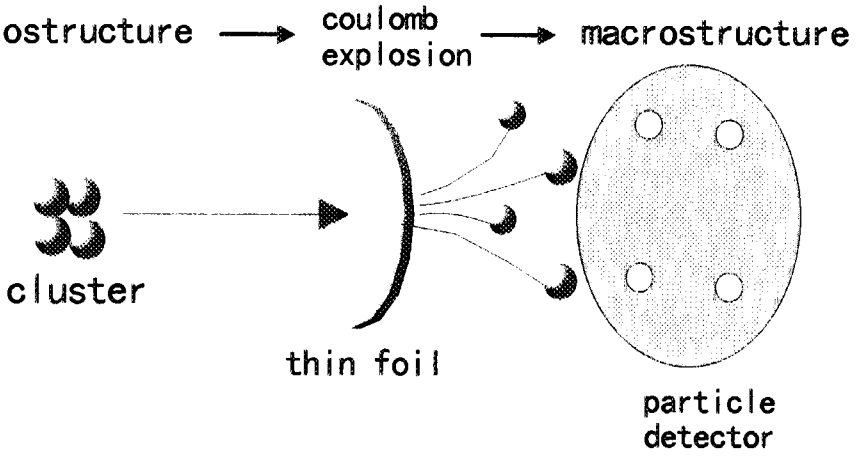

Fig. 1 Schematic diagram of the CEI

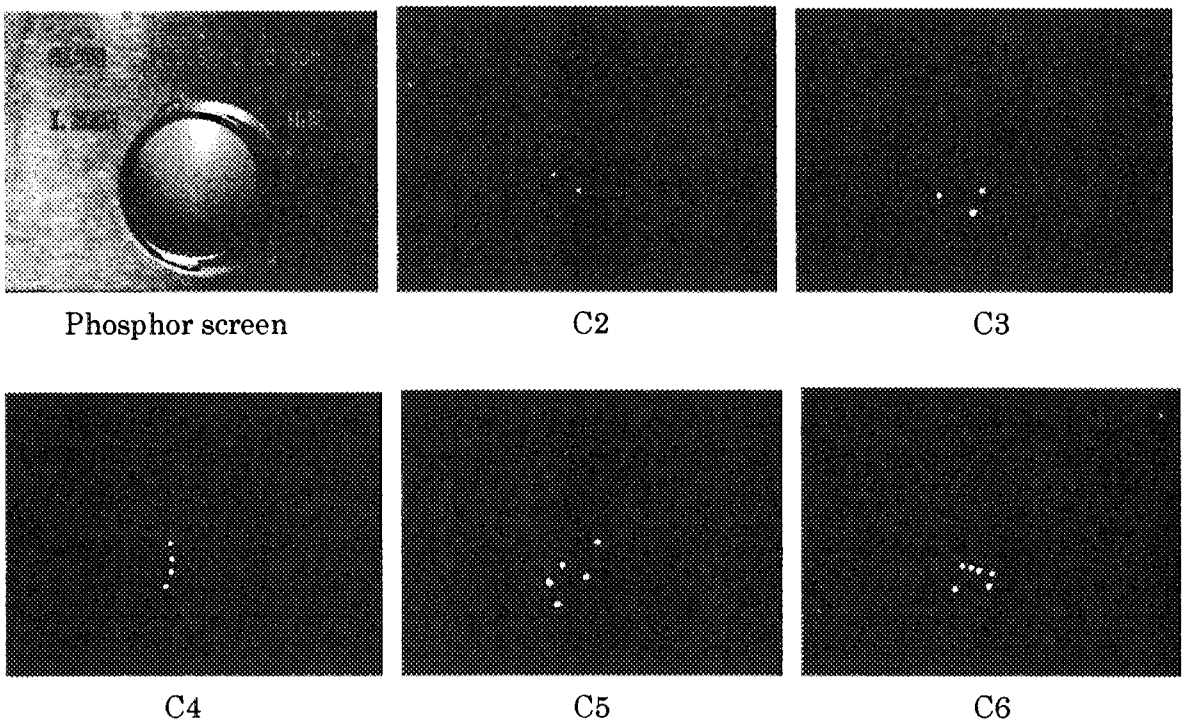

Fig.2 High contrast image of C_{2-6} cluster fragments in phosphor screen

the terminal voltage is set to 3 MV, so that the clusters are accelerated to the energy of 6 MeV.

The CEI experiment was carried out at the multi-purpose chamber connected to the microbeam line[3]. The experimental setup consists of a thin carbon foil (5 $\mu g/cm^2$) , an assembly of microchannel plates (MCP) equipped with phosphor screen as an anode and a video camera. The intensity of the carbon cluster beams is reduced from hundreds nA to several counts per second by means of the mesh attenuator[4] set in the low energy beam line and the fast beam switch in the microbeam line. A MeV Carbon cluster passes through the thin foil where Coulomb explosion occurs. The expanded ions by Coulomb repulsion remaining information of the cluster structure are detected by the MCP placed at the 150 mm downstream of the foil. Hit points of the ions on the MCP are observed by the glimmers on the phosphor screen and recorded by the video camera. The examples of the recorded cluster fragments of C_{2-6} are presented in fig. 2.

4. Conclusion

The preliminary CEI experiment was carried out, and we succeeded in obtaining the fragments of carbon clusters which have the information of the structures by means of the MCP and the video camera. We are planning to obtain and analyze the data automatically.

References

1. Y. Saitoh, K. Mizuhasi, S. Tajima, JAERI-Review 97-015 pp. 240-241
2. Z. Vager, R. Naaman, E. P. Kanter, SCIENCE, Vol. 244, (1989) p426-413
3.T. Kamiya, N. Utsunomiya, E. Minehara, R. Tanaka and I. Ohdomari, Nucl. Instr. and Meth. B64 (1992) p.362-366
4. Y. Nakajima, S. Tajima, JAERI-memo 10-105, (1998)

8. 9 New ion generation method of refractory materials with SF6 plasma

K.Ohkoshi, Y.Saitoh, T.Orimo* and S.Tajima
Advanced Radiation Technology Center, JAERI
*Beam Operation Co. Ltd.

1. INTRODUCTION

The 400kV ion implanter[1] at TIARA facility has been providing variety of ions from proton to bismuth for various experiments. Recently, many kinds of refractory material ions, niobium (Nb), boron (B), and silicon (Si) etc, were requested by users in the research fields of semiconductor development and materials modification. However, it was difficult to generate these ions by the Freeman ion source[2] in our implanter, because the vapor pressures of them at the operation temperature of the source are not enough to produce ions. Accordingly, we developed a new ion generation method with SF6 (sulfur hexa-fluoride) plasma for production of refractory materials with high intensity.

2. ION GENERATION BY THE FREEMAN ION SOURCE

The gas and oven methods are generally used to produce ions by Freeman ion source. The structure of the Freeman ion source is illustrated in Fig.1. In the case where a gas containing an objective element is available, the gas method is used. If the suitable gas can not be obtained, the oven method is used. To produce the vapor of a solid material, an elementary substance or a compound containing an objective element, is inserted into the oven.

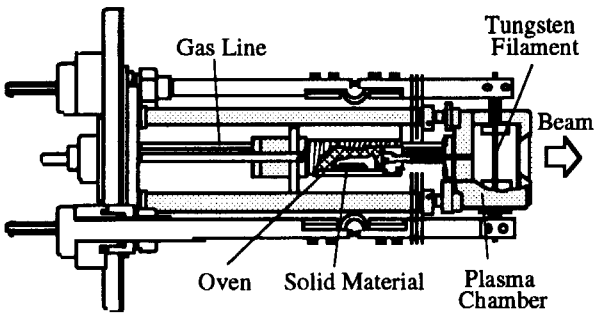

Fig.1 Freeman ion source

However, it is impossible to produce the vapor of refractory materials by the oven method. As for the materials whose vapors are not generated even if those are heated with the oven, the materials are directly installed in the arc plasma of argon (Ar) [3]. However high intensity beam current is not provided in this method. The use of gaseous compounds of solid elements such as fluorides is one of the effective methods. However, the gas containing fluorides tends to be rather harsh and corrosive on the ion sources.

3. OUTLINE OF SF6 PLASMA METHOD

If the high vapor pressure fluoride is directly produced in the ion source through chemical reactions between the solid material and fluorine in the plasma chamber, which is produced by a chemically stable fluoride gas, the amount of the corrosive fluoride in the plasma chamber is extremely reduced and the above drawbacks mentioned in the previous section can be minimized. Therefore, we tried to produce refractory material ions from solid materials by using a plasma generated with chemically stable SF6 gas. We succeeded to obtain the ion beams of B, Si, Nb, titanium, and erbium. Most fluorides of the above elements have much higher vapor pressures than their pure solid materials. For example, BF_3 is gas at normal temperature but pure boron must be heated to about 2000℃ for making the arc plasma to produce material vapor. As an example, the mechanism of B ion generation is shown in Fig.2. In this technique, the sample metals are set in the plasma chamber of the ion source. The SF6 plasma in the ion source involves fluorine ions, sulfur ions, and their neutral elements. The sample materials in the ion source are fluorinated by

the SF6 plasma containing fluoride. The material fluorides with sufficiently high vapor pressure are vaporized and decomposed into fluorine ions and the material ions by the SF6 plasma. The technique is quite simple . It does not need any equipment for evaporating the solid material.

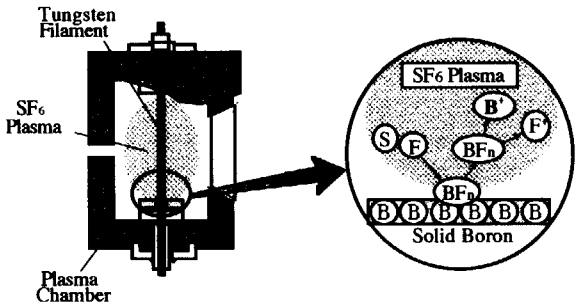

Fig.2 Mechanism of B ion generation

4. EXPERIMENT AND RESULT

To generate B ions, for example, the disk of solid B was set at the bottom of the chamber, where the tungsten filament penetrated the disk. In order to stabilize plasma and to minimize production of the corrosive dirts in the source, the mixture gas of SF6 and Ar was introduced into the chamber. The optimum of ratio of SF6 and Ar of the mixture (SF6(Ar)) was 1:4 in pressure. A mass spectrum of the ions extracted from the source is shown in Fig.3.

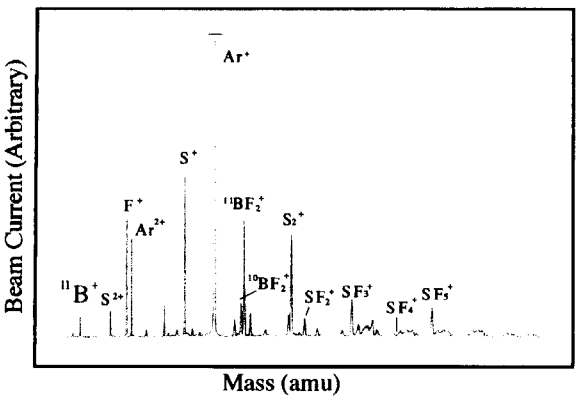

Fig.3 Mass spectrum of ions extracted from source built-in solid B with SF6 (Ar) plasma.

A lot of fragment ions of SF6 and the compound ions of B are observed in the spectrum with $^{11}B^{+}$ ions. Using the same method, other ions of refractory materials were generated. Beam intensities with SF6 (Ar) plasma were 7 to 200 times as much as those with Ar plasma. Topical beam intensities with both plasmas are listed in Table 1.

Table 1 Topical beam intensity of the refractory materials extracted from the source with Ar and SF6 (Ar) plasma

	Ar Plasma	SF6(Ar) Plasma
Nb	0.1 μA	20.0 μA
B	1.0	13.0
Si	0.23	7.0
Ti	1.0	7.0
Er	0.5	10.0

5. SUMMARY

The development of SF6 method allowed to produce many ions of refractory material which were difficult to generate so far. Source handling is very easy so that SF6 gas is chemically stable and nonpoisonous. This method is applicable not only to Freeman source but also to other plasma sources such as ECR ion sources[4].

In the future, we will try to generate ions of other refractory materials and rare earth elements.

REFERENCES

1) S.Tajima et al., JAERI-tech 96-029 (1996)
2) J.H.Freeman,Nucl.instrum. Methods 22, p306 (1963)
3) K.Ohkoshi et al.,TIARA Annual Report (Vol.7), p238 (1997)
4) Y.Saitoh et al., Rev. Sci. Instrum, Vol.69, No.2 ,p703 (1998)

8. 10 Production of Multiply Charged Metallic Ions by MINI-ECR Ion Source with SF_6 Plasma

Y. Saitoh, K. Ohkoshi, and W. Yokota

Advanced Radiation Technology Center, JAERI/Takasaki

1. Introduction

The MINI-ECR[1] was designed to produce medium-multiply-charged ions (Ar^{2+} - Ar^{6+}) with a compact microwave generator (10 GHz, the maximum output power 10 W) of a solid state amplifier. The ion source has been tested for gaseous materials (N_2, O_2, Ar, and Xe) and Ar^{4+} beams of 10 eμA have been observed.

However, production of solid material ions is more difficult than that of gaseous ions, because solid materials have to be vaporized to be introduced into the ECR plasma. Presently, a number of various methods have been used as a means of introducing solid elements into the plasma[2,3,4]. The use of gaseous compounds of a solid element such as fluorides (ex. BF_3, WF_6) is one of the effective methods. However, it has some drawbacks; (1) the gaseous containing fluorides tend to be rather harsh and corrosive on ion sources, (2) BF_3 remains in the source after its use for long time[5], (3) special attention is necessary for treatment of most of fluorides because of their toxic property. If high vapor pressure fluorides are directly produced in the ion source through chemical reactions between the solid materials and fluorine in an ECR plasma, which is produced by a chemically stable fluoride gas, the amount of corrosive fluorides in the ion source is extremely reduced and above drawbacks can be minimized. Therefore, we tried to produce metallic ions from solid materials by using a plasma generated with chemically stable SF_6 gas. We succeeded to obtain the ion beams of B, Nb, Mo, Ta, and W.

2. Refractory material ions production technique with SF_6 plasma

In this technique, sample materials are set in the plasma chamber of the ion source. The SF_6 plasma in the ion source involves fluorine ions, sulfur ions and their neutral elements. Sample materials in the ion source are fluorinated by the SF_6 plasma containing fluorine. The fluorides with sufficiently high vapor pressure are vaporized and decomposed into fluorine ions and the material ions by the SF_6 plasma.

The technique is quite simple. It does not need any equipment for evaporating the solid metal. It can be applied to conventional ECR ion sources exclusively for gaseous ions without any modification.

3. Production of B, Mo, Nb, Ta, and W ions

The experiment was carried out at the ion source test stand biased to 10 kV. The 10 GHz microwave of 10 W was fed to the plasma. An extracted ion beam from the source is analyzed by a 90 degree bending magnet, with a beam trajectory radius of 30 cm. Ion beam current is measured by a Faraday cup placed downstream the bending magnet.

We provided annular metallic samples, which were just fitted to the wall with an extraction hole of the plasma chamber shown in Fig. 1. For producing boron ions, a ceramic sample of boron nitride (BN) was provided because of easy production. Those samples can be utilized repeatedly.

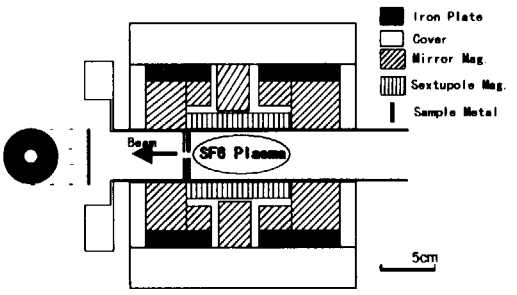

Fig. 1 Schematic cross section of MINI ECR with metallic sample

A typical mass-to-charge spectrum is shown in Fig. 2 for generation of tantalum ions. The observed beam currents for all the elements are summarized in Table 1.

4. Conclusion

The SF_6 plasma method has been tested for three month, and no corrosion has been observed in the ion source. This means that the amount of corrosive gases generated by the method are quite small and the sample metal fluoride is ionized much efficiently in comparison with conventional methods in which the metal gases are fed from outside.

The SF_6 plasma method can be applied for refractory materials and their compounds, which are fluorinated in the room temperature. We expect to apply the method to the materials which react to fluorine at several hundred Celsius degree by means of tuning the ECR plasma heating.

References

[1] Y. Saitoh, W. Yokota, Rev. Sci. Instrum. 67 (3), (1996) 1174

[2] R. Geller, P. Ludwig and G. Mellin, Rev. Sci. Instr. 63 (1992) 2795, and references therein.

[3] R. Harkewicz, P. J. Billquist, J. P. Greens, J. A. Nolen, Jr. and R. C. Pardo, Rev. Sci. Instr. 66 (1995) 2883.

[4] H. Koivisto, J. Arje and M. Numura, Nucl. Instr. Meth. B 94 (1994) 291

[5] R. Harkewicz, J. Stacy, J. Greene, and R. C. Pardo, Rev. Sci. Instr. 65 (1994) 1104.

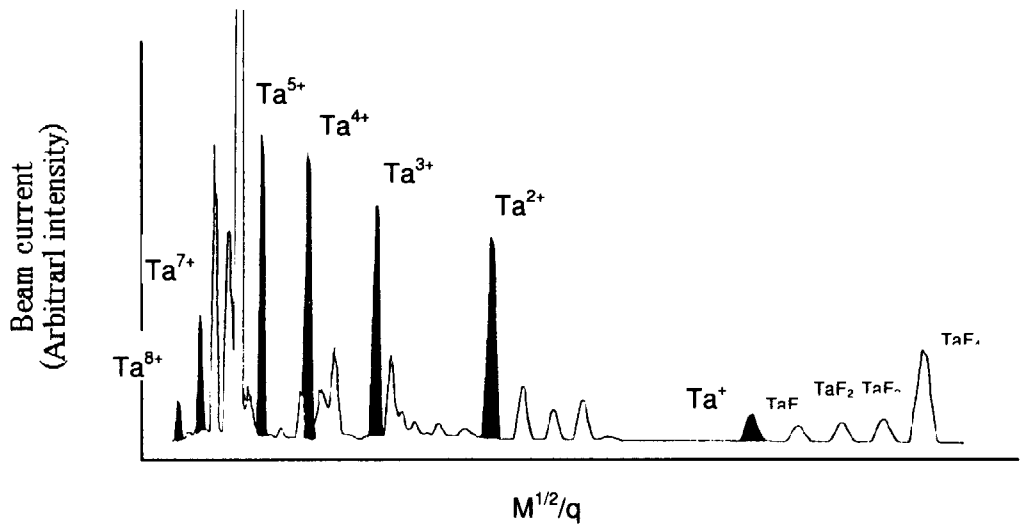

Fig. 2 Mass-to-charge spectrum for tantalum ion generation.

Table 1 Ion beam current for each metal extracted by SF_6 plasma method.

Charge State	1+	2+	3+	4+	5+	6+	7+	8+
^{11}B	6.0 eμA	2.5	0.3					
^{93}Nb	0.46	1.84	2.0	1.38		0.66	0.30	0.18
Σ Mo	0.49	1.85		1.75				
^{181}Ta	0.20	1.43	1.75	2.13	2.28		1.00	0.31
Σ W	0.27	1.07	1.09	1.50	1.69		1.20	0.67

8. 11 Development of micro-PIXE camera

S.Matsuyama, K.Ishii, K.Murozono, K.Goto, H.Yamazaki, S.Iwasaki, T.Sato, S.Yokota*, T.Sakai**, T.Kamiya** and R.Tanaka**

Department of Quantum Science and Energy Engineering, Tohoku University
*Laboratory of Plant and Environmental Research,
Faculty of Agriculture,Tohoku University
**Takasaki Radiation Chemistry Research Establishment, JAERI

1. Introduction

Measurement of spatial distribution of elements in a microscopic region provides invaluable information in medical, biological, botanical and archaeological fields. We combined the microbeam technique[1] with particle-induced X-ray emission (PIXE) analysis which is known to be a novel technique for trace elemental analysis and developed a micro-PIXE system with such characteristics. We call it micro-PIXE camera.

2. Micro-PIXE Camera

A light-ion microbeam apparatus connected to a 3 MV single-ended accelerator in TIARA, JAERI was used in this study. Beam spot size was 0.3 μm with a beam current of 11 pA in this system[2,3]. Figure 1 shows a schematic diagram of beam scanning and data acquisition system for elemental mapping. Proton beams are scanned across the surface of a specimen by two sets of deflection plates which carry sawtooth voltages. The X-rays emitted from the specimen were measured by a Si-PIN diode detector (XR-100T, AMPTEC). In the micro-PIXE camera, X-ray energy and beam position are measured at the same time in order to get spatial distributions of elements. We realized it by combining the beam scanning system of TIARA light-ion microbeam apparatus with the X-ray detection system. Scanning voltages were given by amplifying sawtooth signals generated by a computer and digital-to-analog converters (DAC). The beam position of X-axis or Y-axis is proportional to the scanning voltage for X-axis or Y-axis. The scanning speed is six seconds per one scan at its maximum. Because the higher current density of microbeam deteriorates the status of specimen, the high speed scanning was performed during irradiation.

Figure 2 shows a block diagram of the data acquisition system for X-ray and beam position. The system consists of a multi-parameter data acquisition system and ADCs for X-ray detector signals and for scanning voltage signals. The multi-parameter data acquisition system was manufactured by Laboratory equipment Co. Ltd. Data format of ADC for scanning voltage signals is compatible with that of the ADC for X-ray detector signals. When an X-ray pulse signal enters into one of the ADCs, it triggers a data acquisition cycle. After the analog signals of the detector pulse and a scanning voltage are converted to digital formats, the digital data are saved in a list file. It takes 20 μ seconds for one data acquisition cycle. The list mode data acquisition is useful to observe changes in elemental distributions during irradiation. This system can sort the data for selected element/energy region and generate an elemental map even while the data are accumulated. A large memory size is required in the list mode data acquisition, but it is not so serious since we can utilize large capacity and removable media now. This system can also give a secondary electron image. It is useful to compare the elemental map with the secondary electron image which shows a shape of specimen.

3. Experiment

2 MeV proton beam of a 1 μm spot was used in this study. A leaf epidermis of spiderwort was analyzed to demonstrate the application of micro-PIXE camera to botanical fields. In order to get elemental images of a cell in vivo, the sample target was irradiated in an atmospheric cell settled in a vacuum chamber. Figure 3 shows a mechanism of the atmospheric cell. The sample was fixed on a Kapton foil of 7.5 μm thickness and enclosed with the cell. X-rays from the sample were detected through the Kapton foil. We call this set-up in-air micro-PIXE which reduced sample deterioration caused by irradiation and simplified sample preparation.

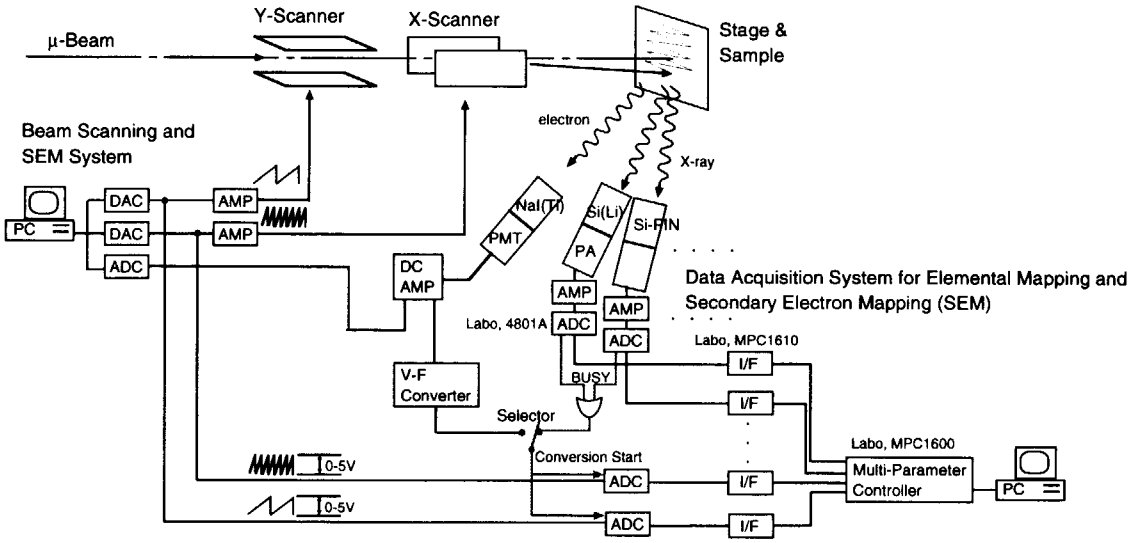

Fig.1 Schematic diagram of beam scanning and data acquisition system for elemental Mapping.

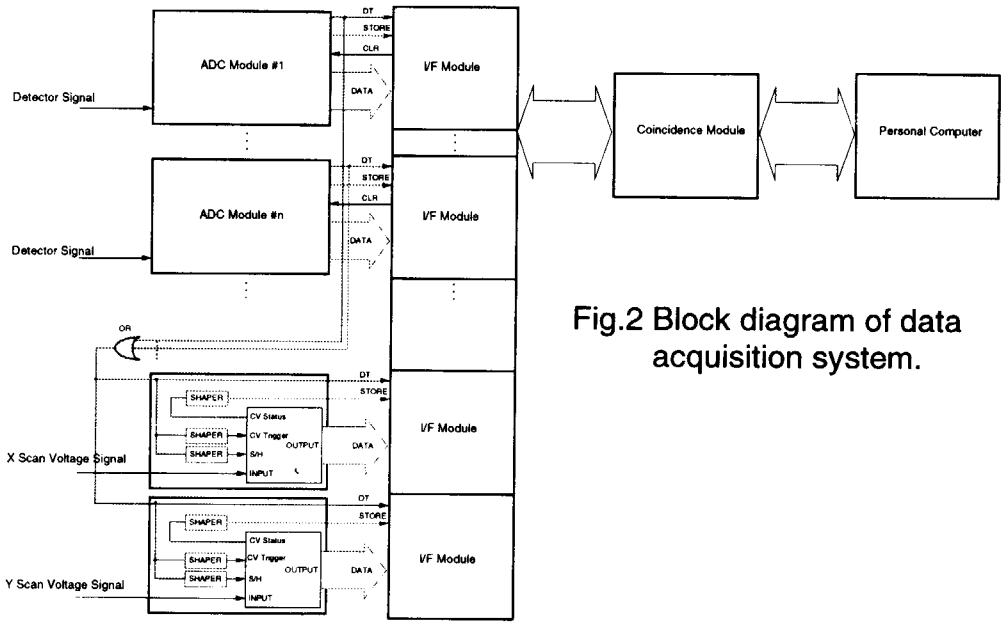

Fig.2 Block diagram of data acquisition system.

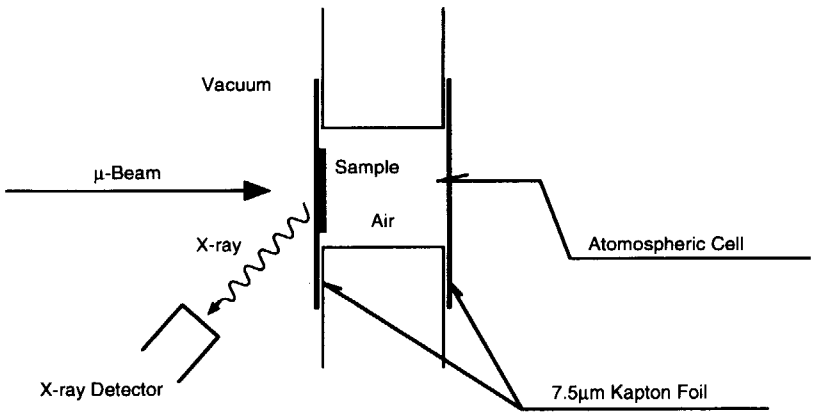

Fig.3 Mechanism of atomospheric cell.

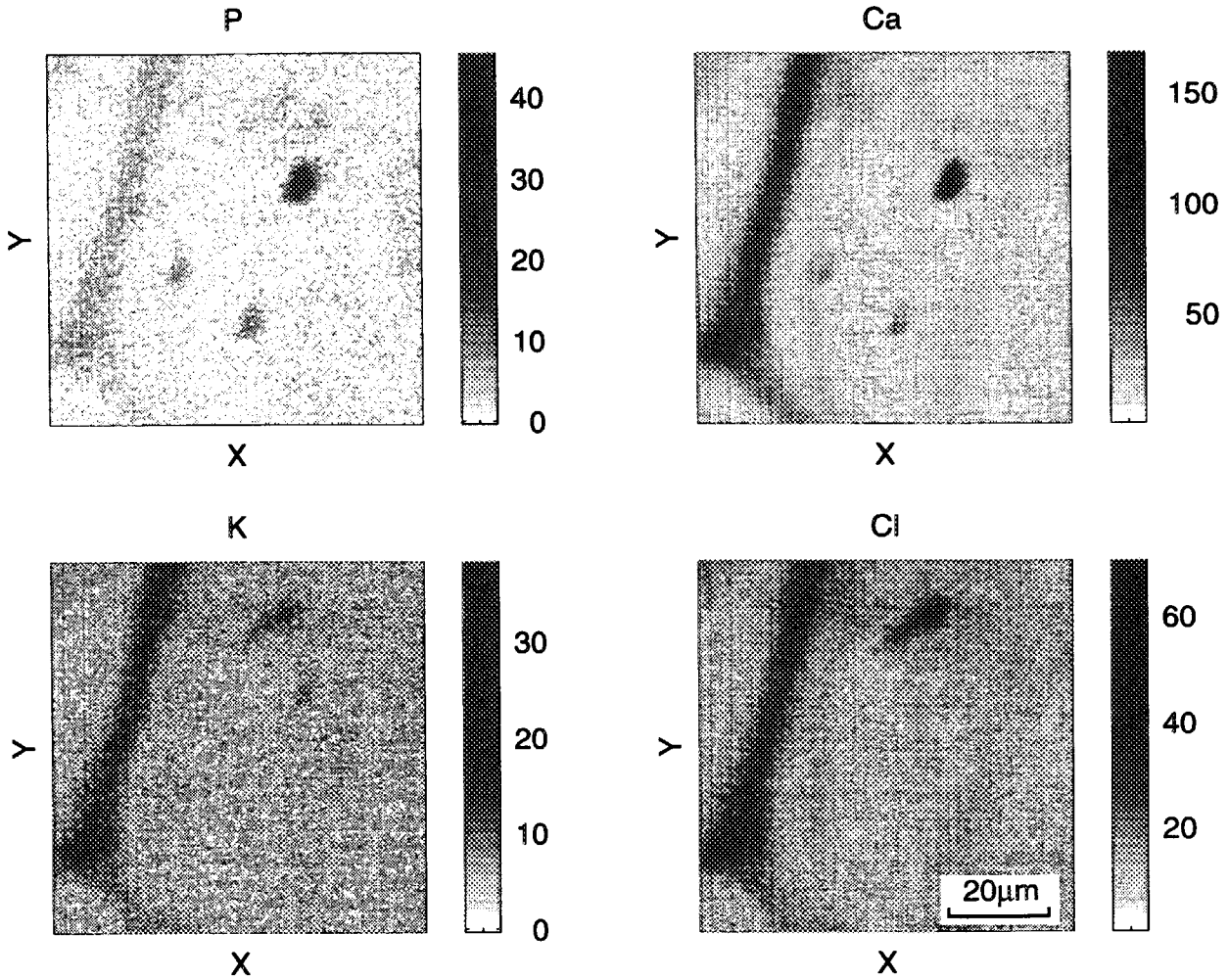

Fig.4 Elemental maps of P, Ca, K and Cl in the leaf epidermis of spiderwort.

Figure 4 shows elemental maps of phosphate(P), calcium(Ca), potassium(K) and chlorine(Cl) in the spiderwort. It took two hours to obtain these images under the beam current of 30 pA. The Ca element is concentrated in a cell wall and a nucleolus. In contrast with the distribution of Ca, the P element is concentrated in only a nucleolus. Each element shows different spatial distribution.

4.Summary

The data acquisition system for micro-PIXE camera was developed. This system is applicable to μ-RBS, STIM and local element analysis combined with the methods mentioned above. As an example of an application to the botanical field, we measured the elemental maps of leaf epidermis of spiderwort and got very clear images.

In this study, we could obtain the images using the in-air micro PIXE camera with an atmospheric cell which was fixed in the vacuum chamber. We are now planning to develop a multi-detectors system to increase the detection efficiency, which will lead to a high speed elemental mapping and reduce radiation damage for the cell samples in vivo.

Acknowledgements

The authors are pleased to acknowledge the assistance of Messrs. Y.Naito and K.Sasaki during the experiments. We wish to thank to Mr. M.Fujisawa for his help in fabrication of the ADCs for scanning voltage signals. We are indebted to Dr. M.Baba for providing the multi-parameter data acquisition system for us.

References

1) F.Watt and G.W.Grime, Principles and Applications of High energy Ion Microbeams (Adam Hilger, Bristol, 1987)
2) T.Kamiya et al., Nucl. Instr. And Meth. B104 (1995) 43
3) T.Kamiya et al., Nucl. Instr. And Meth. B118 (1996) 447

8．12 Development of the technique of the ultra-fine microbeam II

Yasuyuki Ishii, Akira Isoya and Ryuichi Tanaka
Beam Engineering Division, Advanced Radiation Technology Center, JAERI

1. Introduction

The ultra-fine ion beam apparatus has been developed to establish a production technique of a beam of less than 0.1μm in size dia. with beam energy of 100keV order. The basic concept of the apparatus design is the usage of acceleration electrodes which have both characteristics of accelerating and focusing a beam, simultaneously[1,2]. The apparatus consists of an ion source of special duoplasmatron type, two acceleration lenses in series and a beam size measurement system using a knife edge. It was designed and manufactured on the basis of the simulation of beam trajectories. In the process of the ion source development, we obtained a beam of 100eV with an energy spread of about 1eV[3] and very high brightness. In this study, the achievable beam size was estimated.

2. Production of microbeam

The process of the microbeam production[1,2] described on the basis of values estimated using a beam trajectory simulation is as follows. The extracted beam, 0.3mmϕ in size with energy of 100eV order, was accelerated and focused by a series of two acceleration lenses (as shown in Fig.1). At the first acceleration lens, the beam energy reached to about 5keV and the size some μm in diameter. The beam traversed through by a 0.3mm dia. aperture at 140mm downstream of the first acceleration lens to limit the divergence angle within 1×10^{-3}rad. At the second acceleration lens, the beam was subsequently accelerated up to energies of tens keV to 100keV and focused to less than 0.1μm dia.

The size of the microbeam experimentally produced was measured compared to that estimated by the beam trajectory simulation.

3. Estimation of beam sizes

The beam size was estimated through the beam current measurement using the beam size measurement system as shown in Fig.1. The beam current was measured using an aluminum Faraday cup (4mm in dia., 13mm long and suppression voltage about 300V) with gradually change of the knife edge position across the beam.

Several measurements were carried out changing the ion source parameters and the voltage of the second acceleration lens. The beam size measurement result for the beam of 35.7keV at a maximum current of about 100pA is shown in Fig.2 as one example. The beam size was estimated assuming a linear fitting line to the decreasing part in the relation curve of the knife edge position (the readings by a micrometer head) and the beam current.

4. Discussion

Most of experimental results of the beam sizes, down to 0.9μm, are almost equal to those of the beam trajectory simulation results with good reproducibility, although they are larger than the size of 0.1μm. At the beam size of less than 0.9μm, the measured value is different from that of the simulation because of problems, for instance, the unstable beam current measurement and interaction between H_2^+ ions and H_2 residual gas.

The unstable beam current measurement might be due to contribution of secondary electrons produced by the collision between ions scattered at the knife edge and the suppressor electrode. The suppression

electrode shape in the Faraday cup is now modified to minimize the ion collision probability.

The interaction between H_2^+ ions and H_2 residual gas (about 3×10^{-4}Pa) was considered to interfere the focus of the beam, which resulted in increase of the divergence angle of the beam injected in the second acceleration lens. The apparatus is now also improved to achieve the vacuum of less than 1×10^{-5}Pa.

These modifications are anticipated to allow us to produce a beam of 0.1μm in dia. in the next experiment

References

1)A.Isoya, A Universal Method of Producing Ultra-fine microbeam, Proc. Inter. Conf. on Application of Nuclear Techniques. P.334-339, June 1991, Crete, Greece

2)A.Isoya, A Universal Method of Producing Ultra-fine microbeam, Proc. Inter, Conf on Evolution in Beam Application, Nov. 1991, Takasaki, Japan

3)Y.Ishii, A.Isoya and R.Tanaka, Nucl. Instr. Meth. B113(1996)75-77

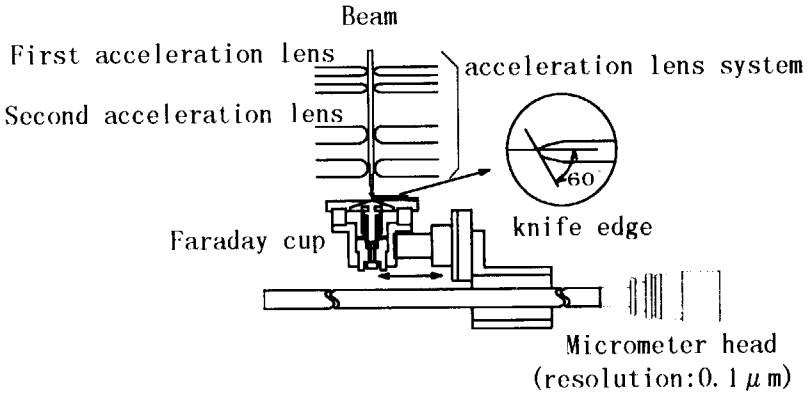

Fig.1 Schematic diagram of beam size measurement system with acceleration lens system.

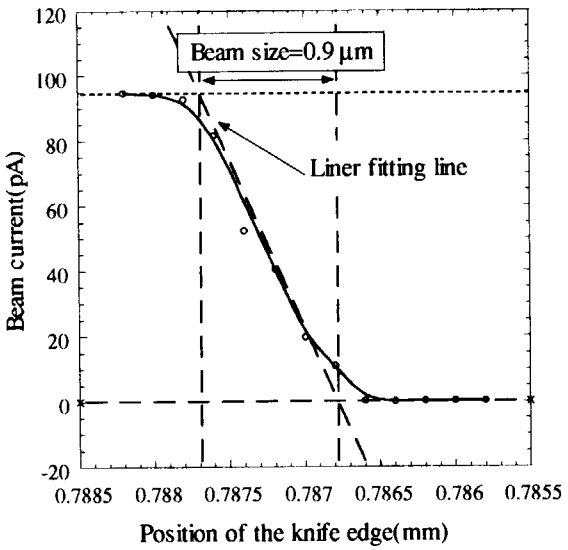

Fig.2 One example of the beam size measurement (beam energy : 35.7keV).

9. Status of TIARA 1997

This is a blank page.

9. 1 UTILIZATION OF TIARA FACILITIES

Utilization and Coordination Division,

Advanced Radiation Technology Center, JAERI

1. Introduction

TIARA is a center of the ion accelerator facilities composed of four ion accelerators, an AVF cyclotron, a 3MV tandem accelerator, a 3MV single-ended accelerator, and a 400kV ion implanter. These accelerators have been fully served for ion beam applications since January 1994.

2. Utilization System

TIARA is opened for public use: it receives applications of the experimental subjects in wide areas once a year from outside users as well as JAERI staffs. The subjects are approved after the official investigation by TIARA General Program Committee(GPC). To attain an effective outcome of the research program, the utilization time of each accelerator is fairly allotted to the subjects three times per year by the Program Advisory Committee (PAC) under the GPC, which are both publicly organized.

Charges for the utilization are remitted in the case that a contract of the joint research between JAERI and a university or a company or that of the projective joint research between JAERI and universities is made. The results of research have to be published at the TIARA Research Review Meeting and in the JAERI TIARA Annual Report. There is another system of visitor use with charges but without the publication duty.

3. Experimental subject approved

Number of subjects using cyclotron approved in FY 1997 for the experiment was 53 while the total number using three electrostatic accelerators was 42 as shown in Table 1. Table 2. shows the number allotted to users under various contracts.

Table 1. Number of experimental subjects at various research fields.

Accelerators / Fields of Research	number of subjects: cyclotron	electrostatic accelerators
Materials for space	4	4
Materials for fusion	2	12
Biotechnology	23	2
Functional material	4	18
RI & nuclear chem.	7	0
Radiation chemistry	5	0
Basic technology	8	6
Others	0	0
total	53	42

Table 2. Number of experimental subjects at various relations with users.

Accelerators / Relations with visitors		number of subjects: cyclotron	electrostatic accelerators
JAERI only	Takasaki Establishment	14	14
	Others	2	7
Cooperative research with university		13	8
Projective joint research between JAERI and universities		14	9
Joint research with private company or govermental institute		9	4
Cooperative & Joint Research		1	0
total		53	42

4. Allotted time to users

The cyclotron has been continuously operated from Monday to Friday. The utilization time for the cyclotron is allotted by the hour. In case of the electrostatic accelerators, on the other hand the utilization time is allotted by the day from 9 a.m. to 6 p.m.: (A mode), 9 a.m. to 10 p.m.: (B mode).

As shown in Table 3, the cyclotron was used at the various research fields, until the electrostatic accelerators were mainly used in the field of functional material. The ratios of allotted time to JAERI staffs were ca. 34% in the cyclotron utilization and ca. 63% in the utilization of other electrostatic accelerators as shown in Table 4.

Table 3. Utilization of accelerators in FY 1997 at various research fields.

Accelerators / Fields of Research	utilization days at each period															
	cyclotron				tandem accelerator				single-ended accelerator				ion implanter			
	8-1	8-2	8-3	total	8-1	8-2	8-3	total	8-1	8-2	8-3	total	8-1	8-2	8-3	total
Material for space	184	128	97	409	11	8	9	28	-	-	1	1	5	7	4	16
Material for fusion	9	0	10	19	11	9	9	29	10	15	16	41	7	4	5	16
Biotechnology	269	209	167	645	4	4	4	12	-	-	-	-	-	-	-	-
Functional material	43	62	37	142	15	17	12	44	28	25	15	68	33	31	25	89
RI & nuclear chem.	112	96	87	295	-	-	-	-	-	-	-	-	-	-	-	-
Radiation chemistry	36	41	22	99	-	-	-	-	-	-	-	-	-	-	-	-
Basic technology	278	204	246	728	13	14	11	38	14	17	12	43	3	3	4	10
total	931	740	666	2337	54	52	45	151	52	57	43	152	48	45	38	131

Table 4. Utilitization of the accelerators in FY 1997 at various relations with users.

Relation with visitors / Accelerators		utilization day at each period															
		cyclotron				tandem accelerator				singl-ended acceler.				ion implanter			
		8-1	8-2	8-3	total	8-1	8-2	8-3	total	8-1	8-2	8-3	total	8-1	8-2	8-3	total
JAERI only	Takasaki Establishment	358	333	228	919	31	25	26	82	27	33	20	80	26	27	25	78
	others	9	0	10	19	4	2	3	9	6	10	12	28	2	1	1	4
Cooperative research with universi.		175	165	111	451	8	11	3	22	14	5	4	23	-	-	-	-
Projective joint research between JAERI and universities		220	131	229	580	10	12	12	34	5	6	5	16	17	12	8	37
Joint research with company or govermental institute		167	109	86	362	1	2	1	4	-	3	2	5	3	5	2	10
Cooperative & Joint Researches		2	2	2	6	-	-	-	-	-	-	-	-	-	-	-	-
Visitors use with charges		114	214	122	450	0	1	4	5	-	2	1	3	2	2	3	7
total		1045	954	788	2787	54	53	49	156	52	59	44	155	50	47	39	136

9. 2 Operation of AVF Cyclotron

K. Arakawa, Y. Nakamura, W. Yokota, M. Fukuda, T. Nara, T. Agematsu, S. Okumura, I. Ishibori, H. Tamura, K. Akaiwa*, To. Yoshida*, S.Ishiro*, A. Matsumura*, H. Suto*, Tu. Yoshida*,Y. Arakawa* and S. Kanou*.

Advanced Radiation Technology Center, JAERI. *Beam Operation Co.,Ltd.

The JAERI AVF cyclotron was smoothly operated according to a beam-time allotment approved in program advisory committee.

The total operation time in the FY 1997 was 3202 hours, and monthly operation times are shown in Fig. 1. The beam time for experiments was 2811 hours in FY 1997. The percentage of time used for experiments including visitors use with charge, beam developments, and tunings were 87.8%, 5.1% and 7.1%, respectively. Thirty-eight kinds of ion species including cocktail beam (M/Q≒5 and 4 ions) were provided for experiments. The accelerated particles and their beam times are also shown in Fig. 2. The beam time for heavy ions was 67% of all as shown in Fig. 2. Regular yearly over-haul was carried out for 5 weeks in the summer.

We have had the following machine troubles; (1) A leakage from bellows, which are used for pressing the contact fingers of the movable shorting plate against the wall of the coaxial type resonator with high pressure air, caused a vacuum in the acceleration chamber woes, and (2)A cooling water leakage (about 50 L) from the baffle slit of the magnetic channel in the acceleration chamber of the cyclotron. About 250 hours of time lost was due to these troubles and we had to cancel or reschedule the beam time for repair.

In order to meet the requests from many groups of researchers, the accelerated particles, their energies and the beam course are changed as shown in Table 1.

Table 1 Frequencies of particle, energy and beam course change in FYs.

FY	Particle	Energy	Beam Course
1994	70	74	145
1995	61	89	186
1996	81	97	188
1997	88	113	206

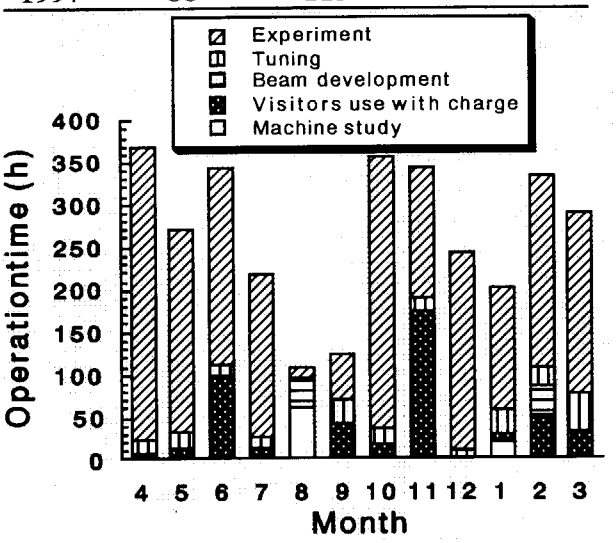

Fig. 1 Monthly operation times in FY1997.

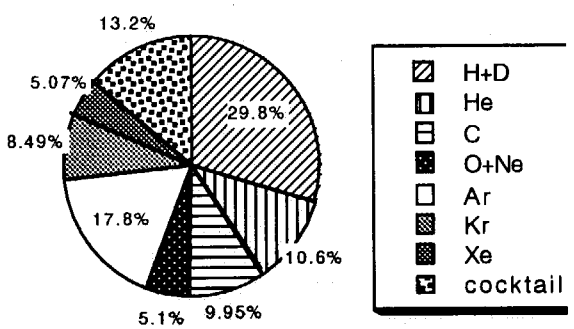

Fig. 2 Beam times of accelerated ions in FY1997.

9. 3 Operation of the Electrostatic Accelerators

S. Tajima, I. Takada, K. Mizuhashi, S. Uno, K. Ohkoshi, Y. Nakajima,
Y. Saitoh, Y. Ishii, T.Kamiya and T. Sakai

Ion Accelerator Operation Division
Advanced Radiation Technology Center, JAERI

1. OPERATION

The three electrostatic accelerators were operated smoothly for various experiments in FY 1997. The total operation time for each accelerator in this fiscal year was 1857 hours for the 3MV tandem accelerator, 2144 hours for the 3MV single-ended accelerator and 1863 hours for the 400kV ion implanter. Yearly operation time for each machine within last seven years are shown in Fig. 1. Yearly operation time are gradually increasing with the years. It was result of the adoption of extended daily operation service.

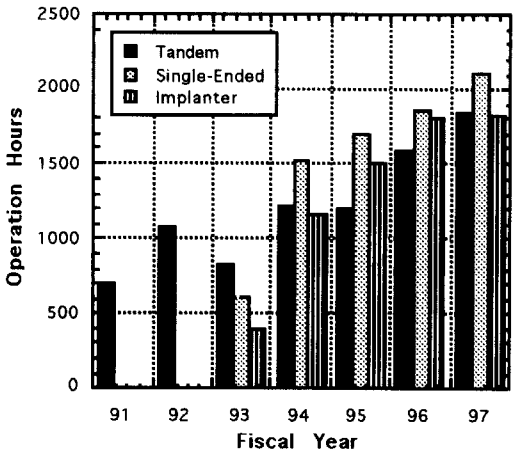

Fig. 1 Yearly Operation Time for Each Electrostatic Accelerator within Last Seven Years.

2. MAINTENANCE

The regular maintenance for the accelerators have taken place in April, August and December. During this term many improvements and renewals for each machine were performed as follows;

For the tandem accelerator; 1) The low-energy accelerating tubes were replaced due to being worn after approximately 8000 hours of service. At the same time of the tube replacement, alignment works between the injection beamline and the tank were carried out. 2) A server which connects control computer to INTERNET was equipped. 3) A gas metering valve feeding nitrogen gas to the terminal stripper was replaced with new one. 4) An ion pump placed high-energy tank end has damaged by vacuum accident and was replaced with the spare one.

For the single-ended accelerator; 5) A new RF ion source was installed after the old source has become considerably worn over one year operation. 6) The plastic tubes for the machine cooling water were replaced with the metal tubes. 7) The resistor assemblies to measure accurate high-voltage of the machine were failed by sparks and were replaced with new ones.

For the ion implanter; 8) A new mesh attenuator was installed on the beamline in front of the switching magnet.

3. MACHINE DEVELOPMENT

We developed new ion generation method which allow to produce the positive ions with high intensity of the refractory materials using SF_6 plasma in the Freeman ion source of the 400kV implanter. The details are described in the separate paragraphs in this report.

In order to extend upward the beam energy range of the 400kV implanter, the practical test of a compact ECR source on the high-voltage deck of the implanter has been promoted. About 1μA of Ar^{3+} was accelerated so far. The ECR source is needed to provide the high-energy ions in excess of 400keV while Freeman source has advantage to generate heavy metal ions. Therefore, the technical point of the development is to keep the compatibility between Freeman type and ECR source.

The developments of the on-line beam monitor which allow to measure beam intensity using the moving probe without beam stopping were carried out. The characteristics of the secondary electron emitted from the probe depended on beam energy and species were measured.

9. 4 RADIATION CONTROL & RADIOACTIVE WASTE MANAGEMENT in TIARA

Safety Division & Utilities and Maintenance Division
Department of Administrative Services. TRCRE. JAERI

1. Radiation Control

1.1 Individual monitoring

(1) Individual monitoring for the radiation workers

Table 1 shows a distribution on effective dose equivalent of the radiation workers in fiscal 1997. The effective dose equivalent values of almost workers were less than 0.2 mSv (minimum detectable dose equivalent).

Maximum dose equivalent was 1.4 mSv/y due to the overhauling of the cyclotron.

(2) Individual monitoring for the visitors and others

Table 2 shows number of persons who have been temporally entered the radiation controlled areas. The effective dose equivalent of all persons were less than 0.2 mSv.

Table 1. Distributions on the effective dose equivalent in fiscal 1997.

Items \ Persons \ Periods		Number of persons			
		1st quarter	2nd quarter	3rd quarter	4th quarter
Distribution range on effective dose equivalent HE:Effective dose equivalent*1(mSv)	HE < 0.2	320	367	356	381
	0.2 ≦ HE ≦ 1.0	4	5	0	9
	1.0 < HE ≦ 5.0	0	0	0	0
	5.0 < HE ≦ 50.0	0	0	0	0
	50.0< HE	0	0	0	0
Persons for radiation control (A)		324	372	356	390
Exposure above 1 mSv	Persons (B)	0	0	0	0
	(B)/(A) ×100(%)	0	0	0	0
Mass effective dose equivalent (Person・mSv)		1.1	3.3	0	3.9
Mean dose equivalent(mSv)		0.00	0.01	0	0.01
Maximum dose equivalent(mSv)		0.5	0.9	0	0.7

*1 Not detected according to internal exposure.

Table 2. Number of temporary entrance persons to radiation controlled areas in fiscal 1997.

Temporary entrance persons \ Persons \ Periods	Number of persons				
	1st quarter	2nd quarter	3rd quarter	4th quarter	Total
Visiter and other	237	278	247	431	1193

1.2 Monitoring of radioactive gases

Table 3 shows the maximum radioactive concentrations and total activities for radioactive gases released from TIARA's stack, during each quarter of fiscal 1997. The least amount of ^{41}Ar, ^{13}N and ^{11}C were detected for some time on operation of the cyclotron, but the pulverized substance (^{65}Zn, etc) were not detected.

Table 3. Monitoring results of released gaseous radioactivities in fiscal 1997.

Nuclide	Items \ Periods	1st quarter	2nd quarter	3rd quarter	4th quarter	Total
^{41}Ar	Maximum concentration (Bq/cm³)	$<4.5\times10^{-5}$	$<4.5\times10^{-5}$	$<4.5\times10^{-5}$	$<4.5\times10^{-5}$	$<4.5\times10^{-5}$
	Total activity (Bq)	1.1×10^{9}	0	0	1.6×10^{9}	2.7×10^{9}
^{13}N	Maximum concentration (Bq/cm³)	$<4.5\times10^{-5}$	—	—	$<4.5\times10^{-5}$	$<4.5\times10^{-5}$
	Total activity (Bq)	2.1×10^{7}	—	—	1.7×10^{7}	3.8×10^{7}
^{11}C	Maximum concentration (Bq/cm³)	$<4.5\times10^{-5}$	—	—	$<4.5\times10^{-5}$	$<4.5\times10^{-5}$
	Total activity (Bq)	5.6×10^{8}	—	—	1.6×10^{8}	7.2×10^{8}
^{65}Zn	Maximum concentration (Bq/cm³)	$<5.4\times10^{-10}$	$<5.4\times10^{-10}$	$<6.6\times10^{-10}$	$<7.0\times10^{-10}$	$<7.0\times10^{-10}$
	Total activity (Bq)	0	0	0	0	0

1.3 Monitoring for external radiation and surface contamination

External radiation monitoring was routinely carried out in/around the radiation controlled areas and surface contamination monitoring was also carried out. Neither unusual value of dose equivalent rate nor contamination were detected.

Figure 1 displays a distribution of the dose equivalent rate at the radiation controlled area in the cyclotron building as an example.

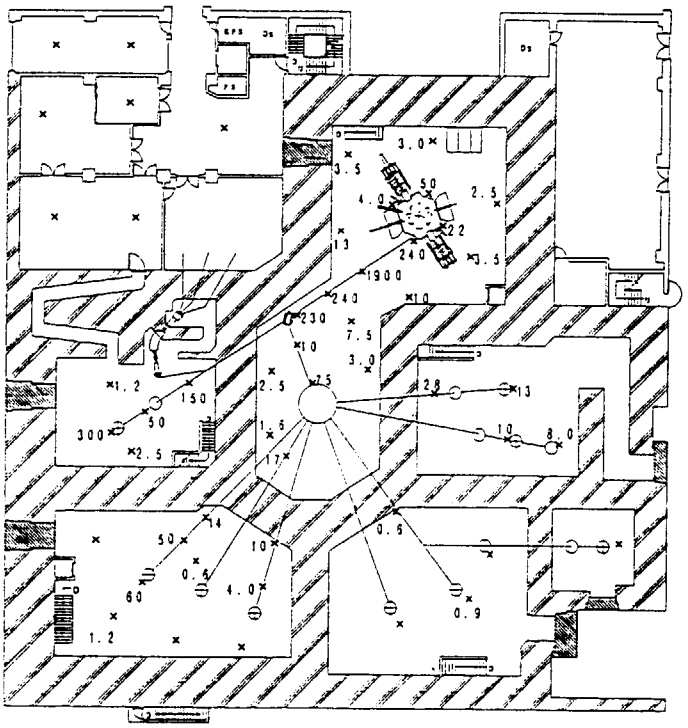

Fig. 1
Dose rate distribution at the radiation controlled area in the cyclotron building.

Date measured :
March 30, 1997
Measuring position :
Indicated with ×
above 1m from floor
Unit : μSv/h
(numerics less than 0.2 μSv/h are not indicated)

Appendix

This is a blank page.

Appendix 1. LIST OF PUBLICATION

A1.1. Publications in Journal

7J01.
H.Kudo, S.Yamamoto, K.Narumi,
Y.Aoki and H.Naramoto
Isotropy of ion-induced electron
emission from crystal targets
bombarded with MeV ions.
Nucl. Instrum. Meth. B132 (1997) 41.
S,I IOM 72023

7J02.
S.Yamamoto, H.Naramoto, K.Narumi,
B.Tuchiya, Y.Aoki and H.Kudo,
Characterization of single-crystalline
Nb films on sapphire by RBS/
channeling technique.
Nucl. Instrum. Meth. B134 (1998) 400.
S IOM 72023

7J03
T.Kojima, H.Sunaga, H.Takizawa and
H.Tachibana
Fluence measurements applied to 5-20
MeV/amu ion beam dosimetry by
simultaneous use of a total absorption
calorimeter and a Faraday cup
Radiat.Phys. Chem. 53(1998)115.
C RCO 71048

7J04
K.Kawatsura, H.Kageyama,
R.Takahashi, D.Hamaguchi, S.Arai,
Y.Aoki, S.Yamamoto, H.Takeshita,
H.Naramoto, T.Kambara, M.Oura,
Y.Kanai and Y.Awaya,
Copper L x-ray spectra measured by a
high resolution ion-induced x-ray
spectrometer
Radiat. Phys. Chem. 49,(1997) 617.
T,S IOM 72025

7J05
K.Kawatsura, T.Inoue, T.Igarashi,
N.Terazawa, S.Arai, Y.Aoki
S.Yamamoto,K.Narumi, H.Naramoto,
T.Yamamoto and H.Uda,
Heavy ion-induced Copper L x-ray
spectra measured with a high
resolution
x-ray crystal spectrometer
Int. J. PIXE(1997) in press
T IOM 72025

7J06
Y.Shimoura, I.Mukouda and K.Sugio,
The influence of dynamical structural
relaxation in point defect clusters on
void formation in irradiated Copper
J.Nucl.Mater. 251(1997) 61.
T,S IOM 72011

7J07
S.Hamada, Y.Miwa, D.Yamaki,
Y.Katano, T.Nakazawa and K.Noda,
Development of a triple beam
irradiation facility
J.Nucl. Mater. 000(1998) in press
T,S,I IOM 72013

7J08
S.Yamamoto, H.Naramoto, K.Narumi,
B.Tsuchiya, Y.Aoki and H.Kudo,
Characterization of singlecrystalline
Nb
films on sapphire by RBS/channeling
technique
Nucl. Inatrum. Meth. B134(1998) 400.
S MAN 72019

7J09
B.Tsuchiya, S.Yamamoto, K.Narumi,
Y.Aoki, H.Naramoto and K.Morita,
Ion irradiation effect on
single-crystalline Cu/Nb and Cu/Nb/Cu
layers on sapphire
Thin Solid Films(1998) in press
S, MAN 72019

7J10
S.Yamamoto, H.Naramoto, B.Tsuchiya, K.Narumi and Y.Aoki,
Characterization of epitaxially grown Cu/Nb multilayer on α-Al_2O_3 with RBS/channeling tecnique
Thin Solid Films (1998) in press
S MAN 72019

7J11
K.Ogura, T.Hattori, M.Asano, M.Yoshida, H.Omichi, N.Nagaoka, H.Kubota, R.Katakai and H.Hasegawa,
Proton response of high sensitivity CR-39 copolymer
Radiat. Meas. 28 (1997)197.
C RCO 71030

7J12
M.Yoshida, M.Asano, H.Omichi, R.Spohr and R.Katakai,
Substrate-specific functional membranes based on etched ion tracks
Radiat. Meas. 28 (1997) 799.
C RCO 71030

7J13
M.Yoshida, M.Asano, T.Suwa, N.Reber, R.Spohr and R.Katakai,
Creation of thermo-responsive ion-track
membranes
Adv. Mater. 9 (1997) 757.
C RCO 71030

7J14
M.Yoshida, N.Nagaoka, M.Asano, H.Omichi, H.Kubota, K.Ogura, J.Vetter, R.Spohr and R.Katakai,
Reversible on-off switch function of ion-track pores for thermo-responsive films based on copolymers consisting of diethylglycol-bis-allylcarbonate and acryloyl-L-proline methyl ester
Nucl. Instrum. Meth. B122(1997) 39.
C RCO 71030

7J15
M.Asai, K.Kawade, H.Yamamoto, A.Osa,M.Koizumi and T.Sekine,
A five-HPGe detector system for γ-γ angular correlation measurements for mass-separated short-lived nuclei
Nucl. Instrum. Meth. A398(1997) 265.
S SCS/NRI 71040

7J16
M.Asai, T.Sekine, A.Osa, M.Koizumi, Y.Kojima, M.Shibata, H.Yamamoto, and K.Kawade,
Energy systematics of low-lying 0+ states in neutron-deficient Ba nuclei
Phys. Rev. C56(1997) 3047.
S,C SCS/NRI 71040

7J17
Y.Kojima, T.Ikuta, M.Asai, A.Taguchi, M.Shibata, H.Yamamoto and K.Kawade,
Measurement of response functions of HPGe detectors for monoenergetic electrons and positrons in an energy range of 0.6-9.0 MeV
Nucl. Instrum. Meth. B126(1997) 419.
S,C SCS/NRI 71040

7J18
Y.Kojima, M.Asai, A.Osa, M.Koizumi, T.Sekine, M.Shibata, H.Yamamoto, K.Kawade and T.Tachibana,
Q_{EC} Measurement of $^{124,125,127-130}$La
J.Phys. Soc. Jpn., in press
S,C SCS/NRI 71040

7J19
K.Umezawa, T.Ito, M.Asada, S.Nakanishi, P.Ding, W.A.Lanford, B.Hjorvarsson,
Adsorption of hydrogen on the Pt(111) surface from low-energy recoil scattering
Surf. Sci. 387(1997) 320.
S MAN 72028

7J20
K.Umezawa, S.Nakanishi, T.Yumura, W.M.Gibson, M.Watanabe, Y.Kido, S.Yamamoto, Y.Aoki and H.Naramoto,
Surface structure analysis of Ni(111)-(/3x/3)R30 -Pb by impact-collision ion scattering
Phys. Rev. B56(1997) 10585.
S MAN 72028

7J21
T.Ito, K.Umezawa and S.Nakanishi,
Epitaxial growth of Ag on Ni(111)
Appl. Surf. Sci. (1998) in press
S MAN 72028

7J22
N.S.Ishioka, H.Matsuoka, S.Watanabe, A.Osa, M.Koizumi, T.Kume, S.Matsuhashi, T.Fujimura, H.Uchida, A.Tsuji and T.Sekine,
Production of positron emitters and application of their labeled compounds to studies on plants
J. Radioanal. Nucl. Chem. in press
C NRI 71034

7J23
Y.Katano, T.Nakazawa, D.Yamaki, T.Aruga, K.Hojou and K.Noda,
Effects of dual and triple beam irradiation with O,He and H-ions on damage structures in single crystal Al_2O_3
Nucl. Instrum. Meth.B116(1996) 230.
T,S,I IOM 72008

7J24
Y.Katano, T.Nakazawa, D.Yamaki, T.Aruga and K.Noda,
Microstructural evolution of single crystalline Al_2O_3 irradiated with single and triple ion beams
J. Nucl. Mater. 233-237(1996) 1325
T,S,I IOM 72008

7J25
Y.Katano, T.Aruga, S.Yamamoto, T.Nakazawa, D.Yamaki and K.Noda,
Cross-sectional observation of damage structures in Al_2O_3 irradiated with multiple beams of H,He and O-ions and after annealing at 1273K
Nucl. Instrum. Meth. B140(1998)152.
T,S,I IOM 72008

7J26
Y.Katano, K.Hojou, T.Nakazawa, D.Yamaki, T.Aruga and K.Noda,
Cavity formation behaviors in single crystal Al_2O_3 irradiated with triple beams of O,He and H ions
Nucl.Instrum. Meth. B141(1998) in press
T,S,I IOM 72008

7J27
Y.Katano, T.Nakazawa, D.Yamaki, T.Aruga and K.Noda,
Damage structures evolution in Al_2O_3 irradiated with multiple beams of H,He and O-ions and after annealing
J. Nucl. Mater. (1998) in press
T,S,I IOM 72008

7J28
T.Kume, S.Matsuhashi, M.Shimazu, H.Ito, T.Fujimura, K.Adachi, H.Uchida, N.Shigeta,H.Matsuoka, A.Osa and T.Sekine,
Uptake and transport of positron-emitting tracer(^{18}F) in plants
Appl. Radiat. Isot. 48(1997) 1035.
C BIT 71016

7J29
H.Hayashi, Y.Okada, H.Mano, T.Kume, S.Matsuhashi, N.S.Ishioka, H.Uchida, and M.Chino,
Detection and characterization of nitrogen circulation through the sieve tubes and xylem vessels of rice planta

Plant and Soil 196(1997) 233.
C BIT 71028

7J30
T.Iwai, N.Sekimura and F.A.Garner,
Viod swelling behavior in ion-irradiated Vanadium alloys
J. Nucl. Mater. 239(1996) 157.
T,S,I IOM 72015

7J31
H.Koizumi, M.Taguchi, H.Namba, T.Ichikawa and H.Yoshida,
Radical formation in the radiolysis of solid adipic acid by γ -rays and heavy ions
Nucl. Instrum. Meth. B132(1997) 633
C RCO 71042

7J32
Y.Saito, K.Ohkoshi and W.Yokota,
Production of multiply charged metallic ions by compact electron cyclotron resonance ion source with SF6 plasma
Rev. of Sci. Instrum. 69(1998) 703.
O ACT 0ff line

7J33
A.Uedono, H.Itoh, T.Ohshima, R.Suzuki, T.Ohdaira, S.Tanigawa, Y.Aoki, M.Yoshikawa, I.Nashiyama, T.Mikado, H.Okumura and S.Yoshida,
Annealing properties of defects in ion-implanted 3C-SiC studied using monoenergetic positron beams
Jpn. J. Appl. Phys. 36(1997) 6650.
S SCS 72004

7J34
H.Itoh, A.Uedono, T.Ohshima, Y.Aoki, M.Yoshikawa, I.Nashiyama, S.Tanigawa, H.Okamura and S.Yoshida
Positron annihilation studies of defects in 3C-SiC hot-implanted with Nitrogen and Aluminum ions
Appl. Phys. A65(1997) 315
S SCS 72004

7J35
H.Itoh, A.Kawasuso, T.Ohshima, M.Yoshikawa, I.Nashiyama, S.Tanigawa, S.Misawa, H.Okumura and S.Yoshida,
Intrinsic defects in cubic Silicon Carbide
Phys. Stat. Sol. (a)162(1997) 173
S SCS 72004

7J36
H.Itoh, T.Ohshima, Y.Aoki, K.Abe, M.Yoshikawa, I.Nashiyama, H.Okumura, S.Yoshida, A.Uedono and S.Tanigawa,
Characterization of residual defects in cubic Silicon Carbide subjected to hot-implantation and subsequent annealing
J. Appl. Phys. 82(1997) 5339
S SCS 72004

7J37
A.Uedono, T.Ohshima, H.Itoh, R.Suzuki, T.Ohdaira, S.Tanigawa, Y.Aoki, M.Yoshikawa, I.Nashiyama and T.Mikado,
Investigation of vacancy-type defects in P^+-implanted 6H-SiC using monoenergetic positron beams
Jpn. J. Appl. Phys. 37(1998) 2422
S SCS 72004

7J38
T.Ohshima, A.Uedono, K.Abe, H.Itoh, Y.Aoki, M.Yoshikawa, S.Tanigawa, and I.Nashiyama,
Characterization of vacancy-type defects and phosphorus-donors introduced in 6H-SiC by ion implantation
Appl.Phys. A submitted
S SCS 72004

7J39

T.Iwasaki, Y.Sakuya, N.Hirakawa, H.Nakashima, Y.Sakamoto, H,Takada and S.Tanaka,
Measurement and analysis of fission reaction distribution of ^{237}Np and ^{238}U in a polyethylene system with a 65MeV neutron source
J. Nucl. Sci. Technol. 35(1998) 169.
C RSH 61045

7J40
M.Baba, Y.Nauchi, T.Iwasaki, T.Kiyosumi, M.Yoshioka, S.Matsuyama, N.Hirakawa, T.Nakamura, Su.Tanaka, S.Meigo, H.Nakashima, Sh.Tanaka and N.Nakao,
Characterization of 40-90 MeV $^{7}Li(p,n)$ neutron source at TIARA using proton recoil telescope and TOF method
Nucl. Instrum. Meth. A. submitted
C RSH 71053

7J41
M.Taguchi, Y.Aoki, H.Namba, R.Watanabe, Y.Matsumoto and H.Hiratsuka,
Fast fluoresence decay of naphthalene induced by Ar ion irradiation
Nucl. Instrum. Meth. B132(1997) 135.
C RCO 61035

7J42
K.Furukawa, S.Ohno, H.Namba, M.Taguchi and R.Watanabe,
Radial dose distribution around a heavy ion's path
Radiat. Phys. Chem. 49(1997) 641.
C RCO 51032

7J43
S.Ohno, K.Furukawa, H.Namba, M.Taguchi and R.Watanabe,
A track structure model based on measurements of radial dose distribution around an energetic heavy ion
MICRODOSIMETRY:
An Interdisciplinary Approach, 31.
C RCO 51032

7J44
M.Taguchi, Y.Matsumoto, H.Namba, Y.Aoki and H.Hiratsuka,
Chemical tracks of heavy ions for 1,2,4,5-Tetracyanobenzene anion radical formation
Nucl. Instrum. Meth. B134(1998) 427.
C RCO 61035

7J 45
M.Taguchi, Y.Matsumoto, M.Moriyama, H.Namba, Y.Aoki and H.Hiratsuka,
Effect of specific energy of heavy ions for 1,2,4,5-Tetracyanobenzene radical anion formation
Nucl. Instrum. Meth B submitted
C RCO 61035

7J46
T.Kamiya, M.Cholewa, A.Saint, S.Plauer, G.J.F.Legge, J.E.Butler and D.J.Vestyck,Jr.,
Secondary electron emission from boron-doped diamond under ion impact: applications in single-ion detection
Appl.Phys. Let. 71(1997) 1875
O ACT off line

7J47
H.Kudoh, T.Sasuga and T.Seguchi,
High energy ion irradiation effects on polymer material-LET dependence of G value of scission of polymethylmethacrylate(PMMA)
Radiat. Phys. Chem. 50(1997) 299.
C RCO 71001

7J48
H.Naramoto, S.Yamamoto, K.Narumi, Y.Aoki, H.Abe and H.Kudo,
Scientific activities on surface modification & characterization of

inorganic materials using ion beams in JAERI/Takasaki
Ionics 23, 261(1997) 35.
S,I IOM/MAN 72032

7J49
H.Naramoto, Y.Aoki, S.Yamamoto and H.Abe,
Comparison of damage growth and recovery in α-Al_2O_3 implanted with Vanadium ions
Nucl. Instrum. Meth. B127(1997) 599.
S,I IOM/MAN 72032

7J50
Z.Q.Ma, Y.F.Zheng and H.Naramoto,
Subsurface modification and relative optical density of synthetic diamond
Appl. Surf. Sci. 119(1997) 181.
I IOM 72032

7J51
N.K.Huang, K.Neubeck, S.Yamamoto, Y.Aoki, H.Abe, K.Narumi, A.Miyashita and H.Naramoto,
The behavior of radiation damage of Nb^+ ion implanted sapphire after annealing at reducing atmosphere
Phys. Stat. Sol. (a) 165(1998) 367.
S,I IOM/MAN 72032

7J52
B.Tsuchiya, S.Yamamoto, K.Narumi, Y.Aoki, H.Naramoto and K.Morita,
Ion irradiation effect on single-crystalline Cu/Nb and Nb/Cu layers on sapphire
Thin Solid Films (1998) accepted for publication
S,I IOM/MAN 72032

7J53
H.Naramoto, S.Yamamoto, Y.Aoki and K.Narumi,
Modified structure of sapphire with ^{51}V ion implantation followed by thermal annealing
Mater. Sci. Eng. (1998) in print
S,I IOM/MAN 72032

7J54
R.Q.Zhang, S.Yamamoto, Z.N.Dai, K.Narumi, A.Miyashita, Y.Aoki and H.Naramoto,
Characterization of natural ilmenite and synthesized FeTiO3 crystals with RBS/PIXE/XRD
Int. J. of PIXE(1998) in print
S IOM/MAN 72032

7J55
W.Yokota, M.Fukuda, S.Okumura, K.Arakawa, Y.Nakamura, T.Nara, T.Agematsu and I.Ishibori,
Performance and operation of a beam chopping system for a cyclotron with multiturn extraction
Rev. Sci. Instrum. 68(4), (1997)1714.
C ACT 71047

7J56
M.Fukuda, S.Okumura and K.Arakawa,
Simulation of spiral beam scanning for uniform irradiation on a large target
Nucl. Instrum. Meth. A396(1997) 45.
C ACT 71046

7J57
J.Isoya, H.Kanda and Y.Morita,
EPR identification of the (100)-split $[B\text{-}N]^+$ interstitialcy in diamond
Phys. Rev. B 56(1997)6392.
C IOM SCS 71031/72027

7J58
J.Isoya, H.Kanda, M.Akaishi, Y.Morita and T.Ohshima,
ESR studies of incorporation of Phosphorus into high-pressure synthetic diamond
Diamond and Related Materials 6(1997) 356.

T, IOM SCS 71031/72027

7J59
H.Watanabe, Y.Kobayashi, S.Yamasaki and K.Kiguchi,
Application of microbeam probes to local irradiation biological systems
Houshasen 23(1), (1997) 63.
C BIT 71009

7J60
Y.Shimomura, I.Mukouda and K.Sugio,
The influence of dynamical structure relaxation in point defect clusters on void formation in irradiated copper
J.Nucl. Mater. 251(1997) 61.
T,S IOM 72011

7J61
A.Tanaka, S.Tano, T.Chantes, Y.Yokota, N.Shikazono and H.Watanabe,
A new arabidopsis mutant induced by ion beams affects flavonoid synthesis with spotted pigmentation in testa
Genes Genet. Sys. 72(1997) 141.
C BIT 71007

7J62
A.Tanaka, H.Watanabe, T.Shimizu, M.Inoue, M.Kikuchi, Y.Kobayashi and S.Tano,
Penetration controlled irradiation with ion beams for biological study
Nucl. Instrum. Meth. B129(1997) 42.
T BIT 72017

7J63
H.Nishimura, M.Inoue, A.Tanaka and H.Watanabe,
Pollen as a transporter of mutations induced by ion beams in *Nicotiana tabacum*
Can. J.Bot. 75(1997) 1261.
C BIT 71012

7J64
T.Sakai, T.Hamano, T.Hirao, T.Kamiya, K.Murozono, J.Inoue, S.Matsuyama, S.Iwasaki and K.Ishii,
Development of a fast multi-parameter data acquisition system for microbeam analyses
Nucl. Instrum. Meth. B136-138(1998) 390.
S ACT 72040

7J65
N.S.Ishioka, T.Sekine and R.M.Lambrecht
Comments on the cross section of ^{186}Re in the ^{186}W(p,n)-and^{186}W(d,2n)-reactions in connection to the paper given by Z.H.Zhu et al. and correction of the calculated yields of ^{186}Re in the ^{186}W(p,n)-reaction
J. Radioanal.Nucl.Chem. in press
C NRI 71034

7J66
H.Yamazaki, M.Tanaka, K.Tsutsumi, K.Ishii, S.Iwasaki, S.Matsuyama, J.Inoue, K.Muruzono and H.Orihara,
A preconcentration technique for water analysis by PIXE
Intern. J. PIXE, 6(3&4),(1996) 471.
O ACT 72040

7J67
T.C.Chu, K.Ishii, M.Kikuchi, K.Muruzono, C.C.Hsu and S.Morita,
Countinuum X-rays produced by 60 keV- and 80 keV-proton bombardment
Intern.J.PIXE, 6(1&2),(1996) 31.
O ACT 72040

7J68
K.Murozono, S.Iwasaki, J.Inoue, K.Ishii and M.Kitamura,
System of pattern analysis in PIXE spectra
Intern. J. PIXE 6(1&2),(1996) 133.

O ACT 72040

7J69
J.Inoue, S.Iwasaki, K.Murozono, K.Ishii and S.Matsuyama,
Use of Si-PIN photodiode X-ray detector for PIXE
Intern. J. PIXE 6(3&4),(1996) 145.
O ACT 72040

7J70
S.Iwasaki, K.Ishii, S.Matsuyama, K.Murozono, J.Inoue, M.Tanaka, H.Yamazaki,
T.Honma, M.Fujioka and H.Orihara,
Facility of PIXE analysis at Tohoku University
Intern. J. PIXE 6(1&2),(1996) 117.
O ACT 72040

7J71
S.Iwasaki, K.Murozono, K.Ishii and M Kitamura,
Towards intelligent spectrum analyzing system for industry-oriented PIXE
Application of Accelerators in Research and Industry, AIP Conference Proc. 392,(1997) 547.
O ACT 72040

7J72
H.Yamazaki, M.Tanaka, K.Tsutsumi, K.Ishii, S.Iwasaki, S.Matsuyama, J.Inoue, K.Murozono and H.Orihara,
Determination of heavy-metal concentrations in water by PIXE analysis using Zr as an internal standard
Intern. J. PIXE 7(1&2),(1997) 31.
O ACT 72040

7J73
S.Yokota, J.Inoue, K.Murozono, S.Matsuyama, H.Yamazaki, S.Iwasaki, K.Ishii and T.Mae,
Application of vertical-beam in-air PIXE to surface analysis of plant root exposed to Aluminum stress
Intern. J. PIXE 7(1&2),(1997) 93.
O ACT 72040

7J74
S.Seki, K.Maeda, Y.Kunimi, S.Tagawa, Y.Yoshida, H.Kudoh, M.Sugimoto, Y.Morita, T.Seguchi and H.Shibata,
Ion beam induced crosslinking reactions in poly(di-n-hexylsilane)
Radiat. Phys. Chem. submitted
C RCO 71045

7J75
K.Mochida, R.Hata, H.Chiba, S.Seki, Y.Yoshida and S.Tagawa,
Radical anions of oligogermanes, Me(Me2Ge)nMe(n=2,3,5 and 10) generated by pulse radiolysis
Chem. Lett. (1998) 263.
C RCO 71044

7J76
S.Seki, H.Shibata, Y.Yoshida, K.Ishigure and S.Tagawa,
Radiation effects on hole drift mobility in polysilanes
Radiat. Phys. Chem. 49(1997) 389.
C RCO 71045

7J77
S.Seki, K.Kanzaki,Y.Kunimi,S.Tagawa, Y.Yoshida, H.Kudoh, M.Sugimoto, T.Sasuga,T.Seguchi and H.Shibata,
LET effects of ion beam irradiation on poly(di-n-hexylsilane)
Radiat. Phys. Chem. 50(1997) 423
C RCO 71045

7J78
S.Seki, K.Kanzaki, Y.Yoshida, S.Tagawa, H.Shibata, K.Asai and K.Ishigure
Positive-negative inversion of silicon based resist materials:Poly(di-n-

hexylsilane) for ion beam irradiation
Jpn. J. Appl. Phys. 36(1997) 5361.
C RCO 71045

7J79
T.Yamaki, Y.Nakashiba, K.Asai, K.Ishigure, S.Seki, S.Tagawa and H.Shibata,
Exciplex formation from amphiphilic polysilanes bearing ammonium moieties
J.Nucl. Mater. 248(1997) 369.
C RCO 71044

7J80
S.Seki, H.Shibata, H.Ban, K.Ishigure and S.Tagawa,
Radiation effects of ion and electron beams on Poly(methylphenylsilane)
Radiat. Phys. Chem. 48(1996) 539.
C RCO 71045

7J81
S.Seki, S.Tagawa, K.Ishigure, K.R.Cromack and A.D.Trifunac,
Observation of silyl radical in γ -radiolysis of solid Poly(dimethyl-silane)
Radiat. Phys.Chem. 46(1996) 217.
C RCO 71044

7J82
Su.Tanaka, M.Fukuda, K.Nishimura, H.Watanabe and N.Yamano,
'IRACM: A code system to calculate induced radioactivity produced by ions and neutrons
JAERI-Data/Code 97-019(1997)
C RSH 71049

7J83
M.Fukuda, S.Okumura and K.Arakawa,
Simulation of spiral beam scanning for uniform irradiation on a large target
Nucl. Instrum. Meth. A396(1997) 45.
O ACT 71047

7J84
T.Sakai, T.Hamano, T.Hirao, T.Kamiya, K.Murozono, J.Inoue, S.Matsuyama, S.Iwasaki and K.Ishii,
Development of a fast multi-parameter data acquisition system for microbeam analysis
Nucl. Instrum. Meth. B136-138(1998) 423.
S,T ACT 72037/72038

7J85
T.Hisamatsu, O.Kawasaki, S.Matsuda and K.Tsukamoto,
Photoluminescence study of silicon solar
cells irradiated with large fluence electrons and protons
Radiat. Phys. Chem. 53(1998) 25.
C SCS 71004

7J86
H.Matsuura, Y.Uchida, T.Hisamatsu and S.Matsuda,
Evaluation of hole traps in 10 MeV proton-irradiated p-type Silicon from hall-effect measurement
Jpn. J.Appl. Phys. to be published
C SCS 71004

A1.2. Publication in Proceedings

7C01
R.Takahashi, D.Hamaguchi,
H.Kageyama, A.Nishihata,
K.Kawatsura, S.Arai, Y.Aoki,
S.Yamamoto, H.Takeshita, H.Naramoto
T.Kambara, M.Oura, Y.Kanai, Y.Awaya,
Y.Horino, Y.Mokuno, A.Chayahara,
A.Kinomura, N.Tsubouti and K.Fujii,
Copper L x-ray spectra measured by a high resolution ion induced x-ray spectrometer
JAERI Conf. 97-003 (1997) 345.
T,S IOM 72025

7C02
R.Takahashi, Y.Nakai, D.Hamaguchi,
T.Nakae, A.Nishihata, T.Shiono,.
K.Kawatsura, S.Arai, Y.Aoki,
S.Yamamoto, H.Takeshita,
H.Naramoto, YHoriono, Y.Mokuno,
K.Fujii and N.Masuda,
Radiation-induced effects in MgO single crystal by 200 keV and 1 MeV
Ni ion implantation
JAERI Conf. 97-003 (1997) 349.
T,S IOM 72025

7C03
K.Kawatsura, H.Kageyama,
T.Hasegawa, T.Terazawa, S.Arai
T.Kambara, M.Oura, Y.Kanai, Y.Aoki,
S.Yamamoto, K.Narumi and
H.Naramoto,
L α and L β x-ray emission spectra of copper induced by 0.075 and 0.75 MeV/u ion impacts
X X . International Conference on the Physics of Electronic and Atomic Collisions (Vienna, July 1997) pp.TH 133
T,S IOM 72025

7C04
M.Sasaki, M.Nakao, N.Nakao,
T.Nakamura and T.Shibata,
Application of self-TOF high energy neutron detector for neutron scattering cross section measurements
Proc. of 98 Radiation Detectors Their Uses KEK(1998)
C RSH 71051

7C05
M.Takebe, K.Abe, Y.Kondo, Y.Satoh,
M.Souda, Y.Kokubun, M.Miyazaki,
Y.Hori and Y.Murakami,
An α -ray image of the imaging plate discriminated from γ -ray and an LET effect on heavy ion irradiations
Proc. of 11th Workshop on Radiation Detectors and their Uses (KEK, February 1997) 1.
C RCO 71043

7C06
K.Abe, T.Kojima, T.Suzuya,
Y.Murakami, K.Saito, K.Toh, T.Sakai
and M.Takebe,
A response of an imaging plate to heavy ion beams and its LET effects
Proc. of 12th Workshop on Radiation Detectors and their Uses (KEK, January 1998)
C RCO 71043

7C07
I.Mukouda, M.Uchida and
Y.Shimomura,
Specimen preparation for TEM by focused ion beam(FIB) device I
Proc. of 8th summer school on electron microscope(Hiroshima, August 1997) 189.
T,S IOM 72011

7C08
K.Umezawa, T.Ito and S.Nakanishi,
Low energy recoil scattering from

hydrogen adsorbed on Ni(111)
Nucl. Instrum. Meth. B(1998)
in press.
(Proc. 13th international Conf. on Ion Beam Analysis, Lisbon, July, 1997)
S MAN 72028

7C09
N.S.Ishioka, H.Matsuoka, S.Watanabe, A.Osa, M.Koizumi and T.Sekine,
A new water target system for the production of ^{18}F and ^{13}N to be used in plant study
Proc. of Synthesis and Applications of Isotopically Labeled Compounds 1997(Philadelphia, Sept. 1997) Edited by J.R.Heys and D.G.Melillo (1998) 669.
C NRI 71034

7C10
H.Matsunami, Y.Arima, K.Watanabe, S.Matsuhashi, N.S.Ishioka, H.Uchida and T.Kume,
$^{13}NO_3$ -N-uptake-site on the common bean root relating to combined nitrogen stress on the root-nodulation
(in Japanese)
The 35th Annual Meeting on Radioisotopes in the Physical Sciences and Industries (Tokyo, June 1998) 6.
C BIT 71017

7C11
T.Kume, S.Matsuhashi, M.Shimazu, H.Ito, T.Fujimura, K.Adachi, H.Uchida, A.Tsuji, N.Shigeta, H.Matsuoka, A.Osa and T.Sekine,
Uptake and transport of positron-emitting tracer in irradiated plants
Proc. of 13th International Plant Nutrition Colloquium (Tokyo, Sept. 1997) 169.
C BIT 71016

7C12
N.Sekimura, Y.Shirao and K.Morishita,
Defect cluster formation in Vanadium under heavy ion irradiation
Proc. of the 4th Japan-China Symposium on Materials for Advanced Energy Systems and Fission and Fusion Engineering 96(1997) 233.
T,S,I IOM 72015

7C13
K.Narumi, S.Yamamoto, A.Miyashita, Y.Aoki and H.Naramoto,
Formation of Vanadium oxide by ion implantation and heat treatment
Proc. of IIT '98(Kyoto, June 1998)
to be published in IEEE
S,I IOM/MAN 72031

7C14
Y.Saito, K.Ohkoshi and W.Yokota,
Production of metallic ions by MINI-ECR with SF6 plasma
Proc. of the 8th Symp. on Beam Eng. of Advanced Material Syntheses(Kyoto, 1997)27.
O ACT

7C15
T.Ohshima, A.Uedono, H.Itoh, K.Abe, R.Suzuki, T.Ohdaira, Y.Aoki, M.Yoshikawa, T.Mikado, H.Okumura, S.Yoshida, S.Tanigawa and I.Nashiyama,
Study on thermal annealing of vacancies
in ion-implanted 3C-SiC by positron annihilation
Proc. of Intern. Conf. on Silicon Carbide III-nitrides and Related Materials (ICSCIII-N'97, August 31-Sept. 5, 1997, Stockholm, Sweden)
Material Science Forum 264-268(1998) 745. Trans. Tech. Publns, Swizerland
S SCS 72004

7C16
K.Abe, T.Ohshima, H.Itoh, Y.Aoki,

M.Yoshikawa, I.Nashiyama and M.Iwami,
Hot-implantation of Phosphorus ions into 6H-SiC
Proc. of Internat. Conf. On Silicon Carbide, III-nitrides and Related Materials
(ICSCIII-N'97, August 31-Sept. 5, 1997, Stockholm, Sweden)
Material Science Forum 264-268(1998) 721. Trans. Tech. Publns, Swizerland
S SCS 72004

7C17
T.Iwasaki, T.Tabei, H.Iwase, N.Hirakawa, Y.Sakamoto and S. Tanaka,
Fission rate distributions of ^{237}Np and ^{238}U for 65MeV quasi-monoenergetic neutrons in polyethylene, Aluminum, Iron and Lead
Proc. ICENES '98(June, 1998, Israel) 195.
C RSH 61045/71052

7C18
M.Takeda, T.Suda, S.Ohnuki, H.Abe and H.Naramoto,
Effect of stress and impurities on radiation-induced amorphization in poly-Si
Proc. of CARET Symposium, Hokkaido University, (1998) 627.
T IOM 72036

7C19
Y.Nauchi, M.Baba, T.Iwasaki, T.Sanami T.Tabei, T.Suzuki, M.Ibaraki, S.Tanaka, H.Nakashima, S.Meigo, H.Takada, N.Nakao, T.Nakamura, Y.Watanabe, M.Harada, T.Nunomiya and N.Hirakawa,
Measurements of (n,xp), (n,xd) double differential cross section of Al and C for neutrons at 75 and 65 MeV
JAERI-Conf. 98-003 proc. 1997symp. Nucl. Data 270.
C RSH 71053

7C20
Y.Nauchi, M.Baba, T.Nunomiya, M.Ibaraki, S.Matsuyama, T.Suzuki, N.Hirakawa,
Particle identification capability of BaF_2 cintillator in the energy region below 20 MeV
Proc of Radiation Detectors and Their Uses,(January, 1997, KEK)
to be published
C RSH 71053

7C21
H.Naramoto, Y.Aoki, S.Yamamoto, P.Goppelt-Langer, M.Gan, J.Zheng and H.Takeshita,
On-site analysis of modified surface using dual beam system
Proc. of 7th Inter. Symposium on Advanced Nuclear Energy Research "Recent Progress in Accelerator Beam Application"(Taksaki, March 1996)
JAERI-Conference 97-003(1997) 113.
S,I IOM/MAN 72032

7C22
Z.N.Dai, S.Yamamoto, A.Miyashita, K.Narumi, Y.Aoki and H.Naramoto,
RBS/Channeling, XRD and Optical characterization of deep ion implantation into single crystalline SiO_2
Proc. of 12th Int.Conf. on ion implantation technology '98(Kyoto, June 22-26, 1998)
S,I IOM/MAN 72032

7C23
M.Fukuda, K.Arakawa, S.Okumura, T.Nara, Y.Nakamura, T.Agematsu, I.Ishibori, W.Yokota and H.Tamura,
Development of cocktail beam acceleration technique for the JAERI AVF cyclotron

Proc. of the 11th Symposium on Accelerator Science Technology, Harima Science Garden City, October 21-23 (1997) 139.
C ACT 71047

7C24
M.Fukuda, S.Okumura, K.Arakawa, I.Ishibori, A.Matsumura and T.Karasawa,
Analysis of a beam centering error measured with a radial main probe
Proc. of the 11th Symposium on Accelerator Science Technology, Harima Science Garden City, October 21-23 (1997) 300.
C ACT 71047

7C25
S.Okumura, K.Arakawa, M.Fukuda, Y.Nakamura, T.Nara, T.Agematsu, I.Ishibori, W.Yokota and H.Tamura,
Status report on the JAERI AVF cyclotron
Proc. of the 11th Symposium on Accelerator Science Technology, Harima Science Garden City, October 21-23 (1997) 338.
C ACT 71047

7C26
Y.Nakamura, I.Ishibori, K.Arakawa and T.Nara,
Estimation of charge exchange cross section for multiply charged ions accelerated in the JAERI AVF cyclotron
Proc. of the 11th Symposium on Accelerator Science Technology, Harima Science Garden City, October 21-23 (1997) 368.
C ACT 71047

7C27
T.Agematsu, K.Arakawa and T.Okumura,
Development of visual beam adjustment method for the beam transport
Proc. of the 11th Symposium on Accelerator Science Technology, Harima Science
Garden City, October 21-23 (1997) 446.
C ACT 71047

7C28
Y.Ishii, A.Isoya and T.Tanaka,
Development of the technique of the ultra-fine microbeam
Proc. of 10th Workshop on Tandem Accelerator and Technology (Tsukuba, July 1997) 105.
O ACT

7C29
Y.Nkamura, I.Ishibori, K.Arakawa and T.Nara,
Estimation of charge exchange cross section for multiply charged ions accelerated in the JAERI AVF cyclotron
Proc. of 11th Symposium on Accelerator Science and Technology (Hyogo, October 1997) 368.
C ACT

7C30
Y.Saitoh, K.Mizuhashi and S.Tajima,
Development of microcluster beam in TIARA
Proc. of 10th Workshop on Tandem Accelerator and Technology (Tsukuba, July 1997) 101.
T ACT 72039

7C31
Y.Kobayashi, H.Watanabe, M.Taguchi, S.Yamasaki and K.Kiguchi,
Application of microbeam probes to local irradiation of biological systems
Proc. of the 3rdInternational Workshop: Microbeam Probes of Cellar Radiation Response(Columbia University, NY, USA.,May 8-9, 1997)

C BIT 71009

7C32
Y.Kobayashi, M.Kikuchi, A.Tanaka and H.Watanabe,
Deinococcus radiodurans does not show RBE peak in LET response
Abst.of the 40th Annual Meeting of the Japan Radiation Research Society (Kyoto,November 5-7, 1997) 286.
C BIT 71008

7C33
T.Sato, N.Ohtake, T.Ohyama, S.Matsuhashi, N.Ishioka, T.Kume and H.Uchida,
Utilization of ^{13}N and ^{15}N for plant nutrition studies
The 35th Annual Meeting on Radioisotopes in the Physical Science and Industries (Tokyo, June 1998) 5.
C BIT 71019

7C34
N.Nemoto, K.Matsuzaki, J.Aoki, T.Akutsu, S.Matsuda, I.Naito, H.Itoh and I.Nashiyama,
Evaluation of single-event upset tolerance on recent commercial memory ICs
3rd ESA Electronic Components Conference, April, 1997)
C SCS 71003

7C35
H.Arai, A.Kawasuso, S.Okada, K.Hirata, Y.Kobayashi and T.Sekiguchi,
Defect analysis in Er-implanted Si and SiO_2/Si by slow positron beam
The 35th Annual Meeting on Radioisotopes in the Physical Science and Industries
(Tokyo, June 1998) 98.
I IOM 72020

7C36
H.Watanabe, A.Tanaka, S.Tano and M.Inoue,
Influence of penetration controlled irradiation with charged particles on tobacco pollen
Proc. of 6th Workshop on "Heavy Charged Particles in Biology and Medicine (Baveno, September 1997)
T BIT 72017

7C37
T.Tobita, M.Suzuki, A.Iwase, K.Aizawa and Y.Idei,
Basic study of irradiation embrittlement caused by γ-rays on light water reactor pressure vessel
36th Annual Meeting of the Atomic Energy Society of Japan
(1998, Mar. Kinki Univ.) 454.
S IOM 72016

7C38
Su.Tanaka, Y.Nakane, Y.Sakamoto, H.Nakashima, Sh.Tanaka, T.Kurosawa, T.Nakamura, N.Nakao and H.Hirayama,
Measurements of neutrons and protons streaming throgh three-legs labyrinth from 68-MeV proton target room
Proc. of 1998 ANS Radiation Protection and Shielding Division Topical Meeting (Nashville Tennessee,USA, April, 1998) II-164.
C RSH 61044

7C39
S.Nagatomi,
Varletal improvement for ornamentals by use of radiations
Proc. of 7th Radiation Process Symposium (1997) 42.
C BIT 71015

7C40
S.Nagatomi, A.Tanaka, H.Watanabe and S.Tano,

Analysis for chimerism of flower color mutants induced by $^{12}C^{5+}$ ion beam irradiation in chrysanthemum
Breeding Sci. (Suppl. 1, 1998) 220.
C BIT 71015

7C41
S.Nagatomi, A.Tanaka, H.Watanabe and S.Tano,
Enlargement of potential chimera on chrysanthemum mutants regenerated from $^{12}C^{5+}$ ion beam irradiation explants.
TIARA Annual Report (1996) 48.
C BIT 71015

7C42
S.Nagatomi,
Application irradiation and in vitro techniques on induced mutation in horticultural crops
Proc. Seminar on Mutation Breeding in Horticultural Crops for Regional Nuclear Cooperation in Asia, Bangkok, (1996) 24.
C BIT 71015

7C43
S.Nagatomi, A.Tanaka, S.Tano and H.Watanabe,
Chrysanthemum mutants regenerated from in vitro explants irradiated with $^{12}C^{5+}$ ion beam
Technical News, Institute of Radiation Breeding, 60(1997) 1.
C BIT 71015

7C44
M.Fukuda, K.Arakawa, S.Okumura, T.Nara, Y.Yamamura, T.Agematsu, I.Ishibori, W.Yokota and H.Tamura,
Development of cocktail beam acceleration technique for the JAERI AVF cyclotron
Proc. of 11th Symposium on Accelerator Science and Technology
(Harima Science Garden City, October 1997) 139.
C ACT 71047

7C45
M.Fukuda, S.Okumura, K.Arakawa, I.Ishibori, A.Matsumura and T.Karasawa,
Analysis of a beam centering error measured with a radial main probe
Proc. of 11th Symposium on Accelerator Science and Technology
(Harima Science Garden City, October 1997) 300.
C ACT 71047

7C46
T.Sakai, T.Hamano and T.Kamiya,
Observation of tracks on CR-39 induced by light ion microbeam irradiation
Proc. of the 34th Seminar on Science and Technology, Small Accelerators and their Application, Tokyo 1997, 261.
S RCO 72038

7C47
S.Matsuda, T.Hisamatsu, O.Kawasaki, T.Nakao, Y.Morita, T.Ohshima and I.Nashiyama,
Electrical characteristics of large fluence 3 MeV or 10 MeV proton irradiated space silicon solar cells
TIARA Annual Report (1996) 5.
C,T SCS 71004,72003

7C48
T.Hisamatsu, S.Matsuda, T.Nakao, Y.Matsumoto, S.T.Taylor and M.Yamaguchi,
Thermal Recovery of degraded space silicon solar cells due to large fluence irradiation
Proc. of the 26th IEEE Photovoltaic Specialists Conference, (Anaheim,CA, 29, September-03, October 1997)991.
C SCS 71004

7C49
S.T.Taylor, M.Yamaguchi, M.Imaizumi,
M.-J.Yang, T.Ito, T.Yamaguchi,
S.Watanabe,
K.Ando, T.Hisamatsu and S.Matsuda,
Microscopic analysis of carrier removal
in heavily irradiated silicon solar cells
Proc. of the 26th IEEE Photovoltaic
Specialists Conference, (Anaheim,
CA,29,September-03, October 1997)
835.
C SCS 71004

7C50
M.Imaizumi, S.T.Taylor, M.Yamaguchi,
T.Hisamatsu and O.Kawasaki,
Analysis of the spectral response of
silicon solar cells irradiated with high
fluence electron/protons
Proc. of the 26th IEEE Photovoltaic
Specialists Conference, (Anaheim,CA,
29,September-03, October 1997) 983.
C SCS 71004

Appendix 2. Type of Research Collaborations

Section of this Report	Research Program Number	Type of Research Collaborations*	Section of this Report	Research Program Number	Type of Research Collaborations*
1.1	71002	JAERI	3.1	71041	Coop.Res.Univ.
1.2	71003	Joint Res.	3.2	71042	Coop.Res.Univ.
1.3	72003	Joint Res.	3.3	71043	Coop.Res.Univ.
1.4	71031/72027	Coop.Res.Univ.	3.4	71044	JAERI
1.5	72002	JAERI	3.5	71045	Coop.Res.Univ.
1.6	72004	JAERI	3.6	71001	JAERI
			3.7	71030	JAERI
2.1	71007	JAERI	3.8	72034	Joint Res.
2.2	71008	JAERI			
2.3	71009	JAERI	4.1	71005	JAERI
2.4	71010	JAERI	4.2	72009	JAERI
2.5	71011	JAERI	4.3	71006	JAERI
2.6	71012/72017	Coop.Res.Univ.	4.4	71032	Coop.Res.Univ.
2.7	71014	Coop.Res.Univ.	4.5	71033	Proj.Res.Univ.
2.8	71015	Joint Res.	4.6	72005	JAERI
2.9	71016	Proj.Res.Univ.	4.7	72006	JAERI
2.10	71017	Proj.Res.Univ.	4.8	72007	JAERI
2.11	71018	Joint.Res.	4.9	72008	Proj.Res.Univ.
2.12	71019	Proj.Res.Univ.	4.10	72010	JAERI
2.13	71020	Joint Res.	4.11	72011	Proj.Res.Univ.
2.14	71021	Joint Res.	4.12	72012	Proj.Res.Univ.
2.15	71022	Joint Res.	4.13	72013	JAERI
2.16	71023	Joint Res.	4.14	72015	Proj.Res.Univ.
2.17	71024	Joint Res.	4.15	72016	JAERI
2.18	71025	Coop.Res.Univ.	4.16	72020	JAERI
2.19	71026	Joint Res.	4.17	72021	JAERI
2.20	71027	Proj.Res.Univ.	4.18	72022	JAERI
2.21	71028	Proj.Res.Univ.	4.19	72023	Proj.Res.Univ.
2.22	71029	Proj.Res.Univ.	4.20	72024	Coop.Res.Univ.
2.23	72018	JAERI	4.21	72025	Coop.Res.Univ.

Section of this Report	Research Program Number	Type of Research Collaborations*
5.1	72019	JAERI
5.2	72028	Coop.Res.Univ.
5.3	72031	JAERI
5.3	72032	JAERI
5.4	72033	Proj.Res.Univ.
5.5	72041	Joint Res.
6.1	71034	JAERI
6.2	71040	Proj.Res.Univ.
6.3	71039	Proj.Res.Univ.
6.4	71035/71038	Proj.Res.Univ.
6.5	off line	JAERI
7.1	71049/72042	JAERI
7.2	71050	Proj.Res.Univ.
7.3	71051	Proj.Res.Univ.
7.4	71052	Proj.Res.Univ.
7.5	71053	Proj.Res.Univ.
8.1	71046	JAERI
8.2	71047	JAERI
8.3	71047	JAERI
8.4	off line	JAERI
8.5	off line	JAERI
8.6	72037	JAERI
8.7	72038	JAERI
8.8	72039	JAERI
8.9	72039	JAERI
8.10	off line	JAERI
8.11	72040	Coop.Res.Univ.
8.12	off line	JAERI

*Joint Res.:Joint research with private company or governmental institution
Coop.Res. Univ.:Cooperative research with a university or ubiversities
Proj.Res.Univ.:The JAERI-Universities Joint Research Project#

For administration of these programs, we appreciate the cooperation of:
Research Center for Nuclear Science and Technology, The University of Tokyo.

Appendix 3. Organization and Personnel of TIARA (FY1997)

1) Organization for the Research and Development of Advanced Radiation Technology

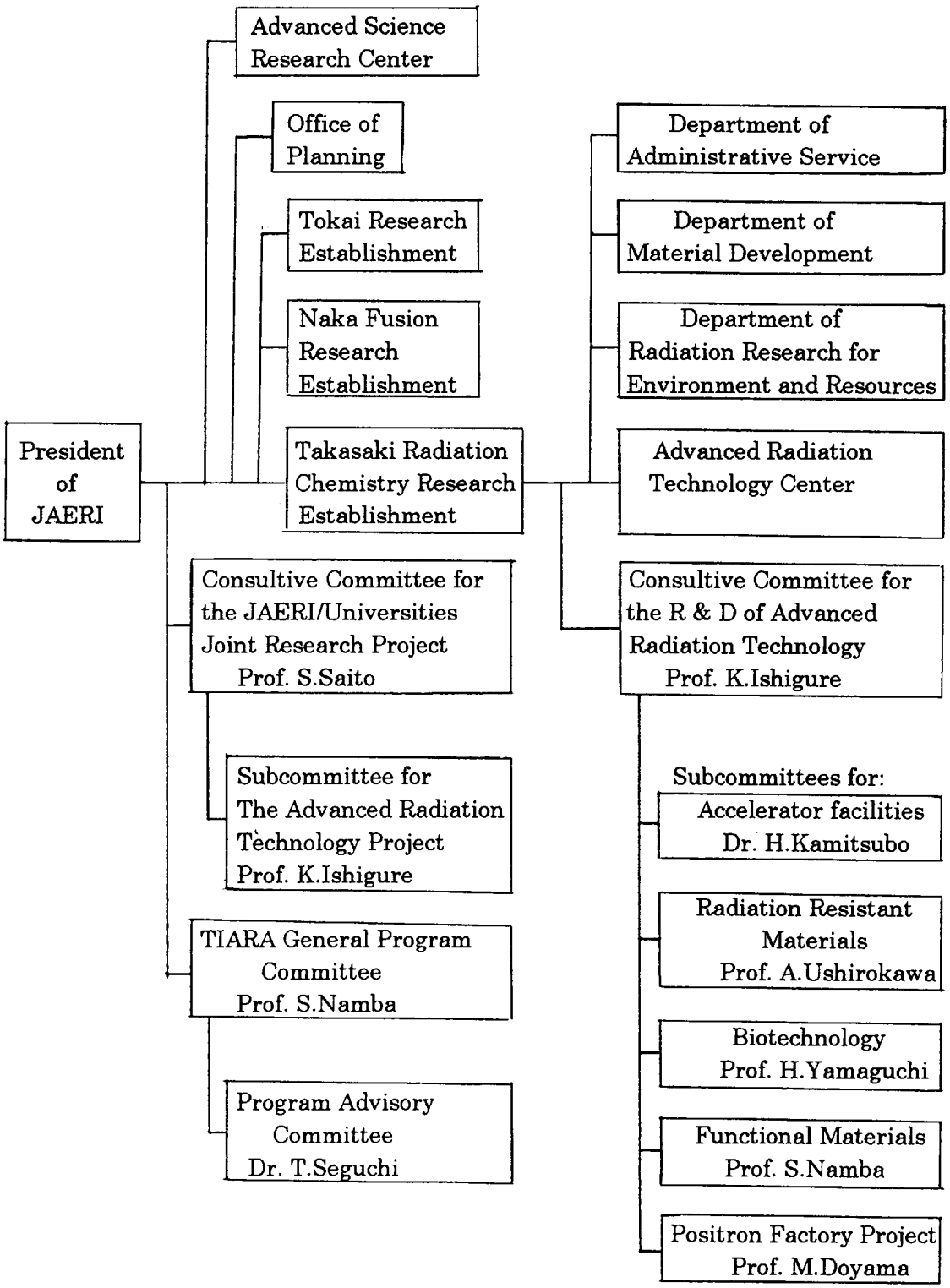

2) Personnel for the Administration, Operation and Control of TIARA

Advanced Radiation Technology Center

Director	R.tanaka
Deputy Director	H.Omichi

Administration Division

General Manager	M.Sawahata
Staff Member	J.Kobayashi, A. Takahashi

Utilization and Coordination Division

General Manager	Y.Kusama/M.Tani
Staff Member	S.Tanaka, K.Nishimura, M.Hosono

Ion Accelerator Operation Division

General Manager	D.Nemoto

Group of Cyclotron Operation

Staff Member	K.Arakawa, Y.Nakamura, T.Nara, T.Agematsu, I.Ishibori, H.Tamura

Group of Electrostatic Accelerators Operation

Staff Member	S.Tajima, I.Takada, K.Mizuhashi S.Uno, K.Ohkoshi, Y.Nakajima

Ion Beam Engineering Division

Head	S.Okada
Staff Member	T.Kojima, W.Yokota, H.Tachibana, M.Fukuda, T.Kamiya, S.Okumura, Y.Saito, Y.Ishii, T.Sakai, A.Kawasuso

Irradiation Service Division

General Manager	K.Yotsumoto
Staff Member	H.Sunaga, T.Kanazawa, T.Ookubo H.Kaneko, Y.Haruyama, H.Takizawa

Department of Administrative Services

Safety Division

Staff Member	T.Niino, T.Sakai

(Radiation Monitoring and Control in TIARA)

Utilities and Maintenance Division

Staff Member	K.Fukuda, Y.Yoshii

(Radioactive Waste Management and Utility Control in TIARA)

国際単位系（SI）と換算表

表1　SI基本単位および補助単位

量	名称	記号
長さ	メートル	m
質量	キログラム	kg
時間	秒	s
電流	アンペア	A
熱力学温度	ケルビン	K
物質量	モル	mol
光度	カンデラ	cd
平面角	ラジアン	rad
立体角	ステラジアン	sr

表2　SIと併用される単位

名称	記号
分，時，日	min，h，d
度，分，秒	°，′，″
リットル	l，L
トン	t
電子ボルト	eV
原子質量単位	u

1 eV=1.60218×10^{-19}J

1 u=1.66054×10^{-27}kg

表3　固有の名称をもつSI組立単位

量	名称	記号	他のSI単位による表現
周波数	ヘルツ	Hz	s^{-1}
力	ニュートン	N	m·kg/s^2
圧力，応力	パスカル	Pa	N/m^2
エネルギー，仕事，熱量	ジュール	J	N·m
工率，放射束	ワット	W	J/s
電気量，電荷	クーロン	C	A·s
電位，電圧，起電力	ボルト	V	W/A
静電容量	ファラド	F	C/V
電気抵抗	オーム	Ω	V/A
コンダクタンス	ジーメンス	S	A/V
磁束	ウェーバ	Wb	V·s
磁束密度	テスラ	T	Wb/m^2
インダクタンス	ヘンリー	H	Wb/A
セルシウス温度	セルシウス度	C	
光束	ルーメン	lm	cd·sr
照度	ルクス	lx	lm/m^2
放射能	ベクレル	Bq	s^{-1}
吸収線量	グレイ	Gy	J/kg
線量等量	シーベルト	Sv	J/kg

表4　SIと共に暫定的に維持される単位

名称	記号
オングストローム	Å
バーン	b
バール	bar
ガル	Gal
キュリー	Ci
レントゲン	R
ラド	rad
レム	rem

1 Å=0.1nm=10^{-10}m

1 b=100fm^2=10^{-28}m^2

1 bar=0.1MPa=10^{5}Pa

1 Gal=1cm/s^2=10^{-2}m/s^2

1 Ci=3.7×10^{10}Bq

1 R=2.58×10^{-4}C/kg

1 rad=1cGy=10^{-2}Gy

1 rem=1cSv=10^{-2}Sv

表5　SI接頭語

倍数	接頭語	記号
10^{18}	エクサ	E
10^{15}	ペタ	P
10^{12}	テラ	T
10^{9}	ギガ	G
10^{6}	メガ	M
10^{3}	キロ	k
10^{2}	ヘクト	h
10^{1}	デカ	da
10^{-1}	デシ	d
10^{-2}	センチ	c
10^{-3}	ミリ	m
10^{-6}	マイクロ	μ
10^{-9}	ナノ	n
10^{-12}	ピコ	p
10^{-15}	フェムト	f
10^{-18}	アト	a

(注)

1．表1－5は「国際単位系」第5版，国際度量衡局1985年刊行による。ただし，1 eVおよび1 uの値はCODATAの1986年推奨値によった。

2．表4には海里，ノット，アール，ヘクタールも含まれているが日常の単位なのでここでは省略した。

3．barは，JISでは流体の圧力を表わす場合に限り表2のカテゴリーに分類されている。

4．EC閣僚理事会指令ではbar，barnおよび「血圧の単位」mmHgを表2のカテゴリーに入れている。

換算表

力	N(=10^{5}dyn)	kgf	lbf
	1	0.101972	0.224809
	9.80665	1	2.20462
	4.44822	0.453592	1

粘度　1Pa·s(N·s/m^2)=10P(ポアズ)(g/(cm·s))

動粘度　1m^2/s=10^{4}St(ストークス)(cm^2/s)

圧力	MPa(=10bar)	kgf/cm^2	atm	mmHg(Torr)	lbf/in^2(psi)
	1	10.1972	9.86923	7.50062×10^3	145.038
	0.0980665	1	0.967841	735.559	14.2233
	0.101325	1.03323	1	760	14.6959
	1.33322×10^{-4}	1.35951×10^{-3}	1.31579×10^{-3}	1	1.93368×10^{-2}
	6.89476×10^{-3}	7.03070×10^{-2}	6.80460×10^{-2}	51.7149	1

エネルギー・仕事・熱量	J(=10^7 erg)	kgf·m	kW·h	cal(計量法)	Btu	ft·lbf	eV
	1	0.101972	2.77778×10^{-7}	0.238889	9.47813×10^{-4}	0.737562	6.24150×10^{18}
	9.80665	1	2.72407×10^{-6}	2.34270	9.29487×10^{-3}	7.23301	6.12082×10^{19}
	3.6×10^6	3.67098×10^5	1	8.59999×10^5	3412.13	2.65522×10^6	2.24694×10^{25}
	4.18605	0.426858	1.16279×10^{-6}	1	3.96759×10^{-3}	3.08747	2.61272×10^{19}
	1055.06	107.586	2.93072×10^{-4}	252.042	1	778.172	6.58515×10^{21}
	1.35582	0.138255	3.76616×10^{-7}	0.323890	1.28506×10^{-3}	1	8.46233×10^{18}
	1.60218×10^{-19}	1.63377×10^{-20}	4.45050×10^{-26}	3.82743×10^{-20}	1.51857×10^{-22}	1.18171×10^{-19}	1

1 cal = 4.18605J（計量法）

= 4.184J（熱化学）

= 4.1855J（15℃）

= 4.1868J（国際蒸気表）

仕事率　1 PS(仏馬力)

= 75 kgf·m/s

= 735.499W

放射能	Bq	Ci
	1	2.70270×10^{-11}
	3.7×10^{10}	1

吸収線量	Gy	rad
	1	100
	0.01	1

照射線量	C/kg	R
	1	3876
	2.58×10^{-4}	1

線量当量	Sv	rem
	1	100
	0.01	1

(86年12月26日現在)